FORMERLY ACTA PHYSICA ACADEMIAE SCIENTIARUM HUNGARICAE

Acta Physica Hungarica

VOLUME 54, NUMBERS 1–2, 1983

EDITOR-IN-CHIEF
I. KOVÁCS

EDITORIAL BOARD
Z. BAY, R. GÁSPÁR, K. NAGY,
L. PÁL, A. SZALAY, I. TARJÁN, B. TELEGDI,
E. WIGNER

Akadémiai Kiadó, Budapest
ACTA PHYS. HUNG. APAHAQ 54 (1–2) 1–220 (1983) HU ISSN 0001-6705

ACTA PHYSICA HUNGARICA

A JOURNAL OF THE HUNGARIAN ACADEMY OF SCIENCES

EDITED BY

I. KOVÁCS

Acta Physica publishes original papers on subjects in physics. Papers are accepted in English, French, German and Russian.

Acta Physica is published in two yearly volumes (4 issues each) by

AKADÉMIAI KIADÓ
Publishing House of the Hungarian Academy of Sciences
H-1054 Budapest, Alkotmány u. 21

Subscription information

Orders should be addressed to

KULTURA Foreign Trading Company
1389 Budapest P.O. Box 149

or to its representatives abroad.

Acta Physica is indexed in Current Contents

ACTA PHYSICA HUNGARICA

EDITORIAL BOARD

Z. BAY, R. GÁSPÁR, K. NAGY, L. PÁL, A. SZALAY, I. TARJÁN, B. TELEGDI, E. WIGNER

EDITOR-IN-CHIEF

I. KOVÁCS

VOLUME 54

AKADÉMIAI KIADÓ, BUDAPEST

1983

ACTA PHYS. HUNG.

CONTENTS

Volume 54

FLUIDS, PLASMAS AND ELECTRIC DISCHARGES

CONDENSED MATTER

INTERDISCIPLINARY

CONTENTS

CONDENSED MATTER

EDITOR'S NOTE

"Hungarica Acta Physica" was the title of the first foreign language physics journal to appear in Hungary. It was published in 1949 in English and German and the Editor was Prof. K. Novobátzky. In the period directly following the Second World War, Hungarian physicists encountered difficulties in publishing their papers abroad, and so the results obtained by them during and after the war appeared in that journal; in this way it became the representative journal of physics in Hungary. For instance it was here in the very first paper that the report appeared of the Hungarian lunar radar experiment for which the equipment had been constructed with several interruptions during the war; the first successful experiment took place only one month after the radio announcement on the American experiment (February 1946). However, only a single volume (6 issues) was published. This was due to the reorganization late in 1949 of the Hungarian Academy of Sciences which had taken over the responsibilities of scientific publishing. A new journal replacing its predecessor was launched under the title "Acta Physica Academiae Scientiarum Hungaricae", with Prof. P. Gombás as Editor (1952–1971). The Editorial Board of the new publication then formulated the following aim:

"The aim of the Hungarian Academy of Sciences in starting the new series of Acta Physica is to contribute to the improvement of the international relations of progressive science, to the further development of science, to the cause of peace and the closer friendship of peoples."

These aims are no less valid to-day.

Some confusion was to arise, however, because the numbering of the volumes of the new journal commenced from 1, which was less than helpful for those not familiar with the history of the two journals. This is one of the reasons for us taking this opportunity to clarify the situation.

From the first issue up to the present time the journal has had the same cover, with the title page in Latin. Unfortunately, however, Latin, the language of science, that was at one time known all over the world, and represented one of the most significant achievements of the Middle Ages, is now gradually dying out; it is taught in fewer and fewer schools and has largely been replaced by English. The principal reason for this was the emigration of European Scientists to the USA during the Second World War causing the centre of the physical sciences to shift from Europe to the USA. In addition,

the favourable development of international relations during the past three decades means that our periodical is no longer the representative of Hungarian physics to-day. The majority of Hungarian physicists no longer send their papers exclusively to the Hungarian Acta but also to the various international journals, authoritative in the particular fields cultivated by the physicists. On the other hand, physicists from abroad find it advantageous to submit their papers to the Hungarian journal — so the latter itself has become international.

In view of these developments the Hungarian Academy of Sciences decided to change over to English on the cover and title page, maintaining the title in Latin, while papers continue to be accepted in English, French, German and Russian.

The Editorial Board has taken this opportunity to simplify the slightly complicated Latin title of the Journal to read "Acta Physica Hungarica", a title which we believe is in better accord with international practice, particularly since the Journal is mostly referred to by that title anyway. The new title "Acta Physica Hungarica" is introduced with the present issue. Advanced printing techniques make it possible for the Journal to appear with a more pleasing colour cover. We wish to emphasize that this is *not* a new journal; the volumes are numbered consecutively. Our aim is to bring ourselves more up to date with these minor changes which, we hope, will prove to be of satisfaction to our authors and to our readers.

Budapest, 3rd May 1983.

Prof. I. Kovács

Acta Physica Hungarica 54 (1—2). pp. 3—8 (1983)

ELECTRON IN EINSTEIN'S UNIFIED FIELD THEORY

J. N. S. KASHYAP

Department of Mathematics, Banaras Hindu University, Varanasi-221005, India

(Received 14 October 1981)

In this paper an exact solution of the field equations of Einstein's unified field theory [7] is obtained for the space-time defined by the most general spherically symmetric metric of Synge in Kruskal coordinates. It describes the gravitational field of electron.

1. Introduction

In general relativity Einstein—Maxwell field equations describe the gravitational field of electron. However, due to 4-potential vector φ_λ, it is considered not to be internally consistent as the field equations for empty space-time. Hence the need of a field theory known as unified field theory was realized. In such a theory matter is treated as absorbed into the field itself. It describes gravitational and electromagnetic phenomena in one and the same framework. Among the unified field theories developed so far Einstein's unified field theory [7] is more applicable from the physical point of view. It has been successful in the study of the hydrogen atom [1], Faraday's electromagnetic induction [2] and the Biot—Savart law for magnetic effect due to current [3]. But it has been shown that it is not possible to describe an electron in the theory [4]. This result throws a dark shadow of suspicion on the sound footed unified theory of Einstein. The present investigation shows that the electron is in total grip of the theory and gives a good account of how the electron is described.

Let us consider the most general spherically symmetric space-time in Kruskal coordinates $(u, \vartheta, \varphi, v)$ defined by the metric [5]

$$ds^2 = -2f\,du\,dv + r^2(d\vartheta^2 + \sin^2\vartheta\, d\varphi^2), \tag{1.1}$$

where f and r are functions of (u, v). Here, the space-time V_4 is the product of a unit sphere S_2 and a 2-space U_2 in the sense that an event of V_4 corresponds to an ordered pair of points, one on S_2 and the other on U_2. The usual polar coordinates (ϑ, φ) belong to S_2 and the coordinates (u, v) belong to U_2. For the metric (1.1) Schwarzschild solution (5) and Reissner—Nordström solution [6] have already been obtained. In the present investigation we impose the field equations of Einstein's unified field theory [7] for the space-time characterized by the metric (1.1) and show how it describes the gravitational field of electron.

2. Field equations

In Einstein's unified field theory the total field is given by the real non-symmetric tensor $g_{\lambda\mu}$ defined as

$$g_{\lambda\mu}=g_{\underline{\lambda\mu}}+g_{\underset{\sim}{\mu\mu}} \tag{2.1}$$

in the usual notations. The symmetric $g_{\underline{\lambda\mu}}$ coincides with the metric tensor of Riemannian space-time and the skew-symmetric $g_{\underset{\sim}{\lambda\mu}}$ is used to interpret the electromagnetic phenomena. Here we consider the total field as characterized by

$$g_{\underline{14}}=-f, \quad g_{22}=r^2, \quad g_{33}=r^2\sin^2\vartheta,$$
$$g_{\underset{\sim}{23}}=e\sin\vartheta, \tag{2.2}$$

all being functions of u and v alone. In (2.2) the symmetric $g_{\underline{\lambda\mu}}$ correspond to the metric (1.1). The field equations used by us are those of Einstein (1953) [7]:

$$g_{\lambda\mu,v}-g_{\alpha\mu}\Gamma^{\alpha}_{\lambda v}-g_{\lambda\alpha}\Gamma^{\alpha}_{v\mu}=0, \tag{2.3a}$$

$$\Gamma^{\mu}_{\underset{\sim}{\mu\mu}}=0, \tag{2.3b}$$

$$R_{\underline{\lambda\mu}}=0, \tag{2.3c}$$

$$R_{[\underset{\sim}{\lambda\mu},v]}=0, \tag{2.3d}$$

where

$$R_{\underline{\lambda\mu}}=\Gamma^{\alpha}_{\underline{\lambda\mu},\alpha}-\frac{1}{2}(\Gamma^{\alpha}_{\underline{\lambda\alpha},\mu}+\Gamma^{\alpha}_{\underline{\mu\alpha},\lambda})+\Gamma^{\beta}_{\underline{\lambda\mu}}\Gamma^{\alpha}_{\underline{\beta\alpha}}-\Gamma^{\beta}_{\underline{\lambda\alpha}}\Gamma^{\alpha}_{\underline{\beta\mu}}-\Gamma^{\beta}_{\underset{\sim}{\lambda\alpha}}\Gamma^{\alpha}_{\underset{\sim}{\beta\mu}}, \tag{2.4}$$

$$R_{\underset{\sim}{\lambda\mu}}=\Gamma^{\alpha}_{\underset{\sim}{\lambda\mu},\alpha}+\Gamma^{\beta}_{\underset{\sim}{\lambda\mu}}\Gamma^{\alpha}_{\underline{\beta\alpha}}\div\Gamma^{\beta}_{\underline{\lambda\alpha}}\Gamma^{\alpha}_{\underset{\sim}{\beta\mu}}-\Gamma^{\beta}_{\underset{\sim}{\lambda\alpha}}\Gamma^{\alpha}_{\underline{\beta\mu}},$$

in the usual notations. Hereafter, the differentiations with respect to u and v are represented throughout by the suffixes 1 and 4, respectively (e.g., $f_1=\partial f/\partial u$, $f_{14}=\partial^2 f/\partial u\partial v$, etc.).

The external field of the isolated charge is the vacuum electrostatic field characterized by

$$J^{\mu}=\frac{1}{2}\eta^{\alpha\beta\lambda\mu}g_{[\underset{\sim}{\lambda\mu},\lambda]}=0, \tag{2.5}$$

where J^{μ} is the charge—current density and $\eta^{\alpha\beta\lambda\mu}$ is Levi—Civita's tensor density. From (2.5) we get

$$e=\text{constant}. \tag{2.6}$$

The field equation (2.3a) determines the affine connections. For the total field (2.2) there are eighteen non-vanishing components of the affine connections and, under

the restriction imposed by (2.5) they are as follows:

$$\Gamma^1_{11} = \frac{f_1}{f}, \quad \Gamma^2_{\underline{12}} = \Gamma^3_{\underline{13}} = \frac{r_1}{Ar},$$

$$\Gamma^1_{22} = \frac{B}{Af} r r_4, \quad \Gamma^1_{33} = \sin^2\vartheta \Gamma^1_{22},$$

$$\Gamma^2_{\underline{24}} = \Gamma^3_{\underline{43}} = \frac{r_4}{Ar}, \quad \Gamma^4_{44} = \frac{f_4}{f},$$

$$F^4_{22} = \frac{B}{Af} r r_1, \quad F^4_{33} = \sin^2\vartheta \, \Gamma^4_{22},$$

$$\Gamma^3_{\underline{23}} \sim \cot\vartheta, \quad \Gamma^2_{33} = -\sin\vartheta\cos\vartheta, \tag{2.7}$$

$$\Gamma^3_{\underset{\sim}{12}} = \frac{e \operatorname{cosec}\vartheta}{Ar^3} r_1, \quad \Gamma^2_{\underset{\sim}{13}} = -\frac{e\sin\vartheta}{Ar^3} r_1,$$

$$\Gamma^3_{\underset{\sim}{24}} = -\frac{e \operatorname{cosec}\vartheta}{Ar^3} r_4, \quad \Gamma^2_{\underset{\sim}{34}} = \frac{e\sin\vartheta}{Ar^3} r_4,$$

$$\Gamma^1_{\underset{\sim}{23}} = \frac{2e\sin\vartheta}{Afr} r_4, \quad \Gamma^4_{\underset{\sim}{23}} = \frac{2e\sin\vartheta}{Afr} r_1,$$

where

$$A = 1 + \frac{e^2}{r^4}, \quad B = 1 - \frac{e^2}{r^4}. \tag{2.8}$$

From (2.7) it is obvious that the field equation (2.3b) is identically satisfied. Making use of (2.7) we obtain the components of $R_{\underline{\lambda\mu}}$ and $R_{\underset{\sim}{\lambda\mu}}$ from (2.4). Consequently, the field equations (2.3c) and (2.3d) take the form:

$$\frac{r_{11}}{r_1} - \frac{f_1}{f} - \frac{A_1}{A} = 0, \tag{2.9a}$$

$$\frac{r_{44}}{r_4} - \frac{f_4}{f} - \frac{A_4}{A} = 0, \tag{2.9b}$$

$$\frac{1}{f}\left(f_{14} - \frac{f_1 f_4}{f}\right) + \frac{2}{Ar} r_{14} + \frac{8e^2}{A^2 r^6} r_1 r_4 = 0, \tag{2.9c}$$

$$B\left(r_{14} + \frac{4e^2}{Ar^5} r_1 r_4\right) + \frac{4e^4}{Ar^9} r_1 r_4 + \frac{B}{r} r_1 r_4 + \frac{Af}{2r} = 0, \tag{2.9d}$$

$$\frac{\partial}{\partial u}\left[\frac{4}{Afr}\left(r_{14} + \frac{2e^2}{Ar^5} r_1 r_4\right)\right] = 0, \tag{2.9e}$$

$$\frac{\partial}{\partial v}\left[\frac{4}{Afr}\left(r_{14} + \frac{2e^2}{Ar^5} r_1 r_4\right)\right] = 0. \tag{2.9f}$$

The field equations (2.9a) and (2.9b) give after integration

$$f = \frac{2\beta}{A} r_1, \quad f = \frac{2\alpha}{A} r_4, \tag{2.10}$$

where $\alpha[\equiv\alpha(u)]$ and $\beta[\equiv\beta(v)]$ are arbitrary functions of integration. From (2.9e) and (2.9f) we obtain

$$r_{14} + \frac{2e^2}{Ar^5} r_1 r_4 = \frac{1}{4} KAfr, \tag{2.11}$$

where K is a constant of integration. Substituting the value of f_1/f from (2.9a) in (2.9c) we have

$$\left(\frac{r_{14}}{r_1} - \frac{A_4}{A}\right)_1 + \frac{2r_1}{Ar}\left(\frac{r_{14}}{r_1} - \frac{A_4}{A}\right) = 0. \tag{2.12}$$

Similarly, from the Eqs. (2.9b) and (2.9c) we get

$$\left(\frac{r_{14}}{r_4} - \frac{A_1}{A}\right) + \frac{2r_4}{Ar}\left(\frac{r_{14}}{r_4} - \frac{A_1}{A}\right) = 0. \tag{2.13}$$

The Eqs (2.12) and (2.13) give, after integration

$$\frac{r_{14}}{r_1} - \frac{A_4}{A} = \frac{\delta}{r^2\sqrt{A}}, \tag{2.14}$$

$$\frac{r_{14}}{r_4} - \frac{A_1}{A} = \frac{\gamma}{r^2\sqrt{A}}, \tag{2.15}$$

where $\gamma\,[\equiv\gamma\,(u)]$ and $\delta[\equiv d(v)]$ are functions of integration. For the values of f given in (2.10) the Eqs. (2.9d) and (2.11) provide

$$B\left(\frac{r_{14}}{r_1} - \frac{A_4}{A}\right) - \frac{e^2}{r^4}\frac{A_4}{A} + \frac{B}{r} r_4 + \frac{\beta}{r} = 0, \tag{2.16}$$

$$B\left(\frac{r_{14}}{r_4} - \frac{A_1}{A}\right) - \frac{e^2}{r^4}\frac{A_1}{A} + \frac{B}{r} r_1 + \frac{\alpha}{r} = 0, \tag{2.17}$$

$$\frac{r_{14}}{r_1} - \frac{A_4}{2A} = \frac{1}{2} K\beta r, \tag{2.18}$$

$$\frac{r_{14}}{r_4} - \frac{A_1}{2A} = \frac{1}{2} K\alpha r. \tag{2.19}$$

From (2.14) and (2.18) we obtain

$$\frac{A_4}{A} = K\beta r - \frac{2\delta}{r^2\sqrt{A}}. \tag{2.20}$$

Similarly, from (2.15) and (2.19) we obtain

$$\frac{A_1}{A} = K\alpha r - \frac{2\gamma}{r^2\sqrt{A}}. \tag{2.21}$$

To find an analogue of Reissner—Nordström solution we further assume

$$Ke^2 = -E^2, \ \gamma = -2m\alpha, \ \delta = -2m\beta. \tag{2.22}$$

The constants m and E can be identified, respectively, with the mass and charge of the electron. Now, making use of (2.14), (2.20) and (2.22) in (2.16) we get

$$r_4 = -\frac{\beta}{B}\left(1 - \frac{2m}{r}\sqrt{A} + \frac{E^2}{r^2}\right). \tag{2.23}$$

Similarly from (2.15), (2.17), (2.21) and (2.22) we get

$$r_1 = -\frac{\alpha}{B}\left(1 - \frac{2m}{r}\sqrt{A} + \frac{E^2}{r^2}\right). \tag{2.24}$$

Putting the value of either r_4 or r_1 from (2.23) and (2.24) in (2.10) we have

$$f = -\frac{2\alpha\beta}{AB}\left(1 - \frac{2m}{r}\sqrt{A} + \frac{E^2}{r^2}\right). \tag{2.25}$$

3. Gravitational field of the electron

We know that

$$dr = r_1 du + r_4 dv, \tag{3.1}$$

which, after using (2.23) and (2.24), gives

$$B\left(1 - \frac{2m}{r}\sqrt{A} + \frac{E^2}{r^2}\right)^{-1} dr = -\alpha du - \beta dv. \tag{3.2}$$

If we put

$$\alpha = -\frac{U_1}{U}, \ \beta = -\frac{V_4}{V}, \tag{3.3}$$

where $U \equiv U(u)$ and $V \equiv V(v)$, then (3.2) and (2.25) take the form

$$B\left(1 - \frac{2m}{r}\sqrt{A} + \frac{E^2}{r^2}\right)^{-1} dr = \frac{dU}{U} + \frac{dV}{V}, \tag{3.4}$$

$$-2f\,du dv = \frac{4}{AB}\left(1 - \frac{2m}{r}\sqrt{A} + \frac{E^2}{r^2}\right)\frac{dU}{U}\cdot\frac{dV}{V}. \tag{3.5}$$

From the Reissner—Nordström solution we find that the product of the coefficients of dr^2 and dt^2 is unity. Taking this point into consideration we define

$$Adt = \frac{dU}{U} - \frac{dV}{V}. \tag{3.6}$$

The relations (3.4) and (3.6) give

$$4\frac{dU}{U}\cdot\frac{dV}{V} = B^2\left(1 - \frac{2m}{r}\sqrt{A} + \frac{E^2}{r^2}\right)^{-2} dr^2 - A^2dt^2. \tag{3.7}$$

Making use of (3.7) in (3.5) we obtain

$$-2f\,dudv = \frac{B}{A}\left(1 - \frac{2m}{r}\sqrt{A} + \frac{E^2}{r^2}\right)^{-1} dr^2 - \\ - \frac{A}{B}\left(1 - \frac{2m}{r}\sqrt{A} + \frac{E^2}{r^2}\right)dt^2. \tag{3.8}$$

Therefore, the metric form (1.1) reduces to

$$ds^2 = \frac{B}{A}\left(1 - \frac{2m}{r}\sqrt{A} + \frac{E^2}{r^2}\right)^{-1} dr^2 + r^2(d\vartheta^2 + \sin^2\vartheta d\varphi^2) - \\ - \frac{A}{B}\left(1 - \frac{2m}{r}\sqrt{A} + \frac{E^2}{r^2}\right)dt^2, \tag{3.9}$$

where A and B are given by (2.8). The line-element (3.9) corresponds to the Reissner—Nordström solution in general relativity and shows how the gravitational field of electron is described in Einstein's unified field theory. If $E=0$ we get the Schwarzschild solution.

Acknowledgement

The author is grateful to Dr. R. Tiwari for his interest in the preparation of this paper.

References

1. J. N. S. Kashyap, Proc. Ind. Nat. Sc. Acad., **43A**, 352, 1977.
2. J. N. S. Kashyap and Shri Ram, Jour. Math. Phys. Sci., **12**, 569, 1978.
3. R. Tiwari and J. N. S. Kashyap, Ind. Jour. Pure Appl. Math., **3**, 896, 1972.
4. R. Tiwari and D. N. Pant, J. Phys. A: Gen. Phys., **5**, 394, 1972.
5. J. L. Synge, Annali di Mathematica pure ed applicata series IV **98**, 239, 1974.
6. Shri Ram and J. N. S. Kashyap, Acta Phys Hung., **41**, 87, 1976.
7. A. Einstein, The Meaning of Relativity (4th ed.), Princeton University Press, Princeton, Appendix II, 130–165, 1953.

Acta Physica Hungarica 54 (1—2), pp. 9—24 (1983)

REARRANGEMENT HEAVY ION COLLISIONS WITH TWO NUCLEON TRANSFER

AHMED OSMAN and S. S. ABDEL-AZIZ

Physics Department, Faculty of Science, Cairo University, Cairo, Egypt

(Received in revised form 27 October 1981)

The theory of heavy ion reactions with two-nucleon transfer is considered. These reactions are considered as one-step direct nuclear reactions. The initial and final channel wave functions are taken as distorted waves describing the two heavy ion interactions through optical model potentials. An analytical expression for the differential cross-section is developed using the distorted wave Born approximation. We considered in the present work the heavy ion reactions with two-nucleon transfer of the incident heavy ion projectiles ^{10}B, ^{16}O and ^{18}O bombarding the heavy target nuclei ^{16}O, ^{26}Mg, ^{42}Ca, ^{48}Ca, ^{60}Ni, ^{74}Ge and ^{76}Ge with incident projectile energies between 50.0 MeV and 100.0 MeV, leaving the residual nuclei in different excited states. Numerical calculations are carried out of the angular distributions of these two-nucleon heavy ion reactions. The agreement between the theoretically calculated differential cross-sections and the experimental data is good. Also, reasonable spectroscopic factors are extracted.

1. Introduction

Recently, heavy ion reactions with one and two-nucleon transfer have been considered by many authors. Baltz et al. [1], Baltz [2] and Bond et al. [3] investigated heavy ion reactions with single nucleon transfer performing DWBA calculations for different heavy ion reactions. In these calculations they used an optical model potential. The imaginary part of the potential is taken to consist of a strongly absorbing volume part describing the small diffusivity and a surface absorptive part with standard diffusivity. This potential gives good results in the nuclear surface region explaining the large cross-sections in the forward angles measured experimentally. Also, this model for the optical potential does not absorb in the nuclear interior. In the case of two nucleon transfer reactions, the bound state configuration is found to depend upon its angular shape which needs using a weakly absorbing volume potential. Osman [4] introduced a theoretical study for ^{6}Li induced reactions as a direct stripping nuclear reaction mechanism. Eisen et al. [5], Pieper et al. [6] and Fortune et al. [7], [8] studied the two-neutron stripping and pick-up reactions for ^{16}O projectiles incident with energy 56 MeV on ^{42}Ca and ^{48}Ca targets. They calculated the angular distributions of these reactions leaving the residual nuclei in their ground states and in the first excited states using both of the cluster and the macroscopic distorted wave Born approximation calculations. The optical model parameters which they used did not

explain the obtained cross-sections for these transfer reactions. In order to compare the theoretically calculated and the experimentally observed cross-sections for the elastic scattering process, they used the extracted parameters in the initial and final channels, where they obtained better fitting for the transfer cross-sections. Feng et al. [9] studied the two-neutron stripping reactions of ^{18}O incident projectiles bombarding ^{48}Ca targets and they obtained very small theoretical values for the cross-sections of these heavy ion transfer reactions. Bond et al [3] measured the angular distributions for the heavy ion reactions of two-nucleon transfer processes in case of ^{16}O and ^{18}O projectiles incident on ^{74}Ge and ^{76}Ge targets. In their study of the case of stripping reaction, they observed a 2^+ state which indicates the existence of interference between the direct and the two step transfer mechanism. They found that the angular distributions for the stripping reactions in the first 2^+ state have the same shapes as that for the pick-up reactions in its ground states. The same two-neutron transfer reactions $^{74}Ge(^{18}O, ^{16}O)^{76}Ge$ and $^{76}Ge(^{16}O, ^{18}O)^{74}Ge$ have been studied by Lemaire and Low [10] using the exact finite coupled channel Born approximation and also by using BCS random phase approximation wave functions. The differential cross-sections of these reactions have been measured which are described by the calculations using optical model potentials. It was found that the ^{18}O has a 2^+ state and exists in the coupled channel Born approximation analysis of the experimental angular distributions of ^{74}Ge ground state. Hamm and Nagatani [11] investigated two-neutron and two-proton heavy ion transfer reactions for ^{10}B projectiles incident with energy 100 MeV on the targets ^{12}C, ^{14}N and ^{16}O. They introduced calculations using the exact finite range distorted wave Born approximation assuming the cluster transfer of the two neutrons or the two protons for the strongly populated level in the mass numbers — 14 and 18 — residual nuclei and for the 2^+ level in the ^{18}O residual nucleus. The shapes of the angular distributions have been fitted using the cluster model approximation and the wave coupling model predictions. Berg et al. [12] measured the differential cross-sections of the transfer heavy ion reactions with incident ^{16}O and ^{18}O projectiles incident on ^{28}Si target nucleus, using the exact finite distorted wave Born approximation for the surface transfer set of the optical model parameters. A theoretical study of heavy ion reactions as a three-body problem has been introduced by Osman [13], [14] using projection operators [15]. Clear features are extracted by comparing the results with Coulomb transfer reactions [16].

In the present work, a theoretical study is introduced for the heavy ion reactions with two-nucleon transfer. Analytical theoretical expression for the differential cross-section is developed. The theory and the expressions are developed using the distorted wave Born approximation. Optical model potentials are used to describe the interaction wave functions in both of the inital and final channels. The parameters of the optical potentials are determined from the fitting of the experimental scattering data of the corresponding heavy ions. These expressions are applied to different rearrangement heavy ion collisions with different two-nucleon transfer. Two-nucleons stripping as well as two-nucleon pick-up reactions are considered. Numerical calcu-

lations are carried out for the heavy ion reactions $^{16}O(^{10}B, ^{8}Li)^{18}Ne$, $^{16}O(^{10}B, ^{8}B)^{18}O$, $^{42}Ca(^{16}O, ^{14}C)^{44}Ti$, $^{48}Ca(^{16}O, ^{14}C)^{50}Ti$, $^{26}Mg(^{18}O, ^{16}O)^{28}Mg$, $^{48}Ca(^{18}O, ^{16}O)^{50}Ca$, $^{60}Ni(^{18}O, ^{16}O)^{62}Ni$, $^{74}Ge(^{18}O, ^{16}O)^{76}Ge$, $^{42}Ca(^{16}O, ^{18}O)^{40}Ca$, $^{48}Ca(^{16}O, ^{18}O)^{46}Ca$ and $^{76}Ge(^{16}O, ^{18}O)^{74}Ge$. The incident energies of the incident heavy ions have values between 50.0 MeV and 100.0 MeV. The aim of the present work is to study the heavy ion reactions with two-nucleon transfer. The use of the DWBA calculations is done to show that the DWBA approximation is suitable for studying such reactions and is able to calculate the differential cross-sections of heavy ion reactions. Another purpose of the present study is the aim of studying the finite-range effects in these reactions. These finite-range effects appear by using finite-range nuclear potentials. The finite-range effects are important in obtaining the correct value of the cross-sections. Then, it is our aim to get the correct values of the spectroscopic and normalization factors. Thirdly, the study of nuclear reactions with two-nucleon transfer gives more information about the energy levels of the captured nucleons in the different shells. Then, in the present study, the DWBA calculations have to be reformulated and modified to include all these effects. Including all these effects, the DWBA approximation is reformulated and modified and evaluated in the present theory for heavy ion reactions with two-nucleon transfer. In the present work, we carried out theoretical calculations for the differential cross-sections of these heavy ion reactions for different values of incident energies and leaving the residual nuclei in different excited states. The calculated angular distributions are compared with the experimental data. From the fitting of the theoretical and the experimental angular distributions, extracted values of the spectroscopic factors are obtained.

In Section 2, we introduce the developed expressions of the differential cross-sections of the heavy ion reactions with two-nucleon transfer using the distorted wave Born approximation. Numerical calculations and results are given in Section 3. Section 4 is left for discussion and conclusions.

2. Expressions of the differential cross-sections with two-nucleon transfer

Let us consider the two-nucleon transfer heavy ion reactions represented as

$$A(C+(a+b))+T\rightarrow R(T+(a+b))+C, \tag{1}$$

where A is the projectile composed of the bound state of the two particles (a, b) and the core C. In the projectile A, let us assume that the particles a and b have relative angular momenta l_a and l_b, respectively. The residual nucleus R has been formed after the reaction process occurs and both of the particles a and b have been captured by the target nucleus T and are bound in R with relative angular momenta l_{n_a} and l_{n_b}, respectively. The transition matrix element T_{fi} of such reaction can be written in the form

$$T_{fi}=\psi_f^{(-)} \mid V_{aC}(r_a)+V_{bC}(r_b) \mid \psi_i^{(+)}. \tag{2}$$

In writing the transition matrix element T_{fi} as in the form given by Eq. (2), we have neglected the potential due to the stripping associated with the Coulomb excitation and another potential between the core C and the target nucleus T, since we are interested in the region outside the nucleus. Let us consider that the coordinates $\mathbf{R}$ and $\mathbf{R}'$ are the separation coordinates between the interacting heavy ions in the initial and final channels, respectively. Then we can write

$$\mathbf{R}=\mathbf{r}_c+\frac{m_{ab}}{m_A}\rho \tag{3}$$

and

$$\mathbf{R}'=\frac{m_T}{m_R}\mathbf{r}_c-\frac{m_{ab}}{m_R}\boldsymbol{\rho}, \tag{4}$$

where $\boldsymbol{\rho}$ is the separation coordinate between the center of mass of the particles a and b and the core C. $\mathbf{r}_c$ is the separation coordinate between the particles C and T. The wave functions $\psi_i^{(+)}$ and $\psi_f^{(-)}$ represent the interaction wave functions in the initial and final channels, respectively, and can be written as

$$\psi_i^{(+)}=\psi^{(+)}(\mathbf{R})\chi_i \tag{5}$$

and

$$\psi_f^{(-)}=\psi^{(-)}(\mathbf{R}')\chi_f, \tag{6}$$

where $\psi^{(+)}(\mathbf{R})$ and $\psi^{(-)}(\mathbf{R}')$ are the distorted wave functions. χ_i is the wave function of the internal motion of the projectile and the target nucleus, while χ_f is the wave function of the internal motion of the residual nucleus R and the ejected particle C. Let us represent both of χ_i and χ_f in the L−S coupling scheme, from which we can represent the wave functions in terms of the relative and center of mass wave functions. Then

$$\chi_i=\sum\begin{Bmatrix} n_i\,\mathscr{L}\,l_a\,lj_aj\,I_c\,m\,\sigma \\ N_i\,S\,l_b\,Lj_b\,\mu_j\mu_c\,M \end{Bmatrix}\circledH\; I_cj(j_aj_b)T(j_aj_b;\,\mathscr{L}\,S)$$

$$\langle n_il,\,N_iL;\,\mathscr{L}\mid n_al_a,\,n_bl_b;\,\mathscr{L}\rangle\,(j\mu_j\,I_c\mu_c\mid I_A\mu_A)$$

$$(lm\,LM\mid\mathscr{L}\mu)(\mathscr{L}\mu\,S\,\sigma\mid j\,\mu_j)\,\Phi_c(\xi)\,\Phi_T(\xi)\,\chi_S^{\sigma}(\sigma_a,\,\sigma_b)$$

$$\chi_{I_c}^{\mu_c}\,\chi_{I_T}^{\mu_T}\,U_{n_il}^{m}(\mathbf{r}_{ab})\,\Phi_{N_iL}^{M}(\boldsymbol{\rho}) \tag{7}$$

and

$$\chi_f=\sum\begin{Bmatrix} n_f\,\mathscr{L}_n\,l_{n_a}\,l_n\,J_a\,J\,I_T\,m_n\,\sigma' \\ N_f\,S'\,l_{n_b}\,L_n\,J_b\,\mu_J\mu_T\,M_n \end{Bmatrix}\circledH\; I_TJ(J_a\,J_b)$$

$$T(J_aJ_b;\,\mathscr{L}_n\,S')\,\langle n_fl_n,\,N_fL_n;\,\mathscr{L}_n\mid n_{f_a}l_{n_a},\,n_{f_b}l_{n_b};\,\mathscr{L}_n\rangle$$

$$(l_nm_n\,L_n\,M_n\mid\mathscr{L}_n\,\mu_n)(\mathscr{L}_n\,\mu_n\,S'\,\sigma'\mid J\,\mu_J)(J\,\mu_J I_T\,\mu_T\mid I_R\,\mu_R)$$

$$\Phi_c(\zeta)\,\Phi_T(\xi)\,\chi_{S'}^{\sigma'}(\sigma_a',\,\sigma_b')\,\chi_{I_c}^{\mu_c}\,\chi_{I_T}^{\mu_T}\,v_{n_fl_n}^{m_n}(\mathbf{r}_{ab})$$

$$\Phi_{N_fL_n}^{*M_n}(\boldsymbol{\eta}). \tag{8}$$

Introducing Eqs. (5), (6), (7) and (8) into Eq. (2), we get for the transition matrix element an expression given as

$$T_{fi}=\sum \begin{Bmatrix} n_i\, n_f\, \mathscr{L}\, l_a\, l_{n_a}\, j_a\, J_a\, l\, l_n\, j\, m\, m_n \\ N_i\, N_f\, \mathscr{L}_n\, l_b\, l_{n_b}\, j_b\, J_b\, L L_n\, J\, M\, M_n \end{Bmatrix} \circledH_{I_T J}(J_a J_b)$$

$$\circledH_{I_C J}(j_a j_b)\; T(J_a J_b;\, \mathscr{L}_n\, S')\; T(j_a j_b;\, \mathscr{L}\, S)\, \langle n_f l_n,\, N_f L_n;\, \mathscr{L}_n \mid$$

$$n_{f_a} l_{n_a},\, n_{f_b} l_{n_b};\, \mathscr{L}_n \rangle\, \langle n_i l,\, N_i L;\, \mathscr{L} \mid n_a l_a,\, n_b l_b;\, \mathscr{L} \rangle$$

$$(l_n m_n\, L_n M_n \mid \mathscr{L}_n \mu_n)\, (\mathscr{L}_n \mu_n\, S'\, \sigma' \mid J\, \mu_J)\, (J\, \mu_J\, I_T\, \mu_T \mid I_R\, \mu_R)$$

$$(lm\, LM \mid \mathscr{L}\, \mu)\, (\mathscr{L}\, \mu\, S\, \sigma \mid j\, \mu_j)\, (j\, \mu_j\, I_c\, \mu_c \mid I_A\, \mu_A) F^{\mu\mu_n}_{\mathscr{L}\mathscr{L}_n}, \tag{9}$$

where the $F^{\mu\mu_n}_{\mathscr{L}\mathscr{L}_n}$ integral is given by

$$F^{\mu\mu_n}_{\mathscr{L}\mathscr{L}_n}=\int v^*_{l_n m_n}(\mathbf{r}_{ab})\, \{V_{aC}(r_a)+V_{bC}(r_b)\}\, U_{lm}(\mathbf{r}_{ab})$$

$$\Phi_{LM}(\boldsymbol{\rho})\, \mathrm{d}\mathbf{r}_{ab}\, \mathrm{d}\boldsymbol{\rho} \int \Phi^*_{L_n M_n}(\boldsymbol{\rho}+\mathbf{r}_c)\, \psi^{*(-)}(\mathbf{R}')\, \psi^{(+)}(\mathbf{R})\, \mathrm{d}\mathbf{r}_c\,. \tag{10}$$

Taylor expansions are used for the distorted waves $\psi^{(+)}(\mathbf{R})$ and $\psi^{*(-)}(\mathbf{R}')$, and also for the bound state wave function $\varphi_{LM}(\boldsymbol{\rho}+\mathbf{r}_c)$. These expansions in partial waves are given by

$$\psi^{(+)}\left(\mathbf{r}_c+\frac{m_{ab}}{m_A}\boldsymbol{\rho}\right)=4\pi\, e^{\frac{m_{ab}}{m_A}\boldsymbol{\rho}\cdot\nabla\psi(+)} \sum_{L'M'} (i)^{L'}\, Y^{M'}_{L'}(\mathbf{k}_i)\; Y^{M'}_{L'}(\mathbf{r}_c)\, \psi^{(+)}(r_c) \tag{11}$$

$$\psi^{*(-)}\left(\frac{m_T}{m_R}\mathbf{r}_c-\frac{m_{ab}}{m_R}\boldsymbol{\rho}\right)=4\pi\, e^{\frac{-m_{ab}}{m_T}\boldsymbol{\rho}\cdot\nabla\psi(-)} \sum_{l'm'} (i)^{l'}(-)^{l'}\, Y^{m'}_{l'}(\mathbf{k}_f)\; Y^{m'}_{l'}(\mathbf{r}_c)\, \psi^{(-)}\left(\frac{m_T}{m_R}\mathbf{r}_c\right) \tag{12}$$

and the bound state wave function can be expanded as

$$\varphi^*_{L_n M_n}(\mathbf{r}_c+\boldsymbol{\rho})=(-1)^{L_n}\, \varphi^*_{L_n M_n}(\mathbf{r}_c-\boldsymbol{\rho})=(-1)^{L_n}\, e^{-\boldsymbol{\rho}\cdot\nabla}\, \Phi^*_{L_n}\, \varphi^*_{L_n M_n}(\mathbf{r}_c).$$

Then

$$\Phi^*_{L_n M_n}(\mathbf{r}_c+\boldsymbol{\rho})=(-1)^{L_n}\, e^{-\boldsymbol{\rho}\cdot\nabla}\, \varphi^*_{L_n}\, Y^{*M_n}_{L_n}(\mathbf{r}_c) \Phi^*_{L_n M_n}(\mathbf{r}_c). \tag{13}$$

The relative motion wave functions of the two captured particles in the projectile $u_{lm}(\mathbf{r}_{ab})$ and in the residual nucleus $v_{l_n m_n}(\mathbf{r}_{ab})$ as well as the center-of-mass bound state wave function $\Phi_{LM}(\boldsymbol{\rho})$ can be taken as Morinigo wave functions [17]. The forms of these wave functions are

$$v^*_{l_n m_n}(\mathbf{r}_{ab})=N(l_n,\, \ldots) r_{ab}^{l_n-1}\, e^{-\chi r_{ab}}\, Y^{*m_n}_{l_n}(\mathbf{r}_{ab}), \tag{14}$$

$$U_{lm}(r_{ab})=N(l,\, \ldots) r_{ab}^{l-1}\, e^{-\chi r_{ab}}\, Y^m_l(\mathbf{r}_{ab})\,, \tag{15}$$

and

$$\Phi_{LM}(\boldsymbol{\rho})=N(L,\, \ldots)\, \rho^{L-1}\, e^{-\chi\rho}\, Y^M_L(\boldsymbol{\rho}). \tag{16}$$

Also we use for both of the potentials $V_{aC}(r_a)$ and $V_{bC}(r_b)$ expressions given in the form of the Yukawa potential as

$$V_{aC}(r_a) = V_{aC}^0 \frac{R_{aC}}{r_a} e^{-\alpha_{aC}(r_a - R_{aC})} \tag{17}$$

and

$$V_{bC}(r_b) = V_{bC}^0 \frac{R_{bC}}{r_b} e^{-\alpha_{bC}(r_b - R_{bC})}. \tag{18}$$

Introducing Eq. (10) into Eq. (9) and making use of Eqs. (11)—(18), and then performing the integration over r_{ab}, we get for the transition matrix element an expression as

$$T_{fi} = 4\pi \sum \begin{Bmatrix} n_i\, n_f\, \mathscr{L}\, l_a\, l_{n_a}\, j_a\, J_a\, l\, l_n\, j\, m\, m_n \\ N_i\, N_f\, \mathscr{L}_n\, l_b\, l_{n_b}\, j_b\, J_b\, L L_n\, J\, M\, M_n \end{Bmatrix} \textcircled{H}^*_{I_T J}(J_a J_b)$$

$$\textcircled{H}_{I_C J}(j_\omega j_b) T(J_a J_b; \mathscr{L}_n S')\; T(j_a j_b; \mathscr{L}\, S) \langle n_f l_n, N_f L_n; \mathscr{L}_n |$$

$$n_{f_a} l_{n_a}, n_{f_b} l_{n_b}; \mathscr{L}_n \rangle \langle n_i l, N_i L; \mathscr{L} \mid n_a l_a, n_b l_b; \mathscr{L} \rangle$$

$$(l_n\, m_n\, L_n\, M_n \mid \mathscr{L}_n\, \mu_n)\, (\mathscr{L}_n\, \mu_n\, S' \sigma' \mid J\, \mu_J)\, (J\, \mu_J\, I_T\, \mu_T \mid I_R\, \mu_R)$$

$$(lm\, LM \mid \mathscr{L}\, \mu)\, (\mathscr{L}\, \mu\, S\, \sigma \mid j\, \mu_j)\, (j\, \mu_j\, I_C\, \mu_C \mid I_A\, \mu_A)$$

$$\sum_{l'm'} \sum_{L'M'} (-1)^{l' + L'_{n_i} l' + L'} \{N(l, \ldots)\}^2\, N(0, \ldots)$$

$$Y_{l'}^{m'}(\mathbf{k}_i)\, Y_{L'}^{M'}(\mathbf{k}_f) \left[\frac{(2L_n+1)(2L'+1)}{(2l'+1)}\right]^{1/2} \begin{pmatrix} L_n & l' & L' \\ 0 & 0 & 0 \end{pmatrix}$$

$$\begin{pmatrix} L_n & l' & L' \\ M_n & m' & M' \end{pmatrix} \int \mathrm{d}r_C r_C^2 F(r_C) \Phi^*_{L_n M_n}(r_C) \Psi^{*(-)}\left(\frac{m_T}{m_R} r_C\right) \Psi^{(+)}(r_C), \tag{19}$$

where

$$F(r_C) = P F_1 + Q F_2, \tag{20}$$

$$P = \frac{V_{aC}^0 R_{aC} e^{\alpha_{aC} R_{aC}}}{\left(B + \dfrac{m_b \alpha_{aC}}{m_{ab}}\right)^{2l+1}} (2l)!, \tag{21}$$

$$Q = \frac{V_{bC}^0 R_{bC} e^{\alpha_{bC} R_{bC}}}{\left(B - \dfrac{m_a \alpha_{bC}}{m_{ab}}\right)^{2l+1}} (2l)!, \tag{22}$$

$$F_1(r_C)=1\Big/\left\{\alpha_{aC}+\chi-\left\{\frac{m_{ab}}{m_R}\left(\frac{2m_{RC}}{\hbar^2}\right)^{1/2}[E_f-V_{RC}(r_C)]^{1/2}-\right.\right.$$

$$-\frac{m_{ab}}{m_A}\left(\frac{2m_{AT}}{\hbar^2}\right)^{1/2}[E_i-V_{AT}(r_C)]^{1/2}-$$

$$\left.\left.-\left(\frac{2\mu_{2nT}}{\hbar^2}\right)^{1/2}[E_{\sigma T}-V_{2nT}(r_c)]^{1/2}\right\}\right\}, \tag{23}$$

$$F_2(r_C)=1\Big/\left\{\alpha_{bC}+\chi-\left\{\frac{m_{ab}}{m_R}\left(\frac{2m_{RC}}{\hbar^2}\right)^{1/2}[E_f-V_{RC}(r_C)]^{1/2}-\right.\right.$$

$$-\frac{m_{ab}}{m_A}\left(\frac{2m_{AT}}{\hbar^2}\right)^{1/2}[E_i-V_{AT}(r_c)]^{1/2}-$$

$$\left.\left.-\left(\frac{2\mu_{2nT}}{\hbar^2}\right)^{1/2}[E_{\sigma T}-V_{2nT}(r_c)]^{1/2}\right\}\right\}. \tag{24}$$

Since the transition matrix element T_{fi} has been given and expressed by Eq. (19), then we get for the differential cross-section of the rearrangement heavy ion collisions with two-nucleon transfer an expression as

$$\frac{d\sigma}{d\Omega}=\frac{m_{AT}^* m_{RC}^*}{(2\pi\hbar^2)^2}\frac{k_f}{k_i}\frac{1}{(2I_A+1)(2I_T+1)}\sum_{\substack{\mu_A\mu_T\\ \mu_C\mu_R}}|T_{fi}|^2. \tag{25}$$

In the present work, an expression for the differential cross-sections of heavy ion reactions with two-nucleon transfer has been evaluated. The DWBA approximation has been used in the present formulation in Section 2. The present formulations of the DWBA differ from previous approximations. The difference is that the finite-range effects in the nuclear potentials have been taken into account in the present formulations. These effects have been solved, evaluated and are given explicitly by the factor $F(r_c)$ as given by expressions (20)—(24). In getting the explicit form of the present formulations, we used the Taylor expressions for the captured nucleons wave function as well as for the distorted wave functions. The local WKB approximation is used also for the $(\bar{V})$ *operators for its operations on the corresponding captured nucleons and distorted wave functions. The obtained factor* $F(r_c)$, due to the finite-range effects which appear only in the present formulations depends on the optical model potentials between the interacting ions. This makes our present formulations for the DWBA different from previous formulae.

3. Numerical calculations and results

In the present work, the heavy ion reactions with two-nucleon transfer have been studied. Theoretical investigations for these reactions are introduced. Expressions for the differential cross-sections have been developed using the distorted wave Born approximation. Numerical calculations are carried out for the angular distributions for different heavy ion reactions. We investigated the two nucleon transfer heavy ion reactions $^{16}O(^{10}B, ^{8}Li)^{18}Ni$ and $^{16}O(^{10}B, ^{8}B)^{18}O$ with ^{10}B projectile ions incident on ^{16}O with an energy of 100 MeV leaving both of the residual nuclei ^{18}Ni and ^{18}O in different excited states. The ^{16}O projectile ions are used in bombarding the ^{42}Ca and ^{48}Ca target nuclei with an energy of 56 MeV in the reactions $^{42}Ca(^{16}O, ^{14}C)^{44}Ti$, $^{48}Ca(^{16}O, ^{14}C)^{50}Ti$ leaving the residual nuclei ^{44}Ti and ^{50}Ti in different excited states. The angular distributions of the two neutron stripping heavy ion reactions $^{26}Mg(^{18}O, ^{16}O)^{28}Mg$ and $^{48}Ca(^{18}O, ^{16}O)^{50}Ca$ have been calculated for ^{18}O projectile ions incident on ^{26}Mg and ^{48}Ca target nuclei with energy 50 MeV. While for the transfer heavy ion reaction $^{60}Ni(^{18}O, ^{16}O)^{62}Ni$ the angular distributions are measured for ^{18}O incident energy 65 MeV leaving the ^{62}Ni residual nucleus in its ground state. In the case of the reaction $^{74}Ge(^{18}O, ^{16}O)^{76}Ge$, the angular distributions are studied for ^{18}O incident energy 75 MeV, leaving the residual nucleus ^{76}Ge in the ground state and its first excited state. Also, two neutron pick-up heavy ion reactions are investigated via the reactions $^{42}Ca(^{16}O, ^{18}O)^{40}Ca$ and $^{48}Ca(^{16}O, ^{18}O)^{46}Ca$, at ^{16}O incident energy of 65 MeV. While differential cross-sections have been calculated for the heavy ion reaction $^{76}Ge(^{16}O, ^{18}O)^{74}Ge$ at ^{16}O incident energy 77.56 MeV leaving the residual nucleus ^{74}Ge in different excited states. Optical model potentials have been used in performing the distorted wave Born approximation calculations. Wood-Saxon potential form is used for the optical potentials. The different values of the different parameters of the optical potentials used in the present work are given in Table I. The present numerical calculations are performed on the CDC 6600 computer. We used in the present calculations the computer program LAJOLLA. This is the international computer program code but it is modified to include the factors which appeared in our present formulations due to the finite-range effects and other different approximations used in Section 2. In the present computations, we used the DWBA computer code programs by using a number of partial waves which range between 20–60 according to each case of the considered heavy-ion reactions separately. Each individual case for the reactions considered needs a computer time between 30 – 65 minutes. With these computer program codes, the differential cross-sections of heavy ion reactions are calculated. The calculated angular distributions are shown in Figs 1–10. The theoretical calculations are shown by the solid curves. The experimental measurements are also given by the points. The present theoretical calculations are fitted to the experimental angular distributions. From this fitting, the spectroscopic factors of these reactions are extracted. The present obtained values of the extracted spectroscopic factors are listed in Table II.

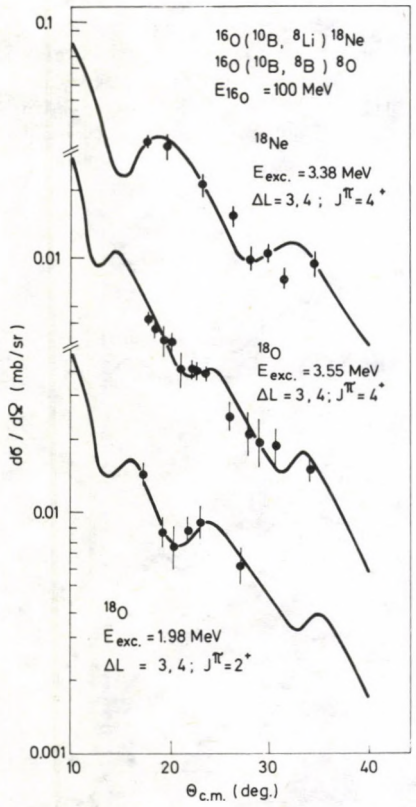

Fig. 1. Differential cross-sections of the reactions $^{16}O(^{10}B, ^{8}Li)^{18}Ne$ and $^{16}O(^{10}B, ^{8}B)^{18}O$ at ^{10}B incident energy 100 MeV leaving the residual nuclei ^{18}Ne and ^{18}O in different excited states. The solid curves are our present DWBA calculations. The optical model parameters are listed in Table I. The points are the experimental data and are taken from reference [11]

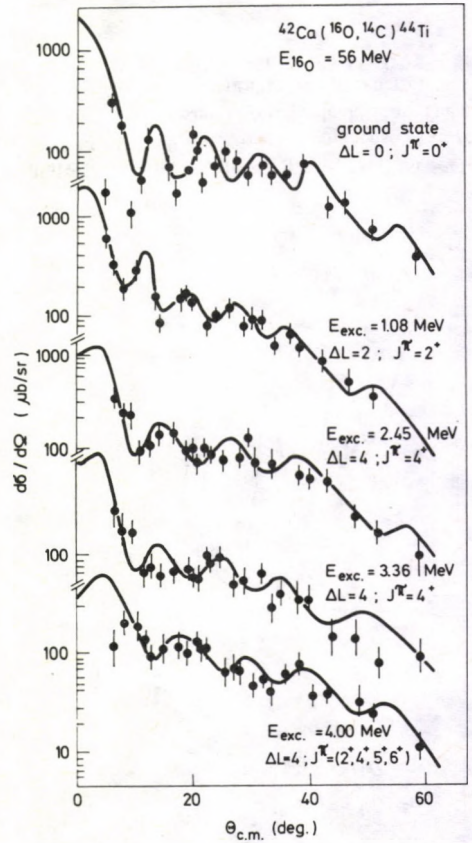

Fig. 2. Differential cross-sections of the reaction $^{42}Ca(^{16}O, ^{14}C)^{44}Ti$ at ^{16}O incident energy 56 MeV leaving the residual nucleus ^{44}Ti in different excited states. The solid curves are our present DWBA calculations. The optical model parameters are listed in Table I. The points are the experimental data and are taken from reference [5]

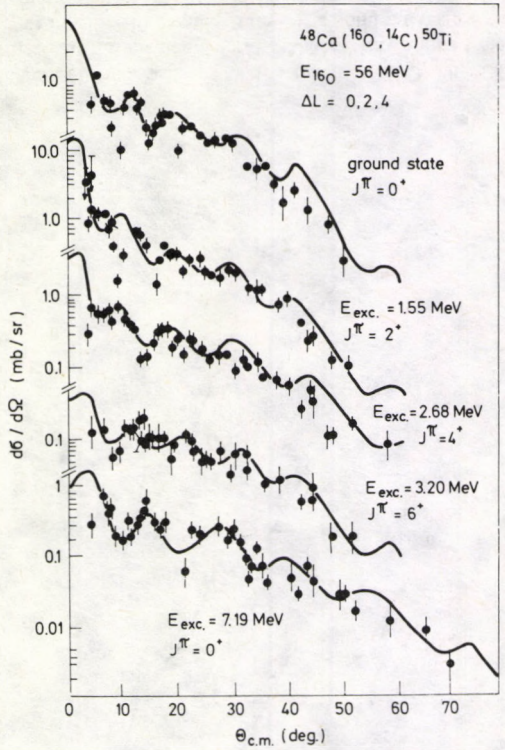

Fig. 3. Differential cross-sections of the reaction $^{48}Ca(^{16}O, ^{14}C)^{50}Ti$ at ^{16}O incident energy 56 MeV leaving the residual nucleus ^{50}Ti in different excited states. The solid curves are our present DWBA calculations. The optical model parameters are listed in Table I. The points are the experimental data and are taken from reference [5]

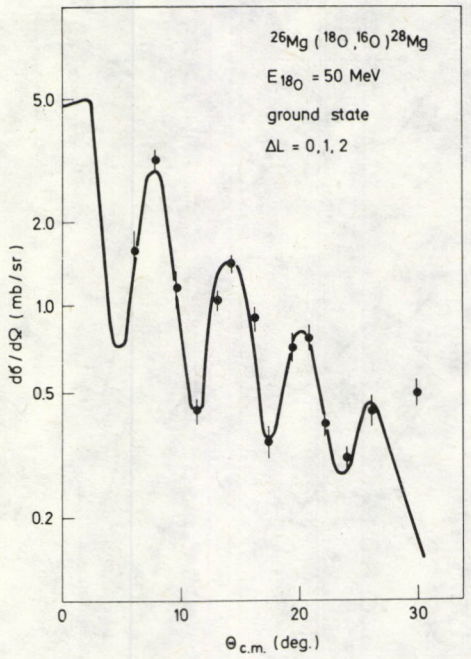

Fig. 4. Differential cross-sections of the reaction $^{26}Mg(^{18}O, ^{16}O)^{28}Mg$ at ^{18}O incident energy 50 MeV leaving the residual nucleus ^{28}Mg in the ground state. The solid curve is our present DWBA calculations. The optical model parameters are listed in Table I. The points are the experimental data and are taken from reference [18] $J^{\pi} = 0^{+}$

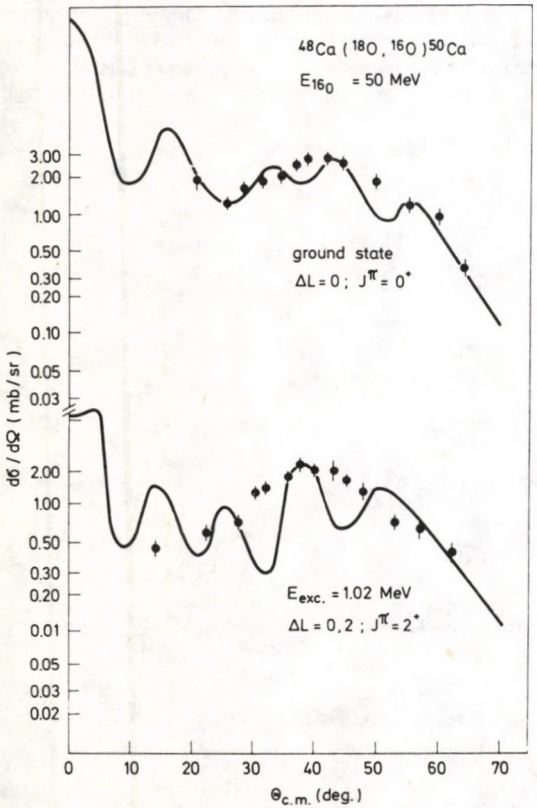

Fig. 5. Differential cross-sections of the reaction $^{48}Ca(^{18}O, ^{16}O)^{50}Ca$ at ^{18}O incident energy 50 MeV leaving the residual nucleus ^{50}Ca in different excited states. The solid curves are our present DWBA calculations. The optical model parameters are listed in Table I. The points are the experimental data and are taken from reference [9]

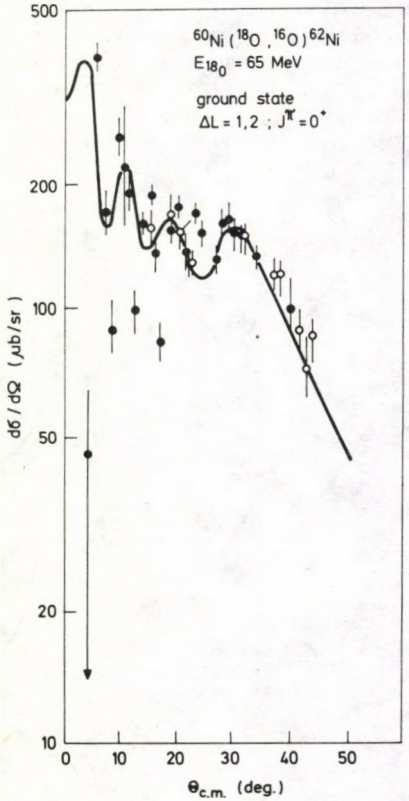

Fig. 6. Differential cross-sections of the reaction $^{60}Ni(^{18}O, ^{16}O)^{62}Ni$ at incident energy 65 MeV leaving the residual nucleus ^{62}Ni in the ground state. The solid curve is our present DWBA calculations. The optical model parameters are listed in Table I. The points are the experimental data and are taken from reference [1]

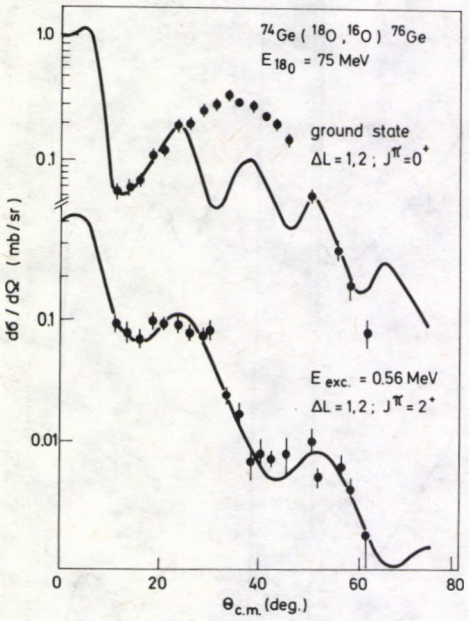

Fig. 7. Differential cross-sections of the reaction ^{74}Ge(^{18}O, ^{16}O)^{76}Ge at ^{18}O incident energy 75 MeV leaving the residual nucleus ^{76}Ge at the ground state and at the 0.56 MeV first excited state. The solid curves are our present DWBA calculations. The optical model parameters are listed in Table I. The points are the experimental data and are taken from reference [10]

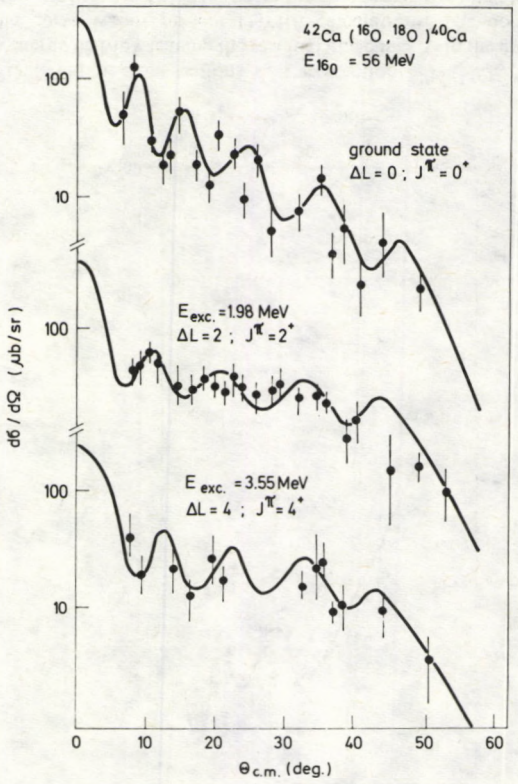

Fig. 8. Differential cross-sections of the reaction ^{42}Ca(^{16}O, ^{18}O)^{40}Ca at ^{16}O incident energy 56 MeV leaving the residual nucleus ^{40}Ca in different excited states. The solid curves are our present DWBA calculations. The optical model parameters are listed in Table I. The points are the experimental data and are taken from reference [5]

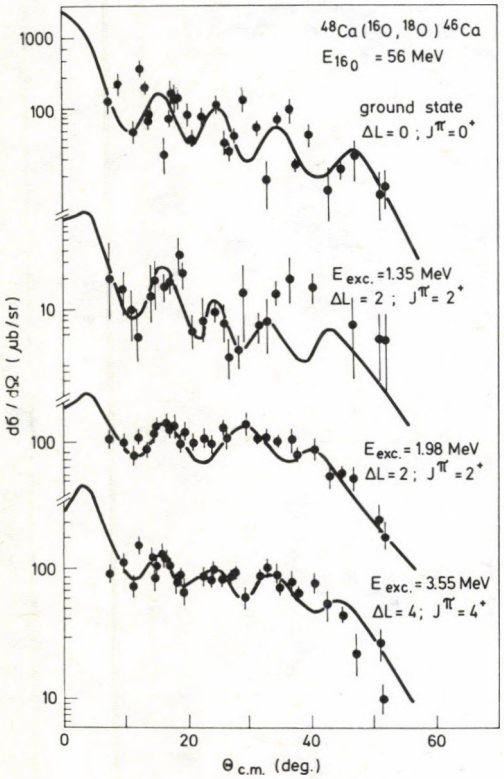

Fig. 9. Differential cross-sections of the reaction $^{48}Ca(^{16}O, ^{18}O)^{46}Ca$ at ^{16}O incident energy 56 MeV leaving the residual nucleus ^{46}Ca in different excited states. The solid curves are our present DWBA calculations. The optical model parameters are listed in Table I. The points are the experimental data and are taken from reference [5]

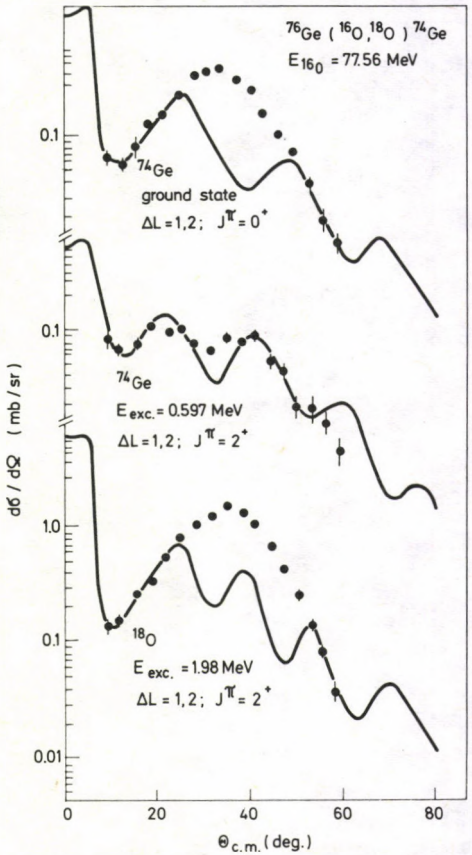

Fig. 10. Differential cross-sections of the reaction $^{76}Ge(^{16}O, ^{18}O)^{74}Ge$ at ^{16}O incident energy 77.56 MeV leaving the residual nucleus ^{74}Ge in different excited states. The solid curves are our present DWBA calculations. The optical model parameters are listed in Table I. The points are the experimental data and are taken from reference [10]

Table I

Optical model parameters

Channel	V_r [MeV]	r_r [fm]	a_r [fm]	W [MeV]	r_w [fm]	a_w [fm]	r_c [fm]
$^{8}Li+^{18}Nc$	100.00	0.970	0.650	40.00	1.180	0.450	1.200
$^{8}B+^{18}O$	100.00	0.070	0.650	40.00	1.180	0.450	1.200
$^{10}B+^{16}O$	100.00	0.970	0.650	40.00	1.180	0.450	1.200
$^{14}C+^{44}Ti$	35.90	1.350	0.900	101.50	1.272	0.286	1.250
$^{14}C+^{50}Ti$	33.90	1.344	0.850	110.20	1.274	0.280	1.250
$^{16}O+^{28}Mg$	33.40	1.321	0.923	10.72	1.251	0.410	1.250
$^{16}O+^{42}Ca$	35.90	1.350	0.960	101.50	1.272	0.286	1.250
$^{16}O+^{48}Ca$	33.90	1.344	0.800	110.20	1.274	0.280	1.250
$^{16}O+^{50}Ca$	97.00	1.210	0.497	59.70	1.140	0.422	1.250
$^{16}O+^{62}Ni$	70.00	8.310	0.400	8.00	8.200	0.500	1.250
$^{16}O+^{76}Ge$ (str.)	14.00	1.355	1.332	36.34	1.260	0.482	1.355
$^{16}O+^{76}Ge$ (pick.)	46.71	1.250	0.583	17.69	1.250	0.583	1.250
$^{18}O+^{26}Mg$	34.40	1.335	0.918	10.84	1.267	0.430	1.250
$^{18}O+^{40}Ca$	35.90	1.350	0.960	101.50	1.272	0.286	1.250
$^{18}O+^{46}Ca$	33.90	1.344	0.800	110.20	1.274	0.280	1.250
$^{18}O+^{48}Ca$	97.00	1.210	0.497	59.70	1.140	0.422	1.250
$^{18}O+^{60}Ni$	70.00	8.680	0.400	8.00	8.200	0.500	1.250
$^{18}O+^{74}Ge$ (str.)	41.92	1.204	0.664	20.937	1.204	0.664	1.204
$^{18}O+^{74}Ge$ (pick.)	19.49	1.332	0.558	17.48	1.316	0.445	1.332

Table II

Extracted spectroscopic factors

Reaction	Incident energy [MeV]	Excitation energy [MeV]	L	J	Spectroscopic factors
$^{16}O(^{10}B, ^{8}Li)^{18}Ne$	100.00	3.380	3, 4	4^+	0.6531
$^{16}O(^{10}B, ^{8}B)^{18}O$	100.00	1.980	3, 4	2^+	0.6628
	100.00	3.550	3, 4	4^+	0.6749
$^{42}Ca(^{16}O, ^{14}C)^{44}Ti$	56.00	0.000	0	0^+	0.6922
		1.080	2	2^+	0.7193
		2.450	4	4^+	0.7225
		3.360	4	4^+	0.7367
		4.000	4	$2^+, 4^+, 5^-, 6^+$	0.7313
$^{48}Ca(^{16}O, ^{14}C)^{50}Ti$	56.00	0.000	0, 2, 4	0^+	0.7038
		1.550	0, 2, 4	2^+	0.6884
		2.680	0, 2, 4	4^+	0.7256
		3.200	0, 2, 4	6^+	0.7164
		7.190	0, 2, 4	0^+	0.7313
$^{26}Mg(^{18}O, ^{16}O)^{28}Mg$	50.00	0.000	0, 1, 2		0.7419

Table II. (cont.)

Reaction	Incident energy [MeV]	Excitation energy [MeV]	L	J	Spectroscopic factors
$^{48}Ca(^{18}O, ^{16}O)^{50}Ca$	50.00	0.000	0	0^+	0.6932
		1.020	0, 2	2^+	0.6318
$^{60}Ni(^{18}O, ^{16}O)^{62}Ni$	65.00	0.000	1, 2	0^+	0.6088
$^{74}Ge(^{18}O, ^{16}O)^{76}Ge$	75.00	0.000	1, 2	0^+	0.6013
		0.560	1, 2	2^+	0.6887
$^{42}Ca(^{16}O, ^{18}O)^{40}Ca$	56.00	0.000	0	0^+	0.6914
		1.980	2	2^+	0.7268
		3.550	4	4^+	0.7093
$^{48}Ca(^{16}O, ^{18}O)^{46}Ca$	56.00	0.000	0	0^+	0.6697
		1.350	2	2^+	0.6284
		1.980	2	2^+	0.7156
		3.550	4	4^+	0.7389
$^{76}Ge(^{16}O, ^{18}O)^{74}Ge$	77.56	0.000	1, 2	0^+	0.6029
		0.597	1, 2	2^+	0.6638
		1.980	1, 2	2^+	0.6087

4. Discussion and conclusions

In the present work, we introduced a study for heavy ion reactions with two nucleon transfer. We developed analytical and theoretical expressions for the differential cross-sections. Numerical calculations for the angular distributions are carried out using the distorted wave Born approximation. In these calculations optical model potentials are used in describing the initial and final channel interactions between the interacting heavy ions. The different parameters of the optical model potentials are determined by fitting the theoretical calculations of the differential cross-sections of the elastic scattering heavy ion reactions with the experimental data. Then, the optical model parameters are fixed. These fixed parameters of the optical model potentials are used in the calculations of the differential cross-section of the heavy ion reactions with two-nucleon transfer. The present theoretical calculations are compared with the experimental measurements. From Figs 1–10, we see that the agreements between the present theoretical calculations of the differential cross-sections and the experimental data are good. The present theoretical calculations produce the oscillatory pattern as well as the maxima and minima of the experimental measurements. Fitting the theoretical calculations of the angular distributions with the experimental data, the spectroscopic factors of the reactions are obtained. The

obtained values of the spectroscopic factors are close to 1. From Table II we can see that the obtained values of the extracted spectroscopic factors are reasonable.

Thus, we can conclude that the present theoretical calculations using the distorted wave Born approximation reproduce the experimental measurements of the differential cross-sections both in shape and in magnitude.

References

1. A. J. Baltz, P. D. Bond, J. D. Garrett and S. Kahana, Phys. Rev., *C*12, 136, 1975.
2. A. J. Baltz, Phys. Rev., *C*13, 668, 1976.
3. P. D. Bond, H. J. Korner, M. C. Lemaire, D. J. Pisano and C. E. Thorn, Phys. Rev., *C*16, 177, 1977.
4. A. Osman, Physics Letters, 34*B*, 478, 1971.
5. Y. Eisen, H. T. Fortune, W. Henning, D. G. Kovar, S. Vigdor and B. Zeidman, Phys. Rev., *C*13, 699, 1976.
6. S. C. Pieper, M. H. Macfarlane, D. H. Gloeckner, D. G. Kovar, F. D. Becchetti, B. G. Harvey, D. L. Hendrie, H. Homeyer, J. Mahoney, F. Pühlhofer, W. von Oertzen and M. S. Zisman, Phys. Rev., *C*18, 180, 1978.
7. H. T. Fortune and D. Kvrath, Phys. Rev., *C*18, 236, 1978.
8. H. T. Fortune, J. R. Powers, R. Middleton, K. Bethge and A. A. Pilt, Phys. Rev., *C*18, 255, 1978.
9. D. H. Feng, T. Tamura, T. K. Udegawa, J. Lynch and K. S. Low, Phys. Rev., *C*14, 1484, 1976.
10. M. C. Lemaire and K. S. Low, Phys. Rev., *C*16, 183 1977.
11. M. Hamm and K. Nagatani, Phys. Rev., *C*17, 586, 1978.
12. G. P. A. Berg, M. A. G. Fernandes, K. Nagatani, J. C. Peng, B. Berthier, J. P. Fovan, J. Gastebois, J. P. Le Fevre and M. C. Lemaire, Phys. Rev., *C*19, 62, 1979.
13. A. Osman, Physics Letters, 37*B*, 135, 1971.
14. A. Osman, Particles and Nuclei (U.S.A.) **3**, 28, 1972.
15. A. Osman, Atomkernenergie, **22**, 62, 1973.
16. A. Osman, Il Nuovo Cimento, **25***A*, 571, 1975.
17. F. B. Morinigo, Phys. Rev., **134**, B1243, 1964.
18. M. Bernas, M. Langevin, J. P. Lefevre, M. C. Mallet-Lemaire, F. Pougheon, P. Roussel, G. Rotbard, M. Roy-Stephan and B. H. Wildenthal, Report Annuaire d'Orsay, France, 1977, p. N. 7.

Acta Physica Hungarica 54 (1—2), pp. 25-39 (1983)

HEAVY ION REACTIONS WITH SINGLE NEUTRON TRANSFER

AHMED OSMAN and S. A. SALEH

Physics Department, Faculty of Science, Cairo University, Cairo, Egypt

(Received in revised form 27 October 1981)

Heavy ion reactions with a neutron transfer are considered. Reactions with the different heavy ions ^{10}B, ^{13}C, ^{14}N, ^{16}O, ^{18}O and ^{32}S are incident on the different targets ^{12}C, ^{16}O, ^{27}Al, ^{28}Si, ^{32}S, ^{40}Ca, ^{48}Ca, ^{54}Fe, ^{60}Ni and ^{208}Pb with the reaction process of a neutron stripping or a neutron pick-up. The energies of the incident heavy ions have values in the range between 36 MeV and 155 MeV. Theory of these transfer reactions is studied using DWBA approximations. Numerical calculations of the differential cross-sections are carried out using the DWBA calculations. Good agreement between the theoretical calculations and the experimental measurements is obtained. From the comparison of the present theoretical calculations and the experimental data of the angular distributions, spectroscopic factors are extracted.

1. Introduction

Stripping and pick-up reactions with a single-neutron transfer have been studied for nuclear reactions with heavy ion projectiles. These reactions are investigated theoretically following different approaches. Garrett et al. [1] studied the $^{27}Al(^{32}S, ^{33}S)\,^{26}Al$ reactions at an incident energy of 100 MeV. Different optical model parameters have been used in comparing the DWBA calculations of the angular distributions with the experimental data. Using ^{16}O projectile with an energy of 139 MeV incident on the heavy target nucleus ^{208}Pb, Becchetti et al. [2] studied the single neutron transfer reactions leading to ^{209}Pb residual nucleus. In their analysis a shift was found between the maxima of the different levels. The theoretical DWBA calculations show that the angular distributions are functions of the Q-value, which is not observed experimentally [2], [3]. Nair et al. [4] measured the differential cross-sections of different single neutron transfer reactions using ^{14}N and ^{10}B incident projectiles. The energies of ^{14}N and ^{10}B ions are 155 and 100 MeV, respectively, which are above the Coulomb barriers in the initial channels. Exact finite-range DWBA approximation is used in calculating the angular distributions. Comparing the theoretically calculated values with the experimental results, the spectroscopic factors are obtained. Osman [5] introduced a theoretical study for ^{6}Li induced reactions as a direct stripping nuclear reaction mechanism. Moffa et al. [6] introduced a theoretical study localizing the heavy ion reactions in both of the coordinate and of the angular momentum spaces. They got a quantum mechanical formula relating the coordinate

with the angular momentum which is compared with the experimental work. A theoretical study of heavy ion reactions as a three-body problem has been introduced by Osman [7], [8] using projection operators [9]. Experimental angular distributions have been measured by Westfall and Zaidi [10] for different heavy ion reactions using ^{13}C projectile with an incident energy of 36 MeV on ^{16}O, ^{28}Si and ^{32}S target nuclei for angles between 4° and 40°.

Clear features are indicated by comparing the results with the exact finite-range DWBA and with Coulomb transfer reactions [11]. The ^{28}Si, $^{40,48}Ca$, $^{54}Fe(^{18}O, ^{17}O)$ single-neutron stripping reactions at a bombarding energy of 50 MeV are studied by Petersen et al [12]. They introduced a comparison between the experimental data and the full-recoil finite-range DWBA analysis. The obtained spectroscopic factors agree with the spectroscopic factors obtained from light ion reactions except for one case. Single neutron transfer reactions for ^{16}O projectile of ^{208}Pb target have been measured by Olmer et al [13] at a bombarding energy of 312.6 MeV. Comparing the DWBA calculations with the experimental results, good agreement is obtained for the relative final-state, but this DWBA analysis fails to predict the absolute energy dependence of the observed transfer cross sections. Nagel [14] applied the exact finite-range Born approximation for the reaction $^{12}C(^{14}N, ^{13}N)^{13}C$ at 100 MeV ^{14}N energy. Nagel observed a disagreement for the 2S transition. The suggested mechanism of this reaction does not succeed in removing the phase discrepancy between the experimental results and the finite-range DWBA predictions for the angular distributions.

In the present work we introduce a theoretical study for heavy ion reactions with single neutron transfer. The heavy ion reactions with single neutron stripping $^{16}O(^{13}C, ^{12}C)^{17}O$, $^{32}S(^{13}C, ^{12}C)^{33}S$, $^{60}Ni(^{13}C, ^{12}C)^{61}Ni$, $^{12}C(^{14}N, ^{13}N)^{13}C$, $^{208}Pb(^{16}O, ^{15}O)^{209}Pb$, $^{28}Si(^{18}O, ^{17}O)^{29}Si$, $^{40}Ca(^{18}O, ^{17}O)^{41}Ca$, $^{48}Ca(^{18}O, ^{17}O)^{49}Ca$ and $^{54}Fe(^{18}O, ^{17}O)^{55}Fe$ are considered. Also, we study the heavy ion reactions with a single neutron pick up $^{16}O(^{10}B, ^{11}B)^{15}O$, $^{16}O(^{14}N, ^{15}N)^{15}O$ and $^{27}Al(^{32}S, ^{33}S)^{26}Al$. The DWBA approximation is considered. In the present work, it is our aim to study the heavy ion reactions with a single neutron transfer. In this study, we show that the DWBA approximation is suitable to calculate the differential cross-sections of such reactions. Also, we aim to study the finite-range effects in such reactions. These finite-range effects are important and appear by using finite-range nuclear potentials. These finite-range effects are important to produce the correct value of the cross-sections. Then we aim to obtain correct values for the spectroscopic and normalisation factors. Then, the DWBA calculations have to be reformulated and modified to include all these effects. Including all these effects, the DWBA approximation is reformulated and modified and evaluated in the present theory for heavy ion reactions with single neutron transfer. This theory is applied to the considered heavy ion reactions. Numerical calculations for the differential cross-sections are carried out using the DWBA calculations. The present theoretically calculated angular distributions are compared with the experimental measurements. From the fitting between the theoretical and experimental values, spectroscopic factors are extracted.

In Section 2, the DWBA approximation for nuclear reactions between heavy ions are introduced. In Section 3, numerical calculations and results are given. Section 4 is left for discussion.

2. The DWBA approximation for heavy ion reactions

The heavy ion reactions with neutron transfer will be considered. These reactions are treated theoretically as direct nuclear reactions. The initial channel is the interaction between the heavy projectile A, incident on the target T. The projectile A is taken to be the bound state of a neutron n and a core C. This direct neutron transfer reaction leads to the final channel of an interaction between the outgoing particle C and the residual heavy nucleus R. The residual nucleus R is taken to consist of a bound neutron n to the projectile T. This reaction is represented as

$$A(n+C)+T\rightarrow C+R(n+T)\,, \tag{1}$$

where n is bound to the core C in the projectile A with relative angular momentum l, while n is bound to T in the residual nucleus R with relative angular momentum L. The transition amplitude for this direct stripping reaction with the neutron transfer [15] is given as

$$T_{fi}=\langle\Psi_f^{(-)}|\,V_{nC}\,|\Psi_i^{(+)}\rangle \tag{2}$$

$\Psi_i^{(+)}$ and $\Psi_f^{(-)}$ are the ingoing and outgoing wave functions describing the reaction processes in the initial and final channels, respectively [16]. These wave functions can be introduced as

$$\Psi_i^{(+)}=\varphi_i\psi^{(+)}\left(\mathbf{r}+\frac{m_n}{m_A}\rho\right), \tag{3}$$

$$\Psi_f^{(-)}=\varphi_f\psi^{(-)}\left(\frac{m_T}{m_R}\mathbf{r}-\frac{m_n}{m_R}\rho\right). \tag{4}$$

$\psi^{(+)}$ and $\psi^{(-)}$ are the ingoing and outgoing wave functions which carry all the distortion effects due to both of the Coulomb and nuclear interactions in the initial and final channels, respectively. φ_i and φ_f are the initial and final non-interacting states of the system and are expressed as

$$\varphi_i=e^{i\mathbf{k}_i\cdot\mathbf{R}}\varphi_{lm}(\boldsymbol{\rho})\varphi_{I_n}^{\mu_n}(\boldsymbol{\xi})\varphi_{I_C}^{\mu_C}(\boldsymbol{\tau})\varphi_{I_T}^{\mu_T}(\boldsymbol{\zeta})\,, \tag{5}$$

$$\varphi_f=e^{i\mathbf{k}_f\cdot\mathbf{R}'}\Phi_{LM}(\mathbf{r}_n)\varphi_{I_n}^{\mu_n}(\boldsymbol{\xi})\varphi_{I_C}^{\mu_C}(\boldsymbol{\tau})\varphi_{I_T}^{\mu_T}(\boldsymbol{\zeta})\,. \tag{6}$$

$\mathbf{R}$ and $\mathbf{R}'$ are the separation coordinates between the projectile A and the target nucleus T in the initial channel and between the outgoing particle C and the residual nucleus R in the final channel, respectively. $\varphi_{I_i}^{\mu_i}$ is the self bound wave function for the particle i. φ_{lm} is the bound state wave function representing the bound state of the neutron n to the core C in the projectile A with relative angular momentum l. Φ_{LM} is also the bound

state wave function of the bound neutron n to T in the residual nucleus R with relative angular momentum L. $\boldsymbol{\rho}$, $\mathbf{r}_n$ and $\mathbf{r}$ are the separation coordinates between n and C, n and T and between C and T, respectively.

Introducing Eqs (3–6) into Eq. (2), we get for the transition amplitude the expression

$$T_{fi}=\sum_{\substack{lj\mu_n \\ m\mu\mu_c}}\sum_{\substack{LJ \\ M\mu\mu_T}} \textcircled{H}\,(l,j)\;\textcircled{H}^{*}(L,J)\,(I_n\mu_n lm|j\mu)\,(j\mu I_C\mu_C|I_A\mu_A)\cdot$$

$$\cdot\,(I_n\mu_n LM|J\mu)\,(J\mu I_T\mu_T|I_R\mu_R)I_{lL}^{mM}\,, \tag{7}$$

with

$$I_{lL}^{mM}=\int \mathrm{d}\boldsymbol{\rho}e^{i\mathbf{Q}\cdot\boldsymbol{\rho}}V_{nC}(\rho)\varphi_{lm}(\boldsymbol{\rho})\int e^{i\mathbf{q}\cdot\mathbf{r}}\Phi^{*}_{(\mathbf{r}+\boldsymbol{\rho})}\psi^{*(-)}\left(\frac{m_T}{m_R}\mathbf{r}-\frac{m_n}{m_R}\boldsymbol{\rho}\right)\cdot\psi^{(+)}\left(\mathbf{r}+\frac{n}{\mathbf{m}_A}\boldsymbol{\rho}\right)\mathrm{d}\mathbf{r}\,, \tag{8}$$

where

$$\mathbf{q}=\mathbf{k}_i-\frac{m_T}{m_R}\mathbf{k}_f \tag{9}$$

and

$$\mathbf{Q}=\frac{m_n}{m_A}\mathbf{k}_i+\frac{m_n}{m_R}\mathbf{k}_f\,. \tag{10}$$

m_i is the mass of the particle i. $\textcircled{H}\,(l,j)$ and $\textcircled{H}^{*}(L,J)$ are the spectroscopic factors.

Taylor expansions are used for the wave functions

$$\Phi^{*}_{LM}(\mathbf{r}+\boldsymbol{\rho})\,,\quad \psi^{(+)}\left(\mathbf{r}+\frac{m_n}{m_A}\boldsymbol{\rho}\right)\text{ and }\psi^{(-)}\left(\frac{m_T}{m_R}\mathbf{r}-\frac{m_n}{m_R}\boldsymbol{\rho}\right)$$

in the form

$$\Psi_i(a\mathbf{r}+b\boldsymbol{\rho})=e^{b\boldsymbol{\rho}\cdot\nabla\Psi_i}\Psi_i(a\mathbf{r})\,. \tag{11}$$

The neutron bound state wave function in the residual nucleus is separated for the radial part as

$$\Phi_{LM}(\mathbf{r})=U_{NL}(r)\,Y_L^M(\hat{\mathbf{r}})\,. \tag{12}$$

The distorted wave functions $\psi^{(+)}$ and $\psi^{(-)}$ are expanded by the partial wave expansion and expressed as

$$\psi^{(+)}(\mathbf{k}_i,\mathbf{r})=4\pi\sum_{\lambda m_\lambda} i^{\lambda}Y^{*m_\lambda}_{\lambda}(\hat{\mathbf{k}}_i)\,Y^{m_\lambda}_{\lambda}(\hat{\mathbf{r}})\psi_\lambda(r) \tag{13}$$

and

$$\psi^{(-)}\left(\mathbf{k}_f,\frac{m_T}{m_R}\mathbf{r}\right)=4\pi\sum_{\mu m_\mu} i^{\mu}Y^{*m_\mu}_{\mu}(\hat{\mathbf{k}}_f)\,Y^{m_\mu}_{\mu}\left(\frac{m_T}{m_R}\mathbf{r}\right)\psi_\mu\left(\frac{m_T}{m_R}r\right). \tag{14}$$

Introducing Eqs (11–14) into Eq. (8), we get

$$I_{lL}^{mM}=(4\pi)^2\sum_{\lambda\mu}\sum_{m_\lambda m_\mu}(-)^\mu(i)^{\lambda+\mu}Y_\lambda^{*m_\lambda}(\hat{\mathbf{k}}_i)\,Y_\mu^{m_\mu}(\hat{\mathbf{k}}_f)\int d\rho\,V_{nC}(\rho)\varphi_{lm}(\rho)\cdot$$

$$\cdot e^{i[\mathbf{Q}-i(\nabla_\Phi+\frac{m_n}{m_A}\nabla_{\psi^{(+)}}-\frac{m_n}{m_R}\nabla_{\psi^{(-)}})]\cdot\boldsymbol{\rho}}\int dr\,r^2e^{i\mathbf{q}\cdot\mathbf{r}}U_{NL}^*(r)\psi_\lambda(r)\psi_\mu^*\left(\frac{m_T}{m_R}r\right)\cdot$$

$$\cdot\int d\Omega_r\,Y_\lambda^{m_\lambda}(\Omega_r)\,Y_\lambda^{*m_\mu}\left(\frac{m_T}{m_R}\Omega_r\right)Y_L^{*M}(\Omega_r)\,. \tag{15}$$

Expanding $e^{i\mathbf{q}\cdot\mathbf{r}}$ in partial spherical harmonics, and collecting all the spherical harmonics and summing them together, we get for Eq. (15) an expression as

$$I_{lL}^{mM}=\sum_{\substack{\lambda\lambda'\mu\\ \nu\sigma}}\sum_{m_\lambda m_{\lambda'}m_\mu\atop m_\sigma m_\Lambda}(4\pi)^{1/2}(-)^{\nu+\mu-\lambda'+m_\nu+m_{\lambda'}}(i)^{\lambda+\mu+\nu}(2\lambda+1)(2\mu+1)\cdot$$

$$\cdot\{(2\nu-2\lambda'+1)(2\nu+1)(2L+1)\}^{1/2}(2\nu_{2\lambda'}+1)^{1/2}(k_i)^{\lambda'}\cdot$$

$$\cdot\left(\frac{m_T}{m_R}k_f\right)^{\nu-\lambda'}\left|k_i-\frac{m_T}{m_R}k_f\right|^{-\nu}(\nu-\lambda'-(m_\nu+m_{\lambda'})\lambda' m_{\lambda'}|\nu-m_\nu)\cdot$$

$$\cdot(\nu m_\nu\lambda m_\lambda|\sigma m_\sigma)(\mu m_\mu LM|\sigma m_\sigma)(\nu-\lambda'-(m_\nu+m_{\lambda'})\mu m_\mu|\Lambda m_\Lambda)\cdot$$

$$\cdot(\lambda'-m_{\lambda'}\lambda m_\lambda|\Lambda m_\Lambda)(\nu_0\lambda_0|\sigma_0)(\mu_0L_0|\sigma_0)(\nu-\lambda_0'\mu_0|\Lambda_0)$$

$$(\lambda_0'\lambda_0|\Lambda_0)P_\Lambda(\cos\varphi)\int dr\,r^2F_{lm}^{nt}(r)j_\nu(qr)U_{NL}^*(r)\psi_\lambda(r)\psi_\mu^*\left(\frac{m_T}{m_R}r\right), \tag{16}$$

where

$$F_{lm}^{nt}(r)=\int d\boldsymbol{\rho}\,V_{nC}(\rho)\varphi_{lm}(\boldsymbol{\rho})e^{i\left[\mathbf{Q}-i\left(\nabla_\varphi+\frac{m_n}{m_A}\nabla_{\psi^{(+)}}-\frac{m_n}{m_R}\nabla_{\psi^{(-)}}\right)\right]}. \tag{17}$$

We use a Morinigo wave function [17] for the bound state of the neutron n in the projectile $\varphi_{lm}(\boldsymbol{\rho})$, and also a Yukawa potential for $V_{nC}(\rho)$ as

$$V_{nC}(\rho)=V_{nC}^0\frac{R_{nC}}{\rho}\,e^{-\alpha_{nC}\cdot(\rho-R_{nC})}. \tag{18}$$

To solve the integral $F_{lm}^{nt}(r)$ as expanded by Eq. (17), we use the following expansion for the exponential

$$e^{i\left[\mathbf{Q}-i\nabla\Phi-i\frac{m_n}{m_A}\nabla_{\psi^{(+)}}+i\frac{m_n}{m_R}\nabla_{\psi^{(-)}}\right]\cdot\boldsymbol{\rho}}=4\pi\sum_{\nu'=0}^{\infty}i^{\nu'},$$

$$j_{\nu'}\left[\left|\mathbf{Q}-i\boldsymbol{\nabla}_{\Phi}-i\frac{m_n}{m_A}\boldsymbol{\nabla}_{\psi^{(+)}}+i\frac{m_n}{m_R}\boldsymbol{\nabla}_{\psi^{(-)}}\right|\rho\right]\cdot$$

$$\cdot\, Y_{\nu'}^{m_{\nu'}}(\hat{\boldsymbol{\rho}})\, Y_{\nu'}^{m_{\nu'}}\left[\mathbf{Q}-i\boldsymbol{\nabla}_{\Phi}-i\frac{m_n}{m_A}\boldsymbol{\nabla}_{\psi^{(+)}}+i\frac{m_n}{m_R}\boldsymbol{\nabla}_{\psi^{(-)}}\right]. \tag{19}$$

The delta ($\boldsymbol{\nabla}$) operators present in Eq. (19) operate on the corresponding wave functions [11] which can be introduced by using the local WKB-approximation as

$$(\nabla^2)^n\psi=(-1)^n\left(\frac{2m^*}{\hbar^2}\right)^n[V(\mathbf{r})-E]^n\psi\,. \tag{20}$$

Then, the finite range form factor $F_{lm}^{nt}(r)$ can be given by the expression

$$F_{lm}^{nt}(r)=4\pi^{1/2}N(l,\ldots)\,V_{nC}^{0}R_{nC}e^{\alpha_{nC}R_{nC}}(2i)^l\Gamma(l+1/2)$$

$$y_l^m[\mathbf{Q}-\hat{P}_{nt}(\mathbf{r})]\,\frac{[\mathbf{Q}-P_{nt}(\mathbf{r})]^l}{\{(\alpha_{nC}+\beta)^2+[\mathbf{Q}-P_{nt}(\mathbf{r})]^2\}^{l+1/2}}\,, \tag{21}$$

where

$$P_{nt}(\mathbf{r})=\sqrt{\frac{2m_{nT}^*}{\hbar^2}[E_{\text{bin}}^{nT}-V_{nT}(\mathbf{r})]}+\frac{m_n}{m_A}\sqrt{\frac{2m_{AT}^*}{\hbar^2}[E_i-V_{\text{opt}}^{AT}(\mathbf{r})]}$$

$$-\frac{m_n}{m_R}\sqrt{\frac{2m_{CR}^*}{\hbar^2}[E_f-V_{\text{opt}}^{CR}(\mathbf{r})]}\,. \tag{22}$$

m_{ij}^* is the reduced mass of the (i,j) bound system, while E_{bin}^{ij} is the binding energy for the bound system of the (i,j) particles. V_{opt}^{ij} is the optical potential for the interaction between the particles i and j.

From Eqs (16) and (21), and introducing it into Eq. (7) determine the transition amplitude, we get an expression for the differential cross-section as

$$\frac{\mathrm{d}\sigma}{\mathrm{d}\Omega}=\frac{m_{AT}^*m_{cR}^*}{(2\pi\hbar^2)^2}\,\frac{1}{(2I_A+1)(2I_T+1)}\sum_{\substack{\mu_A\mu_T\\ \mu_C\mu_R}}|T_{fi}|^2\,. \tag{23}$$

In the present Section, an expression for the differential cross-sections of heavy ion reactions with a single neutron transfer has been evaluated. In the present formulation in Section 2, the DWBA approximation has been used. The present DWBA formulations differ from the previous approximations in that in the present evaluation we took into account the finite-range effects in the nuclear potentials. These effects are solved and are given explicitly by the factor $F_{lm}^{nt}(r)$ as given by expressions (21) and (22). To get an explicit form in the present formulations, we used the Taylor

expansions for the captured neutron wave function as well as for the distorted wave functions. Also, the local WKB approximation is used for the (V) operators for its operations on the corresponding captured neutron and distorted wave functions. The obtained factor, $F^{nt}_{lm}(r)$, due to finite-range effects which appear only in the present formulations, depends on the optical model potentials between the interacting ions. This makes our present formulations for the DWBA different from previous formulae.

3. Numerical calculations and results

Heavy ion reactions with one neutron transfer are studied. The interactions between the heavy ions in the initial and final channels are treated by using the DWBA approximation. Different heavy ion reactions are considered with the heavy ion projectiles ^{10}B, ^{13}C, ^{14}N, ^{16}O, ^{18}O and ^{32}S incident on the different targets ^{12}C, ^{16}O, ^{27}Al, ^{28}Si, ^{32}S, ^{40}Ca, ^{48}Ca, ^{54}Fe, ^{60}Ni and ^{208}Pb. The energies of the projectiles for the different reactions considered have values in the range between 36 MeV and 155 MeV. A theoretical expression for the differential cross-section using DWBA is obtained and is given by Eq. (23). Numerical calculations are performed for the angular distributions for different heavy ion reactions with single neutron transfer.

The neutron stripping heavy ion reactions ^{16}O(^{13}C, ^{12}C)^{17}O and ^{32}S(^{13}C, ^{12}C)^{33}S are studied at ^{13}C incident energy of 36 MeV. The angular distributions are measured for angles between 4° and 40°. The residual nucleus ^{17}O is in an excited state with excitation energy 0.871 MeV, while the ^{33}S residual nucleus in the other reaction is in its ground state. The reaction ^{60}Ni(^{13}C, ^{12}C)^{61}Ni is studied at ^{13}C incident energy of 60.83 MeV leaving the ^{61}Ni residual nucleus in excitation energy 0.284 MeV with total spin $1/2^-$. The neutron stripping reaction ^{12}C(^{14}N, ^{13}N)^{13}C is measured at ^{14}N incident energy of 100 MeV. The residual nucleus ^{13}C of this reaction is left with an excitation energy of 3.09 MeV and total spin $1/2^+$. The ^{16}O ions with an energy of 139 MeV are used as projectiles in the neutron stripping reaction ^{208}Pb(^{16}O, ^{15}O)^{209}Pb leaving the ^{209}Pb residual nucleus in different excited states. ^{18}O ions with energy 50 MeV are used to study different heavy ion reactions with neutron stripping on the different targets ^{28}Si, ^{40}Ca, ^{48}Ca and ^{54}Fe. The outgoing ion is the ^{17}O ion, which in its excited state 0.87 MeV and total spin $1/2^+$ in the case of the reactions ^{28}Si(^{18}O, ^{17}O)^{29}Si, ^{40}Ca(^{18}O, ^{17}O)^{41}Ca and ^{48}Ca (^{18}O, ^{17}O)^{49}Ca. In the case of the reaction ^{54}Fe(^{18}O, ^{17}O)^{55}Fe, the outgoing ^{17}O ion is in its ground state. These reactions are studied in case that the residual nuclei ^{29}Si, ^{41}Ca and ^{49}Ca are in their ground states while the residual nucleus ^{55}Fe is studied in two cases, one is its ground state and the other is when the ^{55}Fe nucleus has excitation energy 0.441 MeV.

Also, we studied here the heavy ion reactions with one neutron pick-up process. The ^{16}O(^{10}B, ^{11}B)^{15}O reaction is studied at ^{10}B incident energy 100 MeV, leaving the ^{15}O residual nucleus in different excited states. In the case of the ^{16}O(^{14}N, ^{15}N)^{15}O reaction, the ^{14}N incident energy is 155 MeV and the ^{15}O residual nucleus is in its

ground state. Also, we studied the $^{27}Al(^{32}S, ^{33}S)^{26}Al$ neutron pick-up heavy ion reaction at ^{32}S incident energy of 100 MeV leaving the residual nucleus ^{26}Al in its ground state.

The differential cross-sections of these reactions are numerically calculated using the present theoretically obtained expressions. In the present DWBA calculations, optical model is used with Wood-Saxon optical potential. The different parameters of the optical potential are given in Table I. The present numerical calculations are performed on the CDC 6600 computer. In the present calculations we used the computer program LAJOLLA. This is the international computer program code but it is modified to include the factors which appeared in our present formulations due to the finite-range effects and other different approximations used in Section 2. In the present computations, we used the DWBA computer code programs by using a number of partial waves which range between 15–40 according to each case of the considered heavy ion reactions separately. Each case for the reactions considered, need a computer time between 20 – 45 minutes according to each case separately. With these computer program codes, the differential cross-sections of heavy ion reactions are calculated. The obtained results of the calculated angular distributions for these reactions are shown in Figs 1–10. The solid curves are our present theoretical calculations. The points are the

Table I

Optical potential parameters

Channel	V [MeV]	r_0 [fm]	a_0 [fm]	W [MeV]	r_I [fm]	a_I [fm]	r_c [fm]
$^{10}B+^{16}O$	14.500	1.300	0.800	6.500	1.315	0.550	1.250
$^{11}B+^{15}O$	14.500	1.300	0.800	6.500	1.315	0.550	1.250
$^{12}C+^{17}O$	100.323	1.140	0.560	12.960	1.284	0.442	0.925
$^{12}C+^{33}S$	100.166	1.235	0.507	8.489	1.234	0.889	1.083
$^{12}C+^{61}Ni$	100.000	1.400	0.600	40.300	1.400	0.600	1.500
$^{13}C+^{16}O$	100.323	1.140	0.560	12.960	1.284	0.442	0.925
$^{13}C+^{32}S$	100.166	1.235	0.507	8.489	1.234	0.889	1.083
$^{13}C+^{60}Ni$	100.000	1.400	0.600	40.300	1.400	0.600	1.500
$^{13}N+^{13}C$	145.000	0.925	0.816	35.300	1.300	0.178	0.925
$^{14}N+^{12}C$	145.000	0.925	0.816	35.300	1.300	0.178	0.925
$^{14}N+^{16}O$	100.000	0.970	0.970	39.500	1.290	0.400	1.250
$^{15}N+^{15}O$	100.000	0.970	0.970	39.500	1.290	0.400	1.250
$^{15}O+^{209}Pb$	40.000	1.310	0.450	15.000	1.310	0.450	1.300
$^{16}O+^{208}Pb$	40.000	1.310	0.450	15.000	1.310	0.450	1.300
$^{17}O+^{29}Si$	60.000	1.200	0.529	15.500	1.140	0.728	1.250
$^{17}O+^{41}Ca$	61.800	1.240	0.528	8.270	1.270	0.727	1.250
$^{17}O+^{49}Ca$	97.000	1.210	0.497	59.700	1.140	0.422	1.250
$^{17}O+^{55}Fe$	66.800	1.210	0.531	41.600	1.200	0.585	1.250
$^{18}O+^{28}Si$	60.000	1.200	0.529	15.500	1.140	0.728	1.250
$^{18}O+^{40}Ca$	61.800	1.240	0.528	8.270	1.270	0.727	1.250
$^{18}O+^{48}Ca$	97.000	1.210	0.497	59.700	1.140	0.422	1.250
$^{18}O+^{54}Fe$	66.800	1.210	0.531	41.600	1.200	0.585	1.250
$^{32}S+^{27}Al$	100.000	0.800	0.500	100.000	0.800	0.500	1.250
$^{33}S+^{26}Al$	100.000	0.800	0.500	100.000	0.800	0.500	1.250

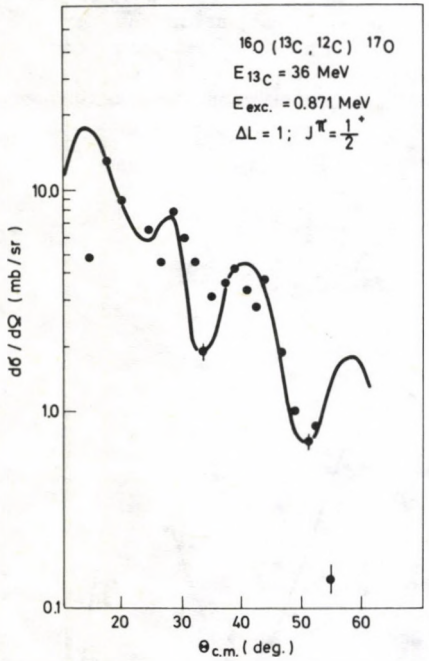

Fig. 1. Differential cross-section of the reaction $^{16}O(^{13}C, ^{12}C)^{17}O$ at ^{13}C incident energy 36 MeV, leaving the residual nucleus ^{17}O in its excited state 0.871 MeV. The solid curve is our present DWBA calculations. The optical model parameters are listed in Table I. The points are the experimental data and are taken from reference [10]

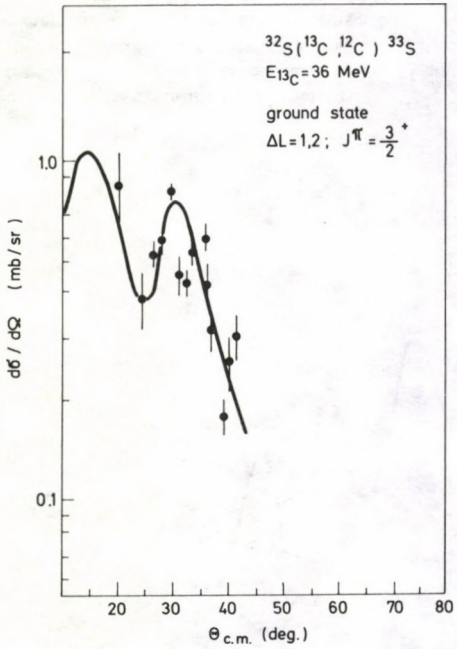

Fig. 2. Differential cross-section of the reaction $^{32}S(^{13}C, ^{12}C)^{33}S$ at ^{13}C incident energy 36 MeV, leaving the residual nucleus ^{33}S in its ground state. The solid curve is our present DWBA calculations. The optical model parameters are listed in Table I. The points are the experimental data and are taken from reference [10]

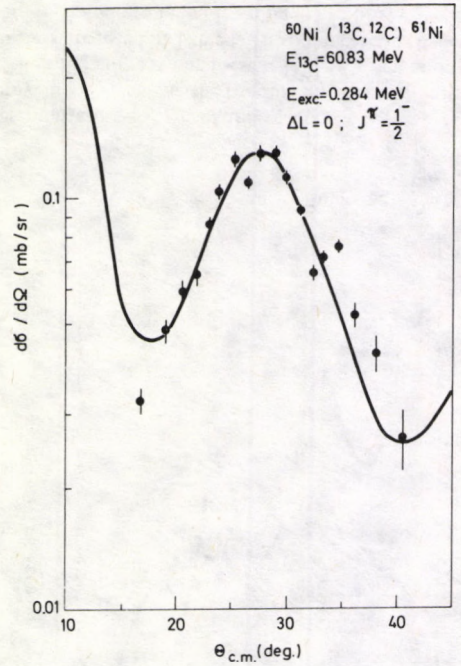

Fig. 3. Differential cross-section of the reaction $^{60}Ni(^{13}C, ^{12}C)^{61}Ni$ at ^{13}C incident energy 60.83 MeV, leaving the residual nucleus ^{61}Ni in its excited state 0.284 MeV. The solid curve is our present DWBA calculations. The optical model parameters are listed in Table I. The points are the experimental data and are taken from reference [6]

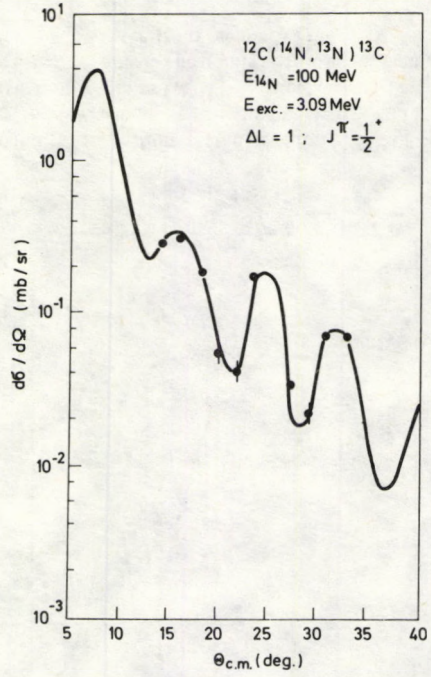

Fig. 4. Differential cross-section of the reaction $^{12}C(^{14}N, ^{13}N)^{13}C$ at ^{14}N incident energy 100 MeV, leaving the residual nucleus ^{13}C in its excited state 3.09 Mev. The solid curve is our present DWBA calculations. The optical model parameters are listed in Table I. The points are the experimental data and are taken from reference [14]

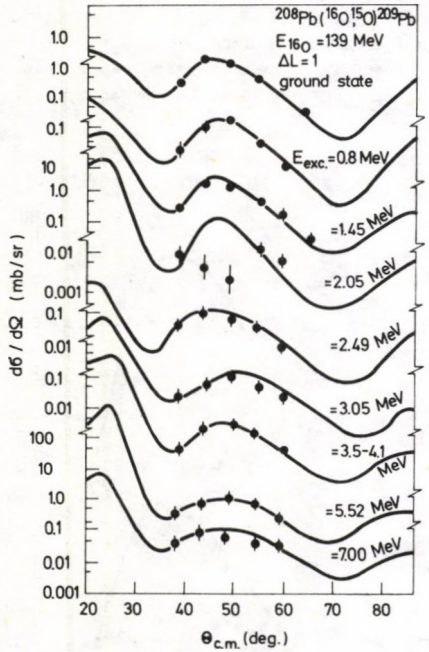

Fig. 5. Angular distributions of the reaction $^{208}Pb(^{16}O, ^{15}O)^{209}Pb$ at incident ^{16}O energy 139 MeV, leaving the ^{209}Pb residual nucleus in different excited states. The solid curve is our present DWBA calculations. The optical model parameters are listed in Table I. The points are the experimental data and are taken from reference [2]

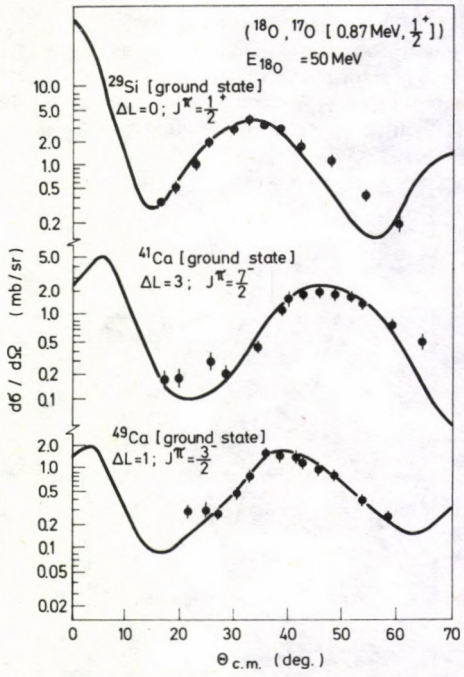

Fig. 6. The differential cross-sections of the reactions ^{28}Si, ^{40}Ca, $^{48}Ca(^{18}O, ^{17}O)$ at incident ^{18}O energy 50 MeV, leaving the residual nuclei in their ground states. The solid curve is our present DWBA calculations. The optical model parameters are listed in Table I. The points are the experimental data and are taken from reference [12]

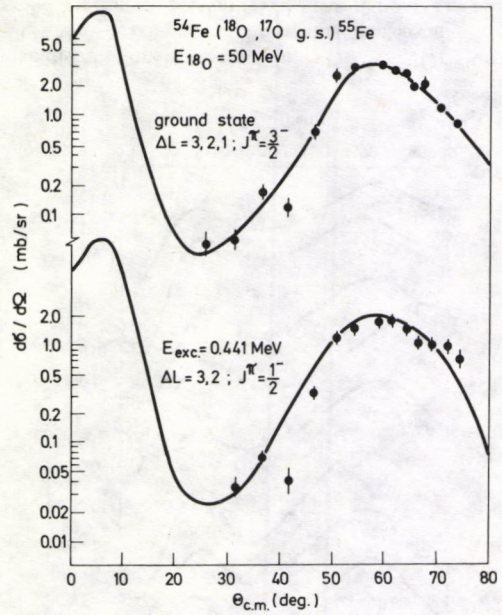

Fig. 7. The differential cross-sections of the reactions ^{52}Fe(^{18}O, ^{17}O)^{55}Fe at ^{18}O incident energy 50 MeV, leaving the residual nucleus ^{55}Fe in different excited states. The solid curve is our present DWBA calculations. The optical model parameters are listed in Table I. The points are the experimental data and are taken from reference [12]

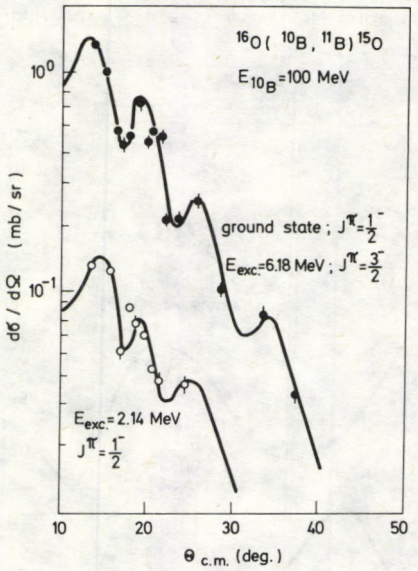

Fig. 8. Angular distribution of the reaction ^{16}O(^{10}B, ^{11}B)^{15}O at ^{10}B incident energy 100 MeV, leaving the residual nucleus ^{15}O in different exicted states. The solid curve is our present DWBA calculations. The optical model parameters are listed in Table I. The points are the experimental data and are taken from reference [4]

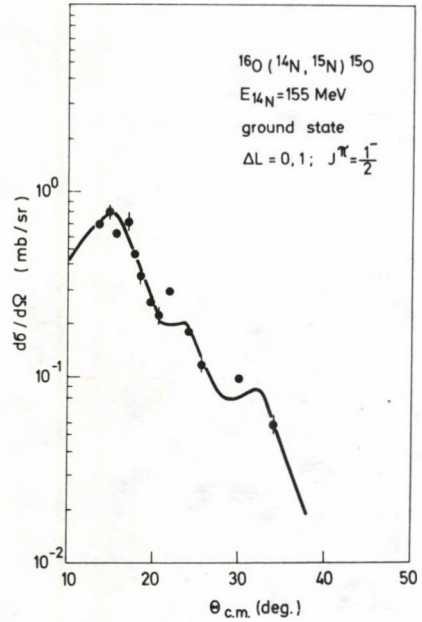

Fig. 9. Angular distribution of the reaction $^{16}O(^{14}N, ^{15}N)^{15}O$ at incident ^{14}N energy 155 MeV, leaving the ^{15}O residual nucleus in its ground state. The solid curve is our present DWBA calculations. The optical model parameters are listed in Table I. The points are the experimental data and are taken from reference [4]

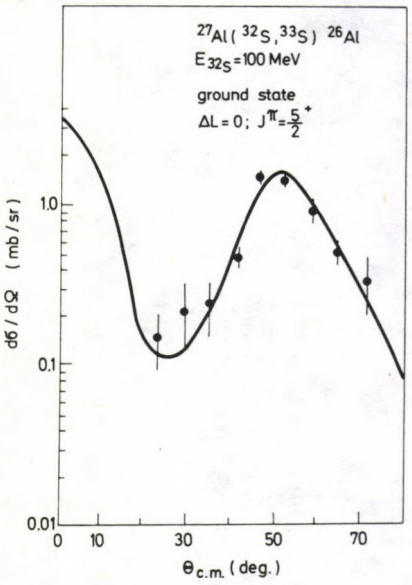

Fig. 10. Differential cross-section of the reaction $^{27}Al(^{32}S, ^{33}S)^{26}Al$ at incident ^{32}S energy 100 MeV, leaving the ^{26}Al residual nucleus in its ground state. The solid curve is our present DWBA calculations. The optical model parameters are listed in Table I. The points are the experimental data and are taken from reference [1]

experimental measurements taken from references [1], [2], [4], [6], [10], [12]–[14]. From the fitting of our present theoretically calculated angular distributions with the experimental measurements, spectroscopic factors are extracted. The extracted values of the spectroscopic factors are listed in Table II.

Table II

Extracted spectroscopic factors

Reaction	Incident energy [MeV]	Excitation energy [MeV]	L	J^π	Spectroscopic factors
$^{16}O(^{13}C, ^{12}C)^{17}O$	36.00	0.871	1	$\frac{1^+}{2}$	0.6138
$^{32}S(^{13}C, ^{12}C)^{33}S$	36.00	0.000	1, 2	$\frac{3^+}{2}$	0.6917
$^{60}Ni(^{13}C, ^{12}C)^{61}Ni$	60.83	0.284	0	$\frac{1^-}{2}$	0.7427
$^{12}C(^{14}N, ^{13}N)^{13}C$	100.00	3.090	1	$\frac{1^+}{2}$	0.7619
$^{208}Pb(^{16}O, ^{15}O)^{209}Pb$	139.00	0.000	1		0.6123
		0.800	1		0.6119
		1.450	1		0.6089
		2.050	1		0.5713
		2.490	1		0.6248
		3.050	1		0.6093
		3.500	1		0.6278
		5.520	1		0.6199
		7.000	1		0.6038
$^{28}Si(^{18}O, ^{17}O)^{29}Si$	50.00	0.000	0	$\frac{1^+}{2}$	0.7315
$^{40}Ca(^{18}O, ^{17}O)^{41}Ca$	50.00	0.000	3	$\frac{7^-}{2}$	0.7598
$^{48}Ca(^{18}O, ^{17}O)^{49}Ca$	50.00	0.000	1	$\frac{3^-}{2}$	0.7624
$^{54}Fe(^{18}O, ^{17}O)^{55}Fe$	50.00	0.000	3, 2, 1	$\frac{3^-}{2}$	0.6719
		0.441	3, 2	$\frac{1^-}{2}$	0.6934
$^{16}O(^{10}B, ^{11}B)^{15}O$	100.00	0.000	0, 1	$\frac{1^-}{2}$	0.7018
		2.140	0, 1	$\frac{1^-}{2}$	0.6985
$^{16}O(^{14}N, ^{15}N)^{15}O$	155.00	0.000	0, 1	$\frac{1^-}{2}$	0.7438
$^{27}Al(^{32}S, ^{33}S)^{26}Al$	100.00	0.000	0	$\frac{5^+}{2}$	0.7549

4. Discussion and conclusions

In the present work, we studied the heavy ion reactions with single neutron transfer. The theoretical calculations are carried out using DWBA calculations. In the present calculations, the parameters of the optical potentials are obtained by performing calculations of the elastic scattering differential cross-sections of the corresponding heavy ion reactions and fitting the theoretical calculations to the experimental data. Then, the optical model parameters are thus obtained and to be used in calculating the neutron transfer reactions between the heavy ions. Different reactions are considered between different heavy ions at different incident energies. The present theoretical calculations produce the oscillatory pattern as well as the maxima and minima of the experimental measurements. From Figs 1–10, we see that the present calculations fit the experimental measurements with good agreement of the angular distributions. Also the present calculations are able to get the right shape and produce the right peaks of the differential cross-sections. From this fitting, the values of the spectroscopic factors are obtained and are close to 1. Table II shows that better spectroscopic factors are extracted from the present calculations.

Thus, we can conclude that the present calculations for heavy ion reactions with single neutron transfer produce the right differential cross-sections in both magnitude and shape.

References

1. J. D. Garrett, H. E. Wegner, T. M. Cormier, E. R. Cosman, O. Hansen and A. J. Lazzarini, Phys. Rev., *C*12, 489, 1975.
2. F. D. Becchetti, B. G. Harvey, D. Kovar, J. Mahoney, C. Maguire and D. K. Scott, Phys. Rev., *C*12, 894, 1975.
3. F. D. Becchetti, B. G. Harvey, D. Kovar, J. Mahoney and M. S. Zisman, Phys. Rev., *C*10, 1346, 1974.
4. K. G. Nair, H. Voit, C. W. Towsley, M. Hamm, J. D. Bronson and K. Nagatani, Phys. Rev., *C*12, 1575, 1975.
5. A. Osman, Physics Letters, **34***B*, 478, 1971.
6. P. J. Moffa, C. B. Dover and J. P. Vary, Phys. Rev., *C*13, 147, 1976.
7. A. Osman, Phys. Letters, **37***B*, 135, 1971.
8. A. Osman, Particles and Nuclei, (U.S.A.) **3**, 28, 1972.
9. A. Osman, Atomkernenergie, **22**, 62, 1973.
10. G. D. Westfall and S.A.A. Zaidi, Phys. Rev., *C*14, 610, 1976.
11. A. Osman, Il Nuovo Cimento, **25***A*, 571, 1975.
12. J. F. Peterson, D. Dehnhard and B. F. Bayman, Phys. Rev., *C*15, 1719, 1977.
13. C. Olmer, M. Mermaz, M. Buonerd, C. K. Gelbke, D. L. Hendrie, J. Mahoney, D. K. Scott, M. H. Macfarlane and S. C. Pieper, Phys. Rev., *C*18, 205, 1978.
14. P. Nagel, Phys. Rev., *C*18, 2617, 1978.
15. N. K. Glendenning and R. J. Ascuitto, Phys. Lett., **47***B*, 332, 1973.
16. N. K. Glendenning, Rev. Mod. Phys., **47**, 659, 1975.
17. F. B. Morinigo, Phys. Rev., **134**, B 1243, 1964.

Acta Physica Hungarica 54 (1—2), pp. 41—48 (1983)

ENHANCED FABRY—PEROT FRINGE VISIBILITY OVER LONG PATH DIFFERENCES USING Se-MgF_2 . . . MULTILAYER COATINGS

S. MOKHTAR, M. S. SHAALAN and W. OSMAN

Length Metrology Department, National Institute of Standards, Cairo, Egypt

(Received in revised form 24 November 1981)

The optical constants of selenium are determined in the red end of the visible spectrum. Reflection and phase characteristics of Se single films are obtained. Highly reflecting Fabry—Perot mirrors are constructed from semiconducting Se films with high refractive index in alteration with dielectric MgF_2 films at λ 644 nm. Reflection coefficients 68%, 74% and 87% were realized for 3, 5 and 7 layer coatings with negligible absorption. Clearly visible F—P fringes are obtained up to Path Differences of 0.12 m, 0.14 m and 0.18 m for the cases of 3, 5 and 7 layer coatings, respectively, employing ordinary sources of spectral radiation.

1. Introduction

Fabry—Perot etalons play an important role in length metrology laboratories, both in absolute wavelength measurement and in investigations concerning properties qualifying certain wavelengths as standards. The half-width and visibility of the F—P fringes are factors of paramount importance. They are both functions of the reflection coefficient of the interferometer's coatings and their spectral dependence [1].

In this paper a multilayer coating system on glass substrate for use at the red end of the visible spectrum is described. Alternate films of semiconductor selenium and dielectric MgF_2 in three, five and seven layers produced high reflection, very low absorption and enhanced visiblity of F—P fringes over relatively longer Path Differences using ordinary spectral radiation sources, thus improving over the use of Ag or Al.

Selenium films were used for their negligible absorption in the red part of the visible spectrum, their ease of evaporation in vacuum and their high refractive index.

* Now on leave to the Physics Department, Faculty of Science, King Abdulaziz University, Jeddah, P. O. Box. 9028, Saudi Arabia.

2. The optical constants of selenium

Selenium optical constants n and k, where $\hat{n} = n - ik$, were determined previously by several workers (Koehler [2], Prosser [3]. Subashiev et al. [4] and Miloslavskii [5]). Techniques based on photometric and polarimetric measurements were used. A method due to Valeev [6] employed transmission measurements of the bare and coated substrate respectively over a wavelength range. He applied the method in case of CdTe films in the i.r. Nomograms were used to extract data on n and k as function of λ. This method is applied here in the visible region in the λ range 600 – 800 nm. For details of the calculations reference [6] may be consulted.

Table I

The optical constants of selenium experimentally determined for a film of a thickness of 700 nm

λ [nm]	Present work		Koehler's results	
	n	k*	n	k
600	2.90	0.029	2.90	0.06
650	2.65	0.026	2.75	0
700	2.63	0.021	2.67	0
750	2.60	0.019	2.63	0
800	2.56	0.018	2.60	0

* Third decimal figures are indicative.

In this work the transmission vs λ information for the uncoated and coated substrate was obtained employing a Zeiss PMQ III spectrophotometer. Values of T are reliable to ± 0.01. Measurements were performed on a Se film of thickness 700 nm determined by weight and a calibrated Edward's crystal oscillator thickness monitor. Thickness of that order approximates quite closely to the bulk behaviour. Selenium was thermally evaporated under vacuum of 10^{-6} mbar onto optically flat substrates to ± 0.001 mm and left in vacuum to attain room temperature. No substrate heating took place. The experimentally determined values of n and k in the wavelength range 600 – 800 nm are given in Table I. Koehler's results [2] in a similar range are included for comparison.

3. Reflection characteristics of single selenium films

Reflection vs wavelength characteristics were obtained for three Se films using a specially designed reflection attachment to the Zeiss PMQ III spectrophotometer. Three films of thickness 160, 180 and 200 nm were deposited in vacuum of 10^{-6} mbar. Thickness was determined interferometrically using Tolansky's method [7]. Values of

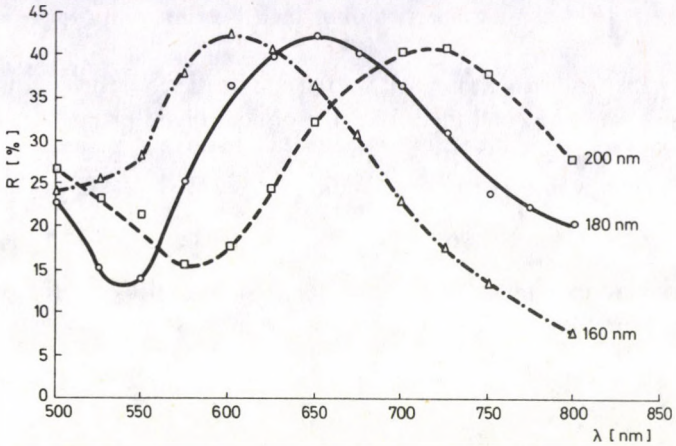

Fig. 1. Experimental variation of the reflectivity of single Se films with wavelength

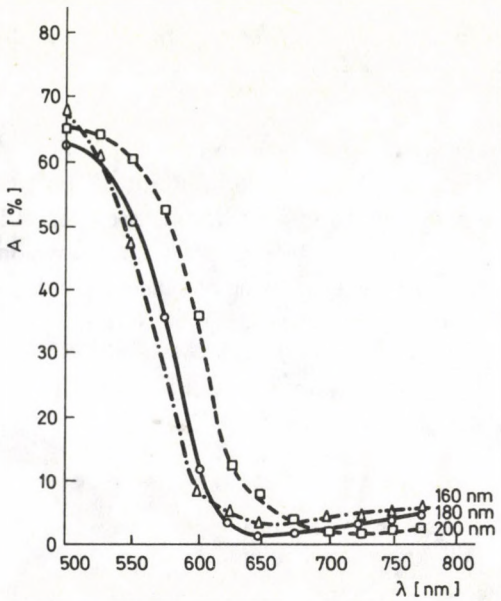

Fig. 2. Experimental variation of absorption of single Se films with wavelength

d are subject to inaccuracies of the order of 1.5 nm. Fig. 1 shows the variation of reflectivity R with wavelength λ at the interface air/film. A film of $d=180$ nm increases the reflectivity of the bare glass substrate from 4% to some 42% at $\lambda=644$ nm with $(nd/\lambda)=0.74$ over a fairly broad band. Fig. 2 shows the variation of the absorption $A=(T+R)-1$, for the three films, with λ. A is less than 2% at λ 44 – 655 nm.

4. The optical phase properties of a single Se film with $(nd/\lambda)=0.75$

The low absorption of Se films in the red and its dielectric behaviour beyond this region in the i.r. may be confirmed from the optical phase properties. According to Born and Wolf [8] the optical phase function F for non-absorbing thin films at a certain wavelength would satisfy the condition

$$F=(2\gamma-B_1-B_2)=(2n\pm 1)\pi,$$

where γ is the change of phase in transmission and B_1 and B_2 are the phase changes upon reflection air/film and dielectric substrate/film, respectively.

Table II

The optical phase properties of a Se single film of thickness $d=180$ nm at $\lambda=644$ nm with $(nd/\lambda)=0.74$

γ	B_1	B_2	$F=(2\gamma-B_1-B_2)$
0.54π	1.01π	1.03π	-0.96π

These phase changes have been determined for a Se film of $d=180$ nm $\pm$ 1.5 nm at $\lambda=644$ nm with $(nd/\lambda)=0.74$ using a two-beam interferometric method previously reported by Barakat et al [9], [10], [11]. The results are given in Table II. The changes of phase are estimated to be accurate to $\pm 6^\circ$ or 0.033π corresponding to some 0.03 of an order separation in the two-beam interference system employed at $\lambda=644$ nm. The order separation is $\lambda/2$. It is clear then that selenium may be expected to behave very nearly as a dielectric in the longer wavelength region of the visible spectrum. This has encouraged its use in multilayer systems exploiting its high refractive index and ease of vacuum evaporation.

5. Se-MgF_2 ... multilayer coatings on glass substrates for $\lambda=644$ nm

The multilayer coating system using Se films of thickness $d=180$ nm and MgF_2 of $\lambda/4$ at $\lambda=644$ nm was prepared on glass substrates by thermal evaporation in vacuum of less than 10^{-6} mbar. Film thickness was controlled during evaporation using an interferometrically calibrated thickness control unit manufactured by Edward's.

Fig. 3 represents the experimental variation of reflectivity with wavelength for three, five and seven layers of Se—MgF_2—Se .... The reflection coefficient is maximum at $\lambda=650$ nm reaching 87% of the incident intensity for the seven layers coating.

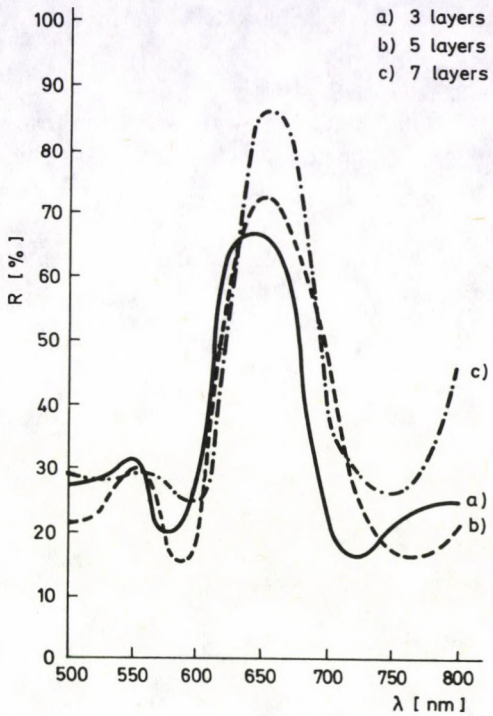

Fig. 3. Experimental variation of reflectance with wavelength for three, five and seven layer Se—MgF_2 ... coatings

Table III

Computed and experimental reflectances of 3, 5 and 7 layer coatings Se—MgF_2—Se

Number of layers	Comp. Ref.	Exp. Ref.
3 layers Se—MgF_2—Se	69%	67%
5 layers Se— ... Se	79%	74%
7 layers Se— ... Se	90%	87%

A computer program was written using a formula due to Vasicek [12] and the Koehler [2] optical constants for selenium to compute the reflectance of 3, 5 and 7 layer coatings. Experimental and computed results are presented in Table III.

6. Experimental variation of F−P fringe visibility with the interferometer's Path Differences

The optical arrangement for securing F—P fringes in transmission is illustrated in Fig. 4. Fringes were photographed on panchromatic glass photographic plates. The plates were calibrated for the red line of $\lambda 644$ nm. A microdensitometer was used to determine maximum and minimum intensities of transmission fringes. Interferometer's plate separations were measured using a special head internal distances measuring

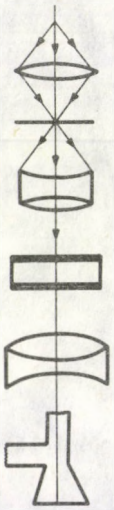

Fig. 4. The optical arrangement for securing F—P transmission fringes

Table IV

Maximum Path Differences at which F—P fringes are visible employing Se—MgF_2 . . . coatings at $\lambda = 644$ nm

Number of layers	Reflectivity	Fringes visible	Fringes vanish
three	67%	at 0.12 m	at 0.20 m
five	74%	at 0.14 m	at 0.23 m
seven	87%	at 0.18 m	at 0.28 m

micrometer. Three cases were investigated where the interferometer's inner surfaces were coated with 3, 5 and 7 layers Se—MgF_2 . . . coatings of reflectivities 67%, 74% and 87%, respectively. Table IV gives the maximum Path Differences at which fringes were still reasonably resolved and visible together with the distances at which they completely vanished.

Fig. 5 shows the experimental variation of V with the interferometer's Path Differences. Plates 1, 2 represent fringes obtained at Path Differences 0.10 and 0.18 m, respectively, for the case of a 7 layer coating.

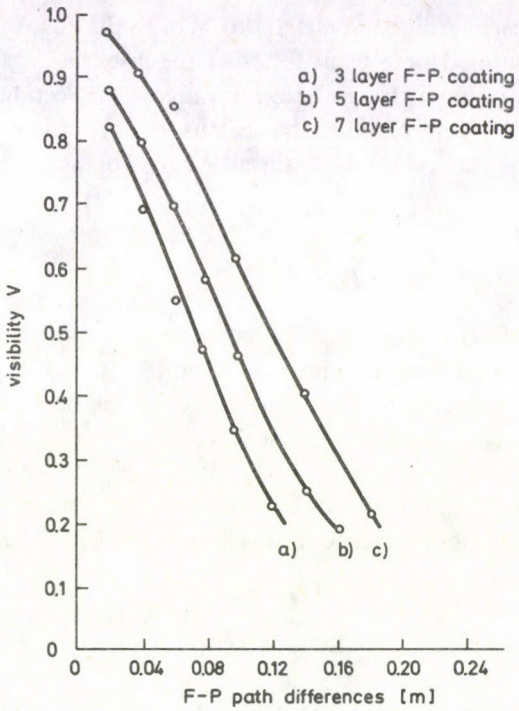

Fig. 5. The variation of the visibility of F—P transmission fringes with the Path Differences

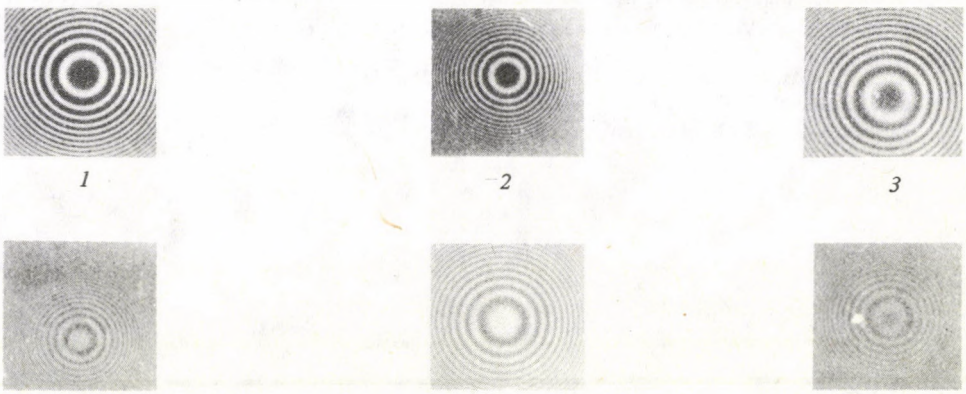

Plates 1—6. 1. F—P rings at a plate separation of 10 cm in case of 7 layer coating. *2.* F—P rings at a plate separation of 18 cm in case of 7 layer coating. *3.* F—P rings at a plate separation of 8 cm in case of 5 layer coating. *4.* F—P rings at a plate separation of 14 cm in case of 5 layer coating. *5.* F—P rings at a plate separation of 10 cm in case of 3 layer coating. *6.* F—P rings at a plate separation of 12 cm in case of 3 layer coating

Plates 3, 4 represent fringes for 0.8 and 0.14 m in the case of 5 layers coating. Plates 5, 6 are those obtained for 0.10 and 0.12 m in the case of a 3 layer coating. It must be noted that loss of definition in fringes belonging to lower reflection coatings is due in an appreciable part to loss of collected beams due to their escape from the interferometer's edges, an effect masterly discussed by Tolansky [1].

7. Discussion

The refractive index values obtained for a Se film of thickness 700 nm are proved to be somewhat lower than those obtained by Koehler [2]. This may explain the 2% difference between computed and experimental reflection coefficients in Table III where computed values are based upon the Koehler constants. However, the high reflection coefficients allowed the use of the Se—MgF_2 ... multilayers as F—P mirrors permitting long Path Differences up to 0.18 m using ordinary spectral sources. This would facilitate interferometric applications in length metrology experimentations.

References

1. S. Tolansky, High Resolution Spectroscopy, Methuen and Co. Ltd. London, 1947.
2. W. F. Koehler, F. K. Odencrant and W. C. White, J.O.S.A., **44,** 109, 1959.
3. V. Prosser, Czech. J. Phys., **10,** 304, 1960.
4. V. K. Subshiev et al, Sov. Phys., Solid State (USA), **6,** 830, 1964.
5. V. K. Milostaveskii and S. Lyashenko, Optics and Spectroscopy, **16,** 80, 1964.
6. A. S. Valeev, Optics and Spectroscopy, **4,** 269, 1963.
7. S. Tolansky, Multiple-Beam Interferometry, London, O.U.P., 1948., p. 149.
8. Born and E. Wolf, Principles of Optics, Pergamon Press, Oxford, 1970.
9. N. Barakat and S. Mokhtar, J.O.S.A., **53,** 1153, 1963.
10. N. Barakat, S. Mokhtar and Abdel-Hadi, J.O.S.A., **54,** 213, 1964.
11. N. Barakat and N. El Kadry, J.O.S.A., **60,** 4, 1970.
12. A. Vasicek, Optics of Thin Films, p. 159, 1960.

Acta Physica Hungarica 54 (1—2), pp. 49—63 (1983)

AN X-RAY STUDY OF As–Se–Te COMPOUNDS

M. F. KOTKATA, A. M. SHAMAH, M. B. EL-DEN and M. K. EL-MOUSLY

Physics Department, Faculty of Science, Ain Shams University, Cairo, Egypt

(Received 26 November 1981)

X-ray measurements of the crystalline and amorphous states of $AsSe_{y-x}Te_x$ compounds, with $y=1.0$ and 2.5 and with $0<x<y$, have shown that the structure of the parent alloys is very sensitive to the addition of Te. Changes with composition and structural features have been discussed and compared with the stoichiometric system As_2Se_3–As_2Te_3. Interplanar spacings, d_{hkl}, and relative intensities, RI, of the recorded reflections are given here for the first time. Two phases, denoted as α- and γ-phases, have been found to exist at $\simeq 20$, 10 and 14 at% Te, for $AsSe_{1-x}Te_x$, $AsSe_{1.5-x}Te_x$, and $AsSe_{2.5-x}Te_x$ systems, in their crystalline states. When Se : Te is equal to 2 : 1, a type of ordering is suggested, similar to either of Bi_2Te_2Se or of As_2Se_3S. The diffraction patterns for the amorphous compounds give a "three stepped hump" pattern with maximum intensity of the second hump step.

1. Introduction

Much work has been done recently on the thermal, electrical and optical properties of the arsenic chalcogenide glasses. Compounds of the type As_2X_3, where X = S, Se, Te, as well as their mixed materials are particularly interesting as they may be obtained as well in crystalline as in glassy forms. In such cases a clear understanding of the properties of the crystalline state can provide a foundation for the investigation of the glassy materials.

Earlier investigations [1 – 3] showed a short-range order for the amorphous As_2Se_3 similar to that of the analogous crystal orpiment, As_2S_3. The texture of As_2Te_3 which possesses a layer structure like that of As_2Se_3 and As_2S_3 suggests a mechanism for the dependence of layer structure on composition [1, 4]. The change in structure with the increase of the coordination number in As_2Te_3 and As_2Se_3 takes place by "wrinking" of the layers. The unit cell of both As_2Se_3 and As_2Te_3 is monoclinic. The latter consists of zigzag chains in which the As atoms are octahedrally and trigonally bonded to Te atoms.

Mixed systems of binaries such as As_2Se_3–As_2Te_3 and As_2Se_3–As_2S_3 have been the subject of detailed investigations [1, 5–8]. The compositional dependence of properties in an alloy system As–Se–Te has also been studied [9, 10]. In the present report, the structural changes with the composition of As–Se–Te compounds have been studied in both glassy and crystalline forms by X-ray diffraction.

2. Sample preparation and X-ray measurements

Three series of As–Se–Te compounds of the general formula $AsSe_{y-x}Te_x$, with $y = 1.0, 1.5$ and 2.5, and with $0 < x < y$, have been prepared as bulk glasses by quenching from the melts [9, 10]. The corresponding polycrystalline forms are obtained by annealing the glassy samples at temperatures between their softening and crystalline temperatures, T_g–T_c, for different soaking times. These are varied between 160-to-260 °C, and between 7-to-60 h, depending on the composition of the examined material [11]. After each annealing period, the sample was left to cool in the oven.

The amorphous and crystalline states have been determined by X-ray diffraction. The amorphous phase yields a diffuse pattern whereas sharp lines indicate the crystalline state. The samples were ground in a quartz mortar to obtain samples in a powder form. A smooth powder specimen surface is produced by mixing the powder with glass in an aluminium holder.

An up-to-date Philips diffractometer has been used with CuKα radiation. The scanning rate (2°/min) and the general operating conditions were kept constant all over the investigation. However, a slow scan, (1/8°/min), was used whenever it proved necessary.

3. Results and discussion

3.1. The amorphous state

The X-ray diffraction patterns for the amorphous $AsSe_{1-x}Te_x$ and $AsSe_{2.5-x}Te_x$ systems are shown in Figs 1 and 2, respectively. The patterns are quite similar to those obtained for the As_2Se_3–As_2S_3 [12], As_2Se_3–As_2Te_3 [5], and for the $(As_2Se_3)_{1-x}(Tl_2Se_3)_x$ [13] glassy compounds. The diffraction patterns show a three stepped hump around the Bragg angles; 12–21, 21–44 and 44–60 degrees, for the first, second, and third step, respectively. The second hump has the highest intensity for the two systems and also occupies the largest angular range. This means that the second step possesses the highest contribution of diffracting atomic planes in the present domains. This has been justified by comparing the diffraction patterns for glassy and crystalline samples of AsSe and $AsSe_{2.5}$, as shown in Figs 3 and 4. These Figures show the presence of the highest number of strongly reflecting planes in the region of the second hump.

As Figs 1 and 2 show, the diffraction patterns of the investigated glassy materials depend on the composition, where a shift of the apex of the second hump step is found in addition to the gradual decrease in intensity of the first step. The displacement in the apex position of the second hump is gradual and monotonic with composition. This is a strong evidence in favour of the assumption that the stepped hump, characteristic of Arsenic-Chalcogenide glasses, is due to the existence of highly reflecting planes of countless randomly distributed diffracting domains in the angular position corresponding to each step.

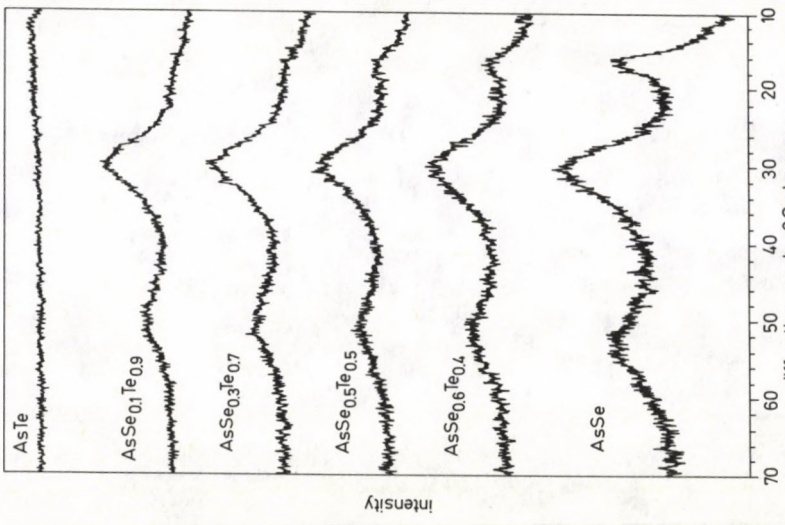
AsTe
AsSe0,1Te0,9
AsSe0,3Te0,7
AsSe0,5Te0,5
AsSe0,6Te0,4
AsSe
intensity
10
20
30
40
50
60
70
diffraction angle 2Θ, degree

Fig. 1

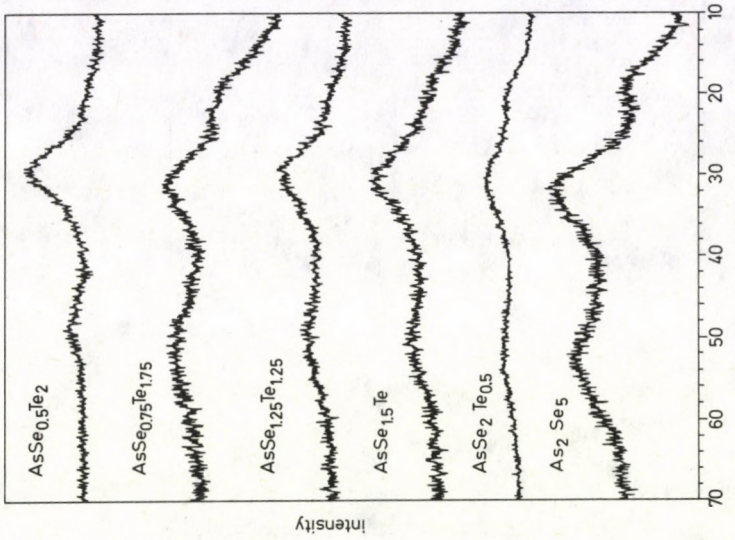
AsSe0,5Te2
AsSe0,75Te1,75
AsSe1,25Te1,25
AsSe1,5Te
AsSe2 Te0,5
As2 Se5
intensity
10
20
30
40
50
60
70
diffraction angle 2Θ, degree

Fig. 2

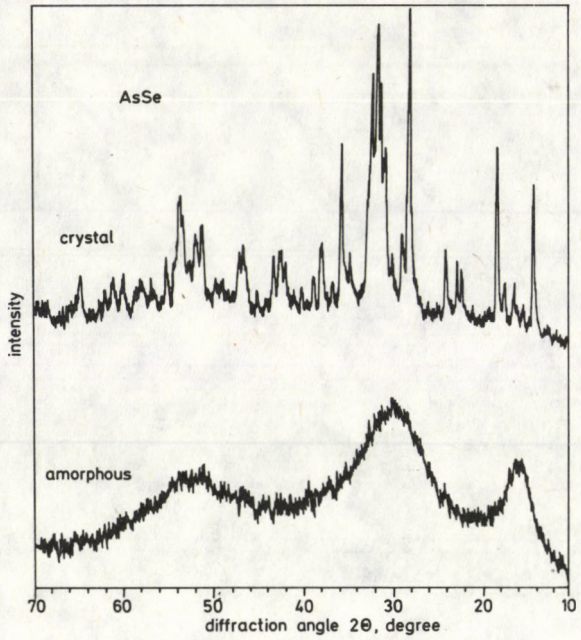
AsSe
crystal
amorphous
intensity
70
60
50
40
30
20
10
diffraction angle 2Θ, degree

Fig. 3

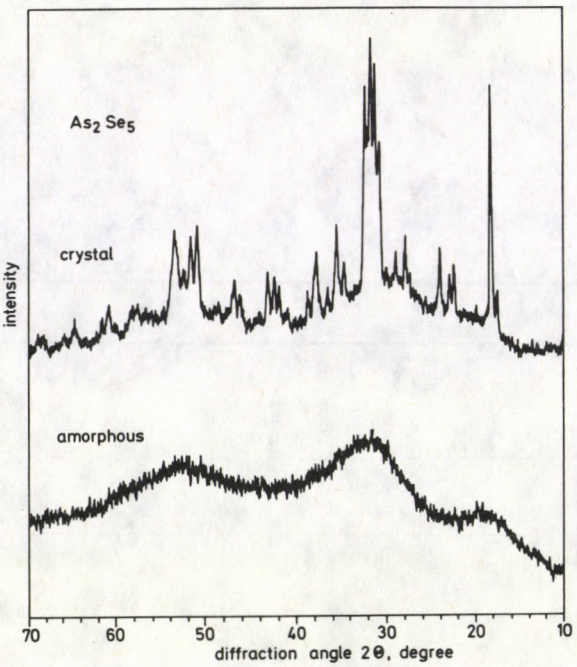
As2 Se5
crystal
amorphous
intensity
70
60
50
40
30
20
10
diffraction angle 2Θ, degree

Fig. 4

3.2. The crystalline state

A: The AsSe–AsTe system

The X-ray diffraction patterns obtained for the AsSe, $AsSe_{0.6}Te_{0.4}$, $AsSe_{0.5}Te_{0.5}$, $AsSe_{0.3}Te_{0.7}$, $AsSe_{0.1}Te_{0.9}$ and AsTe compounds in their crystalline states are depicted in Fig. 5. The Figure shows that the addition of Te to the parent AsSe is accompanied by changes in the diffraction patterns. The strong effect is well demonstrated by the AsSe and $AsSe_{0.1}Te_{0.9}$ diffraction patterns.

The differences in the diffraction pattern of AsSe due to the addition of 20 at% Te, i.e. the composition of $AsSe_{0.6}Te_{0.4}$, might be summarized as follows: i) Around $2\Theta = 16$–$20°$, three peaks ($d = 0.5639$, 0.5149 and 0.426 nm) disappeared and the inten-

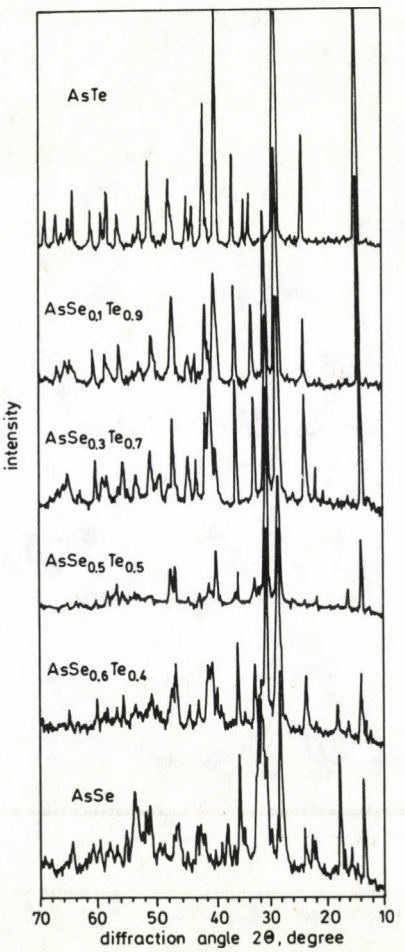

Fig. 5

sity of another peak ($d = 0.4978$ nm) is reduced by about 73%. ii) The intensities of the two peaks around $2\Theta = 22°$ ($d = 0.4032$ and 0.3955 nm) as well as those around $2\Theta = 38°$ ($d = 0.2384$ and 0.2337 nm) disappeared. iii) Around $2\Theta = 30$–$32°$, the peak intensities of the lines of $d = 0.2893$ nm, 0.2866, 0.2805 and 0.2775 nm are reduced by 70, 75, 35 and 35%, respectively. Besides, a well resolved peak developed at $d = 0.283$ nm. iv) The shape of the peaks around $2\Theta = 50$–$54°$ changed.

The changes in the positions, intensities, and shapes of the peaks indicate changes in the AsSe structure due to additional Te atoms. Since the general appearance of the diffraction patterns for AsSe and $AsSe_{0.6}Te_{0.4}$ is the same, the new structure might be considered as a phase based on the AsSe structure where Te atoms might substitute the Se atoms. In other words, a solid solution based on AsSe structure developed, which might be called α-phase. However, the appearance of new lines in the diffraction pattern of $AsSe_{0.6}Te_{0.4}$ indicates the formation of a new phase, which we may call a γ-phase. The two phases might be referred to as a rich Se phase (α-phase), and poor Se phase (γ-phase).

This means that about 20 at% Te in $AsSe_{1-x}Te_x$ compounds is accompanied by phase separation. For compounds of larger Te content, namely $AsSe_{0.5}Te_{0.5}$, $AsSe_{0.3}Te_{0.7}$ and $AsSe_{0.1}Te_{0.9}$, the changes in the diffraction pattern of $AsSe_{0.6}Te_{0.4}$ mentioned above are increased. This indicates that the increase of the number of Te atoms in $AsSe_{1-x}Te_x$ is accompanied by greater changes in the AsSe structure.

By using the AsTe diffraction pattern obtained under the same conditions, it was possible to determine the Bragg lines of the γ-phase (Fig. 5).

Quantitative measurements have been made by measuring the d-spacing for every line in the pattern of each compound together with their relative intensities (I/I_0). The respective data are summarized in Table I. The Table confirms the disappearing and the development of lines as mentioned before. This indicates the formation of the two phases.

An attempt has been made to determine the ratio of the two phases for each compound. The results are collected in Table II.

From the above discussion it can be concluded that phase separation takes place when the Te content reached about 20 at% in the $AsSe_{1-x}Te_x$ compounds.

B: The As_2Se_5–As_2Te_5 system

The X-ray diffraction patterns obtained from the investigated crystalline samples of the $AsSe_{2.5-x}Te_x$ system are presented in Fig. 6. One may conclude from these patterns that some changes are due to the introduction of Te atoms in the parent As_2Se_5. By comparing the patterns of $AsSe_{2.5}$ and $AsSe_{2.0}Te_{0.5}$, clear changes are visible in the ranges $2\Theta = 28$–$30°$, 40–46° and 50–56°. These changes appear as new lines in the diffraction pattern, together with a small shift of the positions of the other lines (2Θ) of the parent sample. The same argument given for the $AsSe_{1-x}Te_x$ system may be applied here, and one may suggest that a phase separation takes place at about

Table I

Measured d-spacing and relative intensities for the observed reflections of the examined compounds of the system $AsSe_{1-x}Te_x$

AsSe		$AsSe_{0.6}Te_{0.4}$		$AsSe_{0.5}Te_{0.5}$		$AsSe_{0.3}Te_{0.7}$		$As_{0.1}Te_{0.9}$		AsTe	
d [nm]	RI	d [nm]	RI	d [nm]	RI	d [nm]	RI	d [nm]	RI	d [nm]	RI
0.6414	50	0.6415	56	0.6364	31	—	—	—	—	—	—
—	—	—	—	—	—	0.6321	71	0.6321	68	0.6325	69
0.5600	15	0.5600	5	—	—	0.5600	3	0.5600	3	—	—
—	—	—	—	0.5466	8	—	—	—	—	—	—
0.4978	59	0.4978	7	—	—	—	—	—	—	—	—
0.4032	17	—	—	—	—	—	—	—	—	—	—
0.3955	20	—	—	—	—	—	—	—	—	—	—
0.3861	7	—	—	—	—	—	—	—	—	0.3850	32
—	—	0.3827	16	0.3811	3	0.3827	37	0.3827	20	—	—
0.3764	22	0.3750	3	—	—	—	—	—	—	—	—
0.3463	5	—	—	—	—	—	—	—	—	0.3326	6
—	—	—	—	0.3238	14	—	—	—	—	—	—
0.3200	100	0.3202	100	—	—	0.3192	100	0.3202	100	0.3186	100
—	—	0.3159	73	—	—	—	—	—	—	—	—
0.3055	12	—	—	—	—	—	—	0.3043	7	—	—
0.3015	20	0.3026	9	—	—	0.3973	30	0.3973	24	0.3978	5
—	—	0.2965	53	0.2966	66	—	—	—	—	—	—
0.2944	55	—	—	—	—	—	—	—	—	—	—
0.2893	75	—	—	0.2933	100	—	—	0.2890	4	—	—
0.2866	93	0.2857	12	0.2840	8	—	—	—	—	—	—
—	—	0.2830	10	—	—	—	—	—	—	—	—
0.2805	79	0.2805	8	—	—	—	—	—	—	—	—
0.2775	49	0.2770	17	—	—	—	—	0.2763	24	—	—
—	—	—	—	0.2755	12	—	—	—	—	0.2755	15
—	—	—	—	0.2740	9	—	—	—	—	—	—
0.2607	20	—	—	—	—	—	—	—	—	—	—
0.2550	55	0.2541	22	0.2534	14	0.2529	41	0.2529	31	0.2528	28
0.2474	10	0.2474	3	—	—	—	—	—	—	—	—
0.2394	22	—	—	—	—	—	—	—	—	—	—
0.2384	21	—	—	—	—	—	—	—	—	—	—
0.2337	12	0.2350	6	0.2337	5			0.2337	20	0.2338	69
0.2263	8	0.2253	18	0.2253	7	0.2253	47	0.2253	13	—	—
—	—	0.2220	17	0.2225	11	—	—	0.2225	24	0.2243	8
—	—	—	—	—	—	—	—	—	—	0.2217	40
0.2185	9	—	—	0.2191	4	—	—	—	—	—	—
0.2165	17	—	—	—	—	—	—	—	—	—	—
0.2141	21	—	—	0.2141	6	—	—	—	—	—	—
0.2136	20	0.2131	8	—	—	0.2126	14	0.2126	9	—	—
—	—	—	—	—	—	—	—	—	—	0.2117	13
0.2066	5	0.2057	7	0.2057	3	0.2057	16	0.2080	10	0.2076	16
0.2020	8	—	—	—	—	—	—	—	—	0.2026	3
—	—	—	—	—	—	—	—	—	—	0.2969	15
0.1960	23	0.1960	17	0.1956	17	0.1952	27	0.1952	27	0.1963	21
0.1944	20	0.1941	11	0.1924	21	0.1924	6	—	—	0.1922	5
0.1845	11	0.1845	6	—	—	0.1841	7	0.1845	8	0.1866	4
—	—	0.1810	10	—	—	—	—	—	—	0.1831	26
—	—	0.1800	8	0.1803	5	0.1806	17	—	—	—	—

Table I. (cont.)

AsSe		$AsSe_{0.6}Te_{0.4}$		$AsSe_{0.5}Te_{0.5}$		$AsSe_{0.3}Te_{0.7}$		$As_{0.1}Te_{0.9}$		AsTe	
d [nm]	RI	d [nm]	RI	d [nm]	RI	d [nm]	RI	d [nm]	RI	d [nm]	RI
0.1796	29	—	—	—	—	—	—	—	—	—	—
0.1771	26	—	—	0.1771	4	—	—	0.1774	7	0.1774	9
—	—	—	—	0.1750	6	—	—	0.1758	7	0.1752	5
0.1734	32	0.1734	6	—	—	0.1743	8	—	—	—	—
0.1719	39	—	—	0.1721	6	—	—	0.1727	4	—	—
0.1760	18	0.1668	7	0.1663	6	0.1668	13	0.1663	12	0.1667	9
—	—	0.1650	5	—	—	0.1650	5	—	—	—	—
—	—	—	—	0.1634	10	—	—	—	—	—	—
0.1625	12	—	—	0.1625	5	—	—	—	—	—	—
—	—	—	—	—	—	—	—	0.1600	9	0.1613	17
0.1595	14	0.1596	5	0.1595	6	0.1597	8	—	—	0.1595	9
0.1582	9	0.1582	4	—	—	0.1580	8	—	—	—	—
0.1553	15	0.1551	8	—	—	—	—	—	—	0.1549	11
—	—	—	—	0.1545	5	0.1545	15	0.1537	11	—	—
0.1525	14	—	—	—	—	—	—	—	—	—	—
0.1507	10	—	—	—	—	—	—	—	—	—	—
0.1490	8	—	—	—	—	—	—	—	—	0.1473	17
—	—	—	—	—	—	—	—	0.1454	6	0.1455	9
0.1445	16	0.1442	5	—	—	0.1442	10	0.1441	9	0.1439	5
0.1435	9	—	—	—	—	—	—	—	—	—	—
—	—	—	—	—	—	0.1405	5	0.1411	9	0.1415	10
—	—	—	—	—	—	—	—	—	—	0.1378	11
—	—	0.1351	5	—	—	—	—	0.1350	8	0.1351	6

Table II

α-phase/γ-phase ratio in $AsSe_{1-x}Te_x$ compounds

Composition	Percentage of atoms			(γ/α) ratio
	As	Se	Te	
AsSe	50	50	—	—
$AsSe_{0.6}Te_{0.4}$	50	30	20	26.4
$AsSe_{0.5}Te_{0.5}$	50	25	25	17.5
$AsSe_{0.3}Te_{0.7}$	50	15	35	38.8
$AsSe_{0.1}Te_{0.9}$	50	5	45	48.5
AsTe	50	—	50	—

14 at% Te. The rich Se phase might be called α-phase, and the poor one γ-phase. The two phases might be referred to as a solid solution of As, Se and Te atoms.

This phase separation appears also in the compounds of a higher Te content, i.e. in $AsSe_{1.5}Te$, $AsSe_{1.25}Te_{1.25}$, $AsSe_{0.75}Te_{1.75}$ and $AsSe_{0.5}Te_2$.

Two methods have been adopted to confirm the formation of two phases in the $AsSe_{2.5-x}Te_x$ system by measuring both the d-spacing and lattice parameters. Table III summarizes the measured d values for the Bragg reflection together with the

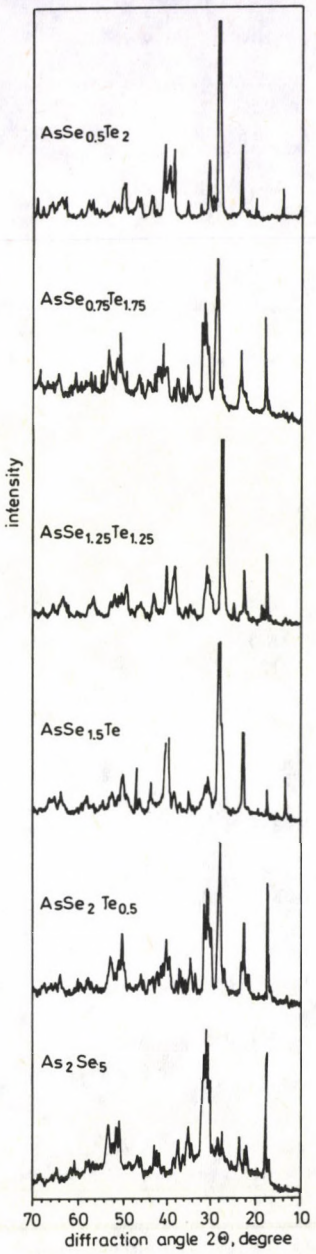
AsSe0.5Te2
AsSe0.75Te1.75
AsSe1.25Te1.25
AsSe1.5Te
AsSe2 Te0.5
As2Se5
intensity
70 60 50 40 30 20 10
diffraction angle 2Θ, degree

Fig. 6

Table III

Measured d-spacing and relative intensities for the observed reflections of examined compounds of the system $AsSe_{2.5-x}Te_x$

$AsSe_{2.5}$		$AsSe_2Te_{0.5}$		$AsSe_{1.5}Te$		$AsSe_{1.25}Te_{1.25}$		$AsSe_{0.75}Te_{1.75}$		$AsSe_{0.5}Te_2$	
d [nm]	RI	d [nm]	RI	d [nm]	RI	d [nm]	RI	d [nm]	RI	d [nm]	RI
—	—	—	—	—	—	—	—	0.7200	6	—	—
—	—	—	—	—	—	—	—	0.6660	5	—	—
—	—	—	—	—	—	0.6414	4	0.6414	6	—	—
—	—	—	—	0.6361	8	—	—	—	—	—	—
—	—	—	—	—	—	—	—	—	—	0.6277	10
—	—	0.5149	9	—	—	—	—	—	—	—	—
0.5116	19	—	—	—	—	0.5116	5	0.5117	12	—	—
—	—	—	—	0.4952	12	—	—	—	—	—	—
0.4929	89	—	—	—	—	0.4929	35	0.4929	66	—	—
0.4208	25	—	—	—	—	—	—	—	—	—	—
—	—	0.4032	16	0.4032	4	0.4032	5	0.4032	13	—	—
0.3911	22	0.3911	16	—	—	0.3861	27	0.3928	14	—	—
—	—	0.3811	49	0.3811	35	—	—	0.3811	42	0.3200	24
—	—	—	—	—	—	0.3764	7	0.3750	18	—	—
0.3748	30	0.3735	24	—	—	0.3735	6	—	—	—	—
0.3300	19	0.3300	7	—	—	0.3300	8	0.3282	8	—	—
0.3238	33	0.3238	18	—	—	—	—	—	—	—	—
—	—	—	—	0.3215	37	—	—	0.3215	18	0.3215	85
—	—	—	—	0.3183	40	0.3183	100	—	—	0.3183	100
—	—	0.3126	100	0.3126	100	—	—	0.3126	100	—	—
0.3116	27	—	—	—	—	—	—	—	—	—	—
—	—	—	—	—	—	—	—	0.3102	77	—	—
—	—	0.3084	67	—	—	—	—	0.3086	68	—	—
—	—	0.3015	9	0.3054	7	—	—	—	—	—	—
0.3004	22	0.2946	44	—	—	0.2944	13	—	—	—	—
0.2922	65	0.2922	34	0.2933	9	—	—	0.2922	36	0.2924	19
0.2904	57	—	—	—	—	—	—	—	—	—	—
0.2890	91	0.2886	7	0.2882	11	0.2893	23	0.2890	66	—	—
—	—	0.2857	70	0.2875	12	0.2866	27	—	—	—	—
0.2840	100	—	—	0.2840	16	—	—	0.2848	68	—	—
0.2821	70	0.2813	41	—	—	0.2821	17	—	—	—	—
0.2796	84	0.2796	59	0.2796	12						
						—	—	0.2796	59	—	—
—	—	—	—	0.2763	7	—	—	—	—	0.2755	5
—	—	0.2614	13	0.2607	3	0.2614	6	—	—	—	—
0.2600	23	—	—	—	—	0.2550	8	0.2600	12	—	—
0.2541	36	0.2541	24	0.2541	8	—	—	—	—	—	—
—	—	—	—	0.2535	9	—	—	0.2535	27	0.2529	5
0.2474	17	0.2468	9	—	—	0.2474	8	0.2468	9	—	—
0.2397	26	0.2410	16	0.2404	7	0.2417	7	0.2397	15	—	—
—	—	0.2380	16	0.2384	5	—	—	0.2380	15	—	—
0.2337	13	0.2343	9	—	—	0.2331	27	0.2337	9	0.2331	24
—	—	—	—	0.2326	9	0.2320	23	—	—	—	—
—	—	0.2280	6	—	—	0.2274	11	0.2286	4	0.2280	18
—	—	—	—	0.2236	31	0.2253	9	—	—	—	—
—	—	0.2225	23	—	—	0.2220	27	—	—	—	—
0.2210	7	0.2210	36	0.2210	30	—	—	0.2210	39	0.2215	25
—	—	0.2170	20	0.2180	9	—	—	—	—	0.2175	2

Table III. (cont.)

$AsSe_{2.5}$		$AsSe_2Te_{0.5}$		$AsSe_{1.5}Te$		$AsSe_{1.25}Te_{1.25}$		$AsSe_{0.75}Te_{1.75}$		$AsSe_{0.5}Te_2$	
d [nm]	RI	*d* [nm]	RI	*d* [nm]	RI	*d* [nm]	RI	*d* [nm]	RI	*d* [nm]	RI
0.2165	15	0.2165	18	—	—	—	—	0.2165	23	—	—
—	—	0.2151	18	—	—	0.2151	5	—	—	—	—
—	—	—	—	—	—	—	—	0.2141	23	—	—
0.2136	18	—	—	—	—	—	—	—	—	—	—
0.2117	10	0.2113	14	—	—	—	—	—	—	0.2117	2
0.2102	20	—	—	—	—	0.2080	11	0.2102	18	—	—
0.2057	12	—	—	—	—	0.2070	12	—	—	0.2066	7
—	—	0.2035	9	0.2048	13	0.2043	3	0.2035	12	—	—
—	—	0.1980	10	—	—	—	—	—	—	—	—
0.1964	12	—	—	—	—	—	—	0.1964	12	0.1952	8
0.1941	17	0.1941	12	0.1944	6	0.1944	9	0.1941	15	—	—
—	—	—	—	0.1913	19	—	—	—	—	0.1917	7
0.1876	11	0.1895	5	0.1906	15	—	—	—	—	—	—
—	—	0.1847	7	0.1841	7	0.1830	17	—	—	0.1830	11
—	—	0.1810	20	0.1810	16	—	—	0.1806	19	0.1820	10
0.1793	36	0.1796	39	0.1803	14	0.1796	13	0.1796	43	0.1793	2
0.1771	33	0.1774	22	0.1774	4	—	—	0.1771	26	0.1774	3
0.1743	22	0.1750	13	0.1750	4	0.1750	11	0.1750	15	0.1743	3
—	—	0.1721	21	0.1724	9	0.1724	9	—	—	—	—
0.1713	36	0.1716	24	—	—	0.1716	9	0.1719	32	—	—
—	—	—	—	0.1697	3	—	—	0.1693	8	—	—
0.1600	12	0.1600	7	—	—	0.1610	10	—	—	0.1610	5
0.1587	11	0.1585	10	—	—	0.1595	7	—	—	0.1590	5
—	—	0.1575	9	0.1573	8	—	—	—	—	—	—
—	—	0.1548	7	0.1548	5	—	—	—	—	0.1545	2
—	—	0.1543	7	—	—	—	—	—	—	—	—
—	—	0.1540	7	—	—	—	—	—	—	—	—
0.1523	13	0.1523	10	0.1523	3	—	—	0.1523	13	—	—
0.1505	9	0.1507	5	—	—	—	—	0.1503	9	—	—
—	—	0.1450	9	—	—	—	—	0.1458	16	—	—
0.1442	10	0.1442	12	0.1446	10	0.1446	9	0.1448	16	0.1450	6
—	—	0.1421	7	0.1418	8	—	—	—	—	0.1420	4
—	—	0.1400	9	—	—	0.1411	7	—	—	0.1410	4
—	—	0.1371	9	—	—	0.1375	5	—	—	0.1377	4
0.1335	10	0.1351	6	0.1351	4	—	—	—	—	—	—

relative intensities of the investigated compounds. The Table shows the formation of new lines resulting from the development of a new phase. Because of the line-resolution problem, only the lattice parameters for the α-phase (Se-rich) have been determined and given in Table IV. The Table shows first the lattice parameters of the α-phase whose unit cell volume is generally larger than those of $AsSe_{2.5}$, as expected. Second, no variation in the lattice parameters appears as one passes from $AsSe_2Te_{0.5}$ upto $AsSe_{0.75}Te_{1.75}$, consequently the unit cell volume does not change. The average values of a, b, c, β and V are: 1.2074, 0.9853, 0.4308 nm, 85° 2Θ and 0.510225 $(nm)^3$, respectively. These two observations indicate that the increase in the lattice parameters

Table IV

The estimated lattice parameters and unit cell volumes of the As_2Se_5–As_2Te_5 compounds

Composition	a [nm]	b [nm]	c [nm]	β°	V [nm^3]
As_2Se_5	1.2052	0.9854	0.4252	87.85	0.504851
$AsSe_{2.0}Te_{0.5}$	1.209±0.002	0.9836±0.001	0.4291±0.001	85.230±0.24	0.508457±0.002
$AsSe_{1.5}Te_{1.0}$	1.198±0.004	0.9851±0.001	0.4305±0.001	85.760±0.41	0.506618±0.009
$AsSe_{1.25}Te_{1.25}$	1.214±0.001	0.9854±0.001	0.4327±0.001	84.588±0.57	0.515214±0.002
$AsSe_{0.75}Te_{1.75}$	1.108±0.002	0.9870±0.001	0.4296±0.001	85.353±0.18	0.510612±0.001

of the α-phase is consistent with the formation of a substitutional solid solution (α-phase) where Te, whose atomic radius (0.143 nm) is larger, replaces the Se atoms of smaller atomic radius (0.116 nm).

Consequently, one may conclude that the structure of the parent compound $AsSe_{2.5}$, is very sensitive to the addition of Te atoms, and an addition of about 14 at% Te is already accompanied by phase separation.

4. Conclusion

The X-ray measurements made on amorphous and crystalline $AsSe_{y-x}Te_x$ systems showed that the structure of these compounds is very sensitive to their compositions. In the amorphous states, three stepped hump diffraction patterns were found with a maximum intensity at the second step. The shift in the apex of the second hump and the decrease in the intensity of the first hump, resulting from increasing Te in the compounds indicate the structural dependence on their compositions.

The structural dependence on the composition has been also found in the crystalline states. In other words, a phase separation has been detected for $AsSe_{0.6}Te_{0.4}$ and $AsSe_2Te_{0.5}$ compounds of $\simeq 20$ and 14 at% Te, respectively. The two phases formed might be denoted as α-phase (rich Se phase) and γ-phase (poor Se phase or rich Te phase).

A phase separation might also be observed for the stoichiometric system $AsSe_{1.5-x}Te_x$ at about 10 at% or higher Te content, as indicated by the diffraction patterns presented in Fig. 7. The $AsSeTe_{0.5}$ compound of Se : Te = 2 : 1 constitutes an exception as shown in Fig. 7. For this compound the diffraction pattern is different from those of smaller or higher at% Te. This means that for such compounds the change from the parent sample, $AsSe_{1.5}$, is not of a phase separation type. One may suggest that the changes in the diffraction pattern are due to some ordering process similar to that observed either for Bi_2Te_2Se [14], of Te : Se = 2 : 1, or for As_2Se_2S [7, 8] of Se : S = 2 : 1. The type of ordering in $AsSeTe_{0.5}$ needs more investigation which is presently being carried out.

In the $AsSe_{1-x}Te_x$ system, the α- and γ-phases have structures based on AsSe (monoclinic) and AsTe (f.c.c.), respectively. The α- and γ-phases found in $AsSe_{1.5-x}Te_x$

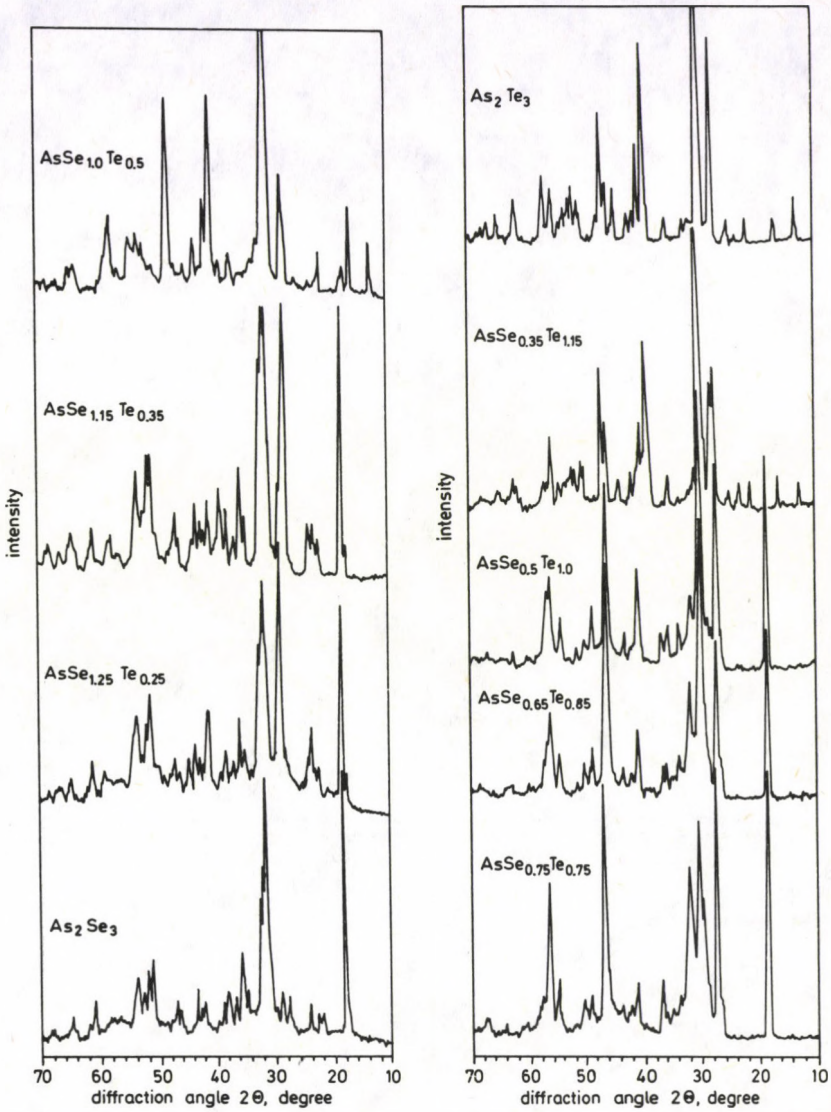

Fig. 7

compounds have structures based on $AsSe_{1.5}$ (monoclinic) and $AsTe_{1.5}$ (monoclinic), respectively. For the $AsSe_{2.5-x}Te_x$ system on the other hand, the α- and γ-phases have structures based on $AsSe_{2.5}$ and $AsTe_{2.5}$, respectively.

Table V summarizes the structural changes with the composition for the three As–Se–Te systems as obtained from X-ray diffraction measurements.

Table V

The structural changes of the As–Se–Te systems with the composition as obtained from X-ray powder diffraction studies

Single phase (α)		Compositional range of two phases α (rich in Se) + γ (rich in Te)	Single phase (γ)	
Parent	Composition of similar structure		Composition of similar structure	Parent
AsSe Monoclinic $a_0 = 0.669$ nm $b_0 = 1.386$ nm $c_0 = 1.000$ nm $\beta = 113.8°$	$AsSe_{1-x}Te_x$ with $x \leqq 0.4$	AsSe–AsTe, with $\geqq 20$ at% Te i.e. from $AsSe_{0.5}Te_{0.5}$ to $AsSe_{0.1}Te_{0.9}$		AsTe F.c.c.: $a_0 = 0.5778$ nm
As_2Se_3 Monoclinic $a_0 = 0.430$ nm $b_0 = 0.994$ nm $c_0 = 1.284$ nm $\beta = 109.1°$	$AsSe_{1.5-x}Te_x$ with $x \leqq 0.25$	As_2Se_3–As_2Te_3, with $\geqq 10$ at% Te i.e. from $AsSe_{1.15}Te_{0.35}$ to $AsSe_{0.50}Te$ with a state of ordering at Se : Te = 2 : 1; $AsSeTe_{0.5}$	$AsSe_{1.5-x}Te_x$ with $x \geqq 1.15$	As_2Te_3 Monoclinic $a_0 = 1.4339$ nm $b_0 = 0.4006$ nm $c = 0.9873$ nm $\beta = 95.0°$
As_2Se_5		As_2Se_5–As_2Te_5, with $\geqq 14$ at% Te i.e. from $AsSe_{2.0}Te_{0.5}$ to $AsSe_{0.5}Te_{2.0}$		As_2Te_5

References

1. A. A. Vaipolin and E. A. Porai-Koshits, Soviet Physics-Solid State, **5,** 178, 1963; **5,** 186, 1963; **5,** 497, 1963.
2. A. T. Ward, Proc. IIIrd Mardi Gras Symposium on Theor. Chemistry, New Orleans, 1971, Adv. in Chem., **110,** 163, 1972.
3. R. Zalien, M. L. Slade and A. T. Ward, Phys. Rev., **B3,** 4257, 1971.
4. A. J. Apling, Electronic and Structural Properties of Amorphous Semiconductors, Ed. P. G. Le-Comber and J. Mort, Academic Press, London, 1973, p. 257.
5. S. A. Saleh, M. F. Kotkata and M. K. El-Mously, Proc. of Math. and Physical Society of Egypt; **42,** 73, 1976; **42,** 83, 1976.
6. E. G. Zhykov, O. I. Dzhaparidze, S. A. Demiovski and N. P. Popova, Izvestiya Akademii Nauk SSSR, Neorgan. Mat., **10,** 1886, 1974.
7. A. M. Shamah, Ph. D. Thesis, Sheffield University, 1979.
8. B. A. Smith, N. Cowlam and A. M. Shamah, Phil. Mag., B, **39,** 111, 1979.
9. M. K. El-Mously, M. F. Kotkata and M. B. El-Den, Egypt. J. Solids, **1,** 166, 1980.
10. M. F. Kotkata and M. B. El-Den, to be published.
11. M. B. El-Den, Ph. D. Thesis, Ain Shams University, 1981.
12. E. S. Ronald, J. Non-Cryst. Solids, **8–10,** 598, 1972.
13. C. A. Majid, P. R. Prager, N. H. Fletcher and J. M. Brettell, J. Non-Cryst. Solids, **16,** 365, 1974.
14. J. R. Drabble and C. H. I. Goodman, J. Phys. Chem. Solids, **5,** 142, 1958.

Acta Physica Hungarica 54 (1—2), pp. 65—70 (1983)

SOME SOLUTIONS OF EINSTEIN—MAXWELL—YUKAWA FIELDS

HIREN B. TRIVEDI and L. K. PATEL

Department of Mathematics, Gujarat University, Ahmedabad 380 009, India

(Received 27 November 1981)

Some exact solutions of Einstein's equations corresponding to source-free electromagnetic fields plus the scalar fields are obtained. The geometry of these solutions is described by an axially symmetric static metric in prolate spheroidal co-ordinates. The details regarding these solutions are also discussed. A three-parameter solutions of static Einstein—Maxwell equations, obtained by Bonnor, is derived as a particular case.

1. Introduction

The importance of exact solutions in the general theory of relativity is quite well-known. Due to the non-linearity of the field equations of general relativity, it is extremely difficult to solve them. Therefore only a handful of exact solutions of these equations are known in the literature. The purpose of the present investigation is to derive some exact axially symmetric static solutions for the interacting electromagnetic and scalar meson fields, which we call Einstein—Maxwell—Yukawa (EMY) fields.

Stephenson [1] has obtained a static spherically symmetric solution of the EMY field equations in which the scalar meson field is associated with a meson of non-zero rest mass μ. According to him such a solution will represent (apart from spin effects) the classical gravitational field of a proton. Thus, it seems worth while to derive exact solutions of EMY field equations. In this paper we shall restrict our analysis to the case $\mu=0$. Therefore now onwards the Yukawa field is supposed to be massless.

Teixeira, Wolk and Som [2] have studied a general class of static cylindrically symmetric solutions of EMY field equations. These solutions reduce to the solutions obtained by Marder [3] in the absence of electromagnetic and scalar fields.

Lal and Khan [4] have obtained a static solution of the EMY field equations. Their solution includes the solutions previously obtained by Patel [5], Singh [6] and Taub [7] as particular cases. They have also derived a non-static solution of these field equations in terms of Einstein—Rosen metric.

Akabari and Patel [8] have obtained various static solutions of EMY field equations in oblate spheroidal coordinates. These solutions reduce to the solutions discussed by Misra [9] in the absence of scalar fields. When the electromagnetic field is switched off in their solutions, they reduce to the solutions obtained by Patel and Trivedi [10].

We shall discuss here some new static solutions of EMY field equations in prolate spheroidal co-ordinates which are generalizations of the electrovac universe discussed by Bonnor [11].

2. The metric and the field equations

We investigate the line element

$$ds^2 = e^{2k}dt^2 - a^2(\xi^2-1)(1-\eta^2)e^{-2k}d\varphi^2 -$$

$$-a^2(\xi^2-\eta^2)e^{2H}\left[\frac{d\xi^2}{\xi^2-1}+\frac{d\eta^2}{1-\eta^2}\right], \tag{1}$$

where K and H are functions of ξ and η only and a is a constant. We number the co-ordinates as

$$x^1=\xi, \quad x^2=\eta, \quad x^3=\varphi \text{ and } x^4=t.$$

In what follows the lower suffixes 1 and 2 after any unknown function imply a partial differentiation with respect to ξ and η respectively. The surviving components of Ricci tensor for the metric (1) are given by

$$R_1^1=\frac{1}{a^2e^{2H}(\xi^2-\eta^2)}[-(\xi^2-1)(H_{11}+2K_1^2)+2\xi K_1-(1-\eta^2)H_{22}+2\eta H_2],$$

$$R_2^2=\frac{1}{a^2e^{2H}(\xi^2-\eta^2)}[-(\xi^2-1)H_{11}-2\xi H_1-(1-\eta^2)(H_{22}+2K_2^2)-2\eta K_2],$$

$$R_3^3=-R_4^4=\frac{1}{a^2e^{2H}(\xi^2-\eta^2)}[(\xi^2-1)K_{11}+2\xi K_1+(1-\eta^2)K_{22}-2\eta K_2],$$

$$\frac{R_2^1}{\xi^2-1}=\frac{R_1^2}{1-\eta^2}=\frac{1}{a^2e^{2H}(\xi^2-\eta^2)}\left[-2K_1K_2+\frac{\xi(H_2+K_2)}{\xi^2-1}-\frac{\eta(H_1+K_1)}{1-\eta^2}\right]. \tag{2}$$

The field equations of space-times containing electromagnetic fields and a zero-mass meson field, but no matter, are

$$R_k^i=-8\pi\,[-F^{ij}F_{kj}+1/4\delta_k^iF_{ab}F^{ab}+g^{ii}V_{,i}V_{,k}], \tag{3}$$

where (i) F_{ik} is the skew-symmetric electromagnetic field tensor which satisfies Maxwell's equations

$$F_{ik}=A_{i,k}-A_{k,i} \tag{4}$$

and

$$F^{ik}{}_{;k}=0 \tag{5}$$

and (ii) V is the zero rest mass scalar field which satisfies

$$\Box V=g^{ij}V_{;ij}=0. \tag{6}$$

Here a comma indicates partial differentiation and a semicolon indicates covariant differentiation.

For the space-time defined by the metric (1), the equation (6) reduces to the usual Laplace's equation. If we assume that V is a function of ξ and η only, the Eq. (6) becomes

$$(\xi^2-1)V_{11}+2\xi V_1+(1-\eta^2)V_{22}-2\eta V_2=0. \tag{7}$$

Here it should be noted that the Eq. (7) is independent of the metric potentials K and H.

Zipoy [12] has shown that the solutions of (7) can be written as a linear combination of Legendre polynomials of integral order l (See also Hobson [13]). Bonnor and Sackfield [14] showed that the solutions for $l=0$ and $l=1$ can be interpreted as a mass monopole and dipole respectively with Euclidean topology.

Following Bonnor [11], let us choose the electrostatic 4-potential A_i — as

$$A_i=\frac{\beta}{\sqrt{8\pi}}\delta_i^4, \tag{8}$$

where β is a function of ξ and η only. The Maxwell's equations (5) gives us the following differential equation for the function β

$$(\xi^2-1)\beta_{11}+2\xi\beta_1+(1-\eta^2)\beta_{22}-2\eta\beta_2=2(\xi^2-1)K_1\beta_1+2(1-\eta^2)K_2\beta_2. \tag{9}$$

We have verified that the entire solution of the EMY field equations (3) is determined by (7), (9) and the following three differential equations:

$$(\xi^2-1)K_{11}+2\xi K_1+K_{22}(1-\eta^2)-2\eta K_2=\frac{1}{2}e^{-2K}[(\xi^2-1)\beta_1^2+(1-\eta^2)\beta_2^2], \tag{10}$$

$$\begin{aligned}2(H_1+K_1)=&\frac{(1-\eta^2)}{\xi^2-\eta^2}[2\xi(\xi^2-1)K_1^2-2\xi(1-\eta^2)K_2^2-4\eta(\xi^2-1)K_1K_2]\\&+\frac{e^{-2K}(1-\eta^2)}{\xi^2-\eta^2}[-\xi(\xi^2-1)\beta_1^2+\xi(1-\eta^2)\beta_2^2+2\eta(\xi^2-1)\beta_1\beta_2]+\\&+\frac{8\pi(\xi^2-1)(1-\eta^2)}{\xi^2-\eta^2}\left[\xi V_1^2-\frac{\xi(1-\eta^2)V_2^2}{\xi^2-1}-2\eta V_1V_2\right],\end{aligned} \tag{11}$$

$$\begin{aligned}2(H_2+K_2)=&\frac{(\xi^2-1)}{\xi^2-\eta^2}[2\eta(\xi^2-1)K_1^2-2\eta(1-\eta^2)K_2^2+4\xi(1-\eta^2)K_1K_2]+\\&+\frac{e^{-2K}(\xi^2-1)}{\xi^2-\eta^2}[-\eta(\xi^2-1)\beta_1^2+\eta(1-\eta^2)\beta_2^2+2\xi(1-\eta^2)\beta_1\beta_2]+\\&+\frac{8\pi(\xi^2-1)(1-\eta^2)}{\xi^2-\eta^2}\left[\frac{\eta(\xi^2-1)V_1^2}{1-\eta^2}-\eta V_2^2+2\xi V_1V_2\right].\end{aligned} \tag{12}$$

We have also verified that the condition of integrability $(H_1+K_1)_2=(H_2+K_2)_1$ for (11) and (12) is satisfied.

A heedful observation of the Eqs (9) and (10) reveals the fact that the determination of the functions β and K does not depend upon the scalar field V. It is evident from the Eqs. (11) and (12) that the determination of the function H depends upon V.

3. The solutions of the field equations

Bonnor [11] has solved the differential equations (9) and (10) with the aid of the method developed by Chandrasekhar [15]. The solution of (9) and (10) can be expressed in the form

$$\beta=U^{-1}V^{-2}(CU-BV) \tag{13}$$

and

$$e^{2K}=U^{-2}V^{-2}(UV-BV-CU)^2 \tag{14}$$

with $U=B+A\eta-\xi$, $V=C+A\eta+\xi$. Here A, B and C are constants of integration satisfying the relation

$$BC=A^2-1. \tag{15}$$

The remaining unknown functions V and H can now be determined from the Eqs (7), (11) and (12).

We limit ourselves to the monopole and dipole solutions of (7). Therefore we consider the following two cases:

(i) $$V=N\log\left(\frac{\xi+1}{\xi-1}\right), \tag{16i}$$

(ii) $$V=L\eta\left[1-\xi^2\log\left(\frac{\xi+1}{\xi-1}\right)\right], \tag{16ii}$$

where N and L are arbitrary constants.

In these two cases the Eqs (11) and (12) yield the following expressions for the function H

$$H=\log\left\{\left[\frac{UV(UV-BV-CU)}{(\xi^2-\eta^2)^2}\right]\left(\frac{\xi^2-1}{\xi^2-\eta^2}\right)^{16\pi N^2}\right\}, \tag{17i}$$

$$H=\log\left\{\left[\frac{UV(UV-BV-CU)}{(\xi^2-\eta^2)^2}\right]\left(\frac{\xi^2-1}{\xi^2\eta^2}\right)^{4\pi L^2}\right\}-$$

$$-4\pi L^2(1-\eta^2)\left[1+\xi\log\left(\frac{\xi+1}{\xi-1}\right)-\frac{1}{4}(\xi^2-1\left\{\log\left(\frac{\xi+1}{\xi-1}\right)\right\}^2\right]. \tag{17ii}$$

Thus the Eqs (13), (14), (15), (16i) and (17i) give us the monopole solution and the Eqs (13), (14), (16 ii) and (17 ii) give us the dipole solution of EMY field equations for the metric (1). It should be noted that there are four arbitrary constants in each of the above mentioned solution of EMY field equations.

For the discussion of details, we restrict our analysis to the monopole solution only. The details regarding the dipole solution can be discussed on similar lines. Instead of using the constants A, B and C, it is physically more significant to use the constants m, e and b defined by (Bonnor [11])

$$m=(C-B)a, \quad e=(C+B)a, \quad -bm=a^2A(B-C). \tag{18}$$

Here m and e are respectively the mass and charge parameters and b corresponds to the distribution of higher multipoles.

The monopole solution of EMY field equations may be written in terms of the spherical polar co-ordinates r, ϑ and φ by means of the transformation

$$a\xi=r-\frac{1}{2}m, \qquad \eta=\cos\ \vartheta. \tag{19}$$

The explicit form of the metric for the monopole solution can be expressed as

$$\begin{aligned} ds^2=&-W^2[P^2Q^{-(3+32\pi N^2)}Z^{32\pi N^2}(Z^{-1}dr^2+d\vartheta^2) \\ &+ZP^{-2}\sin^2\vartheta d\varphi^2]+P^2W^{-2}dt^2, \end{aligned} \tag{20}$$

where

$$\begin{aligned} P&=\left(r-\frac{1}{2}m\right)^2-a^2+b^2\cos^2\vartheta, \\ Q&=\left(r-\frac{1}{2m}\right)^2-a^2\cos^2\vartheta, \\ W&=r^2-\left(b\cos\vartheta+\frac{1}{2}e\right)^2, \\ Z&=\left(r-\frac{1}{2}m\right)^2-a^2, \\ a^2&=b^2+1/4(m^2-e^2). \end{aligned} \tag{21}$$

The electrostatic potential β and the scalar field V can be expressed in terms of r and ϑ as

$$\begin{aligned} \beta&=W^{-1}\left[e\left(r-\frac{1}{2}m\right)-mb\cos\vartheta\right], \\ V&=N\log\left(\frac{2r-m+2a}{2r-m-2a}\right). \end{aligned} \tag{22}$$

As noted by Bonnor [11], the singularity structure of the metric (20) is very complicated. But the singularities are within the region $r=l$ where l stands for the

greater of $|a| + \frac{1}{2}|m|$ and $|b| + \frac{1}{2}|e|$. Therefore the solution described in the metric (20) is meaningful for the following range of the variables:

$$r > l, \quad 0 \leqq \vartheta \leqq \pi, \quad 0 \leqq \varphi \leqq 2\pi, \quad -\infty < t < \infty. \tag{23}$$

It is clear from the result (22) that the scalar field V is real for the region $r > l$.

The following particular cases of the solution (20) may be of physical significance.
(i) $N = 0$. In this case we recover the electrovac universe discussed by Bonnor [11].
(ii) $e = 0$, $m \neq 0$, $b \neq 0$, $N \neq 0$. In this case the solution (20) describes a scalar field generalization of Bonnor's [16] dipole solution. The substitution $N = 0$ in this solution yields the dipole solution of Bonnor with a slight change of notations.
(iii) $b = 0$, $m^2 \neq e^2$, $N \neq 0$. The solution (20) reduces to a scalar field generalization of a non-spherical Weyl solution.
(iv) $b = 0$, $m^2 = e^2$, $N \neq 0$. In this case the solution (20) is equivalent to a scalar field generalization of Reissner—Nordstrom solution with $m^2 = e^2$. Putting $N = 0$, we get the Reissner—Nordstrom solution with $m^2 = e^2$.
(v) $m = 0$, $e = 0$, $N \neq 0$. In this case, the electrostatic potential vanishes. Therefore the solution reduces to a purely zero-mass meson solution. When the scalar field is switched off, the space-time becomes flat. This is a noteworthy feature of this solution.

Thus we have obtained some zero-mass scalar field generalizations of the three-parameter solution of Einstein—Maxwell equations discussed by Bonnor [11]. An interesting feature of these solutions is worth mentioning. The presence of the scalar field does not affect the electrostatic potential and vice-versa. But the scalar field affects the geometry of the space-time because the metric potential H depends on the scalar field V.

Acknowledgement

One of the authors (H.B.T.) is highly indebted to the University Grants Commission, New Delhi, for the award of a junior research fellowship.

References

1. G. Stephenson, Proc. Camb. Phil. Soc., **58,** 521, 1962.
2. A. F. da F. Teixeira, I. Wolk and M. M. Som, J. Math. Phys., **15,** 1756, 1974.
3. L. Marder, Proc. Roy. Soc., *A***244,** 524, 1958.
4. K. B. Lal and M. Q. Khan, Gen. Relativ. Gravitation, **8,** 151, 1977.
5. L. K. Patel, Tensor (N. S.), **29,** 237, 1975.
6. T. Singh, Gen. Relativ. Gravitation, **5,** 657, 1974.
7. A. H. Taub, Ann. Math., **53,** 472, 1951.
8. R. P. Akabari and L. K. Patel, to appear in Quaestiones Mathematicae.
9. M. Misra, Proc. Nat. Inst. Sci. (India), *A***28,** 105, 1962.
10. L. K. Patel and V. M. Trivedi, J. Austral. Math. Soc. (Series-B), **19,** 140, 1975.
11. W. B. Bonnor, J. Phys. A, **12,** 853, 1979.
12. D. H. Zipoy, J. Math. Phys., **7,** 1137, 1966.
13. E. W. Hobson, The Theory of Spherical and Ellipsoidal Harmonics, Cambridge University Press, 1931.
14. W. B. Bonnor and A. Sackfield, Commun. Math. Phys., **8,** 338, 1968.
15. S. Chandrasekhar, Proc. Roy. Soc., *A***358,** 405, 1978.
16. W. B. Bonnor, Z. Phys., **190,** 444, 1966.

Acta Physica Hungarica 54 (1—2), pp. 71—95 (1983)

INVESTIGATIONS OF LONGITUDINAL HOLLOW-CATHODE DISCHARGE

J. MIZERACZYK

Institute of Fluid-Flow Machines, Polish Academy of Sciences
80-925 Gdańsk-Wrzeszcz, Poland

(Received 29 November 1981)

Results of investigations of a longitudinal hollow-cathode discharge are presented for a hollow cathode of 5 mm diameter and a length variable from 8 mm up to 96 mm. Hollow cathodes of such dimensions are used in discharge tubes employed in laser technology.

Axial distributions have been determined for the current density over the cathode surface, discharge current intensity and discharge plasma potential. Also voltage vs current discharge characteristics have been measured.

The measurements have been carried out for discharge in helium at a pressure ranging from 1.67 hPa to 34 hPa. The current intensity varied from 1.86 mA to 250 mA depending on the cathode length.

The investigations covered hollow-cathode discharges in the presence of one anode as well as two anodes located at the opposite ends of the cathode. An axial inhomogeneity of the discharge plasma resulting in nonuniform axial distributions of the cathode and longitudinal currents as well as nonuniform axial distribution of the discharge plasma potential was observed for both cases.

The inhomogeneity of the longitudinal hollow-cathode discharge affects the operation of the laser discharge tube. Some consequences of this inhomogeneity are discussed.

1. Introduction

In the hollow-cathode discharge tubes two principal kinds of electric discharge can be distinguished: the transverse and the longitudinal discharge [1, 2].

The transverse discharge occurs in tubes where the tube geometry and configuration of the electrodes — cathode and anode — makes the electric charge carriers, electrons and ions, move transversely to the hollow cathode axis (Fig. 1a).

It is characteristic of the longitudinal discharge that electrons leaving the cathode surface move towards the anode along the hollow cathode axis (Fig. 1b).

Both the transverse and longitudinal discharge, as well as a discharge of intermediate nature, have been applied for the excitation of lasing in various media [1, 2].

The properties of longitudinal hollow-cathode discharge proved especially convenient for the forming of population inversion in the He – Cd mixture, generating the three basic spectral lines: blue, green and red, which can be mixed to produce white light [3].

The importance of this fact from the viewpoint of possible applications has increased the interest in properties of the longitudinal hollow-cathode discharge. The principal parameters of such discharge which decide whether it is applicable to the excitation of lasing media are the current density distribution over the cathode surface, the discharge plasma current distribution, the cathode fall distribution, the electron energy distribution function, the electron number density distribution, etc.

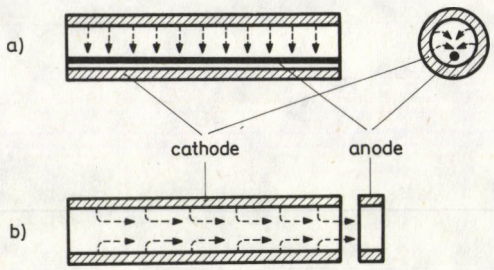

Fig. 1. Schematic diagram of typical hollow cathodes characterized by (a) transverse and (b) longitudinal discharge direction

Papers on the investigations of some of these parameters [4–11] except [9], refer to the longitudinal discharge in hollow cathodes not typical of the laser technology. As the laws of similarity do not hold for the hollow-cathode discharge, the applicability of the results published in [4–11] to the description of the longitudinal hollow-cathode discharge in laser tubes is limited.

This paper presents the results of investigations concerning some properties of the longitudinal discharge in a hollow cathode characterized by parameters typical of discharge tubes used in laser technology.

2. Measuring set-up

The dimensions of the hollow cathode and the measuring range were chosen to be typical of the longitudinal hollow-cathode discharge in lasing mixtures of helium with metal vapours (Cd, Zn, I etc.).

The discharge tube (Fig. 2) consisted of 52 independent annular segments 2 mm thick. The segments were made of stainless steel. Their inner and outer diameters were equal to 5 mm and 20 mm, respectively. Each of the segment rings was separated from the adjacent ones by mica spacers 0.05 mm thick. The rings were put in a pyrex tube in such a way that discharge could occur inside the system of rings only. Separate electric leads to each of the rings made it possible to change the ring polarity freely and to form a hollow cathode of a length variable from 2 mm up to 96 mm. The current to each of the rings could be measured. The measurements were made by measuring the voltage drops across calibrated (6 ohm) resistors connected to respective ring circuits. To

facilitate the measurements the voltage drops across the resistors were transferred to a storage oscilloscope via an electronic commutator. Owing to the use of the commutator the measuring time was reduced to a fraction of a second. This decreased the influence of the working gas temperature changes on the results of measurements. Continuous distributions of the cathode current densities were obtained by smoothing the discrete distributions displayed by the oscilloscope. Fig. 3 gives an example of the smoothing operation. The evaluated accuracy of the measurements made in this way was $\pm 5\%$.

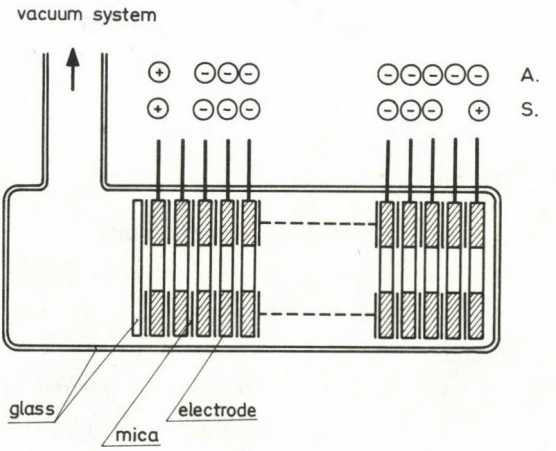

Fig. 2. Hollow cathode draft (52 segments 2 mm thick, with 5 mm I. D.). The polarity of electrodes for asymmetric (A) and symmetric (S) cathode supply is shown

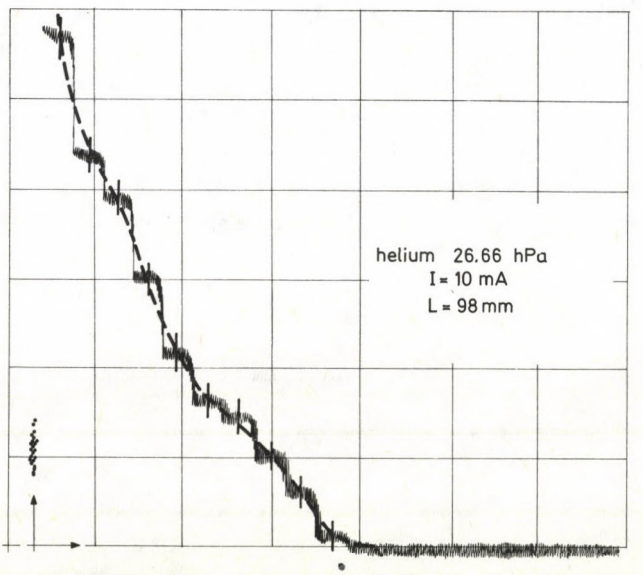

Fig. 3. Oscillograph record showing the cathode current distribution along the hollow cathode. Helium pressure: 26.66 hPa, current intensity; 10 mA, cathode length; 98 mm. The manner of smoothing the stepwise distribution is presented

The experiments included measurements of the density distributions along the cathode and V–I characteristics of the discharge for two geometries of the electrodes: *asymmetric* and *symmetric* (Fig. 2). For the asymmetric electrode configuration the discharge was maintained between the hollow cathode and one annular anode. To obtain a symmetric configuration the hollow cathode was placed between two anode rings ensuring symmetry of the power supply to the discharge. In each case the cathode was separated from each of the anode rings by one distance ring, completely insulated.

It should be noted that in laser tubes designed to obtain a longitudinal hollow-cathode discharge an asymmetric as well as a symmetric arrangement of electrode segments is adopted.

The measurements were carried out for a discharge current intensity and a helium pressure varied from 7.5 mA to 250 mA, and 1.67 hPa to 34 hPa, respectively.

3. Results and discussion

3.1. Introduction

In the longitudinal hollow-cathode discharge two kinds of current can actually be distinguished: the *transverse* or *cathode* current and the *longitudinal* current (Fig. 4). The transverse current of electrons and ions flows between the cathode surface and the negative glow which fills the cathode inside. The longitudinal current is produced mainly by electrons moving in the negative glow region towards the anode. The surface density of the transverse (cathode) current in a particular point of the cathode depends on the cathode fall value and parameters of the negative glow plasma at this point, that is also on the local value of the longitudinal current intensity. The longitudinal electric field in the negative glow causing the motion of electrons towards the anode is responsible for the longitudinal current flow. Thus, between the anode and a point on the cathode surface a specific potential distribution exists which is the resultant of the local cathode fall, longitudinal electric field in the negative glow and sometimes also the anode fall at the anode surface (Fig. 4). This can be written in the following way

$$V = V_a + \int_0^z E(z)\mathrm{d}z + V_c(z), \tag{1}$$

where V is the working voltage, V_a is the anode fall, $E(z)$ is the intensity of electric field in the negative glow at a distance z from the anode, and $V_c(z)$ is the cathode fall at the cathode surface at a distance z from the anode.

It is evident from Eq. (1) that the properties of the longitudinal hollow cathode discharge are determined mainly by the variable distance of the respective cathode surface elements from the anode. As the distance from the anode increases the value of the integral expression (1) increases. This means that at a fixed working voltage the local values of the cathode fall decrease as we go into the cathode. Thus also the

local values of the transverse current intensity vary. For a sufficiently long cathode or relatively low working voltage Eq. (1) may not be satisfied for distances from the anode exceeding a certain finite value $z=\xi$. Physically this means that the depth of penetration of the discharge current into the cathode is limited, so that only part of the

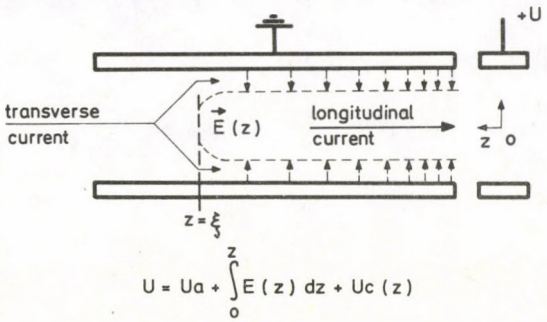

Fig. 4. Transverse and longitudinal current in the hollow cathode (ξ – penetration depth)

cathode surface is covered by the discharge. Obviously, an increase of the working voltage will result in an increase of the depth of current penetration into the cathode.

This inhomogeneity of the longitudinal discharge resulting from the difference in the distances between the anode and the respective cathode elements should be expected in the measurements.

3.2. Asymmetric electrode geometry

Results of measurements of the cathode current density distributions and voltage-current characteristics for the asymmetric electrode configuration are shown in Figs 5ⓐ—ⓖ and 6ⓐ—ⓖ.

In general, the cathode current distribution over the cathode surface is nonuniform independently of the cathode length, helium pressure and discharge current intensity. This is in agreement with considerations in Paragraph 3.1.

As for the form of the cathode current distribution its variations dependent on the current intensity, cathode length and helium pressure are observed. The variations are larger for short cathodes and for the lowest helium pressure equal to 1.67 hPa, as well as for the highest ones, equal to 24 hPa and 34 hPa.

Fig. 7 shows some oscillograph records of the cathode current distribution for different distances between the hollow cathode and the anode, equal to 2 mm and 50 mm, respectively. They show that the form of the cathode current distribution does not depend on the hollow cathode — anode distance. Similar results were obtained for various ranges of variability of the discharge parameters and distance between the hollow cathode and anode.

From Fig. 8 it is evident that for lower values of the current intensity, and corresponding lower working voltages the depth of discharge penetration into the

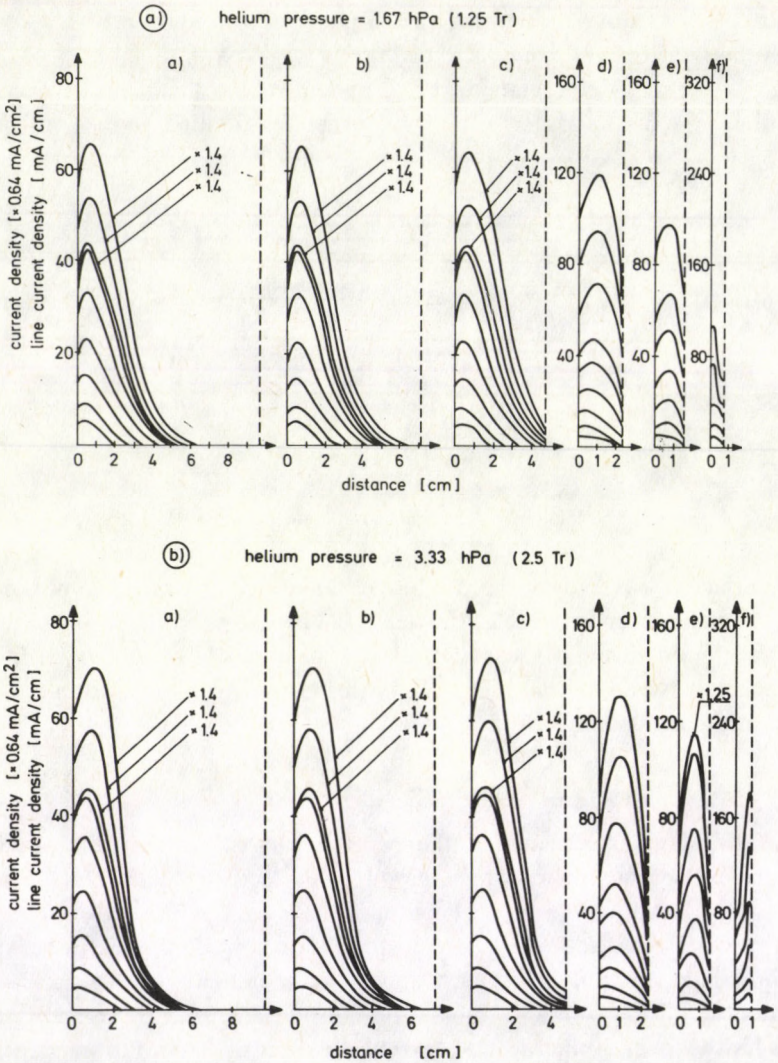

Fig. 5. Distributions of line and surface density of cathode current along the hollow cathode for different cathode lengths, discharge current intensities and helium pressures. Helium pressure: (a) – 1.67 hPa, (b) – 3.33 hPa, (c) – 6.66 hPa, (d) – 10.66 hPa, (e) – 16.66 hPa, (f) – 24 hPa, (g) – 34 hPa. Cathode length: a – 96mm, b – 72 mm, c – 48 mm, d – 24 mm, e – 16 mm, f – 8 mm. The curves, from the lowest one upwards, correspond to the following discharge currents: 7.5 mA, 15 mA, 30 mA, 50 mA, 75 mA, 100 mA, 150 mA, 200 mA and 250 mA. Some distribution curves for high current intensities are missing

cathode is small, independently of the helium pressure. The discharge length, amounting to the penetration depth, increases as the discharge current intensity increases. At the same time for the lowest helium pressures, 1.67 hPa and 3.33 hPa, the discharge length increases but slightly for current intensities above 70 mA. As for the

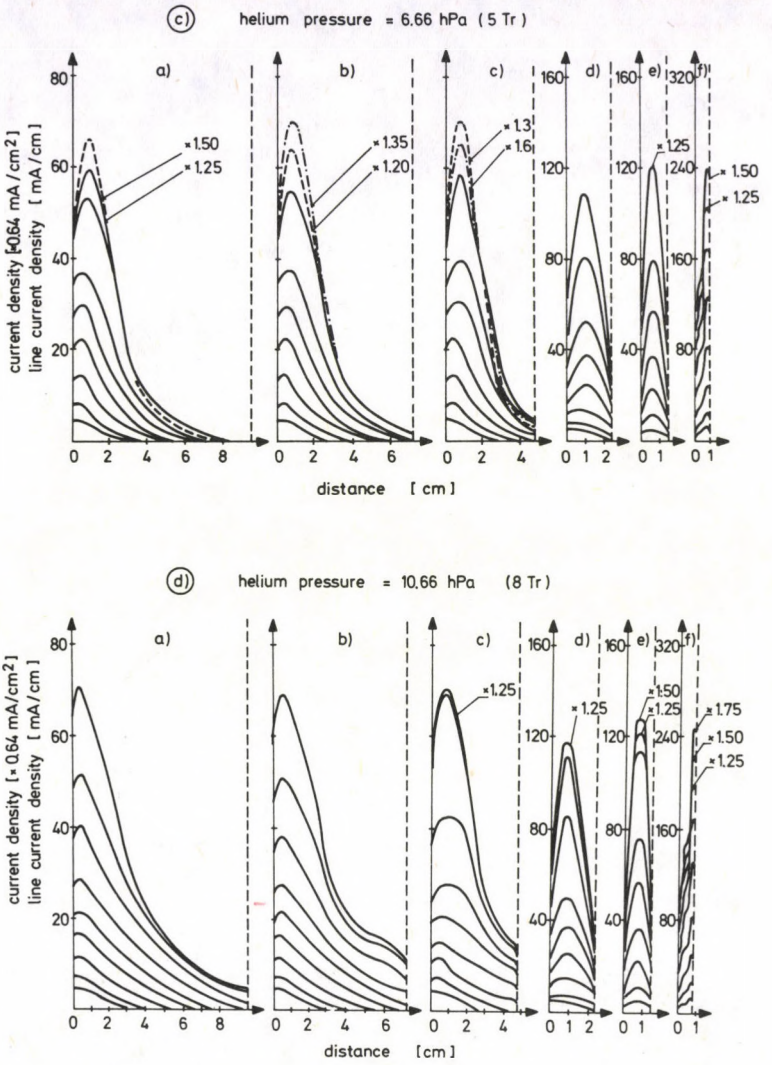

Fig. 5. (cont.)

dependence of the discharge length on the gas pressure it was shown that for a fixed discharge current intensity there is a specific pressure of helium, 16–17 hPa, at which the hollow-cathode discharge length is the largest (Fig. 9). On the other hand, when the working voltage is fixed, the discharge length increases with the helium pressure to reach its steady value on a level characteristic of the particular working voltage at pressures exceeding approximately 20 hPa (Fig. 10).

The results of measurements of the cathode current density can be employed to determine the distributions of the longitudinal current intensity in the hollow cathode.

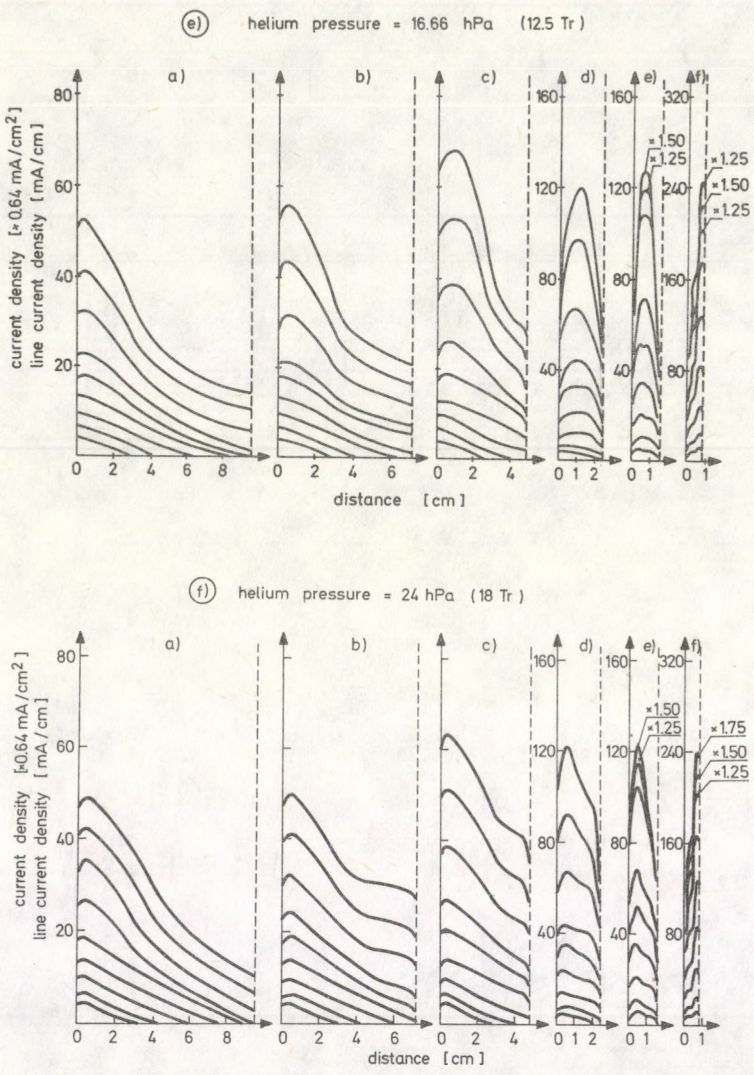

Fig. 5. (cont.)

The dependence of the longitudinal current intensity on the position along the hollow cathode axis is one of features by which this kind of plasma differs from the positive column plasma, where the axial current intensity is constant.

It was shown in [4] and [10] that the cathode current density distributions for hollow cathodes characterized by large diameters, 20 mm and 50 mm, depend for a fixed working gas pressure only on the distance measured from the point defining the discharge penetration depth. Thus they are functions of the quantity $\xi - z$ (see Fig. 4). However, the results of the present work show (Fig. 5) that the cathode current density

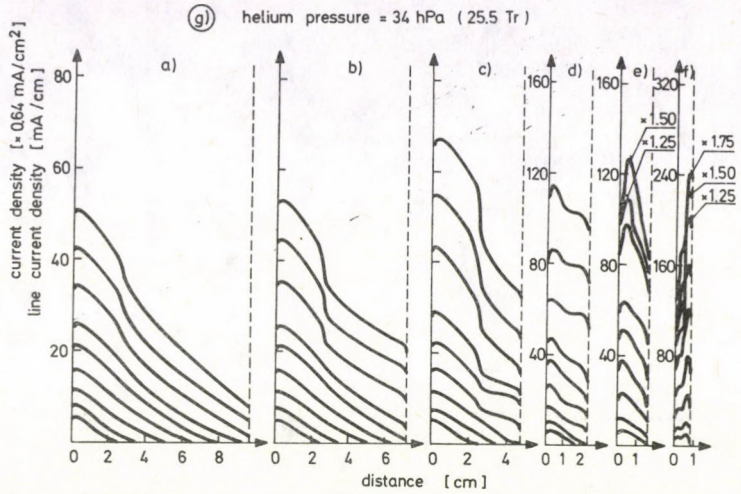

Fig. 5. (cont.)

distributions depend not only on the distance $\xi - z$, but also on the discharge current intensity (and, as in the former case, on the gas pressure).

A similar result was obtained in [6] for a discharge in a hollow cathode of relatively small diameter (14 mm). Based on these results it might be concluded that for a discharge in hollow cathodes characterized by relatively small diameters the relation between the cathode current density and the cathode dimensions and discharge parameters becomes more complex than for cathodes of larger diameters.

This affects directly the method of determining the discharge plasma potential distribution along the hollow cathode axis. It was shown in [4] that for the cathode current density, a function of the distance $\xi - z$ only, it is sufficient, when determining the axial distribution of the discharge plasma potential, to know the working voltage value and the corresponding distribution of the cathode current density. For the reasons presented above this method of determining the plasma potential distribution was inadequate in the case described in this paper.

Therefore, to approximately determine the potential of a plasma inside the hollow cathode measurements were carried out of the floating potential of the odd cathode segments, electrically insulated. The hollow cathode was composed in this case of the even segments. The insulated segments may be regarded as the electric probes. Their floating potential must not differ significantly from the plasma potential.

Fig. 11 shows the results of measurements of the floating potential of insulated segments in the hollow cathode at a selected helium pressure of 16.66 hPa. Based on these measurements it can be concluded that in the hollow-cathode discharge plasma there is a region characterized by a nearly constant potential gradient, i.e. a constant intensity of the longitudinal electric field. This is similar to the situation in the glow

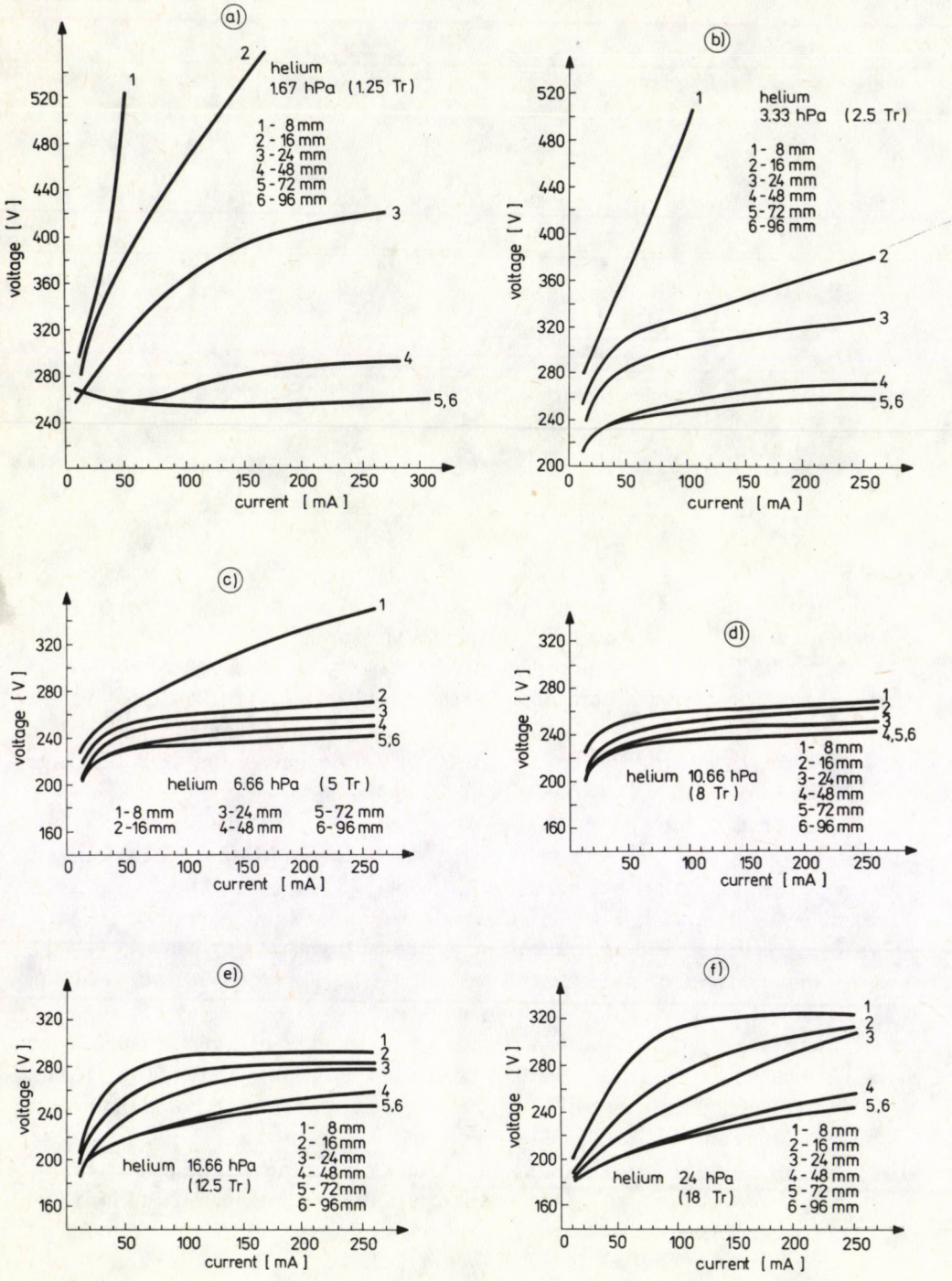

Fig. 6. Voltage–current characteristics for the longitudinal hollow-cathode discharge in cathodes of different lengths. Helium pressure: (a) – 1.67 hPa, (b) – 3.33 hPa, (c) – 6.66 hPa, (d) – 10.66 hPa, (e) – 16.66 hPa, (f) – 24 hPa, (g) – 34 hPa

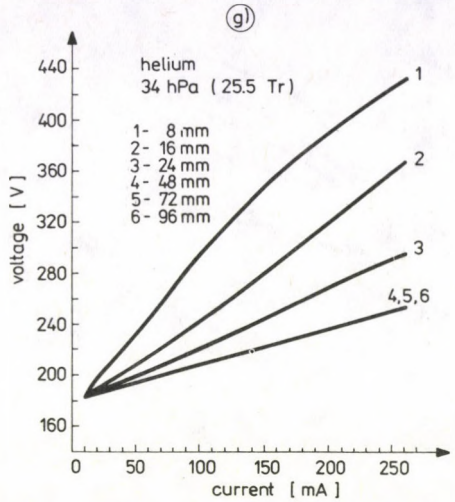

Fig. 6. (cont.)

discharge positive column where the longitudinal electric field is responsible for the drift of electrons toward the anode. Our observation confirms the results of earlier works [7] and [11] where it was suggested that in the longitudinal hollow-cathode discharge three regions may be distinguished, namely the negative glow region, the transient region and the positive column region.

To sum up the results, as presented above, of investigations of the longitudinal hollow-cathode discharge in an asymmetric configuration of electrodes it should be noted that the discharge is inhomogeneous irrespective of the cathode length. The

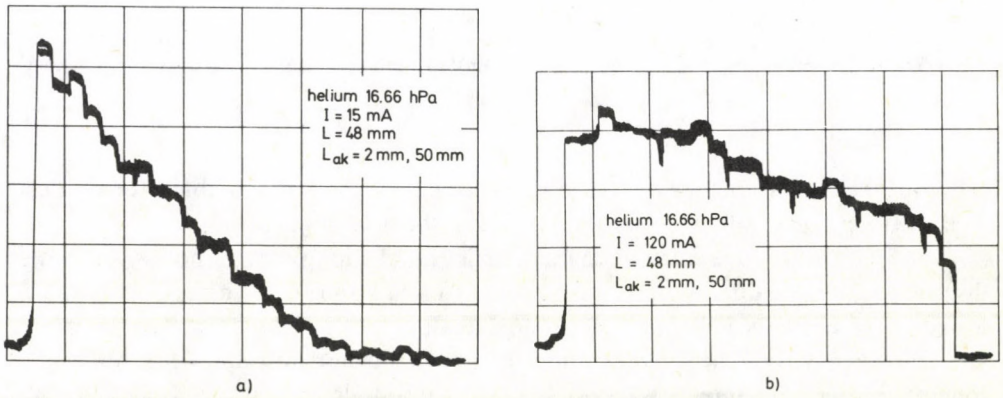

Fig. 7. Examples of double oscillograph records showing the cathode current distributions for different distances between the hollow cathode and anode. The helium pressure was equal to 16.66 hPa, the cathode length was 48 mm and the cathode–anode distance was 2 mm and 50 mm; the current intensity was equal to: a) – 15 mA, b) – 120mA

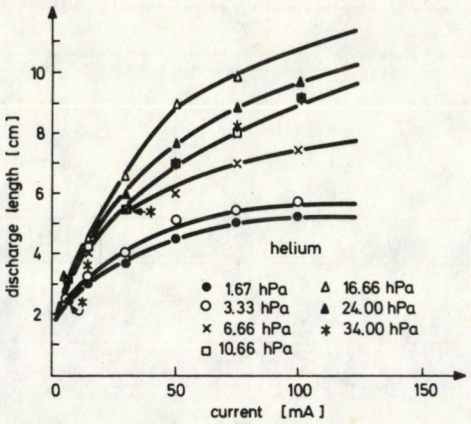

Fig. 8. The hollow-cathode discharge length plotted against the discharge current intensity

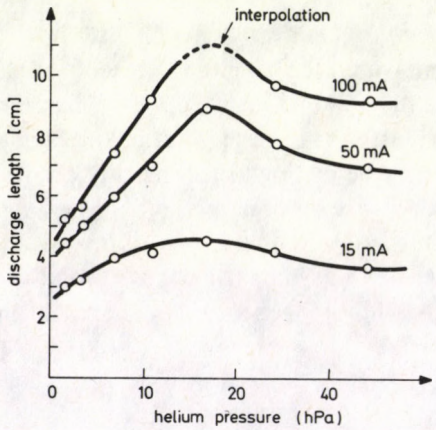

Fig. 9. The hollow-cathode discharge length plotted against the helium pressure for fixed discharge current intensity

inhomogeneity concerns the distributions of the cathode and longitudinal currents as well as the plasma potential distribution along the discharge axis.

As for the voltage–current characteristics for the longitudinal hollow-cathode discharge note that due to the inhomogeneous distributions of both the cathode and longitudinal currents it is impossible to generalize the *V–I* characteristics so as to eliminate their dependence on the cathode length. In this case introducing the notion of longitudinal current intensity reduced to the cathode length unit has no physical meaning. It may only be regarded as the mean value.

From the analysis of voltage–current characteristics and cathode current density distributions it follows that for a fixed gas pressure discharges characterized by

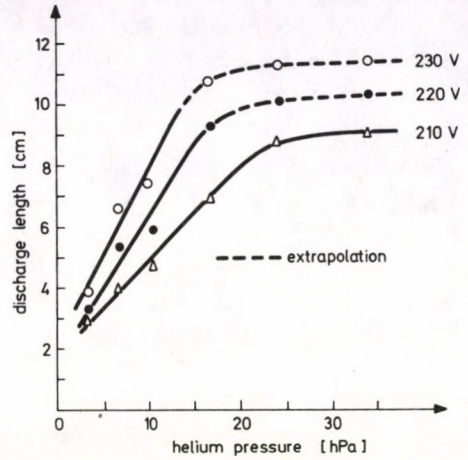

Fig. 10. The hollow-cathode discharge length plotted against the helium pressure for fixed working voltage

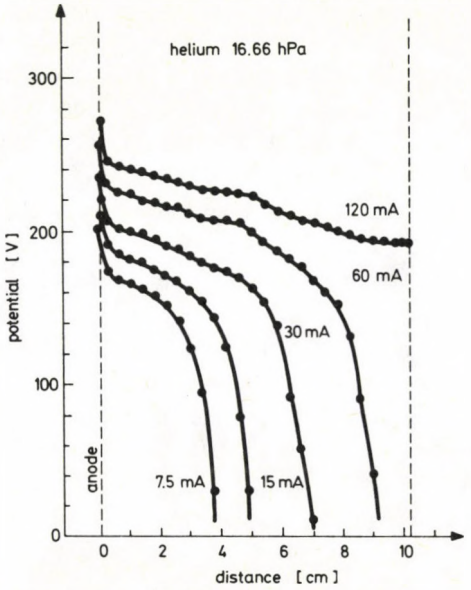

Fig. 11. The floating potential of insulated odd cathode segments for the hollow-cathode discharge with one anode

identical current density distributions occur at the same working voltage, cf. for instance relevant plots for the longest cathodes which are only partly covered by the discharge (Figs 5 and 6). It may happen, however, that identical working voltages correspond to discharges with different cathode current density distributions if only the discharge current intensity and helium pressure remain unchanged. This effect is

characteristic of longer cathodes (96 mm, 72 mm and 48 mm), where for different current density distributions the voltage–current characteristics might sometimes be identical. Such behaviour of the discharge may be explained based on the discussion presented in Paragraph 3.1, which showed that the working voltage depends on the electric field intensity and cathode fall distributions. For different distributions of the cathode current density in the corresponding discharges such distributions of the longitudinal electric field intensity and the cathode fall value may develop that the working voltages for these discharges may happen to be identical.

The characteristics plotted in Fig. 6 show that in most cases the working voltage increases with the current intensity. This is valid also for a discharge covering part of the cathode only, except for the discharge in the longest cathodes (48 mm, 72 mm and 96 mm) at the lowest pressure of helium (1.67 hPa). It is only by this behaviour of the voltage following the current intensity rise in the case of cathode whose part only is covered by the discharge that the hollow-cathode discharge differs from the classical glow discharge with flat or convex cathode.

A glow discharge covering only part of the flat or convex cathode, called *the normal glow discharge*, has three features. First, the current is uniformly distributed over the cathode part covered by the discharge. Second, a rise in the discharge current does not result in the current density growth but causes the area covered by the discharge to increase proportionally to the current intensity rise. Finally, the value of the cathode fall remains unchanged with the discharge current rise until the entire surface of the cathode is covered by the discharge.

When the whole cathode surface is already covered by the discharge a further rise in the discharge current intensity is accompanied by a substantial voltage rise, the current density distributing uniformly over the cathode surface. Such discharge is called an *abnormal discharge*.

It was already mentioned that for the hollow cathode the working voltage increases with the discharge current intensity increase, irrespective of the degree of cathode surface coverage by the discharge. The current density is not constant over the cathode surface covered by it, and this surface does not rise proportionally to the discharge current intensity. The cathode fall is not constant either along the cathode axis. Thus, classical notions concerning the normal and abnormal glow discharge with flat or convex cathode do not apply to the longitudinal hollow-cathode discharge, which was already pointed out in [5]. Nonetheless, the conclusions drawn from this fact are frequently neglected in the literature.

The increase of the working voltage with the growth of the cathode surface area covered by the discharge observed for the hollow-cathode discharge may be explained according to Paragraph 3.1, by the necessity of increasing the voltage to draw the electrons out of cathode regions more and more distant from the anode.

Curves plotted in Figs 12 and 13 show the dependence of the working voltage on the helium pressure for different lengths of the hollow cathode and different intensities of the discharge current. The form of these curves is characteristic of the discharge in

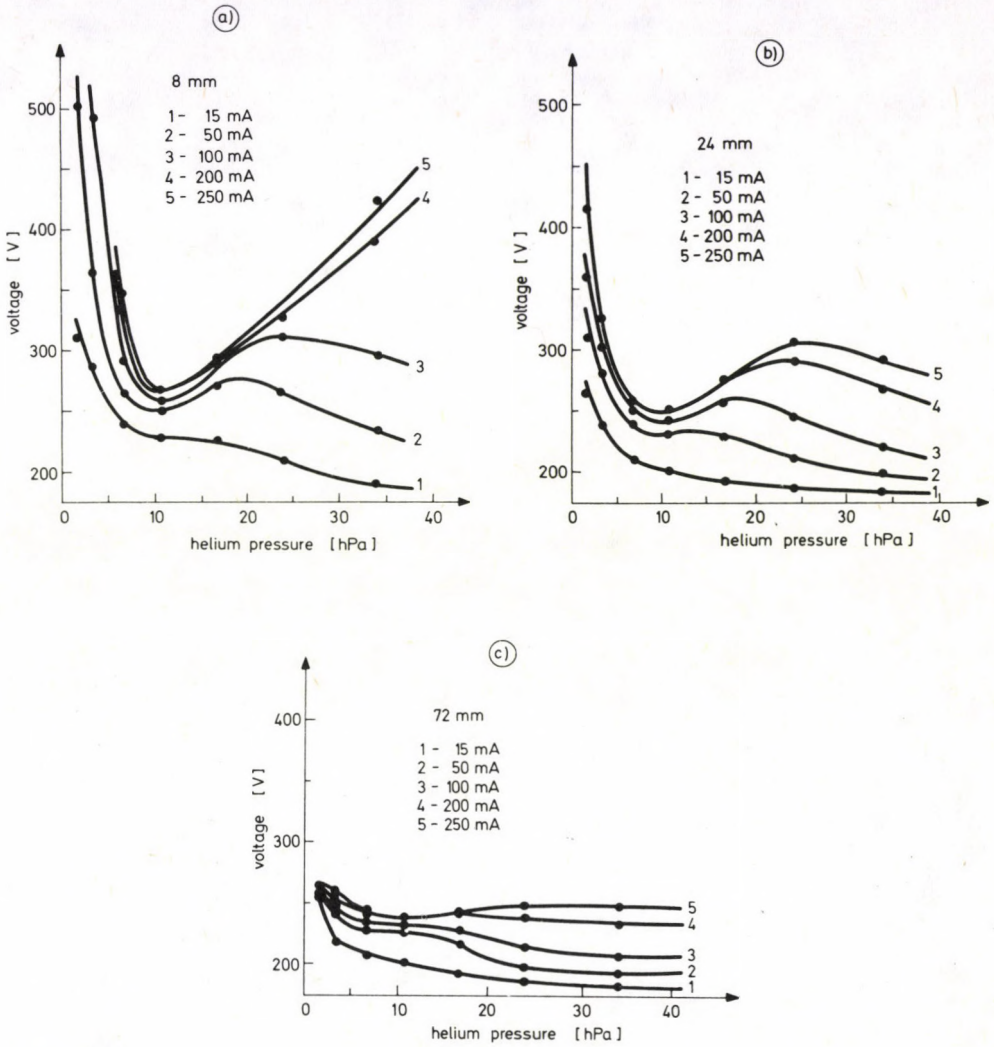

Fig. 12. Working voltage vs helium pressure for different discharge current intensities. Cathode length: a) – 8 mm, b) – 24 mm, c) – 72 mm

which a so-called *hollow-cathode effect* [12] occurs, which consists of the existence of a so-called optimum pressure of the working gas at which a particular intensity of the discharge current is obtained at the lowest working voltage. In the case under consideration the hollow-cathode effect is more distinct for high current intensities and shorter cathodes. It depends thus mainly on the cathode current density.

Figs 14 (a)—(c) show the dependence of the working voltage on the cathode length. It is evident that for a given discharge current intensity the working voltage rises with

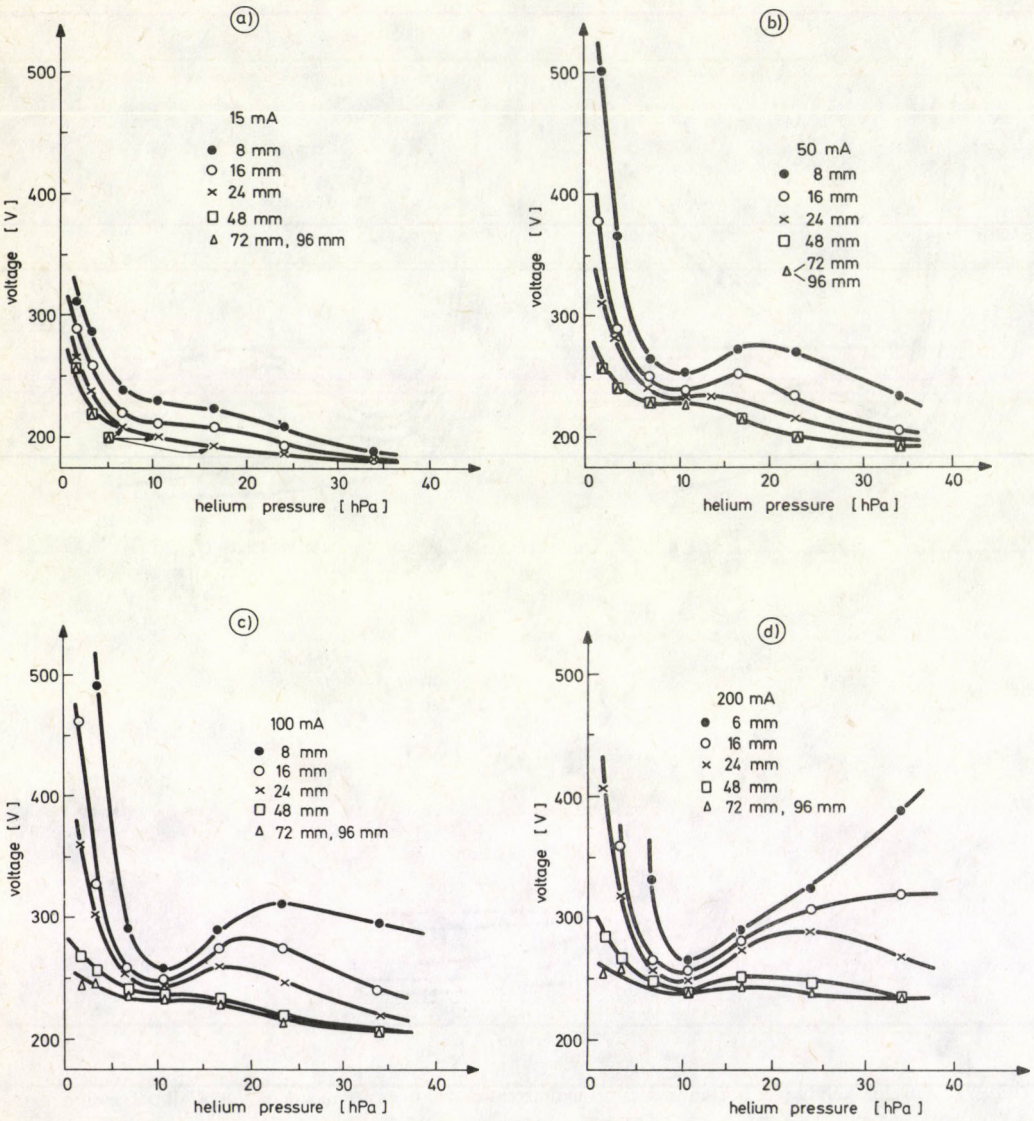

Fig. 13. Working voltage vs helium pressure for different hollow-cathode lengths. Discharge current intensity: (a) – 15 mA, (b) – 50 mA, (c) – 100 mA, (d) – 200 mA, (e) – 250 mA

the cathode length reduction, the rise being the more distinct the lower is the helium pressure.

The analysis of the results obtained leads to the conclusion that this effect can be attributed not only to the cathode current density rise due to the cathode shortening, but also to the resulting changes of the current distribution over the cathode surface.

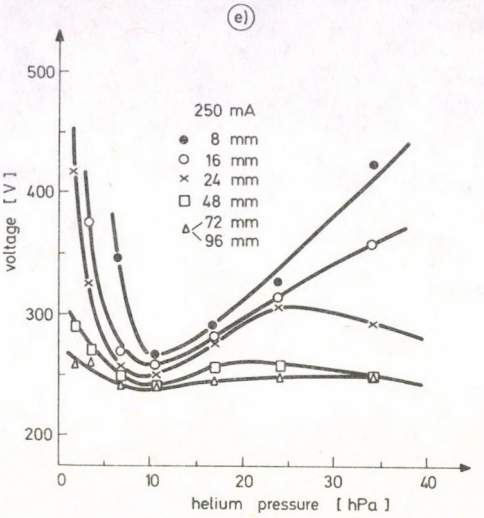

Fig. 13. (cont.)

3.3. Symmetric electrode geometry

The longitudinal discharge in a hollow cathode operating in conjunction with two anodes was investigated for one value of helium pressure, 16.66 hPa, most typical of hollow-cathode lasers.

The results are shown in Figs 15 and 16. In a hollow cathode fed symmetrically the current distribution is symmetric with respect to an axis traversing the cathode centre and dividing the system of electrodes into two asymmetric halves composed of one anode and one half of the original cathode. In order to distinguish such a discharge from the *asymmetric discharge* in a hollow cathode operating in conjunction with one anode, it will be called the *symmetric discharge.*

The symmetric discharge as well as the asymmetric one is characterized by nonuniform distribution over the cathode discharge. To facilitate the evaluation of the extent of this nonuniformity cathode current distributions normalized relative to the corresponding mean values of the current density are shown in Figs 17 and 18. Here the horizontal line on the level of unity represents the normalized uniform distribution of the current density irrespective of the discharge current intensity.

It is evident from Figs 17 and 18 that the cathode current density distribution is most nonuniform for the longest cathodes. The lower the current intensity, the more marked is this nonuniformity. In the extreme case (cathode length of 96 mm, discharge current intensity of 30 mA) the difference between the maximum and minimum value of the current density over the cathode surface is more than twice as large as the corresponding mean value of the current density. Shortening of the cathode or increase of the discharge current intensity results in flattening of the distribution nonuniformities. At the same time the saddle-like distribution curves assume a parabolic shape.

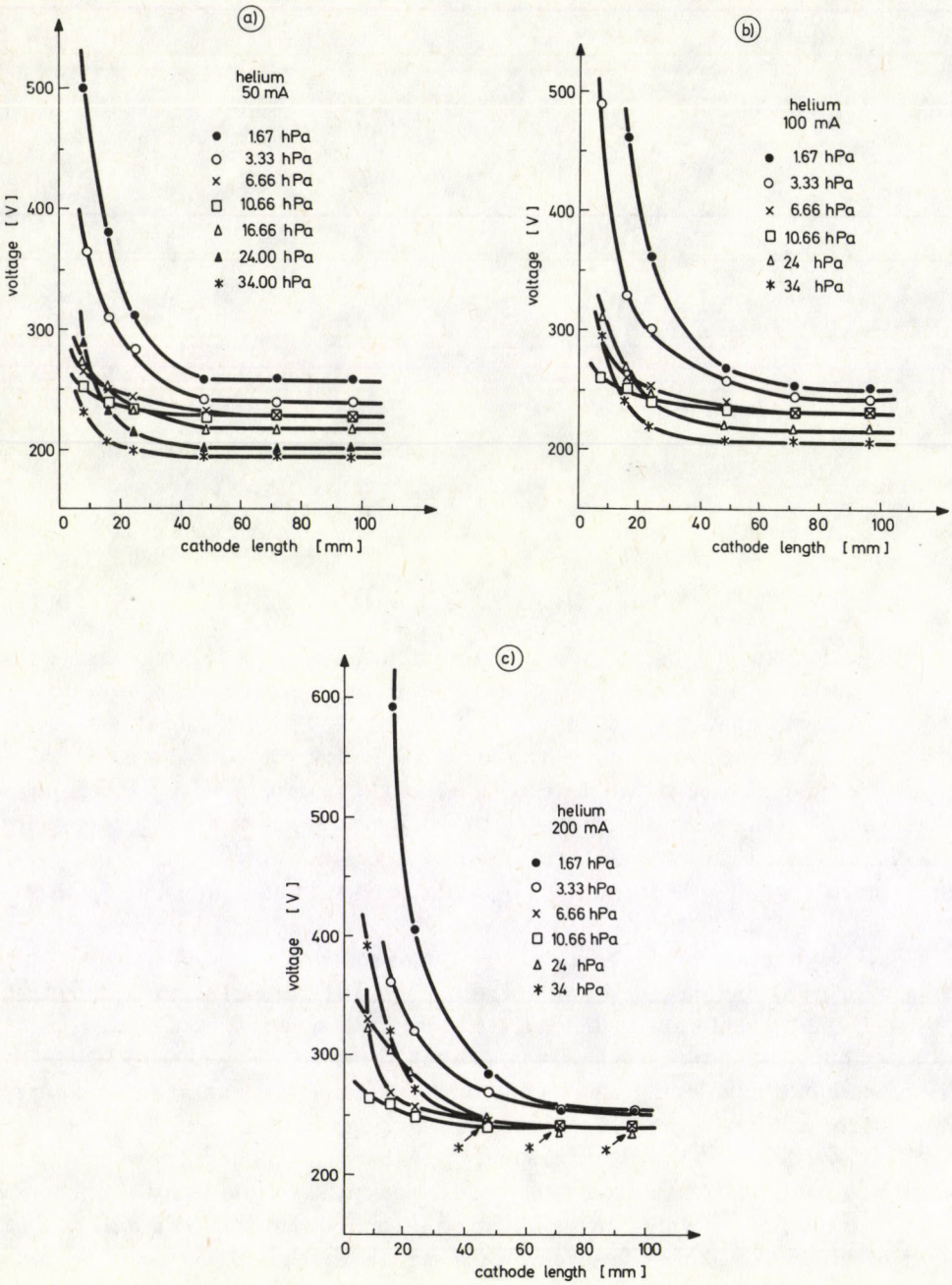

Fig. 14. Working voltage vs hollow-cathode length. Discharge current intensity: (a) – 50 mA, (b) – 100 mA, (c) – 200mA

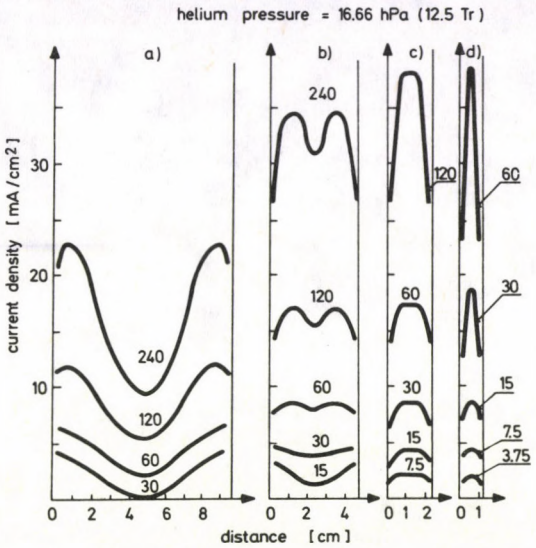

Fig. 15. The cathode current density distribution along the hollow-cathode fed symmetrically. Helium pressure: 16.66 hPa; discharge current intensity: 3.75 mA, 7.5 mA, 15 mA, 30 mA, 60 mA, 120 mA, 240 mA

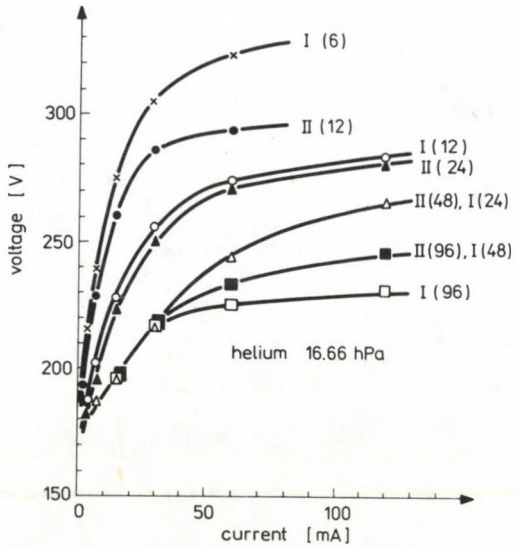

Fig. 16. V–I characteristics for the longitudinal hollow-cathode discharge with (I) one and (II) two anodes. Helium pressure: 16.66 hPa, cathode length: 96 mm, 48 mm, 24 mm, 12 mm and 6 mm. Along the abscissae the anode current intensities are shown

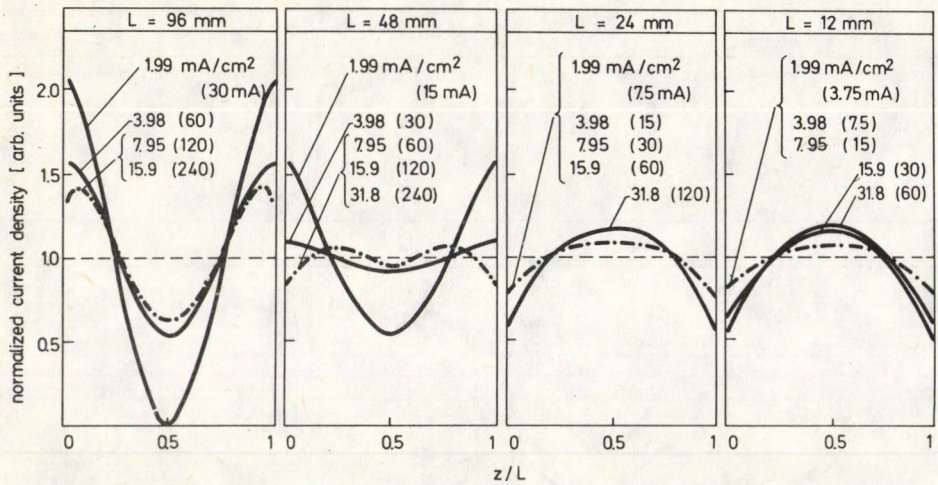

Fig. 17. Cathode current density distributions normalized with respect to the mean value of the current density for the hollow-cathode operating in conjunction with two anodes. Helium pressure: 16.66 hPa, cathode length: 96 mm, 42 mm, 24 mm, 12 mm. Numbers represent mean values of the cathode current density and (in brackets) discharge current intensities, respectively

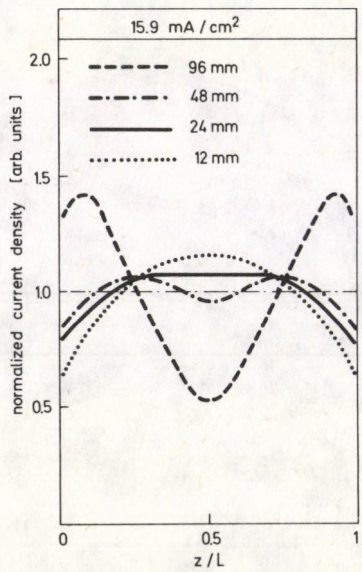

Fig. 18. Discharge density distributions in the hollow-cathode operating in conjunction with two anodes, normalized with respect to the mean value of the cathode current density. Helium pressure: 16.66 hPa, cathode length: 96 mm, 48 mm, 24 mm, 12 mm; mean value of the cathode current density: 15.9 mA/cm^2

This makes it possible to obtain a uniform or nearly uniform distribution of the cathode current density. For instance, a nearly uniform distribution of the cathode current density may be expected for a discharge in a hollow cathode 48 mm long if only the discharge current is kept within the 30 mA–60 mA interval (cf. Fig. 17). Note, however, that this uniformity of the cathode current density is accompanied by a nonuniform distribution of the longitudinal discharge current. Thus, the hollow-cathode discharge in the presence of two anodes is, as a whole, inhomogeneous.

The symmetry of cathode current density distributions in a hollow-cathode discharge where two anodes are used suggests that the discharge consists of two parts, each of them belonging mainly to its anode and the adjacent half of the cathode. The structure of the symmetric discharge may be explained better on the basis of a comparison of working voltages and cathode current density distributions for symmetric and asymmetric discharges, and also for an asymmetric discharge with a cathode shortened by half (Figs 16 and 19), termed briefly the *asymmetric half-discharge*. The following conclusions can be drawn from this comparison:

For the longest cathode (96 mm) all of the above mentioned three distributions of the cathode current density are identical irrespective of the type of discharge, unless the anode current intensity exceeds 15 mA. Potentials of anodes corresponding to these distributions are the same. This means that the symmetric discharge is then composed of two mutually independent asymmetric discharges, each of them occurring only between its anode and the adjacent cathode half. The presence or absence of one asymmetric discharge does not affect the other discharge. Likewise, the symmetric discharge may be regarded as composed of two asymmetric half-discharges.

With a rise of the discharge current intensity in the longest cathode the distributions of the cathode current density in the asymmetric discharge begin to differ from the other two distributions, which remain indistinguishable. The difference appears mainly because in the asymmetric discharge the current may be distributed over an area larger than in the remaining two cases. Consequently, the mean value of the cathode current density per unit length of the cathode surface covered by the discharge is lower, and therefore the working voltage for the asymmetric discharge is lower, too (see e.g. Fig. 16). Similar conclusions may be obtained from the analysis of the discharge in the 48 mm hollow cathode. In spite of insignificant differences between the forms of distributions of cathode current densities for the symmetric discharge and corresponding asymmetric half-discharge the symmetric discharge may still be regarded as consisting of two, nearly independent asymmetric half-discharges.

For cathodes shorter than 48 mm both parts of the symmetric discharge affect each other and cease being independent. This results in differences in the forms of the cathode current density distributions and changes of anode voltages of the symmetric discharge and asymmetric half-discharge. The shorter the cathodes, the larger these differences.

It follows from the above discussion that for the range of parameters as considered here the symmetric discharge in a hollow cathode whose length is 48 mm or

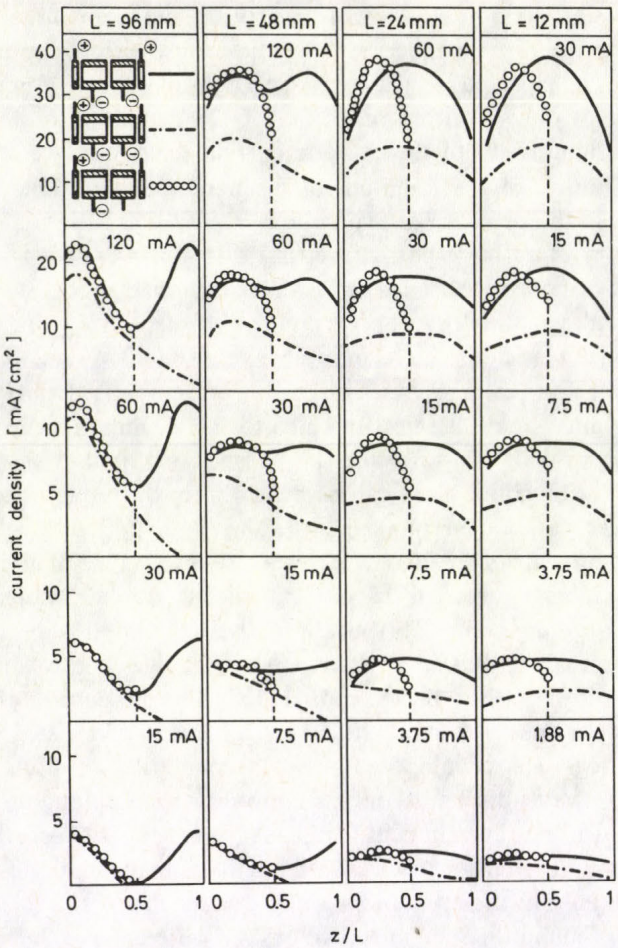

Fig. 19. A comparison of cathode current density distributions for the symmetric discharge (solid line), asymmetric discharge (dash-dot line), and asymmetric half-discharge (circles). Helium pressure: 16.66 hPa, cathode length 96 mm, 48 mm, 24 mm, 12 mm. Current intensities shown (1.88 mA up to 120 mA) denote the anode current values

more may be regarded approximately as composed of two independent asymmetric half-discharges. On the other hand, for cathodes shorter than 48 mm both parts of the discharge interact, which leads to changes in the working voltage value and form of the cathode current density distributions.

The decrease, occurring in the latter case, of the anode voltages in the symmetric discharge compared with the asymmetric half-discharge characterized by the same intensity of the anode current possibly results from the presence of the so-called *pendel electrons* [13] in the central region of the cathode equidistant from both anodes. The presence of such electrons, causing additional ionization of the gas, should lead to a

drop of the working voltage. Besides, in the symmetric discharge the contribution of photons to the production of electrons on the cathode surface in the intermediate region is larger than in the case of two asymmetric half-discharges where photons are more likely to escape outside. This may be another reason for the working voltage decrease for the symmetric discharge.

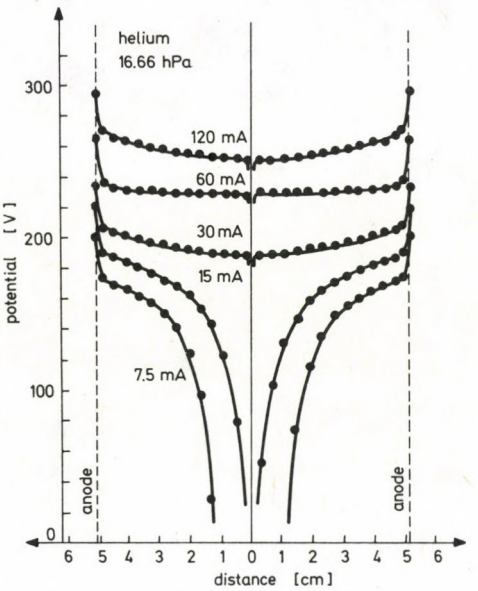

Fig. 20. The floating potential of insulated odd cathode segments in the hollow-cathode discharge with two anodes for different intensities of the anode currents

For the symmetric discharge, as for the asymmetric one, the plasma potential distribution along the cathode was estimated by measuring the floating potential of electrically insulated odd cathode segments (Fig. 20). The measurement confirmed the presence in the discharge of a region of nearly constant longitudinal electric field intensity, suggesting the existence in this region of a plasma exhibiting properties of the positive column.

4. Concluding remarks

The results of investigations presented in this paper lead to the following conclusion:

The longitudinal discharge in a hollow cathode having dimensions typical of the laser technology is axially inhomogeneous irrespective of the configuration of the electrodes, anode and cathode — symmetric or asymmetric. Axial distributions of the

cathode current density and longitudinal current as well as axial distributions of the plasma potential are, as a rule, nonuniform. From this point of view minor differences only have been observed between the longitudinal discharge in hollow cathodes typical of laser tubes and the classical hollow-cathode discharge [4–11].

An appropriate choice of the cathode length and current intensity for the symmetric discharge will ensure a uniform cathode current density distribution. However, this will not provide for a uniform distribution of the longitudinal current and corresponding uniform axial distributions of the plasma potential and cathode fall.

The presence in some regions of the discharge plasma of a constant electric field suggests that the plasma in these regions has properties of the positive column plasma of glow discharge.

The properties of the longitudinal hollow-cathode discharge for which only part of the cathode surface is covered by the discharge differ essentially from those of the normal glow discharge between flat or convex electrodes. It is therefore inappropriate to call the former using the classical term "normal glow discharge" rather than "normal hollow-cathode discharge".

The inhomogeneity of the longitudinal hollow-cathode discharge affects the operation of the laser tube considerably. First of all a nonuniform excitation of laser levels along the cathode axis should be expected. Therefore a considerable part of the hollow cathode may be inactive from the viewpoint of lasing even when filled with discharge plasma. This reduces the so called active length of the laser tube. Nonuniform current and plasma potential distributions may result in nonuniform cathodic sputtering and heating of the cathode surface leading to a shortened lifetime of the device.

If operated with a mixture of gases the effect of cataphoresis may be expected to occur in the hollow cathode due to the presence of the longitudinal electric field. Such an effect is undesirable as it might make the continuous laser operation difficult to maintain (e.g. in the $He–Kr^+$ laser).

The investigations of the symmetric discharge showed that for a laser tube filled with alternating cathode and anode segments an increase of the number of segments for the tube length and discharge current intensity fixed results in a decrease of the working voltage.

The results presented in this paper do not provide a complete answer as to the optimum length of the hollow cathode with longitudinal discharge to be used for lasers. It follows from the analysis of uniformity of the cathode current density distribution and working voltage value for the asymmetric and symmetric discharges that in laser technology the most appropriate application of cathodes is the following: cathodes of a length of 12 to 24 mm are suitable for asymmetric power supply, and those of a length of 24 to 48 mm are suitable for a symmetric configuration. Then the cathode current density distributions are relatively uniform and the working voltages necessary to ensure the appropriate current density are not very high.

However, to answer the question mentioned above fully the microscope parameters of the hollow-cathode discharge plasma should be measured. These are mainly the axial distributions of the electron energy distribution function and electron concentration. An analysis of the results of such measurements should provide the answer required.

Acknowledgment

The author extends his gratitude to Mr. J. Ziemann for his ingenious technical help during the measurements, W. Piechocki, M. Sc., for his assistance in the processing of the results and Dr. H. Szczepańska for reviewing the manuscript and valuable remarks.

References

1. W. K. Schuebel, A. Review of Hollow Cathode Laser Development, Proc. Conf. Lasers 79, 431, Orlando, 1979.
2. K. Rozsa, Z. Naturforsch., **35A,** 649, 1980.
3. J. Fujii, IEEE J. Quantum Electronics, QE-**11,** 111, 1975.
4. W. Weizel, G. Müller, Ann. der Physik, **6,** 417, 1956.
5. B. I. Moskalev, Rozrjad s połom katodom, Energia, Moskva, 1969, 52–62.
6. Je. T. Kuczerenko, Je. W. Zykova, L. N. Makosevskaja, Ukr. fiz. Zhurn., **17,** 2063, 1972.
7. Je. W. Zykova, Je. T. Kuczerenko, Ukr. fiz. Zhurn., **21,** 1549, 1976.
8. A. Rutscher, Die Hohlkathodenentladung-Physikalische Grundlagen und Anwendungen, Arbeitstagung Physik und Technik des Plasmas, Physikalische Gesellschaft der DDR, Karl Marx-Stadt 1974, 265–276.
9. K. Fujii, IEEE J. Quantum Electronics, QE-**15,** 35, 1979.
10. W. Ohlendorf, Zeit. Phys., **167,** 123, 1962.
11. W. I. Moskalev, The Structure of Plasmas Inside the Hollow Cathode of the Glow Discharge, 9th Int. Conf. Phenom. Ionized Gases, Bucuresti, 1969, 166.
12. G. Francis, The Glow Discharge at Low Pressure, Handbuch der Physik, Band XXII, Gasentladungen II, Springer Verlag, 1956, 97–99.
13. H. Helm, Z. Naturforsch., **27a,** 1812, 1972.

Acta Physica Hungarica 54 (1—2), pp. 97—99 (1983)

A COMPARISON BETWEEN ROSEN AND EINSTEIN THEORY OF GRAVITATION

G. CALLEGARI

Istituto di Fisica della Universitá di Ferrara, Ferrara, Italy

and

L. BARONI

Istituto di Fisica della Universitá di Bologna, Bologna, Italy

(Received 11 December 1981)

In this paper a method is given to compare Rosen's theory of gravitation and Einstein's theory of gravitation on the ground of the emission of gravitational radiation by a binary system with a compact companion. The conclusion is that the emission of gravitational radiation deduced from Rosen's theory is three orders of magnitude greater than foreseen by Einstein's theory.

Rosen's bimetric theory of gravitation [1] predicts the existence of dipole gravitational radiation and this is due to violation of the equivalence principle for strongly self-gravitating bodies [2].

Gravitational and inertial masses differ appreciably when the gravitational field is strong (e.g. in a neutron star) and therefore dipole radiation is possible. Will and Eardley [2] calculate the rate of change of the orbital energy E of a binary system due to dipole gravitational radiation and find:

$$\frac{dE}{dt} = \frac{20G}{9c^3}\mu^2(s_1 - s_2)^2 |\mathbf{r}|, \tag{1}$$

where $\mathbf{r}$ is the distance between the two stars, μ the reduced inertial mass and

$$s_{1,2} = \frac{1}{2}(Gm_{1,2}c^2)^{-1} \int_{V_{1,2}} \frac{\rho(\mathbf{x})\rho(\mathbf{x}')}{|\mathbf{x}-\mathbf{x}'|} d\mathbf{x}d\mathbf{x}'$$

with with ρ the rest-mass density.

The main difficulty with Rosen's theory is the wrong sign in the above formula according to which gravitational radiation emission increases the energy of the system. To overcome this difficulty Rosen [3] has shown on the ground of the Wheeler–Feyman absorber theory [4] that gravitational radiation is to be found only in the form of standing waves and therefore physical systems emitting gravitational radiation cannot lose or gain energy in an appreciable amount although a gravitational detector does respond to gravitational waves. From now on we shall refer to this theory as WFR

suggestion. A direct verification of this phenomenon has been suggested by Fortini et al. [5].

An indirect evidence could come from the observations of the period changes of the binary pulsar PSR 1913+16 as predicted by Taylor et al. [6] on the ground of general relativity. If the predicted value is observed both the bimetric theory of gravitation and the WFR suggestion would be invalidated.

If, on the other hand, the detected changes in the period are not in complete agreement with the Einstein's theory of gravitation, then general relativity can be rescued only by the WFR suggestion.

In this case, however, Einstein's theory should compete with other theories of gravitation including the bimetric theory itself. Therefore if the WFR suggestion is real, it is no longer possible to discriminate between the Rosen and Einstein theories as proposed by Will and Eardley [2] through the period changes in a system like PSR 1913+16.

In this work we show that it is possible to distinguish between the two theories by measuring the "intensity" of gravitational radiation.

We must remember that in the framework of the WFR suggestion what is measured by a gravitational wave detector is the energy exchanged by the system with the standing gravitational wave and in this case formula (1) gives a measure of the amplitude of the wave.

For our purpose it is convenient to choose binary systems in which the dipole radiation strength (as predicted by the bimetric theory) is much different from that of quadrupole radiation (as predicted by general relativity). A binary system formed by two neutron stars is not well suited because dipole radiation depends critically, through the term $s_1 - s_2$, on the masses of the stars as pointed out by Will and Eardly [2]. If, however, we consider a binary system formed by a neutron and a normal star, the gravitational wave emission does not depend critically on the masses: in fact for a normal star $s \sim 10^{-6}$ and for a neutron star $s \sim 10^{-1}$. Besides this, such systems are relatively abundant in our galaxy ($\sim 10^3$–10^4) [7].

The ratio Q between the energy exchanged by dipole emission in the bimetric theory $\left(\frac{dE}{dt}\right)$ D. R. and the energy exchanged by the quadrupole emission in general relativity $\left(\frac{dE}{dt}\right)$ G. R. is easily calculated on the ground of a paper by Will [8] and turns out to be

$$Q = \left(\frac{dE}{dt}\right)_{\text{D.R.}} \Big/ \left(\frac{dE}{dt}\right)_{\text{G.R.}} = \frac{5}{8} \frac{\xi}{K_1} \frac{c^2}{v^2} |s_1 - s_2|^2, \tag{2}$$

where ξ and K_1 are dimensionless parameters. Their values in the present case are $\xi = -\frac{20}{3}$ and $K_1 = -\frac{21}{2}$. In Table I calculated Q values for some X-emitting binary systems are given.

Table I

Calculated values for X-emitting binary systems

	Binary period [s]	Visible companion	Neutron star velocity [cm/s]	Q
Cyg X-1	$4.83\ 10^5$	20 M	$2.49\ 10^7$	5760
Cen X-3	$1.8\ 10^5$	16 M	$3.21\ 10^7$	3460
SMC X-1	$2.67\ 10^5$	25 M	$3.27\ 10^7$	3340
Vel X-1	$1.73\ 10^5$	25 M	$2.3\ 10^7$	6750

As one can see, if the bimetric theory is correct, gravitational radiation should be three orders of magnitude greater than foreseen by general relativity.

References

1. N. Rosen, J. Gen. Rel. Grav., **4,** 435, 1973.
2. C. M. Will and D. M. Eardley, Ap. J., **212,** L 91, 1977.
3. N. Rosen, Lett. Nuovo Cimento, **19,** 249, 1977.
4. J. A. Wheeler and R. P. Feynmann, Rev. Mod. Phys., **17,** 157, 1945.
5. P. Fortini, F. Fuligni and C. Gualdi, Lett. Nuovo Cimento, **23,** 345, 1978.
6. J. H. Taylor, L. A. Fowler and P. M. McCullogh, Nature, **277,** 437, 1979.
7. G. Callegari and A. M. Nobili, Mem. Soc. Astr. It., **4,** 21, 1977.
8. C. M. Will, Ap. J., **214,** 826, 1977.

Acta Physica Hungarica 54 (1—2), pp. 101—109 (1983)

INTERACTION OF AN OBLIQUELY INCIDENT ELECTROMAGNETIC WAVE WITH COLLISIONAL, MAGNETIZED AND MOVING PLASMA SLAB

Y. P. SINGH and A. S. SHEKHAWAT

Department of Physics, University of Rajasthan, Jaipur, India

(Received 11 December 1981)

Interaction of an electromagnetic wave incident obliquely on a homogeneous, magnetized, collisional and moving plasma slab is investigated. The effects of plasma slab velocity ($\beta = v/c$), electron density (ω_p/ω), and angle of incidence (ϑ) on reflection, transmission and absorption coefficients are discussed numerically. It is observed that for higher densities of plasma the reflection coefficient decreases with increase in the angle of incidence, whereas for lower densities of plasma the reflection coefficient remains constant up to $\vartheta = 35°$, afterwards it increases rapidly and becomes greater than unity. For lower plasma frequency the absorption coefficient has an oscillatory behaviour.

Introduction

It is well known that electromagnetic waves can propagate in a homogeneous and isotropic plasma. It is of interest to know how such waves interact when arriving at an interface of collisional, magnetized and moving plasma slab. The problem of electromagnetic interaction with a moving plasma slab is of considerable importance in the fields of ionospheric studies, re-entry communication, black out problems, meteorology etc., and have received considerable attention of many workers including Yeh [1]; Collier and Tai [2]; Jain et al. [3]; Tiwari et al. [4]; Phalswal and Varma [5]; Phalswal et al. [6]; and Phalswal and Singh [7]. However, Phalswal and Singh [7] have studied the problem for moving plasma slab in the presence of an external static magnetic field.

The object of the present paper is to provide a theoretical expression for power reflection (R), transmission (T) and absorption (A) coefficients for p-polarized wave for a moving, homogeneous collisional plasma slab in the presence of an obliquely applied static magnetic field B, by solving Maxwell's equations under necessary boundary conditions. The effects of plasma density (ω_p/ω), slab velocity (β) and angle of incidence ϑ have been studied numerically.

Formulation of the problem

Consider a collisional plasma slab (with sharp boundaries at $Z=0$ and $Z=d_0$), which is embedded in a uniform static magnetic field B. The static magnetic field is always at an arbitrary angle ϑ with propagation vector K. The plasma slab can move with any uniform velocity v in x-direction, so that there will be no Doppler shift in frequency for the reflected and transmitted waves. Let us also consider two reference frames: the primed frame being fixed in the moving plasma slab and the unprimed frame is attached with e.m. wave source. Thus the two reference frames are in relative motion.

Following Appleton's equation (Heald and Wharton [8]) we get the complex refractive index in the primed frame as:

$$\tilde{\mu}'^2 = \left[1 - \frac{\omega_p'^2/\omega'^2 \sin^2 \vartheta'}{\sin^2 \vartheta' - \frac{\omega_b^2}{\omega'^2} \sin^4 \vartheta - (1-\omega_p'^2/\omega'^2)\cos^2 \vartheta'} - \right.$$

$$\left. - \frac{iv'}{\omega'} \frac{\omega_p'^2}{\omega'^2} \frac{\{1+\omega_b'^2/\omega'^2 \sin^2 \vartheta' + 3\cos^2 \vartheta'/\sin^2 \vartheta'\}}{\left\{1-\omega_b'^2/\omega'^2 \sin^2 \vartheta' - (1-\omega_p'^2/\omega'^2)\frac{\cos^2 \vartheta'}{\sin^2 \vartheta'}\right\}^2} \right], \tag{1}$$

where $\tilde{\mu}'$, ω_p', ω', v' and ω_b' are the complex refractive index, plasma frequency, angular frequency, collisional frequency and cyclotron frequency of the electrons in the primed system, respectively, ignoring ion dynamics. Now following Sommerfeld [9] the incident field equations for p-polarized wave in the unprimed system are:

$$B_y = B_0 \exp\left[-i(K\cos\vartheta\, Z + K\sin\vartheta\, x - \omega t)\right],$$

$$E_y = 0, \tag{2}$$

where B_0, K and ω are the amplitude of the incident magnetic field, the wave vector in the positive direction of the Z-axis and the angular frequency of wave, respectively.

Further following Phalswal and Singh [7] in primed frame and matching the tangential electric and magnetic fields at the interfaces $Z'=0$ and $Z'=d'$ we obtain

$$A_{r_1}' = B_0' \frac{1-K_s'/K'}{1+K_s'/K'}, \tag{3}$$

$$G_t' = \frac{2B_0'}{1+K_s'/K'}, \tag{4}$$

where

$$K' = \omega'/c,$$
$$K_s' = \omega'/c \cdot \tilde{\mu}', \tag{5}$$

$$K'_s = \frac{\omega'}{c}\left[1 - \frac{\omega'^2_p/\omega'^2 \sin^2\vartheta'}{\sin^2\vartheta' - \frac{\omega'^2_b}{\omega'^2}\sin^4\vartheta - \left(1-\frac{\omega'^2_p}{\omega'^2}\right)\cos^2\vartheta'} - \right.$$

$$\left. - \frac{iv'}{\omega'}\frac{\omega'^2_p}{\omega'^2}\frac{\{1+\omega'^2_b/\omega'^2\sin^2\vartheta' + 3\cos^2\vartheta'/\sin^2\vartheta'\}}{\{1-\omega'^2_b/\omega'^2\sin^2\vartheta' - \left(1-\frac{\omega'^2_p}{\omega'^2}\right)\cos^2\vartheta'/\sin^2\vartheta'\}^2}\right]^{\frac{1}{2}}, \tag{6}$$

$$\tilde{\mu}' = \mu' - i\chi' = k'^{1/2}. \tag{7}$$

B'_0, Ar', G'_i are arbitrary constants, μ', χ' and k' are the real refractive index, attenuation index and dielectric constants, respectively. K' and K'_s are wave vectors in free space and plasma slab in primed frame, respectively. From Eqs (2)–(7), matching the tangential electric and magnetic fields at $Z=0$, we obtain (Heald and Wharton [8]) the average power reflection, transmission and absorption coefficients as

$$R' = \frac{\gamma'_p\left[1+(1-2\gamma'_p)\exp\left(-\frac{4\omega'\chi'd'}{c}\right)\right]}{1-\gamma'^2_p\exp\left(-\frac{2\omega'\chi'd'}{c}\right)},$$

$$T' = \frac{(1-\gamma'_p)^2\exp\left(-\frac{2\omega'\chi'd'}{c}\right)}{1-\gamma'^2_p\exp\left(-\frac{4\omega'\chi'd'}{c}\right)}, \tag{8}$$

$$A' = \frac{(1-\gamma'_p)\left[1-\exp\left(-\frac{2\omega'\chi'd'}{c}\right)\right]}{1-\gamma'_p\exp\left(-\frac{2\omega'\chi'd'}{c}\right)},$$

where

$$\gamma'_p = \left|\frac{A'_r}{B'_0}\right|^2 = \frac{(1-K'_r)^2+K'^2_i}{(1+K'_r)^2+K'^2_i}. \tag{9}$$

K'_r and K'_i are real and imaginary parts of K'_s/K', and are given by

$$K'_r = \left\{\frac{\sqrt{A'^2_1+B'^2_1}+A'_1}{2}\right\}^{1/2},$$

$$K'_i = \left\{\frac{\sqrt{A'^2_1+B'^2_1}-A'_1}{2}\right\}^{1/2},$$

with

$$A_1' = 1 - \frac{\omega_p'^2/\omega'^2 \sin^2 \vartheta'}{\sin^2 \vartheta' - \frac{\omega_b'}{\omega'^2} \sin^4 \vartheta' - \left(1 - \frac{\omega_p'^2}{\omega'^2}\right) \cos^2 \vartheta'},$$

$$B_1' = \frac{v'}{\omega'} \frac{\omega_p'^2}{\omega'^2} \frac{\{1 + \omega_b'^2/\omega'^2 \sin^2 \vartheta' + 3\cos^2 \vartheta'/\sin^2 \vartheta'\}}{\left\{1 - \frac{\omega_b'^2}{\omega'^2} \sin^2 \vartheta' - (1 - \omega_p'^2/\omega'^2) \frac{\cos^2 \vartheta'}{\sin^2 \vartheta'}\right\}^2}. \tag{10}$$

Similar calculations will give reflected and transmitted fields at the two interfaces of the slab in the unprimed frame.

Now making use of phase invariance (Pauli [10]), the variance of Maxwell's equations with respect to the Lorentz transformation (Sommerfeld [9]), and satisfying the boundary conditions, we obtain the equations of transformation from primed to unprimed frame as

$$\omega' = \alpha(\omega - vK) = \alpha\omega(1 - \beta),$$

$$K' = \alpha\left[K - \frac{\omega v}{c^2}\right] = \alpha K(1 - \beta),$$

$$K^{(r_1)} = \alpha(K' - \frac{\omega'\beta}{c}) = \alpha^2 K(1 - \beta)^2,$$

$$K^{(r_2)} = \alpha\left(K_s' - \frac{\omega'\beta}{c}\right) = \alpha^2 K(1 - \beta)(D - \beta) = K_s^{(t_1)},$$

$$K^{(t_2)} = \alpha\left(K' + \frac{\omega'\beta}{c}\right) = \alpha^2 K(1 - \beta)^2,$$

$$\omega^{(r_1)} = \alpha(\omega' - K'\beta c) = \alpha^2\omega(1 - \beta)^2,$$

$$\omega^{(r_2)} = \alpha(\omega' - K_s'\beta c) = \alpha^2\omega(1 - \beta)(1 - D\beta) = \omega^{(t_1)},$$

$$\omega^{(t_2)} = \alpha(\omega' + K'\beta c) = \alpha^2\omega(1 - \beta^2),$$

$$d = \frac{d'}{\alpha} = \frac{d_0}{\alpha}, \qquad v' = \alpha v,$$

$$\gamma_p = \gamma_p' \left(\frac{1 - \frac{vK}{\omega}}{1 + \frac{vK^{(r)}}{\omega^{(r)}}}\right) = \frac{(1 - K_r)^2 + K_i^2}{(1 + K_r)^2 + K_i^2} \left(\frac{1 - \beta}{1 + \beta}\right)^2, \tag{11}$$

$\alpha = \dfrac{1}{\sqrt{1 - \beta^2}}$, $\beta = \dfrac{v}{c}$, d_0 is the proper thickness of the slab. c = velocity of light.

$$D = \left[1 - \frac{\omega_p'^2/\omega'^2 \sin^2 \vartheta'}{\sin^2 \vartheta' - \frac{\omega_b'^2}{\omega'^2} \sin^4 \vartheta' - (1-\omega_p'^2/\omega'^2)\cos^2 \vartheta'} - \right.$$

$$\left. - \frac{iv'}{\omega'} \frac{\omega_p'^2}{\omega'^2} \frac{\{1+\omega_b'^2/\omega'^2 \sin^2 \vartheta' + 3\cos^2 \vartheta'/\sin^2 \vartheta'\}}{\left\{1-\omega_b'^2/\omega'^2 \sin^2 \vartheta' - (1-\omega_p'^2/\omega'^2)\frac{\cos^2 \vartheta'}{\sin^2 \vartheta'}\right\}^2} \right]^{1/2},$$

$$K_r = \left[\frac{\sqrt{A_1+B_1}+A_1}{2}\right]^{1/2}, \qquad K_i = \left[\frac{\sqrt{A_1+B_1}-A_1}{2}\right]^{1/2},$$

with

$$A_1 = 1 - \frac{\omega_p^2/\omega^2 \sin^2 \vartheta}{\alpha^2(1-\beta)^2 \sin^2 \vartheta - \omega_b^2/\omega^2 \sin^4 \vartheta - Q_0 \cos^2 \vartheta},$$

$$B_1 = \frac{\gamma}{\omega} \cdot \frac{\omega_p^2}{\omega^2} \frac{[\alpha^2(1-\beta)^2 + \omega_b^2/\omega^2 \sin^2 \vartheta + \alpha^2(1-\beta)^2 3\cos^2 \vartheta/\sin^2 \vartheta]}{[\alpha^2(1-\beta)^2 - \omega_b^2/\omega^2 \sin^2 \vartheta - Q_0 \cos^2 \vartheta/\sin^2 \vartheta]},$$

$$Q_0 = [\alpha^2(1-\beta)^2 - \omega_p^2/\omega^2]. \tag{12}$$

When the slab is moving in the x-direction, there would be no Doppler shift in the frequency for the reflected and transmitted waves. Thus the angle of incidence remains invariant in this case.

Reflection, transmission and absorption coefficients

Now following Phalswal et al [6] and Phalswal and Singh [7], we obtain reflection, transmission and absorption power coefficients in the unprimed frame

$$R = \frac{\gamma_p\left[1+(1-2\gamma_p)\exp\left(-\frac{4\omega\chi d_0}{c\cdot\alpha}\right)\right]}{1-\gamma_p^2 \exp\left(-\frac{4\omega\chi d_0}{c\cdot\alpha}\right)},$$

$$T = \frac{(1-\gamma_p)^2 \exp\left(-\frac{2\omega\chi d_0}{c\cdot\alpha}\right)}{1-\gamma_p^2 \exp\left(-\frac{4\omega\chi d_0}{c\cdot\alpha}\right)},$$

$$A = \frac{(1-\gamma_p)\left[1-\exp\left(-\frac{2\omega\chi d_0}{c\cdot\alpha}\right)\right]}{1-\gamma_p \exp\left(-\frac{2\omega\chi d_0}{c\cdot\alpha}\right)}. \tag{13}$$

Results and discussion

For $\omega_p = 0$, i.e. in the absence of plasma the reflection and absorption coefficients reduce to zero. In case of collisional ($\nu \neq 0$), magnetized ($\omega_b \neq 0$) and $\vartheta = 90°$, i.e. for the normal incidence case the reflection coefficient (R) in Eq. (9) reduces to the similar one obtained by Phalswal and Singh [7]. In case of collisional ($\nu \neq 0$), unmagnetized ($\omega_b = 0$) for $d_0 = \infty$ the reflection coefficient (R) in the Eq. (9) reduces similarly to the one obtained by Phalswal and Varma [5]. Taking $\gamma/\omega_p = 0.01$, $\frac{\omega}{C} = d_0 = 10$ cm, the effects of the plasma density (ω_p/ω), the slab velocity ($\beta = v/c$) and the angle (ϑ) are plotted in Figs 1–3.

Fig. 1 shows the variation of reflection, absorption and transmission coefficients with slab velocity ($\beta = v/c$) for $\omega_p/\omega = 0.5$, 1.5; $(\omega_b/\omega_p)^2 = 5$ and $\vartheta = 30°$, 45°. When the slab moves away from the e.m.w. source, then for $\omega_p/\omega = 1.5$, $\vartheta = 45°$ the reflection coefficient (R_3) decreases with β, but the absorption coefficient increases slightly and remains constant over a wide range of velocity; whereas for the case in which the

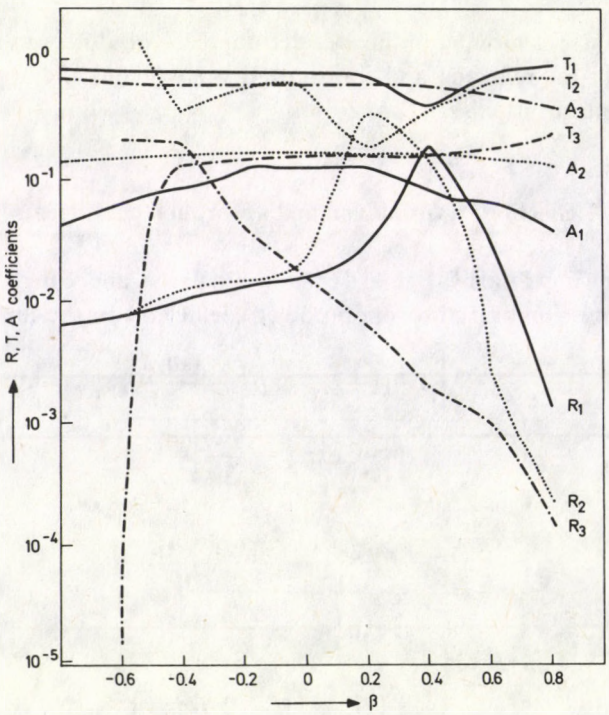

Fig. 1. Variation of R, T and A with a plasma slab velocity ($\beta = v/c$) —— $\omega_p/\omega = 0.5$, $\nu/\omega_p = 0.01$, $\omega_b/\omega_p = 5.0$, $\vartheta = 30°$, ... $\vartheta = 45°$, $-.-.-$ $\omega_p/\omega = 1.5$, $\nu/\omega_p = 0.01$, $\omega_b/\omega_p = 5.0$, $\vartheta = 45°$

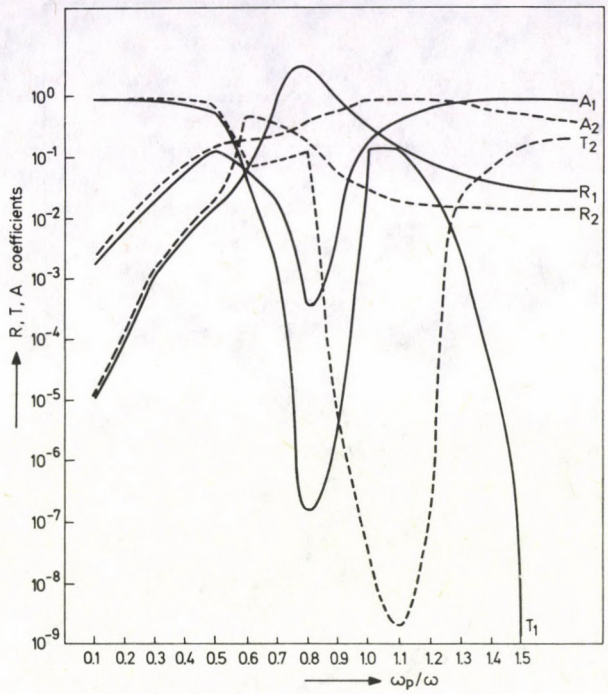

Fig. 2. Variation of R, T and A as a function of plasma density (ω_p/ω) — $\nu/\omega_p = 0.01$, $\omega_b/\omega_p = 5.0$, $\beta = 0$, $\vartheta = 30°$, – – – – $\nu/\omega_p = 0.01$, $\omega_b/\omega_p = 5.0$, $\beta = 0.001$, $\vartheta = 45°$

plasma slab moves towards the e.m.w. source the reflection coefficient increases, but the absorption coefficient shows a slight decreasing effect up to $\beta = -0.4$ and at $\beta = -0.6(A_3)$ becomes more than unity. The transmission coefficient shows a slight increase at a very high velocity of plasma slab, but when it moves towards the e.m.w. source it suddenly decreases to minimum at $\beta = -0.6$, it becomes almost zero. For a plasma frequency less than the wave-frequency $(\omega_p/\omega) = 0.5$ and $\vartheta = 30°$, the absorption coefficient (A_1) shows a negligible variation at extremes i.e. at a very high frequency of plasma slab, whereas the transmission coefficient shows a decrease at $\beta = 0.4$, otherwise the variation is almost negligible. However, the reflection coefficient (R_1) is maximum at $\beta = 0.4$ and it decreases in limits $\beta \gtrless 0.2$. Similarly if we change the angle of incidence to 45°, there is a shift in the maxima of reflection coefficient (R_2) at $\beta = 0.2$ and the minimum of transmission coefficient also shows a shift at $\beta = 0.2$. The variations in absorption coefficient are negligible.

In Fig. 2 the R, A and T are plotted as a function of plasma density (ω_p/ω) for $\beta = 0$, 0.001, $(\omega_b/\omega_p)^2 = 5$ and $\vartheta = 30°$, 45°; the reflection coefficient is maximum and greater than unity when $\omega_p/\omega = 0.7$ to 0.8. It decreases in the limit $\omega_p/\omega > 0.8 < 0.7$. The absorption and transmission coefficients are minimum at $\omega_p/\omega = 0.8$, then the transmission coefficient again increases up to $\omega_p/\omega = 1.1$, after that transmission

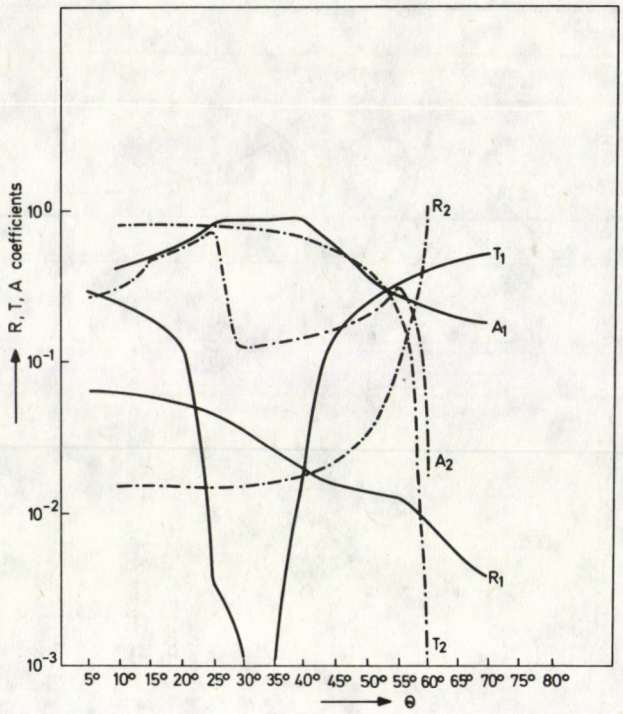

Fig. 3. Variation of R, T and A as a function of angle incidence (ϑ) in degrees —— $\nu/\omega_p = 0.01$, $\omega_p/\omega = 1.5$, $(\omega_b/\omega_p)^2 = 5.0$, $\beta = 0$, $-.-.-$ $\nu/\omega_p = 0.01$, $\omega_p/\omega = 0.5$, $(\omega_b/\omega_p)^2 = 5.0$, $\beta = 0$

coefficient (T_1) shows a rapid decrease and at density $\omega_p/\omega = 1.5$ it becomes quite negligible, whereas the absorption is fairly constant. When $\beta = 0.001$ and the incident angle is 45°, the reflection coefficient (R_2) is maximum at $\omega_p/\omega = 0.6$ and it decreases in the limit $\omega_p/\omega \gtrless 0.6$. There is an increase in the absorption coefficient (A_2) with density up to $\omega_p/\omega = 1.0$ and then it remains constant. However, the transmission coefficient (T_2) has the minimum value at $\omega_p/\omega = 1.1$ and then it increases in the limit $\omega_p/\omega \gtrless 1.1$.

In Fig. 3 the variations of R, A and T are shown with the angle of incidence ϑ at $\omega_p/\omega = 1.5, 0.5$; $\beta = 0$ and $(\omega_b/\omega_p)^2 = 5$. For a higher density of plasma ($\omega_p/\omega = 1.5$) with the increase in the angle of incidence the reflection coefficient (R_1) decreases whereas absorption coefficient (A_1) remains constant up to 35° and after that it also decreases. The transmission coefficient (T_1) remains negligible from 30° to 35°, however, at other angles it increases. For lower plasma frequency ($\omega_p/\omega = 0.5$), the reflection coefficient (R_2) remains constant up to 35° after that (R_2) increases and becomes greater than unity at 60°. The transmission coefficient shows a reverse effect, up to 40° it remains constant and afterwards it decreases exponentially and becomes negligible at 60°. However, the absorption coefficient (A_2) shows an oscillatory behaviour with the angle of incidence as shown in Fig. 3.

Acknowledgement

The authors express their sincere thanks to Dr. N. L. Varma for many valuable discussions and suggestions.

References

1. C. Yeh, J. Appl. Phys., **37,** 3079, 1966.
2. J. R. Collier and C. T. Tai, IEEE Trans., MTT-**13,** 441, 1965.
3. P. K. Jain, D. Singh, P. N. Gupta and S. K. Tolpadi, IEEE Trans., AP-**21,** 743, 1973.
4. G. N. Tiwari and S. K. Tolpadi, Indian J. Radio and Space Phys., **6,** 114, 1977.
5. D. R. Phalswal and N. L. Varma, Indian J. Radio and Space Phys., **7,** 182, 1978.
6. D. R. Phalswal, Y. P. Singh and N. L. Varma, Acta Phys. Hung., **48,** 68, 1980.
7. D. R. Phalswal and Y. P. Singh, Proc. Indian National Science Academy, **46A,** 470, 1980.
8. M. A. Heald and C. B. Wharton, Plasma Diagnostics with Microwaves, John Wiley and Sons Inc., N.Y., 130, 1965.
9. A. Sommerfeld, Electrodynamics, Academic Press Inc., N. Y., 280, 1952.
10. W. Pauli, Theory of Relativity, Pergamon Press Inc., N. Y., 94, 1958.

Acta Physica Hungarica 54 (1—2), pp. 111—118 (1983)

ON THE CHARACTERISTICS OF THE OXIDATION OF VANADIUM EFFECTED BY A CONTINUOUS BEAM OF LASER LIGHT

F. V. BUNKIN, N. A. KIRICHENKO, B. S. LUKYANCHUK, A. V. SIMAKHIN, G. A. SHAFEEV
Lebedev Physical Institute, Moscow, USSR

and

L. NÁNAI, I. HEVESI
Department of Experimental Physics, József Attila University, Szeged, Hungary

(Received 19 February 1982)

The CW CO_2 laser induced oxidation of vanadium was investigated. On the surface of vanadium grew a V_2O_5 layer. During the oxidation of vanadium most of the V_2O_5 formed was in the liquid state. Times needed for melting of V_2O_5 were measured for various polarizations of CW CO_2 laser light. Some interesting stochastic phenomena were observed during the oxidation of vanadium.

Investigations into the laser-induced chemical processes on the surface of solids have recently aroused considerable interest [1]. The principal characteristic of processes like these is the fact that they generally take place under conditions of considerable nonequilibrium. The reason for this is the fast change in temperature on the surface of the object resulting from a significant change in the absorptivity of the substance. The dynamics of the so-called thermochemical phenomena is highly complex. Namely, the chemical processes effected by laser light have as concomitants various phenomena of instability and self-induced oscillations.

An important product of chemical synthesis is related empirically to the oxidation of metals. The oxidation of a number of metals (e.g. Cu, Fe, W, Ti, Al) effected by laser light in the atmosphere has been investigated by many researchers [1]. Nevertheless, there are no research results available for the oxidation of several, practically important substances, e.g. various semiconductors and basic materials for chemistry and technology. V_2O_5 can be quoted as an example of such a substance showing semiconductor properties, and known, above all, as a catalyst [1–3].

The present paper is a report on the experimental results gained from the oxidation of the vanadium metal effected by a CW CO_2 laser light in the atmosphere.

The block-scheme of the experimental arrangement can be seen in Fig. 1.

The surface of a $5 \times 5 \times 0.1$ mm^3 metal plate of vanadium was illuminated, at right angle, by CW CO_2 laser of type ИЛГН-701. The temperature (T) and its derivate (dT/dt) were recorded with the help of a chromel-alumel thermocouple alloyed into the back surface of the object, and by a loop oscillograph (type H-115).

A typical oscillogramme is presented in Fig. 2.

As Fig. 2 shows, the change in the temperature of the object and in the speed of its heating points to the non-constant quality of absorptivity A. The change in A is related to the fact that during the oxidation of vanadium a "metal + oxide" absorbent system was formed. Following the method described in [4], with the data shown in Fig. 2, the

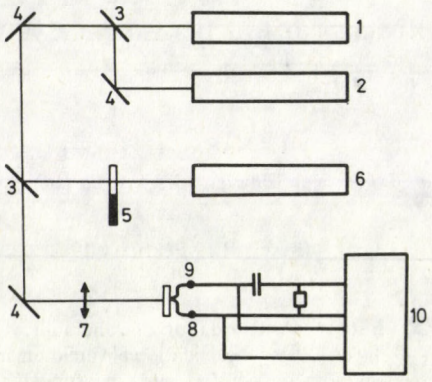

Fig. 1. Experimental setup: 1 – CW He–Ne laser, 2 – CW CO_2-laser, 3 – beamsplitters, 4 – metallic mirrors, 5 – chopper, 6 – calorimeter, 7 – lens, 8 – thermopile, 9 – sample, 10 – loop oscillograph

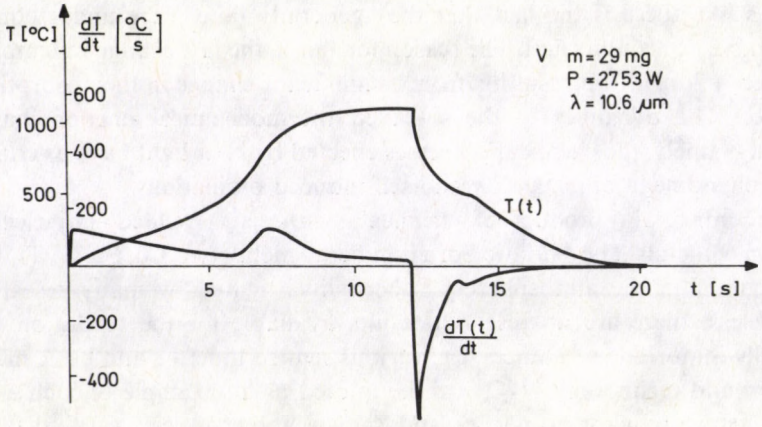

Fig. 2. Typical oscillogramme of the laser heated V sample

temperature dependence of absorptivity, i.e. the function $A(T)$ presented in Fig. 3, can be determined.

At the initial stage of heating absorptivity A of the object is equal to absorptivity $A_0 = 0.08$ obtained for pure vanadium metal at a wavelength of $\lambda = 10.6$ μm [5]. At the subsequent stages, the increase of thickness x of the oxide layer is in direct proportion

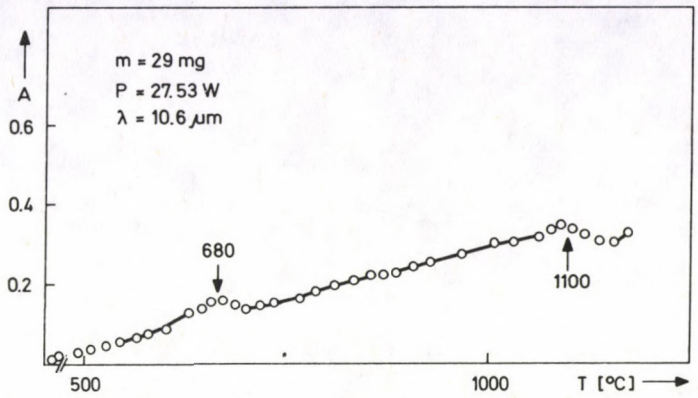

Fig. 3. Temperature dependence of absorptivity in terms of data shown in Fig. 2

to the increase of absorptivity A of the sample. Theoretically, the function $A(x)$ can be given as follows [4]:

$$A(x)=1-|r|^2,$$

$$r=\frac{r_{12}e^{-2i\psi}+r_{23}}{e^{-2i\psi}+r_{12}r_{23}},\quad r_{23}=\frac{r_{12}-r_{13}}{r_{12}r_{13}-1},\quad \psi=\frac{2\pi x}{\lambda}\sqrt{\varepsilon}, \tag{1}$$

$$r_{12}=\frac{1-\sqrt{\varepsilon}}{1+\sqrt{\varepsilon}},\quad r_{13}\approx -1+\frac{A_0}{2}(1-i),\quad \sqrt{\varepsilon}=n+i\kappa.$$

ε, n, κ and λ are the dielectric constant, refractive index, absorption index and wavelength, respectively.

The results of experiments with structure analysis and ion "back-scattering" show that an essential proportion of the oxide layer is made up of V_2O_5. The experimental results with respect to the latter are presented in Fig. 4.

Fig. 5 shows a picture of the surface of a vanadium sample oxidized by CO_2 laser light, taken with a conventional microscope. The microcrystal structure characteristics of V_2O_5 can be distinguished clearly.

For $\lambda=10.6$ μm, the optical constants have the assumed values of $n=0.8$, $\kappa=1$ and the absorptivity is calculated as $A_0=0.08$, then the shape of the theoretical curve $A(x)$, determined in terms of formula (1) has the form presented in Fig. 6.

When comparing Fig. 3 with Fig. 6, it becomes obvious that the shape of function A obtained experimentally is more complex than that obtained by calculation. First of all, it can be established that, as the evidence of the experiments proves the oxide layer to be as thick as 100 μm, thereby fulfilling condition $\alpha x \gg 1$ (where $\alpha=\frac{4\pi\kappa}{\lambda}$ is the

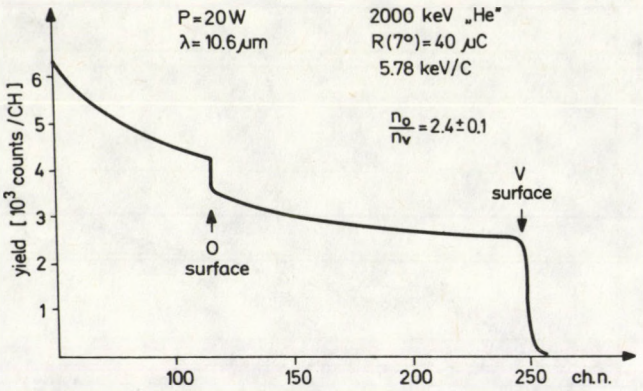

Fig. 4. "Back scattering" curve of an oxidized V sample

absorption coefficient), absorptivity A is determined unequivocally by the optical parameters of the oxide layer:

$$A = \frac{4n}{(n+1)^2+\kappa^2}. \tag{2}$$

This shows that the difference between the theoretical (calculated value $A=0.75$ (Fig. 6)) and the experimental value $A=0.35$ (Fig. 3) can be explained by a change in the optical parameters during the heating. The characteristic of this change is presented in Fig. 7, where function $n(\kappa)$ formed in terms of connection

$$n = \frac{2-A_0}{A_0}\left(1-\sqrt{1-\frac{A_0}{(2-A_0)^2}(1+\kappa^2)}\right) \tag{3}$$

is drawn at $A=0.35$ [4].

Another fact throwing further light on this problem when comparing Fig. 3 with Fig. 6 is that the experimental curve $A(T)$ shows anomalies at $T=680\,^{\circ}C$ and $T=1100\,^{\circ}C$. These anomalies cannot be connected with the interference oscillation experienced for $A(T)$ when using other substances, because V_2O_5 exhibits stronger absorptivity at a wavelength of $\lambda=10.6$ μm ($\alpha\lambda \gg 1$).

The anomaly discernible at $T=680\,^{\circ}C$ is related to the fact that the optical properties vary when V_2O_5 is converted from the solid phase to the liquid phase (the melting point of V_2O_5 is $T=680\,^{\circ}C$ [2]). And the anomaly experienced at $T=1100\,^{\circ}C$ can be explained by the fact that during the heating the frequency of the plasma undergoes a change and shifts to shorter wavelengths, because the concentration of the free charge carriers of the oxide layer increases [5].

One of the characteristics of our experiments most worthy of interest is that during the oxidation of vanadium most of the V_2O_5 formed was in the liquid state. Among others this is suggested by the oscillogramme in Fig. 2 too, making quite

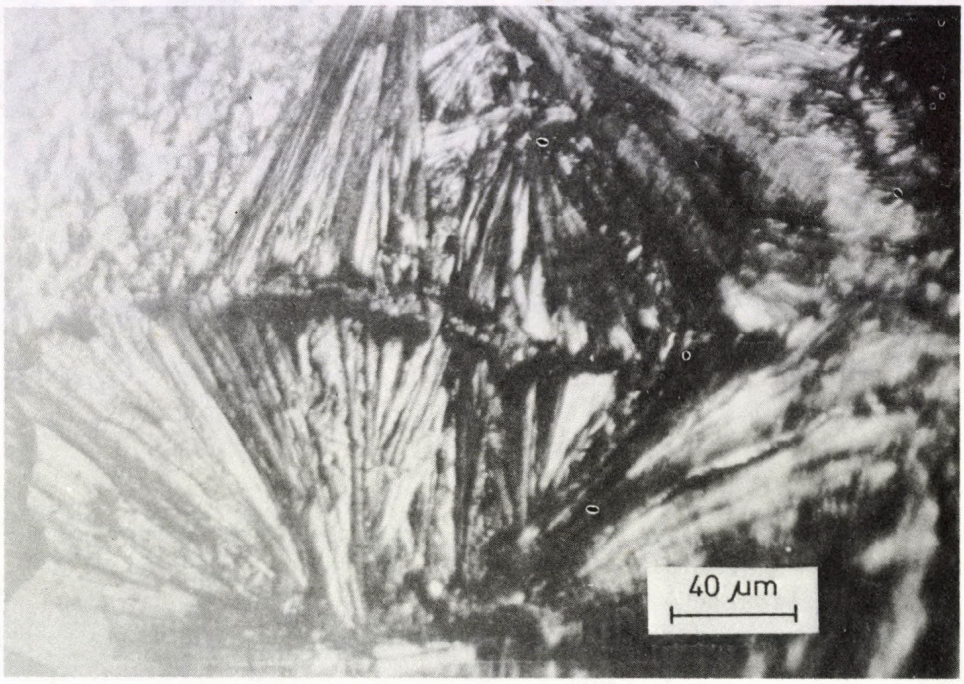

Fig. 5. Microscopical picture of an oxidized V sample

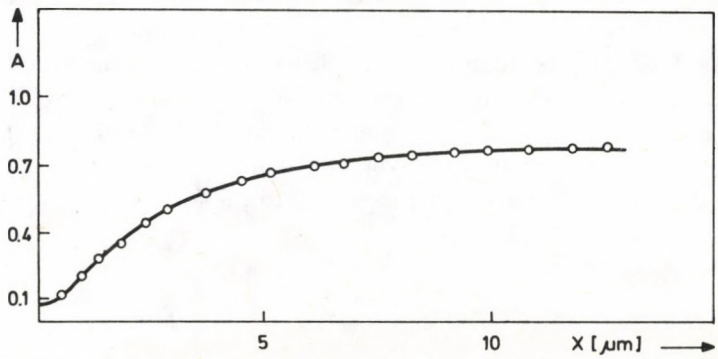

Fig. 6. Theoretical curve $A(x)$ calculated using formula (1)

obvious that at the heating stage the energy absorption related to latent melting heat of fusion is considerably lower than the energy emanating at the cooling phase.

In our experiments the dependence of activation time t_a on the angle of incidence Θ of the laser light was also investigated. It is a well-known fact [6] that for highly absorbent oxides, such as V_2O_5, curve $t_a(\Theta)$ can be assumed to show a low minimum at about 55°. The minimum results from the fact that, for angles of incidence near

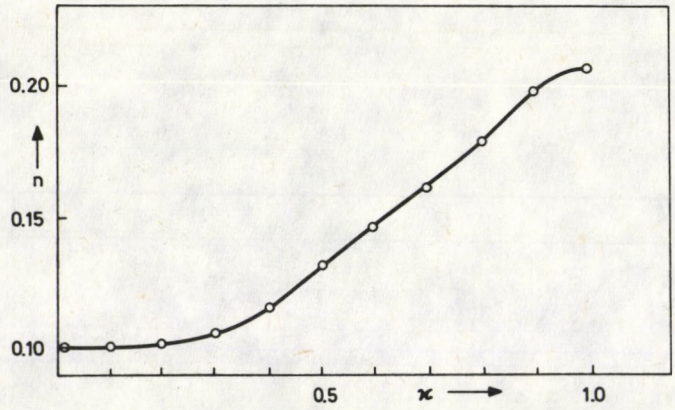

Fig. 7. Function $n(\kappa)$ on condition that $A=0.35$

Brewster's angle, the beam of light polarized parallel to the plane of incidence gets absorbed in a high degree. It may be noted that the "depth" and "position" of the minimum depend strongly on power P of the incident radiation [6]. In this connection, it is note worthy that, when investigating into the inflammation of tungsten excited by CO_2 laser light [6], a very low minimum shown on curve $t_B(\Theta)$ has been observed (where t_B is the time of the inflammation). The power of CO_2 laser light used in [6] was 700 W (the power of laser light used by us for the present investigations was 40 W).

Times $t_a(\Theta)$, needed for melting V_2O_5, can be seen in Fig. 8, plotted against the angle Θ of incidence of the laser light, for various polarizations.

In Fig. 8, despite the small power employed, it is clearly discernible that for a perpendicular polarization ($\perp$) $t_{a\perp}(\Theta)$ will increase monotonically (curve 2), while for a parallel polarization ($\|$), $t_{a\|}(\Theta)$ has a minimum (curve 1). The depth of the minimum of function $t_{a\|}(\Theta)$ depends on the optical constants of the oxide layer [6] as well as on the power of laser light, and is in direct proportion to the following quantity:

$$L=\frac{\kappa^2}{\frac{n^4}{n^2-1}\cdot A_0^2}. \tag{4}$$

On the evidence of the experiments, function $t_{a\|}(\Theta)$ has no minimum for Cu_2O, at $\lambda=10.6\ \mu m$ and at 40 W. The difference in the shapes of functions $t_{a\|}(\Theta)$ Cu and V targets is due to the great difference between the L-s: in system $Cu+Cu_2O$ $L=5\cdot 10^{-3}$, while in $V+V_2O_5$ $L=11$.

At last, it should be noted that during the laser induced oxidation of vanadium in the atmosphere some interesting stochastic phenomena could be observed. Having achieved a steady state (stationary) temperature, the dT/dt curve showed in certain cases regular oscillations (Fig. 9).

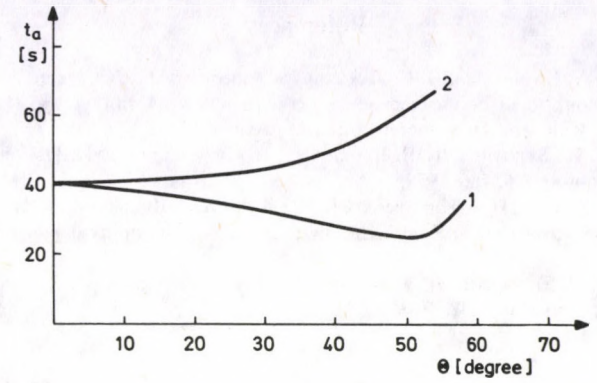

Fig. 8. Activation time vs the angle of incidence of laser light for various polarizations

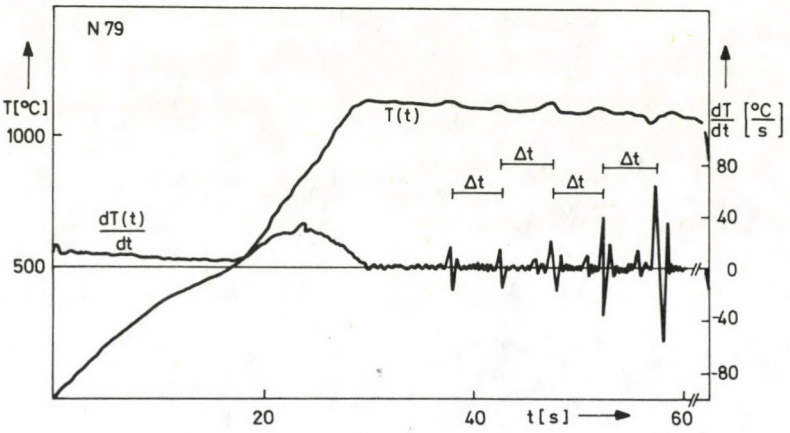

Fig. 9. Typical oscillogramme showing stochastic oscillations

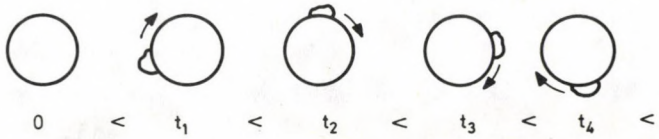

Fig. 10. Behaviour of a CO_2 laser irradiated plate showing regular oscillations in subsequent moments

The period of the oscillations (~ 5 s) was of a relatively constant duration. Simultaneously with the appearance of the oscillations, a luminous spot could be seen circulating around the irradiated area of the sample, and the period of this was in good agreement with the period of the oscillations of dT/dt (Fig. 10).

The above stochastic processes are connected to non-linear interactions caused by a strong positive feed-back; investigations into this feed-back are now in progress.

References

1. Ф. В. Бункин, Н. А. Кириченко, Б. С. Лукьянчук, Известия АН СССР сер. физ., **45,** 1018, 1981.
2. Ред. Г. В. Самсонов, Физико-химические свойства окислов, Металлургия, Москва, 1980.
3. А. А. Абдуллаев, Кандидатская диссертация, Москва, 1971.
4. М. И. Арзуов, А. И. Барчуков, Ф. В. Бункин, Н. А. Кириченко, В. И. Конов, Б. С. Лукьянчук, Квантовая электроника, **6,** 466, 1979.
5. В. И. Бойко, Ф. В. Бункин, Н. А. Кириченко, В. И. Конов, Б. С. Лукьянчук, Л. Нанаи, В. И. Токарев, И. Хевеши, Тезисы докладов 4. Конференции по лазерам и их применениям, стр. 130, Лейпциг, 1981.
6. М. И. Арзуов, А. И. Барчуков, Ф. В. Бункин, Н. А. Кириченко, В. И. Конов, Б. С. Лукьянчук, Квантовая электроника, **6,** 2232, 1979.

Acta Physica Hungarica 54 (1—2), pp. 119—124 (1983)

DETERMINATION OF THE REFRACTIVE INDEX, THE ABSORPTION COEFFICIENT AND THE THICKNESS OF AMORPHOUS V_2O_5 THIN FILMS FROM REFLECTANCE INTERFERENCE SPECTRA

LIEM PHAN*, L. MICHAILOVITS and I. HEVESI

Institute of Experimental Physics, József Attila University, Szeged, Hungary

(Received 23 February 1982)

The absorption coefficient, refractive index and thickness of amorphous vanadium pentoxide thin films have been determined from reflectance interference spectra in the wavelength range of 450–710 nm. In the photon energy range of 2.15–2.70 eV the wavelength dependence of the absorption coefficient obeys Urbach's rule.

Introduction

The optical properties of amorphous transition metal oxides have received much attention during the last decade [1–4] since these oxides in thin film form could have considerable application in digital display devices. Most of the studies deal with WO_3 thin films [1, 2]; relatively little attention has been paid to vanadium pentoxide [3, 4].

In this paper we present optical data of amorphous V_2O_5 thin films obtained by vacuum deposition. We show that applying a new improved method based on the ideas of A. M. Goncharenko [5] the absorption coefficient, refractive index and thickness of the films can be obtained from a single reflectance interference spectrum.

The method

The sample structure used is shown in Fig. 1. The film to be characterized is of uniform thickness d and complex refractive index $\bar{n}_2 = n_2 - ik_2$. If the film is weakly absorbing, i.e. $n_2 \gg k_2$ the reflectance R for normal incidence is given by [5]

$$R = \frac{(\sqrt{r_1} - \sqrt{r_2}\eta)^2 + 4\sqrt{r_1 r_2}\eta \sin^2 \psi}{(1 - \sqrt{r_1 r_2}\eta)^2 + 4\sqrt{r_1 r_2}\eta \sin^2 \psi}, \tag{1}$$

* Department of Physics, University of Hanoi, Viet-Nam.

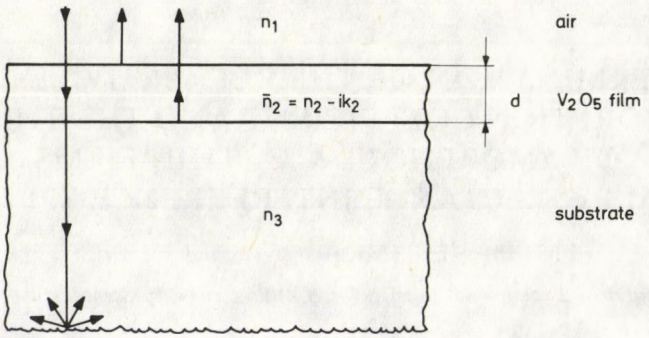

Fig. 1. Sample arrangement for reflectance measurement

where

$$r_1 = \frac{(n_2 - n_1)^2 + k_2^2}{(n_2 + n_1)^2 + k_2^2}, \tag{1a}$$

$$r_2 = \frac{(n_2 - n_3)^2 + k_2^2}{(n_2 + n_3)^2 + k_2^2}, \tag{1b}$$

$$\eta = \exp\left(-\frac{4\pi}{\lambda} k_2 d\right), \tag{1c}$$

$$\psi = -\frac{2\pi}{\lambda} n_2 d. \tag{1d}$$

Examination of Eq. (1) for the conditions under which maxima and minima occur produces the following results:

If $n_2 > n_1$ and $n_2 > n_3$ the light reflected from the $n_2 - n_1$ interface undergoes a phase change of π, from which it follows that maxima in R occur, when

$$\left(m + \frac{1}{2}\right)\lambda_{\max} = 2n_2 d, \tag{2}$$

where m is an integer (the order of the interference) and λ denotes the wavelength of the incident light. The maximum value of R at this wavelength is

$$R_{\max} = \left(\frac{\sqrt{r_1} + \sqrt{r_2}\eta}{1 + \sqrt{r_1 r_2}\eta}\right)^2. \tag{3}$$

Minima in R occur, when

$$m\lambda_{\min} = 2n_2 d \tag{4}$$

and the minimum value of R at the corresponding wavelength is

$$R_{\min} = \left(\frac{\sqrt{r_1} - \sqrt{r_2}\eta}{1 - \sqrt{r_1 r_2}\eta} \right)^2 . \tag{5}$$

The $R_{\min}$ values at $\lambda_{\max}$ and $R_{\max}$ values at $\lambda_{\min}$ can be obtained by applying the approximation procedure given in [6]. Introducing

$$A \equiv \frac{1+\sqrt{R_{\max}}}{1-\sqrt{R_{\max}}} \quad \text{and} \quad B \equiv \frac{1+\sqrt{R_{\min}}}{1-\sqrt{R_{\min}}},$$

from Eqs (3) and (5) follows that

$$r_1 = \frac{\sqrt{AB}-1}{\sqrt{AB}+1}, \tag{6}$$

and

$$\sqrt{r_2}\eta = \frac{\sqrt{\frac{A}{B}} - 1}{\sqrt{\frac{A}{B}} + 1}. \tag{7}$$

If $n_1 = 1$ we can write

$$n_2 = \frac{(r_1+1)+\sqrt{(r_1+1)^2-(r_1-1)(k_2^2+1)}}{1-r_1}, \tag{8}$$

$$\sqrt{r_2}\eta = \sqrt{\frac{(n_2-n_3)^2+k_2^2}{(n_2+n_3)^2+k_2^2}} \exp\left(-\frac{4\pi}{\lambda} k_2 d \right). \tag{9}$$

The values of n_2, k_2 and d can be determined by the following iterative approximation method: Supposing that $k_2 = 0$ the first approximation value of n_2 can be obtained from Eq. (8). The film thickness d may then be determined from the position of an extremum and Eqs (2) or (4). Finally, Eq. (9) gives the first approximation value of k_2. Repeating this procedure the values of n_2, k_2 and d can be determined with the desired accuracy.

The integer m can be calculated from Eqs (2) and (4), supposing that the change in the refractive index between two neighbouring maxima and minima is negligibly small.

The value of the refractive index n_3 of the substrate can be obtained from

$$R = \left(\frac{n_3 - 1}{n_3 + 1} \right)^2 .$$

Experimental details

The V_2O_5 films were prepared by vacuum evaporation of V_2O_5 powder (purum, Reanal, Hungary) from vanadium boats in $<2\times10^{-3}$ Pa vacuum. During evaporation the substrates were held at room temperature.

The reflectance of the film and its substrate was measured as a function of the wavelength by an Optica Milano CF 4 DR spectrophotometer supplied with an integrating sphere at nearly normal incidence ($\pm4°$). An aluminium mirror was used as reflectance standard. To prevent reflection from the substrate–air interface, the back side of the substrate was roughened and blackened.

Results

In Fig. 2 the measured reflectance interference spectrum of a V_2O_5 film of 500 ±25 nm thickness is shown. The values of n_2 and k_2 calculated from this spectrum by the iterative method presented before are given in Fig. 3. The optical constants obtained from reflectance spectra of different samples of slightly different thicknesses were in good agreement indicating that with this relatively simple method correct values for the absorption coefficient, refractive index and thickness of the V_2O_5 films

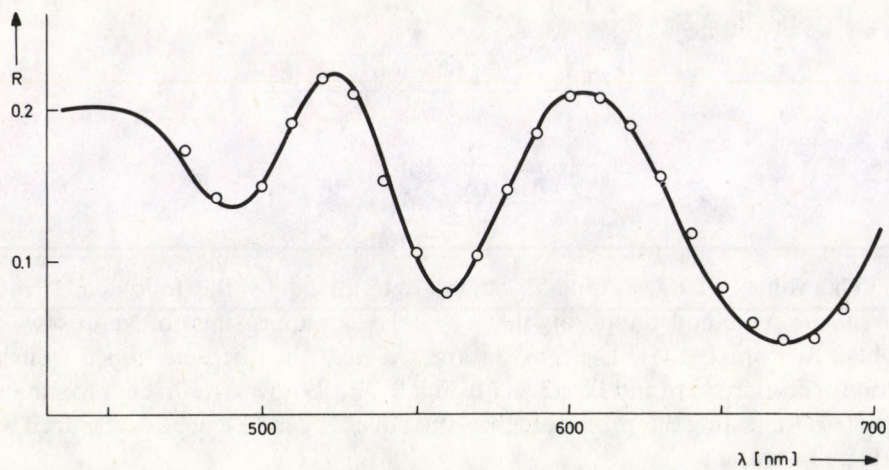

Fig. 2

can be obtained. From the n_2, k_2 and d data we recalculated the reflectance spectrum at different wavelengths. These points are marked by open circles in Fig. 2. The agreement between the measured and calculated values is very good, which verifies the applicability of the approximation procedure used.

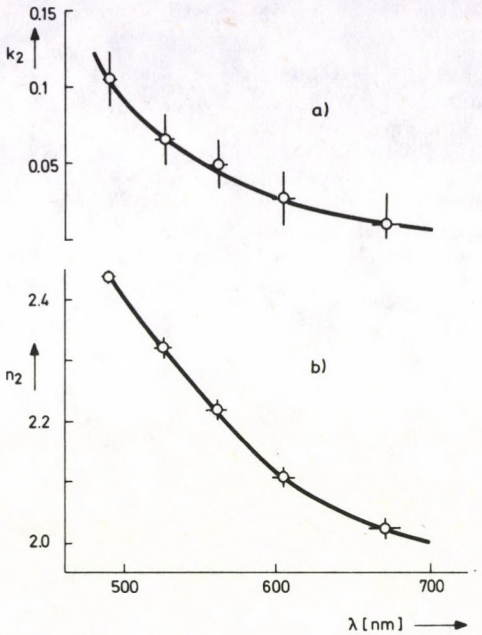

Fig. 3

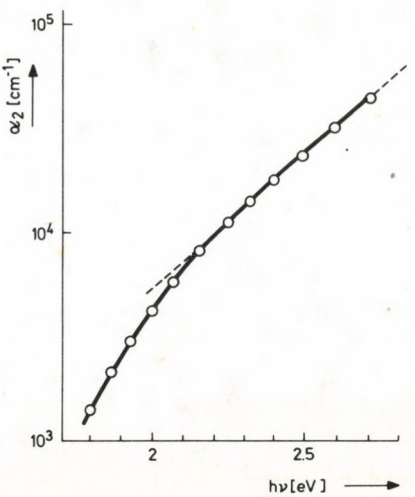

Fig. 4. Dependence of the absorption coefficient on photon energy

Hevesi et al [7, 8] pointed out that the long wave tail of V_2O_5 single crystals showed an exponential dependence on photon energy. From the results presented in Fig. 4 it can be seen that the absorption coefficient of the amorphous V_2O_5 layers obtained by vacuum evaporation obeys Urbach's rule between 2.15 and 2.70 eV.

References

1. J. Livage, J. Phys. (France), **42** suppl. C4-981, 1981.
2. R. J. Colton, A. M. Guzman and J. W. Rabalais, J. Appl. Phys., **49,** 409, 1978.
3. A. I. Gavrilyuk, N. M. Reinov and F. A. Chudnovskii, Pis'ma v Zh. Tekh. Fiz. (USSR), **5,** 1227, 1979.
4. E. F. Ryannel', V. I. Gaman and V. M. Kalygina, Izv. VUZ Fiz. (USSR), No. 2, 102, 1976.
5. A. M. Goncharenko and F. I. Fedorov, Opt. i Spektr., **14,** 94, 1963.
6. A. C. Valeev, Opt. Spektr., **15,** 500, 1963.
7. Z. I. Bodó and I. Hevesi, Phys. Stat. Sol., **20,** K45, 1967.
8. Nguyen The Quang and I. Hevesi, Acta Phys. et Chem., **20,** 285, 1974.

Acta Physica Hungarica 54 (1—2), pp. 125—137 (1983)

MAGNETORESISTANCE AND ELECTRON SCATTERING MECHANISMS IN GALLIUM ARSENIDE

B. PŐDÖR

Research Laboratory for Inorganic Chemistry of the Hungarian Academy of Sciences
*1502 Budapest, Hungary**

(Received 6 May 1982)

Results of magnetoresistance measurements performed at 300K and 77K on GaAs single crystals having electron concentrations in the range of 10^{16} to 10^{18} cm^{-3} were analysed using the concept of effective relaxation time $\tau_{eff} \sim \varepsilon^{r_{eff}}$ where r_{eff} is the effective scattering exponent. The values of r_{eff} deduced from the experiments are in accordance with dominant polar optical phonon and space-charge scattering at room temperature as well as with dominant ionized impurity scattering with an admixture of space-charge scattering at liquid nitrogen temperature. Results for the Hall factor at these two temperatures are also presented; at 300K $r_H \approx 1$, but at 77K it changes appreciably with the carrier concentration.

1. Introduction

The magnetoresistance coefficients measured on semiconductors in low magnetic field contain useful information about the band structure and scattering mechanisms of the semiconductor under investigation. In the case of a semiconductor having a simple band structure, e.g. a spherical minimum of the conduction band at the centre of the Brillouin zone with a dispersion law of $E = \hbar^2 k^2 / 2m^*$, the longitudinal magnetoresistance vanishes, the transversal component is isotropic, and its coefficient depends only on the scattering mechanisms [1]. In many respect, n-type GaAs is close to this picture of the "ideal" semiconductor. Its conduction band minimum is spherical and is located at the centre of the Brillouin zone [2, 3]. The only deviation is the slight nonparabolicity of the conduction band [3], which manifests itself above about 5×10^{17} cm^{-3} electron concentration [4]. Therefore the magnetoresistance coefficients measured on GaAs make it possible for us to draw conclusions about the relevant scattering mechanisms. The analysis is not simple because in n-type GaAs combinations of different types of scattering mechanisms dominate the mobility.

Calculations for lattice scattering mechanisms were performed recently by several authors, notably by Rode [5], Fletcher and Butcher [6], Pődör and Nádor [7], (see also the reviews of Rode [8] and of Nag [9]). According to these calculations, at room temperature polar optical phonon scattering is by far the strongest electron scattering mechanism due to the lattice. At a temperature of 77K the three lattice

* Present address: Department of Electronic and Electrical Engineering, University of Ife, Ile–Ife Nigeria

scattering mechanisms — polar optical phonon, acoustic phonon and piezoelectric scattering — have roughly the same weight.

In low mobility crystals with an intermediate and a high electron and impurity concentration and presumably with a substantial compensation (mainly such crystals are of interest in this work), ionized impurity scattering and scattering on space-charge regions [10 to 14], also play an important role.

Space-charge scattering in semiconductors is caused by space-charge regions that form around localized composition and impurity concentration inhomogeneities. This mechanism was first proposed by Weisberg [10] to explain anomalously low mobilities in GaAs. Later, Conwell and Vassel [15] proposed a simple model where the space-charge scattering relaxation time was given by

$$\tau_{SC}=(N_{SC}Qv)^{-1},$$

from which the space-charge mobility is obtained as

$$\mu_{SC}=\frac{4e}{3(2\pi m^* k_B T)^{1/2} N_{SC} A},$$

where N_{SC} is the volume density of the space-charge scattering centres, which can vary widely depending on the properties of the sample, Q is the cross-sectional area of the centres, and v is the electron velocity. This differs by a numerical factor of $4/3\pi^{1/2}=0.7523$ from the original formula due to Weisberg [10].

Recently [16, 17], however, instead of the space-charge scattering mechanism, scattering on localized potential was proposed and analysed by Chattopadhyay [17], using the scattering cross section for such potential considered by Faulkner [18] and Dean [19] (c.f. also the earlier work by Anselm and Askerov [20], also in the review [21]). This scattering cross section also predicts a mobility contribution varying inversely as the square root of the temperature, under certain simplifying considerations.

It can be concluded that in practical cases the carrier scattering and the electron transport is dominated by the combination of two or three or even more simultaneously acting scattering mechanisms.

The transport coefficients are straightforwardly evaluated in the relaxation time approximation. With one notable exception, for the relevant scattering mechanisms, the relaxation time is a power function of the electron energy $\tau \sim \varepsilon^r$ where the exponent r has a half integer value [1]. Polar optical phonon scattering cannot be described with a relaxation time aprroach [1, 2, 22]. For limited temperature ranges, however, an effective exponent using the relaxation time approach can also be introduced for polar optical phonon scattering according to Ehrenreich [23], Kuzel [24] and Voronina et al. [25].

In the present paper megnetoresistance measurements performed at temperatures of 300K and 77K on strongly doped and compensated GaAs will be analysed

using two different models to account for the combined scattering effects which prevail in this range of concentration and temperature.

The first model is based on the calculations of Kravchenko et al. [26], who calculated the galvanomagnetic coefficients for n-type GaAs taking into account the inelastic scattering on the polar optical phonons, and the usual elastic scattering mechanisms, describable with the relaxation time approximation, but have neglected the effects of space-charge scattering. The second model is based on a relaxation time-type approach using a single scattering exponent r_{eff} in the expression for the effective relaxation time, $\tau_{\text{eff}} \sim \varepsilon^{r_{\text{eff}}}$. A similar analysis of the different transport coefficients with some applications to GaAs has been made by Emelyanenko et al. [27], and of the thermoelectric power of GaAs by Hamerly and Heller [28]. The theoretical bases of this latter model will be summarized in the next paragraph.

2. Theoretical background for the relaxation time-type model

In the relaxation time approximation the magnetoresistance coefficient ξ and the Hall factor, defined as the ratio of the Hall mobility to the drift mobility $r_{\text{H}} = \mu_{\text{H}}/\mu$ are expressed as (see e.g. [1])

$$\xi = \frac{\langle\tau^3\rangle\langle\tau\rangle}{\langle\tau^2\rangle^2} - 1, \tag{1}$$

$$r_{\text{H}} = \frac{\langle\tau^2\rangle}{\langle\tau\rangle^2}. \tag{2}$$

If the relaxation time is a power function of the carrier energy, i.e. $\tau \sim \varepsilon^r$ then ξ and r_{H} can be expressed with the help of the Fermi integrals (see e.g. [1]), as

$$r_{\text{H}} = \frac{3\left(2r+\frac{3}{2}\right)F_{2r+\frac{1}{2}}(\zeta)F_{\frac{1}{2}}(\zeta)}{2\left(r+\frac{3}{2}\right)^2[F_{r+\frac{1}{2}}(\zeta)]^2}, \tag{3}$$

$$\xi = \frac{\left(3r+\frac{3}{2}\right)\left(r+\frac{3}{2}\right)F_{3r+\frac{1}{2}}(\zeta)F_{r+\frac{1}{2}}(\zeta)}{\left(2r+\frac{3}{2}\right)^2[F_{2r+\frac{1}{2}}(\zeta)]^2} - 1 \qquad r \neq -\frac{1}{2}$$

$$= \frac{\left(r+\frac{3}{2}\right)F_{r+\frac{1}{2}}(\zeta)[1+\exp -\zeta]^{-1}}{\left(2r+\frac{3}{2}\right)^2[F_{2r+\frac{1}{2}}(\zeta)]^2} - 1, \qquad r = \frac{1}{2}, \tag{4}$$

where $F_n(\zeta) = \int_0^\infty \varepsilon^n [1 + \exp(\varepsilon - \zeta)]^{-1} d\varepsilon$ are the Fermi integrals. For the case of classical statistics the Fermi integrals are reduced to gamma functions.

For a given r with increasing degeneracy, i.e. with increasing ζ, the values of r_H and ξ decrease in a monotonous way, and for $\zeta \to \infty$ $r_H = 1$ and $\xi = 0$.

Eqs (3) and (4) are supplemented with the relationship between the carrier concentration (Hall coefficient) and the Fermi level

$$n = \frac{r_H}{eR_H} = N_C F_{\frac{1}{2}}(\zeta), \tag{5}$$

where $N_C = 4\pi(2m^* k_B T/h^2)^{\frac{3}{2}}$. Using Eqs (3), (4) and (5) the Fermi level ζ, and the theoretical value of the magnetoresistance coefficient ξ can be calculated from the measured value of the Hall coefficient for a specified scattering mechanism, i.e. for a given value of the exponent r. This procedure can also be reversed, and from the measured values of ξ and R_H the values of ζ, the scattering factor r_H, and the "effective" exponent r_{eff} can be deduced. However, this reversed procedure yields two sets of values for r_{eff} and ζ due to the forms of the curves corresponding to Eq. (4). This property of ξ and of r_H was already noted by Kuzel [24] in the context of calculating the effective exponent r_{eff} for polar optical phonon scattering from different transport coefficients. In practical cases the solution can be made unambiguous using supplementary informations about the scattering processes.

3. Experimental techniques and results

The samples used in the measurements were cut out from single crystals grown by the horizontal Bridgman method. The crystals had a room temperature electron concentration ($n_H = 1/eR_H$) between 1×10^{16} and 2×10^{18} cm^{-3}, at 77K the electron concentration was between 1×10^{16} and 2×10^{17} cm^{-3}. Some of the high concentration samples were not investigated at low temperatures. The electron mobility was correspondingly low, between 2000 and 4000 cm^2/Vs at room temperature and between 2000 and 6000 cm^2/Vs at 77K.

Conductivity, Hall coefficient and mobility were measured by the usual d.c. compensation method on bar shaped samples with six alloyed contacts, between temperatures of 300 and 77K. Magnetoresistance was also measured by the usual d.c. compensation method at temperatures of 300 and 77K as described in our earlier work [29].

In Fig. 1 some typical results of the mobility versus temperature measurements are presented. Fig. 2 shows some typical curves of the low field magnetoresistance measurements. From their slope the magnetoresistance coefficient $\xi = \Delta\rho/\rho\mu_H^2 B^2$ was determined. The results for $n_H = 1/eR_H$, μ_H, and ξ for temperatures of 300K and 77K are collected in Table I.

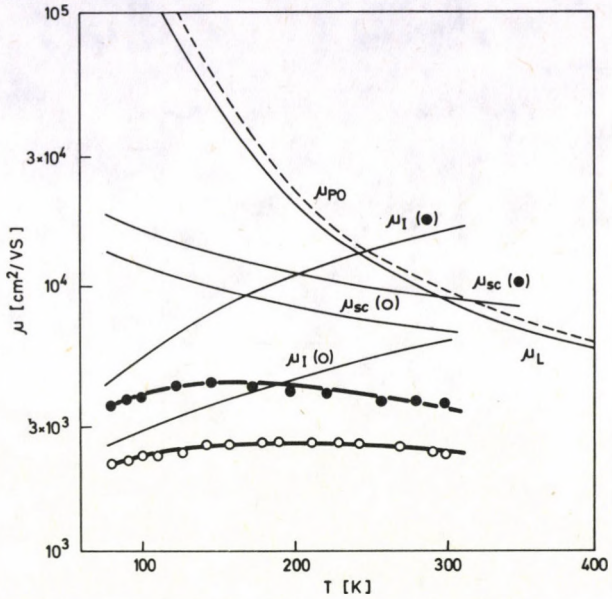

Fig. 1. Mobility versus temperature. Theoretical values for polar optical phonon scattering (PO – – –), and lattice scattering (L ——) are shown, the fits to the experimental data using lattice mobility, ionized impurity mobility (I) and space-charge scattering (SC) are also presented

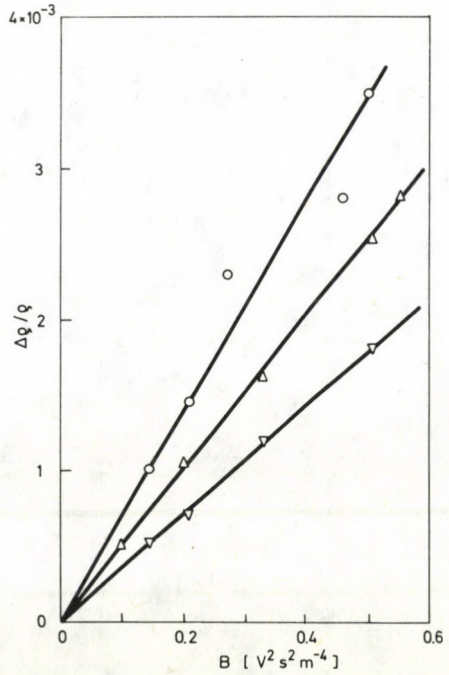

Fig. 2. Magnetoresistance measured at room temperature versus the square of the magnetic field. ○ — $n=8.1\times10^{16}$ cm^{-3}, △ $n=3.7\times10^{17}$ cm^{-3}, 801 ≅ — $n=1.6\times10^{18}$ cm^{-3}

Table I

Results and analysis of magnetoresistance measurements

Sample No	n_{300K} [cm^{-3}]	$\mu_{H\,300K}$ [cm^2/Vs]	ξ_{300K}	n_{77K} [cm^{-3}]	$\mu_{H\,77K}$ [cm^2/Vs]	ξ_{77K}	r_{eff} 300K	r_{eff} 77K	$K = N_a/N_d$
1	1.9×10^{16}	2650	0.17	1.3×10^{16}	4200	0.51	−0.43	1.47	0.79
2	2.7×10^{16}	2800	0.24	1.5×10^{16}	6800	0.30	−0.48	1.09	0.73
3	4.0×10^{16}	3300	0.078	3.0×10^{16}	3500	0.29	−0.31	1.10	0.75
4	8.1×10^{16}	3850	0.047	6.7×10^{16}	4000	0.17	−0.24	0.90	0.51
5	1.7×10^{17}	3500	0.086	1.5×10^{17}	3200	0.20	−0.33	1.14	0.59
6	1.9×10^{17}	2750	0.11	2.1×10^{17}	2000	0.30	−0.38	1.50	0.63
7	4.8×10^{17}	2550	0.060	–	–	–	−0.30	–	0.54
8	1.6×10^{18}	1950	0.085	1.6×10^{18}	1400	–	−0.50	–	0.55

Note: $n = 1/eR_H$

4. Analysis of the experimental results. I. Mobility

Before presenting the results of the analysis of magnetoresistance measurements, we would like to make a concise survey of the dominant scattering mechanisms operating in *n*-type GaAs which are relevant for the present work. At a temperature of 77K the lattice limited mobility is more than an order of magnitude greater than the mobilities measured in our samples, therefore the effects of lattice scattering can be safely neglected. The mobility at this temperature is dominated by ionized impurity scattering for electron concentrations greater than about 10^{15} cm^{-3}. In most cases besides ionized impurity scattering, scattering on space charge regions also plays an important role [10 to 15].

At 300K the dominant lattice scattering mechanism is the polar optical phonon scattering, other lattice scattering mechanisms make only a small contribution to the mobility [2, 6, 7, 30]. Besides polar optical phonon scattering, ionized impurity scattering and space-charge scattering play an important and in some cases, dominant role, depending on the carrier concentration, compensation degree, etc. [10 to 15].

Fig. 1 presents also the results of an analysis of the mobility versus temperature curves in terms of mobilities limited by lattice scattering, ionized impurity scattering and space-charge scattering. Theoretical values of the lattice limited mobility are taken from the earlier work of the present author [7], ionized impurity scattering is accounted for by the Brooks—Herring formula, making allowance for the degeneration (see e.g. [21]), and space-charge scattering is described with the formula discussed in the Introduction. For reference the contribution of polar optical phonon scattering to the lattice limited mobility is also separately depicted [7]. The results of this mobility analysis, which is typical for the other samples investigated in this work demonstrate the points made above, and are in full accordance with the results of previous mobility analysis on higher purity epitaxial layers, performed by the present author [12].

5. Analysis of the experimental results. II. Magnetoresistance

Kravchenko et al [26] have calculated the magnetoresistance coefficient, ξ, and presented curves of it in function of $\mu_H/\mu_{H,\,\text{lattice}}$ for different electron concentrations at temperatures of 300 and 77K. They have taken into account the lattice scattering mechanisms and ionized impurity scattering, but neglected space-charge scattering. Our experimental data for ξ are compared with the results of the model due to Kravchenko et al [26] in Figs 3 and 4.

As can be seen in Fig. 3 the measured values of ξ at room temperature are generally greater than the corresponding theoretical values calculated in [26] for the respective electron concentrations, but in most of the cases the discrepancy is not too important, taking into account the inherent errors in measuring the magnetoresistance

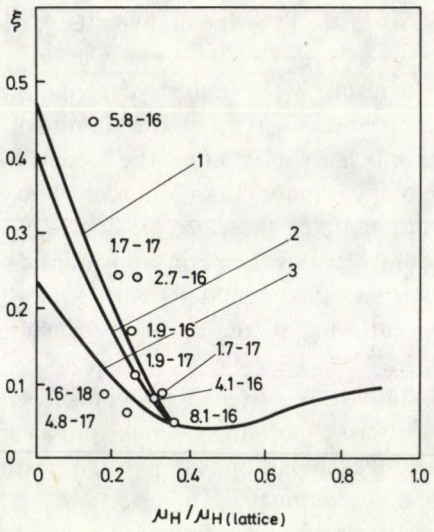

Fig. 3. Comparison of the room temperature values of ξ with the theoretical curves of Kravchenko et al [26]. 1 — $n = 10^{16}$ cm^{-3}, 2 — $n = 10^{17}$ cm^{-3}, 3 — $n = 10^{18}$ cm^{-3}

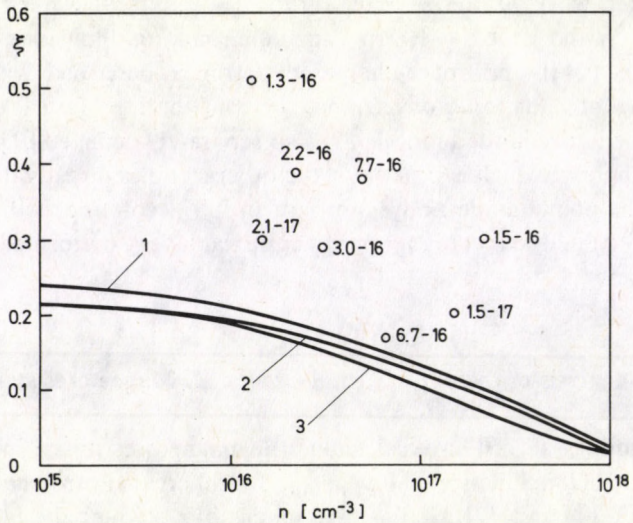

Fig. 4. Comparison of the 77K values of ξ with the theoretical predictions of Kravchenko et al [26]. Values of $\mu_H/\mu_{H,\,\text{lattice}}$ for the curves are $1-6\times10^{-3}$, $2-1\times10^{-2}$, $3-2\times10^{-2}$

coefficients. But as the data presented in Fig. 4 show, the measured values of ξ at 77K are consistently higher than the theoretical values calculated from the curves of Kravchenko et al [26]. In both Figures the data points are identified with the corresponding values of $n_H = 1/eR_H$. It is supposed here that the discrepancy between

our experimental data and the theoretical predictions presented in [26] are chiefly caused by the fact that, while in our samples space-charge scattering plays an important role in determining the mobility and also the other transport coefficients, the theoretical calculations referred to above have not included this type of scattering mechanism.

Therefore our magnetoresistance measurements were reinterpreted on the basis of the relaxation time-type approach using a single scattering exponent, r_{eff}, based on the model presented above.

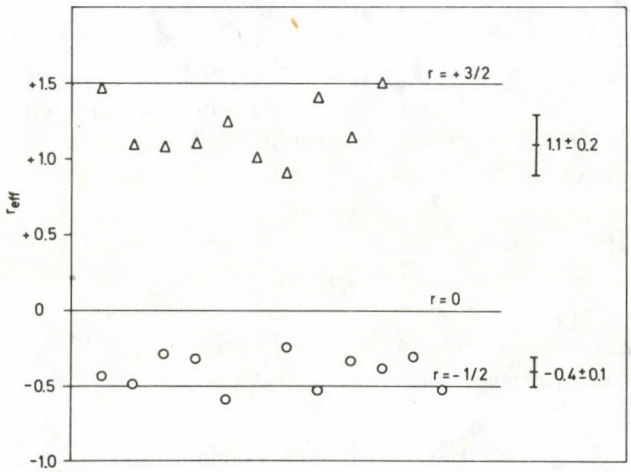

Fig. 5. Values of the effective scattering exponent r_{eff} at room temperature (○) and at 77K (△)

As it has been already mentioned in the preceding Paragraph, such an analysis gives two values of r_{eff} for each measured value of the magnetoresistance coefficient ξ. One of them is negative, the other one is positive. The values of r_{eff} for the room temperature measurements are presented in Table I and Fig. 5. Only the values of $r_{\text{eff}} < 0$ are shown, because as will be discussed these values have physical meaning in this case. The positive values of r_{eff} showed a wide scatter between 0.3 and 1.0. Two lines are drawn in Fig. 3 for $r = 0$ corresponding to polar optical phonon scattering in the low temperature limit ($T \ll \Theta_D$) and for $r = -1/2$ corresponding to space-charge scattering [15] or to acoustic phonon scattering, which latter is not relevant at room temperature. Using the results of Kuzel [24], a better estimation can be made for r valid for polar optical phonon scattering. With $\Theta_D = 420$K we have $\Theta_D/T = 1.4$ and for this value different transport coefficients result in a value of $r = -(0.35 - 0.45)$ for polar optical phonon scattering. From our measurements we have (see Fig. 5) $r_{\text{eff}} = -0.4 \pm 0.1$ which can be readily interpreted supposing that the dominant scattering mechanism in our samples at room remperature is due to the combination of polar optical phonon and space-charge scatterings. This interpretation is in accordance with other works on

mobility in GaAs [11, 12, 31, 32] and with the conclusions drawn from the analysis of thermoelectric power measurements by Hamerly and Heller [28]. We think that the positive values of r_{eff}, mentioned above, cannot be reconciled with dominant polar optical phonon scattering with any combination of ionized impurity scattering, even with neglecting the effects of space-charge scattering, which neglection, according to our opinion, would be unjustified.

The values of r_{eff} for 77K temperature are shown also in Table I and Fig. 5. Because at this temperature ionized impurity scattering is by far the strongest scattering mechanism, which is characterized by $r = +3/2$, in this case the negative values of r_{eff} have no meaning. The values of r_{eff} with three exceptions where they are close to $+3/2$ show a wide scatter around about 1, more exactly $r_{eff} = 1.1 \pm 0.2$. In those samples where $r_{eff} \approx 3/2$ the scattering is nearly pure ionized impurity scattering (c.f. [33]). The value of $r_{eff} \approx 1.1$ can be interpreted supposing dominant impurity scattering with an admixture of another scattering mechanism with a lower value of r, presumably space-charge scattering. As it was already mentioned, lattice scattering is not significant in our samples at low temperatures.

In Table II we have compiled the values of r_{eff} for different temperatures determined in this work, by Emelyanenko et al. [27], Hamerly and Heller [28] and Voronina et al. [25] for all samples having similar electron concentrations, except for the samples measured by Voronina et al [25], which were high purity epitaxial layers, with electron concentrations of the order of 10^{14} cm^{-3}.

Table II

Values of r_{eff} determined in this work and in the literature

T [K]	Measured transport coefficient	r_{eff}	Reference
77	magnetoresistance	1.1 ± 0.2	this work
100	magnetoresistance	0.6 ± 0.1	[27]
100	thermoelectric and thermomagnetic effects	$(0.2-0.4)$	[27]
300	magnetoresistance	-0.4 ± 0.1	this work
300	thermoelectric power	$-(0.2-0.7)$	[28]
300	magnetoresistance	$-(0.27-0.4)$	[25]
300	Hall factor	$-(0.37-0.47)$	[25]

It can be seen from Table II that the values of r_{eff} determined from different transport coefficients at 300K are in a good agreement with each other. For high purity epitaxial samples, in the temperature range of 150—300K, where polar optical phonon scattering is dominant, r_{eff} remains nearly constant [25]. In the case of samples with greater impurity content, the value of r_{eff} increases continuously as the temperature is lowered showing the increasing role of ionized impurity scattering.

An interesting byproduct of the analysis presented above is the determination of the scattering factor r_H for the concentration range of our samples and for the given

scattering process. The value of r_H as function of the electron concentration ($n_H = 1/eR_H$) at 300K and 77K is presented in Fig. 6.

At 300K, for the concentration range of interest in this work, r_H is close to 1. In the range of $10^{16} - 10^{17}$ cm^{-3} it decreases from 1.10 to about 1.05, then remains constant at a value of 1.05 ± 0.05. According to Fletcher and Butcher [6] for pure lattice scattering $r_H = 1.16$, our calculations, using the method proposed by Rode and Knight

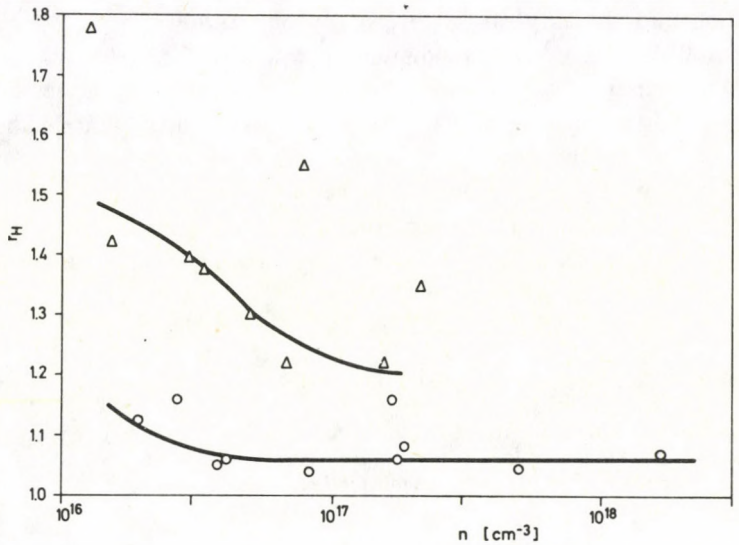

Fig. 6. Concentration dependence of the Hall scattering factor, r_H, at room temperature (○) and at 77K (△)

[30], gave $r_H = 1.18$. Lattice scattering is dominant below about 5×10^{15} cm^{-3} electron concentration (without compensation), therefore we can conclude that with increasing n, r_H quickly decreases to about 1. Our results agree well with the experimental results of Baranskii et al. [34], who obtained experimentally $r_H = 1.0$, for the electron concentration range of $1 \times 10^{15} - 1 \times 10^{18}$ cm^{-3}.

At a temperature of 77K the value of r_H in our low mobility samples for $n \approx 10^{16}$ cm^{-3} is about 1.5 and gradually decreases with increasing n to about 1.2. According to Fletcher and Butcher [6] and according to our own estimations for lattice scattering $r_H = 1.10$. The value of r_H presumably increases from this value in the concentration range of $10^{14} - 10^{16}$ cm^{-3} to about 1.5, its maximum value, then it decreases again. But different compensation degrees can modify this behaviour. According to the measurements of Baranskii et al [34] in the concentration range of $1 \times 10^{15} - 1 \times 10^{18}$ cm^{-3} r_H decreases from 1.12 to 1.0 in variance with the results presented above. It is not yet clear what the reason is for this disagreement.

6. Conclusions

From the analysis presented above the following conclusions can be drawn:

i) With the help of the quantity r_{eff} introduced through the relation $\tau_{\text{eff}} \sim \varepsilon^{r_{\text{eff}}}$ a consistent description of magnetoresistance and mobility measurements on GaAs can be given. The concept of r_{eff} is also useful for the description of other transport properties as was referred to above.

ii) From the magnetoresistance measurements it could be inferred that for the concentration and mobility range covered by our samples, polar optical phonon scattering and space-charge scattering dominate the mobility at room temperature, and ionized impurity scattering with an admixture of space-charge scattering is the relevant scattering mechanism at 77K. These results are in accordance with the results of direct mobility measurements.

iii) It is established that the scattering factor at 300K is nearly equal to unity in a wide concentration range and shows a more pronounced dependence on the electron concentration at 77K at least for the concentration and mobility range covered by our samples.

7. Acknowledgements

Grateful acknowledgements are due to Mrs. N. Nádor for her contributions in developing the ideas on the general role of space-charge scattering. The experimental part of this work was performed during the affiliation of the author with the Research Institute for Technical Physics of the Hungarian Academy of Sciences, Budapest.

References

1. E. H. Putley, The Hall Effect and Related Phenomena, London, Butterworths, 1960.
2. H. Ehrenreich, Phys. Rev., **120,** 1951, 1960.
3. C. Hilsum, In: Progress in Semiconductors, Ed. A. F. Gibson, London, Heywood Co. Ltd., **9,** 137, 1965.
4. H. Piller, Proc. Int. Conf. Semicond. Phys., Kyoto, 1966, p. 206.
5. D. L. Rode, Phys. Rev., *B2,* 1012, 1970.
6. K. Fletcher and P. N. Butcher, J. Phys. C: Solid State Phys., **5,** 212, 1972.
7. B. Pődör and N. Nádor, Acta Phys. Hung., **37,** 317, 1974.
8. D. L. Rode, In: Semiconductors and Semimetals, Ed. R. K. Willardson, A. C. Beer, Acad. Press, New York, Vol. 10, p. 1, 1975.
9. B. R. Nag, Electron Transport in Compound Semiconductors, Springer Verlag, Berlin, 1980.
10. R. L. Weisberg, J. Appl. Phys., **33,** 1817, 1962.
11. T. Katoda and T. Sugano, J. Electrochem. Soc., **121,** 1066, 1974.
12. B. Pődör, N. Nádor and I. Bertóti, phys. stat. sol. (a), **29,** 173, 1975.
13. Y. Kushiro, T. Seimiya, O. Sinbori and T. Kobayashi, J. Appl. Phys., **48,** 1636, 1977.
14. G. B. Stringfellow, J. Appl. Phys., **50,** 4178, 1979.
15. E. M. Conwell and M. O. Vassel, Phys. Rev., **166,** 797, 1968.
16. G. B. Stringfellow and H. Künzel, J. Appl. Phys., **51,** 3254, 1980.
17. D. Chattopadhyay, Phys. Rev., *B23,* 2956, 1981.
18. R. A. Faulkner, Phys. Rev., **175,** 991, 1968.
19. P. J. Dean, J. of Luminescence, **1—2,** 398, 1970.
20. А. И. Ансельм, Б. М. Аскеров, Физика твердого тела, **3,** 3668, 1961.

21. В. И. Фистуль, Сильно легированные полупроводники, Изд. Наука, Москва, 1967.
22. S S. Devlin, In: Physics of II—VI Compounds, Ed. M. Aven, J. S. Prener, Amsterdam, North-Holland, 1967, p. 549.
23. H. Ehrenreich, J. Appl. Phys. (Suppl.), **32,** 2155, 1961.
24. R. Kuzel, Can. J. Phys., **47,** 2261, 1969.
25. Т. И. Воронина, О. В. Емельяненко, В. Н. Наследов, Д. Д. Недеогло, Физ. и тех. полупроводников, **7,** 1382, 1973.
26. A. F. Kravchenko, S. Kubálková, B. V. Morozov, V. G. Polovinkin, and E. M. Skok, Phys. Stat. Sol. (b) **72,** 221, 1975.
27. О. В. Емельяненко, З. Ш. Овсюк, В. Г. Сидоров, В. А. Скрипкин, Всесоюзная конференция по физическим свойствам полупроводников A^3B^5 и A^2B^6 1965, Баку, Изд. АН Азерб. ССР, 1967, стр. 193.
28. R. G. Hamerly and M. W. Heller, J. Appl. Phys., **42,** 5585, 1971.
29. B. Pődör, Acta Phys. Hung., **27,** 449, 1969.
30. D. L. Rode and S. Knight, Phys. Rev., *B***3,** 2534, 1971.
31. H. Ikoma, J. Phys. Soc. Japan, **25,** 1069, 1968.
32. В. В. Батавин, В. М. Михаэлян, Г. В. Попова, В. Н. Федоренко, Физ. и тех. полупроводников, **6,** 84, 1972.
33. B. Pődör and C. Ivánka, Acta Phys. Hung., **25,** 115, 1968.
34. П. И. Баранский, Г. В. Долганникова, Э. П. Сеитов, Укр. Физ. Журн. **17,** 137, 1972.

Acta Physica Hungarica 54 (1—2), pp. 139—146 (1983)

INVESTIGATION OF ANTI-STOKES FLUORESCENCE IN MIXED RHODAMINE 6G—MALACHITE GREEN SYSTEMS

A. BUJKO, C. BOJARSKI and R. BUJKO

*Institute of Physics, Technical University, Gdańsk, Poland**

(Received 20 May 1982)

Concentrational changes of the fluorescence quantum yield and emission anisotropy were measured for rhodamine 6G (donor) in the presence of malachite green (acceptor) in glycerin — alcohol solutions, excited in the anti-Stokes and Stokes regions. Reduction of the nonradiative energy transfer efficiency in the case of anti-Stokes excitation was observed. The results of measurements proved to be in good agreement with the theory [10] which allows for a multistep mechanism from donor to acceptor energy transfer for Stokes as well as anti-Stokes excitation. However, in the latter case this agreement could have been obtained for a clearly lower value of the absolute donor fluorescence yield.

1. Introduction

Investigations of concentrational changes of the photoluminescence (PL) quantum yield η/η_0 in rhodamine solutions have shown that for excitation in the anti-Stokes (AS) region the PL concentrational quenching is less intense than for the Stokes (S) excitation [1—3]. It should be emphasized that this effect is significantly weaker than the analogous one observed in the case of emission anisotropy (Weber's red edge effect [4—6]). For this reason an especially careful determination of inactive absorption was necessary to ensure the evaluation of true η/η_0 values. However, for PL self-quenching nonluminescent dimers are mainly responsible for inactive absorption. For them the extinction coefficient $\varepsilon''(\nu)$ in the AS region is usually much larger than the extinction coefficient $\varepsilon'(\nu)$ for monomers. Besides, for $\nu < \nu_{0-0}$ values of both coefficients may be highly inaccurate, as the absorption spectra for dimers and monomers are calculated from a family of absorption curves corresponding to different dye concentrations rather than being directly measured. Therefore a two-component system seems to be better suited for investigations, because for such a system the donor and acceptor absorption spectra may be determined with higher accuracy than resolved monomer and dimer spectra.

In this paper we discuss results of measurements of the quantum yield, and emission anisotropy concentrational changes for the fluorescence in a two-component system in which molecules of rhodamine 6G act as donors and those of malachite green as acceptors.

* Address: Instytut Fizyki, Politechnika Gdańska, ul. Majakowskiego 11/12, 80-952 Gdańsk, Poland.

2. Experimental

Three series of glycerin-alcohol solutions of rhodamine 6G (donor) and malachite green (acceptor) were prepared. Rhodamine 6G ($C_{26}H_{27}O_3N_2Cl$, m.w. = 450.98) and malachite green ($C_{25}H_{26}N_2O_4$, m.w. = 418.53) were purified in the normal way by recrystallization. Anhydrous analytically pure glycerin mixed with 25% of methanol (p. a.) without any further purification was used as solvent. Dye concentrations were adjusted by weighing in such a way so as to ensure for each series of solutions a constant ratio of the malachite green concentration (C_M) to the square of rhodamine 6G concentration (C_R) ($C_M/C_R^2 = K$). For the respective series this ratio amounted to $K_1 = 76\ \mathrm{dm^3 \cdot mol^{-1}}$, $K_2 = 1895\ \mathrm{dm^3 \cdot mol^{-1}}$ and $K_3 = 7581\ \mathrm{dm^3 \cdot mol^{-1}}$ for systems I, II and III, respectively.

The quantum yield and flourescence spectra were measured for samples frontally excited with the aid of a Q-400 mercury lamp. An SPM-2 monochromator was used to select wavelengths $\lambda_1 = 546$ nm and $\lambda_2 = 578$ nm for the S and AS excitation, respectively ($\lambda_{0-0} = 544$ nm). An IF 625 Ca filter was used for observations. For measurements of the quantum yield and fluorescence spectra a device described elsewhere [7] was adopted. The absorption spectra were measured with a VSU2-P spectrophotometer. For emission anisotropy (EA) excitation also the Q-400 mercury lamp was applied. The measurements of EA were carried out using a device described in [8]. Corrections for secondary fluorescence were introduced for EA, while in the case of quantum yield corrections for secondary fluorescence as well as anisotropy of the spatial distribution of fluorescence were applied, as in [9]. All measurements were made at 293K.

The actual values of the PL quantum yield were determined on the basis of the relation

$$\frac{\eta}{\eta_0} = \left(\frac{\eta}{\eta_0}\right)'\left[1 + \frac{1-x}{x}\left(\frac{\varepsilon_M}{\varepsilon_R}\right)_{\lambda_{ex}}\right], \tag{1}$$

where $(\eta/\eta_0)'$ is the PL quantum yield with no correction for inactive absorption by the acceptor, ε_M and ε_R are extinction coefficients for malachite green and rhodamine 6G, respectively, and $x = C_R/(C_R + C_M)$. For AS excitation the correction factor in (1) may reach high values. For instance, for $\lambda_{ex} = 578$ nm the expression in square brackets changes from 4 to 438 for the concentration in system III variable between $6.3 \times 10^{-6}\ \mathrm{mol \cdot dm^{-3}}$ and $9.1 \times 10^{-4}\ \mathrm{mol \cdot dm^{-3}}$. Analogous changes corresponding to excitation at $\lambda_{ex} = 546$ nm wavelength cover the range (1 – 2.1). The accuracy with which the correction factor may be determined depends mainly on the accuracy of measurement of the extinction coefficient for rhodamine 6G. To increase this accuracy the coefficient ε_R was measured in the AS region, using cuvettes of appropriately large thickness. The maximum error associated with the determination of the correction factor was evaluated to be equal to 1.2%, the error in determination of the mole content of rhodamine 6G in the solution having been neglected.

3. Results and discussion

Fig. 1 shows the absorption and fluorescence spectra for rhodamine 6G as well as the absorption spectrum for malachite green in glycerin–alcohol solutions. The substantial overlaps of the fluorescence and absorption spectra of rhodamine 6G, as well as the rhodamine 6G fluorescence spectrum and the absorption spectrum of malachite green provide for efficient energy migration among the donor molecules and its transfer to the acceptor. Values of critical concentrations C_0 and distances R_0 for the processes under consideration are specified in Table I. Fig. 2 presents the results of measurements of concentrational changes of the quantum yield η/η_0 and emission anisotropy r/r_0 for fluorescence of rhodamine 6G in the presence of malachite green, fluorescence occurring as a result of Stokes and anti-Stokes excitation. The solid lines showing concentrational changes of η/η_0 for S excitation were calculated from the formula [10]

$$\frac{\eta}{\eta_0} = \frac{1-f(\gamma)}{1-\alpha_0\alpha f(\gamma)}, \tag{2}$$

where

$$f(\gamma)=\pi^{1/2}\gamma\cdot\exp(\gamma^2)[1-erf(\gamma)], \tag{3}$$

$$\gamma=\gamma_R+\gamma_M=\frac{\pi^{1/2}}{2}\left(\frac{C_R}{C_{0R}}+\frac{C_M}{C_{0M}}\right); \qquad \alpha=\frac{\gamma_R}{\gamma_R+\gamma_M}. \tag{4}$$

Here C_{0R}, C_{0M} are critical concentrations and α_0 is the probability of absence of the energy degradation in the process of energy migration between rhodamine molecules. The values of C_{0R} and C_{0M} were calculated for the absolute value of rhodamine 6G PL quantum yield equal to $\eta_0=0.85$ as given in [11]. The value of the orientation factor $\langle\kappa^2\rangle$ for the lowest concentration was assumed to equal 2/3 [12]. Consequently $\tau_r \ll \tau_l$ was assumed, where τ_r is the rotation time for rhodamine 6G molecules and τ_l is the excitation energy localization time. In [13] it was shown that an increase of concentration of active molecules in a solution may result in a decrease of τ_l leading to $\tau_r \gg \tau_l$. Then $\langle\kappa^2\rangle=0.476$ [14, 15]. The values of $\langle\kappa^2(\gamma)\rangle$ for intermediate concentration were calculated in a similar way as in [13, 16]. The Figure shows the good agreement of experimental results for S excitation with theoretical curves of η/η_0 (empty circles and solid lines).

An equally good agreement of experimental and theoretical [relation (2)] values of η/η_0 was obtained for AS excitation (black circles and dashed lines). This, however, was achieved for the values of critical concentration C_{0R} and C_{0M} higher by 46% than those assumed for Stokes excitation. Note that the rise of critical concentration caused by the red shift of fluorescence spectrum for AS excitation does not exceed several percent [2]. Thus, the increased values of C_{0R} and C_{0M} may be obtained only on assumption of a drop of the absolute PL quantum yield for rhodamine 6G subject to AS excitation to $\eta_0'=0.40$.

Table I

Characteristic data for rhodamine 6G — malachite green systems in glycerin — alcohol solutions

T [K]	Viscosity [Pa · s]	λ_{ex} [nm]	η_0 [—]	C_{0R} [mol · dm^{-3}]	C_{0M} [mol · dm^{-3}]	R_{0R} [nm]	R_{0M} [nm]
293	0.124	546	0.85	3.18×10^{-3}	1.92×10^{-3}	4.99	5.91
		578	0.40	4.64×10^{-3}	2.80×10^{-3}	4.40	5.21

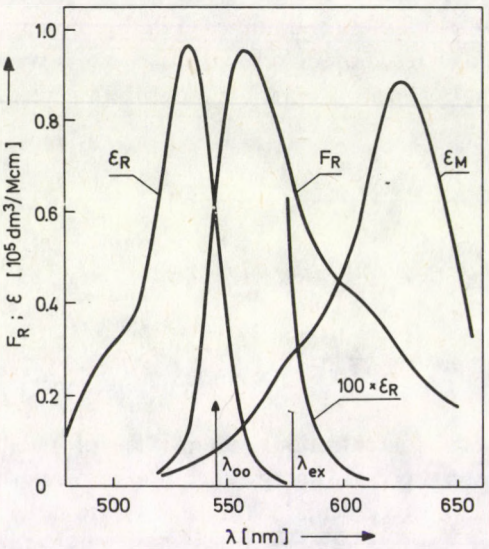

Fig. 1. Absorption (ε_R) and fluorescence (F_R) spectra for rhodamine 6G and absorption spectrum (ε_M) for malachite green in a glycerin–alcohol solution; $100 \times \varepsilon_R$ — a 100 times magnified part of the rhodamine 6G absorption band

Also shown in Fig. 2 are concentrational changes of the PL emission anisotropy for the same systems subject to S and AS excitation. Experimental results for system I fall satisfactorily well along theoretical curves given by [17]

$$\frac{r}{r_0} = (1 - \alpha\alpha_0 f)\left[1 + \frac{1}{2}\frac{(\alpha\alpha_0 f)^2}{1 - \frac{3}{4}(\alpha\alpha_0 f)^2}\right], \tag{5}$$

where $f \equiv f(\gamma)$, α_0 and α correspond to those in (2). The solid and dashed lines were calculated for the same absolute yield values as the corresponding quantum yield curves. This applies also to the remaining systems. For systems II and III theoretical curves do not describe the experimental results as well as those for system I. This may

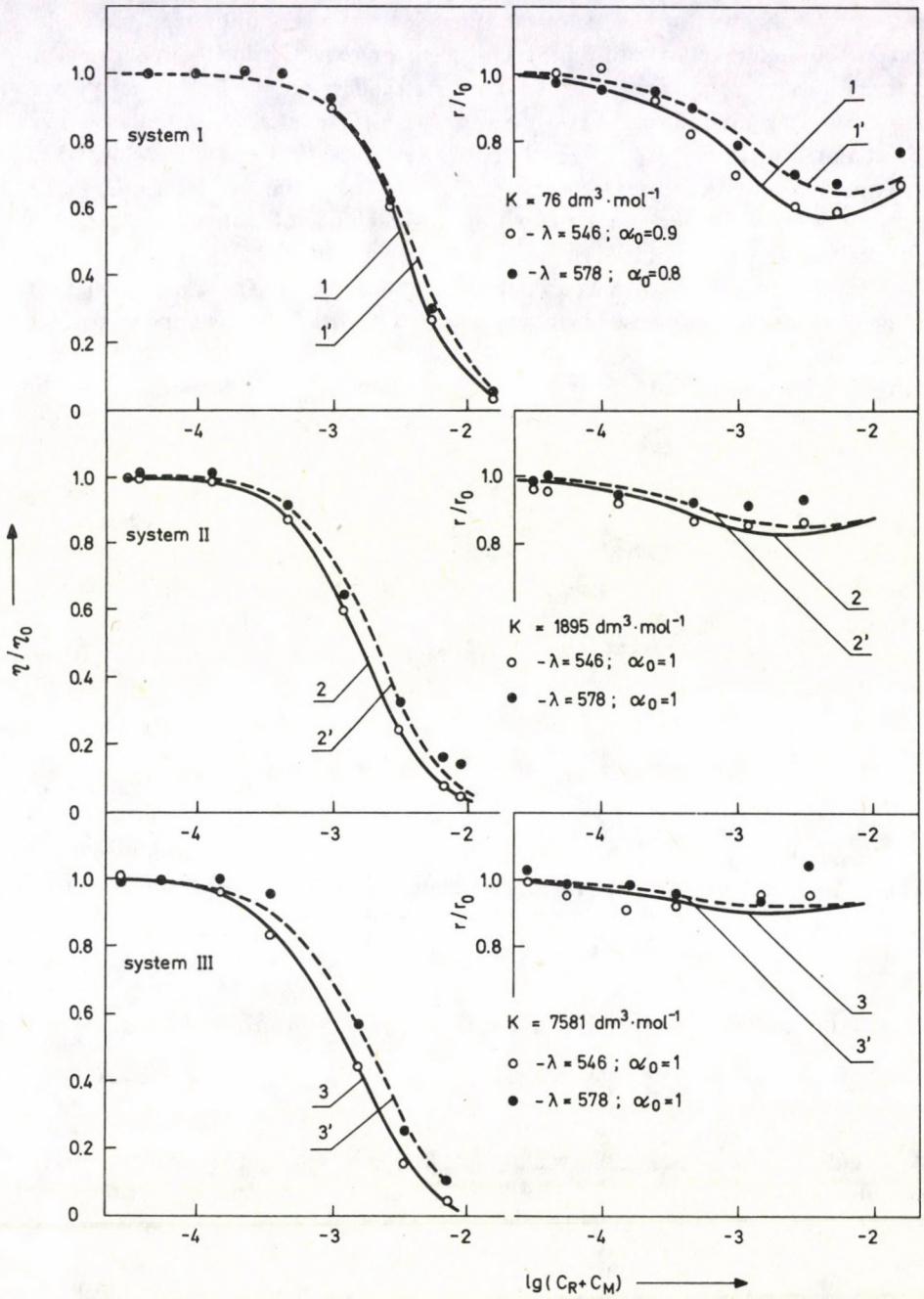

Fig. 2. Concentrational changes of the quantum yield η/η_0 and emission anisotropy r/r_0 for fluorescence of rhodamine 6G in the presence of malachite green in glycerin–alcohol solutions. Solid and dashed lines for η/η_0 have been calculated from formula (2), while those for r/r_0 — from formula (5); curves 1, 2, 3 correspond to $\eta_0 = 0.85$, curves 1′, 2′, 3′ — to $\eta_0' = 0.40$

be caused by neglecting in Eq. (5) of the quenching by malachite green molecules present in the luminescence centre [18] as well as by reduction of the measurement accuracy, resulting from strong quenching of the rhodamine 6G PL in the systems investigated. This quenching is also responsible for the effect of repolarization, exhibited markedly enough for systems I and II. Repolarization was already observed for systems characterized by strong quenching of PL by dimers [17, 19, 20]. For systems under consideration the participation of rhodamine 6G dimers in quenching may be neglected. It is known that rhodamine 6G in glycerin, and also in ethyl alcohol, exhibits nearly concentration-independent absorption spectra. The same is valid for glycerin–alcohol solutions as used in the experiments reported. On assumption that for the solution of rhodamine 6G under consideration $K = 0.11\ \mathrm{dm^3 \cdot mol^{-1}}$ as for rhodamine 6G in ethanol [21] the ratio C''/C_M, which is highest for system I, does not exceed 0.11% ($C''/C_M \approx K/K_i$, where $K = C''/C'^2$ is the dimerization constant, K_i are values of the constant defining C_M for the respective systems; C'' and C' are the concentrations of dimers and monomers, respectively).

The Rayleigh scattering of exciting light on active molecules is another factor which may affect experimental values of η/η_0 in the AS region. Table II shows the values of errors caused by omission of the effect of light scattering when calculating the true values of η/η_0 according to Eq. (1). The values of coefficient ε_R for $\lambda > 578$ nm were obtained by extrapolation (cf. Fig. 3) of $\varepsilon_R(\nu)$ values as described by an approximate equation given by Erickson [22, 23]

$$\varepsilon(\nu) = \varepsilon(\nu_{0-0}) \cdot \exp\left[\frac{h}{kT}(\nu - \nu_{0-0})\right], \tag{6}$$

where ν_{0-0} is the frequency of purely electronic transition. The extinction coefficient associated with scattering, ε', was calculated using the relation [24, 25]

$$\varepsilon' = \frac{1}{C} \cdot \frac{8 \cdot \pi}{3} R,$$

where R is the scattering cross-section and C is the dye concentration. The values of R were measured for $\lambda = 632.8$ nm wavelength; for other wavelengths the relation $R \sim \frac{1}{\lambda^4}$ was adopted. It is evident from Table II that in the case of AS excitation at 578 nm the effect of light scattering is negligible, while in the longer wavelength region its omission may result in substantial errors. It should be emphasized that omission of the light scattering effect in the problem under consideration leads to reduction of true η/η_0 values.

Note that for system I, which is characterized by the lowest K, differences between the course of yield curves for S and AS excitation are relatively small compared with those for systems II and III, where PL quenching by malachite green is markedly stronger. The reverse is observed for the emission anisotropy, where system I

Table II

Errors in true values of η/η_0 due to the neglecting of the effect of exciting light scattering

λ [nm]	ε_R $\left[\frac{dm^3}{mol \cdot cm}\right]$	ε' $\left[\frac{dm^3}{mol \cdot cm}\right]$	$\frac{\varepsilon'}{\varepsilon_R}$ [—]	$\frac{\Delta\eta/\eta_0}{\eta/\eta_0}$ [%]
546	5.26×10^4	11.7×10^{-2}	2.23×10^{-7}	0.002
578	437	9.94×10^{-2}	2.14×10^{-4}	0.02
625	0.631	6.83×10^{-2}	1.08×10^{-1}	10
632.8	0.1955	6.50×10^{-2}	3.41×10^{-1}	25
648	0.0562	5.91×10^{-2}	1.05	51

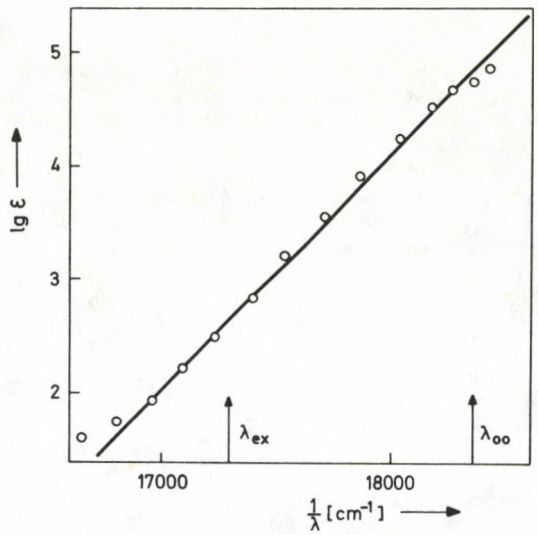

Fig. 3. The anti-Stokes part of the rhodamine 6G absorption band

exhibits the largest differences between the curves. The small differences between r/r_0 for S and AS excitation are the obvious results of the strong PL quenching by the acceptor for systems II and III.

In should be pointed out that the true values of η/η_0 could have been determined in our case more accurately than for systems where the PL quenching depends on the presence of nonluminescent dimers. Good agreement of experimental results for η/η_0 and r/r_0 with those calculated according to (2) and (5) was obtained for values of parameters determined based on independent measurements (see Table I). The probability α_0 was the only parameter of the theory that was determined from the best fit of experimental results to theoretical curves. It was equal, for system I, to 0.9 and 0.8

for S and AS excitation, respectively. Also the results of η/η_0 and r/r_0 measurements obtained for AS excitation could have been described correctly with relations (2) and (5), however, for a much lower absolute yield. This confirms the Vavilov law [26–28] stating that a drop of the absolute yield should be expected in the AS region. Another explanation of the lower efficiency of the energy transfer process for AS excitation is also possible, and may be attributed to an inhomogeneous broadening of the absorption and fluorescence bands of interacting molecules [29–31].

Acknowledgement

This work was carried out under the Research Project MR. I. 5.

Reference

1. C. Bojarski, A. Bujko, J. Dudkiewicz and R. Twardowski, Z. Naturforsch., **30***a*, 1091, 1975.
2. C. Bojarski, A. Bujko, R. Bujko and R. Twardowski, Acta Phys. et Chem. Szeged, **23**, 93, 1977.
3. C. Bojarski, A. Bujko, R. Bujko and R. Twardowski, Acta Phys. Polon, *A***54**, 713, 1978.
4. G. Weber, Biochem. J., **75**, 335, 1960.
5. S. R. Anderson and G. Weber, Biochemistry, **8**, 371, 1969.
6. J. Eisinger, A. A. Lamola, J. W. Longworth and W. B. Gratzer, Nature, **226**, 113, 1970.
7. C. Bojarski, G. Obermueller and J. Kuśba, Z. Nauk. Politechn. Gdańsk, **181**, 2, 1971 (in Polish).
8. J. Dudkiewicz, Z. Nauk. Politechn. Gdańsk, **181**, 121, 1971 (in Polish).
9. A. Budó and I. Ketskeméty, Acta Phys. Hung., **14**, 167, 1962.
10. C. Bojarski and J. Domsta, Acta Phys. Hung., **30**, 145, 1971.
11. J. P. Webb, W. C. Mc Colgin, O. G. Peterson, D. L. Stockman and J. H. Eberly, J. Chem. Phys., **53**, 4227, 1970.
12. Th. Förster, Ann. Physik, Leipzig, **2**, 55, 1948.
13. C. Bojarski and J. Dudkiewicz, Chem. Phys. Letters, **67**, 450, 1979.
14. M. D. Galanin, Zh. Eksper. Theor. Phys. USSR, **28**, 485, 1955.
15. M. Z. Maksimov and I. M. Rozman, Opt. i Spektr., **12**, 606, 1962.
16. C. Bojarski and E. Grabowska, Z. Naturforsch., **35***a*, 1030, 1980.
17. C. Bojarski, J. Luminescence, **5**, 413, 1972.
18. C. Bojarski, J. Luminescence, **9**, 40, 1974.
19. L. Szalay, B. Sárkány and E. Tombácz, Acta Phys. et Chem. Szeged, **11**, 21, 1965.
20. C. Bojarski and J. Dudkiewicz, Z. Naturforsch., **26***a*, 1028, 1971.
21. C. Bojarski and E. Grabowska, Acta Phys. Polon., *A***60**, 397, 1981.
22. L. E. Erickson, J. Luminescence, **5**, 1, 1972.
23. R. Beserman, G. Curie and D. Curie, J. Luminescence, **8**, 326, 1974.
24. M. B. Huglin, Light Scattering from Polymer Solutions, Academic Press, London, New York, 1972.
25. L. Woliński, K. Witkowski and Z. Turzyński, Makrom. Chemie, **180**, 2399, 1979.
26. S. I. Vavilov, Collected Papers Acad. Sci. USSR, Moscow–Leningrad, 1952, Vol. 2, p. 373.
27. L. Kozma, E. Farkas and M. Fekete, Acta Phys. et Chem. Szeged, **16**, 97, 1970.
28. I. Ketskeméty and L. Kozma, Acta Phys. Hung., **29**, 331, 1970.
29. J. N. Bodunov, J. V. Kolobkova and V. L. Ermolajev, Opt. i Spektr., **44**, 2, 1978.
30. J. N. Bodunov and V. A. Malyshev, Opt. i Spektr., **46**, 3, 1979.
31. J. N. Bodunov, V. A. Malyshev, S. V. Jakovlev, Zh. Prikl. Spektrosk., **32**, 5, 1980.

Acta Physica Hungarica 54 (1—2), pp. 147—153 (1983)

A LAGRANGIAN FORMULATION IN MAGNETOFLUID DYNAMICS

I. MERCHES

Faculty of Physics, Alexandru Joan Cuza University, Iasi 6600, Romania

(Received 20 May 1982)

By using Clebsch representations for all necessary vector fields, an action principle for a compressible, inviscid, one-component magneto-fluid, undergoing isentropic motion in an electromagnetic field, is given.

1. Introduction

There are many papers regarding the derivation of the equations of magnetofluid dynamics from an action principle. One of the first and most important problems arising in such derivations is the construction of a Lagrangian density, suitable for the considered magnetofluid model.

Regardless of the particular cases which are under discussion, there exist certain rules (or procedures) used in the derivation of the set of equations describing the behaviour of the magnetofluid system. One of these rules says that the electromagnetic field **E**, **B** is expressed in terms of either the well-known potentials **A**, Φ [e.g. 1–7] or the so called "generalized antipotentials" [8]. On the other hand, the fluid velocity field **v** is usually represented in terms of a set of Clebsch potentials, and an interaction term as well. Both electromagnetic and Clebsch potentials are taken as variational parameters. But we should mention that this procedure is not compulsory: the Clebsch representation of the velocity field can be obtained as a result of the variation.

The main purpose of the present paper is to give a variational principle for an inviscid, conducting fluid, and show that the representation of *all* vector fields in terms of Clebsch potentials is not only a possible, but also a useful method in the Lagrangian approach of magnetofluid dynamics.

2. Construction of the Lagrangian density

Let our model of magnetofluid be an inviscid, one-component, compressible fluid, which undergoes isentropic motion in the electromagnetic field **E**, **B**. If we denote by ρ and ρ^e the mass and charge densities, and suppose that the particle number density

n is identical to the charge carrier density n^e, then we may write $\rho^e/\rho = e/m$, which is an invariant in our non-relativistic approximation.

Hamilton's principle requires

$$\delta S = \delta \iiint \mathscr{L} \, dx \, dz \, dt = 0, \tag{1}$$

where the action S is formed by three parts: one belongs to the electromagnetic field, one to the fluid, and one gives the interaction between the two physical systems. Then the Lagrangian density will have the same composition and we choose

$$\mathscr{L}^{em} = \frac{1}{2} k_0 E_i E_i - \frac{1}{2\mu_0} B_i B_i , \tag{2}$$

$$\mathscr{L}^{\text{fluid}} = \frac{1}{2} \rho v^2 - \rho\varepsilon - \alpha[\partial_t \rho + \partial_i(\rho v_i)] - \beta\rho(\partial_t s + v_i \partial_i s) , \tag{3}$$

$$\mathscr{L}^{\text{int}} = \rho^e(v_i A_i - \Phi) . \tag{4}$$

In these formulas, Φ and $\mathbf{A}$ are the scalar and vector potentials, ε and s are the internal energy and the entropy per unit mass, while α and β are two Lagrangian multipliers. It is assumed that $k \sim k_0$ and $\mu \sim \mu_0$, where k and μ are the permittivity and the permeability of the fluid.

Before going further, we shall briefly discuss the significance of the Lagrangian densities (2), (3), and (4). The expression (2) is the Lagrangian density of the electromagnetic field *in vacuo;* it is known as *the Larmor invariant*. Since $\rho^e = \frac{e}{m}\rho$, we may write (4) as

$$\mathscr{L}^{\text{int}} = \frac{e}{m} \rho(v_i A_i - \Phi) . \tag{5}$$

We deliberately left at the end the Lagrangian density (3), given by Herivel [9], because we want to work on it. First, one observes that the equation of continuity and the equation of conservation of entropy play the role of two constraint equations. On the other hand, the analytical mechanics formalism says that Euler–Lagrange equations

$$\frac{\partial \mathscr{L}}{\partial \varphi^{(s)}} - \frac{\partial}{\partial x_J}\left(\frac{\partial \mathscr{L}}{\partial \varphi^{(s)}_{,J}}\right) = 0 \qquad (J = \overline{1,4}\,; \qquad s = 1, 2, \ldots) , \tag{6}$$

where $x_1 = x$, $x_2 = y$, $x_3 = z$, $x_4 = t$, and $\varphi^{(s)}$ stand for variational parameters, are form-invariant with respect to the "divergence transformation"

$$\mathscr{L}'(x_J, \varphi^{(s)}, \varphi^{(s)}_{,J}) = \mathscr{L}(x_J, \varphi^{(s)}, \varphi^{(s)}_{,J}) +$$

$$+ \frac{\partial}{\partial x_k} F_K(x_J, \varphi^{(s)}) \qquad (J, K = \overline{1,4}) , \tag{7}$$

if the domain of integration is fixed, and the variational parameters $\varphi^{(s)}$ take fixed values on the boundary which limits the integration domain. Here and throughout this paper the Einstein's summation convention is used.

Making allowance for (7), we shall add the term

$$\frac{\partial}{\partial x_j}(\rho\alpha v_j)=\frac{\partial}{\partial t}(\rho\alpha)+\frac{\partial}{\partial x_i}(\rho\alpha v_i) \qquad (i=\overline{1,3})$$

to Eq. (3) and get

$$\mathscr{L}^{\text{fluid}}=\frac{1}{2}\rho v_i v_i-\rho\varepsilon+\rho(\partial_t\alpha+v_i\partial_i\alpha)- \\ -\beta\rho(\partial_t s+v_i\partial_i s)\,. \tag{8}$$

In view of (2), (5), and (8), we shall write our Lagrangian density as

$$\mathscr{L}=\frac{1}{2}k_0E_iE_i-\frac{1}{2\mu_0}B_iB_i+\frac{e}{m}\rho(v_iA_i-\Phi)+\frac{1}{2}\rho v_iv_i-\rho\varepsilon+ \\ +\rho(\partial_t\alpha+v_i\partial_i\alpha)-\beta\rho(\partial_t s+v_i\partial_i s)\,. \tag{9}$$

3. The Lagrangian formulation. First method

The fundamental system of equations describing the behaviour of our fluid include: Maxwell's equations

$$\varepsilon_{ijk}\partial_jE_k+\partial_tB_i=0\,; \qquad \partial_iB_i=0\,, \tag{10a, b}$$

$$\varepsilon_{ijk}\partial_j(\mu_0^{-1}B_k)=\rho^e v_i+\partial_t(k_0E_i)\,; \qquad \partial_i(k_0E_i)=\rho^e\,, \tag{11a, b}$$

the equation of motion

$$\partial_t v_i+v_k\partial_k v_i=-\frac{1}{\rho}\partial_i p+\frac{e}{m}E_i+\frac{1}{\rho}\varepsilon_{imk}j_m\Omega_k\,, \tag{12}$$

as well as Ohm's law, the equation of state, and the equations of conservation of mass and entropy. Part of these equations have already been used in the construction of the Lagrangian density (9). The first group of Maxwell's equations (10a, b) serve to define the electromagnetic field **E**, **B** in terms of potentials **A**, Φ:

$$E_i=-\partial_i\Phi-\partial_tA_i\,; \qquad B_i=\varepsilon_{ijk}\partial_jA_k\,. \tag{13a, b}$$

In view of these considerations, we shall take as independent variational parameters Φ, A_j, v_j, α, s, ρ. Making allowance for the Euler–Lagrange equations (6), where $\mathscr{L}$ is given by (9), one obtains:

$$(\Phi) \qquad \partial_i(k_0E_i)-\rho^e=0\,, \tag{14}$$

$$(A_i) \qquad \varepsilon_{ijk}\partial_j(\mu_0^{-1}B_k)-\rho^e v_i-\partial_t(k_0E_i)=0\,, \tag{15}$$

$$(v_i) \qquad v_i+\partial_i\alpha-\beta\partial_i s+\frac{e}{m}A_i=0\,, \tag{16}$$

$$(\alpha) \qquad \partial_t\rho+\partial_i(\rho v_i)=0\,, \tag{17}$$

$$(s) \qquad \partial_t\beta+v_i\partial_i\beta-T=0, \tag{18}$$

$$(\rho) \qquad \frac{1}{2}v_iv_i-\varepsilon-\frac{p}{\rho}+\partial_t\alpha+v_i\partial_i\alpha+\frac{e}{m}(v_iA_i-\Phi)=0\,. \tag{19}$$

The first two equations (14) and (15) are just Maxwell's source equations (11a, b). Eq. (16) is a generalized Clebsch transformation, α, β, and s being a set of Clebsch potentials. In the derivation of the last two equations (18) and (19) we used the fundamental thermodynamical equation of reversible processes

$$T\mathrm{d}s=\mathrm{d}\varepsilon(\rho,s)+p\mathrm{d}\left(\frac{1}{\rho}\right). \tag{20}$$

By eliminating the Lagrangian multipliers α, β from Eq. (16), (18), and (19), we shall arrive at the equation of motion (12). To do this, one takes the gradient of (19). The result is:

$$\mathbf{v}\times\operatorname{curl}\mathbf{v}+(\mathbf{v}\cdot\nabla)\mathbf{v}-\nabla\varepsilon-\rho^{-1}\nabla p+\rho^{-2}p\nabla\rho+\partial_t(\nabla\alpha)+$$

$$+(\nabla\alpha)\times\operatorname{curl}\mathbf{v}+(\mathbf{v}\cdot\nabla)(\nabla\alpha)+(\nabla\alpha\cdot\nabla)\mathbf{v}+\frac{e}{m}\nabla(\mathbf{v}\cdot\mathbf{A}-\Phi)=0\,.$$

In view of (16), (18) and (20), we still have:

$$\left(\beta\nabla s-\frac{e}{m}\mathbf{A}\right)\times\operatorname{curl}\mathbf{v}+(\mathbf{v}\cdot\nabla)\mathbf{v}-T\nabla s-\rho^{-1}\nabla p-\partial_t\mathbf{v}+\partial_t(\beta\nabla s)-$$

$$-\frac{e}{m}\partial_t\mathbf{A}+(\mathbf{v}\cdot\nabla)(\nabla\alpha)+(\nabla\alpha\cdot\nabla)\mathbf{v}+\frac{e}{m}\nabla(\mathbf{v}\cdot\mathbf{A}-\Phi)=0\,.$$

But

$$\partial_t(\beta\nabla s)=(\nabla s)\partial_t\beta-(\beta\nabla s)\times\operatorname{curl}\mathbf{v}-\beta(\mathbf{v}\cdot\nabla)(\nabla s)-\beta(\nabla s\cdot\nabla)\mathbf{v}\,,$$

$$(\mathbf{v}\cdot\nabla)(\nabla\alpha)=-(\mathbf{v}\cdot\nabla)\mathbf{v}+\beta(\mathbf{v}\cdot\nabla)(\nabla s)+(\nabla s)(\mathbf{v}\cdot\nabla\beta)-\frac{e}{m}(\mathbf{v}\cdot\nabla)\mathbf{A}\,,$$

so that, after some reduction and arrangement of the terms, we are left with

$$-\frac{\mathrm{d}\mathbf{v}}{\mathrm{d}t}+\frac{1}{\rho}\mathbf{j}\times\mathbf{B}+\frac{e}{m}\mathbf{E}-\frac{1}{\rho}\nabla p=0\,,$$

i.e. the desired equation of motion (12).

4. The Lagrangian formulation. Second method

The definition of the electromagnetic field **E**, **B** in terms of the electromagnetic potentials and their use as variational parameters is a well-known procedure. A little more unusual is, in our opinion, the representation of the electromagnetic field in terms of Clebsch potentials. In the following we shall show that this representation is very useful in our variational formulation.

Starting with one of Grad's [10] ideas, let the vector potential **A** be defined in terms of the Clebsch potentials ξ, η, ζ as

$$A_i = -\xi_{,i} + \eta\zeta_{,i} \qquad (\xi_{,i} = \partial_i \xi)\,. \tag{21}$$

If one introduces this definition in (13a, b), one gets:

$$E_k = -\Phi^*_{,k} + \zeta_{,t}\eta_{,k} - \eta_{,t}\zeta_{,k}\,, \tag{22a, b}$$

$$B_k = \varepsilon_{kjm}\eta_{,j}\zeta_{,m}\,,$$

where

$$\Phi^* = \Phi - \xi_{,t} + \eta\zeta_{,t}\,. \tag{23}$$

As one observes, the definition (21) makes it possible to express the electromagnetic field in terms of three scalar functions Φ^*, η, ζ, instead of four quantities A_i, Φ. These functions appear as Clebsch potentials of the vector potential **A**. They may be called *second-order potentials* or *superpotentials.*

In view of (16) and (22), all vector fields interfering in the Lagrangian density (9) can be expressed in terms of Clebsch potentials. In order to choose these potentials as variational parameters, we make some arrangement of the terms in (9), and get

$$\mathscr{L} = \frac{1}{2}k_0 E_i E_i - \frac{1}{2\mu_0}B_i B_i - \frac{e}{m}\rho\Phi^* - \frac{1}{2}\rho v_i v_i - \rho\varepsilon +$$

$$+ \rho\alpha_{,t} - \beta\rho s_{,t} - \frac{e}{m}\rho\xi_{,t} + \frac{e}{m}\rho\eta\zeta_{,t}\,. \tag{24}$$

Taking as independent variational parameters $\Phi^*, \eta, \xi, \alpha, \beta, s, \rho$, and having in mind the transformation ((see (16))

$$v_k = -\alpha_{,k} + \beta s_{,k} - \frac{e}{m}(-\xi_{,k} + \eta\zeta_{,k})\,, \tag{25}$$

one obtains from (6):

$$(\Phi^*) \qquad \partial_i(k_0 E_i) - \rho^e = 0\,, \tag{26}$$

$$(\eta) \qquad [\varepsilon_{ijk}\partial_j(\mu_0^{-1}B_k) - \rho^e v_i - \partial_t(k_0 E_i)]\partial_i\zeta = 0\,, \tag{27}$$

$$(\xi) \qquad \partial_t\rho^e + \partial_i(\rho^e v_i) = 0\,, \tag{28}$$

$$(\alpha) \qquad \partial_t\rho + \partial_i(\rho v_i) = 0\,, \tag{29}$$

$$(\beta) \qquad \partial_t s + v_i \partial_i s = 0\,, \tag{30}$$

$$(s) \qquad \partial_t \beta + v_i \partial_i \beta - T = 0\,, \tag{31}$$

$$(\rho) \qquad -\frac{e}{m}\Phi^* - \frac{1}{2} v_i v_i - \varepsilon - \frac{p}{\rho} + \partial_t \alpha - \beta \partial_t s +$$

$$+ \frac{e}{m}(-\partial_t \xi + \eta \partial_t \zeta) = 0\,. \tag{32}$$

One easily recognizes the source Maxwell's equations (it is assumed that $\zeta_{,i} \neq 0$), the equations of conservation of charge, mass, and entropy, and the Eq. (18) and (19) as well. Using the already known procedure, we take the gradient of (32):

$$-\frac{e}{m}\nabla\Phi^* - \mathbf{v} \times \operatorname{curl} \mathbf{v} - (\mathbf{v} \cdot \nabla)\mathbf{v} - \nabla\varepsilon - \rho^{-1}\nabla p + \rho^{-2} p \nabla\rho +$$

$$+ \partial_t(\nabla\alpha) - (\nabla\beta)\partial_t s - \beta\partial_t(\nabla s) + \frac{e}{m}\nabla(-\partial_t\xi + \eta\partial_t\zeta) = 0\,. \tag{33}$$

But, in view of (25)

$$\partial_t(\nabla\alpha) = -\partial_t \mathbf{v} + \partial_t\beta(\nabla s) + \beta\partial_t(\nabla s) -$$

$$-\frac{e}{m}[-\nabla(\partial_t\xi) + \partial_t\eta(\nabla\zeta) + \eta\partial_t(\nabla\zeta)]\,,$$

$$\operatorname{curl} \mathbf{v} = \nabla\beta \times \nabla s - \frac{e}{m}\nabla\eta \times \nabla\zeta\,,$$

so that, after performing some reduction in (33), we are left with the expected equation of motion (12)

$$\frac{\mathrm{d}\mathbf{v}}{\mathrm{d}t} + \rho^{-1}\nabla p - \frac{\rho^e}{\rho}(\mathbf{E} + \mathbf{v} \times \mathbf{B}) = 0\,.$$

5. Discussion

We have started this investigation based on the idea that all variational parameters (except for ρ) are Clebsch potentials. As one can see, the result is in complete agreement with that obtained by a "classical" method in Section 3. The advantage of this procedure is threefold: (i) it allows a symmetric formulation of the variational principle; (ii) it provides some extra information about the behaviour of the magnetofluid (e.g. the equation of conservation of charge); (iii) the equation of motion can be deduced in a simple way.

One can also see that the Eqs (19) and (32) are Bernoulli-type equations. Since $p'_J = v_J + \frac{e}{m} A_J = -\alpha_{,J} + \beta s_{,J} = \partial S'/\partial x_J \; (J = \overline{1,4})$ is the generalized momentum per unit mass, the Eq. (32) may be written as

$$\frac{\partial S'}{\partial t} + \kappa = 0 , \tag{34}$$

where

$$\kappa = \frac{1}{2} v^2 + \varepsilon + \frac{p}{\rho} + \frac{e}{m} \Phi \tag{35}$$

is the Hamiltonian per unit mass of the magnetofluid. Eq. (34) is similar to the usual Hamilton–Jacobi equation, S' being the action per unit mass. This comes to prove that our formalism is opened to various applications.

References

1. S. Katz, Phys. Fluids, **4,** 345, 1961.
2. C. H. Su, Phys. Fluids, **4,** 1376, 1961.
3. T. S. Lundgren, Phys. Fluids, **6,** 898, 1963.
4. M. G. Calkin, Can. J. Phys., **41,** 2241, 1963.
5. D. R. Wells, J. Plasma Phys., **4,** part 4, 645, 1970.
6. J. P. Dougherty, J. Plasma Phys., **11,** part 2, 331, 1974.
7. H. Rund, D. R. Wells & L. C. Hawkins, J. Plasma Phys., **20,** part 3, 329, 1978.
8. I. Merches, Phys. Fluids, **12,** 2225, 1969.
9. J. W. Herivel, Proc. Camb. Phil. Soc., **51,** 344, 1955.
10. H. Grad, Proc. of the Symposium on Electromagnetic and Fluid Dynamics of Gaseous Plasma, Polytechnic Institute of Brooklyn, April 1961, p. 37.

Acta Physica Hungarica 54 (1—2), pp. 155—159 (1983)

SOLUTIONS OF THE SU(1, 1) SPIN COEFFICIENT EQUATIONS WITH NON-GEODESIC EIGENRAYS

B. LUKÁCS

Central Research Institute for Physics
1525 Budapest, Hungary

(Received 2 June 1982)

The integration of the spin coefficient equations of spatially symmetric vacuum is carried out for non-geodesic eigencongruences and vanishing shear parameter. Two different solutions, a special Einstein–Rosen metric and a solution belonging to the spatially symmetric analogons of the Papapetrou-type metrics are obtained. The corresponding electrovac class of common eigenrays contains only Ernst counterparts of the vacuum metrics.

1. Introduction

The spin coefficient technique has yielded many new exact solutions of the Einstein equation of the general relativity. If one does not assume any symmetry for the spacetime, the four dimensional Newman–Penrose equations can be analytically solved for geodesic rays (principal null congruences) [1, 2, 3]. When the space-time has a non null symmetry, the spin coefficient formalism can be reformulated in a three dimensional background space [4, 5] and for timelike symmetry the vacuum equations have been integrated both for $\kappa=0$, $\sigma\neq 0$, [6] and for $\kappa\neq 0$, $\sigma=0$ [7]. (The asymptotically good Kerr solution is among the $\kappa=\sigma=0$ metrics). These solutions have nongeodesic rays because the eigenrays are the three dimensional projections of the rays if and only if $\sigma=0$. [4] It is interesting that the more general $\kappa\sigma=0$ class does not contain any generalization of the Kerr solution.

Since the structure of the spin coefficient equations does not become more complicated if one chooses space-like symmetry instead of the timelike one, it is obvious to try to integrate the two cases mentioned above for spatial symmetry too. (If $\kappa=\sigma=0$, the metric is algebraically special, and even the four-dimensional equations can be integrated). In fact, the general solution is known if $\kappa=0$, $\sigma\neq 0$, [8] which class does not contain also any generalization of the Kerr metric. In this paper we integrate the opposite $\kappa\neq 0$, $\sigma=0$ case. The analogous stationary solutions are very special: two different metrics exist, which do not have any arbitrary parameter except for a trivial constant conformal factor [7].

For the cases investigated till now, if the vacuum equations were integrable, the corresponding electrovac solutions of common eigenrays could be obtained too. Thus we will investigate this more general case.

Since the integrational process runs on the same way as in [7], we will not go into details of identical steps. In Section 2 we give the equations to be solved. Section 3 shows the way of the integration. Finally, in Section 4, we give the explicit form of the solution and discuss its behaviour.

2. The field equations

The general formulation of the 3 dimensional spin coefficient method for spatially symmetric space-times can be found in [5]. Since the orthonormality relations do not fully determine the triad vectors, the equations can be simplified by choosing a triad in which

$$G_- = \varepsilon = 0 . \tag{2.1}$$

The second condition can always be fulfilled, the first is not met only if the solution does not have eigenrays, which case is exceptional [5]. Since this paper deals with the solutions in which the shear parameter of the eigenray congruence vanishes, both conditions can be fulfilled. Then the basic vector l is the tangent vector of the congruence, and a rotation around l

$$\mathbf{m}' = \mathbf{m}e^{iC^\circ}; \qquad DC^\circ = 0 \tag{2.2}$$

remains free, by means of which a phase with vanishing D derivative can be removed from one of κ, σ or G_+. [5]

The conditions (2.1) restrict the triad, but not the metric. For the metric, our assumption is that

$$\sigma = H_- = 0, \qquad \kappa \neq 0 . \tag{2.3}$$

(The first condition does not mean that the eigenray congruence is shearfree, because $[\sigma]$ is not the shear if $\kappa \neq 0$. The second can be interpreted such that the eigenrays of the G and H fields coincide.) With these assumptions the field equations are as follows: [5, 9]

$$D\rho - \bar{\delta}\kappa = \kappa\tau + \kappa\bar{\kappa} - \rho^2 - G_0\bar{G}_0 - H_0\bar{H}_0 ,$$

$$D\tau = -\rho\tau + \bar{\kappa}\rho - G_0\bar{G}_- - H_0\bar{H}_- ,$$

$$DG_0 = (-2\bar{\rho} + G_0 - \bar{G}_0)G_0 + \bar{\kappa}G_+ - H_0\bar{H}_0 ,$$

$$DH_0 = \left(-2\bar{\rho} + \frac{3}{2}G_0 - \frac{1}{2}\bar{G}_0\right)H_0 + \bar{\kappa}H_+ ,$$

$$DG_+ - \delta G_0 = \kappa G_0 - (\bar{\rho} + \bar{G}_0)G_+ - \bar{H}_0 H_+ ,$$

$$DH_+ - \delta H_0 = \left(\kappa + \frac{1}{2}G_+\right)H_0 - \left(\bar{\rho} + \frac{1}{2}(\bar{G}_+ - \bar{G}_0)\right)H_+ ,$$

$$\delta\kappa = \kappa\bar{\tau} - \kappa^2 ,$$

$$\delta\rho = -(\rho-\bar{\rho})\kappa - G_0 G_+ - \bar{H}_0 H_+ ,$$

$$\delta\tau + \overline{\delta\tau} = -2\tau\bar{\tau} + \rho\bar{\rho} - G_0\bar{G}_0 - G_+\bar{G}_- - H_0\bar{H}_0 - H_+\bar{H}_- ,$$

$$\bar{\delta}G_0 = -(\bar{\kappa}+\bar{G}_-)G_0 - \bar{H}_- H_0 ,$$

$$\bar{\delta}H_0 = -\left(\bar{\kappa}+\frac{1}{2}\bar{G}_-\right)H_0 ,$$

$$\bar{\delta}G_+ = (\rho-\bar{\rho})G_0 - (\tau+\bar{G}_-)G_+ - \bar{H}_- H_+ ,$$

$$\bar{\delta}H_+ = (\rho-\bar{\rho})H_0 - \left(\tau+\frac{1}{2}\bar{G}_-\right)H_+ , \tag{2.4}$$

where

$$D\delta - \delta D = -\bar{\rho}\delta + \kappa D ,$$

$$\delta\bar{\delta} - \bar{\delta}\delta = \tau\delta - \bar{\tau}\bar{\delta} - (\rho-\bar{\rho})D . \tag{2.5}$$

In order to obtain the metric, we first apply the commutators on the field quantities. Then, writing the known derivatives into the obtained equations, we may get further differential equations. When the system has become closed, proper coordinates are to be chosen, in which the Eqs (2.4–5) become partial differential equations of the first order. Integrating these equations, the three dimensional quantities g_{ik}, **G** and **H** are obtained, whence the metric and the electromagnetic potential can be reconstructed.

We must note that every solution of the Einstein–Maxwell equations contains two trivial arbitrary constant parameters. The first is a constant conformal (homothetic) factor in ds^2 and its square root in the electromagnetic potential, the second is a constant duality angle in the complexified electromagnetic potential [10, 11].

3. Integration of the field equations

First let H_0 be zero. Then Eqs (2.4) show that $\mathbf{H}=0$, i.e. there is vacuum. Now **G** must not vanish, because this would lead to the trivial Minkowskian line element only. If $G_0 \neq 0$, applying the first of the commutators (2.5) on $\ln G_0$, a new equation for κ is obtained:

$$D\kappa = \left(\rho - \kappa\frac{\bar{G}_-}{\bar{G}_0}\right)\kappa . \tag{3.1}$$

Then, applying the same commutator on $\ln\kappa$, the result is as follows:

$$\bar{\rho} = \bar{\kappa}\frac{G_+}{G_0} \Rightarrow D\kappa = 0 , \tag{3.2}$$

which means that κ can be made real and positive by means of the transformation (2.2).

Finally, derivating the algebraic identity (3.2) by δ, we obtain:

$$G_+ = 0 \Rightarrow \rho = 0 . \tag{3.3}$$

Writing these results into the field equations, it is seen that

$$D\tau = D\gamma = 0 , \qquad \gamma^2 = G_0 \bar{G}_0 , \tag{3.4}$$

$$2\kappa\tau = \gamma^2 .$$

Thus τ is also real and positive.

If $H_0 \neq 0$, the first of the commutators (2.5) is to be applied on both in G_0 and $\ln H_0$. We obtain Eq. (3.1) again, and a new algebraic equation

$$G_0 H_+ = G_+ H_0 \Rightarrow (\mathbf{G} \times \mathbf{H}) = 0 . \tag{3.5}$$

(The field equations show again that G_0 must not vanish.) Applying the first of the commutators on $\ln \kappa$, we obtain the Eq. (3.2) again, whence, letting δ on it,

$$\rho = G_+ = H_+ = 0 \tag{3.6}$$

and the system of equations has become closed.

Now a coordinate system is to be chosen. Since the remaining equations have the same structure (except for some signs) as in [7], the convenient coordinate system is also the same (except for the change in the index numbers $1 \to 0$, $2 \to 1$, $3 \to 2$), and, mutatis mutandis, we can perform the same integrational process again. For vacuum, there are two different solutions:

$$\mathrm{d}s^2 = F^2 \{ \mathrm{ch}\,(2T)\,[e^{\rho^2}(\mathrm{d}T^2 - \mathrm{d}\rho^2) - \rho^2\,\mathrm{d}\Phi^2] - \mathrm{ch}^{-1}\,(2T)\,(\mathrm{d}z + \rho^2\,\mathrm{d}\varphi)^2 \} \tag{3.7}$$

and

$$\mathrm{d}s^2 = F^2 \{ e^{2T}[e^{\rho^2}(\mathrm{d}T^2 - \mathrm{d}\rho^2) - \rho^2\,\mathrm{d}\Phi^2] - e^{-2T}\,\mathrm{d}z^2 \} . \tag{3.8}$$

Here we have introduced canonical coordinates.

Eq. (3.5) shows that **G** and **H** are parallel vectors. Thus, if $|q^0| < 1$, the electrovac solutions are Ernst counterparts of the vacuum ones. [11]. When $|q^0| \geqq 1$, Ernst's method cannot be applied [12]. Nevertheless, having written the result (3.6) into the field equations (2.4), two sets of the equations are obtained. The first set contains the differential equations for $\ln H_0$; on the right hand sides of these equations H_0 does not occur. The remaining equations are differential equations for the spin coefficients and G_0, and on the right hand sides of them H_0 occurs only in the combination $G_0 \bar{G}_0 + H_0 \bar{H}_0$. Thus the way of the integration is independent of the ratio G_0/H_0, i.e. the counterpart solutions remain valid for $|q^0| \geqq 1$ too. Therefore we will not explicitly calculate these solutions here. The counterpart solutions have two (one complex) extra parameters, one of which is the trivial duality angle, and the other is the charge parameter.

4. The behaviour of the solutions

As in the stationary case, there are two vacuum solutions, without any nontrivial arbitrary parameters. The solutions have two commuting space-like Killing vectors:

$$K_1 = (0, 0, 1, 0), \tag{4.1}$$

$$K_2 = (0, 0, 0, 1).$$

This fact may be interpreted as cylindrical symmetry. In the second metric the two Killing vectors are mutually orthogonal, in the first they are not, and the Killing vector of direction z (with respect to which the $3+1$ decomposition of the "3 dimensional relativity" has been done) is not hypersurface orthogonal. If the symmetry were timelike, the first line element would be stationary, and the second static. For space-like symmetry, such a distinction might be also possible, but there are no conventional distinguishing terms.

The second line element is a special Einstein–Rosen solution [13]. The first is a new solution, nevertheless, in it

$$\varphi = \varphi(f), \tag{4.2}$$

i.e. this solution belongs to a class analogous to the Papapetrou solutions of the stationary problem [14].

The electrovac solutions are of similar behaviour as the vacuum ones. Thus, having integrated the whole $\kappa\sigma = 0$ class of both the stationary and the spatially symmetric problems, we have not obtained any generalization of the Kerr and Kerr–Newman metrics for which $\kappa = \sigma = 0$ [15].

Acknowledgements

The author would like to thank Drs. Z. Perjés and J. Kóta for illuminating discussions.

References

1. E. T. Newman and L. Tamburino, J. Math. Phys., **3,** 902, 1962.
2. E. T. Newman, L. Tamburino and T. W. Unti, J. Math. Phys., **4,** 915, 1963.
3. T. W. Unti and R. J. Torrence, J. Math. Phys., **7,** 535, 1966.
4. Z. Perjés, J. Math. Phys., **11,** 3383, 1970.
5. B. Lukács, Acta Phys. Hung., **41,** 137, 1976.
6. J. Kóta and Z. Perjés, J. Math. Phys., **13,** 1695, 1972.
7. J. Kóta, B. Lukács and Z. Perjés, Proc. 8th Marcel Grossmann Meeting, North–Holland, 1982, p. 203.
8. B. Lukács, KFKI Report, 73–38.
9. B. Lukács, KFKI Report, 73–26.
10. F. J. Ernst, J. Math. Phys., **15,** 1409, 1974.
11. F. J. Ernst, Phys. Rev., **168,** 1415, 1968.
12. B. Lukács and Z. Perjés, Gen. Rel. Grav., **4,** 161, 1973.
13. A. Einstein and N. Rosen, J. Franklin Inst., **223,** 43, 1937.
14. A. Papapetrou, Ann. Phys., **12,** 309, 1953.
15. Z. Perjés, Int. J. Theor. Phys., **10,** 217, 1974.

Acta Physica Hungarica 54 (1—2), pp. 161—187 (1983)

ON THE INTENSITY ANOMALIES IN THE FULCHER-α BANDS OF THE H_2 MOLECULE

I. KOVÁCS

Department of Atomic Physics, Physical Institute, Technical University
1521 Budapest, Hungary

B. P. LAVROV, M. V. TYUTCHEV

Department of Optics and Spectroscopy, Institute of Physics, Leningrad State University
Leningrad, 198904, USSR

and

V. I. USTIMOV

Department of Theoretical Physics, Institute of Physics, Leningrad State University
Leningrad 198904, USSR

(Received 16 June 1982)

The experimental investigation and theoretical analysis of the anomalies observed earlier in the rotational structure of the H_2 Fulcher-α band system is carried out. The anomaly consists in the substantial deviation between the measured intensity ratios of *R* and *P* lines starting from the same rotational level and the values predicted by the Hönl–London formulas. For the first time the quantitative interpretation of this phenomenon is given on the basis of the nonadiabatic theory of the perturbation of the rotational levels of the upper $d^3\Pi_u^+$ state by the other $^3\Sigma_u'^+$ electronic-vibrational states of the molecule. The influence of the vibration-rotation interaction is also discussed and taken into account.

Introduction

More than 40 years ago N. Ginsburg and G. H. Dieke [1] observed the anomalies of the intensity distributions in the rotational structure of Fulcher-α emission bands ($d^3\Pi_u^+$, $v' - a^3\Sigma_g^+$, v'' radiative transitions) of the H_2 molecule. The measured ratios I_R/I_P of the intensities of pairs of *R* and *P* branch lines starting from the same rotational levels differ sufficiently from that predicted by the well-known Hönl–London formulae.

Later Dieke tried to explain these peculiarities in the relative transition probabilities by the perturbation of the initial $d^3\Pi_u^+$ state by the other electronic states of the molecule [2]. But the nonadiabatic theory developed by him was found to be in serious disagreement with the experimental data.

In the work of D. Villarejo et al. [3] an attempt was made to explain the dependencies of the ratios of the line strengths of *R* and *P* branch lines on the rotational quantum number in the framework of an adiabatic theory but taking into account the

vibration-rotation interaction. However, the results of numerical calculations for Fulcher-α bands have shown that the effect is rather weak and cannot explain the observed phenomenon either.

The goal of the present work is to give an adequate explanation of the peculiarities in the relative line strengths on the basis of experimental investigations and theoretical analysis.

First of all more detailed experimental studies of the relative line strengths were carried out. The technique used here and the results are described in §1. §2 is devoted to theoretical analysis, the purpose of which is to derive and to examine simple analytical formulae for the dependencies of radiative transition probabilities on the rotational quantum number of upper level. The comparison of the theory and the experiment is discussed in §3. In conclusion, the main results of the work are summarized.

§1. Experimental studies

In the optically thin plasma the intensity of the electronic vibro-rotational line[1] belonging to the spontaneous emission band spectra $I^{n'v'J'}_{n''v''J''}$ is connected with the population density of upper level $N_{n'v'J'}$ and corresponding transition probability $A^{n'v'J'}_{n''v''J''}$ by the well-known expression

$$I^{n'v'J'}_{n''v''J''} = N_{n'v'J'} A^{n'v'J''}_{n''v''J''} hc\nu^{n'v'J''}_{n''v''J''}, \tag{1-1}$$

where n' and n'' denote sets of quantum numbers describing the initial and final electronic states of the molecule, v', v'' and J', J'' are vibrational and rotational quantum numbers, respectively, $\nu^{n'v'J'}_{n''v''J''}$ is the wave number of the $n', v', J' \to n'', v'', J''$ transition.

According to wave mechanics $A^{n'v'J'}_{n''v''J''}$ may be related to the electronic vibro-rotational line strength $\sum_M |R^{n'v'J'}_{n''v''J''}|^2$ [5] by

$$A^{n'v'J'}_{n''v''J''} = \frac{64\pi^4}{3h} (\nu^{n'v'J'}_{n''v''J''})^3 \frac{\sum_M |R^{n'v'J'}_{n''v''J''}|^2}{g_{J'}}, \tag{1-2a}$$

where $g_{J'}$ is the degree of degeneracy of the initial state.

If the vibration-rotation interaction is negligible, the expression (1–2a) is simplified and the so-called rotational line strength $S_{J'J''}$ may be introduced by

$$\sum_M |R^{n'v'J'}_{n''v''J''}|^2 = |R^{n'v'}_{n''v''}|^2 S_{J'J''}, \tag{1-2b}$$

[1] "Intensity of the spectral line" hereafter refers to the energy of quanta belonging to the transition emitted by unit volume in unit time to all directions.

where $R^{n'v'}_{n''v''}$ is the matrix element of the dipole moment on the electronic and vibrational wavefunctions. In the Franck–Condon approximation the v' and v'' dependency of $|R^{n'v'}_{n''v''}|^2$ may also be factorized as the Franck–Condon factor. (For further details on the quantum-mechanical theory of electronic-rotational radiative transitions see the monograph [5]).

The ratio of the intensities of two lines starting from the same rotational level does not depend on the initial level population density and is connected with the corresponding ratio of line strengths.

For example this ratio for R and P branch lines:

$$\frac{I^{n'v'J'}_{n''v''J'-1}}{I^{n'v'J'}_{n''v''J'+1}} = \frac{\sum\limits_M |R^{n'v'J'}_{n''v''J'-1}|^2}{\sum\limits_M |R^{n'v'J'}_{n''v''J'+1}|^2} \left(\frac{\nu^{n'v'J'}_{n''v''J'-1}}{\nu^{n'v'J'}_{n''v''J'+1}}\right)^4. \tag{1–3a}$$

For $d^3\Pi_u$ and $d^3\Sigma_g^+$ states of the H_2 molecule the spin-multiplet splitting is known to be small in comparison with the rotational constant B_e. (The triplet structure of the emission bands was not resolved in our and G. H. Dieke's experiments). So in both states rotational levels may be characterized by the quantum number N of the total angular momentum without allowance for electron spin. Then the formula (1–3a) in our case may be rewritten as

$$S(N') = \frac{S[R(N'-1)]}{S[P(N'+1)]} = \left(\frac{\nu_P}{\nu_R}\right)^4 \frac{I[R(N'-1)]}{I[P(N'+1)]}. \tag{1–3b}$$

Thus for the experimental determination of $S(N')$ it is necessary to measure at once the intensities of R and P lines with the same upper level and belonging to the same electronic-vibrational bands.

For the studies of the intensity distributions among the rotational structure of molecular bands the spectrophotometrical system must in general possess sufficiently high spectral resolution and light sensitivity. These two requirements contradict each other and it is not easy to fulfil both requirements in one apparatus. Then it is advisable to use two spectral systems with different characteristics. For example the identification of the rotational lines may be carried out under maximum brightness conditions in the light source when the line intensities may be disturbed by reabsorption. In this case it is most important to achieve higher spectral resolution even by decreasing the sensitivity. However, for the measurements of the intensities of widely separated weak lines higher sensitivity is necessary and a lower resolution is sufficient.

The experimental set-up used in the present work was analogous to that of our previous papers [6, 7]. The schematic diagram of the experimental apparatus is shown in Fig. 1. It consists of the gaseous discharge light source and two analogous

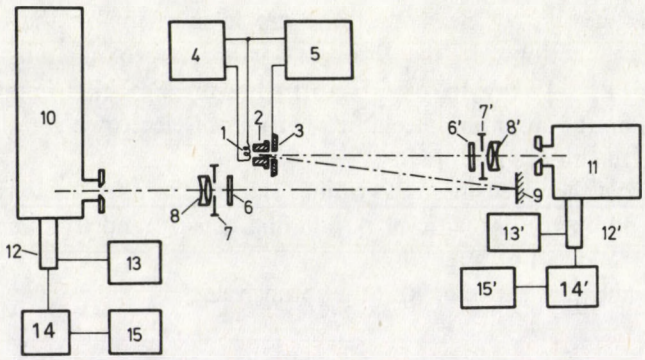

Fig. 1. Schematic diagram of the experimental apparatus: 1-hot oxide cathode; 2-capillary; 3-anode; 4, 5-stabilized power supply circuits; 6, 6′-light filters; 7, 7′-aperture stops; 8, 8′-achromatic objectives; 9, 9′-plane mirror; 10-long-focus Ebert–Fastie monochromator; 12, 12′-FEU-79 photomultipliers; 13, 13′-stabilized rectifiers; 14, 14′-dc amplifiers; 15, 15′-automatic electronic potentiometers

spectrophotometrical systems which differ only in the dispersion and transmission of monochromators. In the first system (6–10, 12–15) the 2.65 m Ebert–Fastie type monochromator (10) was used with a grating of 1800 lines/mm (in first-order), which provided a spectral resolution of 0.01–0.02 nm. In the second system (6′–8′, 11–15′) the 0.75 meter Czerny–Turner type monochromator (11) with a grating of 1200 lines/mm was employed in second order and had somewhat smaller dispersion but a considerably higher transmission. An alternative use of the two systems generally improved the performance of the experimental set-up. The simultaneous application of both systems, however, increased the amount of information available on the intensity measurements of the same spectral lines and the reliability of the experimental data.

The determine the relative spectral sensitivity of the photoelectric systems we measured the spectrum of two tungsten ribbon lamps of different geometry having glass and sapphire windows.

In the wavelength range 520–750 nm the sensitivity values obtained with various lamps (at three different temperatures of the ribbon for each lamp) differ on the average by less than 5–6%. For the pair of lines the error was not larger than 1.2%.

As light source an arc discharge through a 1.5 mm diameter capillary was used. The construction of the discharge device was described earlier [8]. In the experiment described here the discharge device was filled with spectrally pure hydrogen rectified by passing through heated nickel. Previous investigations [7] have shown that in the range of discharge currents $i = 0.05$–0.35 A and gas pressures $P = 67$–1600 Pa various secondary effects (for example reabsorption) do not influence the value of the line intensities. So the basic measurements were carried out at $i = 0.08$, 0.15 and 0.3 A and $P = 533$ and 1600 Pa.

Just like in the work [1] the main difficulty restricting the number of measured ratios $S(N')$ consists in the accidental overlapping of the spectral lines belonging to

different electronic-vibrational bands. In the emission spectrum of the hydrogen molecule various branches, bands and even band systems are usually superimposed due to the anomalous high values of vibrational and rotational constants. In some cases two or more different lines lie so close to each other that on account of Doppler broadening and/or the insufficient resolution of the spectral apparatus it is impossible to resolve them for the intensity measurements. This situation may be called accidental overlapping. It should be noted that in this case the measured ratios (1–3b) have to be changed owing to the variation of discharge conditions.

This spectrum has not yet been fully identified in spite of the extensive work carried out on this problem. Many lines are not identified unambiguously, even in the most complete available tables of the H_2 spectral line wavelengths [9]. Therefore "a priori" it is impossible to select unambiguously the pairs of lines suitable for the determination of the ratios $S(N')$. Let us illustrate this on the example of the (2–2) Fulcher-α band.

Table I shows the wavelengths of R and P branch lines of interest to us and some other lines lying in their neighbourhood. The line intensities shown in Table I can be used only as a qualitative indication of the true intensities because they are only eye estimates on an approximately logarithmic scale. Columns 2, 3 and 4 of Table I represent the intensities obtained under different gas pressure and power conditions of a microwave electrodeless discharge light source.

It can be seen from the Table that some lines ($R0$, $R3$, $R5$, $P3$ and $P4$) are identified unambiguously and it is neecessary to study the intensity distribution in the corresponding branches experimentally to improve this earlier identification based on the measurements of the line wavelengths only [10].

In addition to this, with the aid of tables like Table I the overlappings in the bands can be analysed conveniently. For this purpose the line wavelength measurements were combined with spectral measurements of intensity distributions in the vicinity of the lines interesting for the determination of the ratios $S(N')$. Three situations have occurred:

1. Both lines of R and P branches starting from the same rotational level are free from overlapping. It means that an obstacle line nearest to the spectral line of interest to us is displaced outside the contour of the Fulcher line. As an example the neighbourhood of (2–2) $P5$ Fulcher-α line is shown in Fig. 2a. It is seen that the emission of the 636.2337 nm and 636.2706 nm lines nearest to (2–2) $P5$ is hardly probable to be included into the measured value of (2–2) $P5$ line intensity. This Figure also shows that our spectral apparatus made it possible to distinguish between two lines separated by a distance of 0.0048 nm in the spectrum (see lines 636.4618 nm and 636.4666 nm in Fig. 2a).

2. One of the lines indispensable for the determination of line strengths ratio (1–3a) may be overlapped ((2–2) $P7$ line in Fig. 2b) whereas another line of the pair is to be free from blending ((2–2) $R5$ in Fig 2b). So the ratio $S(N')$ thus obtained may be

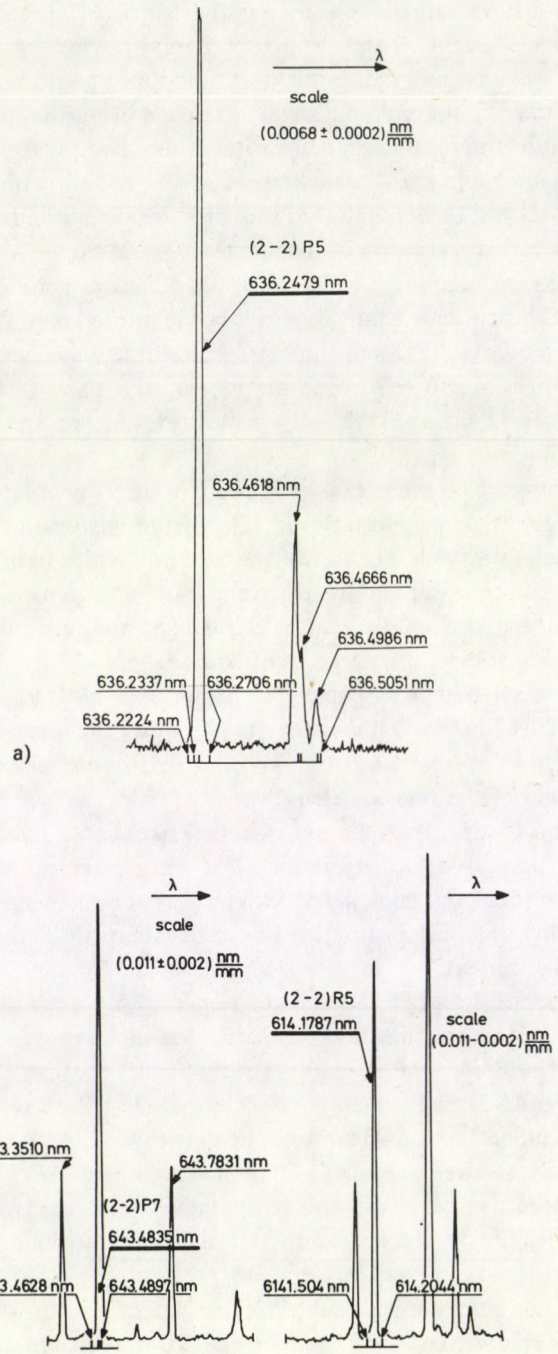

Fig. 2. (For caption see next page)

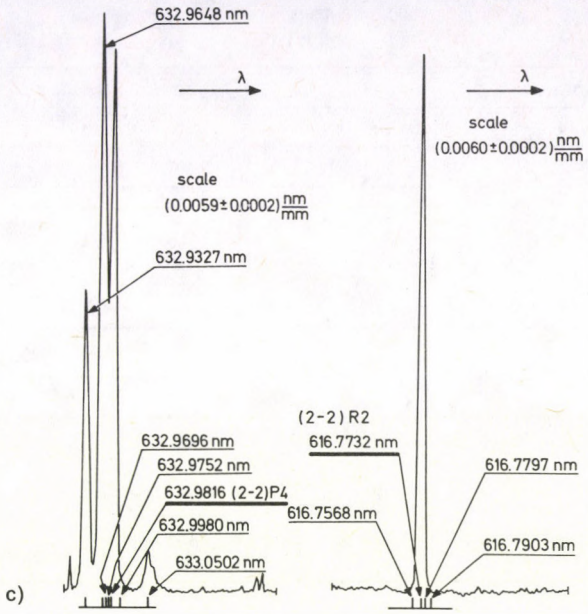

Fig. 2. Typical results of the measurements of spectra in the vicinity of lines for the (2 – 2) band: a) $N' = 4$, b) $N' = 6$ and c) $N' = 3$

over- or underestimated to some extent. For example, the ratio $S(N')$ for $v' = v'' = 2$ and $N' = 6$ seems to be probably underestimated.

3. Both lines of the pair may be overlapped by some lines of unknown intensity. In this case it may be impossible to determine the $S(N')$ (See e.g. Fig. 2c).

Such an analysis is useful in understanding the nature of intensity distributions in the branches. But it cannot provide an unambiguous answer to the question whether the measured ratio $S(N')$ obtained in the experiment corresponds to that of line strengths $S(N')$.

To solve this problem a series of experiments have been carried out under various regimes in gaseous discharge light source. It is quite clear that for the lines free from overlapping their intensity ratio (closely connected with $S(N')$) has to be independent of the discharge conditions. The purpose of this series was to select such line pairs.

The order of the measurements was as follows. The intensities of R and P lines of the pair were measured one after another three times. Then the corresponding three values of $S(N')$ were calculated and averaged. After that the discharge conditions (pressure or current) were altered and the same procedure has been repeated.

As an example in Table IIa the results obtained at various discharge currents are presented for $v' = v'' = 2$ and $N' = 6$ transitions. It is known (see Table I and Fig. 2b) that the (2–2) $P7$ line ($N' = 6$) can be overlapped by the (4–0) $P4$ line ($N' = 3$) belonging to the 2K→2B electronic transition (in Dieke's notation). So when the current i is increased

Table I
(2–2)

R-branch					*P*-branch				
λ [nm]	Intensity			Notation	λ [nm]	Intensity			Notation
1	2	3	4	5	1	2	3	4	5
620.0927	10	7	–	–					
620.0954	–	–	–	–	627.1118	–	–	2	
620.1185	29	25	19	R0	627.1311	27	23	17	P2
620.0185	29	25	19	3A-2C (1-0) 2	627.1390	–	–	–	–
620.1423	6	–	–	–	627.1547	3	–	–	–
618.2730	10	7	–	–	629.9173	9	2	–	–
618.2990	29	28	24	R1	629.9423	31	28	23	P3
618.3220	6	–	–	–	629.9423	31	28	23	X-2B (0-6) R2
					632.9648	24	–	20	–
					632.9696	–	–	15	–
616.7568	–	–	–	–	632.9752	15	–	–	–
616.7732	24	21	19	R2	632.9816	15	23	24	P4
616.7797	3	–	–	–	632.9816	15	23	24	3D-2B (3-10) P4
616.7903	–	–	–	–	632.9780	–	–	–	–
615.5466	3	–	–	–	636.2224	3	5	–	–
615.5629	24	22	23	R3	636.2337	3	–	–	–
615.5629	24	22	23	Z-2B (1-6) P1	636.2479	24	24	24	P5
615.5629	24	22	23	3D-2B (0-4) P6	636.2706	2	–	–	–
615.5860	3	–	–	–					
614.6670	2	2	–	2-2B (2-9) R0	639.7216	–	–	2	–
614.6901	17	15	20	R4	639.7445	17	15	18	P6
614.6931	–	–	–	3D-2B (0-4) P5	639.7662	1	–	–	–
614.7222	2	2	–	–					
614.1504	5	4	–	3E-2C (3-1) P3	643.4628	2	–	–	–
614.1787	15	15	20	R5	643.4835	19	18	22	P7
614.1787	15	15	20		643.4897	–	–	–	2K-2B (4-0) P4
614.2044	2	2	–	–					
614.0576	1	–	–	–	647.4366	1	2	–	Y-2C (2-1) R2
614.0724	1	2	–	R6	647.4551	2	5	4	P8
614.0954	11	–	–	–	647.4551	2	5	4	4f-3B (2-0) R1
					647.4551	2	5	4	3f-2c (0-1) R3
					647.4773	–	2	2	–

Table IIa

i [mA]	$\frac{S[R5]}{S[P7]}$			$\left\langle \frac{S[R5]}{S[P7]} \right\rangle$
	No. 1	No. 2	No. 3	
30	0.45	0.53	0.48	0.49 ∓ 0.02
65	0.53	–	0.51	0.52 ∓ 0.01
150	–	0.53	0.55	0.54 ∓ 0.01
300	0.57	0.53	0.53	0.54 ∓ 0.02
400	0.54	0.55	0.55	0.55 ∓ 0.01

Table IIb

v'	N'	v''	$\frac{S[R(N-1)]}{S[R(N+1)]}$, $p=467$ Pa			$\frac{S[R(N-1)]}{S[P(N+1)]}$,
			$i=0.08$ A	$i=0.15$ A	$i=0.3$ A	$i=0.15$ A, $p=1600$ Pa
0	1	0	1.48∓0.04	1.28∓0.02	0.99∓0.02	1.14∓0.02
	2	0	1.59∓0.02	1.45∓0.01	1.52∓0.02	1.66∓0.02
	3	0	0.92∓0.02	1.23∓0.01	–	1.57∓0.02
	4	0	0.85∓0.02	0.86∓0.01	0.84∓0.02	0.83∓0.02
	5	0	0.44∓0.02	0.42∓0.01	0.47∓0.01	0.46∓0.01
	6	0	0.66∓0.02	0.67∓0.01	0.67∓0.02	0.67∓0.01
	7	0	0.75∓0.02	0.74∓0.01	0.71∓0.02	0.79∓0.02
	8	0	0.58∓0.02	0.57∓0.02	0.58∓0.02	0.58∓0.02
1	1	0	2.49∓0.06	3.50∓0.06	3.96∓0.06	9.2∓0.2
		1	1.79∓0.02	1.80∓0.01	1.76∓0.02	1.80∓0.02
	2	0	1.36∓0.02	1.35∓0.03	1.34∓0.02	1.38∓0.02
		1	1.34∓0.02	1.37∓0.01	1.37∓0.02	1.37∓0.02
	3	0	1.47∓0.03	1.42∓0.01	1.36∓0.02	1.34∓0.02
		1	1.67∓0.02	1.99∓0.03	2.39∓0.02	2.23∓0.02
	4	0	–	–	–	–
	5	1	18.8 ∓0.1	18.0 ∓0.3	9.1∓0.2	8.4∓0.1
	6	1	4.26∓0.07	5.57∓0.05	7.4∓0.2	7.8∓0.2

Table IIc

v'	N'	v''	$\frac{S[R(N-1)]}{S[R(N+1)]}$, $p=467$ Pa			$\frac{S[R(N-1)]}{S[P(N+1)]}$,
			$i=0.08$ A	$i=0.15$ A	$i=0.3$ A	$i=0.15$ A, $p=1600$ Pa
2	1	1	1.66∓0.01	1.65∓0.03	1.64∓0.02	–
		2	1.69∓0.04	1.68∓0.02	1.63∓0.03	1.64∓0.02
	2	1	1.06∓0.02	1.07∓0.02	1.10∓0.03	1.08∓0.02
		2	1.08∓0.02	1.11∓0.03	1.09∓0.02	1.09∓0.02
	3	1	0.93∓0.03	0.96∓0.02	0.93∓0.04	0.94∓0.02
		2	–	–	–	–
	4	1	14.50∓0.5	8.3 ∓0.1	6.5 ∓0.2	10.5 ∓0.2
		2	0.73∓0.02	0.71∓0.01	0.73∓0.02	0.72∓0.01
	5	1	–	–	–	–
		2	0.99∓0.02	1.00∓0.02	1.24∓0.02	2.48∓0.04
	6	1	0.66∓0.02	0.67∓0.02	0.67∓0.02	0.66∓0.02
		2	0.54∓0.01	0.56∓0.01	0.56∓0.01	0.53∓0.02
3	1	2	1.56∓0.03	1.58∓0.02	1.56∓0.03	1.62∓0.03
		3	1.44∓0.02	1.43∓0.02	1.45∓0.02	1.50∓0.02
	2	2	1.02∓0.02	1.01∓0.01	1.03∓0.02	1.01∓0.03
		3	0.97∓0.02	0.97∓0.02	0.95∓0.02	0.95∓0.03
	3	2	1.89∓0.06	2.10∓0.04	2.33∓0.03	2.15∓0.02
		3	0.77∓0.01	0.73∓0.02	0.75∓0.02	0.73∓0.03

Table IId

v'	v''	N'
0	0	1
0	0	2
0	0	3
1	0	1
1	0	3
1	1	3
1	1	5
1	1	6
2	1	2
2	1	4
2	2	5
3	2	3
3	3	1

the gas temperature also increases. The relative contribution of the obstacle line (4–0) $P4$ starting from the rotational level with lower rotational quantum number N has to be decreased and the measured $S(N')$ must come nearer to the true value of the line strengths ratio. Nevertheless, it is probable that the highest measured value $S(6)=0.55\pm0.01$ remains somewhat underestimated.

The typical results obtained with the first spectral system (Fig. 1) are shown in Tables IIb and IIc for three different currents and two pressures. It can be seen from these data that the measured ratios of the intensities for the lines with v', v'' and N' summarized in Table IId change noticeably. This fact, together with the above mentioned analysis of the line contours and wavelengths, shows that they are overlapped. It is impossible to use them for the determination of $S(N')$ values, therefore these transitions were excluded from our further consideration.

The Fulcher-α bands starting from the $d^3\Pi_u^+$, $v'=1$ state are known to be perturbed irregularly due to the close position of perturbed and perturbing ($e^3\Sigma_u^+$, $\tilde{v}=4$) rotational levels. So the intensities of corresponding R and P lines differ greatly from those predicted by Hönl–London formulas. These lines are inconvenient for the determination of relative line strengths $S(N')$ and have been omitted from the present work.

If we propose a regular character of the perturbation for $d^3\Pi_u^+$, $v'=0, 2, 3$ states taking into account: i) the displacement of perturbed and perturbing levels, ii) the behaviour of N'-dependences of Λ-doubling and, iii) the character of changes in the intensity distributions among the branches during the variation of discharge conditions, some sudden change in the monotonies in these distributions have to be interpreted as due to accidental overlapping. So in some cases the true values of the intensities may be determined by graphical interpolation of N'-dependences of the intensities in the branches.

For example such intensity distributions for the R and P branches of the (0–0) band obtained at constant gas pressure and three different discharge currents are

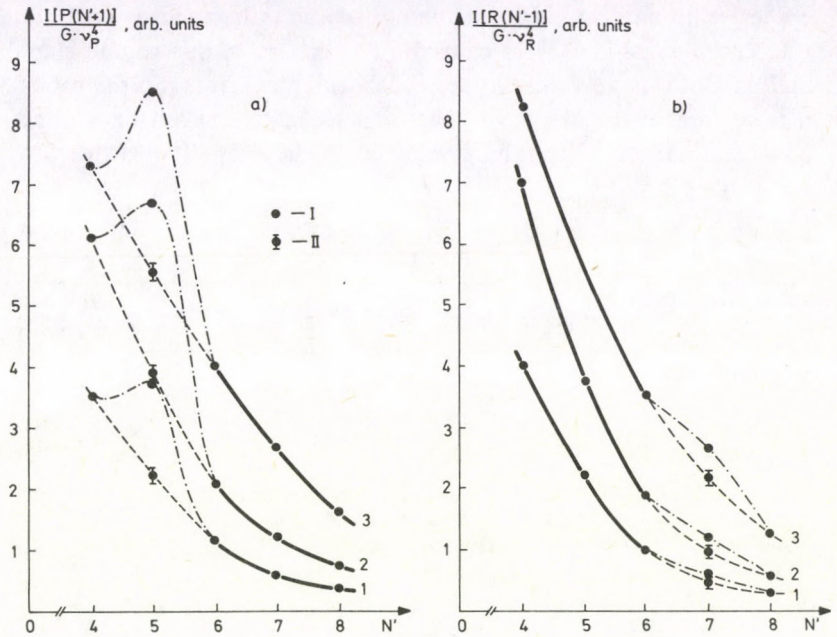

Fig. 3. Intensity distributions in the R and P branches of the (0−0) band at different discharge currents: $i = 0.08$ A (curve 1). 0.15 A (2) and 0.3 A (3). I — values obtained in the experiment, II — results of graphical interpolation

shown in Fig. 3. Factor G accounts for the nuclear spin orientation, with $G = 1$ for odd values of N' (parahydrogen) and $G = 3$ for even N' (orthohydrogen). It can be seen from the Figure that the (0–0) $P6$ $N' = 5$ and (0–0) $R6$ ($N' = 7$) lines have anomalous high intensities. So neither of the ratios $S(5)$ and $S(7)$ can be determined directly from the experimental data. However, they may be graphically interpolated. The errors of the determination and the way of their estimation are also indicated in Fig. 3 for $i = 0.08$ A, 0.15 A and 0.3 A. The ratio $S(N')$ for $v' = v'' = 2$ and $N' = 5$ has been obtained in the same manner.

The fact that some ratios are independent of the discharge conditions in the experiment may be due to two reasons.

1. The obstacle lines (nearest neighbours) inside the spectral widths of the lines are those of negligibly low intensity and so their existence does not influence the determination of the relative line strength ratio.

2. The range of variation of the discharge conditions is not wide enough for the dependence to be noticeable, but one of the lines (or both of them) is overlapped.

It is clear that the second reason seems to be less probable and so we selected all the pairs of lines independent of the discharge conditions for further investigation. It should be noted here that unfortunately this is still possible and the erroneous values of $S(N')$ thus obtained could not be recognized in a purely experimental way.

After the preliminary investigations described above the intensity measurements of the selected number of lines were carried out. The aim of this second step of the experimental part of our work was to decrease incidental errors. So the ratios $S(N')$ have been measured in the same way but 6 times under certain fixed conditions ($i=0.15$ A and $P=533$ Pa). The values obtained in the present work for $S(N')$ are presented in Table III.

Table III

N'	$v'-v''$	v'			$\frac{H[R(N\text{-}1)]}{H[P(N+1)]}$
		0	2	3	
1	0	–	1.67∓0.02	–	2.00
	1	–	1.65∓0.02	1.58∓0.02	
	0	–	1.10∓0.01	0.96∓0.02	
2	−1	–	1.09∓0.04	–	1.50
	1	–	–	1.01∓0.01	
	0	–	–	0.74∓0.02	
3	−1	–	0.96∓0.05	–	1.33
	1	–	0.94∓0.01	–	
4	0	0.84∓0.01	0.72∓0.01	–	1.25
5	0	0.74∓0.03*	0.65∓0.03*	–	1.20
6	0	0.67∓0.01	0.55∓0.01	–	
	1	–	0.66∓0.01	–	1.17
7	0	0.60∓0.04*	–	–	1.14
8	0	0.58∓0.01	–	–	1.125

It can be seen from Table III that the difference generally possible between the line strengths $S(N')$ obtained from the intensities of the bands having the same upper and different lower vibrational levels is unnoticeably weak for the transitions studied here. So the ratios $S(N')$ may be associated with the vibrational quantum number of upper state, i.e. with v'. For clarity, the data are also presented in graphical form (Figs 4a, b, c), where experimental points corresponding to various diagonal and non-diagonal bands starting from the levels with the same v' are specially marked.

The values obtained earlier by Ginsburg and Dieke [1] are also shown in Fig. 4. They are generally in good agreement with the results of our measurements. Certainly, our data appear to be more realistic due to the higher dispersion of our spectroscopic equipment and the more precise knowledge of the sensitivity of the spectrophotometric systems.

The corresponding ratios of Hönl–London factors are also shown in Fig. 4 as well as the relative line strengths $S(N')$ calculated by Villarejo et al. [3] with adiabatic theory accounting for the influence of vibration-rotation interaction on the Franck–Condon factors. It is quite clear that there is actually a difference between the measured ratios $S(N')$ and those calculated in the framework of adiabatic theory. The difference increases with the growth of N'.

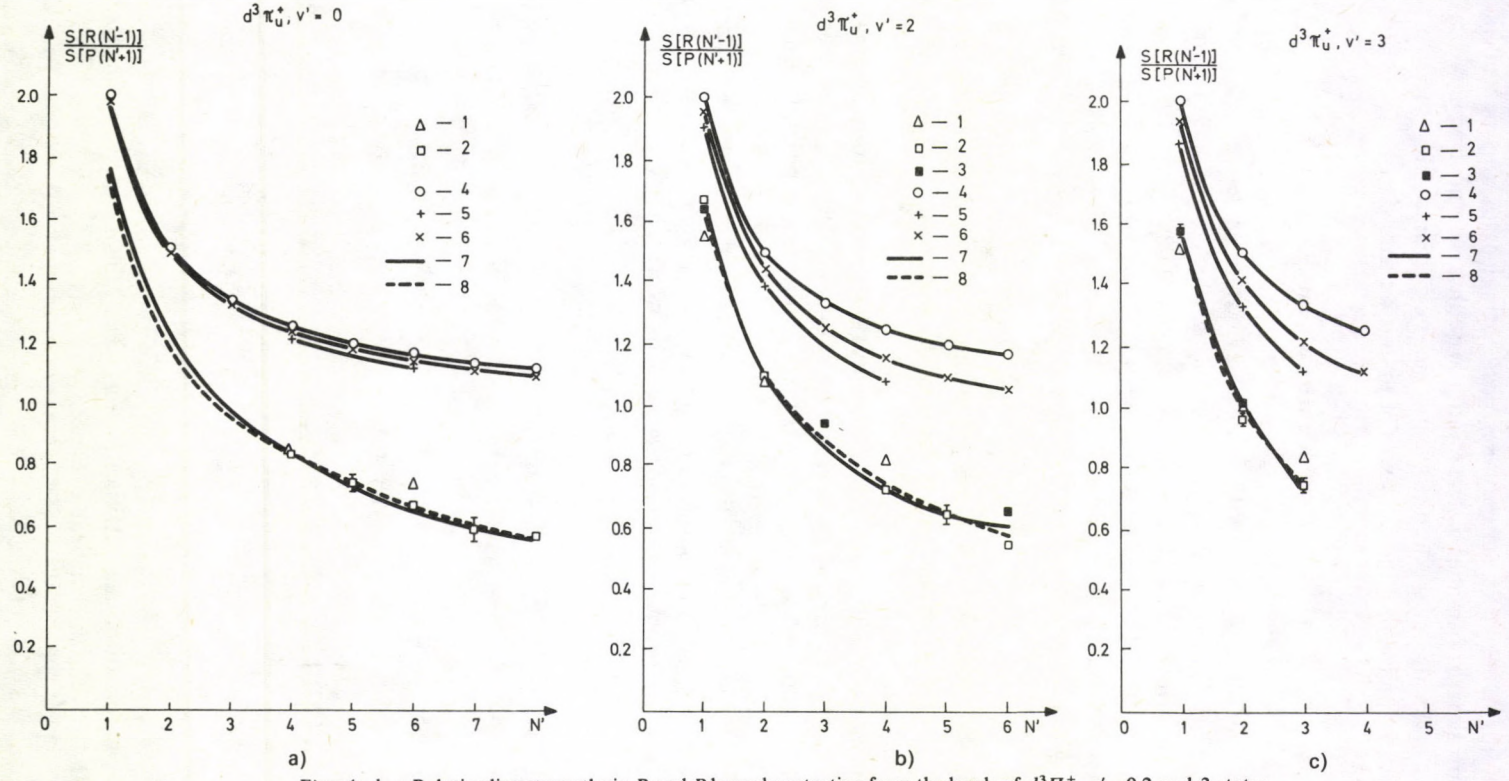

Figs. 4a, b, c. Relative line strengths in R and P branches starting from the levels of $d^3\Pi_u^+$, $v'=0,2$ and 3 states

Experiment: 1 — data of [1]: 2 and 3 — results of the present work.

Theory: 4 — ratios of corresponding Hönl–London factors; 5 — adiabatic approximation with the values of Franck–Condon factors obtained with "RKR" and "ab initio" potentials in [3]; 6 — adiabatic approximation with the values of Franck–Condon factors calculated in the present work using the Morse–Pekeris potentials in (2—24); 7, 8 — non-adiabatic theory, calculations by means of the formulas (2—13a), (2—22), respectively

Therefore, in deriving simple analytical formulae for the dependences of radiative transition probabilities on the rotational quantum number N' in our case it is necessary to make use of the non-adiabatic theory accounting for the interaction between electronic vibro-rotational states of the molecule.

§ 2. Theoretical treatment

Unknown non-adiabatic wave functions may be represented in the form of series expansion over the complete set of basis functions which are eigenfunctions of the Schrödinger equation written in the adiabatic approximation. Constructed in such a way the total wave function may be substituted into the Schrödinger equation written in a general form. Then one obtains an infinite set of algebraic equations for the coefficients of the series expansion. This cannot be solved in a general way, so two relatively simple cases are considered in particular: 1. the perturbation of ${}^3\Pi_u^+, v'$ state mainly due to the interaction with only one ${}^3\Sigma_u'^+, \tilde{v}'$ electronic-vibrational state of the molecule; and 2. the perturbation caused by the interaction with an indefinite number of perturbing $\Sigma_u'^+, \tilde{v}'$ states but lying so far from the perturbed $d^3\Pi_u^+, v'$ state that the interaction may be considered weak.

In both cases we neglect generally possible $\Pi-\Delta$ and $\Pi-\Pi$ interactions. It will be seen in §3 that available experimental data for N'dependences of the line strengths of Fulcher-α bands in the emission spectrum of the H_2 molecule can be explained without including these effects in the theoretical scheme.

The so-called pure Hund's limiting case b) is used throughout the analysis, because no triplet splitting can be observed either in the upper, or in the lower state, and so the spin-orbit and spin-spin interactions can be neglected.

2.1. Two interacting electronic-vibrational states $({}^3\Pi(b)\leftrightarrow{}^3\Sigma'^+)$

Let us consider the line strengths $S(N')$ for ${}^3\Pi_u^+, v'\rightarrow a^3\Sigma_g^+, v''$ transition, where the rotational levels of upper state are perturbed by some other ${}^3\Sigma'^+, \tilde{v}$ state. So only the $({}^3\Pi_{J-1}, {}^3\Sigma_{J-1}'^+)$, $({}^3\Pi_J, {}^3\Sigma_J'^+)$ and $({}^3\Pi_{J+1}, {}^3\Sigma_{J+1}'^+)$ perturbations exist. The matrix elements for this case are (e.g. see [5] pp. 259 and 260):

$$\begin{aligned}\langle {}^3\Pi_{J-1}^-|H|{}^3\Sigma_{J-1}'^+\rangle &= \eta\sqrt{8(J-1)J}\,,\\ \langle {}^3\Pi_J^+|H|{}^3\Sigma_J'^+\rangle &= \eta\sqrt{8J(J+1)}\,,\\ \langle {}^3\Pi_{J+1}^-|H|{}^3\Sigma_{J+1}'^+\rangle &= \eta\sqrt{8(J+1)(J+2)}\,,\end{aligned} \tag{2–1a}$$

where

$$\eta = \frac{1}{8\pi^2\mu}\left\langle {}^3\Pi, v', J\left|\frac{L_\xi}{r^2}\right|{}^3\Sigma'^+, \tilde{v}, J\right\rangle (BL_\xi)\,({}^3\Pi, {}^3\Sigma'^+)\,. \tag{2–1b}$$

L_ξ is the ξ component of the matrix of the resultant orbital angular momenta of the electrons, and r is the internuclear distance.

Accordingly, the perturbed eigenfunctions expressed by the unperturbed eigenfunctions assume the following form

$$\begin{aligned}
\langle {}^3\Pi^-_{J-1}, J|^p &= S^{(1)}_\Pi(J)\langle {}^3\Pi^-_{J-1}, J| + S^{(1)}_\Sigma(J)\langle {}^3\Sigma'^+_{J-1}, J|\,,\\
\langle {}^3\Pi^+_J, J|^p &= S^{(2)}_\Pi(J)\langle {}^3\Pi^+_J, J| + S^{(2)}_\Sigma(J)\langle {}^3\Sigma'^+_J, J|\,,\\
\langle {}^3\Pi^-_{J+1}, J|^p &= S^{(3)}_\Pi(J)\langle {}^3\Pi^-_{J+1}, J| + S^{(3)}_\Sigma(J)\langle {}^3\Sigma'^+_{J+1}, J|\,,
\end{aligned} \tag{2–2}$$

where

$$S^{(i)}_\Pi(N) = \frac{\eta\sqrt{8N(N+1)}}{\sqrt{(F^{(p)}_N - F_N)^2 + 8\eta^2 N(N+1)}}\,;\quad S^{(i)}_\Sigma(N) = \frac{F^{(p)}_N - F_N}{\sqrt{(F^{(p)}_N - F_N)^2 + 8\eta^2 N(N+1)}}\,; \tag{2–3}$$

and if $i=1,\ 2,\ 3$ then $N=J-1,\ J,\ J+1$ and $\langle {}^3X, J| = \Phi_0({}^3X), R^X(r)u^X$ are the eigenfunctions for case b) Φ_0, R and u are the electronic, the vibrational and the rotational part, respectively. Π^+ and Π^- denote the following

$$\begin{aligned}
\langle {}^3\Pi^+_\Omega| &= \frac{1}{\sqrt{2}}[\langle {}^3\Pi_{+\Omega}| + \langle {}^3\Pi_{-\Omega}|]\,,\\
\langle {}^3\Pi^-_\Omega| &= \frac{1}{\sqrt{2}}[\langle {}^3\Pi_{+\Omega}| - \langle {}^3\Pi_{-\Omega}|]\,.
\end{aligned} \tag{2–4}$$

(This agrees only for ${}^3\Pi_J$ with the notation used in [5]).

As can be easily seen from Fig. 5 the line strengths of the R and P branches observed in an identical upper state are composed of sums of line strengths of the following (actually coincident) branches

$$\begin{aligned}
S[P^{(p)}(J+1)] &= S[P^{(p)}_1(J+2)] + S[{}^PQ^{(p)}_{12}(J+1)] + S[{}^PR^{(p)}_{13}(J)] +\\
&+ S[P^{(p)}_2(J+1)] + S[{}^PQ^{(p)}_{23}(J)] + S[P^{(p)}_3(J)]\,,\\
S[R^{(p)}(J-1)] &= S[R^{(p)}_1(J)] + S[R^{(p)}_2(J-1)] + S[{}^RQ^{(p)}_{21}(J)] +\\
&+ S[R^{(p)}_3(J-2)] + S[{}^RQ^{(p)}_{32}(J-1)] + S[{}^RP^{(p)}_{31}(J)]\,,
\end{aligned} \tag{2–5}$$

where (p) means the perturbed branches.

Of the amplitudes pertaining to these line strengths the one for $P^{(p)}_1(J+2)$ will be the following:

$$\begin{aligned}
R_Z[P^{(p)}_1(J+2)] &= \langle {}^3\Pi^-_{J-1}, J+1|{}^pM_Z|{}^3\Sigma^+_{J-1}, J+2\rangle =\\
&= S^{(1)}_\Pi(J+1)\langle {}^3\Pi^-_{J-1}, J+1|M_Z|{}^3\Sigma^+_{J-1}, J+2\rangle +\\
&+ S^{(1)}_\Sigma(J+1)\langle {}^3\Sigma'^+_{J-1}, J+1|M_Z|{}^3\Sigma^+_{J-1}, J+2\rangle =\\
&= S^{(1)}_\Pi(J+1)D^P_{\Pi\Sigma}\sqrt{\frac{J(2J+5)}{2(2J+3)}} + S^{(1)}_\Sigma(J+1)D^P_{\Sigma'\Sigma}\sqrt{\frac{(J+1)(2J+5)}{2J+3}}\,,
\end{aligned} \tag{2–6}$$

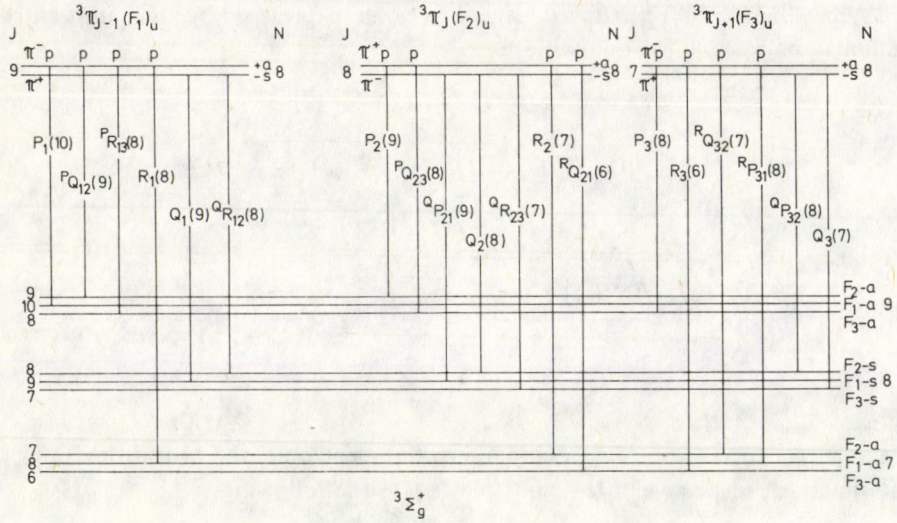

Fig. 5. Diagram for illustration of the branches starting from the same upper state (e.g. $N'=8$) of a $^3\Pi \rightarrow {}^3\Sigma$ transition

where we have used the unperturbed amplitudes given in Table IV, in which

$$D^i_{\Pi\Sigma}(J'') = \langle \Sigma v'' J'' | M_\eta | \Pi v' J' \rangle = \\ = \iint \Phi_0(^3\Sigma^+) R^{\Sigma}_{v''J''} M_\eta \Phi_0(^3\Pi) R^{\Pi}_{v'J'} r^2 dr d\tau \,, \tag{2-7a}$$

$$D^i_{\Sigma'\Sigma}(J'') = \langle \Sigma v'' J'' | M_\zeta | \Sigma' \tilde{v}' J' \rangle = \\ = \iint \Phi_0(^3\Sigma^+) R^{\Sigma}_{v''J''} | M_\zeta | \Phi_0(^3\Sigma'^+) R^{\Sigma'}_{\tilde{v}'J'} \, r^2 dr \, d\tau \,, \tag{2-7b}$$

where sign i means P, Q, R, for $J''=J'+1$, $J''=J'$, $J''=J'-1$, respectively.

Producing the amplitudes in a similar way for the other branches as well, the corresponding line strengths will be given by the squares of these:

$$S[P_1^{(p)}(J+2)] = \frac{J(2J+5)}{2(2J+3)} \left[S^{(1)}_\Pi (J+1) D^P_{\Pi\Sigma} + S^{(1)}_\Sigma (J+1) D^P_{\Sigma'\Sigma} \sqrt{\frac{2(J+1)}{J}} \right]^2 ,$$

$$S[{}^P Q_{12}^{(p)}(J+1)] = \frac{J}{2(J+1)^2} \left[S^{(1)}_\Pi (J+1) D^Q_{\Pi\Sigma} + S^{(1)}_\Sigma (J+1) D^Q_{\Sigma'\Sigma} \sqrt{\frac{2(J+1)}{J}} \right]^2 ,$$

$$S[{}^P R_{13}^{(p)}(J)] = \frac{J}{2(J+1)^2(2J+1)(2J+3)} \Big[S^{(1)}_\Pi (J+1) D^R_{\Pi\Sigma} + \\ + S^{(1)}_\Sigma (J+1) D^R_{\Sigma'\Sigma} \sqrt{\frac{2(J+1)}{J}} \Big]^2 ,$$

$$S[P_2^{(p)}(J+1)] = \frac{J^2(J+2)}{2(J+1)}\left[S_{\Pi}^{(2)}(J)D_{\Pi\Sigma}^{P} + S_{\Sigma}^{(2)}(J)D_{\Sigma'\Sigma}^{P}\sqrt{\frac{2(J+1)}{J}}\right]^2, \tag{2-8}$$

$$S[{}^{P}Q_{23}^{(p)}(J)] = \frac{J}{2(J+1)^2}\left[S_{\Pi}^{(2)}(J)D_{\Pi\Sigma}^{Q} + S_{\Sigma}^{(2)}(J)D_{\Sigma'\Sigma}^{Q}\sqrt{\frac{2(J+1)}{J}}\right]^2,$$

$$S[P_3^{(p)}(J)] = \frac{J(2J-1)}{2(2J+1)}\left[S_{\Pi}^{(3)}(J-1)D_{\Pi\Sigma}^{P} + S_{\Sigma}^{(3)}(J-1)D_{\Sigma'\Sigma}^{P}\sqrt{\frac{2(J+1)}{J}}\right]^2.$$

Summing up and calculating the same for the R branches we obtain in a good approximation (neglecting the small differences between D^Q and D^R, D^P in (2–8) in the summation procedure)

$$S[P^{(p)}(J+1)] = \frac{3(J+1)[2J\eta D_{\Pi\Sigma}^{P} + (F_J^{(p)} - F_J)D_{\Sigma'\Sigma}^{P}]^2}{(F_J^{(p)} - F_J)^2 + 8\eta^2 J(J+1)}, \tag{2-9a}$$

$$S[R^{(p)}(J-1)] = \frac{3J[2(J+1)\eta D_{\Pi\Sigma}^{R} - (F_J^{(p)} - F_J)D_{\Sigma'\Sigma}^{R}]^2}{(F_J^{(p)} - F_J)^2 + 8\eta^2 J(J+1)}. \tag{2-9b}$$

Be the observed Λ-type doublet $\Delta\nu^{\Lambda}({}^3\Pi_{N'})$ equal to $F_{N'}^{(p)} - F_{N'}$ for all three components when the perturbing Σ term is below the perturbed Π term:

$$F_{N'}^{(p)} - F_{N'} = \Delta\nu^{\Lambda}({}^3\Pi_{N'}). \tag{2-10}$$

The relations are illustrated in Fig. 6.

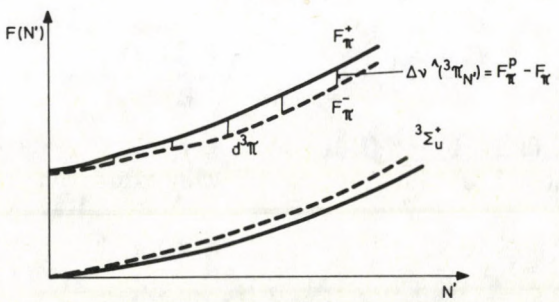

Fig. 6. In this schematic Figure the solid lines represent the perturbed energies; the dashed lines represent the energies for the hypothetical case of no interaction between two states; the unperturbed $d^3\Pi$ state coincides with the F_{Π}^{-} state and so $F_{\Pi}^{P} - F_{\Pi}^{-}$ gives the observed Λ-type doublet

Table IV

Branches	$^3\Pi(b)-{}^3\Sigma^+(b)$	$^3\Sigma'^+(b)-{}^3\Sigma^+(b)$
$P_1(J)$	$+D^P_{\Pi\Sigma}\sqrt{\frac{(J-2)(2J+1)}{2(2J-1)}}$	$+D^P_{\Sigma'\Sigma}\sqrt{\frac{(J-1)(2J+1)}{2J-1}}$
$^PQ_{12}(J)$	$-D^Q_{\Pi\Sigma}\sqrt{\frac{J-1}{2J^2}}$	$-D^Q_{\Sigma'\Sigma}\sqrt{\frac{1}{J}}$
$^PR_{13}(J)$	$-D^R_{\Pi\Sigma}\sqrt{\frac{J}{2(J+1)^2(2J+1)(2J+3)}}$	$-D^R_{\Sigma'\Sigma}\sqrt{\frac{1}{(J+1)(2J+1)(2J+3)}}$
$P_2(J)$	$+D^P_{\Pi\Sigma}\sqrt{\frac{(J-1)^2(J+1)}{2J^2}}$	$+D^P_{\Sigma'\Sigma}\sqrt{\frac{(J-1)(J+1)}{J}}$
$^PQ_{23}(J)$	$-D^Q_{\Pi\Sigma}\sqrt{\frac{J}{2(J+1)^2}}$	$-D^Q_{\Sigma'\Sigma}\sqrt{\frac{1}{J+1}}$
$P_3(J)$	$+D^P_{\Pi\Sigma}\sqrt{\frac{J(2J-1)}{2(2J+1)}}$	$+D^P_{\Sigma'\Sigma}\sqrt{\frac{(J+1)(2J-1)}{2J+1}}$
$R_1(J)$	$-D^R_{\Pi\Sigma}\sqrt{\frac{(J+1)(2J+3)}{2(2J+1)}}$	$+D^R_{\Sigma'\Sigma}\sqrt{\frac{J(2J+3)}{2J+1}}$
$R_2(J)$	$-D^R_{\Pi\Sigma}\sqrt{\frac{J(J+2)^2}{2(J+1)^2}}$	$+D^R_{\Sigma'\Sigma}\sqrt{\frac{J(J+2)}{J+1}}$
$^RQ_{21}(J)$	$+D^Q_{\Pi\Sigma}\sqrt{\frac{J+1}{2J^2}}$	$-D^Q_{\Sigma'\Sigma}\sqrt{\frac{1}{J}}$
$R_3(J)$	$-D^R_{\Pi\Sigma}\sqrt{\frac{(J+3)(2J+1)}{2(2J+3)}}$	$+D^R_{\Sigma'\Sigma}\sqrt{\frac{(J+2)(2J+1)}{2J+3}}$
$^RQ_{32}(J)$	$+D^Q_{\Pi\Sigma}\sqrt{\frac{J+2}{2(J+1)^2}}$	$-D^Q_{\Sigma'\Sigma}\sqrt{\frac{1}{J+1}}$
$^RP_{31}(J)$	$+D^P_{\Pi\Sigma}\sqrt{\frac{J+1}{2J^2(2J-1)(2J+1)}}$	$-D^P_{\Sigma'\Sigma}\sqrt{\frac{1}{J(2J-1)(2J+1)}}$

By using (2–9a, b) and (2–10) one obtains for the ratio of the perturbed line strengths of the R and P branches the following expression

$$S(N') = \frac{S[R(N'-1)]}{S[P(N'+1)]} = \frac{N'}{N'+1}\left[\frac{2(N'+1)\eta D^R_{\Pi\Sigma} - \Delta\nu^A(^3\Pi_{N'})D^R_{\Sigma'\Sigma}}{2N'\eta D^P_{\Pi\Sigma} + \Delta\nu^A(^3\Pi_{N'})D^P_{\Sigma'\Sigma}}\right]^2. \quad (2\text{–}11)$$

In the simplest case of reliability of the so-called Franck–Condon approximation (see e.g. [7]) the matrix elements (2–7a) and (2–7b) are proportional to $f^R_{\Pi\Sigma}, f^P_{\Pi\Sigma}, f^R_{\Sigma'\Sigma},$

$f^P_{\Sigma'\Sigma}$ the corresponding overlap integrals of the vibrational wave functions of the upper and lower state:

$$D^R_{\Pi\Sigma}(v', N'; v'', N'-1) = M_{\Pi\Sigma}(v', v'')\langle \Pi, v', N' | \Sigma, v'', N'-1\rangle = M_{\Pi\Sigma}(v'v'')f^R_{\Pi\Sigma},$$

$$D^P_{\Pi\Sigma}(v', N'; v'', N'+1) = M_{\Pi\Sigma}(v', v'')\langle \Pi, v', N' | \Sigma, v'', N'+1\rangle = M_{\Pi\Sigma}(v'v'')f^P_{\Pi\Sigma}, \quad (2\text{–}12a)$$

$$D^R_{\Sigma'\Sigma}(\tilde{v}', N'; v'', N'-1) = M_{\Sigma'\Sigma}(\tilde{v}', v'')\langle \Sigma', \tilde{v}', N' | \Sigma, v'', N'-1\rangle = M_{\Sigma'\Sigma}(\tilde{v}', v'')f^R_{\Sigma'\Sigma},$$

$$D^P_{\Sigma'\Sigma}(\tilde{v}', N'; v'', N'+1) = M_{\Sigma'\Sigma}(\tilde{v}', v'')\langle \Sigma', \tilde{v}', N' | \Sigma, v'', N'+1\rangle = M_{\Sigma'\Sigma}(\tilde{v}', v'')f^P_{\Sigma'\Sigma}. \quad (2\text{–}12b)$$

Using (2–12a) and (2–12b) we get for (2–11)

$$S(N') = \frac{N'}{N'+1}\left[\frac{2(N'+1)\tau(N')f^R_{\Pi\Sigma} - \Delta v^A({}^3\Pi_{N'})f^R_{\Sigma'\Sigma}}{2N'\tau(N')f^P_{\Pi\Sigma} + \Delta v^A({}^3\Pi_{N'})f^P_{\Sigma'\Sigma}}\right]^2, \quad (2\text{–}13a)$$

where

$$\tau(N') = \frac{\eta(N')M_{\Pi\Sigma}(v'v'')}{M_{\Sigma'\Sigma}(v', v'')}. \quad (2\text{–}13b)$$

Neglecting in (2–13a) the usually weak effect of vibration-rotation interaction in radiation processes we obtain the following expression

$$S(N') = \frac{N'}{N'+1}\left[\frac{2(N'+1)\tau(N') - \Delta v^A({}^3\Pi_{N'})}{2N'\tau(N') + \Delta v^A({}^3\Pi_{N'})}\right]^2, \quad (2\text{–}14a)$$

taking into account only the effect of perturbation between a $^3\Pi$ and $^3\Sigma$ states.

Neglecting the effect of vibration-rotation interaction in the perturbation matrix element (2–1a), too, we get the following

$$S(N') = \frac{N'}{N'+1}\left[\frac{2(N'+1)\tau - \Delta v^A({}^3\Pi_{N'})}{2N'\tau + \Delta v^A({}^3\Pi_{N'})}\right]^2. \quad (2\text{–}14b)$$

In this case, of course, η and so τ do not depend on N' either.

In the case of two far lying terms it would be suitable to introduce instead of the difference of the perturbed and unperturbed terms, $F^{(P)} - F$, the difference of the perturbed and perturbing terms, $F_\Pi(N') - F_{\Sigma'}(N') = \nu(\Pi, \Sigma')$ where

$$\nu(\Pi, \Sigma') \sim \text{const.} > 8\eta^2 J(J+1). \quad (2\text{–}15)$$

Here it is supposed that the perturbation effect is so small in comparison with the term distance that the perturbed position of the perturbed and perturbing terms can be substituted by the unperturbed position of these terms and the term differences do not change with the rotational quantum number. According to the well known perturbation calculation [5] we obtain

$$F^{(p)}_{N'} - F_{N'} = -\frac{\nu(\Pi, \Sigma')}{2} + \sqrt{\left(\frac{\nu(\Pi, \Sigma')}{2}\right)^2 + 8\eta^2 N'(N'+1)} \sim \frac{8\eta^2 N'(N'+1)}{\nu(\Pi, \Sigma')}. \quad (2\text{–}16)$$

Putting (2–16) in (2–14b) we get

$$S(N') = \frac{N'}{N'+1}\left[\frac{2(N'+1)\tau - \dfrac{8\eta^2 N'(N'+1)}{\nu(\Pi,\Sigma')}}{2N'\tau + \dfrac{8\eta^2 N'(N'+1)}{\nu(\Pi,\Sigma')}}\right]^2 \sim \frac{N'+1}{N'}\left[\frac{1-\gamma N'}{1+\gamma(N'+1)}\right], \tag{2–17}$$

where the last small square terms in the numerator and denominator of the last expression have been neglected. Here

$$\gamma = 8\frac{\eta M_{\Sigma'\Sigma}}{\nu(\Pi,\Sigma')M_{\Pi\Sigma}}. \tag{2–18}$$

Otherwise the results are the same as in the case of a $^1\Pi^+ \to {}^1\Sigma^+$ transition perturbed by a $^1\Sigma'^+$ state, but they differ from Dieke's results [2], who has neglected the so-called interference terms.

2.2. Low interaction of $^3\Pi(b)$ state with an indefinite number of Σ', $\tilde{v}'$ states

This case may be treated in the first order of the well-known perturbation theory. Particularly for the ratio of line strengths of the members of R and P branches of $d^3\Pi_u$, $v', N' \to a^3\Sigma_g^+$, v'', N'' the transition starting from the same initial level (after averaging over initial and summing over final spin projections) can be easily obtained as

$$S(N') = \frac{N'+1}{N'}\left|\frac{D^R_{\Pi\Sigma}(N'-1)}{D^P_{\Pi\Sigma}(N'+1)}\right|^2\left[\frac{1-N'\gamma^R(N')}{1+(N'+1)\gamma^P(N')}\right], \tag{2–19a}$$

where

$$\gamma^R(N') \equiv \gamma(N', N'')|_{N''=N'-1}; \qquad \gamma^P(N') = \gamma(N', N'')|_{N''=N'+1}, \tag{2–19b}$$

$$\gamma(N', N'') = \frac{1}{8\pi^2\mu}\sum_{\Sigma', \tilde{v}'}\frac{\langle \Pi, v', N'\left|\dfrac{L_\xi}{r^2}\right|\Sigma', \tilde{v}', N'\rangle\langle \Sigma, v'', N''|M_\xi|\Sigma', \tilde{v}', N'\rangle}{(F_{\Pi v'}(N') - F_{\Sigma', \tilde{v}'}(N'))\langle \Sigma, v'', N''|M_\eta|\Pi, v', N'\rangle}$$

μ is the reduced mass of nuclei and $F_{\Pi v'}(N') - F_{\Sigma', \tilde{v}'}(N')$ are the term differences between perturbed and perturbing levels.

For the applicability of the theory it is necessary that

$$\frac{N'|\gamma(N', N'')|}{4} \ll 1. \tag{2–19c}$$

Depending on the vibrational (v', v'') and rotational (N', N'') quantum numbers the magnitudes $\gamma(N', N'')$ may be obtained either theoretically by numerical calculation of the electronic wave functions or semiempirically by finding the values which give the best fit to the experimental data on relative line strengths $S(N')$. (As in the previous case

we are not interested in vibrational dependencies, therefore the indices v', v'' are omitted in (2–19a)).

From the structure of formulae (2–19b) it can be seen that $\gamma(N', N'')$ has to depend more weakly on N'' than on the initial rotational quantum number N'. Indeed, the N''dependence (leading to a difference between γ^R and γ^P) can be due to the vibration-rotation interaction only, namely to the dependencies of matrix elements of dipole moment over vibrational wave functions on the rotational quantum numbers. (It should be noted that these matrix elements for the same (R or P) lines enter into the numerator (for $\Sigma' \to \Sigma$ transition) and the denominator (for $\Pi \to \Sigma$) of (2–19b) and may compensate each other to some extent. It is sufficient also that they are put under the sign of summation).

The dependence of $\gamma(N', N'')$ on N' may be caused by the N'-dependences of the matrix element for the $\frac{L_\xi}{r^2}$ operator and the term differences $F_{\Pi v'}(N') - F_{\Sigma' v''}(N')$ as well.

Although, generally speaking, both dependencies (on N' and N'') should be rather weak, their weaknesses have to be of different order. If we neglect the weaker N''dependence (or the effect of vibration-rotation interaction in the perturbation terms of (2–19b)), then formula (2–19a) is reduced to

$$S(N') = \frac{N'+1}{N'} \left| \frac{D^R_{\Pi\Sigma}(N'-1)}{D^P_{\Pi,\Sigma}(N'+1)} \right|^2 \left[\frac{1 - N'\gamma(N')}{1 + (N'+1)\gamma(N')} \right]. \tag{2–20}$$

The determination of the matrix elements entering into (2–20) meets with significant difficulties because the modern methods to solve the adiabatic Schrödinger equation numerically cannot ensure the necessary precision to describe adequately the effect of vibration-rotation interaction (see below §3). So in deriving the N dependences of relative line strengths accounting for the effect we shall use simple analytical expressions for the matrix elements instead of the results of numerical calculations. According to Tipping and Chackerian [11] in the case of weak vibration-rotation interaction the analytical forms of the squares of the amplitudes in the first approximation are as follows:

$$\begin{aligned} [D^R_{\Pi\Sigma}(N'-1)]^2 &= \tilde{M}^2_{\Pi\Sigma}(v', v'')[1 + a(v'v'')N'], \\ [D^P_{\Pi\Sigma}(N'+1)]^2 &= \tilde{M}^2_{\Pi\Sigma}(v', v'')[1 - a(v'v'')(N'+1)], \end{aligned} \tag{2–21}$$

where $\tilde{M}_{\Pi\Sigma}(v', v'')$ and $a(v', v'')$ are independent of the rotational quantum numbers N', N''. Then substituting the restricted series into the formula (2–20), making the necessary transformations and neglecting the small square terms (see 2–19c) one obtains

$$S(N') = \frac{N'+1}{N'} \left[\frac{1 - N'\tilde{\gamma}(N')}{1 + (N'+1)\tilde{\gamma}(N')} \right], \tag{2–22}$$

where $\tilde{\gamma}(N')=\gamma(N')-a(v'v'')$ accounts for both effects: the vibration-rotation interaction in the radiative transition and the N-dependence of the matrix element combination (2–15a) describing perturbing interactions between various electronic-vibrational states of the molecule. The effective values of $\tilde{\gamma}(N')$ may be also obtained either theoretically by numerically calculating the electronic wave functions or semiempirically by finding the values which give the best fit to the experimental data about $S(N')$.

If one neglects the vibration-rotation interaction

$$S(N')=\frac{N'+1}{N'}\left[\frac{1-N'\gamma(N')}{1+(N'+1)\gamma(N')}\right], \tag{2–23}$$

which coincides with the previous expression. So in any experimental studies the two different effects cannot be distinguished.

It should be noted that formula (2–23) coincides with (2–17) if one considers the perturbation to be caused by the single electronic-vibrational state of a molecule.

2.3. Transition to formulas of adiabatic theory

If the perturbation is negligible, whereas the vibration-rotation interaction remains sufficient, then the non-adiabatic formulas derived in the present work must turn into that obtained in the adiabatic theory. For this transition it is necessary to put the corresponding terms describing the perturbations [Δv in (2–11), and $\gamma(N', N'')$ in (2–19a)] equal to zero. Then

$$S(N')=\left|\frac{D^R_{\Pi\Sigma}(N'-1)}{D^P_{\Pi\Sigma}(N'+1)}\right|^2\frac{N'+1}{N'}. \tag{2–24}$$

This expression is identical to that used by Villarejo et al. [3]. If the vibration-rotation interaction can also be neglected for the transition under study the ratio of line strengths becomes equal to that predicted by the well-known Hönl–London formulas

$$S(N')=\frac{N'+1}{N'}. \tag{2–25}$$

§ 3. Comparison of theoretical and experimental results

As it was seen in §1 the Hönl–London formulas are in contradiction with the experiment. The attempt by Villarejo et al. to improve the adiabatic theory in the framework of Franck–Condon approximation by taking into account the influence of vibration-rotation interaction on the corresponding overlap integrals was not successful either [3]. The interaction proved to be rather weak to account for the observed deviation although it was noticeable for the transition under study.

This situation is illustrated in Figs 4a, b, c where one can see $S(N')$ values calculated by (2–24) in adiabatic approximation by numerically solving the

Schrödinger equation with Rydberg–Klein–Rees potential in [3] (curve 5) and with Morse–Pekeris potential in the present work (curve 6).[2]

We have carried out calculations not only for the additional verification of the previous results obtained by Villarejo et al. but, in principle, to include the vibration-rotation interaction into the non-adiabatic theory (formulas (2–13a), and (2–19a)). Unfortunately, the comparison of the results of two independent numerical computations in (2–20) based on different methods shows that for the $d^3\Pi_n \to a^3\Sigma_g^+$ transition in the H_2 molecule the modern methods of Franck–Condon factor calculations give an uncertainty comparable to the order of the effect of vibration-rotation interaction (see Fig. 4, curves 5 and 6).[3]

Both methods have their own advantages and disadvantages. In the literature there is no generally accepted answer to the question which of them gives better or more correct results (see e.g. references and discussion in [4] pp. 73–75). Therefore, in the further analysis of the applicability of nonadiabatic theoretical models we shall use, on the one hand, in (2–13a) the Franck–Condon factors calculated with Morse–Pekeris potential, on the other hand, in (2–22), the expressions based on the analytical form (2–21) for squares of amplitudes D taking into account the weakness of vibration-rotation interaction obtained in the numerical calculations mentioned above.

Earlier, the only non-adiabatic theoretical scheme was developed for pure p- and d-complexes [5]. The formulas in this scheme have been verified in the analysis of rotational distributions in certain emission bands of N_2 [13] and He_2 [5] molecules but they have been found not to be valid for the triplet term $3p$-complex of the H_2 molecule because in our case the conditions of existence of the pure p and d complex are not fulfilled (e.g. $B_\Pi = B_\Sigma = B$; $\eta = \dfrac{B}{\sqrt{2}}, \dfrac{D_{\Pi\Sigma}}{D'_{\Sigma\Sigma}} = \sqrt{2}, \tau = B$).

Let us proceed to the comparison of formulas (2–13a) and (2–22) with the experimental data. The values of parameters $\tau(N')$ and $\tilde{\gamma}(N')$ entering into these formulas calculated with the measured ratios $S(N')$ from Table III and $\Delta v^A(^3\Pi)$ data adopted from [2] (see in Tables Va, b, c) are presented in Fig. 7. It can be seen that: i) the results obtained from diagonal and non-diagonal band intensities coincide within the error limits of the experiment; ii) decrease of $\tau(N')$ and $\tilde{\gamma}(N')$ with the growth of N' observed here may be described by a linear function with good accuracy (see Table VI).

For $\tilde{\gamma}(N')$ this dependence is rather weak (comparable to the experimental uncertainty) and may be interpreted as:

[2] The deviation from the Franck–Condon approximation, i.e. the weak dependence of the electric dipole moment on the internuclear distance observed for $d^3\Pi_n \to a^3\Sigma_g^+$ transition in our previous paper [7] was found to have practically no influence upon the ratios $S(N')$. So in formula (2–24) Franck–Condon factors may be used instead of squares of amplitudes $D^{R,P}_{\Pi\Sigma}(N')$ with an accuracy much better than the precision of the experiment.

[3] It should be noted that when neglecting the effect of vibration-rotation interaction our computer procedure gives results coinciding with those obtained by Spindler [12] with an accuracy better than 0.1%.

Table Va*
$d^3\Pi_u^+ (v'=0)$

N'	$S^0(N')$	$\Delta v^A(^3\Pi_{N'})$	$S^C(N')$ (2−14b)	$f^R_{\Pi\Sigma}(N'-1)$	$f^P_{\Pi\Sigma}(N'+1)$	$f^R_{\Sigma'\Sigma}(N'-1)$	$f^P_{\Sigma'\Sigma}(N'+1)$	$S^C(N')$ (2−13a)
4	0.84	3.87	0.74	0.9618	0.9679	0.1998	0.1870	0.84
5	0.74	5.22	0.68	0.9609	0.9683	0.2021	0.1867	0.73
6	0.67	6.14	0.65	0.9600	0.9686	0.2044	0.1866	0.66
7	0.60	6.40	0.68	0.9591	0.9688	0.2069	0.1868	0.62
8	0.58	6.50	0.71	0.9582	0.9690	0.2095	0.1874	0.57

Table Vb*
$d^3\Pi_u^+ (v'=2)$

N'	$S^0(N')$	$\Delta v^A(^3\Pi_{N'})$	$S^C(N')$ (2−14b)	$f^R_{\Pi\Sigma}(N'-1)$	$f^P_{\Pi\Sigma}(N'+1)$	$f^R_{\Sigma'\Sigma}(N'-1)$	$f^P_{\Sigma'\Sigma}(N'+1)$	$S^C(N')$ (2−13a)
1	1.66	0.96	1.57	0.8195	0.8298	0.0316	0.0327	1.66
2	1.10	2.64	1.05	0.8157	0.8327	0.0315	0.0334	1.10
3	0.95	4.75	0.84	0.8116	0.8353	0.0315	0.0343	0.87
4	0.72	6.87	0.74	0.8075	0.8374	0.0316	0.0355	0.73
5	0.65	8.41	0.71	0.8032	0.8394	0.0320	0.0371	0.65
6	0.61	8.87	0.73	0.7989	0.8409	0.0326	0.0392	0.61

Table Vc*
$d^3\Pi_u^+ (v'=3)$

N'	$S^0(N')$	$\Delta v^A(^3\Pi_{N'})$	$S^C(N')$ (2−14b)	$f^R_{\Pi\Sigma}(N'-1)$	$f^P_{\Pi\Sigma}(N'+1)$	$f^R_{\Sigma'\Sigma}(N'-1)$	$f^P_{\Sigma'\Sigma}(N'+1)$	$S^C(N')$ (2−13a)
1	1.58	1.98	1.45	0.9643	0.9664	0.1938	0.1894	1.57
2	0.98	4.40	1.01	0.9635	0.9669	0.1957	0.1884	1.01
3	0.74	6.41	0.89	0.9627	0.9675	0.1976	0.1876	0.72

* *Note.* The columns 2 show the mean values of the intensity ratios observed in different transitions belonging to the same upper levels, the columns 3 are the observed values of the Λ-type doublets [2], the columns 4 give the theoretical calculated values of the intensity ratios from (2 − 14b) with constant τ values (for the numerical values of τ see Table VI), columns 5, 6, 7, 8 show the Franck–Condon factors calculated theoretically, and the last columns represent the values of the intensity ratios calculated theoretically from (2 − 13a) with $\tau(N')=\tau_0-\tau_1 N'$ (for the numerical values of τ_0 and τ_1 see Table VI)

Table VI

v'	$\bar{\tau}$	$\tau(N')=\tau_0-\tau_1 N'$		$\bar{\gamma}$	$\gamma(N')=\gamma_0-\gamma_1 N'$	
		τ_0	τ_1		γ_0	γ_1
0	3.3±0.8	1.34±0.05	$(1.06\pm0.07)10^{-1}$	0.042±0.002	0.052±0.002	$(1.60\pm0.05)10^{-3}$
2	5.9±1.3	0.369±0.004	$(2.53\pm0.01)10^{-1}$	0.059±0.006	0.068±0.001	$(2.57\pm0.04)10^{-3}$
3	9.0±2.5	3.1±0.2	$(6.1\pm0.9)10^{-1}$	0.085±0.003	0.081±0.002	$-(2.0\pm0.9)10^{-3}$

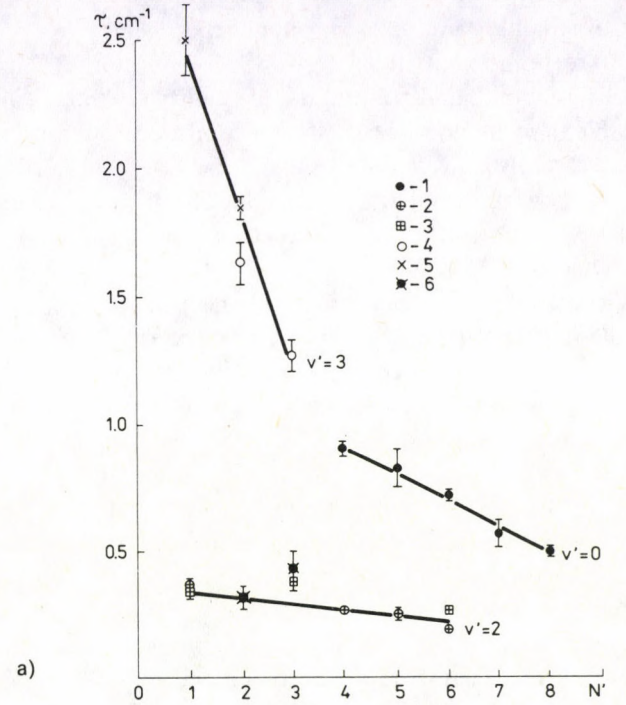

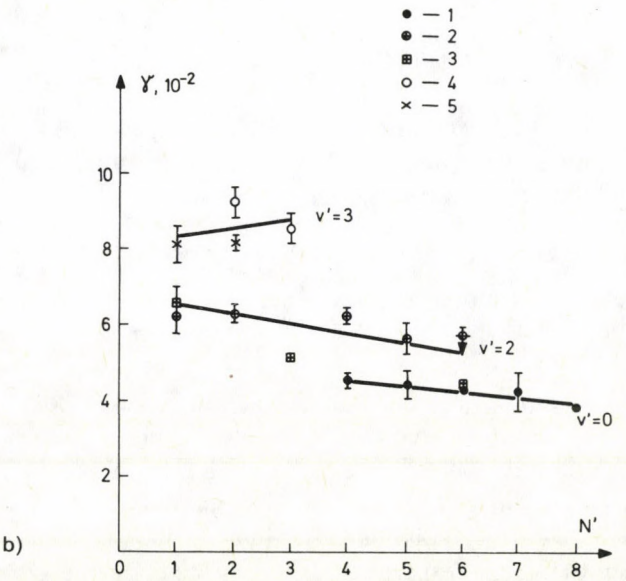

Figs. 7a, b. N'-dependences of $\tau(N')$ and $\tilde{\gamma}(N')$ obtained from (0–0) (1), (2–2) (2), (2–1) (3), (2–3) (6), (3–3) (4) and (3–2) (5) transitions. Solid lines are the results of linear approximation by the least square method

1. an effect of small systematic error of the experiment;

2. small square terms omitted in derivation of formula (2–22) although the absolute values of $\tilde{\gamma}(N')$ are found to fulfil the inequality (2–19c);

3. a noticeable contribution of the effect of vibration-rotation interaction;

4. N'-dependence of the term differences in (2–19b).

In any case the weakness of the N'-dependence of $\tilde{\gamma}(N')$ observed here is in accordance with the "a priori" view of the situation.

The dependence of $\tau(N')$ on N' seems to be due to points 1. and 3. mentioned. In this case $\tau(N')$ shows the dependence on N' of the perturbation matrix elements separately from the matrix elements of the radiative transitions. From the relatively stronger variation of $\tau(N')$ as compared to $\tilde{\gamma}(N')$ it follows that the latter is compensated to a certain extent by the dependence of the perturbation matrix element.

The dependencies of the ratios $S(N')$ on N' for the bands with $v'=0$, 2 and 3 calculated by formulas (2–13a), (2–22) with the linear approximations of the N'-dependences of $\tau(N')$ and $\tilde{\gamma}(N')$ are presented in Figs 4a, b, c. It can be seen that both theories generally are in good agreement with the experimental data. So in our case the interaction with several (or even with an infinite number of) states is equivalent to that with a single effective electronic-vibrational state.

Thus the comparison of theoretical and experimental results shows that the intensity anomalies in rotational structure of the Fulcher-α bands of the H_2 molecule are caused mainly by the perturbation of the upper $d^3\Pi_u^+$, v' states due to the interactions with other ${}^3\Sigma_u'^+$, $\tilde{v}$ states of the molecule.

Conclusion

The main goal of the present work was to understand whether the non-adiabatic quantum approach is capable of describing the radiative transition probabilities in the case of a perturbed upper state when the simple formulas of adiabatic theory are not valid.

We have chosen for the investigation of radiative transition probabilities one of the simplest situations, a simplest neutral molecule and a lowest triplet Π emitting electronic state. Nevertheless, up to now the reiterated attempts to solve the problem (see Introduction) have failed.

The results of our work show that the non-adiabatic theory based on the consideration of interactions between the electronic-vibrational states of the molecule and taking into account the relatively weak effect of vibrational-rotational interaction makes it possible to explain all available experimental data on the line strengths of $d^3\Pi_u^+$, v', $N' \rightarrow a^3\Sigma_g^+$, v'', N'' radiative transitions in the H_2 molecule. Thus the agreement between theory and experiment indicates the correctness of the proposed theoretical scheme and seems to confirm our knowledge of the structure of the molecule.

The adequate theoretical description of the investigated transition makes it possible to obtain the corresponding radiative transition probabilities semiempirically, by finding the values of fitting parameters from the finite volume of experimental data on the relative line strengths and calculating the line strengths for electronic-vibro-rotational transitions with arbitrary vibrational and rotational quantum numbers by means of the formulas of the theory.

In particular, the line strength values for the R and P branches of Fulcher-α bands of hydrogen obtained in the present work have shown considerable deviations from those predicted by the formulas of adiabatic theory, the difference increasing with the growth of v' and N'. This circumstance has to be taken into account in the determination of the rotational level population densities of $d^3\Pi_u^+$, v' states of the H_2 molecule in non-equilibrium ionized molecular gases and plasma.

Moreover, it should be emphasized that theoretical and experimental investigations analogous to the present work may be applied for the determination of the electronic-vibro-rotational radiative transition probabilities in diatomic molecules. Due to the difficulties of purely theoretical calculations of electronic wave functions such a semiempirical approach (widely applied to obtain electronic-vibrational transition probabilities [4]) seems to be most promising.

References

1. N. Ginsburg and G. H. Dieke, Phys. Rev., **59,** 632, 1941.
2. G. H. Dieke, Phys. Rev., **60,** 523, 1941.
3. D. Villarejo, R. Stockbauer and M. G. Inghram, J. Chem. Phys., **50,** 1754, 1969.
4. L. A. Kuznetzova, N. E. Kuz'menko, Yu. Ya. Kuzyakov and Yu. A. Plastinin, Veroyatnosty Opticheskih Perehodov Dvuhatomnih Molekul (In Russian: Optical Transition Probabilities in Diatomic Molecules), Nauka, Moscow, 1980.
5. I. Kovács, Rotational Structure in the Spectra of Diatomic Molecules, Akadémiai Kiadó, Budapest and Adam Hilger Ltd. London, 1969.
6. B. P. Lavrov and D. K. Otorbaev, Opt. Spektrosk., **45,** 1074, 1978. (Opt. Spectrosc. (USSR), **45** (6), 859, 1978.)
7. T. V. Kirbjat'eva, B. P. Lavrov, V. N. Ostrovsky, M. V. Tyutchev, V. I. Ustimov, Opt. Spektrosk., **52,** 39. 1982.
8. B. P. Lavrov, L. P. Schischatzkaya, Optico Mechanicheskaya Promishlennost, **11,** 58, 1979.
9. The Hydrogen Molecule Wavelength Tables of G. H. Dieke, ed. by Crosswhite, N. Y., 1972.
10. B. P. Lavrov and D. K. Otorbaev, Opt. Spektrosk., **44,** 617, 1978. (Opt. Spectrosc. (USSR), **44** (3), 360, 1978.)
11. R. H. Tipping and C. Chackerian, J. Mol. Spectr., **88,** 352, 1981.
12. R. J. Spindler, J. Q. S. R. T., **9,** 597, 627, 1041, 1969.
13. P. K. Carroll, J. Chem. Phys., **58,** 3897, 1973.

Acta Physica Hungarica 54 (1—2), pp. 189—212 (1983)

ELECTRONIC SPECTRUM OF NdO

L. A. KALEDIN and E. A. SHENYAVSKAYA

Institute for High Temperatures, Moscow, USSR

I. KOVÁCS

Department of Atomic Physics, Technical University, 1521 Budapest, Hungary

(Received 30 June 1982)

Emission and absorption spectra of NdO have been obtained in the 500–1100 nm region. Vibrational and rotational analyses have been carried out. The rotational analysis shows that there are at least 4 low-lying states which give rise to absorption bands. The observed Λ-type doubling has been interpreted by the theoretical formula produced for the intermediate case between Hund's case a) and b) of a $^5\Pi$ state. The anomalous high values and the opposite sign of the centrifugal constants D have been explained by the heterogeneous perturbations.

Introduction

The electronic structure of rare earth monoxides has been of considerable interest for many years because of the great uncertainty in the calculated thermodynamic properties of these gases, which arises from the unavoidable use of estimated molecular properties in the computation of high temperature thermal functions. In recent years the CeO [12, 13] and PrO [10, 14, 15] molecules have been extensively studied, and the experimental information obtained seems to be sufficiently complete to understand their electronic structure.

Till now the electronic spectrum of NdO has not been analyzed. In a short communication [1] we reported on the preliminary results of the rotational analysis of 3 bands of NdO. This paper deals with the analysis of the most intense band systems of NdO in the region 500–1100 nm.

1. Experimental

Emission and absorption spectra of NdO were obtained by using a vacuum furnace with a tantalum heater [2] heating the neodymium oxide Nd_2O_3 to temperatures about 2000–2200 °C. The emission spectrum was recorded in the region 500–1100 nm, the absorption spectrum was obtained only between 500–800 nm because of the unavailability of a suitable source of continuous spectrum in the infrared region.

Plates for the vibrational analysis were taken in a PGS-2 spectrograph with a dispersion of about 0.2 nm/mm (grating with 600 lines per mm, blaze angle corresponding to a wavelength of 1900 nm). Plates for the rotational analysis were taken in our Laboratory by a spectrograph constructed ($f = 3000$ nm) in VI–XII orders of grating (300 lines per mm, 200 mm long, blaze angle corresponding to the wavelength of 6000 nm) with a dispersion of 0.03–0.1 nm/mm and an actual resolving power of about 300 000–400 000.

The samples of Nd_2O_3 containing both the natural neodymium and the isotope ^{142}Nd were used. Rotational analysis was carried out for ^{142}NdO.

Different glass filters and a predisperser were used to block out overlapping orders. An iron hollow cathode lamp provided a reference spectrum and measurements were carried out using an IZA-2 comparator. The precision of the measurement is considered to be about of 0.02 cm^{-1} for sharp unblended lines.

All the intense band heads of NdO listed in [3] were observed in this work.

2. Vibrational analysis

Numerous bands (~ 400) were measured in the region 500–1100 nm. According to the Wigner–Witmer correlation rules atoms of Nd ($S \geqq 2$) and O ($2 \leqq 1$) lead to molecular states of high multiplicity [3–9]. But as in case of CeO and PrO all the transitions appear to be singlet ones. About sixty bands were arranged into 8 systems (or subsystems). Table I gives the wavelengths and the wavenumbers of band heads and their assignments. The systems are marked by Roman numerals in the order of their wavelength positions in the spectrum. Two single 0–0 bands of the systems IV and V, for which the rotational analysis was carried out, are included in Table I.

The assignments of the 0–0 bands were facilitated by the observation of the spectrum of the natural isotope mixture: the $\Delta v \neq 0$ bands seem to have the band heads and the rotational structure broadened by isotopic shift, unlike the $\Delta v = 0$ bands on spectrograms taken with low dispersion.

The 0–0 bands of the systems V–X were observed in absorption. The VII (0–0) band at 689.7 nm is the most prominent in absorption and it probably corresponds to the very strong band at 680.2 nm observed in the absorption spectrum of the matrix isolated NdO molecule at 4 K [4]. However, it is very difficult to guess to which band the other very strong band at 566.8 nm observed in the neon matrix corresponds.

Table II gives the vibrational constants calculated from band heads. The vibrational constants in lower states have close values, and their $\Delta G_{1/2}$ are in agreement with the infrared band observed in the neon matrix. So the results of the matrix study cannot be used for distinguishing the transitions terminating in the ground state.

Table I

Band heads of NdO and their assignments

λ_{air} [nm]	ν_{vac} [cm^{-1}]	Assignment System	$v'-v''$	λ_{air} [nm]	ν_{vac} [cm^{-1}]	Assignment System	$v'-v''$
1974.92	9300.5	I	0–1	772.26	12945.4	III	3–1
1033.75	9670.9	II	0–1	761.45	13129.2	VI	0–1
988.57	10112.8	II	3–3	741.04	490.8	V	0–0
986.11	138.0	I	0–0	733.00	638.8	VII	1–2
975.20	251.5	II	2–2	731.53	666.3	VII	0–1
962.48	387.0	II	1–1	781.70	910.1	VI	2–2
951.08	511.5	II	0–0	717.02	942.8	VI	1–1
950.39	519.2	III	2–3	715.76	967.4	VI	0–0
942.82	603.6	III	1–2	705.60	14168.5	VIII	3–4
934.61	696.7	III	0–1	703.37	213.4	VIII	2–3
921.83	845.0	I	2–1	702.30	235.0	IX	0–2
915.81	916.3	I	1–0	701.07	260.0	VIII	1–2
913.15	948.1	II	3–2	698.80	306.4	VIII	0–1
901.47	11090.0	II	2–1	689.71	494.9	VII	0–0
890.66	224.4	II	1–0	665.91	15012.8	IX	1–2
880.43	355.0	III	2–2	664.30	049.3	VIII	2–2
873.37	446.8	III	1–1	663.34	071.1	X	0–2
872.00	464.9	VI	0–3			IX	0–1
865.98	544.4	III	0–0	662.09	099.6	VIII	1–1
848.16	787.0	II	3–1	659.82	151.2	VIII	0–0
837.94	931.0	II	2–0	630.74	849.9	IX	1–1
832.91	12002.9	III	4–3	629.10	891.3	VIII	2–1
831.85	018.1	VII	0–3	628.57	904.7	X	0–1
826.09	101.9	III	3–2	628.19	914.4	IX	0–0
819.47	199.7	III	2–1	626.92	946.7	VIII	1–0
813.14	294.6	III	1–0	601.53	16619.7	IX	2–1
		VI	0–2	599.01	689.5	IX	1–0
808.25	369.1	IV	0–0	597.89	720.7	X	1–1
791.69	627.8	II	3–0	597.36	735.6	VIII	2–0
784.34	746.1	III	5–3	597.08	743.6	X	0–0
780.07	815.8	VII	1–3	572.59	17459.7	IX	2–0
778.58	840.3	VII	0–2	570.31	529.8	X	2–1
778.27	845.4	III	4–2	569.33	559.6	X	1–0
				538.36	18569.7	X	2–0

Table II

Vibrational constants of ^{142}NdO* (in cm^{-1})

System	ν_e	ω'_e	$\omega'_e x'_e$	ω''_e	$\omega''_e x''_e$
I	10166.7(9)	790.4	6.0	835.7**	
II	10572.2(9)	722.7(9)	4.4(2)	842.4(9)	1.0(2)
III	11590.4(10)	754.6(8)	1.2(2)	848.8(13)	1.0(3)
VI	13976.8(4)	826.0(7)	6.1(2)	842.6(4)	2.1(1)
VII	14511.4(3)	798.1(2)**		831.7(4)	1.5(1)
VIII	15177.5(7)	798.4(10)	2.1(3)	850.3(6)	2.4(2)
IX	15943.7(16)	784.6(19)	3.7(6)	845.1(19)	2.1(6)
X	16754.5(10)	822.9(13)	3.4(1)	844.2(13)	2.7(1)

* The numbers in parentheses are the uncertainty in the last digit that corresponds to two standard deviations

** $\Delta G_{1/2}$

3. Rotational analysis

The wave numbers of rotational lines in the 0–0 bands of the systems I–V, VII, VIII and X and in the 1–0 band of system I are given in Table IV. The lines overlapped by other band lines are marked with asterisks. Those lines which are badly blended are indicated by two asterisks. The lines which form the bandhead are marked by "*h*".

All but two of the analyzed bands (the 0–0 and 1–0 bands of system I) consist of *R*, *Q* and *P* branches. The relative numbering for these bands has been established by finding agreement between the combination differences $\Delta_1 F$: $R(J)-Q(J)=Q(J+1)-P(J+1)$ for the upper state and $R(J)-Q(J+1)=Q(J)-P(J+1)$ for the lower state. The relative numbering for the bands of the system I has been found by finding agreement between the combination differences $\Delta_2 F''=R(J-1)-P(J+1)$ for both the 0–0 and the 1–0 bands. The absolute numbering has been found by the requirement that $\Delta_2 F(J)=4B(J+1/2)$ plotted as a function of J should tend to zero at $J=-1/2$.

The rotational constants and the band origins (see Table III) have been calculated by the least-squares techniques using the equations

$$\Delta_1 F=2B(J+1)-4D(J+1)^3, \tag{3.1}$$

$$\Delta_2 F=4B(J+1/2)-8D(J+1/2)^3, \tag{3.2}$$

$$R(J-1)+P(J)=2\nu_0+2(B'-B'')J^2-2(D'-D'')J^2(J^2+1). \tag{3.3}$$

Since the multiplet structure is not obvious in the spectrum the assignments of electronic transitions can be carried out only using case c) designation (i.e. $\Omega'-\Omega''$). It is rather difficult to observe the lowest J lines of the transitions, especially in the spectra obtained at temperatures as high as in this experiment. The weak first lines are often overlapped by the other lines of the same band or of the other. The assumed electronic assignment (see Table III, "Remarks" column) should not be considered final, but very probable.

The short description of the rotational structure and the proposed electronic assignment are given below for all analyzed bands.

System I. 986.1 nm (0–0) *and* 916.8 nm (1–0)

Bands consist of single lines of the *R* and *P* branches. $I(R)\approx I(P)$. The lines at lowest J numbers unblended in the 0–0 band are $R(5)$ and $P(6)$, and in the 1–0 band $P(5)$. Besides, in the 0–0 band the weak lines which can be assigned to $Q(4)$, $Q(5)$ and $Q(7)$ were measured. For this reason the system I was assigned to $(\Omega'=4)-(\Omega''=4)$ transition.

The upper state of the 0–0 band is perturbed. The "extra"-lines were measured for $42\leqq J\leqq 49$. The $B'-B''$ and ν_0 methods, invented by Gerő and developed by one of us (I. K.) [5] were applied for the determination of the constants of the perturbing state

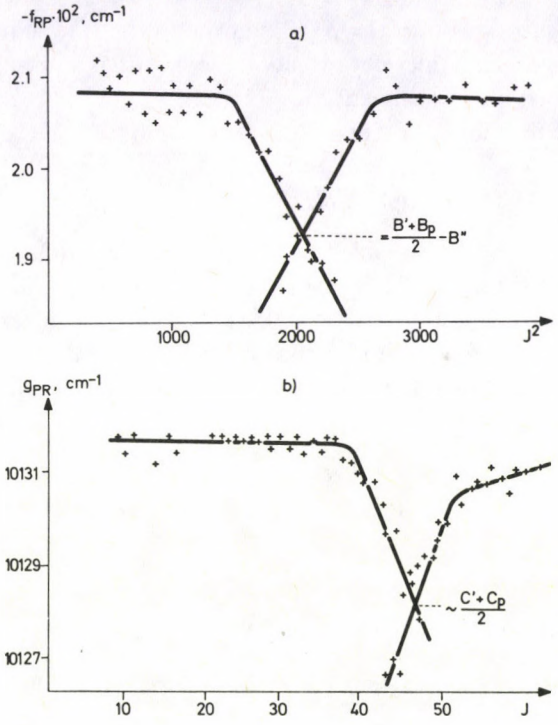

Fig. 1. Determination of the constants of the perturbing state in the $\tilde{I}$ (0–0) band.
a) $B'-B''$ curve; b) g-curves giving the spacing of the vibrational levels of the interacting states

(see Fig. 1) and the zone of perturbation. Constants of the perturbed state were calculated as usual, excepting the zone of perturbation ($37 \leqq J \leqq 53$). Provided that the D-values of the interacting states are equal, the calculation of the perturbation-matrix element H_{AB} using the formula:

$$F_{1,2} = \frac{F_A + F_B}{2} \pm \sqrt{\left(\frac{F_A - F_B}{2}\right)^2 + |H_{AB}|^2}\,, \tag{3.4}$$

where F_A, F_B and F_1, F_2 mean the unperturbed and the perturbed energies, respectively, gives $H_{AB} = 0.91 \pm 0.02$ cm^{-1}, which does not depend on J.

System II. 951 nm (0–0)

The band consists of the doubled R, Q and P branches. $I(Q) > I(P) > I(R)$. The splitting in the band can be represented by the formula

$$\begin{aligned} \Delta\nu(J) &= R_a(J-1) - R_b(J-1) = \\ &= Q_a(J) - Q_b(J) = \\ &= P_a(J+1) - P_b(J+1), \end{aligned} \tag{3.5}$$

which is valid for substates with $\Omega=2$ [6] and shows that the splitting occurs in the upper state. The theoretical interpretation of these splittings will be given in Section 4. The assumed electronic assignment $(\Omega'=2)-(\Omega''=3)$ is in agreement with the observation of the first lines, $Q(3)$ and $R(3)$. (See Section 4.)

System III. 866 nm (0–0)

The band consists of the doubled R, Q and P branches. $I(Q)>I(P)>I(R)$. The Λ-doubling is unusual, it changes the sign with increasing J. It is unlikely that both states are splitted, because in this case the difference of the line components in the P and R branches equals the difference of the Λ-type doublings of the upper and lower states, and in the Q branch it equals their sum. So when the splitting of the R_a and R_b lines changes sign and is equal to zero, the splitting in the Q branch cannot be equal to zero.

Table III

Rotational constants and band origins (in cm^{-1})***

Band [nm]	Assignment	Band origin	B'	$D'\cdot 10^7$	B''	$D''\cdot 10^7$	Remarks
986.1	I(0–0)	10132.0(1)* 10125.9(1)**	0.3408(1)* 0.3440(5)**	2.3(3)*	0.3617(1)	3.6(1)	4–4
915.8	I(1–0)	10911.33(1)	0.3373(2)	0.2(5)	0.3615(1)	2.8(6)	4–4
951.0	II(0–0)	10506.06(2)	0.3401(1)[a] 0.3403(1)[b]	2.3(2)[a] 3.5(1)[b]	0.361o(1)	2.7(2)	2–3, 3–4****
866.0	III(0–0)	11539.77(3)	0.3351(2)[a] 0.3350(2)[b]	−21.9(5)[a] −22.4(4)[b]	0.3613(1)	2.0(2)	1–2
808.3	IV(0–0)	12365.92(1)	0.3222(2)	−28.0(7)	0.3625(2)	4.2(7)	0–1
741.0	V(0–0)	13472.38(1)	0.3592(2)	6.0(7)	0.3662(1)	7.2(5)	$\Delta\Omega=1$, $\Omega''\leqq 5$
689.7	VII(0–0)	14495.89(1)	0.3560(1)	8.7(6)	0.3623(2)	3.8(5)	$\Delta\Omega=-1$, $\Omega''\leqq 7$
659.8	VIII(0–0)	15151.33(1)	0.3579(1)	1.9(5)	0.3612(1)	0.1(4)	$\Delta\Omega=1$, $\Omega''\leqq 5$
597.1	X(0–0)	16737.93(2)	0.3397(2)	−5.2(23)	0.3614(1)	1.3(8)	3–4

* constants for the perturbed state
** constants for the perturbing state
[a] — constants for the a levels
[b] — constants for the b levels
*** The numbers in parentheses are the uncertainty in the last digit that corresponds to two standard deviations.
**** The assignment 2–3 follows from the observation of the first lines, but the more probable assignment 3–4 from the Λ-type doubling analysis (See Section 4.)

As Table III shows the valuc of the centrifugal stretching constant has negative sign and differs considerably from the value calculated from the Kratzer relation. The Λ-type doubling and the anomalous behaviour of the centrifugal constant will be theoretically interpreted in Section 4.

System IV. 808.3 nm (0–0)

The band consists of the single R, Q and P branches. $I(Q)>I(P)>I(R)$. The combination defect was not detected. The observation of the unblended $Q(1)$ line and the intensity distribution led to the electronic assignment $(\Omega'=0)-(\Omega''=1)$. The regular course of the branches is violated for $J'>39$. Here, too, the centrifugal constant D shows anomalous behaviour which is theoretically interpreted in Section 4.

System V. 741.0 nm (0–0)

The band consists of the single R, Q and P branches. $I(Q)>I(R)>I(P)$. No combination defect occurs. Because of the small difference $B'-B''$ the R lines are not overlapped. The R lines presented in Table IV begin with $R(0)$. But the R lines with $0 \leqq J \leqq 4$ are not regular and seem to be doubled, so their assignments are not certain. From the analysis it follows strictly: $\Delta\Omega=+1$ and $\Omega'' \leqq 5$.

System VII. 689.7 nm (0–0)

The band consists of the single R, Q and P branches. $I(Q)>I(P)>I(R)$. The R lines are not overlapped, but they are very weak at low values of J. From the analysis it follows that $\Delta\Omega=-1$ and $\Omega'' \leqq 7$. The regular course of branches is violated at $J>39$.

System VIII. 658.8 nm (0–0)

The band consists of the single R, Q and P branches. $I(Q)>I(R)>I(P)$. The R lines are not overlapped by the other band lines. Their intensity decreases sharply at $J<5$. There are many unidentified lines in this band. It cannot be excluded that the R lines at $J<5$ which are weak and diffuse are erroneous. The rotational analysis gives $\Delta\Omega=+1$ and $\Omega'' \leqq 5$.

System X. 597.1 nm (0–0)

The band consists of the single R, Q and P branches. $I(Q)>I(P)>I(R)$. The first lines $R(4)$, $Q(4)$ and $P(4)$, which are not overlapped, imply that the band corresponds to the $(\Omega'=3)-(\Omega''=4)$ transition. The theoretical interpretation of the anomalous behaviour of the centrifugal constant D will be given in Section 4.

4. Theoretical part

a. The Λ-type doubling

The transitions $(\Omega'=2)-(\Omega''=3)$ and $(\Omega'=1)-(\Omega''=2)$ show Λ-type doublets. In order to describe the observed splittings theoretically we assume in the first step that the upper states of these transitions are a $^5\Pi_2$ and a $^5\Pi_1$ term, respectively. The formulas of the Λ-type doublets valid in the neighbourhood of Hund's case a) and b) $^5\Pi$

terms were given by Kovács and Péczeli [6]. These are for $^5\Pi_2$ and $^5\Pi_1$ terms in the neighbourhood of the Hund's case a) the following:

$$\Delta\nu(^5\Pi_2) = f(^5\Pi_2)\,(J-1)J(J+1)\,(J+2), \tag{4.1a}$$

$$\Delta\nu(^5\Pi_1) = f(^5\Pi_1)J(J+1), \tag{4.1b}$$

where

$$f(^5\Pi_2) = \frac{C_0(17Y-16)+C_1(Y-2)\,(11Y-8)+12C_2Y(Y-2)\,(Y-3)}{Y(Y-2)^2\,(Y-4)^2}, \tag{4.2a}$$

$$f(^5\Pi_1) = \frac{2C_0(5Y+6)+3C_1(Y+2)Y+C_2(Y+2)Y^2}{(Y+2)Y^2}, \tag{4.2b}$$

and $Y=A/B$ (A = multiplet splitting constant), C_0, C_1, C_2 are constants.

The tendencies of the observed splittings show that the formula (1a) may be sufficient for the state $^5\Pi_2$ but the formula (1b) for the state $^5\Pi_1$ is unsuitable. In the latter case, namely, the splitting as function of the rotational quantum number about $J\sim 50$ changes its sign. In order to explain this phenomenon we produce the Λ-type doublet formula for the $^5\Pi_1$ term valid in the intermediate case between Hund's case a) and b). and b). For a detailed treatment see [17].

The wave function of a $^5\Pi_1$ state in the intermediate case is as follows:

$$\psi(^5\Pi_J^{\pm}) = S_{3,J}\psi(^5\Pi_3^{\pm}) + S_{2,J}\psi(^5\Pi_2^{\pm}) + S_{1,J}\psi(^5\Pi_1^{\pm}) + \\ + S_{0,J}\psi(^5\Pi_0^{\pm}) + S_{-1,J}\psi(^5\Pi_{-1}^{\pm}), \tag{4.3}$$

where

$$\psi(^5\Pi_\Omega^{\pm}) = \frac{1}{\sqrt{2}}[\psi(^5\Pi_{+\Omega}) \pm \psi(^5\Pi_{-\Omega})] \qquad (\Omega = 3, 2, 1, 0, -1)$$

are the wave functions of Hund's case a) and the $S_{\Omega,J}$ transformation matrix elements have the following forms:

$$S_{3,J} = f_J(Y)\sqrt{\frac{6(J-2)\,(J-1)\,(J+2)\,(J+3)}{C_J(J)}}; \quad S_{2,J} = -(Y-3)f_J(Y)\sqrt{\frac{6(J-1)\,(J+2)}{C_J(J)}},$$

$$S_{1,J} = f_J(Y)g_J(Y)\sqrt{\frac{1}{C_J(J)}} \tag{4.4}$$

$$S_{0,J} = (Y-1)g_J(Y)\sqrt{\frac{6J(J+1)}{C_J(J)}}; \quad S_{-1,J} = g_J(Y)\sqrt{\frac{6J^2(J+1)^2}{C_J(J)}},$$

where

$$C_J(J) = 6f_J(Y)^2(J-1)\,(J+2)\,[(Y-3)^2+(J-2)\,(J+3)] + f_J(Y)^2g_J(Y)^2 + \\ + 6g_J(Y)^2J(J+1)\,[(Y-1)^2+J(J+1)], \tag{4.5}$$

$$f_J(Y) = (Y-1)\,(Y-6)-2J(J+1); \qquad g_J(Y) = (Y-3)\,(Y+2)-2(J-2)\,(J+3).$$

(Substituting $Y=0$, we get the form valid in pure Hund's case b) [7]).

In the case of $^5\Pi$ terms, perturbation by the $^5\Sigma$ terms affects the originally coinciding components differently and therefore a splitting occurs. Using the formula (4.3) the perturbation matrix elements between the $^5\Pi_J^{\pm}$ and $^5\Sigma_\Omega^{\pm}$ states will be

$$H(^5\Pi_J^{\pm}{}^5\Sigma_2^{\pm}) = S_{3,J}H(^5\Pi_3^{\pm}{}^5\Sigma_2^{\pm}) + S_{2,J}H(^5\Pi_2^{\pm}{}^5\Sigma_2^{\pm}) + S_{-1,J}H(^5\Pi_{-1}^{\pm}{}^5\Sigma_2^{\pm}),$$

$$H(^5\Pi_J^{\pm}{}^5\Sigma_1^{\pm}) = S_{2,J}H(^5\Pi_2^{\pm}{}^5\Sigma_1^{\pm}) + S_{1,J}H(^5\Pi_1^{\pm}{}^5\Sigma_1^{\pm}) + S_{0,J}H(^5\Pi_0^{\pm}{}^5\Sigma_1^{\pm}) +$$
$$+ S_{-1,J}H(^5\Pi_1^{\pm}{}^5\Sigma_1^{\pm}), \tag{4.6}$$

$$H(^5\Pi_J^{\pm}{}^5\Sigma_0^{\pm}) = S_{1,J}H(^5\Pi_1^{\pm}{}^5\Sigma_0^{\pm}) + S_{0,J}H(^5\Pi_0^{\pm}{}^5\Sigma_0^{\pm}),$$

where (see e.g. [5] pp. 54–55)

$$H(^5\Pi_3^{\pm}{}^5\Sigma_2^{\pm}) = 2\eta\sqrt{(J-2)(J+3)}; \qquad H(^5\Pi_2^{\pm}{}^5\Sigma_2^{\pm}) = 2(\xi+2\eta);$$

$$H(^5\Pi_{-1}^{\pm}{}^5\Sigma_2^{\pm}) = \mp(-1)^{\Sigma}2\eta\sqrt{(J-1)(J+2)}; \qquad H(^5\Pi_2^{\pm}{}^5\Sigma_1^{\pm}) = 2\eta\sqrt{(J-1)(J+2)};$$

$$H(^5\Pi_1^{\pm}{}^5\Sigma_1^{\pm}) = \sqrt{6}(\xi+2\eta); \tag{4.7}$$

$$H(^5\Pi_0^{\pm}{}^5\Sigma_1^{\pm}) = \mp(-1)^{\Sigma}2\eta\sqrt{J(J+1)}; \qquad H(^5\Pi_1^{\pm}{}^5\Sigma_1^{\pm}) = \mp(-1)^{\Sigma}2(\xi+2\eta);$$

$$H(^5\Pi_1^{\pm}{}^5\Sigma_0^{\pm}) = [\pm 1-(-1)^{\Sigma}]\eta\sqrt{J(J+1)}; \qquad H(^5\Pi_0^{\pm}{}^5\Sigma_0^{\pm}) = [\pm 1-(-1)^{\Sigma}]\sqrt{3}(\xi+2\eta)$$

and $\xi = (AL_\xi)(^5\Pi^5\Sigma)$, $\eta = (BL_\xi)(^5\Pi^5\Sigma)$. A denotes the coefficient of the spin-orbit coupling, B is the rotational constant, $L_\xi(^5\Pi^5\Sigma)$ denotes the matrix element of the component of the electronic orbital angular momentum in the ξ direction, perpendicular to the molecular axis for the stationary molecule. On the right sides of the formulae (4.7) the upper or lower sign are to be used according to the $^5\Pi^+$ or the $^5\Pi^-$ term, respectively, and in the exponent $\Sigma = 0$ or 1 according as the perturbing $^5\Sigma$ term is Σ^+ or Σ^-. The spin–spin and spin–rotation interactions are neglected here.

If the multiplet spacing is large as compared to the spacing of the components, the perturbation calculation for non-degenerate systems in the first approximation yields for the perturbed energies:

$$F^p(^5\Pi_J^{\pm}) = F(^5\Pi_J^{\pm}) + \sum_k \frac{1}{\nu(^5\Pi^5\Sigma_k)}\left[|H(^5\Pi_J^{\pm}{}^5\Sigma_{2,k}^{\pm})|^2 + \right.$$
$$\left. + |H(^5\Pi_J^{\pm}{}^5\Sigma_{1,k}^{\pm})|^2 + |H(^5\Pi_J^{\pm}{}^5\Sigma_{0,k}^{\pm})|^2\right]. \tag{4.8}$$

Written out in detail the Λ-type doublet assumes the form instead of (4.1b)

$$\Delta\nu(^5\Pi_J) = F^p(^5\Pi_J^+) - F^p(^5\Pi_J^-) =$$
$$= \frac{f_J(Y)g_J(Y)}{C_J(J)}\left\{2C_0\left[2g_J(Y) + 3\frac{g_J(Y)}{f_J(Y)}(Y-1)^2\right] + 3C_1[(Y-1)g_J(Y) - \right.$$
$$-2(Y-3)(J-1)(J+2)] +$$
$$\left. + C_2[12((J-2)(J+3)-(Y-3)(Y-1))(J-1)(J+2) + f_J(Y)g_J(Y)\right\}J(J+1), \tag{4.9}$$

where

$$C_0 = 12\sum_k \frac{(-1)^\Sigma(\xi+2\eta)^2}{\nu(^5\Pi^5\Sigma_k)}; \qquad C_1 = 32\sum_k \frac{(-1)^\Sigma(\xi+2\eta)\eta}{\nu(^5\Pi^5\Sigma_k)},$$

$$C_2 = 8\sum_k \frac{(-1)^\Sigma\eta^2}{\nu(^5\Pi^5\Sigma_k)}. \tag{4.10}$$

The last member of (4.9) gives a possibility for the change of sign in the Λ-type doublet. Therefore neglecting the effects of the terms containing the constants C_0, C_1 and assuming $\Delta\nu(^5\Pi_J)\,(J\sim 50)=0$ we obtain from (4.9) $Y=195\ \mathrm{cm}^{-1}$. Substituting this value in the formula (4.9) and fitting to the observed Λ-type splitting we get $C_2=[2.05\pm 0.10]\cdot 10^{-4}\ \mathrm{cm}^{-1}$ and the solid line curve in Fig. 2. The agreement between the observed and calculated splittings is fairly good, apart from a short region between $J=20$ and 30.

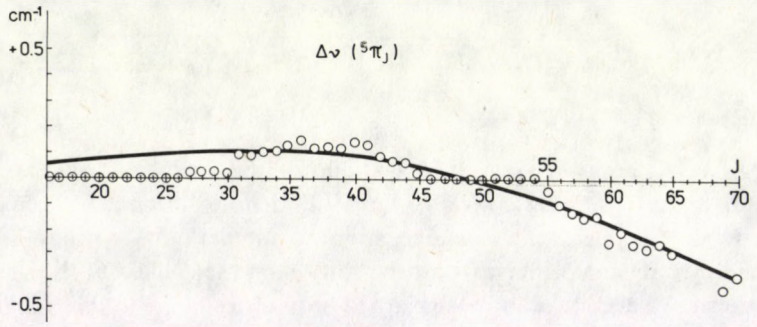

Fig. 2. The mean values of the Λ-type doubling observed in the P, Q and R branches on the III (0–0) band. In Eq. (4.9) of the theoretical curve $C_0=C_1=0$, $C_2=[2.05\pm 0.10]\cdot 10^{-4}\ \mathrm{cm}^{-1}$, $Y=195\ \mathrm{cm}^{-1}$. (RMS $=0.045\ \mathrm{cm}^{-1}$)

When we suppose moreover that the upper state of the $(\Omega'=2)-(\Omega''=3)$ transition is another component of the same $^5\Pi$ state and substituting in (4.2a) the values of C_2 and Y given above, we get

$$f(^5\Pi_2) = \frac{12C_2(Y-3)}{(Y-2)(Y-4)^2} \sim 6.71\cdot 10^{-8}\ \mathrm{cm}^{-1}. \tag{4.11a}$$

Using this value the formula (4.1a) yields a curve near to the solid line curve in Fig. 3 for the Λ-type doubling of the $^5\Pi_2$ state.

This agreement is, however, illusory. This supposition namely contradicts the fact that in the observed region of the rotational quantum number J with the value Y given before the condition of the application of the formula (4.1a) valid in the neighbourhood of Hund's case a) is not fulfilled that is $Y \gg 2J$ is not valid. Therefore, similarly as for the $^5\Pi_1$ term, the Λ-type doublet formula for the $^5\Pi_2$ term valid in the intermediate case between Hund's case a) and b) should also be produced.

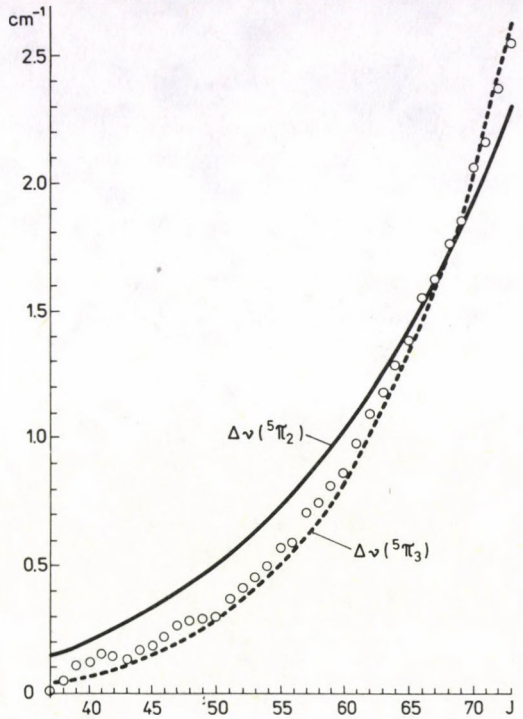

Fig. 3. Mean values of the Λ-type doubling observed in the P, Q and R branches on the II (0–0) band. In Eq. (4.11d) of the solid line curve $Y \geqq 1000\ \mathrm{cm}^{-1}$ and the constants C_0, C_1, C_2 should be chosen suitably. The same curve can be obtained from Eq. (4.1a) with $f(^5\Pi_2) = [7.69 \pm 0.13] 10^{-8}\ \mathrm{cm}^{-1}$ (RMS = 0.11 cm^{-1}). In Eq. (4.11e) of the dashed line curve $f(^5\Pi_3) = [1.70 \pm 0.01] \cdot 10^{-11}\ \mathrm{cm}^{-1}$ (RMS = 0.05 cm^{-1})

In a manner similar to that for the $^5\Pi_1$ term it is necessary to give at first the forms of the transformation matrix element valid for the $^5\Pi_2$ term in the intermediate case. These are

$$S_{3,J+1} = -f_{J+1}(Y)\sqrt{\frac{8(J-2)(J-1)(J+2)(J+3)}{C_{J+1}(J)}};$$

$$S_{2,J+1} = (Y-8-u^-)f_{J+1}(Y)\sqrt{\frac{2(J-1)(J+2)}{C_{J+1}(J)}};$$

$$S_{1,J+1} = f_{J+1}(Y)g_{J+1}(Y)\sqrt{\frac{3}{C_{J+1}(J)}}; \qquad (4.11b)$$

$$S_{0,J+1} = (Y+4+u^+)g_{J+1}(Y)\sqrt{\frac{2J(J+1)}{C_{J+1}(J)}};$$

$$S_{-1,J+1} = g_{J+1}(Y)\sqrt{\frac{8J^2(J+1)^2}{C_{J+1}(J)}},$$

where

$$u^{\pm}=\sqrt{(Y-2)^2+4J(J-2)}\pm(Y-2);f_{J+1}(Y)=Yu^{+}-4J;\ g_{J+1}(Y)=$$
$$=(Y-4)u^{-}+4(J-2);\ C_{J+1}(J)=2f_{J+1}(Y)^2(J-1)(J+2)[(Y-8-u^{-})^2+$$
$$+4(J-2)(J+3)]+3f_{J+1}(Y)^2g_{J+1}(Y)^2+$$
$$+2g_{J+1}(Y)^2J(J+1)[(Y+4+u^{+})^2+4J(J+1)]. \tag{4.11c}$$

The Λ-type doublet formula for the $^5\Pi_2$ term derived for the intermediate case by the procedure treated before, making use of the transformation matrix elements (4.11b), is the following:

$$\Delta\nu(^5\Pi_{J+1})=\frac{f_{J+1}(Y)g_{J+1}(Y)}{C_{J+1}(J)}\left\{2C_0\left[4g_{J+1}(Y)+\frac{g_{J+1}(Y)}{f_{J+1}(Y)}(Y+4+u^{+})^2\right]+\right.$$
$$+C_1[3(Y+4+u^{+})g_{J+1}(Y)+4(Y-8-u^{-})(J-1)(J+2)]+$$
$$+C_2[4((Y-8-u^{-})(Y+4+u^{+})-4(J-2)(J+3))](J-1)(J+2)+$$
$$\left.+3f_{J+1}(Y)g_{J+1}(Y)\right\}J(J+1). \tag{4.11d}$$

Putting in formula (4.11d) for C_0, C_1, C_2 and Y the values determined before for the $^5\Pi_1$ term, we get a substantial deviation from the observed splittings, in particular for higher J values (e.g. $\Delta\nu(70)=0.66$ cm^{-1} instead of 2.07 cm^{-1}). The investigation of the formula (4.11d) shows that in the case of $Y<1000$ cm^{-1} it is impossible to approach the observed splittings with C_0, C_1, C_2 values of the same sign. On the other hand, if $Y\geqq 1000$ cm^{-1} the problem will be undetermined for the constants Y, C_0, C_1, C_2 that is to say there will be an infinite number of possibilities for the suitable constants and in the case of any arbitrary selection of the suitable constants we get the solid line curve as in Fig. 3. In the case of these relatively high values of Y, namely, the condition of the application of the formula (4.1a) valid in the neighbourhood of Hund's case a) is more or less fulfilled. That means that in the case of a Λ-type doublet of this $^5\Pi_2$ term the formula (4.1a) valid in the neighbourhood of Hund's case a) is applicable and gives a good approximation, if $Y\geqq 1000$ cm^{-1} with $f(^5\Pi_2)=[7.69\pm 0.13]10^{-8}$cm^{-1}. It seems then that this $^5\Pi_2$ term does not belong to the same electronic state as the $^5\Pi_1$ term discussed before. On the other hand, to determine the exact numerical values of the constants Y, C_0, C_1, C_2 we should know the Λ-type doublings of the other components of the same multiplet state belonging to this $^5\Pi_2$ term.

In any case a much better agreement can be obtained if $\Omega'=3$ would be supposed instead of $\Omega'=2$ with the aid of the following formula valid in the neighbourhood of Hund's case a) [6]:

$$\Delta\nu(^5\Pi_3)=f(^5\Pi_3)(J-2)(J-1)J(J+1)(J+2)(J+3), \tag{4.11e}$$

where $f(^5\Pi_3)=[1.70\pm0.01]\cdot 10^{-11}$ cm^{-1} (for the detailed form of $f(^5\Pi_3)$ see [6]). In Fig. 3 the dashed line shows the theoretical calculated values according to (4.11e). That means: in spite of the observed first lines (where, however, the $P(3)$ line was not detected, the $Q(3)$ line coincides with the $R(32)$ line and $R(3)$ can be accidental) a $^5\Pi_3\rightarrow{}^5\Delta_4$ transition is more probable than a $^5\Pi_2\rightarrow{}^5\Delta_3$ transition.

b. The anomalous D-values

In the upper states of $(\Omega'=1)-(\Omega''=2)$, $(\Omega'=0)-(\Omega''=1)$ and $(\Omega'=3)-(\Omega''=4)$ transitions the centrifugal constants D have opposite signs and in the first two cases anomalously high values ($-22.9\cdot 10^{-7}$ cm^{-1}, $-28.0\cdot 10^{-7}$ cm^{-1} and $-5.2\cdot 10^{-7}$ cm^{-1}). This phenomenon can be interpreted as a perturbation of another term where, though the perturbing term lies sufficiently far from the perturbed term so as not to cross it, it is nevertheless near enough for the variation of term distances with the rotational quantum number not to be negligible in comparison to the distance of the perturbing term [16]. According to the well known perturbation calculation the perturbed term will be in the first approximation

$$F^p_\Omega(J)=F_\Omega(J)+\frac{|H(\Omega,\Omega')|^2}{\nu(\Omega,\Omega')}. \tag{4.12}$$

In this case in the first approximation it can be written

$$\nu(\Omega,\Omega')=\nu+(B_\Omega-B_{\Omega'})J(J+1), \tag{4.13}$$

where the distance of the vibrational levels is denoted now by ν and B_Ω and $B_{\Omega'}$ denote the rotational constants of the perturbed and perturbing terms, respectively.

Using (4.13) expanding the reciprocal values occurring in (4.12) we obtain

$$\frac{1}{\nu(\Omega,\Omega')}\sim\frac{1}{\nu}\left[1-\frac{(B_\Omega-B_{\Omega'})J(J+1)}{\nu}\right]. \tag{4.14}$$

Let $\Omega'=\Omega\pm1$ so that $\Delta\Lambda=\pm1$, $\Delta\Sigma=0$ and $\Lambda\neq0$, $\Lambda'\neq0$, then the perturbation matrix elements have the following form [5]:

$$H(\Omega,\Omega\pm1)=2\eta\sqrt{J(J+1)-\Omega(\Omega\pm1)} \tag{4.15}$$

and the perturbed term will be in the first approximation

$$F^p_\Omega(J)=F_0+B_\Omega J(J+1)-D_\Sigma J^2(J+1)^2+\frac{4\eta^2}{\nu}[J(J+1)-\Omega(\Omega\pm1)].$$

$$\left[1-\frac{(B_\Omega-B_{\Omega\pm1})J(J+1)}{\nu}\right]=\bar{F}_0+\bar{B}_\Omega J(J+1)-\bar{D}_\Omega J^2(J+1)^2, \tag{4.16}$$

where

$$\bar{F}_0 = F_0 - \frac{4\eta^2}{\nu}\Omega(\Omega\pm 1);\ \bar{B}_\Omega = B_\Omega + \frac{4\eta^2}{\nu}\left[1 + \frac{\Omega(\Omega\pm 1)(B_\Omega - B_{\Omega\pm 1})}{\nu}\right], \quad (4.17)$$

$$\bar{D}_\Omega = D_\Omega + \frac{4\eta^2}{\nu^2}(B_\Omega - B_{\Omega\pm 1}).$$

The sign of the last term in the expression of $\bar{D}_\Omega$ depends on the sign of $B_\Omega - B_{\Omega\pm 1}$, therefore when $B_{\Omega\pm 1} > B_\Omega$ it can be negative and of greater absolute value as compared to D_Ω. This gives a possible explanation for the negative $\bar{D}_\Omega$ values.

Discussion

Table III gives the molecular constants derived from the rotational analysis. It is readily seen that the transitions analyzed have no common upper states. However, it cannot be excluded that the systems I and X with assumed $\Omega'' = 4$ (the combination differences are equal up to $J = 31$ within the error limit of measurements) and the systems IV and VII have the lower states in common. So the analysis has shown that the NdO molecule has at least 4 states which give rise to absorption bands.

Table IV

Wavenumbers of band lines of NdO

System I Band 986.1 nm			
J	*R*	*Q*	*P*
4		10131.58	
5	10135.50	31.37	
6	35.96	31.12	10127.00
7	36.36	30.82	26.12
8	36.69		
9	37.00		24.07
10	37.26		22.93*
11	37.48		21.86*
12	37.60		20.62
13	37.78		
14	37.96h		18.07
15	37.96h		16.83
16	37.96h		15.50
17	37.96h		14.08
18			12.64*
19	37.78		11.20*
20	37.60		09.69*
21	37.39		08.14
22	37.17		06.54
23	36.84		04.89
24	36.55		03.19
25	36.17		01.50
26	35.78		10099.72

Table IV (cont.)

System I Band 986.1 nm				
J	*R*		*P*	
27	10135.32		10097.91	
28	34.85		96.08	
29	34.32		94.17	
30	33.75		92.26	
31	33.14		90.26	
32	32.48		88.27	
33	31.79		86.21	
34	31.07		84.15	
35	30.29		82.00	
36	29.47		79.84	
37	28.63		77.60	
38	27.74		75.33	
39	26.85		73.06	
40	25.89		70.75	
41	24.93	22.93*	68.38	
42	23.93	22.01	66.03	
43	22.93*	21.06	63.60	61.58
44	21.86	20.02	61.17	59.29
45	20.82	18.97	58.73	56.87
46	19.75	17.82	56.28	54.44
47	18.69	16.60	53.83	51.98
48	17.58	15.33	51.32	49.36
49		14.01	48.78	46.71
50		12.64		44.01
51		11.20		41.28
52		09.69		38.45
53		08.20		35.63
54		06.62		32.71
55		04.98		29.77
56		03.32		26.78
57		01.61		23.75
58		10099.85		20.66
59		98.07		17.52
60		96.21		14.36
61		94.30		11.15
62		92.38		07.90
63		90.41		04.62

System I Band 916.8 nm		
J	*R*	*P*
4	10914.20*	
5	14.64*	10907.28
6	15.04*	06.26
7	15.35*	05.23
8	15.65*	04.18
9	15.89	03.09

Table IV (cont.)

System I Band 916.8 nm		
J	*R*	*P*
10	10916.08	10901.94
11	16.34h	00.72
12	16.34h	10899.47
13	16.34h	98.17
14	16.34h	96.82
15	16.34h	95.41
16	16.23	93.96
17	16.23**	92.48
18	15.95	90.93
19	15.65*	89.51**
20	15.35*	87.71
21	15.04*	86.01
22	14.64*	84.29
23	14.20*	82.52
24	13.74	80.69
25	13.22	78.82
26	12.64	76.90
27	12.05	74.94
28	11.37	72.93
29	10.67	70.88
30	09.93	68.78
31	09.12	66.64*
32	08.28	64.44
33	07.40	62.19
34	06.45	59.92
35	05.49	57.59
36	04.47	55.24
37	03.40	52.80
38	02.28	50.36
39	01.13	47.83
40	10899.91	45.29
41	98.68	42.74**
42	97.39	40.03

System II Band 951.0 nm						
J	R_a	R_b	Q_a	Q_b	P_a	P_b
3	10508.59	10508.59	10505.88*	10505.88*		
4	09.09	09.09	05.64	05.64	10502.88	10502.88
5	09.53	09.53	05.48	05.48	01.99	01.99
6	09.99	09.99	05.14*	05.14*	01.07	01.07
7	10.23*	10.23*	04.82	04.82	00.03	00.03
8	10.59*	10.59*	04.49	04.49	10499.05	10499.05
9	10.88*	10.88*	04.12	04.12	97.94*	97.94*
10	11.16*	11.16*	03.68	03.68	96.88	96.88
11	11.37*	11.37*	03.22	03.22	95.73	95.73
12	11.53*	11.53*	02.71*	02.71*	94.53	94.53

Table IV (cont.)

System II Band 951.0 nm						
J	R_a	R_b	Q_a	Q_b	P_a	P_b
13	10511.69	10511.69	10502.18	10502.18	10493.29	10493.29
14	11.81[h]	11.81[h]	01.56	01.56	92.03	92.03
15	11.81[h]	11.81[h]	00.89*	00.89*	90.73	90.73
16	11.81[h]	11.81[h]	00.21	00.21	89.37	89.37
17	11.81[h]	11.81[h]	10499.49	10499.49	87.97	87.97
18	11.69	11.69	98.72*	98.72*	86.53	86.53
19	11.53*	11.53*	97.94*	97.94*	85.04	85.04
20	11.37*	11.37*	97.07	97.07	83.49*	83.49*
21	11.16*	11.16*	96.18	96.18	81.92	81.92
22	10.88*	10.88*	95.25*	95.25*	80.30	80.30
23	10.59*	10.59*	94.26*	94.26*	78.65	78.65
24	10.23*	10.23*	93.24	93.24	76.93	76.93
25	09.84	09.84	92.18	92.18	75.17	75.17
26	09.40	09.40	91.07	91.07	73.39	73.39
27	08.93	08.93	89.92	89.92	71.55	71.55
28	08.41	08.41	88.71	88.71	69.68	69.68
29	07.85	07.85	87.50*	87.50*	67.75	67.75
30	07.22	07.22	86.20	86.20	65.80	65.80
31	06.59	06.59	84.87	84.87	63.81	63.81
32	05.88*	05.88*	83.49*	83.49*	61.77	61.77
33	05.14*	05.14*	82.07	82.07	59.63	59.63
34	04.34	04.34	80.61	80.61	57.55	57.55
35	03.51	03.51	79.11	79.11	55.34	55.34
36	02.71	02.71	77.56	77.56	53.11*	53.11*
37	01.81	01.75	75.96	75.96	50.80*	50.80*
38	00.89	00.73	74.36	74.36	48.53	48.50
39		10499.77	72.70	72.61	46.22	46.14
40		98.72*	71.00*	70.87	43.83	43.75
41	10497.69	97.51	69.26	69.11	41.41	41.30
42	96.61	96.46	67.43	67.30	38.95	38.83
43		95.25*	65.59	65.46	36.42	36.30
44	94.26*	94.04	63.72	63.56	33.87	33.73
45	92.99	92.76	61.77	61.60	31.26	31.09
46	91.70	91.40	59.83	59.63	28.61	28.44
47	90.36	90.06	57.81	57.55	25.95	25.73
48	88.97	88.71	55.76	55.49	23.23	22.97
49	87.50*	87.24	53.67	53.36	20.45	20.17
50	86.08	85.72	51.45	51.15	17.64	17.33
51	84.52		49.28	48.93	14.81	14.47
52	83.04	82.60	47.09	46.68	11.91	11.51
53	81.42	80.93	44.84	44.38	08.96	08.55
54	79.83	79.23	42.56	42.02	06.00*	05.54
55	78.12	77.56	40.19	39.64	02.96	02.48
56	76.42	75.67	37.82	37.20	10399.92	10399.35
57	74.62	73.92	35.38	34.71	96.82	96.20
58	72.84	72.03	32.91	32.16	93.68	92.98
59	71.00*	70.13	30.41	29.58	90.51	89.72
60	69.11	68.12	27.84	26.97	87.20	86.39
61		66.13	25.25	24.27	83.96	83.08
62	65.27	64.08	22.63	21.53	80.67	79.69
63			19.96	18.78	77.36	76.27

Table IV (cont.)

System II Band 951.0 nm

J	R_a	R_b	Q_a	Q_b	P_a	P_b
64	10461.22	10459.83	10417.25	10415.97	10373.97	10372.81
65	59.91	57.55	14.47	13.09	70.54	69.25
66	57.00	55.34	11.69	10.17	67.07	65.66
67		53.11*	08.84	07.24	63.58	62.07
68	52.62	50.80*	06.00*	04.23	60.03	58.39
69	50.33	48.23	03.09	01.19		
70	48.00	45.87	00.10	10398.07		
71		43.36	10397.13	94.93		
72	43.36		94.12	91.74		
73			91.04	88.48		

System III Band 866.0 nm

J	R_a	R_b	Q_a	Q_b	P_a	P_b
3					11537.57*	11537.57*
4					36.63	36.63
5			11539.06	11539.06	35.69*	35.69*
6	11543.42*	11543.42*	38.69	38.69	34.70*	34.70*
7	43.68*	43.68*	38.34*	38.34*	33.65	33.65
8	43.93*	43.93*	37.91	37.91	32.57*	32.57*
9	44.09*	44.09*	37.43	37.43	31.42	31.42
10	44.28*	44.28*	36.88*	36.88*	30.20	30.20
11	44.38h	44.38h	36.31	36.31	28.89	28.89
12	44.38h	44.38h	35.69*	35.69*	27.67	27.67
13	44.38h	44.38h	34.99	34.99	26.30	26.30
14	44.38h	44.38h	34.30	34.30	24.92	24.92
15	44.28*	44.28*	33.52	33.52	23.47	23.47
16	44.09*	44.09*	32.69*	32.69*	21.96	21.96
17	43.93*	43.93*	31.82	31.82	20.40*	20.40*
18	43.68*	43.68*	30.92	30.92	18.83*	18.83*
19	43.42*	43.42*	29.97	29.97	17.20*	17.20*
20	43.12	43.12	28.98*	28.98*	15.53*	15.53*
21	42.78	42.78	27.95	27.95	13.80	13.80
22	42.38	42.38	26.87*	26.87*	12.06	12.06
23	41.96	41.96	25.77	25.77	10.30	10.30
24	41.52	41.52	24.64	24.64	08.46	08.46
25	41.03	41.03	23.47*	23.47*	06.60	06.60
26	40.50	40.50	22.27*	22.27*	04.71	04.71
27	39.97	39.97	21.04*	20.99*	02.77	02.77
28	39.43	39.43	19.79*	19.74	00.81	00.81
29	38.87	38.87	18.49	18.44	11498.84	11498.84
30	38.34*	38.16	17.20*	17.13	96.82	96.82
31		37.57*	15.86	15.87	94.78	94.78
32		36.88*	14.49	14.42	92.70	92.70
33		36.13	13.11	13.03	90.67	90.59
34	35.53	35.40	11.72	11.61	88.58	88.47
35	34.85	34.70	10.30	10.17	86.45	86.37

Table IV (cont.)

System III Band 866.0 nm						
J	R_a	R_b	Q_a	Q_b	P_a	P_b
36	11534.12	11534.03	11508.88	11508.76	11484.32	11484.22
37		33.30	07.44	07.32	82.19	82.04*
38	32.69*	32.57	05.99	05.87	80.02	79.90
39	31.93	31.82	04.55	04.43	77.88	77.75
40	31.20	31.08	03.09	02.96	75.70*	
41	30.48	30.33	01.63	01.51	73.54	73.37
42	29.71	29.62	00.19	00.08	71.36	71.22
43	28.98*	28.89	11498.72	11498.60	69.12*	69.12*
44	28.23	28.23	97.27	97.19		
45	27.51	27.51	95.83	95.76	64.87	64.87
46	26.87*	26.87*	94.37	94.37	62.62	62.62
47	26.14	26.14	92.96	92.96	60.52	60.52
48	25.50	25.50	91.56	91.56	58.37	58.37
49	24.81	24.81	90.17	90.17	56.26	56.26
50	24.21	24.21	88.80	88.80	54.14	54.14
51	23.47	23.47	87.48	87.48	52.07	52.07
52	22.80	22.80	86.10	86.10	50.02	50.02
53	22.27*	22.27*	84.65	84.65	47.86	47.86
54	21.54	21.54	83.30	83.30	45.74	45.74
55	20.99*	21.04*	81.99	82.04	43.72	43.72
56	20.40		80.66	80.81	41.66	41.66
57	19.79*	19.94	79.36	79.49		
58	19.12	19.26	78.07			
59		18.83*	76.76			
60	17.99	18.15	75.45	75.70		
61	17.36	17.57	74.14	74.39		
62			72.81	73.10		
63	16.17	16.44				
64	15.53*	15.78	70.12			
65	14.96	15.25	68.84	69.12*		
66		14.63				
67		14.03				
68		13.42				
69	12.41	12.83				
70	11.85	12.22				
71		11.61				

Table IV (cont.)

System IV Band 808.3 nm			
J	*R*	*Q*	*P*
1	12367.19*	12365.86	12365.27*
2	67.63*	65.69	64.45
3	68.05*	65.50*	63.52
4	68.32*	65.27*	62.49
5	68.57*	64.74*	61.51*
6	68.73*	64.27	60.29*
7	68.90h	63.72	59.18*
8	68.90h	63.11*	57.90
9	68.73*	62.26*	56.52
10	68.57*	61.51*	55.08*
11	68.32*	60.60	53.54
12	68.05*	59.65	51.92
13	67.63*	58.63	50.20*
14	67.19*	57.53	48.51
15	66.74	56.36	46.68
16	66.16	55.08*	44.77
17	65.50*	53.81	42.85*
18	64.74*	52.43	40.76
19	63.96	50.98	38.68
20	63.11*	49.49	36.51
21	62.26*	47.92	34.28
22	61.26	46.30	31.99
23	60.29*	44.66	29.68
24	59.18*	42.85*	27.25
25	58.06	41.07	24.81*
26	56.84	39.22*	22.26
27	55.62	37.33	19.70
28	54.33	35.35	17.07
29	53.02	33.37	14.39
30	51.62	31.29	11.67
31	50.20*	29.18	08.89
32	48.74	27.04	06.07
33	4716	24.81*	03.14
34	45.58	22.56	00.26
35	44.01	20.29	12297.28
36	42.36	17.97	94.29
37	40.76	15.65	91.23
38	39.22*	13.33	88.28
39		11.02	85.15

Table IV (cont.)

System V Band 741.0 nm			
J	*R*	*Q*	*P*
0	13473.14		
1	73.72		
2	74.47		
3	75.22		
4	75.94		
5	76.54		
6	77.16		
7	77.76	13472.08	
8	78.38	71.95	
9	78.97	71.82	
10	79.55	71.66	
11	80.10	71.47	
12	80.66	71.34	
13	81.16	71.14	
14	81.70	70.94	
15	82.21	70.74	13460.04
16	82.70	70.49	59.05
17	83.17	70.26	58.00*
18	83.67	70.01	57.11
19	84.10	69.77	56.10
20	84.54	69.47	55.15*
21	84.95	69.18	54.15
22	85.42	68.88	53.12
23	85.79	68.56	52.10
24	86.13	68.23	51.00
25	86.51	67.87	49.95
26	86.87	67.51	48.86
27	87.22	67.16	37.66
28	87.59	66.82	46.72
29	87.92	66.46	45.76
30	88.24	66.04	44.65
31	88.53	65.61	43.42
32	88.80	65.20	42.22
33	89.06	64.75	41.16
34	89.36	64.31	39.91
35	89.59	63.86	38.81
36	89.83	63.39	37.66
37	90.05	62.89	36.44
38	90.26	62.41	35.21
39	90.45	61.86	34.04
40	90.60	61.34	32.75
41	90.73*	60.79	31.51
42	90.89h	60.21	30.23
43	90.89h	59.61	28.99
44	90.73*	58.90	27.63
45	90.73*	58.00*	26.19
46	90.73*	57.33	24.56
47	90.73*	56.56	23.18
48	90.73*	55.89	21.68
49	90.73*	55.15*	20.24**
50		54.58	18.87
51			17.63

Table IV (cont.)

System VII Band 689.7 nm			
J	*R*	*Q*	*P*
7	14501.22		
8	01.90		
9	02.46		
10	02.99		
11		14495.04	14487.17*
12	04.16	94.92	86.33
13	04.69	94.77	85.49*
14	05.25	94.56	84.61
15	05.79	94.39	83.73
16	06.25	94.19	82.80
17	06.78	93.96	81.90
18		93.73	80.90
19	07.69	93.49	79.99
20	08.12	93.21	79.01
21	08.55	92.92	77.99
22	08.97	92.65	77.01
23	09.31	92.32	76.01
24	09.75	92.00	74.96
25	10.11	91.66	73.93
26	10.47	91.29	72.86
27	10.74	90.90	71.78
28	11.08	90.50	70.68
29	11.32	90.10	69.52
30	11.64	89.66	68.48
31	11.81	89.19	67.23
32	12.09	88.72	66.07
33	12.35	88.24	64.88
34	12.51	87.70	63.65
35	12.68	87.17*	62.43
36	12.80	86.65	61.18
37	12.96	86.07	59.90
38	13.02	85.49*	58.60
39		84.82	57.34

System VIII Band 659.8 nm			
J	*R*	*Q*	*P*
2	15153.47		
3	54.15		
4	54.85		
5	55.54		
6	56.22		
7	56.88		
8	57.56		
9	58.18		
10	58.85		
11	59.47		
12	60.11		

Table IV (cont.)

System VIII Band 659.8 nm			
J	*R*	*Q*	*P*
13	15160.73		15141.36
14	61.34		40.61
15	61.98		39.73
16	62.55		38.89
17	63.18		38.19
18	63.80	15150.16	37.30
19	64.36	49.97	36.49
20	64.88	49.86	35.65
21	65.50	49.70	34.82
22	65.98	49.54	33.83
23	66.54	49.38	32.99
24	67.11		32.05
25	67.60	49.13	31.15
26	68.14	48.82	30.19
27	68.66	48.65	29.32
28	69.23	48.40	28.46
29	69.75	48.30	27.49
30	70.19	48.04	26.53
31	70.67	47.80	25.60
32	71.17	47.58	24.67
33	71.65	47.31	23.75
34	72.13	47.05	22.71
35	72.53	46.81	21.75
36	72.97	46.50	20.75
37	73.34	46.24	19.78
38	73.78	45.88	18.76
39	74.20	45.57	17.75
40	74.58	45.28	16.73
41	74.91	44.94	15.73
42	75.37	44.59	14.61
43	75.50	44.16	13.51
44			12.39
45			11.18

System X Band 597.1 nm			
J	*R*	*Q*	*P*
4	16740.89*	16737.43	16734.73
5	41.37*	37.24	33.85
6	41.81	37.02	32.90
7	42.20	36.72	31.96
8	42.56*	36.38	30.91
9	42.81*	36.01	29.84*
10	43.07*	35.56	28.77
11	43.29*	35.16	27.63
12	43.46*	34.64	26.47
13	43.59*	34.05	25.21*
14	43.64h	33.47	23.95
15	43.64h	32.82	22.64
16	43.64h	32.09	21.25*
17	43.59*	31.36	19.80

Table IV (cont.)

System X Band 597.1 nm			
J	*R*	*Q*	*P*
18	16743.59*	16730.63	16718.39
19	43.46*	29.84*	16.88
20	43.29*	29.00	15.38
21	43.07*	28.06	13.80
22	42.81*	27.15	12.19
23	42.56*	26.18	10.52
24	42.28	25.21*	08.87
25	42.01	24.20	07.16
26	41.63	23.18	05.43
27	41.37*	22.14	03.70
28	41.10	21.15	01.94
29	40.89*	20.14	00.19
30		19.21	16698.50
31			96.82

All the bands in the visible region reveal perturbations: the picking out of branches with J values larger than those indicated in Table IV is complicated by very strong perturbations in the upper states.

The results of this work and the experimental data recently obtained on the spectrum of FdO [8, 9] apparently contradict the wide-spread idea that the electronic states of the molecules containing rare earth elements must be necessarily in Hund's case c) [10, 11].

References

1. Л. А. Каледин, Е. А. Шенявская, Опт. и спектр., **47,** 1015, 1979.
2. E. A. Shenyavskaya, I. V. Egorova and V. N. Lupanov, J. Mol. Spectr., **47,** 355, 1973.
3. A. Gatterer, J. Junkes and E. W. Salpeter, "Molecular spectra of metallic oxides", Ed. Specola Vaticana, 1957.
4. R. L. DeKock and W. Weltner, J. Phys. Chem., **75,** 514, 1971.
5. I. Kovács, Rotational Structure in the Spectra of Diatomic Molecules, Akadémiai Kiadó, Budapest and Adam Hilger Ltd. London, 1969.
6. I. Kovács and I. Péczeli, J. Mol. Spectr., **88,** 264, 1981.
7. I. Kovács and M. I. M. El-Agrab, Acta Phys. Hung., **43,** 185, 1977.
8. B. R. Yadav and F. B. Rai, J. Mol. Spectr **89,** 1, 1981.
9. R. J. Van Zee, R. F. Ferrante, K. J. Zeringue and W. Weltner, J. Chem. Phys., **75,** 5297, 1981.
10. M. Dulick, R. W. Field, J. C. Beaufils and J. Schamps, J. Mol. Spectr., **87,** 278, 1981.
11. Л. Д. Ландау, Е. М. Лифшиц, Квантовая механика нерелятивистская теория, Москва, 1963, стр. 363.
12. R. F. Barrow, R. M. Clements, S. M. Harris and P. P. Jenson, Astrophys. J., **229,** 439, 1979.
13. C. Linton, M. Dulick, R. W. Field, P. Carette and R. F. Barrow, J. Chem. Phys., **74,** 189, 1981.
14. M. Dulick, R. W. Field and J. Cl. Beaufils, J. Mol. Spectr., **87,** 268, 1981.
15. E. A. Shenyavskaya and L. A. Kaledin, J. Mol. Spectr., **91,** 22, 1982.
16. I. Kovács, Proc. Roy. Ir. Acad., **60A,** 15, 1959.
17. I. Kovács, J. Mol. Spectr. **98,** 41, 1983.

Acta Physica Hungarica 54 (1—2), pp. 213—215 (1983)

SHORT COMMUNICATION

MHD NATURAL CONVECTION AND MASS TRANSFER THROUGH A HORIZONTAL POROUS CHANNEL

A. RAPTIS

Department of Mechanics, School of Physics, University of Ioannina
Ioannina, Greece

(Received 16 November 1981)

The study of the effects of natural convective (free convection) flow through a porous medium plays an important role in many industrial processes. For this reason Raptis et al. [3, 4] recently studied the free convection and mass transfer through a porous medium bounded by a infinite vertical plate.

The flow of a viscous, incompressible, electrically conducting fluid between two infinite parallel plates in the presence of a uniform transverse magnetic field was studied by Katagiri [1]. The motion of the fluid is induced by the impulsive motion of one of the plates. Muhuri [2] extended the study of the above problem when one of the plates starts moving with a uniform acceleration and there is a uniform suction and injection at the plates.

Recently Raptis and Tzivanidis [5] studied the mass transfer effects on the flow past an accelerated infinite vertical plate with variable heat flux on the plate. Also Raptis and Tzivanidis [6] studied the effects of mass transfer, free-convection currents and heat sources on the Stokes' problem for an infinite vertical plate.

The object of the present paper is to study the effects of the natural convection and mass transfer of a conducting fluid through a very porous medium bounded by two horizontal and unmoving plates, by the presence of a magnetic field assuming uniform axial temperature and concentration variations along the plates. The magnetic Reynolds number is considered to be small so that the induced magnetic field is negligible and the magnetic field is normal to the plates.

In this problem, the x'-axis and y'-axis are respectively taken along and perpendicular to the parallel plates with the origin on the lower plate. The two plates are considered to be of infinite extent so that the motion is independent of x' (except

pressure). Then the equations for the steady motion in x' and y' directions for the velocity field $(u', 0)$ are:

$$0 = -\frac{\partial p'}{\partial x'} + \mu \frac{d^2 u'}{dy'^2} - \frac{\mu}{K'} u' - \sigma B_0^2 u', \tag{1}$$

$$0 = -\frac{\partial p'}{\partial y'} - \rho' g, \tag{2}$$

where μ is the coefficient of viscosity, p' is the pressure, σ is the electric conductivity, B_0 is the magnetic field normal to the plates and all the other variables are defined by Raptis et al. [3].

Assuming a uniform axial temperature variation and a uniform axial concentration variation along the plates the temperature and the concentration can be written respectively as

$$\begin{aligned} T' - T_0 &= L_1 x' + \vartheta'(y'), \\ C' - C_0 &= L_2 x' + C_1'(y'), \end{aligned} \tag{3}$$

where L_1, L_2 are constants, C' is the concentration, T' is the temperature and T_0, C_0 are a reference temperature and concentration, respectively.

The density variation which is going to be used in Eq. (2) is given by the equation of state

$$\rho' = \rho_0 [1 - \beta(T' - T_0) - \beta^*(C' - C_0)], \tag{4}$$

where ρ_0 denotes the density of a reference state, β is the coefficient of volume expansion and β^* is the coefficient of thermal expansion with concentration. Putting Eqs (3) and (4) into (2) and after integrating we get

$$\begin{aligned} p' = &-\rho_0 g y' + \rho_0 g \beta L_1 x' y' + \rho_0 g \beta^* L_2 x' y' + \\ &+ \rho_0 g \beta \int \vartheta' dy' + \rho_0 g \beta^* \int C_1' dy' + R(x'). \end{aligned} \tag{5}$$

Eliminating p' from Eqs (1) and (5) and taking into account that all the fluid properties are assumed constant except that the influence of the density variation with the temperature is only considered in the body force term, then after introducing the dimensionless quantities

$$P_x = -\frac{L^3}{\rho_0 \nu^2} \frac{dR}{dx'}, \qquad y = \frac{y'}{L}, \qquad u = \frac{u' L}{\nu P_x}, \tag{6}$$

(where L is the distance between the plates), we get

$$\frac{d^2 u}{dy^2} - K^{-1} u - Mu = Gy + G^* y - 1, \tag{7}$$

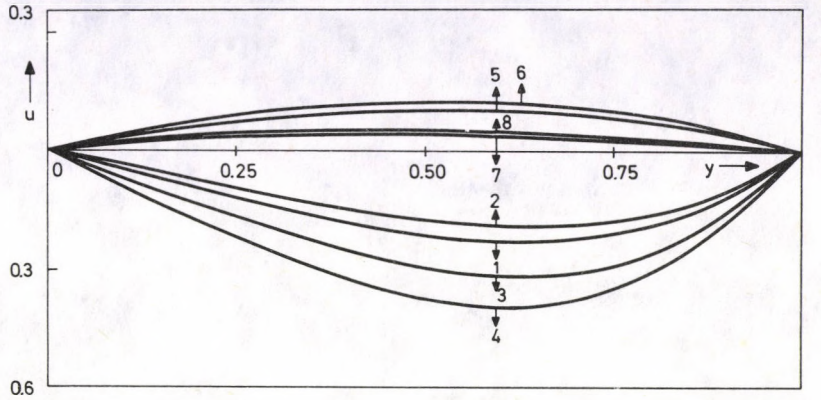

Fig. 1. Velocity profiles: 1: $G=4$, $G^*=3$, $K=0.3$, $M=1$, 2: $G=4$, $G^*=3$, $K=0.3$, $M=4$, 3: $G=4$, $G^*=5$, $K=0.3$, $M=1$, 4: $G=4$, $G^*=5$, $K=2$, $M=1$, 5: $G=-4$, $G^*=3$, $K=0.3$, $M=1$, 6: $G=-4$, $G^*=3$, $K=0.3$, $M=4$, 7: $G=-4$, $G^*=5$, $K=0.3$, $M=1$, 8: $G=-4$, $G^*=5$, $K=2$, $M=1$

where $G^*=\dfrac{\beta g L^4 L_1}{\nu^2 P_X}$ (Grashof number), $G=\dfrac{\beta^* g L^4 L_2}{\nu^2 P_X}$ (modified Grashof number) $M=\dfrac{\sigma B_0^2 L^2}{\nu \rho_0}$ (magnetic parameter) and $K=\dfrac{K'}{L^2}$ (permeability parameter).

Since $P_X>0$, the positive and negatives values of L_1 correspond to heating and cooling, respectively, $(G \gtrless 0)$ along the channel plates.

The solution of Eq. (7) satisfying the non-slip conditions $u(0)=0$ and $u(1)=0$ at both plates is

$$u=\frac{1}{\sqrt{K^{-1}+M}}\left[\frac{1}{e^{m_2}-e^{m_1}}\left[-(e^{m_2}+G+G^*-1)e^{m_1 y}+(e^{m_1}+G+G^*-1)e^{m_2 y}\right]-\right.$$

$$\left.-(G+G^*)y+1\right], \tag{8}$$

where

$$m_1=\frac{1}{\sqrt{K^{-1}+M}}, \qquad m_2=-\frac{1}{\sqrt{K^{-1}+M}}.$$

The effects of the Grashof number, modified Grashof number, permeability parameter and magnetic parameter on the velocity field are shown in Fig. 1.

References

1. M. Katagiri, J. Phys. Soc. (Japan), **17,** 393, 1962.
2. P. K. Muhuri, J. Phys. Soc. (Japan), **18,** 1671, 1983.
3. A. Raptis, C. Perdikis and G. Tzivanidis, J. Phys. D: Appl. Phys., **14,** L99, 1981.
4. A. Raptis, G. Tzivanidis and N. Kafousias, Letter in Heat and Mass Transfer, **8,** 417, 1981.
5. A. Raptis and G. Tzivanidis, Acta Mech., **39,** 43, 1981.
6. A. Raptis and G. Tzivanidis, Astrophys. and Space Science, **78,** 351, 1981.

BOOK REVIEWS

Structural Stability in Physics

Springer Series in Synergetics,
Editors: W. Güttinger and H. Eikemeier, Springer-Verlag, Berlin, Heidelberg, New York, 1979 pp. VIII + 311, 108 figures

This Volume contains the Proceedings of two International Symposia on Applications of Catastrophe Theory and Topological Concepts in Physics, held at the Institute for Information Sciences, University of Tübingen, FRG, May 2–6 and December 11–19, 1978. The May Symposium centred around the granting of a honorary doctors degree to René Thom, by the Faculty of Physics of the University of Tübingen, in recognition of his theory on structural stability and morphogenesis. The May Symposium was followed by a second one on the same subject in December. Attended by more than 50 scientists, it provided an opportunity for mathematicians, physicists, chemists etc. to exchange ideas about the subjects mentioned above.

The first part of this Volume begins with Thom's reflections about the role of catastrophe theory in Natural Philosophy. E. C. Zeeman summarizes the use of catastrophes for modeling in sciences and W. Güttinger provides a short sketch of recent trends in applying catastrophe theory to physics. In the second chapter recent developments in the theory of random waves, fractals and diffraction catastrophes are outlined. The papers of the third chapter deal with attempts to use catastrophe techniques in spaces with infinitely many dimensions and to establish links with bifurcation theory. The contributions of the fourth chapter centre around the topological classification of singularities in ordered media, flow fields and wave fronts. The fifth chapter is devoted to topics in statistical mechanics and phase transitions. The papers of the sixth chapter deal with both the mathematical aspects and the physical significance of the soliton concept, whose topological background is still almost unexplored. The last chapter on dynamical systems crosses the boundaries of physics and concludes with an overall view on chaos with many fascinating problems.

In summing up, the papers of these Proceedings are interesting, and fascinating but, at the same time, a little "chaotic".

I. Gyarmati

HARTMUT M. PILKUHN: *Relativistic Particle Physics*

(Texts and Monographs in Physics) Springer-Verlag, Berlin, Heidelberg, New York, 1979, pp. XII + 427, 85 figures

The book contains an excellent in-depth summary of the questions in particle physics, viewed from the basis of personal and intimate experience.

One wonders how the author can produce so many illuminating short cuts in order to make ample space for practical calculations. All the argumentations are strict and require the intristic knowledge of the armaments attacking the problems of particle physics.

The material is presented in eight chapters. The first one is devoted to one-particle problems, starting from Lorentz invariance, Klein-Gordon, Pauli and Dirac equations, including Coulomb scattering. The second chapter describes two particle problems, decay rates, cross sections kinematics, unitarity, scattering by a 4-potential, Breit equations, etc., Chapter 3 turns to the field of radiation and presents quantum electrodynamics. Unitarity and analyticity are discussed in detail. Chapter 4 introduces the particle zoo, including new particles and charm. The following chapter describes weak interactions, e.g. β-decay, neutrino experiments, the Weinberg-Salam model, CVC,

PCAC, etc. Chapters 6, 7 and 8 treat the analyticity and strong interactions, particular hadronic processes and particular electromagnetic processes in collision with atoms and nuclei. Appendices A.-C., contain special functions, SU_2 and SU_3, units and particle tables. QCD is hardly mentioned. The orientation in these topics is facilitated by means of an extensive list of references and a comprehensive index.

The book is highly recommended to graduate students as well as to researchers involved in high energy physics.

K. L N.

WALTER THIRRING: *Lehrbuch der Mathematischen Physik 4.*
Quantenmechanik grosser Systeme

Springer, Wien–New York, 1980, X + 268 pages

"Im Kontrast zum reversiblen, indeterministischen Character der zugrundeliegenden Quantengesetze verhalten sich makroskopische Körper irreversibel und deterministisch. Wie lässt sich der scheinbare Widerspruch verstehen?" These are the first sentences of this textbook of statistical mechanics. The clear formulation of the question expresses the sharp and demanding logic of the author. The treatment of statistical mechanics makes use of the mathematics, introduced in the former Volumes (mainly in the first Volume) and of the presentation of quantum mechanics, as introduced in the third Volume.

The style of the book is similar to the former Volumes: it is exact and compact; more simple and more abstract proofs are given than usual. The important applications are included. The whole series is warmly recommended to those physicists who hate handwaving arguments and who are masochistic enough to enjoy modern mathematics. Luckily enough, there are plenty of them.

G. Marx

The (p, n) Reaction and the Nucleon-Nucleon Force

Editors: C. D. Goodman, S. M. Austin, S. D. Bloom, J. Rapaport and G. R. Satchler
Plenum Press, New York and London, 1980

The thick, handsome volume contains the Proceedings of the Conference on the (p, n) Reaction and the Nucleon-Nucleon Force held in Telluride, Colorado, 29–31 March, 1979. This topic is closely related to those of the Gull Lake Conference (The Two-Body Force in Nuclei, ed. by S. M. Austin and G. M. Crawley, Plenum, 1972) and of the Tucson Conference (Effective Interactions and Operators in Nuclei, ed. by B. R. Barrett, Springer, 1975). However, as is testified by the Proceedings, this Conference is more than an up-to-date review of the same topic. It is richer than the previous reviews first of all in the detailed discussion of medium-energy and mesonic effects. On the other hand, unlike the Tucson Conference, this meeting was motivated by experiments, and, as the scope of experimental facilities has recently widened substantially, so has the topic that was to be covered by the Conference.

In fact, the meeting was prompted by the emergence of the first results from the Indiana University Cyclotron Facility. This makes it possible to study (p, n) reactions between 50 and 200 MeV, a region completely inaccessible for accurate measurements previously.

The significance of the (p, n) reaction for nuclear physics is twofold. First, since the strongest (p, n) transitions, those conserving the target isospin, are caused primarily by the isovector terms of the effective nucleon-nucleon force, they are unique tools to study these interaction terms. Second, as these transitions lead to some of the basic excitations of nuclei, they reveal fundamental aspects of nuclear structure and excitability.

Two of the most important transitions are those that go to the ground state analogue and to the spin-flip isospin-flip (Gamow–Teller) giant resonance. The analogue state is defined by all its quantum numbers being equal to those of the ground state of the neighbouring isobaric nucleus except, of course, for the isospin projection. The Gamow–Teller resonance is an excitation, over the ground state, that carries spin-parity (and isospin) $1^+(1)$. The former process is due to the scalar-isovector interaction term and the existence of the neutron excess density of the target nucleus. The latter one is caused by the vector-isovector term and the existence of the spin-isospin-flip excitation mode. It is this transition that has lately attracted particular interest since the Indiana measurements have confirmed the conjecture that the Gamow–Teller mode is concentrated into a well-defined giant resonance, which is excited very neatly through (p, n) at such a high bombarding energy.

Most of the papers in this Volume are concerned with these aspects. The effective interactions are discussed both in the context of their theoretical derivation and of their extraction from experimental data. The analysis of experiments poses the question

of reaction mechanism, and this also receives due attention in the Volume. The picture is completed by the reviews on the hadronic analogues of the (p, n) process (pion and kaon charge exchange, (^{3}He, t) and (n, p) reactions) as well as the electromagnetic excitation of the Gamow–Teller states. The list of authors contains plenty of prominent names.

R. G. Lovas

Interacting Bose–Fermi Systems in Nuclei

Editor: F. Iachello, Plenum Press, New York and London, 1981, pp. 412

Ettore Majorana International Science Series. Physical Sciences, Volume 10

This Volume contains the 41 talks presented at the second workshop on interacting Bose–Fermi systems in nuclei, Erice, Sicily, June 12–29, 1980. Thus, it is a companion volume to the earlier "Interacting Bosons in Nuclear Physics" (Volume 1, 1979 in the above series). While Volume 1 presents the investigations in the Interacting Boson Model up to 1978, this Volume presents the subsequent results from 1979, 1980 (Part I), and also the generalization of the model to odd-A nuclei (Part II).

The 28 talks in Part I treat the successes and limitations of the Interacting Boson Model applied to even–even nuclei (phenomenology, microscopic studies, extensions, application to reactions, classical limit, and related topics).

Since the original model was not able to describe the collective states of even–odd nuclei, a suitable extension has been worked out by Iachello and Scholten. This Interacting Boson Fermion Model is treated in the remaining talks in Part II. Phenomenological, microscopic and supersymmetry aspects of the new exciting model are equally described in the Volume.

This excellent, nice, well organized, valuable book can be recommended those who are interested in the new developments of the nuclear structure.

G. Pócsik

Developments in the Theory of Fundamental Interactions

Proceedings of the XVIIth Winter School of Theoretical Physics, Karpacz, Poland, February 22–March 6, 1980. Editors: L. Turko and A. Pekalski. Harwood Academic Publishers, Chur–London–New York, 1981.

The annual "Winter School of Theoretical Physics" held in Karpacz, Poland, is usually devoted to quantum field theory and elementary particle physics. The various lectures published in this Volume are devoted to recent developments in the theory of strong interactions, supersymmetric field theories, in particular, supergravity.

After the spectacular triumph of field theoretic methods, in particular Yang-Mills gauge theories, exciting new ideas have been put forward in the description of the strong and electromagnetic interactions for the possible unification of all interactions and for subquarks and lepton structures. Of these, perhaps the most beautiful ideas are related to supersymmetry. Many theorists share the opinion that supersymmetry may be a very important and relevant new principle above the energy scale of $\simeq 1000$ GeV.

The Volume reviewed here contains lectures on supergravity (L. Brink, A. Van Proyen, P. Breitenlohner, E. Sokatchev) as well as lectures on the more general properties of supersymmetric field theories (P. Fayet, J. T. Lopuszanski, J. Lukierski).

Other authors contributed lectures on Quantum Chromo Dynamics. Both the phenomenological aspects (O. W. Greenberg, J. Hietarinta, J. Kripfganz, R. D. Peccei, J. Ranft, etc.) and the nonperturbative aspects (W. J. Zakrzewski, I. Ya. Aref'eva, V. F. Müller, T. T. Wu, etc.) are considered.

Although some of the ideas presented in these lectures proved to be not very practical, most of the lectures describe very recent and important developments.

The Volume can be recommended to professional field theorists.

Z. Kunszt

Acta Electronica

Revue trimestrielle éditée par les laboratoires d'électronique et de physique appliquée, Paris
Rédacteurs scientifiques: Ginette Pouvesle, rédacteur en chef Rita Hubac, rédacteur en chef adjoint Annie Mircea
Abonnement (4 numéros) France 120 F, Étranger: 160 FF

All four issues of Vol. 23 are devoted to the same topic: the study of GaAs based microwave devices, as carried out by French researchers. The works give a detailed insight into the state of art concerning research and, partly, technology in French laboratories. For example Vol. 23 No. 2 presents papers as follows:

Introduction by J. L. Teszner; GaAs FET: analytical model and equivalent circuit by D. Boccon-Gibod; Noise behaviour and practical realization of GaAs microwave FET-s for microwaves by P. Baudet; Power GaAs MESFET: design and technology by P. Baudet; FET microwave characterization; noise figure, gain, power measurements on microwave bench by M. Binet, P. Baudet; FET automatic microwave characterization by M. Parisot, M. Binet, A. Rebier; GaAs MESFET reliability study by D. Meignant; Modelling of submicrometer gate FET by B. Cernez, A. Cappy, G. Salmer, E. Constant.

This Volume of the Journal can be recommended to engineers specializing in the field of microwave electronics. This way of presenting so many papers on the same topic — in this case GaAs based microwave devices — offers the possibility to compare French results and problems with the results achieved and the problems encountered by researchers in other countries.

M. Somogyi

Manuscript received by Akadémiai Kiadó: 30 August 1982
Manuscript received by the Printers; 13 September 1982
Date of publication 22 August 1983

PRINTED IN HUNGARY
Akadémiai Nyomda, Budapest

NOTES TO CONTRIBUTORS

I. PAPERS will be considered for publication in Acta Physica Hungarica only if they have not previously been published or submitted for publication elsewhere. They may be written in English, French, German or Russian.

Papers should be submitted to

Prof. I. Kovács, Editor
Department of Atomic Physics, Technical University
1521 Budapest, Budafoki út 8, Hungary

Papers may be either articles with abstracts or short communications. Both should be as concise as possible, articles in general not exceeding 25 typed pages, short communications 8 typed pages.

II. MANUSCRIPTS

1. Papers should be submitted in three copies.
2. The text of papers must be of high stylistic standard, requiring minor corrections only.
3. Manuscripts should be typed in double spacing on good quality paper, with generous margins.
4. The name of the author(s) and of the institutes where the work was carried out should appear on the first page of the manuscript.
5. Particular care should be taken with mathematical expressions. The following should be clearly distinguished, e.g. by underlining in different colours: special founts (italics, script, bold type, Greek, Gothic, etc.); capital and small letters; subscripts and superscripts, e.g. x^2, x_3; small *l* and l; zero and capital O; in expressions written by hand: *e* and *l*, *n* and *u*, *v* and v, etc.
6. References should be numbered serially and listed at the end of the paper in the following form: J. Ise and W. D. Fretter, Phys. Rev., **76**, 933, 1949.

For books, please give the initials and family name of the author(s), title, name of publisher, place and year of publication, e.g.: J. C. Slater, Quantum Theory of Atomic Structures, I. McGraw-Hill Book Company, Inc., New York, 1960.

References should be given in the text in the following forms: Heisenberg [5] or [5].

7. Captions to illustrations should be listed on a separate sheet, not inserted in the text.
8. In papers submitted to Acta Physica all measures should be expressed in SI units.

III. ILLUSTRATIONS AND TABLES

1. Each paper should be accompanied by three sets of illustrations, one of which must be ready for the blockmaker. The other sets attached to the copies of the manuscript may be rough drawings in pencil or photocopies.
2. Illustrations must not be inserted in the text.
3. All illustrations should be identified in blue pencil by the author's name, abbreviated title of the paper and figure number.
4. Tables should be typed on separate pages and have captions describing their content. Clear wording of column heads is advisable. Tables should be numbered in Roman numerals (I, II, III, etc.).

IV. RETURN OF MATERIAL

Owing to high postage costs, the Editorial Office cannot undertake to return *all* material not accepted for any reason for publication. Of papers to be revised (for not being in conformity with the above Notes or other reasons) only *one* copy will be returned. Material rejected for lack of space or on account of the Referees' opinion will not be returned to authors outside Europe.

Periodicals of the Hungarian Academy of Sciences are obtainable at the following addresses:

AUSTRALIA
C.B.D. LIBRARY AND SUBSCRIPTION SERVICE
Box 4886, G.P.O., *Sydney N.S.W. 2001*
COSMOS BOOKSHOP, 145 Ackland Street
St. Kilda (Melbourne), Victoria 3182

AUSTRIA
GLOBUS, Höchstädtplatz 3, *1206 Wien XX*

BELGIUM
OFFICE INTERNATIONAL DE LIBRAIRIE
30 Avenue Marnix, *1050 Bruxelles*
LIBRAIRIE DU MONDE ENTIER
162 rue du Midi, *1000 Bruxelles*

BULGARIA
HEMUS, Bulvar Ruszki 6, *Sofia*

CANADA
PANNONIA BOOKS, P.O. Box 1017
Postal Station "**B**", *Toronto, Ontario M5T 2T8*

CHINA
CNPICOR, Periodical Department, P.O. Box 50
Peking

CZECHOSLOVAKIA
MAD'ARSKÁ KULTURA, Národní třida 22
115 66 Praha
PNS DOVOZ TISKU, Vinohradská 46, *Praha 2*
PNS DOVOZ TLAČE, *Bratislava 2*

DENMARK
EJNAR MUNKSGAARD, Norregade 6
1165 Copenhagen K

FEDERAL REPUBLIC OF GERMANY
KUNST UND WISSEN ERICH BIEBER
Postfach 46, *7000 Stuttgart 1*

FINLAND
AKATEEMINEN KIRJAKAUPPA, P.O. Box 128 *SF- 00101 Helsinki 10*

FRANCE
DAWSON-FRANCE S. A., B. P. 40, *91121 Palaiseau*
EUROPÉRIODIQUES S. A., 31 Avenue de Versailles, *78170 La Celle St. Cloud*
OFFICE INTERNATIONAL DE DOCUMENTATION ET LIBRAIRIE, 48 rue Gay-Lussac
75240 Paris Cedex 05

GERMAN DEMOCRATIC REPUBLIC
HAUS DER UNGARISCHEN KULTUR
Karl Liebknecht-Straße 9, *DDR-102 Berlin*
DEUTSCHE POST ZEITUNGSVERTRIEBSAMT Straße der Pariser Kommüne 3–4, *DDR-104 Berlin*

GREAT BRITAIN
BLACKWELL'S PERIODICALS DIVISION
Hythe Bridge Street, *Oxford OX1 2ET*
BUMPUS, HALDANE AND MAXWELL LTD.
Cowper Works, *Olney, Bucks MK46 4BN*
COLLET'S HOLDINGS LTD., Denington Estate *Wellingborough, Northants NN8 2QT*
WM. DAWSON AND SONS LTD., Cannon House *Folkstone, Kent CT19 5EE*
H. K. LEWIS AND CO., 136 Gower Street
London WC1E 6BS

GREECE
KOSTARAKIS BROTHERS INTERNATIONAL BOOKSELLERS, 2 Hippokratous Street, *Athens-143*

HOLLAND
MEULENHOFF-BRUNA B. V., Beulingstraat 2,
Amsterdam
MARTINUS NIJHOFF B.V.
Lange Voorhout 9–11, *Den Haag*
SWETS SUBSCRIPTION SERVICE
347b Heereweg, *Lisse*

INDIA
ALLIED PUBLISHING PRIVATE LTD., 13/14
Asaf Ali Road, *New Delhi 110001*
150 B-6 Mount Road, *Madras 600002*
INTERNATIONAL BOOK HOUSE PVT. LTD.
Madame Cama Road, *Bombay 400039*
THE STATE TRADING CORPORATION OF INDIA LTD., Books Import Division, Chandralok 36 Janpath, *New Delhi 110001*

ITALY
INTERSCIENTIA, Via Mazzé 28, *10149 Torino*
LIBRERIA COMMISSIONARIA SANSONI, Via Lamarmora 45, *50121 Firenze*
SANTO VANASIA, Via M. Macchi 58
20124 Milano
D. E. A., Via Lima 28, *00198 Roma*

JAPAN
KINOKUNIYA BOOK-STORE CO. LTD.
17-7 Shinjuku 3 chome, Shinjuku-ku, *Tokyo 160-91*
MARUZEN COMPANY LTD., Book Department, P.O. Box 5050 Tokyo International, *Tokyo 100-31*
NAUKA LTD. IMPORT DEPARTMENT
2-30-19 Minami Ikebukuro, Toshima-ku, *Tokyo 171*

KOREA
CHULPANMUL, *Phenjan*

NORWAY
TANUM-TIDSKRIFT-SENTRALEN A.S., Karl Johansgatan 41–43, *1000 Oslo*

POLAND
WĘGIERSKI INSTYTUT KULTURY, Marszalkowska 80, *00-517 Warszawa*
CKP-I W, ul. Towarowa 28, *00-958 Warszawa*

ROUMANIA
D. E. P., *Bucuresti*
ILEXIM, Calea Grivitei 64–66, *Bucuresti*

SOVIET UNION
SOJUZPECHAT — IMPORT, *Moscow*
and the post offices in each town
MEZHDUNARODNAYA KNIGA, *Moscow G-200*

SPAIN
DIAZ DE SANTOS, Lagasca 95, *Madrid 6*

SWEDEN
GUMPERTS UNIVERSITETSBOKHANDEL AB
Box 346, *401 25 Göteborg 1*

SWITZERLAND
KARGER LIBRI AG, Petersgraben 31, *4011 Basel*

USA
EBSCO SUBSCRIPTION SERVICES
P.O. Box 1943, *Birmingham, Alabama 35201*
F. W. FAXON COMPANY, INC.
15 Southwest Park, *Westwood Mass. 02090*
READ-MORE PUBLICATIONS, INC.
140 Cedar Street, *New York, N.Y. 10006*

YUGOSLAVIA
JUGOSLOVENSKA KNJIGA, Terazije 27, *Beograd*
FORUM, Vojvode Mišića 1, *21000 Novi Sad*

Index: 26.022

3802

FORMERLY ACTA PHYSICA ACADEMIAE SCIENTIARUM HUNGARICAE

Acta Physica Hungarica

VOLUME 54, NUMBERS 3–4, 1983

EDITOR-IN-CHIEF
I. KOVÁCS

EDITORIAL BOARD
Z. BAY, R. GÁSPÁR, K. NAGY,
L. PÁL, A. SZALAY, I. TARJÁN, B. TELEGDI,
E. WIGNER

Akadémiai Kiadó, Budapest
ACTA PHYS. HUNG. APAHAQ 54 (3-4) 221-373 (1983) HU ISSN 0001-6705

ACTA PHYSICA HUNGARICA

A JOURNAL OF THE HUNGARIAN ACADEMY OF SCIENCES

EDITED BY

I. KOVÁCS

Acta Physica publishes original papers on subjects in physics. Papers are accepted in English, French, German and Russian.

Acta Physica is published in two yearly volumes (4 issues each) by

AKADÉMIAI KIADÓ
Publishing House of the Hungarian Academy of Sciences
H-1054 Budapest, Alkotmány u. 21

Subscription information

Orders should be addressed to

KULTURA Foreign Trading Company
1389 Budapest P.O. Box 149

or to its representatives abroad.

Acta Physica is indexed in Current Contents

CONTENTS

Acta Physica Hungarica 54 (3—4), pp. 221—230 (1983)

INVESTIGATION OF THE ELECTRICAL CONDUCTIVITY OF γ-IRRADIATED SODIUM SILICATE GLASSES CONTAINING MULTIVALENCE Cu IONS

A. TAWANSI, S. EL-KONSOL

Physics Department, Mansoura University and Reactor and Neutron Physics Department, Atomic Energy Establishment, Cairo, Egypt

A. F. BASHA

Physics Department, Cairo University, Cairo, Egypt

and

M. M. MORSI

Glass Research Division

National Research Center, Cairo, Egypt

(Received in revised form 19 December 1981)

The present investigation deals with a study of the γ-radiation effects on the d.c. electrical resistivity of SiO_2-Na_2O-CaO glasses containing Cu^0, Cu^+, Cu^{2+} and a mixture of Cu^+ and Cu^{2+} ions over the temperature (T) range from 300 to 630 K. The applicability of the polaron hopping conduction mechanism has been established from the reciprocal temperature dependence of $\ln \rho/T$ for the samples under investigation. The electrical resistivity is found to decrease by increasing the TM valency which enhances the hopping process. The post-irradiation effect due to ionizing gamma-radiation is investigated within the framework of the electron (and hole) trapping theory, and an average value of 0.45 is obtained for the parameter Δ, characterizing traps with an exponentially decreasing number below the conduction band.

1. Introduction

Many papers have been published [1] on the electronic conductivity of oxide glasses containing a single transition metal (TM) oxide, which can remain in the glass in two (or more) different valence states. However, to our knowledge, little has been reported in the literature [1 – 3] on glasses containing two or more different 3*d* TM oxides together.

Transition metal additives can be used to probe the oxidation state of glasses because their site symmetry determines the ordering of the ligand-field splitting of their *d*-levels and hence the energies of intra-atomic (Laporte-forbidden) transitions [4].

Many glasses containing transition-metal ions, for instance vanadium or iron, are semiconductors. It is generally recognized that the conductivity in such glasses is due to the presence of ions of more than one valency, for instance V^{4+} and V^{5+} and

Fe^{2+} and Fe^{3+}; an electron can pass from one ion to another, and the process is similar to impurity conduction in nickel oxide [5].

The group IB atoms occupy covalent sites; Cu in Se is known to be of a fourfold coordinated state, $\langle 4 \rangle$ [6]. This shows the remarkable influence that the relatively weakly bound, but compact, *d*-orbitals possess, in general, the valence properties of the noble metals and their compounds.

The Cu(I) atom occupies a covalent site with formal charge Cu^{1+} and has a diamagnetic response in chalcogenide glasses [7], whereas a Cu(II) atom, which probably occupies an ionic site Cu^{2+}, gives a paramagnetic response from its d^9 configuration [4].

The present work is an investigation of the d.c. electrical resistivity of SiO_2-Na_2O-CaO glass containing Cu, Cu^+, Cu^{2+} and a mixture of Cu^+ and Cu^{2+} ions. The effect of gamma ionizing radiation on the conduction mechanism is studied and a prediction for the trap distribution according to Fowler's model is presented.

2. Experimental

2.1. Sample preparation

The raw materials used in preparing the glass specimens were acid-washed quartz powder and reagent grade chemicals in the form of carbonates or oxides.

A batch giving 100 g glass of the composition 62.4 $SiO_2-16.69\ Na_2O-20.91$ CaO mole% were mixed thoroughly. To this batch CuO was added as shown in Table I. The mixed batch (with the added ingredients was placed in Pt 2% Rh crucible

Table I
Amounts (in g) of CuO added to 100 g glass of the mentioned composition

Sample No	CuO	Valency of Cu	Remarks
G-I	0.1	Cu^0	melted under reducing conditions
G-II	0.1	Cu^+	melted under reducing conditions
G-III	0.1	Cu^{2+}	melted under normal conditions
G-IV	0.1	Cu^0 & Cu^+	melted under reducing conditions

and melted at 1723 ± 10 K for 3 h in a gas-fired furnace. After melting, the glass was cast into plates and annealed at 773 K for 4 h, then ground and polished to get the form of disks of dimensions $10 \times 10 \times 3$ mm.

Samples in which copper is in the oxidation state 0 or +1 were prepared as described above after 2 – 12 g of oxalic acid was added.

2.2. Irradiation facilities and electrical measurements

A ^{60}Co gamma cell model 220 (233 TBq) was used as a source of γ-radiation. The glass specimens were exposed to different doses with a gamma dose rate of 10.5 Gy s^{-1} at room temperature.

The d.c. electrical resistivity of the irradiated specimens was measured at two hours after irradiation. A simple indirect method was used to measure the resistivity. The electrical circuit consists of the glass sample connected in series with a d.c. stabilized power supply and a standard resistance ($10^5\ \Omega$) across which an X – Y recorder is connected. The X – Y recorder is of Philips PM 8141 type with an accuracy $\pm 0.25\%$ and maximum sensitivity 50 μV/cm. The voltage drop across the standard resistance is recorded and the resistivity of the glass sample is calculated.

3. Results and discussion

First, it seems important to mention that for mixed oxide silicate glasses, like that used in the present work, Zachariasen's random network model had a central role in ideas of glass structure [8]. Although the model may need some modification when used to describe medium range order in certain systems, it usually gives a good description and classification of the short range order and coordinations in terms of the concepts of network-forming (covalent) and network-modifying atoms; for exceptions see Weyl and Marboe [9].

Figure 1 depicts the reciprocal temperature dependence of $\ln(\rho/T)$ for the untempered and unirradiated G-I, G-II, G-III and G-IV glasses. It is seen that each curve can be divided into two regions: the lower temperature region where the resistivity increases with temperature and the higher temperature region where ρ decreases as T increases. Moreover, for most of the second region there is a linear relation between $\ln(\rho/T)$ and $1/T$. The electrical resistivity behaviour in the first region may be attributed to the effect of moisture and humidity content in the samples used. On the other hand, the linear part of the higher temperature region, to which we pay more attention can be interpreted as follows. Schmid [10] predicted that, for oxide glasses containing TM ions, if the 3*d* electron is highly localized and the interaction with phonons is strong enough, a small polaron will be formed, and at high temperatures it will move by a hopping process assisted by optical phonons. Austin and Mott [11] have reviewed the conduction in small polaron systems. They also suggested that the electron transfer in TM-ion glasses can be ascribed to this small polaron hopping between two localized TM-ion centres. Glasses containing Cu^+ can apparently exist in a conducting and a non-conduction state [12], and this may be associated with a rearrangement of the glass so that the hole in Cu^{2+} is taken up in a bond.

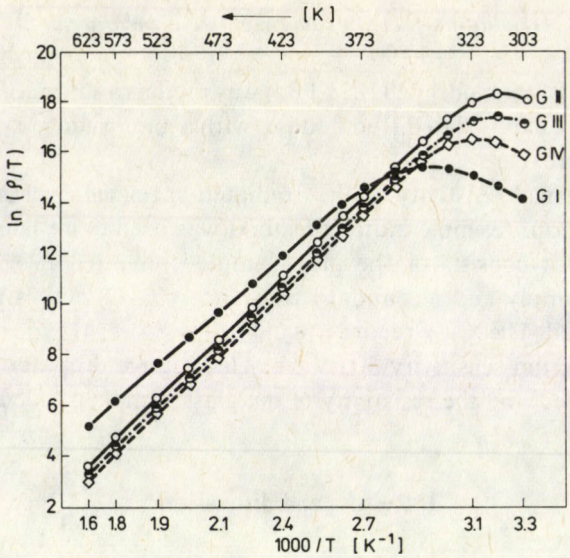

Fig. 1. The reciprocal temperature dependence of $\ln(\rho/T)$ for the intempered and unirradiated glasses

For the glasses used in the present work a suitable formula for the conductivity σ is [11]:

$$\sigma = C(1-C)(e^2/RKT)\exp(-2\alpha R - W/KT). \tag{1}$$

For the resistivity ρ, Eq. (1) can be written as:

$$\ln(\rho/T) = \ln[RK/e^2\, C(1-C)] + 2\alpha R + W/KT. \tag{2}$$

Here R is the mean distance between the ions, C and $(1-C)$ are the proportions of Cu^+ and Cu^{2+}, respectively, α is the rate of decay of the wave function ($\psi \sim \exp(-\alpha R)$) of an electron on Cu^{2+}, and

$$W = W_H + \frac{1}{2} W_D .$$

W_H is the energy of polaron formation and W_D is the Miller–Abrahams term. W_D is called also the disorder energy, which is the energy difference between initial and final sites due to variations in the local arrangements of the TM ions. It is seen from Eq. (2) that as the value of C increases the electrical resistivity decreases. This agrees with Fig. 1. It might be said that for a multivalency element, the increase in the order of its valence state will decrease its stability. This will enhance the hopping process and the electrical resistivity will be decreased. It is important to note there that glass G-IV (of mixed Cu^+ and Cu^{2+} ions) is of lowest resistivity value in the linear part. This is attributed to the suggestion that hopping between neighbouring ions of different valences is evidently more favourable energetically than hopping between ions of the

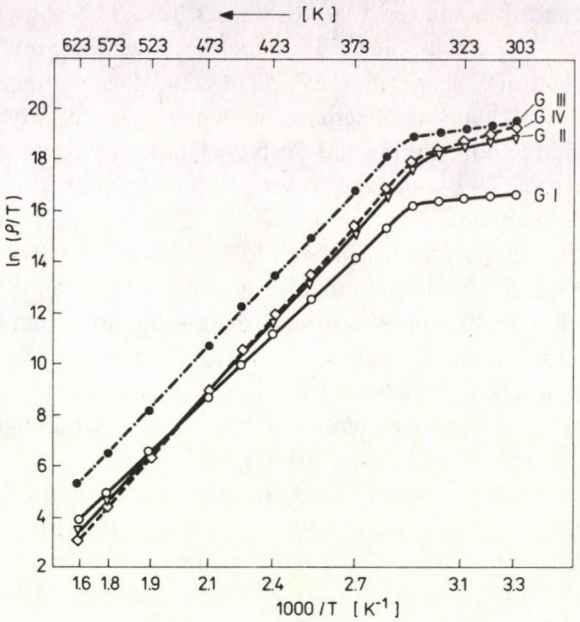

Fig. 2. The reciprocal temperature dependence of ln (ρ/T) for the annealed glasses at 673 K for 5 h

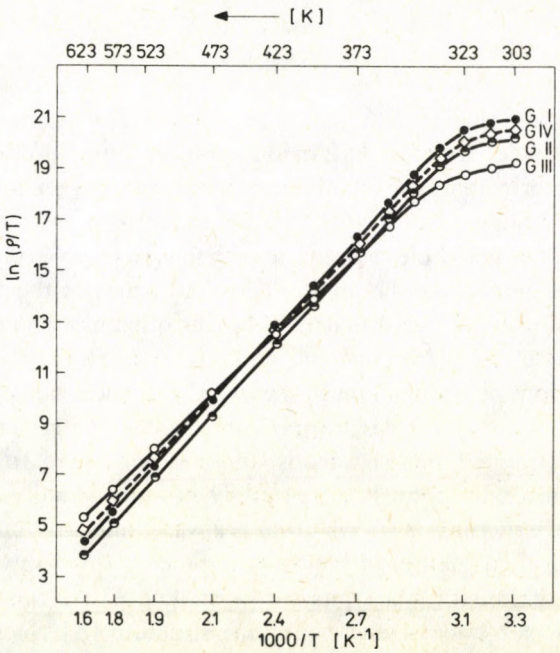

Fig. 3. Ln (ρ/T) as a function of $1/T$ for the studied glasses after irradiation with γ-radiation dose of 1300 Gy

same valency [3], and thus the resistivity decreases. Also, it is shown that the lower temperature limit of the linear part of the reciprocal temperature dependence of $\ln(\rho/T)$ decreases with increasing the TM valency. In other words, the temperature range of applicability of relation (2) increases with increasing the TM valency. Such a result is fairly acceptable, considering that the higher TM valence states contain a large number of hopping sites. This is why the polaron hopping process does not need a high temperature to predominate.

The electrical resistivity was measured for all the prepared samples after their annealing at 673 K for 5 h, and the plots of $\ln(\rho/T)$ as a function of $1/T$ are given in Fig. 2. This second annealing process affects mainly the lower temperature region, and a resistivity transition temperature T_0 is seen to distinguish between two stages of behaviour obeying Eq. (2). In fact, the existence of resistivity transition temperature is characteristic for most insulating materials, and its value depends significantly on the changes in sample treatment and composition [13].

Figure 3 depicts the reciprocal temperature dependence of $\ln(\rho/T)$ for glass samples irradiated with γ-dose value of 1300 Gy. It is seen that for most of the linear parts of these curves the resistivity values are of the same order of magnitude for different TM valence states. Comparing the results of this Figure with those in Fig. 1, it is seen that the resistivity increases by irradiation. Also, it is clear that the temperature range of applicability of Eq. (2) increases by this ionizing γ-radiation. It might be thought that the reaction

$$Cu^{+} + h\nu = Cu^{2+} + e$$

takes place together with the formation of colour centres. Thus, gamma irradiation of sodium silicate glasses containing TM oxides induces trapped-hole and trapped-electron centres. The principal type of hole traps may be an oxygen atom bridging Na and/or Cu atoms or bridging two Na (or Cu) atoms. On trapping a hole it forms the alkali-oxygen (or Cu-oxygen) hole centre. The second type of hole traps is Cu^{+} which forms Cu^{2+} after trapping a hole. The main electron trap may be the preexisting voids of molecular dimensions in the glass matrix [14]. The other electron trap is the Cu^{2+} ion which produces Cu^{+} after trapping occurs. In the present analysis, as the dose of gamma radiation is low, recombination of the two carriers will be neglected, in other words, only the electrons and holes trapped (in reference to recombining) will be considered. Having trapped their electrons, the TM ions tend to cluster. As the temperature rises, clustering proceeds more rapidly, producing major agglomerations. Moreover, in silicate structures, a silicon atom is always linked to four oxygen atoms [14], so a short range correlation of the SiO_4 tetrahedra (probably between 5 and 1.0 nm) was suggested, similar to the α-phase in crystalline quartz. It is well known that most glasses process sub-microscopic crystalline structure [5]. Such structures are helices or chains of silica. Averaged over the volume of the glass, the substructure is basically random, but over distances up to about 1.0 nm there is some correlation

between adjacent SiO_4 tetrahedra. It is the substructure which forms the same electron trap as in bulk silica glass.

Figure 4 shows the reciprocal temperature dependence of $\ln(\rho/T)$ for samples of G-II before and after irradiation with different doses (900, 1300, 1900 and 2500 Gy). It is seen that for higher doses the temperature range of applicability of Eq. (2) increases. This might be attributed to the suggestion that for higher gamma doses there is an increase in the probability of hopping sites formation at lower temperatures.

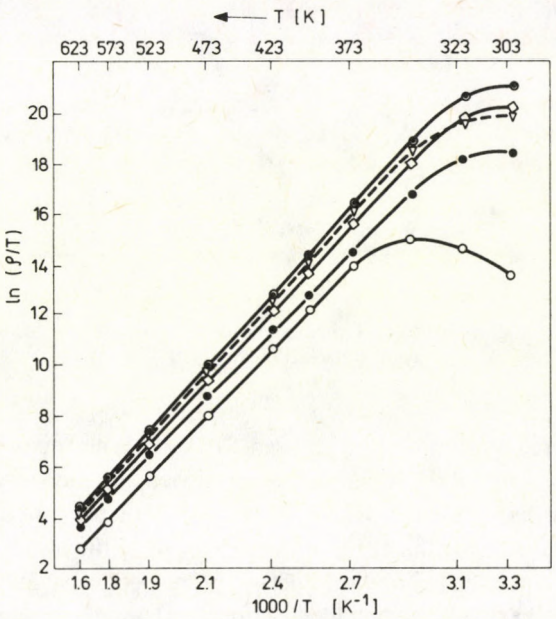

Fig. 4. The reciprocal temperature dependence of $\ln(\rho/T)$ for glass G-II before and after irradiation with different γ-ray doses

⊙—⊙—⊙ 2500 Gy, □—□ 1300 Gy, ▽—▽—▽ 1900 Gy ●—●—● unirr. ○—○—○ 900 Gy

Moreover, it is seen in Fig. 4 that for a gamma-irradiated sample with 900 Gy dose the electrical resistivity is lower than that for the nonirradiated sample. This might be due to the increase of hopping sites by the ionizing gamma-rays. However, for doses higher than 900 Gy the resistivity increases due to the impeding effect of charge carrier scattering and the decrease in its mobility. For such disordered systems the resistivity is proportional to a generalized dwelling time that may include back-and-forth hopping effects. This dwelling time characterizes the possibility of leaving the site and returning [15].

It is important to say that the electrical resistivity temperature dependence was measured for all the prepared samples after irradiation with different gamma doses.

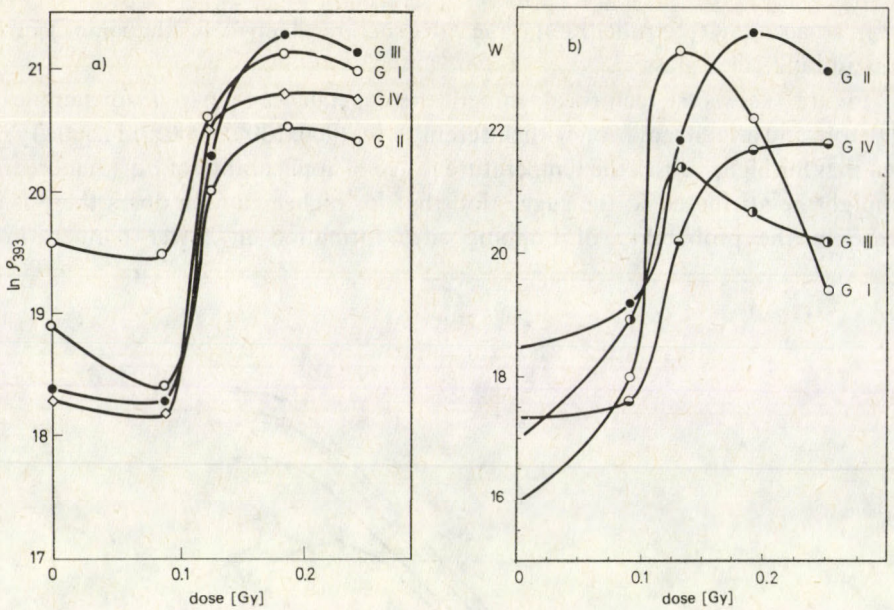

Fig. 5. The effect of dose, for all the prepared samples, on each of: (a) the resistivity measured at 393 K and (b) the activation energy W

The used doses were the same as those used for G-II. The reciprocal temperature dependence of $\ln(\rho/T)$ for all those samples were carried out and were found to behave in the same way as that shown in Fig. 4, so they are not presented here.

Figures 5a and b show the effect of dose on each of the logarithm of resistivity measured at 393 K and the activation energy W, respectively, for all the prepared samples. The curves in these Figures have a similar character in which the values of resistitity, and activation energy, tend to reach the maximum at higher irradiation doses. To interpret this result we write Eq. (2) in the form:

$$\ln(\rho/T) = \ln B + W/KT, \tag{3}$$

where

$$B = \frac{RK}{C(1-C)} e^{2\alpha R}. \tag{4}$$

Using the data of $\ln(\rho/T)$ reciprocal temperature dependence at $T = 393$ K to calculate $\ln B$ and plotting $\ln B$ against gamma dose for each glass, Fig. 6 is obtained. This Figure shows that as the gamma dose increases $\ln B$ increases, reaching a maximum value, then it decreases. It seems likely that the essential factor affecting the value of $\ln B$ is α. Consequently, the tendency of $\ln \rho_{393}$ to reach maximum values (in Fig. 5a) at higher gamma doses might be attributed to the decrease in the value of α. This is because C, R and W change slightly with gamma dose.

The obtained results can be discussed in terms of the model suggested by Fowler [16] to explain the induced conductivity in insulating materials due to ionizing radiation. According to this model, the measured conductivity σ after irradiation will be the sum of the induced and static conductivities. Consequently, the calculated activation energy W will be the sum of an irradiated activation energy W_x and the depth W_0 below the conduction level. The model predicts that the induced conductivity σ_x during irradiation should vary with radiation intensity or dose rate S according to the relation:

$$\sigma_x = aS^{\Delta}, \tag{5}$$

where a is proportionality constant and Δ has the theoretical value between 0.5 and 1, depending on the given substance and the distribution of electron (and hole) traps.

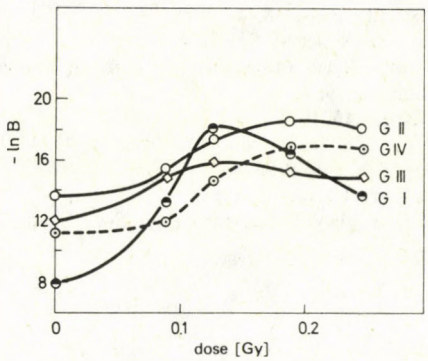

Fig. 6. The factor ln B as a function of the γ-radiation dose

Now, in order to obtain some information about the distribution of trapping centres in glasses we shall make use of the equation:

$$\sigma_x = \sigma_0 S^{\Delta} e^{-W_x/kT}. \tag{6}$$

This equation was used for the first time by one of the authors [17] to explain the post irradiation effects in mica on the basis of the electron trapping theory. Later on [18] it was used to calculate the characteristic parameter Δ for some ferroelectric crystals. In the present work, it can find further experimental evidence for its applicability to glasses.

The parameter Δ was calculated using Eq. (6) and an average value of $\Delta = 0.46 \pm 0.05$ was obtained. This implies, according to Fowler's model, that the electron (and hole) traps distribution in the glasses considered here is exponential in depth.

References

1. M. A. C. G. Van de Graaf, K. J. de Vries and A. J. Burgraff, Phys. Chem. Glasses, 1453, 1973.
2. L. D. Bogomolova, T. F. Dolgolenko, V. N. Lazukin and I. V. Filatova, Sov. Phys. Solid State, **15,** 2477, 1974.
3. A. K. Bandyopadhyay and J. O. Isard, J. Phys. D, Appl. Phys., Vol. **10,** 1977.
4. J. Robertson, Phil. Mag. B., **41,** 177, 1980.
5. N. F. Mott and E. A. Davis, Electronic Processes in Noncrystalline Materials, Clarendon Press, Oxford, 1971.
6. S. A. Hunter, A. Bienenstock and T. M. Hayes, Structure of Noncrystalline Materials. Ed. P. H. Gaskell, Taylor and Francis Ltd, London, 1977.
7. P. C. Taylor, P. C. Friebele and S. G. Bishop, Physics od Semiconductors. Ed. B. L. H. Wilson, Institute of Physics, Bristol, 1978.
8. W. H. Zachariasen, J. Am. Chem. Soc., **54,** 3841, 1932.
9. W. A. Weyl, and E. C. Marboe, Constitution of Glasses, Wiley, New York, 1964.
10. A. P. Schmid, J. Appl. Phys., **39,** 3140, 1968.
11. I. G. Austin and N. F. Mott, Adv. Phys., **18,** 41, 1969.
12. C. F. Drake and I. F. Scanlan, J. Noncryst. Solids, **4,** 434, 1970.
13. J. F. Kircher and R. E. Bowman, Effect of Radiation on Materials and Components. Reinhold Publishing Corporation, New York, London, 1964.
14. G. Brown, J. of Material Science, **10,** 1975.
15. B. Movaghar, B. Pohlmann and W. Schimacher, Phil. Mag., B, **41,** 49, 1980.
16. J. F. Fowler, Proc. Roy. Soc., **236,** 646, 1956.
17. A. F. Basha, M. Sc. Thesis, Cairo University, 1969.
18. A. F. Basha, M. Amin and A. A. Elwy, Proc. Math. Phys. Soc. (Egypt), No. 45, 171, 1978.

Acta Physica Hungarica 54 (3—4), pp. 231—247 (1983)

OPTICAL ABSORPTION SPECTRA OF $NdCl_3$ COMPLEXES IN SOLUTION

S. V. J. LAKSHMAN and S. BUDDHUDU

Spectroscopic Laboratories, Department of Physics
Sri Venkateswara University, Tirupati, India 517 502

(Received 27 April 1982)

Spectral investigation of Nd^{3+} in $NdCl_3$, $MgCl_2$, $CaCl_2$, $CdCl_2$ and NH_4Cl complexes have been carried out. For the first time the second derivative spectra of these five Nd^{3+} complexes have been studied. From the observed features of the $^4F_{5/2}$ and $^4G_{5/2}$ bands, crystal field (A_{20}, A_{40}) parameters were evaluated assuming C_{3h} symmetry for the Nd^{3+} in these complexes. The Slater—Condon (F_2, F_4, F_6), spin—orbit (ξ_{4f}), nephelauxetic (β), bonding (δ) and Judd—Ofelt intensity (T_2, T_4, T_6) parameters are evaluated. Theoretical estimates of spectral intensities calculated from Judd—Ofelt and electric (S_{ed})-magnetic (S_{md}) dipole line strength methods are in good agreement with the observed values.

Introduction

The absorption and fluorescence spectra of neodymium ion incorporated in various crystal lattices have been extensively studied. [1–4]. Electron spin resonance studies of Nd^{3+} diluted with lanthanum chloride have been carried out by Brower [5] and Clarke [6].

Carnall et al [7], Tandon [8] and Jeanlouis [9] have reported the solution absorption spectrum of neodymium ion and correlated the observed energy levels and spectral intensities of the bands with the theoretically calculated values of energies and intensities.

Since no optical absorption studies have so far been reported earlier in the literature for the trivalent neodymium ion in $MgCl_2$ $CaCl_2$, $CdCl_2$ and NH_4Cl complexes, the authors have undertaken the present investigation of work. For the first time, the second derivative spectra of these complexes have been studied by the authors.

Experimental studies

To the saturated solutions of magnesium chloride, calcium chloride, cadmium chloride and ammonium chloride, one mole per cent of $NdCl_3$ was added. In addition to these four solutions 1 mole per cent $NdCl_3$ solution was also prepared in the present investigation.

Absorption spectrum of $NdCl_3$ complexes in the wavelength region 270–830 nm was carried out on a Perkin—Elmer 551 recording spectrophotometer. Second derivative spectra of these complexes were also recorded in this wavelength region by using a derivative accessory to the spectrophotometer. The Perkin—Elmer 551 recording spectrophometer records the spectrum in the range of 850 nm to 200 nm.

The near infrared spectrum from 750 nm to 1100 nm was recorded on a Carl-Zeiss specord 61 recording spectrophotometer. Since there is no derivative accessory for this spectrophotometer, only normal spectra were recorded.

The intensity of a band is a measured in terms of a quantity known as oscillator strength (f). The experimental value of the oscillator strength (f) is expressed in terms of the molar extinction coefficient (ε) and the energy of the transition in wavenumbers (ν) by the following relation [10]

$$f = 4.32 \times 10^{-9} \int \varepsilon \, d\nu , \tag{1}$$

where $d\nu$ is the half band width. The molar extinction coefficient (ε) at a given energy (ν) is computed from the Beer—Lambert law

$$\varepsilon = \frac{A}{cl} , \tag{2}$$

where c is the concentration of the system in moles/lit, l is the light path in solution (cm) and A is the absorptivity or optical density. In the present work $c = 1$ mole per cent, $l = 1$ cm light path hence the absorbance (A) itself becomes the extinction coefficient (ε). The refractive indicies (n) of the $NdCl_3$ complexes were measured on PZ0 Warszawa 3275 refractometer.

Theory

The observed energy levels of rare earth ions in solution are fitted by a least squares fit method. The Slater—Condon (F_2, F_4, F_6) and spin-orbit (ξ_{4f}) parameters for the free ion and the ion in solution may not differ very much. Therefore the correction factors ΔF_2, ΔF_4, ΔF_6 and $\Delta\xi_{4f}$ for the ion in solution are evaluated by the least squares method. The energy E_j of the jth level may be written in terms of the changes in the parameters by Taylor-series expansion as follows

$$E_j = E_{0j} + \frac{dE_j}{dF_2} \Delta F_2 + \frac{dE_j}{dF_4} \Delta F_4 + \frac{dE_j}{dF_6} \Delta F_6 + \frac{dE_j}{d\xi_{4f}} \Delta\xi_{4f} , \tag{3}$$

where E_{0j} is the zero-order energy of the jth level and $\frac{dE_j}{dF_2}$, $\frac{dE_j}{dF_4}$, $\frac{dE_j}{dF_6}$ and $\frac{dE_j}{d\xi_{4f}}$ are the partial derivatives. The numerical values of zero-order energy and partial derivatives are given by Wong [11]. Using the experimental energy levels for E_j and the numerical values of zero-order energy and partial derivatives, a number of linear equations equal

to the number of observed levels were formed. By employing the least-squares method, the values of ΔF_2, ΔF_4, ΔF_6 and $\Delta\xi_{4f}$ were calculated. These were added to the zero-order parameters to obtain the parameters F_2, F_4, F_6 and ξ_{4f} for the five Nd^{3+} complexes studied. Thus

$$\begin{aligned} F_2 &= F_2^0 + \Delta F_2 , \\ F_4 &= F_4^0 + \Delta F_4 , \\ F_6 &= F_6^0 + \Delta F_6 , \\ \xi_{4f} &= \xi_{4f}^0 + \Delta\xi_{4f} , \end{aligned} \tag{4}$$

where F_2^0, F_4^0, F_6^0 and ξ_{4f}^0 are the zero-order parameters [11]. The r.m.s. deviation is calculated from the formula

$$\sigma = \left(\frac{\Sigma \Delta i^2}{N}\right)^{1/2} , \tag{5}$$

where Δi is the deviation of the ith level and N is the number of levels fitted.

Spectral intensities

Theoretical estimates of intensities for the observed bands were made following the methods of

(a) Judd—Ofelt;

(b) Electric (S_{ed}) and magnetic (S_{md}) dipole line strengths.

(a) *Judd—Ofelt method*

Judd [12] and Ofelt [13] independently showed the oscillator strength of an induced electric dipole transition to be related to the energy of the transition $\nu(cm^{-1})$ and squares of the matrix elements of the unit tensor operators U^λ connecting the initial and final states (ψJ and $\psi' J'$) via three phenomenological parameters $T_\lambda (\lambda = 2,4 \,\&\, 6)$. As per theory

$$f_{ed} = \sum_{\lambda = 2,4,6} T_\lambda \nu (f^N \psi J \| U^\lambda \| f^N \psi' J')^2 . \tag{6}$$

Evaluation of reduced matrix elements $(f^N \psi J \| U^\lambda \| f^N \psi' J')$ in (i) LS and (ii) Intermediate coupling cases.

(i) *LS coupling*

The evaluation of reduced matrix elements is made using the formula

$$(f^N\psi J'\|U^\lambda\|f^N\psi' J')=$$
$$=(-1)^{S+L+J+\lambda}[(2J+1)(2J'+1)]^{1/2}\begin{Bmatrix} JJ'\lambda \\ L'LS \\ L'LS \end{Bmatrix}(f^N SL\|U^\lambda\|f^N SL'). \tag{7}$$

The right hand side matrix elements of $(f^N SL\|U^\lambda\|f^N SL')$ are taken from the tables of Nielson and Koster [14] and the values of the 6j symbol $\begin{Bmatrix} JJ'\lambda \\ L'LS \end{Bmatrix}$ (for $\lambda=2, 4\&6$) are taken from the tables of Rotenberg [15].

(ii) *Intermediate coupling*

The calculation of the reduced matrix elements in an intermediate field is illustrated for a typical transition like ${}^4D_{1/2}\rightarrow{}^2P_{1/2}$ belonging to $(Nd^{3+})4f^3$ configuration. The energy matrix for $j=\dfrac{1}{2}$ is a 2×2 matrix given as [16, 17]

$$\begin{array}{c|cc} & |{}^4D_{1/2}\rangle & |{}^2P_{1/2}\rangle \\ |{}^4D_{1/2}\rangle & (90F_2+108F_4-1728F_6)-E_1 & -(5/2)^{1/2}\xi \\ |{}^2P_{1/2}\rangle & -(5/2)^{1/2}\xi & \left(120F_2+291F_4+1092F_6-\dfrac{3}{2}\right)-E_2 \end{array}$$

We write

$$\begin{aligned} |{}^4D'_{1/2}\rangle &= C_1|{}^4D_{1/2}\rangle + C_2|{}^2P_{1/2}\rangle, \\ |2P'_{1/2}\rangle &= C_3|{}^2P_{1/2}\rangle + C_4|{}^4D_{1/2}\rangle, \end{aligned} \tag{7a}$$

where C_1, C_2, C_3 and C_4 are the eigenvectors corresponding to the intermediate fields $|{}^4D'_{1/2}\rangle$ and $|{}^2P'_{1/2}\rangle$, respectively. Now we have

$$\begin{aligned} ({}^4D'_{1/2}\|U^\lambda\|{}^2P'_{1/2}) &= [(C_1|{}^4D_{1/2}\rangle + C_2|{}^2P_{1/2}\rangle)\|U^\lambda\|(C_3|{}^2P_{1/2}\rangle + C_4|{}^4D_{1/2}\rangle)] \\ &= [C_1C_4\langle{}^4D_{1/2}\|U^\lambda\|{}^4D_{1/2}\rangle + C_2C_3\langle{}^2P_{1/2}\|U^\lambda\|{}^2P_{1/2}\rangle]. \end{aligned} \tag{7b}$$

There will be no cross terms involving ${}^4D_{1/2}$ with ${}^2P_{1/2}$, since the matrix element between different spin states are zero.

The values of the reduced matrix elements $\langle{}^4D_{1/2}\|U^\lambda\|{}^4D_{1/2}\rangle$ and $\langle{}^2P_{1/2}\|U^\lambda\|{}^2P_{1/2}\rangle$ in LS coupling are easily determined from Eq. (7). From these and the eigenvectors (C_1, C_2, C_3 and C_4) obtained by solving energy matrices [16, 17] the reduced matrix element $({}^4D'_{1/2}\|U^\lambda\|{}^2P'_{1/2})$ for the intermediate coupling case are calculated using Eq. (7b). The reduced matrix elements are thus transformed from the

LS basis states to the physical coupling scheme prior to being squared and substituted in Eq. (6). The squared values of Eq. (7b) were substituted in Eq. (6) and using f_{expt} for f_{ed} the values of T_λ parameters were evaluated by the least squares fit method.

(b) *Method of electric* (S_{ed}) *and magnetic* (S_{md}) *dipole line strengths*

Theoretical spectral intensity f can be evaluated by the relation

$$f = \frac{8\pi^2 mcv}{3he^2(2J+1)}\left[\frac{(n^2+2)^2}{gn} S_{ed} + nS_{md}\right], \tag{8}$$

where n = refractive index of the medium
S_{ed} = electric dipole line strengh
S_{md} = magnetic dipole line strength
m = mass of an electron
c = velocity of light, h = Planck's constant
e = energy of an electron in coulombs
v = energy of the band in cm^{-1}, J = value of initial level J

$$S_{ed} = e^2\left[1.085\times 10^{11}\frac{n(n^2+2)}{q}\right]^{-1}(2J+1)\sum_{\lambda=2,4,6} T_\lambda(f^N\psi J\|U^\lambda\|f^N\psi' J')^2 \tag{9}$$

(symbols have the same significance as described in Eqs. (6, 7 and 8)), and

$$S_{md} = \frac{e^2h^2}{16\pi^2m^2c^2}(\psi J\|L+2S\|\psi' J')^2 . \tag{10}$$

Values of $\|L+2S\|^2$ are as given hereunder (since selection rule is $\Delta J = 0, \pm 1$)
$J' = J$

$$(SLJ\|L+2S\|SL, J') = gJ(J+1)(2J+1) \tag{11}$$

where

$$g = 1 + \frac{J(J+1)+S(S+1)-L(L+1)}{2J(J+1)} \tag{12}$$

$J' = J-1$

$$(SLJ\|L+2S\|SL, J-1) = \left[\frac{(S+L+J+1)(S+L+1-J)(J+S-L)(J+L-S)}{4J}\right] \tag{13}$$

$J' = J+1$

$$(SLJ\|L+2S\|SL, J+1) = \left[\frac{(S+L+J+2)(S+J+1-L)(L+J+1-S)(S+L-J)}{4(J+1)}\right] \tag{14}$$

The matrix elements calculated from Eqs. (11–14) were transformed into the intermediate coupling scheme before computation of the magnetic dipole contribution represented by Eq. (10).

Results and discussion

The observed UV – Vis and NIR spectra of $NdCl_3$ complexes are shown in Figs 1–5 and Figs 1a–5a, respectively. The assignment of electronic transitions to the eighteen observed bands of Nd^{3+} in $NdCl_3$, $MgCl_2$, $CaCl_2$, $CdCl_2$ and NH_4Cl was straightforward.

By the method of least squares the Slater—Condon and spin—orbit parameters were evaluated and presented in Table II. Theoretical energies were next calculated with these parameters and are presented in Table I alongwith the experimental values.

The energy matrices for $4f^3$ configuration have been diagonalized on an IBM 370/155 computer to compute the eigenvalues and eigenvectors for $NdCl_3$ complexes with the Slater—Condon and spin—orbit parameters (Table II). The eigenvectors thus obtained were used in the calculation of the squared reduced matrix elements $\|U^{\lambda}\|^2$ for the observed terms. The values of electric (S_{ed}), magnetic (S_{md})

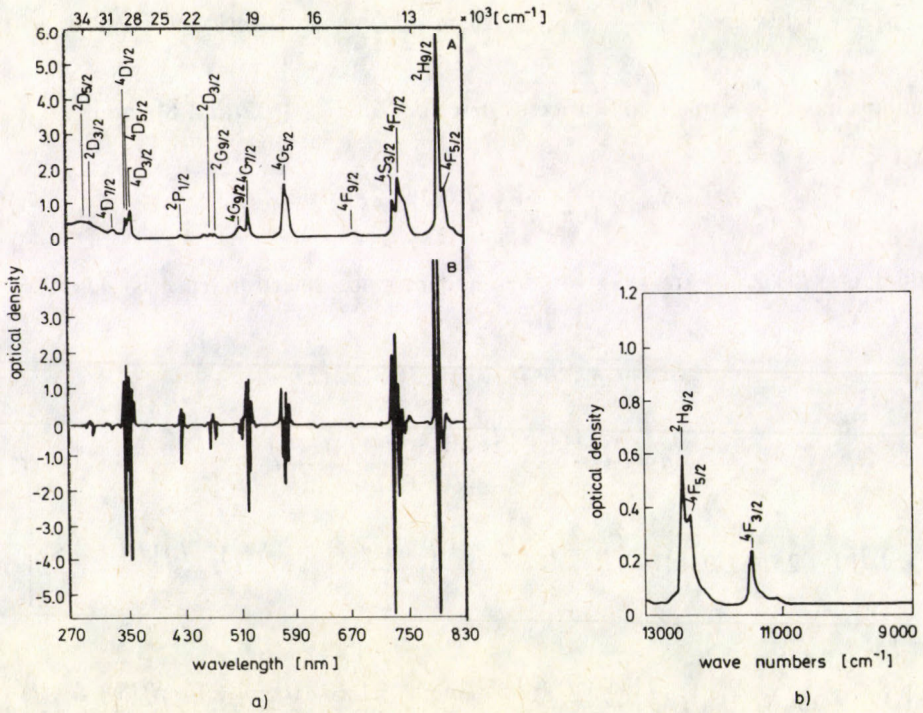

Fig. 1a. Absorption spectrum of Nd^{3+}: $NdCl_3$ (a) normal (b) second derivative
Fig. 1b. Near infrared absorption spectrum of Nd^{3+}: $NdCl_3$

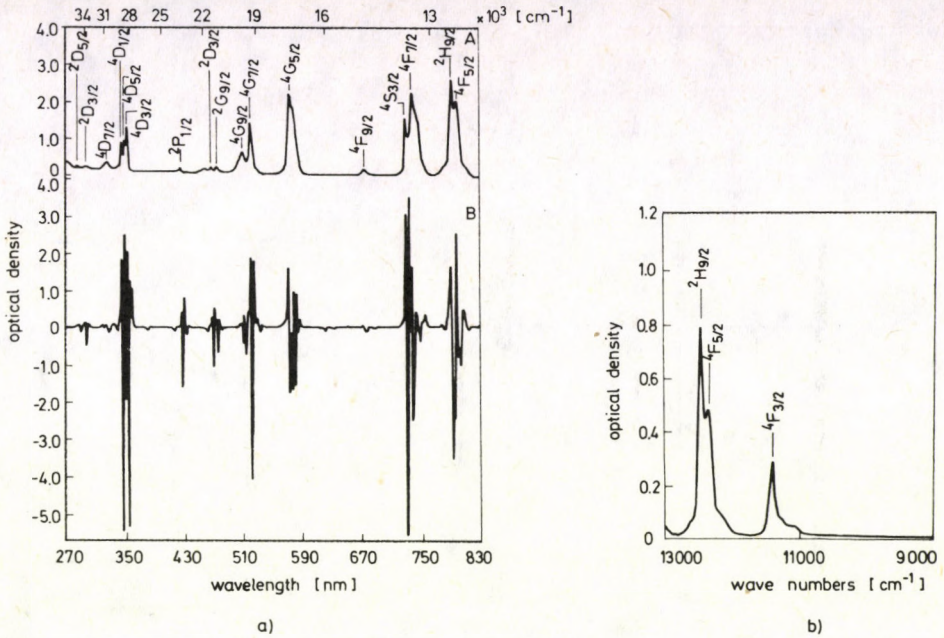

Fig. 2a. Absorption spectrum of $Nd^{3+}:MgCl_2$ (a) normal (b) second derivative
Fig. 2b. Near infrared absorption spectrum of $Nd^{3+}:MgCl_2$

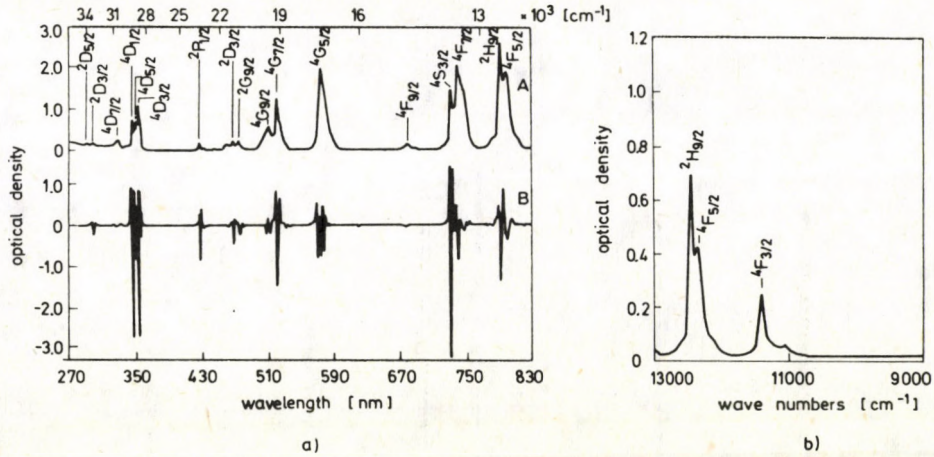

Fig. 3a. Absorption spectrum of $Nd^{3+}:CaCl_2$ (a) normal (b) second derivative
Fig. 3b. Near infrared absorption spectrum of $Nd^{3+}:CaCl_2$

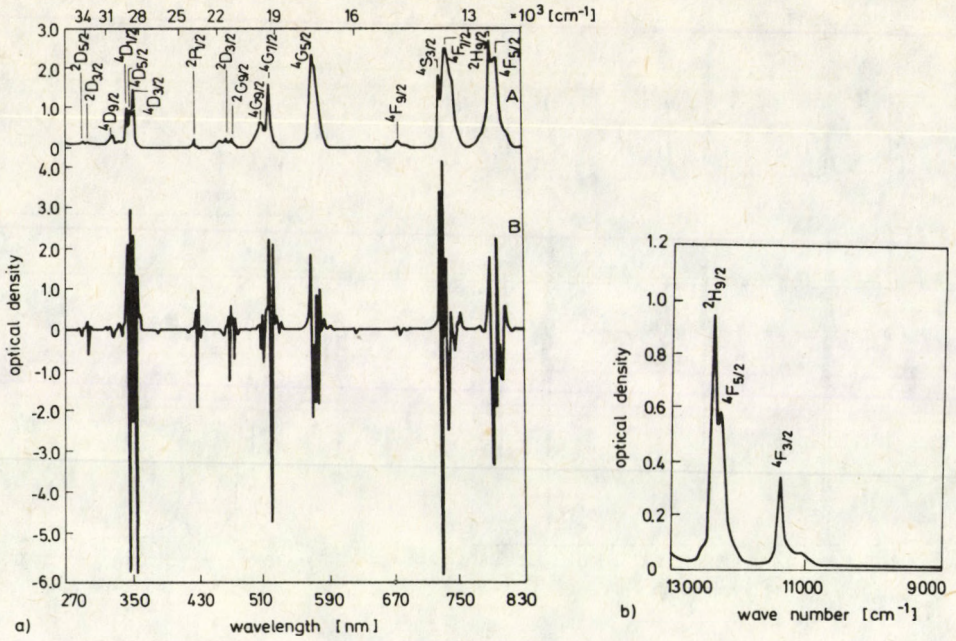

Fig. 4a. Absorption spectrum of Nd^{3+}:$CdCl_2$ (a) normal (b) second derivative
Fig. 4b. Near infrared absorption spectrum of Nd^{3+}:$CdCl_2$

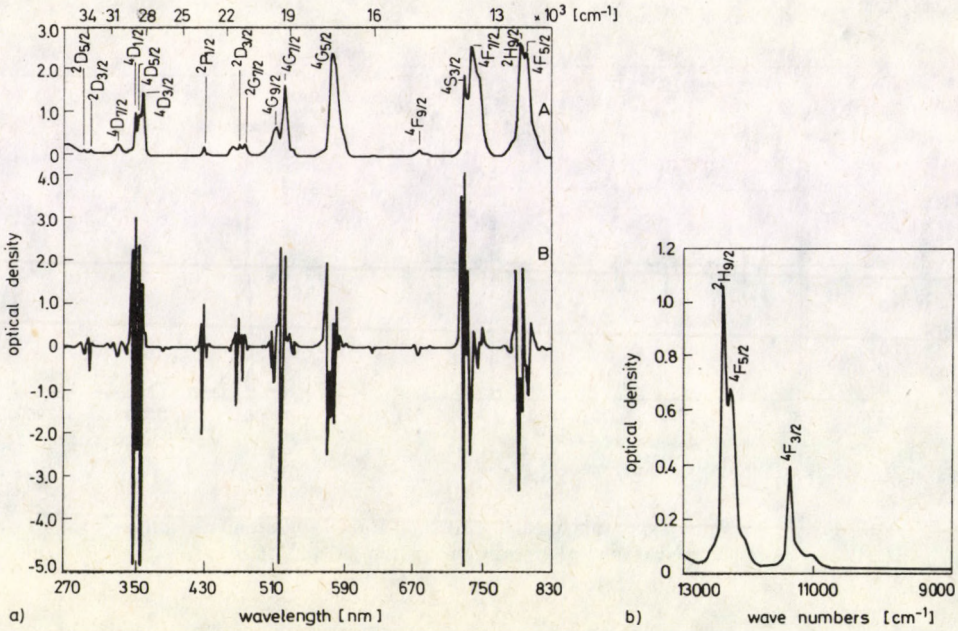

Fig. 5a. Absorption spectrum of Nd^{3+}:NH_4Cl (a) normal (b) second derivative
Fig. 5b. Near infrared absorption spectrum of Nd^{3+}:NH_4Cl

Table I

Experimental and calculated energy levels for Nd^{3+} complexes in solution

Energy levels	Nd^{3+} in $NdCl_3$		Nd^{3+} in $MgCl_2$		Nd^{3+} in $CaCl_2$		Nd^{3+} in $CdCl_2$		Nd^{3+} in NH_4Cl	
	E_{expt} cm^{-1}	E_{calc} cm^{-1}	E_{expt} cm^{-1}	E_{calc} cm^{-1}	E_{expt} cm^{-1}	E_{calc} cm^{-1}	E_{expt} cm^{-1}	E_{calc} cm^{-1}	E_{expt} cm^{-1}	E_{calc} cm^{-1}
$^2D_{5/2}$	34347	34429	34 447	34 419	34 305	34 416	34 433	34 406	34 364	34 415
$^2D_{3/2}$	33 323	33 304	33 445	33 305	33 323	33 281	33 401	33 268	33 357	33 293
$^4D_{7/2}$	30 360	30 384	30 305	30 340	30 306	30 364	30 488	30 303	30 357	30 372
$^4D_{1/2}$	28 653	28 736	28 735	28 741	28 653	28 371	28 818	28 707	28 614	28 732
$^4D_{5/2}$	28 327	28 389	28 309	28 392	28 249	28 371	28 369	28 360	28 329	28 335
$^4D_{3/2}$	28 051	28 107	28 090	29 114	28 011	28 087	28 169	28 075	28 105	28 050
$^2P_{1/2}$	23 365	23 316	23 364	23 317	23 256	23 300	23 364	23 283	23 310	23 214
$^2D_{3/2}$	21 277	21 243	21 322	21 243	21 277	21 219	21 299	21 214	21 277	21 239
$^2G_{9/2}$	20 921	21 009	20 965	20 921	21 018	20 988	20 986	20 980	21 008	21 002
$^4G_{9/2}$	19 531	19 431	19 569	19 436	19 418	19 416	19 512	19 411	19 455	19 436
$^4G_{7/2}$	19 139	19 053	19 157	19 056	19 084	19 032	19 194	19 019	19 120	19 044
$^4G_{5/2}$	17 246	17 066	17 261	17 070	17 201	17 054	17 291	17 048	17 236	17 066
$^4F_{9/2}$	14 749	14 652	14 738	14 654	14 727	14 464	14 749	14 706	14 639	14 646
$^4S_{3/2}$	13 687	13 585	13 643	13 587	13 605	13 578	13 661	13 575	13 642	13 582
$^4F_{7/2}$	13 387	13 385	13 513	13 387	13 477	13 377	13 514	13 374	13 495	13 582
$^2H_{9/2}$	12 555	12 632	12 563	12 641	12 563	12 614	12 587	12 602	12 579	12 630
$^4F_{5/2}$	12 438	12 468	12 477	12 415	12 420	12 492	12 405	12 402	12 461	12 410
$^4F_{3/2}$	11 370	11 406	11 375	11 409	11 370	11 399	11 385	11 395	11 380	11 405
r.m.s. deviation	±81.0		±91.0		±74.0		±111.0		±75.0	

Table II

Slater—Condon (F_2, F_4 and F_6), spin—orbit (ξ_{4f}) and refractive index (n) for $NdCl_3$ complexes in solution

Parameters	Nd^{3+} in $NdCl_3$	Nd^{3+} in $MgCl_2$	Nd^{3+} in $CaCl_2$	Nd^{3+} in $CdCl_2$	Nd^{3+} in NH_4Cl
F_2	328.13	327.93	328.08	327.97	328.00
F_4	51.14	51.25	50.99	50.91	51.16
F_6	5.32	5.31	5.32	5.32	5.31
ξ_{4f}	856.00	855.66	856.05	856.81	855.02
n	1.3317	1.3834	1.3635	1.3595	1.3772

dipole line strengths for the $NdCl_3$ complexes are presented in Table III. Theoretical estimates of oscillator strengths calculated from Judd—Ofelt and electric (S_{ed})-magnetic (S_{md}) dipole line strength methods are in good agreement with the experimental values. The values of experimental and calculated oscillator strengths for the $NdCl_3$ complexes are given in Table IV.

Bonding

The nephelauxetic ratio (β) has been calculated as

$$\beta = v_c / v_a \tag{15}$$

where v_c and v_a refer to the energies of the corresponding transitions in the complex and aquo ion, respectively. In the evaluation of bonding parameter (δ), the average nephelauxetic ratio $\bar{\beta}$ was used. The bonding parameter (δ) has been calculated [2, 18]

$$\delta = \frac{1 - \bar{\beta}}{\bar{\delta}} \times 100 . \tag{16}$$

The bonding will be covalent or ionic depending upon the positive or negative nature of the value. The following Table gives the details of the nephelauxetic ratio $\bar{\beta}$ and bonding parameter (δ) for Nd^{3+} complexes.

Complex	Nephelauxetic ratio ($\bar{\beta}$)	Bounding parameter (δ)
Nd^{3+}: $MgCl_2$	1.0014	−0.1431
Nd^{3+}: $CaCl_2$	0.9994	0.0585
Nd^{3+}: $CdCl_2$	1.0017	−0.1707
Nd^{3+}: NH_4Cl	1.0006	−0.0063

Since δ values are negative for Nd^{3+} in $MgCl_2$, $CdCl_2$ and NH_4Cl complexes, the nature of bonding is ionic in these complexes. The positive nature of δ for Nd^{3+} in $CaCl_2$ suggests covalent bonding in this complex.

Table III

Electric (S_{ed}), magnetic (S_{md}) dipole line strengths for $NdCl_3$ complexes in solution

Energy levels	Nd^{3+} in $NdCl_3$		Nd^{3+} in $MgCl_2$		Nd^{3+} in $CaCl_2$		Nd^{3+} in $CdCl_2$		Nd^{3+} in NH_4Cl	
	S_{ed} ($\times 10^{22}$)	S_{md} ($\times 10^{22}$)	S_{ed} ($\times 10^{22}$)	S_{md} ($\times 10^{22}$)	S_{ed} ($\times 10^{22}$)	S_{md} ($\times 10^{22}$)	S_{ed} ($\times 10^{22}$)	S_{md} ($\times 10^{22}$)	S_{ed} ($\times 10^{22}$)	S_{md} ($\times 10^{22}$)
$^4D_{7/2}$	1.67	0.229	2.20	0.003	2.60	0.007	2.91	0.007	2.49	0.008
$^4D_{1/2}$	35.76	0	50.18	0	44.98	0	57.65	0	59.29	0
$^4D_{5/2}$	12.66	0	17.75	0	17.47	0	20.94	0	20.06	0
$^4D_{3/2}$	30.70	0	43.52	0	39.76	0	50.62	0	51.41	0
$^2P_{1/2}$	4.66	0	6.83	0	6.01	0	8.24	0	8.00	0
$^2D_{3/2}$	3.80	0	3.74	0	3.34	0	3.89	0	4.23	0
$^2G_{9/2}$	6.33	0.016	6.89	0.002	5.82	0.008	7.74	0.005	9.13	0.002
$^4G_{9/2}$	19.22	0.021	24.38	0.008	23.46	0.015	26.99	0.008	27.57	0.088
$^4G_{7/2}$	35.72	0.007	46.94	0.017	50.63	0.016	44.71	0.001	52.09	0.022
$^4G_{5/2}$	170.40	0	227.59	0	221.88	0	197.80	0	231.90	0
$^4F_{9/2}$	12.27	0.059	15.24	0.001	16.28	0.065	15.22	0.001	17.07	0.023
$^4S_{3/2}$	53.29	0	64.70	0	64.49	0	72.18	0	69.55	0
$^4F_{7/2}$	59.19	0.010	72.38	0.034	71.21	0.045	83.02	0.019	81.11	0.041
$^2H^9_{/2}$	23.97	0.015	31.82	0.007	33.07	0.011	36.26	0.050	35.49	0.005
$^4F_{5/2}$	123.20	0	157.41	0	152.00	0	178.50	0	176.20	0
$^4F_{3/2}$	43.11	0	59.92	0	56.07	0	68.58	0	66.79	0

Table IV

Experimental and theoretical estimates of oscillator strengths ($f \times 10^6$) of the observed bands for $NdCl_3$ complexes in solution

Energy levels	(i) Nd^{3+} in $NdCl_3$			(ii) Nd^{3+} in $MgCl_2$			(iii) Nd^{3+} in $CaCl_2$			(iv) Nd^{3+} in $CdCl_2$			(v)Nd^{3+} in NH_4Cl		
	f_{expt}	f^a_{calc}	f^b_{calc}	f_{expt}	f^a_{calc}	f^b_{calc}	f_{expt}	f^a_{calc}	f^b_{calc}	f_{expt}	f^a_{calc}	f^b_{calc}	f_{expt}	f^a_{calc}	f^b_{calc}
$^4D_{7/2}$	0.07	0.12	0.12	0.15	0.09	0.09	0.12	0.10	0.11	0.13	0.12	0.12	0.12	0.10	0.10
$^4D_{1/2}$	1.21	1.32	1.32	1.61	1.93	1.92	1.48	1.70	1.70	1.49	2.18	2.18	1.51	2.26	2.26
$^4D_{5/2}$	0.56	0.46	0.46	0.86	0.67	0.67	0.73	0.65	0.65	0.84	0.78	0.78	1.00	0.76	0.76
$^4D_{3/2}$	1.03	1.11	1.11	1.44	1.63	1.63	1.28	1.47	1.46	1.75	1.87	1.87	1.63	1.92	1.92
$^2P_{1/2}$	0.11	0.14	0.14	0.23	0.21	0.21	0.18	0.18	0.19	0.22	0.25	0.25	0.18	0.25	0.25
$^2D_{3/2}$	0.08	0.10	0.10	0.18	0.11	0.11	0.15	0.09	0.09	0.17	0.11	0.10	0.19	0.12	0.12
$^2G_{9/2}$	0.10	0.17	0.17	0.23	0.19	0.19	0.19	0.16	0.16	0.23	0.21	0.21	0.30	0.26	0.26
$^4G_{9/2}$	0.32	0.49	0.48	0.52	0.64	0.64	0.93	0.60	0.60	0.69	0.61	0.69	0.56	0.71	0.72
$^4G_{7/2}$	0.83	0.88	0.89	1.33	1.20	1.20	1.13	1.12	1.28	1.47	1.28	1.12	1.61	1.32	1.32
$^4G_{5/2}$	3.75	3.79	3.79	5.23	5.24	5.24	5.01	5.03	5.00	4.47	3.83	4.49	5.29	5.32	5.31
$^4F_{9/2}$	0.09	0.22	0.25	0.12	0.30	0.30	0.12	0.30	0.34	0.14	0.29	0.30	0.17	0.35	0.33
$^4S_{3/2}$	0.59	0.94	0.94	0.86	1.18	0.78	1.16	1.16	1.18	0.97	1.30	1.29	0.17	0.35	0.33
$^4F_{7/2}$	1.07	1.02	1.02	1.25	1.31	1.31	1.13	1.26	1.26	1.38	1.47	1.47	0.92	1.26	1.26
$^2H_{9/2}$	1.49	0.39	0.41	1.57	0.53	0.53	1.55	0.55	0.55	1.72	0.60	0.60	1.49	0.59	0.59
$^4F_{5/2}$	1.88	1.98	1.97	1.97	2.62	2.62	2.45	2.49	2.49	2.77	2.93	2.93	2.84	2.92	2.92
$^4F_{3/2}$	0.79	0.63	0.63	1.21	0.91	0.91	1.00	0.84	0.84	1.52	1.03	1.02	1.51	1.01	1.01
r.m.s. deviation		±0.127			±0.309			±0.162			±0.414			±0.357	

where a, b are from Eqs (6 and 8)

Hypersensitive transition

Transitions where intensities are particularly sensitive to the host and follow the selection rule.

$$\Delta J \leqq 2, \qquad \Delta L \leqq 2 \qquad \text{and} \qquad \Delta S \leqq 0$$

are termed hypersensitive transition. For Nd^{3+}, the transition $^4G_{5/2} \leftarrow {}^4I_{9/2}$ is the hypersensitive transition. The parameter T_2 varies with the environment, at the same time parameter T_4 also varies even more and T_6 by about the same amount. A strong correlation exists between T_2 and the oscillator strengths of the observed bands which does not exist for T_4 and T_6 (It is because the above selection rules hold good for T_2).

Complex	$T_2(\times 10^9)$	$T_4(\times 10^9)$	$T_6(\times 10^9)$	$f(\times 10^6)$
Nd^{3+} in NH_4Cl	0.209	0.227	0.368	5.32
Nd^{3+} in $MgCl_2$	0.208	0.256	0.374	5.24
Nd^{3+} in $CaCl_2$	0.191	0.299	0.405	5.03
Nd^{3+} in $CdCl_2$	0.151	0.276	0.303	3.83
Nd^{3+} in $NdCl_3$	0.142	0.289	0.416	3.79

The oscillator strengths of the observed bands which are calculated with T_2, T_4 and T_6 are given in Table IV for all the Nd^{3+} complexes studied.

Crystal field splittings

Second derivative spectra of $NdCl_3$ complexes in different hosts show splitting in the electronic states $^4F_{5/2}$ and $^4G_{5/2}$ into two and three levels, respectively.

Since C_{3h} symmetry is common to trichlorides, we assumed the same symmetry for Nd^{3+} ion in all the complexes studied in the present work. In C_{3h} symmetry, $^4F_{5/2}$ and $^4G_{5/2}$ terms are expected to be split into three levels each designated as $\pm 1/2$, $\pm 3/2$ and $\pm 5/2$ crystal quantum states.

Table V

Operator equivalents in the intermediate field for Nd^{3+} complexes in solution

Complexes	Terms	$\langle j\|\|\alpha\|\|j\rangle$	$\langle j\|\|\beta\|\|j\rangle$	$\langle j\|\|v\|\|j\rangle$
Nd^{3+}:$NdCl_3$	$^4F_{5/2}$	0.014 70	0.001 43	0
	$^4G_{5/2}$	0.003 85	0.004 24	0
Nd^{3+}:$MgCl_2$	$^4F_{5/2}$	0.013 80	0.001 22	0
	$^4G_{5/2}$	0.003 38	0.003 91	0
Nd^{3+}:$CaCl_2$	$^4F_{5/2}$	0.014 11	0.001 33	0
	$^4G_{5/2}$	0.003 63	0.004 06	0
Nd^{3+}:$CdCl_2$	$^4F_{5/2}$	0.013 80	0.001 29	0
	$^4G_{5/2}$	0.003 45	0.004 12	0
Nd^{3+}:NH_4Cl	$^4F_{5/2}$	0.014 47	0.001 38	0
	$^4G_{5/2}$	0.003 75	0.004 11	0

Within a pure f^N configuration, the potential E_{CF} for C_{3h} symmetry may be written as

$$E_{CF} = A_{20}O_{20}\alpha_j + A_{40}O_{40}\beta_j + A_{60}O_{60}\nu_j + A_{66}O_{66}\nu_j, \tag{17}$$

where A_{20}, A_{40}, A_{60} and A_{66} are crystal field parameters, O_{20}, O_{40}, O_{60} and O_{66} are the operator matrix elements and α_j, β_j and ν_j are the operator equivalent factors. These α_j, β_j and ν_j factors are available in literature for all the states required in the above calculation except for the transitions $^4D_{5/2} \rightarrow {}^4F_{5/2}$, $^4G_{5/2}$; $^2D_{5/2} \rightarrow {}^2D'_{5/2}$, $^2F_{5/2}$, $^2F'_{5/2}$; $^2D'_{5/2} \rightarrow {}^2F_{5/2}$, $^2F'_{5/2}$, $^4F_{5/2} \rightarrow {}^4G_{5/2}$; $^2F_{5/2} \rightarrow {}^2F'_{5/2}$. The operator equivalent factors for these transtions are evaluated following the usual procedure of Judd [16] and are presented hereunder.

Transitions	α_j	β_j	ν_j
$^4D_{5/2} \rightarrow {}^4F_{5/2}$	0.0661	0.0090	0
$^4D_{5/2} \rightarrow {}^4G_{5/2}$	0.0121	−0.0002	0
$^2D_{5/2} \rightarrow {}^2D'_{5/2}$	−0.0118	−0.0025	0
$^2D_{5/2} \rightarrow {}^2F_{5/2}$	0.0185	−0.0014	0
$^2D_{5/2} \rightarrow {}^2F'_{5/2}$	0.0158	0.0028	0
$^2D'_{5/2} \rightarrow {}^2F_{5/2}$	−0.0097	−0.0033	0
$^4F_{5/2} \rightarrow {}^4G_{5/2}$	0.0347	0.0035	0
$^2D_{5/2} \rightarrow {}^2F_{5/2}$	−0.0227	0.0031	0
$^2F_{5/2} \rightarrow {}^2F'_{5/2}$	0.0447	−0.0018	0

The operator equivalent factors α_j, β_j, ν_j in the intermediate coupling case are calculated and presented in Table V. The operator matrix elements O_{20}, O_{40}, O_{60} and O_{66} are taken from Hufner [19].

The band maxima positions for the split components of $^4F_{5/2}$ and $^4G_{5/2}$ levels in Nd^{3+} complexes are given in Table VI. The energy difference between the two components observed for $^4F_{5/2}$ in the second derivative spectrum of $NdCl_3$ complexes could belong to the energy difference between the crystal quantum states of one set of the following

$$\begin{array}{ccc} \pm 1/2 & \text{and} & \pm 3/2 \\ \pm 3/2 & \text{and} & \pm 1/2 \\ \pm 1/2 & \text{and} & \pm 5/2 \\ \pm 5/2 & \text{and} & \pm 1/2 \\ \pm 3/2 & \text{and} & \pm 5/2 \\ \pm 5/2 & \text{and} & \pm 3/2 \end{array}$$

Table VI

Observed crystal field energy levels of $^4F_{5/2}$ and $^4G_{5/2}$ with their crystal quantum states in $NdCl_3$ complexes in solution

Energy levels	μ	Nd^{3+} in $NdCl_3$ $E\,[cm^{-1}]$	Nd^{3+} in $MgCl_2$ $E\,[cm^{-1}]$	Nd^{3+} in $CaCl_2$ $E\,[cm^{-1}]$	Nd^{3+} in $CdCl_2$ $E\,[cm^{-1}]$	Nd^{3+} in NH_4Cl $E\,[cm^{-1}]$
$^4F_{5/2}$	$\pm 5/2$	12 415	12 408	12 420	12 427	12 412
	$\pm 1/2$	12 458	12 441	12 465	12 465	12 444
$^4G_{5/2}$	$\pm 3/2$	17 180	17 188	17 210	17 182	17 202
	$\pm 5/2$	17 250	17 249	17 286	17 272	17 282
	$\pm 1/2$	17 284	17 279	17 311	17 301	17 306

Similarly the energy difference between two components of any three of the observed levels of $^4G_{5/2}$ could belong to one of the above six sets of crystal quantum states. Since the value of v_j is zero for $^4F_{5/2}$ and $^4G_{5/2}$ states, we then have the potential E_{CF} for these states as

$$E_{CF} = A_{20} O_{20} \alpha_j + A_{40} O_{40} \beta_j . \tag{18}$$

From the known α_j, β_j, O_{20}, and O_{40} values the crystal field parameters A_{20}, A_{40} were evaluated by solving 36 equations (six each belonging to $^4F_{5/2}$ and $^4G_{5/2}$ states). The crystal field parameters which were of the same order of parameters reported in literature were chosen as the appropriate parameters. With these parameters, the position of the third component level (which was not taken in earlier calculation) of $^4G_{5/2}$ was calculated and it is interesting to note that this is in good agreement with the experimental value.

After the crystal quantum states were fixed for the levels of Nd^{3+} in $NdCl_3$ complex, the crystal quantum numbers were assigned to the split levels of $^4F_{5/2}$ and $^4G_{5/2}$ states in the other Nd^{3+} complexes from the nature and position of the component levels. By solving simultaneous equations, the appropriate crystal field parameters were evaluated. The crystal quantum numbers assigned to the levels are also presented in Table VI. The calculated splittings are shown in Fig. 6. The crystal field parameters are presented in the following Table.

Crystal field parameters	Nd^{3+} in $NdCl_3$	Nd^{3+} in $MgCl_2$	Nd^{3+} in $CaCl_2$	Nd^{3+} in $CdCl_2$	Nd^{3+} in NH_4Cl
A_{20}	130.15	129.52	115.18	126.22	100.62
A_{40}	−101.04	−94.29	−71.59	−85.60	−69.85

	$^4F_{5/2}$				$^4G_{5/2}$			
	μ	Calc [cm^{-1}]	μ	Obs [cm^{-1}]	μ	Calc [cm^{-1}]	μ	Obs [cm^{-1}]
$Nd^{3+}:NdCl_3$	$\pm 3/2$	22.09	$\pm 3/2$		$\pm 3/2$	76.16	$\pm 3/2$	17 180
		11.17				97.48		70
	$\pm 5/2$	10.92	$\pm 5/2$	12 415	$\pm 5/2$	−21.32	$\pm 5/2$	17 250
		43.50		43		33.52		34
	$\pm 1/2$	−32.58	$\pm 1/2$	12 458	$\pm 1/2$	−54.84	$\pm 1/2$	17 284
$Nd^{3+}:MgCl_2$	$\pm 3/2$	17.05	$\pm 3/2$		$\pm 3/2$	65.49	$\pm 3/2$	17 188
		6.08				83.23		61
	$\pm 5/2$	10.97	$\pm 5/2$	12 408	$\pm 5/2$	−17.74	$\pm 5/2$	17 249
		39.02		33		30.00		30
	$\pm 1/2$	−28.05	$\pm 1/2$	12 441	$\pm 1/2$	−47.74	$\pm 1/2$	17 279
$Nd^{3+}:CaCl_2$	$\pm 3/2$	13.86	$\pm 3/2$		$\pm 3/2$	51.48	$\pm 3/2$	17 210
		3.29				64.74		76
	$\pm 5/2$	10.57	$\pm 5/2$	12 420	$\pm 5/2$	−13.26	$\pm 5/2$	17 286
		35.00		45		24.96		25
	$\pm 1/2$	−24.43	$\pm 1/2$	12 465	$\pm 1/2$	−38.22	$\pm 1/2$	17 311
$Nd^{3+}:CdCl_2$	$\pm 3/2$	16.45	$\pm 3/2$		$\pm 3/2$	62.61	$\pm 3/2$	17 182
		5.78				79.41		89
	$\pm 5/2$	10.77	$\pm 5/2$	12 427	$\pm 5/2$	−16.80	$\pm 5/2$	17 271
		38.00		38		29.00		30
	$\pm 1/2$	−27.23	$\pm 1/2$	12 465	$\pm 1/2$	−45.80	$\pm 1/2$	17 301
$Nd^{3+}:NH_4Cl$	$\pm 3/2$	14.46	$\pm 3/2$		$\pm 3/2$	50.89	$\pm 3/2$	17 202
		5.70				64.38		80
	$\pm 5/2$	8.76	$\pm 5/2$	12 412	$\pm 5/2$	−13.49	$\pm 5/2$	17 282
		31.99		32		23.91		24
	$\pm 1/2$	−23.23	$\pm 1/2$	12 444	$\pm 1/2$	−37.40	$\pm 1/2$	17 306

Fig. 6. The observed and calculated splittings of $^4F_{5/2}$ and $^4G_{5/2}$ levels in the second derivative spectra of $NdCl_3$ complexes. Here μ is the crystal quantum number

Acknowledgements

One of the authors (SB) is grateful to Dr. J. L. Rao for recording the spectra. His thanks are due to the CSIR (New Delhi, India) for awarding him a senior research fellowship.

References

1. B. R. Judd and R. Lowden, Proc. Roy. Soc. (London), **A251,** 127, 1959.
2. S. P. Sinha, Spectrochim Acta, **22,** 57, 1966.
3. V. J. Rao, Ind. J. Pure & Appl. Physics, **11,** 833, 1973.
4. H. M. Crosswhite, H. Crosswhite, H. Crosswhite, F. W. Kaseta and R. Sarup, J. Chem. Phys., **64,** 1981, 1976.
5. K. L. Brower, H. J. Stapleton and E. O. Brower, Phys. Rev., **150,** 198, 1966.
6. R. M. Clarke, Phys. Rev. Lett. **27,** 638, 1971.
7. W. T. Carnall, P. R. Fields and R. Rajnak, J. Chem. Phys., **49,** 4412, 1968.
8. S. P. Tandon, Spectroscopy Lett., **7,** 515, 1974.
9. Jeanlouis, Chem. Phys., **33,** 385, 1979.
10. W. T. Carnall, H. Crosswhite and H. M. Crosswhite, Energy Level Structure and Transition Probabilities of the Trivalent Lanthanides in LaF_3, Argonne National Laboratory, Argonne, Illinois, U.S.A., 1978.
11. E. Y. Wong, J. Chem. Phys., **35,** 544, 1961.
12. B. R. Judd, Phys. Rev., **127,** 750, 1962.
13. G. S. Ofelt, J. Chem. Phys., **37,** 511, 1962.
14. C. W. Nielson and G. F. Koster, Spectroscopic Coefficients for p^n, d^n and f^n Configuration. MIT Press, Cambridge, Massachusetts, 1964.
15. M. Rotenberg, R. Bivins, N. Metropolis and J. R. Wooten, 3*j* and 6*j* Symbols. MIT Press, Cambridge, Massachusetts, 1959.
16. B. R. Judd, Proc. Roy. Soc. (London), **A251,** 134, 1959.
17. G. Racah, Phys. Rev., **62,** 438, 1942.
18. S. P. Tandon, P. C. Mehta and K. Tandon, Optics Commun., **1,** 352, 1970.
19. S. Hufner, Optical Spectra of Transparent Rare Earth Compounds. Academic Press, New York, 1978.

Acta Physica Hungarica 54 (3—4), pp. 249—266 (1983)

ON THE BEHAVIOUR OF THE UHF METHOD NEAR THE "CRITICAL POINT"

I. MAYER

Central Research Institute for Chemistry of the Hungarian Academy of Sciences
1525 Budapest, Hungary

(Received 17 August 1982)

The properties of the unrestricted Hartree—Fock (UHF) wave function are discussed with particular attention to the vicinity of the "critical point" where the UHF wave function starts to differ from the restricted Hartree—Fock (RHF) one. By considering the simplest analytically solvable model, the origin of the critical point is analysed, based on the decomposition of the DODS determinant in terms of the full CI wave functions. It is shown that the UHF energy curve departs from the RHF one by exhibiting a discontinuity of the second derivative. (The first derivative of the UHF energy is continuous for any system.) The wave function obtained by *subsequent* spin projection of the UHF wave function (i.e. without performing orbital reoptimization) gives a discontinuity already for the first derivative of the energy, showing that this procedure is inapplicable to calculate potential curves.

1. Introduction; a numerical example

The "unrestricted" Hartree-Fock (UHF) method applying single determinant DODS ("different orbitals for different spins") wave function is, as is well known, probably the simplest one accounting for a part of the correlation energy and correcting the improper dissociation behaviour of the usual "restricted" Hartree—Fock (RHF) method using doubly filled orbitals. However, it is known that in many cases the UHF method fails to give solutions differing from the RHF one. Often, e.g. for the H_2 molecule [1, 2], the UHF orbitals are "split" (i.e. we obtain really different orbitals for different spins) only at larger internuclear distances.

The present paper deals mainly with the consideration of a very simple analytically solvable model problem, devoted to obtain a better qualitative understanding of this phenomenon. Our interest will be focused on the effects which take place in the vicinity of the "critical point" where the splitting of the UHF orbitals starts. This was motivated by some problems encountered in our former *ab initio* study [3] of the potential curves of the B—H molecule given by different one-electron methods, and were not solvable by means of numerical calculations only. For this reason, before going to consider the analytical model, we shall briefly recall, from a slightly different point of view, some results of these calculations:

It was found that the RHF curve shows the known incorrect dissociation properties and the UHF solution does not differ from the RHF one up to relatively

large interatomic distances (~ 3.4 a.u.). With the further increase of the internuclear separation the UHF potential curve departs *quite smoothly* from the RHF one (Fig. 1) and then very quickly approaches a correct asymptotic energy value. The most impressing is the behaviour (see Fig. 1) of the potential curve obtained by performing the spin projection of the UHF wave function (UHF + SP method). As the separation of the RHF and UHF curves occurs, the UHF + SP curve at first decreases with the increase of the internuclear distance, then goes over a minimum and starts to increase only at $R_{BH} \sim 3.6$ a.u. (A correct potential curve would increase monotonically at these separations.) The complete potential curves are shown and discussed in [3]. The UHF + SP procedure should be distinguished from the spin projected extended Hartree—Fock (EHF) method [4, 5] in which the spin projected wave function itself is optimized variationally. For the B—H molecule the EHF method gave a potential curve which had a well-balanced shape and was correct not only qualitatively but at least semiquantitatively at all interatomic distances [3].

We were not able to follow numerically how exactly the UHF + SP curve approaches the RHF one with the further decrease of the internuclear distance, since it

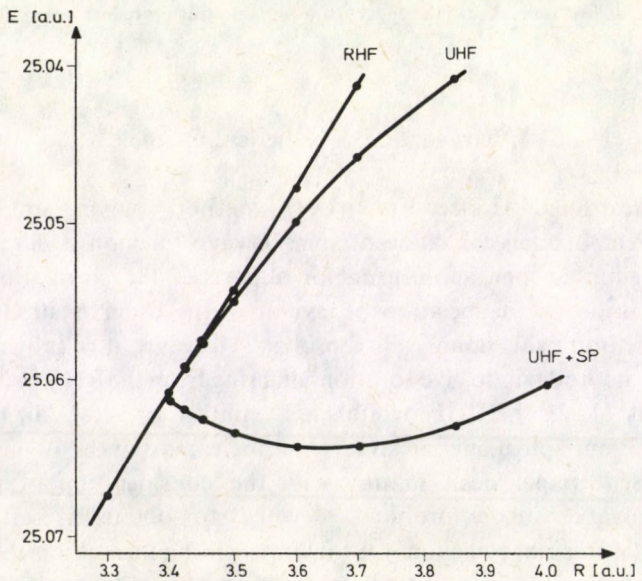

Fig. 1. Potential curves of the BH molecule near the "critical point"

became impossible to obtain converged UHF solutions reliably differing from the RHF ones [3]. Nevertheless, the inspection of Fig. 1 (which is essentially a part of Fig. 1 in [3], drawn with larger scales on both axes) suggests that it seems rather unlikely that the UHF + SP curve will take a very short turn and then approach smoothly the RHF one, as the UHF curve does. On the contrary, one may expect that the UHF + SP curve

will meet the RHF one quite sharply at an internuclear distance about 3.395 a.u. This expectation is in agreement with the behaviour of the overlap integrals λ_{UHF} of the corresponding orbitals* obtained by performing the pairing of the UHF ones. Fig. 2 shows how the lowest λ_{UHF} depends on the interatomic distance. It is most probable that the curve $\lambda_{UHF(min)}$ crosses sharply the unity level at the same internuclear distance $R \approx 3.395$ a.u. where the energy curves meet each other. This means that this point is the "critical" one, in which all the UHF orbitals become doubly filled (all $\lambda_{UHF} = 1$), thus coincide with the RHF ones, and in this point we shall really have $E_{UHF+SP} = E_{UHF} = E_{RHF}$ for the energies. In other words, as far as such conclusions may be drawn merely

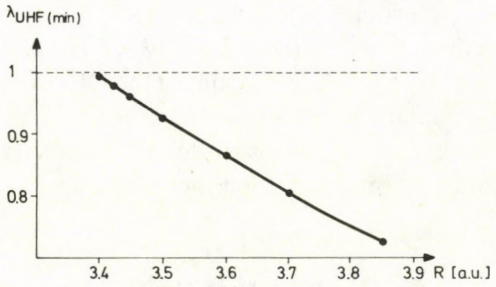

Fig. 2. The lowest overlap integral of the UHF corresponding orbitals for the BH molecule as a function of the internuclear distance

on the basis of numerical calculations, these results indicate that at this point the specific UHF solution differing from the RHF one disappears completely. (If the specific UHF solution would exist everywhere but approach the RHF one so closely that they become indistinguishable numerically, then all three energy curves would approach smoothly each other, as well as the curve $\lambda_{UHF(min)}$ the unity level.)

Now, there appear different questions concerning the behaviour of the potential curves and wave functions in the vicinity of the critical point. These questions are related, of course, not only to the calculations described in [3].

The most important problem probably consists in a deeper understanding of the origin of the "critical point". Furthermore, the RHF and UHF curves coincide with each other at the internuclear distances smaller than the critical one and become slowly separated when the internuclear distance increases. Apparently both curves are continuous and smooth. Nevertheless, as Pulay emphasized [7], it follows from the properties of Taylor expansions that at least for one of these two curves there must be a discontinuity in some of the (higher) derivatives. In fact, if all the derivatives would be

* According to the known "pairing theorem" [6] it is always possible to find unitary transformations of the orbitals which ensure without changing the many-electron determinant wave function that the orbitals a_i and b_i filled with spins α and β,respectively, become not only orthonormalized but also "paired": $\langle a_i \mid b_j \rangle = \lambda_i \delta_{ij} (0 \leqq \mid \lambda_i \mid \leqq 1)$. The paired orbitals are often called "corresponding orbitals". In the case of the B—H molecule the pairing led also to a well-pronounced localization of the orbitals, the lowest $\mid \lambda_i \mid$ always corresponded to the B—H bond.

continuous, the curves would coincide everywhere, because it would be possible to expand them into a common Taylor series around an arbitrary point within the interval of the internuclear distances smaller than the critical one. There the curves are identical and, therefore, all the derivatives occurring in their Taylor expansion are equal.

The above problem is closely related to the fate of the specific UHF solution at the internuclear distances smaller than the critical one: whether or not the UHF solution has an analytical continuation in this interval, corresponding again to a stationary (even if not minimum) energy value.

It seems also desirable to obtain a better understanding, why the existence of the critical point leads to the sharp departure of the UHF + SP potential curve from the RHF one and to that of the λ_{UHF} curve from the level $\lambda = 1$. It is also of interest to discuss the qualitative differences between the behaviour of the UHF and spin projected EHF methods: the RHF wave function represents a particular solution of both UHF and EHF equations, but only in the EHF case exists for all internuclear distances a distinct (specific) solution with an energy lower than the RHF one.

2. The simplest model

In order to obtain a qualitative answer for the problems raised above, we decided to perform an analytical study of the most simple model system for which these questions have a meaning at all. The model problem selected is that of the H_2 molecule treated at the CNDO level of integral approximation, or — which is mathematically the same — the PPP model for the π-electrons of the ethylene molecule.

Let us denote by χ_1 and χ_2 the two atomic orbitals (AO-s) and introduce the notations h_{ij} and γ_{ij} for the elements of the one-electron (core) and Coulomb integral matrices. Any wave function with the projection $S_z = 0$ of the resulting spin can be expressed as a linear combination of the four determinants which can be built up of the pure AO-s χ_1, χ_2 and have $S_z = 0$. By diagonalizing the 4 by 4 Hamiltonian matrix in the space of these four determinants one easily finds the solutions (cf. [8], for instance) of the full CI problem, which give the exact energies and wave functions for the model under consideration. The exact ground state wave function is a Weinbaum's type spatially symmetric singlet with the energy

$$E_{S1} = t + \frac{\gamma}{2} - \frac{1}{2}\sqrt{\gamma^2 + 16\beta^2}, \tag{1}$$

where we have introduced the notations

$$\begin{aligned} t &= 2h_{11} + \gamma_{12}; \\ \beta &= h_{12} < 0; \\ \gamma &= \gamma_{11} - \gamma_{12} > 0. \end{aligned} \tag{2}$$

It is evident that the inequalities indicated in (2) hold for any reasonable electronic model-Hamiltonian.

There is another symmetric singlet solution having the energy

$$E_{S2} = t + \frac{\gamma}{2} + \frac{1}{2}\sqrt{\gamma^2 + 16\beta^2}, \tag{3}$$

as well as an antisymmetric singlet with the energy

$$E_{SA} = t + \gamma, \tag{4}$$

and a single (antisymmetric) triplet wave function having the energy

$$E_T = t. \tag{5}$$

It is easy to see that the energy of the ground state singlet is always lower than that of the triplet while the other two singlets lie above the triplet.

The RHF wave function is uniquely determined by the symmetry of the model and coincides with the simplest LCAO-MO wave function:

$$\Psi_{RHF} = \hat{\mathcal{A}}\,[\varphi(1)\alpha(1)\varphi(2)\beta(2)], \tag{6}$$

where the orbital φ is defined as

$$\varphi = \frac{1}{\sqrt{2}}(\chi_1 + \chi_2), \tag{7}$$

and $\hat{\mathcal{A}}$ is the antisymmetrizer.

The RHF energy is

$$E_{RHF} = t + \frac{\gamma}{2} + 2\beta. \tag{8}$$

A DODS determinant wave function may be written as

$$\Psi_{DODS} = \hat{\mathcal{A}}\,[a(1)\alpha(1)b(2)\beta(2)], \tag{9}$$

where

$$a = \frac{1}{\sqrt{1+q^2}}(\chi_1 + q\chi_2); \qquad b = \frac{1}{\sqrt{1+q^2}}(\chi_2 + q\chi_1). \tag{10}$$

The orbitals a and b are related by the symmetry transformation, as it is usually obtained for the UHF orbitals of the systems of this type.

Assuming the coefficient q to be real, we obtain the energy of the DODS function as

$$E_{DODS} = t + 4\beta p + 2\gamma p^2, \tag{11}$$

where

$$p = \frac{q}{1+q^2}. \tag{12}$$

It follows from (12) that the following inequality holds for the parameter p:

$$|p| \leqq \frac{1}{2}, \tag{13}$$

otherwise q becomes complex. The limiting value $|p| = 1/2$ is achieved if $|q| = 1$. In turn, if $p = 1/2$ then $q = 1$ and the DODS wave function reduces to the RHF one. As it is easy to see, the overlap of the DODS orbitals a and b is $\lambda = \langle a|b\rangle = 2p$.

Let us require the energy (11) to be stationary under the variation of the orbital coefficients (i.e., under the variation of the quantity q). We have

$$\frac{dE_{\text{DODS}}}{dq} = \frac{dE_{\text{DODS}}}{dp} \cdot \frac{dp}{dq} = 0. \tag{14}$$

Therefore, (11) will be stationary either if $\frac{dp}{dq} = 0$ or if $\frac{dE_{\text{DODS}}}{dp} = 0$. In the first case we find $\frac{dp}{dq} = 0$ if $1 - q^2 = 0$, i.e. $q = \pm 1$. The upper sign corresponds to the RHF wave function (6), the lower to a determinant in which the antibonding orbital $\frac{1}{\sqrt{2}}(\chi_1 - \chi_2)$ is doubly filled. Thus, as expected, the RHF wave function is a particular solution of the UHF problem. The specific UHF solution is obtained if the condition

$$\frac{dE_{\text{DODS}}}{dp} = 0 \tag{15}$$

is fulfilled. By performing the differentiation, we obtain the condition of the stationary energy as

$$p = -\frac{\beta}{\gamma} = \frac{|\beta|}{\gamma}. \tag{16}$$

If $\gamma \geqq 2|\beta|$, $p \leqq 1/2$, and we may find from (12) two real values (q_1 and q_2) of q ensuring the fulfilment of (16). Thus we obtain two UHF wave functions which, however, differ only by the interchange of the spins α and β or that of the AO-s χ_1 and χ_2 in (10), since $q_1 = 1/q_2$. By substituting (16) into (11) we have for their energy the value $t - 2\beta^2/\gamma$. If, however, $\gamma < 2|\beta|$, we have $p > 1/2$, therefore by substituting the value of p prescribed by the stationarity condition (16) we obtain from (12) complex roots for the quantity q which was assumed to be real. It may be shown by a slightly more involved analysis that the situation is not changed if we permit the two UHF orbitals to have quite arbitrary, even complex, orbital coefficients (cf. [2]). In this most general case we obtain again exactly the same UHF solutions as above, and if $\gamma < 2|\beta|$, the condition of the stationary energy for the specific UHF solution leads to complex roots for a quantity which is defined as an absolute value, and must be, therefore, real. Consequently, the point in which $\gamma = 2|\beta|$ is the "critical point" where the specific UHF solution ceases to

exist and there is *no analytical continuation* of the specific UHF solution beyond the critical point. Since the UHF energy is defined as the minimum possible energy which may be obtained by using single determinant wave functions, we must write

$$E_{\mathrm{UHF}} = \begin{cases} t - \dfrac{2\beta^2}{\gamma} & \text{if} \quad \gamma \geqq 2|\beta|\,, \qquad (17a) \\ E_{\mathrm{RHF}} & \text{if} \quad \gamma < 2|\beta|. \qquad (17b) \end{cases}$$

It is easy to see that $E_{\mathrm{UHF}} < E_{\mathrm{RHF}}$ if there exists the specific UHF solution and that $E_{\mathrm{UHF}} = E_{\mathrm{RHF}}$ in the critical point $\gamma = 2|\beta|$. Here the UHF wave function also becomes identical with the RHF one and, therefore, $\lambda = 2p = 1$. According to the above discussion, the absence of the analytical continuation of the UHF wave function in the interval $\gamma < 2|\beta|$ may be connected with the fact that the overlap integral $\lambda = 2p = 2|\beta|/\gamma$ cannot exceed unity in the absolute value.

The complete disappearance of the specific UHF solution in the case of $\gamma < 2|\beta|$ means that the RHF solution becomes the absolute minimum on the energy-hypersurface for the single determinant wave functions. In the interval $\gamma > 2|\beta|$, however, the RHF energy represents not a minimum but only a saddle point, and there is a pair of symmetrically situated minima corresponding to the two UHF wave functions differing from each other by interchanging the AO-s χ_1 and χ_2 or the spins α and β. As the critical point is approached ($\gamma/|\beta| \to 2$), the UHF minima become more shallow and move closer to the RHF saddle point (λ tends to 1) until they coincide with the latter (and with each other) when $\gamma = 2|\beta|$. It is easy to see that in this critical point not only the first derivative of the energy $\mathrm{d}E_{\mathrm{DODS}}/\mathrm{d}q$ is equal zero, but the second derivative $\mathrm{d}^2E_{\mathrm{DODS}}/\mathrm{d}q^2$ vanishes, too. Therefore, in the vicinity of the critical point the energy hypersurface becomes extremely flat in the directions corresponding to the orbital splitting; this is also in accordance with the numerical experience [3].

3. The origin of the "critical point"

Since the orbital splitting is permitted, the UHF method means the use of a more flexible trial wave function in the variational procedure than the RHF one. It seems worthwhile to discuss why such an increased flexibility can lead to a considerable energy gain in one geometric interval but becomes completely ineffective in another. For this purpose we shall consider the expansions of different SCF-type functions as linear combinations of the exact (full CI) eigenfunctions of the model-Hamiltonian characterizing our system.

The RHF wave function is a superposition of the two symmetric singlet eigenfunctions having the energies (1) and (3), with the weights (squares of the coefficients)

$$\frac{(1+x)^2}{2(1+x^2)} \quad \text{and} \quad \frac{(1-x)^2}{2(1+x^2)},$$

respectively. Here

$$x = \frac{\sqrt{\gamma^2 + 16\beta^2} + \gamma}{4|\beta|} > 1 \tag{18}$$

is the ratio of the coefficients at the covalent and ionic terms in the exact (full CI) ground-state eigenfunction. As known, the ionic terms are strongly exaggerated in the RHF wave function: they have the same weight as the covalent ones. Accordingly, the highest CI wave function consisting mainly of these ionic terms* appears with a considerable coefficient in the expansion of the RHF wave function.

The single determinant DODS wave function (9) is not an eigenfunction of the total spin ($\hat{S}^2$) but is a mixture of singlet and triplet components. In our analytic model the two symmetric singlet and the triplet eigenfunctions have the weights

$$\frac{(2p+x)^2}{2(1+x^2)}, \quad \frac{(2px-1)^2}{2(1+x^2)} \quad \text{and} \quad \frac{1-4p^2}{2},$$

respectively. (The antisymmetric singlet does not appear in the expansion.) If $p = 1/2$, we come back to the RHF case. When p decreases from this value, the weight of the higher singlet decreases too, until it becomes zero at $p = 1/2x$. This value of p, however, is not reached in the UHF case, i.e. if we perform the variational optimization of the *single* DODS determinant wave function. Really, the triplet energy (5) is lower than that of the highest singlet but the triplet component appears not simply in place of the latter. With the decrease of p the weight of the exact ground state (lowest singlet) also decreases and, since $E_T > E_{S1}$, this effect is connected with an energy increase.**

Performing the variational optimization of the UHF wave function we seek for the best compromise between these effects. It is clear that one obtains a specific UHF solution differing from the RHF one only if (at the given value of the parameters) the factors leading to the energy gain are able to overcompensate those which are connected with a loss in the energy. Thus, in our case the net energy effect due to the orbital splitting may be written as

$$E_{\text{DODS}} - E_{\text{RHF}} = (1-2p)\left[2|\beta| - \frac{\gamma}{2}(1+2p)\right], \tag{19}$$

and, as easy to see, it really cannot be negative if $\gamma < 2|\beta|$, since $(1-2p) \geqq 0$ and $(1+2p) \leqq 2$. In this case, therefore, the decrease of the weight of the exact ground state in the DODS wave function prevents the orbital splitting.

* For the higher symmetric singlet the ratio between the coefficients at the covalent and ionic terms is given by $x' = -1/x$, and, therefore, $|x'| < 1$.

** A characteristic numerical example for the sharp decrease of the overlap between the UHF and exact ground state wave functions as compared with the RHF case may be found in [9, 10]. (We note here that the lowest triplet energy for the π-electron model of butadiene discussed in [9] is -76.634 eV and not -67.634 eV as it was misprinted.)

From a more physical point of view, the above results may be interpreted as follows. Permitting the orbital splitting we can decrease the weight of the ionic terms overestimated by the RHF wave function but, at the same time, the appearance of the triplet component in the DODS wave function leads to the decrease of the bond order between the atoms, too. (The bond order is 1 for the RHF case and decreases to $2p$ in the DODS one.) As the internuclear distance decreases, the value $\gamma=\gamma_{11}-\gamma_{12}$ giving the difference of the energy between the purely ionic and covalent configurations decreases, while the bonding parameter β increases in the absolute value. Now, it may happen that starting from some value of the internuclear distance (from the "critical point") the energy loss connected with the decrease of the bond order overweights the effect due to the improvement in the ionic terms, and therefore, no orbital splitting will take place. The competition of these effects becomes very perspicuous if we rewrite (19) as

$$E_{\mathrm{DODS}}-E_{\mathrm{RHF}}=2|\beta|(1-2p)-\frac{\gamma}{2}(1-4p^2). \tag{20}$$

Similar arguments may be used to explain qualitatively the observation [3] (see also Fig. 1 in [2]) that the UHF potential curve approaches the (correct) asymptotic value *too* quickly when the interatomic distance increases. In the limit of the infinite interatomic separations the lowest singlet and triplet CI energies become equal due to the absence of the interaction between the atoms, but the triplet energy approaches the common asymptotic value from above while the singlet energy from below. As the energy difference between the ionic and covalent configurations increases with increasing interatomic distance, the orbital splitting and thus the weight of the triplet component in the UHF wave function also increase, until the weights of the triplet and of the singlet become equal in the limit of infinite separations. At intermediate interatomic distances the UHF potential curve represents some mean between the singlet and triplet curves, and this places it close to the asymptotic level. In other terms, as the interatomic distance increases, it becomes quickly of minor importance from the point of view of the UHF energy (as compared with that of reducing the weight of the ionic terms) that the large triplet component is connected with the decrease of the bond order. This means that at these distances the UHF method *underestimates* the remaining binding effects though the latter still have an important influence on the detailed shape of the exact potential curve. It may be of interest to note that the bond order $D_{12}=2x/(1+x^2)$ for the exact full CI wave function is always less than 1. Therefore, the RHF method *overestimates* the energy effects connected with the bond order term, and the same holds, of course, for the UHF wave function in the interval where it coincides with the RHF one.

One can conclude that the single determinant UHF wave function does not have enough flexibility for both to describe adequately the binding effects and to reduce effectively the weight of the ionic terms, and gives, therefore, a too quick transition between the limiting cases for which essentially only one of these factors is taken into account.

If we subject the DODS determinant to spin projection then the triplet component disappears and the wave function

$$\Psi_{SP}=\hat{\mathcal{O}}^S\Psi_{DODS}=\hat{\mathcal{O}}^S\hat{\mathcal{A}}\,[a(1)\alpha(1)b(2)\beta(2)]= \tag{21}$$

$$=\frac{1}{2}\{\hat{\mathcal{A}}\,[a(1)\alpha(1)b(2)\beta(2)]-\hat{\mathcal{A}}\,[a(1)\beta(1)b(2)\alpha(2)]\}$$

becomes a linear combination of the two symmetric singlets only. (Here $\hat{\mathcal{O}}^S$ is Löwdin's spin projection operator for the singlet state [4].) This means that in our case the spin projection restores not only the correct spin properties but also the spatial symmetry of the wave function. A similar situation may often be encountered [9–11]. The energy corresponding to the wave function (21) can be given as

$$E_{SP}=t+\frac{4\gamma p^2+8\beta p}{1+4p^2}. \tag{22}$$

In the UHF+SP method we perform the spin projection of the UHF wave function, i.e., take the orbitals which minimize the energy (11) of the *single* DODS determinant. Then, for the interval $\gamma>2|\beta|$ we have $p=|\beta|/\gamma$ and (22) becomes

$$E_{UHF+SP}=t-2\frac{|\beta|^2}{\gamma}\cdot\frac{2}{1+4|\beta|^2/\gamma^2}. \tag{23}$$

Obviously, $E_{UHF+SP}<E_{UHF}<E_{RHF}$ in all cases when $\gamma>2|\beta|$ and the specific UHF solution differing from the RHF one exists at all. It is easy to see that in these cases the UHF+SP method leads to an improvement also for the quality of the wave function (weight of the true ground state in the superposition) as compared with both RHF and UHF methods. The effect which can be obtained in the UHF+SP case is, however, quite sensitive to the relations between the parameters β and γ (and is, in general, strongly system dependent [11]). In particular, E_{UHF+SP} also tends to E_{RHF} when the critical point is approached: there the UHF wave function becomes identical to the RHF one which is automatically a pure singlet. In the UHF+SP method we apply the UHF value $p=|\beta|/\gamma$ of the orbital splitting parameter, which is based on a delicate equilibrium between the different factors influencing the energy of the *single determinant*. The changes in the parameters of the system may shift considerably the position of this equilibrium (the degree of splitting of the UHF orbitals) and lead at the same time to only moderate changes in the resulting UHF energy, as the different competing factors discussed above cancel the effect of each other to a large extent. Since the triplet component playing a central role in determining the UHF energy is excluded by the spin projection, no such cancellation takes place for the UHF+SP wave function and the latter will be "out of balance" and may exhibit even a wrong qualitative dependence of the energy on the parameters characterizing the system.

Thus the spurious extrema on the UHF + SP curve discussed in the Introduction may be immediately connected with the not truly variational character of this method: we optimize another wave function than we really do use.

As mentioned above, in the UHF case the presence of the triplet component prevents the parameter p to reach the value $1/2x$ at which the highest singlet disappears from the expansion of the DODS determinant. This becomes, however, possible if we use the spin projected wave function directly as trial function in the variational procedure (EHF method), since in this case the triplet component is excluded from the very beginning. In other words, setting $p=1/2x$, the spin projected determinant (21) becomes identical with the exact ground state wave function. This is in agreement with the known fact that the EHF procedure is equivalent to the full CI in any two electrons — two orbitals case. (This is not valid, of course, for models with more than two electrons and/or orbitals.)

It seems worthwhile to consider the behaviour of the EHF method also by performing directly the variation of the expression (22) for the energy of the spin projected determinant (21). Requiring the energy (22) to be stationary under the variation of the orbital coefficients, i.e., under the variation of the quantity q in (10), we obtain the condition

$$\frac{\mathrm{d}E_{\mathrm{SP}}}{\mathrm{d}q} = \frac{\mathrm{d}E_{\mathrm{SP}}}{\mathrm{d}p} \cdot \frac{\mathrm{d}p}{\mathrm{d}q} = 0. \tag{24}$$

The solutions of (24) correspond either to $\frac{\mathrm{d}p}{\mathrm{d}q} = 0$, or to $\frac{\mathrm{d}E_{\mathrm{SP}}}{\mathrm{d}p} = 0$. Therefore, similarly to the UHF case, the RHF-type wave functions for which $\frac{\mathrm{d}p}{\mathrm{d}q} = 0$; $q = \pm 1$ give particular solutions for the EHF problem, too. The specific EHF solution, however, may be obtained from the condition $\frac{\mathrm{d}E_{\mathrm{SP}}}{\mathrm{d}p} = 0$. Then the differentiation of (22) gives

$$p = \frac{\gamma \pm \sqrt{\gamma^2 + 16\beta^2}}{8\beta} \tag{25}$$

which, as it is easy to see, coincides with the condition $p=1/2x$, discussed above, if we select the negative sign*. By substituting this value of p into (22) we can check explicitly that the EHF energy is really equal to that of the exact ground state CI solution.

In the EHF case we have for the coefficient q the equation

$$\frac{q}{1+q^2} = \frac{\gamma - \sqrt{\gamma^2 + 16\beta^2}}{8\beta}, \tag{26}$$

* The positive sign in (25) corresponds to $p=-x/2$; in this case the spin projected wave function (21) becomes identical to the highest symmetric singlet CI solution.

which has always real, positive solutions. Thus, in contrast to the UHF case, the specific EHF solution differing from the RHF one exists at any values of the parameters. According to the above discussion, this difference between the behaviour of the UHF and EHF methods may be connected with the fact that in the EHF case there are no such factors, as the reduction of the bond order due to the triplet component in the UHF case, which could prevent the orbital splitting.*

4. The derivatives at the critical point

At the critical point $\gamma = 2|\beta|$ the specific UHF solution coincides with the RHF one and ceases to exist. Therefore, we have at this point a transition from one branch of the solutions of Eq. (14) ($dE_{DODS}/dp = 0$) to another ($dp/dq = 0$). As we have seen, the UHF energy changes continuously at this transition and we shall show that the same holds for its first derivative, too. In fact, according to (8) the derivative of the RHF energy can be written as

$$\frac{dE_{RHF}}{dr} = \frac{dt}{dr} + \frac{1}{2}\frac{d\gamma}{dr} + 2\frac{d\beta}{dr}, \tag{27}$$

where r is the internuclear distance. For the interval $\gamma > 2|\beta|$ (i.e. $r > r_c$, where r_c is the internuclear distance corresponding to the critical point) we have for the derivative of the UHF energy (17a)

$$\frac{dE_{UHF}}{dr} = \frac{dt}{dr} - \frac{4\beta}{\gamma}\frac{d\beta}{dr} + \frac{2\beta^2}{\gamma^2}\frac{d\gamma}{dr}. \tag{28}$$

Since the right-hand sides of (27) and (28) are equal ar $r = r_c$ ($\gamma = 2|\beta|$) and the UHF energy curve coincides with the RHF one when $\gamma < 2|\beta|$, we obtain

$$\left.\frac{dE_{UHF}}{dr}\right|_{r=r_c+0} = \left.\frac{dE_{UHF}}{dr}\right|_{r=r_c-0} = \left.\left(\frac{dt}{dr} + \frac{1}{2}\frac{d\gamma}{dr} + 2\frac{d\beta}{dr}\right)\right|_{r=r_c}, \tag{29}$$

i.e., the first derivative of the UHF energy changes continuously when passing the critical point. This conclusion is in agreement with the general result of Meyer and Pulay, valid also for the many-nuclear molecules, according to which the first derivative of any SCF energy can be determined from the wave function alone, without the knowledge of the derivatives of the orbital coefficients [14, 15]. In other words, the

* For some larger systems the splitting of the different orbital pairs may become competitive due to the specific spin-coupling scheme [12, 13] inherent in the many-electron EHF wave function. This problem is, however, beyond the scope of the present paper.

coincidence of the RHF and UHF wave functions at the critical point predetermines the equality of the first derivatives of the corresponding energies, too. (We shall return to this question later.) No such considerations apply, however, for the derivative of the UHF+SP energy as the UHF+SP method is not strictly speaking an SCF (variational) one. For the UHF+SP energy we have again $dE_{UHF+SP}/dr = dE_{RHF}/dr$ if $\gamma > 2|\beta|$, since in this interval the UHF+SP wave function also coincides with the RHF one, while for $\gamma > 2|\beta|$ we obtain from (23)

$$\frac{dE_{UHF+SP}}{dr} = \frac{dt}{dt} - \frac{4\beta}{(\gamma^2+4\beta^2)^2}\left[2\gamma^3\frac{d\beta}{dr} + (4\beta^3 - \beta\gamma^2)\frac{d\gamma}{dr}\right]. \tag{30}$$

At the critical point (30) becomes

$$\left.\frac{dE_{UHF+SP}}{dr}\right|_{r=r_c+0} = \left.\left(\frac{dt}{dr} + \frac{d\beta}{dr}\right)\right|_{r=r_c}. \tag{31}$$

The right-hand side of (31) differs from (27), therefore the UHF+SP energy curve has a discontinuity of first derivative at the critical point. An exception is possible only if the additional condition $\frac{1}{2}\, d\gamma/dr = d|\beta|/dr$ also holds at $r = r_c$. (In this case the ratio $2|\beta|/\gamma$ determining the existence or absence of the specific UHF solution has a zero derivative.) This would represent, however, a rather unrealistic assumption since γ and $|\beta|$ must change in opposite directions when the internuclear distance increases.

For the parameter p the value $p = 1/2$ is kept until $\gamma < 2|\beta|$, therefore $\left.\frac{dp}{dr}\right|_{r=r_c-0} = 0$. For the interval, where the specific UHF solution exists, $p = -\beta/\gamma$, and accordingly

$$\left.\frac{dp}{dr}\right|_{r=r_c+0} = -\frac{1}{\gamma}\left.\left(\frac{1}{2}\frac{d\gamma}{dr} + \frac{d\beta}{dr}\right)\right|_{r=r_c}. \tag{32}$$

Since the right-hand side of (32) differs from zero (except the unrealistic case discussed above), the parameter p also exhibits a discontinuity of its derivative at the critical point. This means that the overlap integral $\lambda = 2p$ of the UHF orbitals departs sharply, i.e. with a non-horizontal tangent, from the unity level when passing the critical point. (As $\frac{dp}{dq} = 0$ at the critical point, the ratio q of the LCAO coefficients departs from unity by having a vertical tangent.)

We shall discuss briefly that the continuity of the UHF energy derivative may be attributed to the fact that an infinitesimal splitting of the orbitals (i.e. an infinitesimal lowering of the parameter p with respect to the value $p = 1/2$) does not lead to any first order energy change in the critical point: by performing the differentiation in (20) we obtain that $\partial(E_{DODS} - E_{RHF})/\partial p$ is zero here. This interrelationship is, in fact, not

restricted to our simple model but may be used to show that the UHF energy curve must always have a derivative equal to that of the RHF one in the critical point:

The critical point separates the intervals where the RHF energy is stable and where it is unstable with respect to the orbital splitting. If only an infinitesimal splitting is considered, the partial derivative of the energy difference $E_{\mathrm{DODS}} - E_{\mathrm{RHF}}$, taken according to the appropriate parameter characterizing the orbital splitting in the energetically most favourable direction,* must have opposite signs in these intervals. Therefore this derivative is zero in the critical point.

The energy E_{DODS} is a continuous function of the orbital splitting parameter as well as of the different quantities (one- and two-electron integrals) characterizing the system. The latter depend on the internuclear distance, of course. The UHF energy is nothing else than the DODS energy obtained by substituting the SCF value for the orbital splitting parameter; this SCF value also changes with the internuclear distance. Therefore, in order to obtain the change of the UHF energy caused by an infinitesimal change of the internuclear distance, one has to determine the derivative of the DODS energy in a well defined direction in the space of its arguments, which is prescribed by the changes in the different parameters under the influence of the changing internuclear distance. This means that the full derivative of $E_{\mathrm{UHF}} - E_{\mathrm{RHF}}$, taken according to the internuclear distance can be written as a sum of the partial derivatives of $E_{\mathrm{DODS}} - E_{\mathrm{RHF}}$ according to these different quantities, each multiplied by the full derivative of the corresponding parameter. At the critical point the partial derivative according to the splitting parameter must be zero as discussed above. Now, the partial derivatives of $E_{\mathrm{DODS}} - E_{\mathrm{RHF}}$ according to the one- and two-electron integrals must be taken by keeping the splitting parameter fixed at its value corresponding to the critical point, where the UHF and RHF wave functions coincide with each other. This just means that no orbital splitting is considered; under this limitation $E_{\mathrm{DODS}} - E_{\mathrm{RHF}}$ is identically zero, of course, and all its derivatives vanish. Thus the derivative of the UHF vs RHF energy difference is zero in the critical point and the UHF and RHF curves have equal derivatives.

The above considerations may be well illustrated on our simple model. In fact, denoting by $\Delta E = E_{\mathrm{DODS}} - E_{\mathrm{RHF}}$ and by p_u the SCF value (16) of p, we have according to (20)

$$\left.\frac{\mathrm{d}(E_{\mathrm{UHF}} - E_{\mathrm{RHF}})}{\mathrm{d}r}\right|_{r=r_c} = \left.\frac{\mathrm{d}(\Delta E)}{\mathrm{d}r}\right|_{\substack{p=p_u \\ r=r_c}} =$$

$$= \left[\frac{\partial(\Delta E)}{\partial(|\beta|)} \cdot \frac{\mathrm{d}|\beta|}{\mathrm{d}r}\right]_{\substack{p=p_u \\ r=r_c}} + \left[\frac{\partial(\Delta E)}{\partial\gamma} \cdot \frac{\mathrm{d}\gamma}{\mathrm{d}r}\right]_{\substack{p=p_u \\ r=r_c}} +$$

* We need not specify here the nature of this parameter, only require that it must be continuous and have continuous (one side) derivative at the critical point, as well as that E_{DODS} must be its continuous and continuously differentiable function. (In our simple model the parameter p fulfils, the coefficient q does not fulfil these conditions.)

$$+\left[\frac{\partial(\Delta E)}{\partial p}\cdot\frac{\mathrm{d}p}{\mathrm{d}r}\right]\Bigg|_{\substack{p=p_u\\r=r_c}}=\left[2(1-2p)\frac{\mathrm{d}|\beta|}{\mathrm{d}r}\right]\Bigg|_{\substack{p=p_u\\r=r_c}}-$$

$$-\left[\frac{1}{2}(1-4p^2)\frac{\mathrm{d}\gamma}{\mathrm{d}r}\right]\Bigg|_{\substack{p=p_u\\r=r_c}}+\left[4(\gamma p-|\beta|)\frac{\mathrm{d}p}{\mathrm{d}r}\right]\Bigg|_{\substack{p=p_u\\r=r_c}}. \tag{33}$$

The first two terms vanish simply because $p_u=\frac{1}{2}$ at $r=r_c$, the third is zero since $\gamma=2|\beta|$ also holds at the critical point.

Turning to the second derivatives, we obtain by performing the differentiation in (27) and (28)

$$\frac{\mathrm{d}^2E_{\mathrm{RHF}}}{\mathrm{d}r^2}=\frac{\mathrm{d}^2t}{\mathrm{d}r^2}+\frac{1}{2}\frac{\mathrm{d}^2\gamma}{\mathrm{d}r^2}+2\frac{\mathrm{d}^2\beta}{\mathrm{d}r^2} \tag{34}$$

and

$$\frac{\mathrm{d}^2E_{\mathrm{UHF}}}{\mathrm{d}r^2}=\frac{\mathrm{d}^2t}{\mathrm{d}r^2}-\frac{4\beta}{\gamma}\frac{\mathrm{d}^2\beta}{\mathrm{d}r^2}+2\frac{\beta^2}{\gamma^2}\frac{\mathrm{d}^2\gamma}{\mathrm{d}r^2}-\frac{4}{\gamma}\left(\frac{\mathrm{d}\beta}{\mathrm{d}r}-\frac{\beta}{\gamma}\frac{\mathrm{d}\gamma}{\mathrm{d}r}\right)^2, \tag{35}$$

respectively.* At the critical point $r=r_c$ we have $\gamma=2|\beta|=-2\beta$, therefore

$$\frac{\mathrm{d}^2E_{\mathrm{UHF}}}{\mathrm{d}r^2}\Bigg|_{r=r_c+0}=\frac{\mathrm{d}^2E_{\mathrm{RHF}}}{\mathrm{d}r^2}\Bigg|_{r=r_c}-\left[\frac{1}{\gamma}\left(\frac{\mathrm{d}\gamma}{\mathrm{d}r}-2\frac{\mathrm{d}|\beta|}{\mathrm{d}r}\right)^2\right]\Bigg|_{r=r_c}. \tag{36}$$

According to (17)

$$\frac{\mathrm{d}^2E_{\mathrm{UHF}}}{\mathrm{d}r^2}\Bigg|_{r=r_c-0}=\frac{\mathrm{d}^2E_{\mathrm{RHF}}}{\mathrm{d}r^2}\Bigg|_{r=r_c}.$$

Eq. (36) shows, therefore, that the second derivative of the UHF energy has a discontinuity at the critical point, except the physically unrealistic case ($\mathrm{d}\gamma/\mathrm{d}r=2\mathrm{d}|\beta|/\mathrm{d}r$ at the critical point) discussed above.

5. Conclusions

The above analysis is based mainly on the consideration of the simplest model. It seems, however, evident that the use of the ZDO assumption for the integrals does not change the main features of the problem. Thus, for instance, the formulae (8) and (17)

* There is no need to consider the second derivative of the UHF + SP energy, since already the first derivative has a discontinuity at the critical point.

for the RHF and UHF energies, respectively, remain valid also in the *ab initio* case, if one uses Löwdin-orthogonalized basis functions and replaces β by

$$\beta' = \beta + \langle \chi_1(1)\chi_2(2) | r_{12}^{-1} | \chi_2(1)\chi_2(2) \rangle$$

and γ by

$$\gamma' = \gamma + K_{12}.$$

($K_{12} = \langle \chi_1(1)\chi_2(2) | r_{12}^{-1} | \chi_2(1)\chi_1(2) \rangle$ is the exchange integral for the pair of the orbitals χ_1 and χ_2.) Therefore, until $\beta' < 0$, the results obtained for the conditions of the existence of the specific UHF solution as well as for the derivatives of the RHF and UHF energy curves also require only these substitutions. Some other formulae become slightly more complicated; their changes, however, may not influence the qualitative aspects of the problem. The main conclusions remain valid also if we turn to the consideration of more complicated models with more than two electrons and/or basis orbitals. In fact, one can easily generalize for other systems the physical picture which we used to rationalize, how the energy of the single DODS determinant UHF wave function results from a compromise between different effects acting in the opposite directions. One obtains a specific UHF solution differing from the RHF one only if the orbital splitting can give a net energy lowering. Therefore, at the "critical point", where the UHF wave function starts to differ from the RHF one, the first order effects of the different competing factors influencing the UHF vs RHF energy difference fully compensate each other. This conclusion is not restricted to the simple model considered and consequently the UHF energy curve must always depart from the RHF one quite smoothly, i.e. by having a continuous first derivative equal in the critical point to that of the RHF curve. As the triplet etc. components are excluded by the spin projection, no such compensation takes place for the UHF + SP vs RHF energy difference; this leads to the discontinuity in the derivative of the UHF + SP energy. Since the RHF and the specific UHF wave functions correspond to different branches of solution of the variational problem for the single determinants, the parameters characterizing the UHF wave function (as orbital coefficients or overlaps of the corresponding orbitals), though they coincide with the RHF values at the critical point, have discontinuous derivatives here. Only the first order effects of the orbital splitting are compensated at the critical point but not the higher order ones; the UHF energy curve has a discontinuity of the second derivative.

These results indicate that one can use the UHF method for studying potential curves except if the second derivative is needed in the interval close to the critical point. One has, however, to take into account also that probably the UHF potential curve will give a too quick transition to the asymptotic region when the internuclear distance increases. The UHF + SP method may perhaps give a better asymptotic behaviour (cf. Fig. 1 in [3]); it is, however, not adequate for studying whole potential curves or surfaces. The analysis presented above indicates that the pathological behaviour of the UHF + SP curve found in [3] is connected with the essentially nonvariational character of the UHF + SP method and not with the particular system studied; similar

artefacts may be expected in other cases as well. The potential curves given by the EHF method (and also by the "Half Projected HF" one [16, 17]) are expected to have well-balanced shapes, much more correct than those of the UHF curves.

Finally, we should like to make some more general remarks based on the differences between the behaviour of the UHF and spin projected EHF methods. First, the existence of the specific EHF solution in the interval where the UHF wave function does not differ from that RHF one indicates that probably a similar situation can be encountered for other (e.g. spatial) symmetries, too. In other words, if one permits the breaking of a symmetry restriction and despite of this obtains a wave function which possesses automatically the correct symmetry, this fact does not necessarily mean that the corresponding projected method (in which the symmetry breaking wave function projected on the appropriate symmetry subspace is used as variational one) will not give a lower energy. Furthermore, the continuous behaviour of the EHF wave function suggests that it is hardly a strict approach to treat [2, 18] the appearance of the critical point for the UHF wave function as a sort of electronic phase transition ("Mott transition"). The critical point is connected with the limitations inherent in both RHF and UHF methods and has only a very slight, if any, connection with the problem that whether the localized or the delocalized description of the electronic structure is more adequate for a given system. This conclusion is in concordance with the recent UHF crystal orbital results of [19], where it was discussed that the instability of a "metallic" RHF solution towards the orbital splitting occurs when the RHF wave function is very bad, and therefore the appearance of the DODS solution cannot really be used to describe metal—insulator transitions.

Acknowledgement

The author is indebted to Dr. J. Tiňo, Dr. V. Klimo, Dr. M. Kertész and, especially, Dr. P. Pulay for the interesting discussions which stimulated him to a large extent to perform the analysis presented here.

References

1. C. A. Coulson and I. Fischer, Phil. Mag., **40,** 386, 1949.
2. H. Fukutome, Progr. Theor. Phys., **47,** 1156, 1972.
3. I. Mayer, Int. J. Quantum Chem., **14,** 29, 1978.
4. P.-O. Löwdin, Phys. Rev., **97,** 1509, 1955.
5. P.-O. Löwdin, p. 601 in Quantum Theory of Atoms, Molecules and Solid State, Academic Press, New York, 1966; W. A. Goddard III, J. Chem. Phys., **48,** 450, 1968; I. Mayer, J. Ladik and G. Biczó, Int. J. Quantum Chem., **7,** 583, 1973; I. Mayer, Adv. Quant. Chem., **12,** 189, 1980 and references therein.
6. A. T. Amos and G. G. Hall, Proc. Roy. Soc., **A263,** 483, 1961.
7. P. Pulay, private communication.
8. I. N. Kinev and N. N. Tyutyulkov, Opt. i Spektr., **43,** 222, 1977.
9. I. Mayer, Int. J. Quantum Chem., **8,** 363, 1974.
10. I. Mayer, Acta Phys. Hung., **39,** 133, 1975.
11. I. Mayer and M. Kertész, Int. J. Quantum Chem., **9,** 527, 1975.

12. G. W. Pratt Jr., Phys. Rev., **92,** 278, 1953.
13. R. Pauncz, Alternant Molecular Orbital Method, Saunders, Philadelphia, 1967.
14. W. Meyer and P. Pulay, p. 44 in Proc. of the Second Seminar on Computation Problems of Quantum Chemistry, Strasbourg, France, 1972, Eds. G. H. Dierksen, B. T. Sutcliffe and A. Veillard, München, 1973.
15. P. Pulay, p. 153 in Modern Theoretical Chemistry. Vol. 4, Ed. H. F. Schaefer III., Plenum Press, New York, 1977.
16. Y. G. Smeyers, An. Fis. (Madrid), **67,** 17, 1971.
17. Y. G. Smeyers and L. Doreste Suarez, Int. J. Quantum Chem., **7,** 687, 1973; Y. G. Smeyers and A. M. Bruceña, ibid., **14,** 641, 1978.
18. J. B. Goodenough, Magnetism and the Chemical Bond, Interscience, New York, 1963.
19. M. Kertész, J. Koller and A. Ažman, Phys. Rev., **B19,** 2034, 1979.

Acta Physica Hungarica 54 (3—4), pp. 267—275 (1983)

DEBYE–WALLER FACTORS FOR THIN FILM DIFFRACTION

K. STACHULEC

Politechnika Swiętokrzyska, 25-314 Kielce, Poland

(Received 2 September 1982)

The Debye–Waller factors for low energy electron diffraction (LEED) for thin films are considered in harmonic and anharmonic approximation. The numerical calculation for some parameters describing thin film dynamics of the lattice particle in the case of the high temperature limit is presented. The results show an interesting distribution of the Debye–Waller factor in the direction perpendicular to the thin film surface as well as its anisotropic character.

1. Introduction

We consider the temperature dependence of the low energy electron diffraction by thin films. In order to describe the relation between parameters describing the temperature properties of thin film scattering we present a derivation of the Debye–Waller factors for thin films in harmonic approximation (Sections 2, 3) and we generalize the obtained formulas for the case of anharmonic crystals using the pseudoharmonic approximation (Section 4). The expressions obtained for the temperature, scattering angle and thickness dependence of the Debye–Waller factors are discussed in Section 5, where we present some numerical computation results.

2. Derivation of the Debye–Waller factor for thin films

We consider a film situated in a Cartesian coordinate system with z-axis oriented in the direction perpendicular to the surface of the film. We divide the film into n layers determined by atoms belonging to the crystallographic planes parallel to the surface of the film. The position of an atom in plane is given by the two-dimensional vector $\mathbf{j}$, and the layers are labelled by v. The dynamics of the crystal lattice of thin films are determined by the Hamiltonian in the harmonic approximation

$$H = \frac{1}{2}\sum_{v\mathbf{j}s}(P^s_{v\mathbf{j}})^2/M_{v\mathbf{j}} + \frac{1}{2}\sum_{v\mathbf{j}s}\sum_{v'\mathbf{j}'s'} A^{ss'}_{v\mathbf{j}v'\mathbf{j}'}\,\delta R^s_{v\mathbf{j}}\delta R^{s'}_{v'\mathbf{j}'}, \tag{1}$$

where $P^s_{v\mathbf{j}}$ and $\delta R^s_{v\mathbf{j}}$ are the 2-components of the momentum and the displacement

operators, respectively, belonging to the $(v\mathbf{j})$-th atom. $A^{ss'}_{v\mathbf{j}v'\mathbf{j}'}$ denote the tensor elements of the interaction forces, $M_{v\mathbf{j}}$ is the mass of the $(v\mathbf{j})$-th atom.

In the representation in which the Hamiltonian (1) has the diagonal form [1]:

$$H = \sum_{\mathbf{q}\lambda\mu} \hbar w_{\mathbf{q}\lambda\mu}\left(n_{\mathbf{q}\lambda\mu} + \frac{1}{2}\right) \tag{2}$$

the displacement $\delta\mathbf{R}_{v\mathbf{j}}$ can be written as follows

$$\delta\mathbf{R}_{v\mathbf{j}} = \left(\frac{\hbar}{2MN^2n}\right)^{1/2} \sum_{\mathbf{q}\lambda\mu} \frac{e_{\mathbf{q}\lambda\mu}}{\sqrt{w_{\mathbf{q}\lambda\mu}}} T^{\mathbf{q}}_{v\lambda}\, e^{i\mathbf{q}\mathbf{j}}(a_{\mathbf{q}\lambda\mu} + a^{+}_{\mathbf{q}\lambda\mu}), \tag{3}$$

where $w_{\mathbf{q}\lambda\mu}$ are the frequency eigenvalues, $n_{\mathbf{q}\lambda\mu}$ denotes the average number of phonons in the $(\mathbf{q}\lambda\mu)$-state, N is the number of the atoms in the each atomic layer parallel to the surface, and n is the total number of the atomic layers of the film. $\mathbf{q}$ represents the propagation vector in two-dimensional space belonging to the first Brillouin zone. The operator $\hat{e}_{\mathbf{q}\lambda\mu}$ denotes the transformed polarisation vector, and $T^{\mathbf{q}}_{v\lambda}$ are the transformation coefficients in the direction perpendicular to the surface of the film. $a_{\mathbf{q}\lambda\mu}a^{+}_{\mathbf{q}\lambda\mu}$ are the creation and annihilation operators of a phonon in $(\mathbf{q}\lambda\mu)$-state, respectively.

By means of the expression (3) we can calculate the mean square displacement $\langle \delta R^2_{vj}\rangle$ of the $(v\mathbf{j})$-th atom in the film. The result is:

$$\langle(\delta R_{vj})^2\rangle = \left(\frac{\hbar}{2MN^2n}\right) \sum_{\mathbf{q}\lambda\mu} (T^{\mathbf{q}}_{v\lambda}\,\hat{e}_{\mathbf{q}\lambda\mu})^2 \frac{\operatorname{cth}\left(\dfrac{\hbar w_{\mathbf{q}\lambda\mu}}{2kT}\right)}{w_{\mathbf{q}\lambda\mu}} = B_v. \tag{4}$$

This result can be used to determine the temperature dependent atomic potential $V_T(\mathbf{r}-\mathbf{R}_{v\mathbf{j}})$ of the $(v\mathbf{j})$-th atom in the film, supposing that we know it at the temperature $T = 0$K. Namely, let us denote by $V_0(\mathbf{r}-\mathbf{R}_{v\mathbf{j}})$ the scattering potential of the (vj)-th atom in the film at zero temperature, thus following [2] we can determine V_T

$$V_T(\mathbf{r}-\mathbf{R}_{v\mathbf{j}}) = \left(\frac{1}{2\pi B_v}\right)^{3/2} \int V_0(\mathbf{u}-\mathbf{R}_{v\mathbf{j}}) e^{-\frac{|\mathbf{r}-(\mathbf{u}=_{vj})|^2}{2B_v}} d^3u. \tag{5}$$

We consider now, as an example, the diffraction of the electrons by the film. In this case $V_0(\mathbf{r}-\mathbf{R}_{v\mathbf{j}})$ can be written in the standard way

$$V_0(\mathbf{r}-\mathbf{R}_{v\mathbf{j}}) = -\sum_n \frac{Ze^2\alpha_n}{|\mathbf{r}-\mathbf{R}_{v\mathbf{j}}|} e^{-\beta_n|\mathbf{r}-\mathbf{R}_{v\mathbf{j}}|}, \tag{6}$$

where the numerical coefficients α_n and β_n are given for different atoms by Tietz [3]. In this case the temperature dependent potential of the $(v\mathbf{j})$-th atom $V_T(\mathbf{r}-\mathbf{R}_{v\mathbf{j}})$ can be

calculated by means of Eq. (6) and Eq. (5), and as a result we obtain

$$V_T(\mathbf{r}-\mathbf{R}_{vj}) = -\frac{Ze^2}{2|\mathbf{r}-\mathbf{R}_{vj}|}\sum_n \alpha_n F_n(|\mathbf{r}-\mathbf{R}_{vj}|)e^{\frac{\beta_n^2 B_v}{2}}, \tag{7}$$

where $F_n(|\mathbf{r}-\mathbf{R}_{vj}|)$ is given by

$$F_n(|\mathbf{r}-\mathbf{R}_{vj}|) = e^{-\beta_n|\mathbf{r}-\mathbf{R}_{vj}|}\left[1-\Phi\left(\beta_n\sqrt{\frac{B_v}{2}}-\frac{|\mathbf{r}-\mathbf{R}_{vj}|}{\sqrt{2B_v}}\right)\right]$$

$$-e^{\beta_n|\mathbf{r}-\mathbf{R}_{vj}|}\left[1-\Phi\left(\beta_n\sqrt{\frac{B_v}{2}}+\frac{|\mathbf{r}-\mathbf{R}_{vj}|}{\sqrt{2B_v}}\right)\right] \tag{8}$$

and

$$\Phi(X) = \frac{2}{\sqrt{\pi}}\int_0^x e^{-t^2}\,\mathrm{d}t.$$

For the above determined potential one can calculate the scattering amplitude of the $(v\mathbf{j})$-th atom in thin film in the first Born approximation at a given temperature. The result is

$$f_T(\mathbf{K}, v\mathbf{j}) = -\frac{m}{2\pi\hbar^2}\sum_0^\infty 4\pi r^2 V_T(\mathbf{r}-\mathbf{R}_{vj})\frac{\sin(\mathbf{Kr})}{Kr} =$$

$$= \frac{2mZe^2}{\hbar^2}\sum_n \frac{\alpha_n}{\beta_n^2+K^2}e^{-i\mathbf{K}\mathbf{R}_{vj}}e^{-\frac{K^2B_v}{2}}, \tag{9}$$

where $\mathbf{K}$ denotes the scattering vector.

The total scattering amplitude of the thin film can be written in the following way

$$f_T(K,n) = \sum_{v\mathbf{j}}\left(\frac{2mZe^2}{\hbar^2}\sum\frac{\alpha_n}{\beta_n^2+K^2}\right)e^{-i\mathbf{K}\mathbf{R}_{vj}}e^{-\frac{K^2B_v}{2}} = \sum_{v=1}^{n} f_v^0(\mathbf{K},S)e^{-\frac{K^2B_v}{2}}, \tag{10}$$

where $f_v^0(K,S)$ denotes the scattering amplitude of the (v)-th atomic layer at the temperature $T=0\mathrm{K}$, and S stands for the value of the surface area. Because only the B_v quantities are temperature dependent in the expression (10) the temperature effect of the diffraction is described by the exponential factors

$$g_v = e^{-\frac{K^2B_v}{2}}$$

which corresponds to the Debye–Waller factor in the bulk theory, but in the thin film case it is the position dependent quantity and should be calculated for each atomic layer parallel to the surface.

3. A model for the factor g_v calculation

The g_v-factor can be expressed by the Debye–Waller coefficient $W_v = \frac{1}{2} K^2 B_v$ in the form

$$g_v = e^{-W_v} \tag{11}$$

and we will calculate the Debye–Waller coefficients W_v. In order to calculate the coefficient W_v we have to know the dispersion relation of the phonons in thin film and the quantity $T^{\mathbf{q}}_{v\lambda}$.

The phonon theory of thin films elaborated by Wojtczak and Zajac [1] allows us to write the quantity $T^{\mathbf{q}}_{v\lambda}$ in the general form

$$T_{v\lambda} = A_\lambda \cos(\alpha_\lambda v + \beta_\lambda), \tag{12}$$

where α_λ and β_λ can be obtained from the boundary conditions, dependent on the structure and orientation of the film. For simple cases they are determined in [1]. A_λ in Eq. (12) are the normalization constants. In order to obtain an analytical result for the Debye–Waller coefficients we chose a simple dispersion relation [5]

$$w_{\mathbf{q}\lambda 1} = w_{\mathbf{q}\lambda 2} = w_m \left[\sin^2 \frac{q_x a}{2} + \sin^2 \frac{q_y a}{2} + \frac{A'}{A} \sin^2 \frac{\alpha_\lambda}{2} \right]^{1/2}; \quad w_m = \sqrt{\frac{4A}{M}},$$

$$w_{\mathbf{q}\lambda 3} = \bar{w}_m \left[\sin^2 \frac{q_x a}{2} + \sin^2 \frac{q_y a}{2} + \frac{B'}{B} \sin^2 \frac{\alpha_\lambda}{2} \right]; \quad \bar{w}_m = \sqrt{\frac{B4}{M}}, \tag{13}$$

where A, A and B, B denote the force constants.

Inserting the relation (4) and (12) into Eq. (11) we have:

$$W_v = \frac{\hbar K^2}{4MN^2 n} \sum_{q\lambda} A_\lambda^2 \cos^2(\alpha_\lambda v + \beta_\lambda) \cdot$$

$$\cdot \left\{ \sin^2 \Theta \cos^2 \varphi \frac{\operatorname{cth}(\hbar w_{\mathbf{q}\lambda 1}/kT)}{w_{\mathbf{q}\lambda 1}} + \sin^2 \Theta \sin^2 \varphi \frac{\operatorname{cth}(\hbar w_{\mathbf{q}\lambda 2}/kT)}{w_{\mathbf{q}\lambda 2}} + \right.$$

$$\left. + \cos^2 \Theta \frac{\operatorname{cth}(\hbar w_{\mathbf{q}\lambda 3}/kT)}{w_{\mathbf{q}\lambda 3}} \right\}. \tag{14}$$

The sum over $\mathbf{q}$, due to the periodic conditions which are fulfilled in the direction parallel to the plane of the film, can be replaced by an integral using the relation

$$\sum_q (\ldots) \Rightarrow \frac{S}{4\pi^2} \int_{-\frac{\pi}{a}}^{\frac{\pi}{a}} \int_{-\frac{\pi}{a}}^{\frac{\pi}{a}} dq_x dq_y (\ldots)$$

thus Eq. (14) becomes

$$W_v = \frac{\hbar K^2}{4MN^2 n} \sum_{\lambda=1}^{n} T_{v\lambda}^2 \{I_1(\lambda) \sin^2 \Theta + \cos^2 \Theta I_3(\lambda)\}, \tag{15}$$

where

$$I_1(\lambda) \cong \frac{4N^2 kT}{\pi \hbar w_m^2} \ln \left(1 + \frac{2}{\varepsilon_A \sin^2 \frac{\alpha_1}{2}}\right)^{1/2}; \quad \left(\varepsilon_A = \frac{A'}{A}\right), \tag{16}$$

$$I_3(\lambda) \cong \frac{4N^2 kT}{\pi \hbar \bar{w}_m^2} \ln \left(1 + \frac{2}{\varepsilon_B \sin^2 \frac{\alpha_1}{2}}\right)^{1/2}; \quad \left(\varepsilon_B = \frac{B'}{B}\right) \tag{17}$$

and we have made the use of the fact that in our model $W_{q\lambda 1} = W_{q\lambda 2}$.

Let us introduce the following quantity

$$\begin{aligned} \eta_v(n) &= \frac{1}{n} \sum_{\lambda=1}^{n} T_{v\lambda}^2 \ln \left(1 + \frac{2}{\varepsilon_A \sin^2 \frac{\alpha_\lambda}{2}}\right)^{1/2}, \\ \gamma_v(n) &= \frac{1}{n} \sum_{\lambda=1}^{n} T_{v\lambda}^2 \ln \left(1 + \frac{2}{\varepsilon_B \sin^2 \frac{\alpha_\lambda}{2}}\right)^{1/2}, \end{aligned} \tag{18}$$

thus we can rewrite Eq. (15) in the form

$$\begin{aligned} W_v &= \frac{K^2 kT}{\pi M w_m^2} \eta_v(n) \left[\sin^2 \Theta + \frac{w_m^2}{\bar{w}_m^2} \frac{\gamma_v(n)}{\eta_v(n)} \cos^2 \Theta\right] = \\ &= \frac{K^2 kT}{4\pi A} \eta_v(n) [1 + \xi_v(n) \cos^2 \Theta], \end{aligned} \tag{19}$$

where

$$\xi_v(n) = \frac{w_m^2}{\bar{w}_m^2} \frac{\gamma_v(n)}{\eta_v(n)} - 1 \tag{20}$$

and can be called the anisotropy coefficients of the Debye–Waller factors of thin films.

From the last form for quantity W_v one can see the anisotropic character of the Debye–Waller factor as well as its position and the thickness dependence.

4. Debye–Waller factors in pseudoharmonic approximation

The model for the Debye–Waller factors calculation presented in the last paragraph for thin films can be easily generalised to the case of anharmonic approximation [4, 7, 8]. It is known [4, 7] that the solution of the Green function equation in the pseudoharmonic approximation has the same form as in harmonic approximation but the frequencies of the phonons are renormalized by some temperature coefficient $\alpha(T)$ as follows

$$\tilde{w}^2_{\mathbf{q}\lambda\mu} = \alpha^2(T) w^2_{\mathbf{q}\lambda\mu},$$

where $w_{\mathbf{q}\lambda\mu}$ are the harmonic frequency and $\alpha(T)$ is defined by [4]

$$\alpha^2(T) = 1 - 36 \left\langle \frac{(\delta \mathbf{R}_{v\mathbf{j}} - \delta \mathbf{R}_{v'\mathbf{j}'})^2}{a^2} \right\rangle .$$

Using the same renormalization constant for all branches μ the pseudoharmonic Debye–Waller factors take the same form as in the harmonic model, namely

$$\tilde{W}_v = \frac{K^2 k\, T}{4\pi A} \cdot \tilde{\eta}_v(n) \left[1 + \xi_v(n) \cos^2 \Theta\right],$$

where by $\tilde{W}_v$ we denote the Debye–Waller coefficients in the pseudoharmonic model and $\tilde{\eta}_v(n)$ is given by

$$\tilde{\eta}_v(n) = \frac{\eta_v(n)}{\alpha^2(T)} \tag{21}$$

and

$$\tilde{W}_v = \frac{1}{\alpha^2(T)} W_v. \tag{22}$$

One can see that the anisotropy coefficients $\xi_v(n)$ are the same as in the harmonic model. From the above formulas it is evident that the anharmonic model of the film even in its simple pseudoharmonic approximation changes the temperature dependence of the LEED amplitude.

5. Numerical results

In this Section we present the results we have obtained numerically using the formula for the Debye–Waller factors of thin films derived in Section 3 in the harmonic and pseudoharmonic approximation (Section 4). All numerical computations are done for the film of $n = 10$ atomic layers, with an asymmetric boundary condition and with s.c. structure. The orientation of the considered sample is chosen as [001]. For this case we have $\beta_\lambda = -\alpha_\lambda/2$ and $\alpha_\lambda = \dfrac{\pi\lambda}{2n}$. In Fig. 1 we present the obtained distribution of the

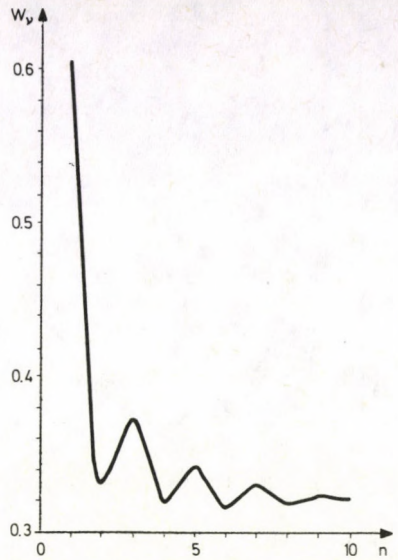

Fig. 1. Debye–Waller factor distribution in the direction perpendicular to the surface ($\varepsilon_A = 0.5$, $\varepsilon_B = 0.5$, $\bar{\varepsilon} = 1$, $\Theta = 180°$)

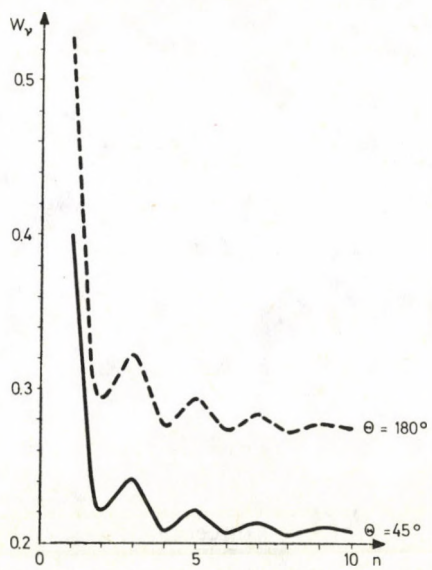

Fig. 2. Debye–Waller factor distribution in the direction perpendicular to the surface, for different angles ($\varepsilon_A = 0.8$, $\varepsilon_B = 0.9$, $\bar{\varepsilon} = 1$)

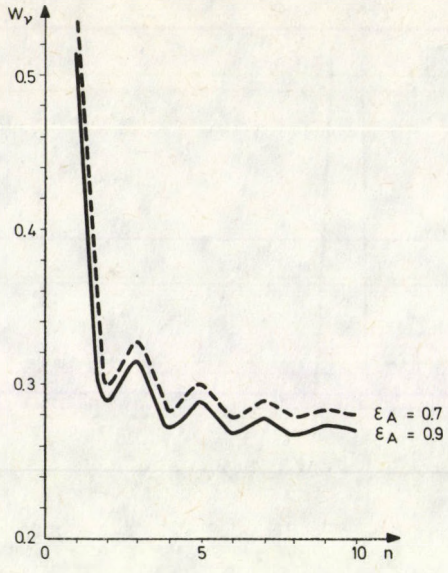

Fig. 3. Debye–Waller factor distribution in the direction perpendicular to the surface, for different parameters ($\varepsilon_B = 0.9$, $\bar{\varepsilon} = 1$, $\Theta = 180°$)

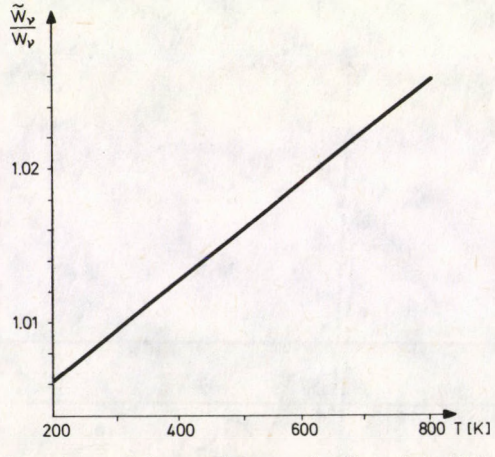

Fig. 4. Temperature dependence of the pseudoharmonic effect of the Debye–Waller factor

Debye–Waller factors in the thickness direction of the thin film. In Fig. 2 we show the same distribution but for two different angles of the diffraction. Next, in Fig. 3 we present the distribution of the Debye–Waller factors for different surface parameters ε_A. The results of the harmonic and pseudoharmonic approximation for the Debye–Waller factors are compared in Fig. 4, where we show the curve of the temperature dependence of the quantity $\frac{\tilde{W}_v}{W_v}$.

Acknowledgement

The author is much indebted to Professor L. Wojtczak for stimulating discussions and helpful criticism throughout the work.

References

1. L. Wojtczak and S. Zajac, Bulletin de L'Académie Polonaise des Sciences, **16,** 527, 1968.
2. K. Stachulec, ZN PS., **f,** 147, 1977 (in Polish).
2. T. G. Strand and T. Tietz, Nuovo Cimento, **41B,** 89, 1966.
4. T. Siklós, The Thermodynamic Green's Function Method in the Self-Consistent Phonon Theory of Anharmonic Crystals, Report KFKI-1981-43, Budapest, 1981; T. Siklós, Acta Phys. Hung., **30,** 181, 1971; **30,** 193, 1971; **30,** 301, 1971; **34,** 327, 1973.
5. A. Corciovei and A. Berinde, J. de Physique, **24,** 89, 1963.
6. A. Stachulec, Acta Phys. Hung., **51,** 243, 1981.
7. J. Zimnicki, Acta Phys. Hung., **30,** 27, 1975.
8. L. Wojtczak and K. Stachulec, Phys. Stat Sol. (b), **70,** K165, 1975.

Acta Physica Hungarica 54 (3—4), pp. 277—285 (1983)

COMPOSITION CHANGES IN Ni—Au, Ni—Pd and Ni—Cu ALLOYS DUE TO SPUTTERING— A COMPUTER SIMULATION

J. LÁSZLÓ, L. FÜSTÖSS and J. GIBER

Physical Institute of the Technical University, 1521 Budapest, Hungary

(Received in revised form 7 September 1982)

The authors have used the RETTUPS Monte Carlo computer model for the simulation of the sputtering process. After the setting of the program for pure targets the sputtering features of binary alloy targets have been modelled by simulating a mean event. The composition changes of the surface close layers in Ni—Au, Ni—Pd and Ni—Cu have been examined, comparing the results to experimental data of the literature. The sputtering has been executed by 1 keV Ar^+ ions. The influence of the mass ratio and that of the binding energy ratio of the components on the sputtering features have also been investigated. As a conclusion the qualitative measure of surface enrichment in these target systems could be determined.

Introduction

The ion sputtering of multicomponent alloys has become the research area of the recent years. As there were already a large number of experimental data available for the sputtering yields of pure metals [1], the attention of researchers has been drawn to multicomponent targets. Surface enrichment, preferential sputtering [2, 3, 4] and cascade mixing [5, 6, 7] are characteristically important questions to solve in multicomponent targets and these tasks require the observation of the ion bombarded surfaces.

The development of this kind of research work is mostly due to Auger Electron Spectroscopy [8, 9, 10, 11, 12]. Anyway, we can accept the sputtering features of a multicomponent target only, if the so-called steady state sputtering is already reached [13], i.e. the sputtering yield ratios of the bulk correspond to the stoichiometric ratios for the components. That is the way how Shimizu [14] and later Betz and his co-workers [15, 16] have carried out special Auger examination procedures, which may result in a qualitative estimation of the measure of surface enrichment or preferential sputtering in binary alloy targets. The target is bombarded by ions within UHV environments and the sputtered material is deposited on a substrate placed close to the target surface. During the sputtering they examine the surface of both the target and the substrate by AES. Obviously, from the assumption of the steady state sputtering, the target surface corresponds to the bulk conditions, while the surface of

the substrate shows a temporary, altered surface composition. A ratio results from the Auger intensity ratios measured this way, which is thus characteristic to the degree of surface enrichment (or depletion). Betz and co-workers have worked out another similar method. They measure the Auger intensity ratios originated from scribed or fractured surfaces of the target and from the sputtered areas within UHV environments and draw a conclusion for the stationary value of surface enrichment.

There is not only an experimental way leading to the examination of the influences of ion sputtering and the understanding of the complex processes in the target material. Many researchers use analytical methods (mostly by approximately resolving the Boltzmann transport equation [5, 17]) to find out, how the composition of the target changes due to ion bombardment. Others apply computer simulations [18, 19, 20, 21, 22] accepting the measured sputtering features as the test of their models. These authors expect from their models to serve predictions on unknown features.

The model

One sort of the simulations models the target as a gaslike material. We could not use this approximation, as we do not have an appropriate method to take into account the different kinds of particles by the collision cross sections [23]. The other type of models simulating an amorphous target [20] can probably show a realistic picture of the sputtering process, but the computational difficulties do not allow us to use this possibility. For a good synopsis of the physical problems, easy handling and limited computer time we chose first a monocrystal target model, by which we could obtain results comparable to experimental data, and which were also suitable to predict qualitatively correct sputtering features.

For the simulation of the collision dynamics, we have chosen the binary collision approximation, and every interactive particle has a screened Coulomb potential. The choice of the interaction potential can be explained by its reasonable fitting feature besides the economic point of view of the computer time. Therefore the applied screening function was the Bohr function [24]:

$$V(r) = V_c(r) \exp(-r/a),$$

where $V(r)$ is the applied potential, $V_c(r)$ is the Coulomb potential and

$$a = k \frac{a_B}{(Z_1^{2/3} + Z_2^{2/3})^{1/2}},$$

where a_B is the first Bohr radius, Z_1 and Z_2 are the atomic numbers and k is the fitting parameter. This function connected to a reasonably chosen maximum impact parameter ($p = d/\sqrt{8}$, where d is the lattice constant) has become useful to describe the collision processes in a crystal target which is built up from nonoverlapping spheres.

The modelling of the collisions and the characteristics of the crystal depend to a great extent on the choice of the special energy values, as the displacement, threshold and binding energies. Let us consider a collision, where the initial kinetic energy of the primary particle is E_1, and after the scattering $E_1 - E_T$, where E_T is the transfer energy. The lattice atom can be displaced, if $E_T > E_d$ (where E_d is the displacement energy) and it can be added to the cascade so with an energy $E_T - E_b$, where E_b is the binding energy. The active, moving particles are followed in the program as far as their energy decreases below E_c, where E_c is the threshold energy. A moving particle can replace a lattice atom on its site, if $E_T > E_d$ and E_1 is less than the minimum of E_c and E_d. In our model E_c is a constant value that corresponds to the isotropic surface binding model [20]. A common value of 3.5 eV proved to be suitable for the metals under investigation. The other two energy values are chosen to be equal to the cohesive energy of the crystal [25]. If E_c was chosen according to the planar model [21, 26, 27], (i.e. the velocity of the moving particle perpendicular to the surface corresponded to the velocity contained in threshold energy E_c), then the low energy edge of the sputtered particle spectrum slightly decreased.

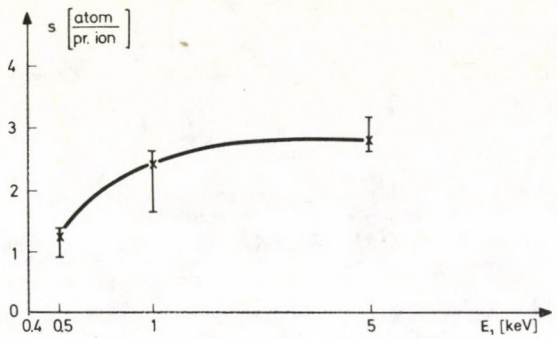

Fig. 1. The sputtering yields of Ni vs the primary energy. The bombarding particles are Ar^+ ions. The deviation bars denote the measured results

To test our model we have begun our investigations on pure metal targets. Since we had enough experimental results for comparison to our calculated ones for nickel [1] and since Ni produces an f.c.c. lattice, a structure well-suiting our model, we have used a Ni monocrystal target bombarded by Ar^+ ions with the primary energy of 1 keV.

In Fig. 1 the sputtering yield of Ni is shown as a function of the primary energy. The results are in satisfactory agreement with the measured data (deviation bars) [1]. Further on we will always speak about normal incident angle, and about the (100) incident plane of the crystal.

Results

The change of the surface composition in binary alloys was examined by the model in Ni—Au, Ni—Pd and Ni—Cu systems. First of all we were interested in how the mass ratios and the binding energy ratios influence the composition change, the preferential sputtering.

In Table I one can see the binding energy values (E_b) from the literature [6, 28], the experimental sputtering yields (S_{exp}) [2], the binding energies used in the calculation (E_b^x) and the calculated yields for pure materials (S_{calc}). The fitting parameter is always 1.1 here according to the tested simulation for Ni.

Table II contains the mass and binding energy ratios [6, 28].

Table I

Binding energy and sputtering yields

	E_b[eV]	S_{exp}[1 keV, Ar^+]	S_{calc}[1 keV, Ar^+]	E_b^*[eV]
Au	3.8	3.6	3.2	3.5
Pd	3.9	3.1	3.0	3.8
Cu	3.5	3.6	3.8	3.5
Ni	4.45	2.2	2.4	4.6

Table II

Mass and binding energy ratios

	Ni—X	M_{Ni}/M_X	$E^*_{b\,Ni}/E^*_{b\,X}$
X	Au	0.298	1.314
	Pd	0.550	1.211
	Cu	0.924	1.314

From the different compositions we could infer the influence of the mass ratio [29] in the case of Ni—Cu resembling Ni—Au, while in the cases of Ni—Pd to Ni—Au and of Ni—Pd to Ni—Cu we could obtain information on the influence of the binding energy ratios [30].

For the first time now let us consider a solid solution crystal target consisting of A and B types of atoms. We examine the behaviour of this sample after sputtering by 1 keV Ar^+ ions. The atomic mass and binding energy of the different types of atoms are different.

In Fig. 2 one can see the sputtering yield ratio (S_A/S_B) vs the concentration ratio of the target (C_B/C_A). The function parameter is the mass ratio ($\mu = M_B/M_A$). The binding energy is the same for the components. The decreasing slope of the linear functions shows the physically understandable fact that during the development of the cascade only a smaller amount of atoms with bigger mass displaces from the lattice site.

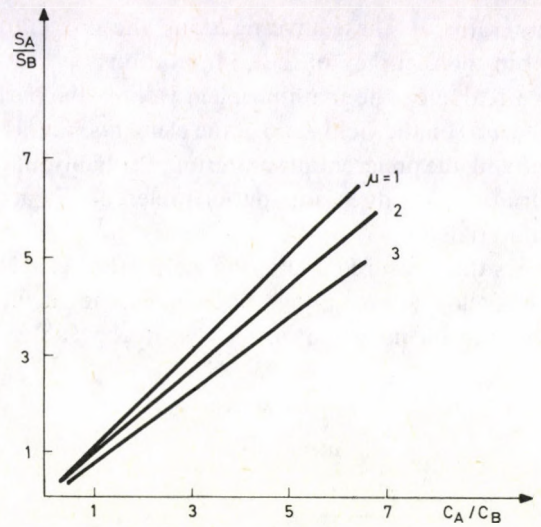

Fig. 2. The sputtering yield ratio (S_B/S_A) of a target consisting of A and B types of atoms vs the concentration ratio of these elements (C_B/C_A). The function parameter is their mass ratio ($\mu = M_B/M_A$). The binding energies are the same ($E_{bA} = E_{bB}$)

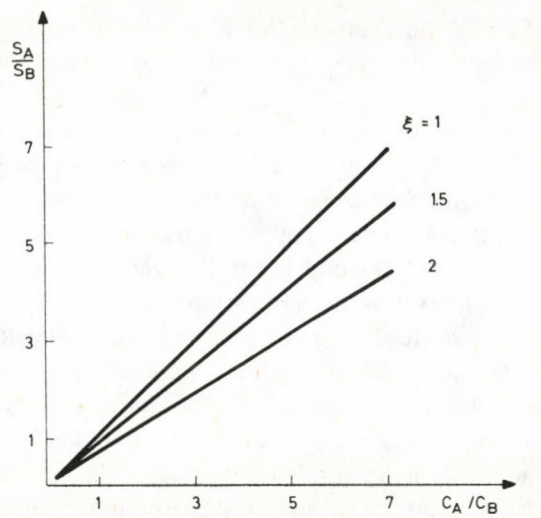

Fig. 3. Similar functions to those of Fig. 2. The function parameter is the binding energy ratio ($\xi = E_{bB}/E_{bA}$). The masses are the same ($M_A = M_B$)

In Fig. 3 the case is similar, but the function parameter is the binding energy ratio ($\xi = E_{bB}/E_{bA}$), and the mass is the same for the components.

According to these investigations we concluded that the sputtering yield ratio is more sensitive to the change of the binding energy ratio of the components, than to that

of the atomic mass ratio. In these investigations the concentration ratio has no significant role within the accuracy of the computations.

Considering a real alloy the main problem is, how the partial sputtering yield ratio of the alloy depends on the yield ratio of the elements. This is the first question to deal with, when studying the preferential sputtering. Probably, that component will be enriched on the surface which does not sputter preferentially according to the yield ratio of the pure materials.

Table III shows the measured sputtering yield ratios [16, 28] of pure materials (S_A/S_B (pure)), those of alloys (S_A/S_B (alloy)), and, finally, the calculated ratios (S_A/S_B) in the cases of the alloys under investigation. A = Ni in the Table.

Table III

Sputtering yield ratios

$A-B$		S_A/S_B(alloy)	S_A/S_B (pure)	S_A/S_B
B	Au	—	0.55	0.673
	Pd	0.67	0.71	0.78
	Cu	0.625	0.611	0.72

As our RETTUPS Monte Carlo simulation program registers the number of the displaced and stopped atoms in every atomic plane, the possibility is given to determine depth profiles.

The program models the average collision cascade induced by one bombarding particle, and the kinetics in a model cannot be followed without memory. For substitution we applied the following conceptual model. Let us consider the depth distribution of the sputtered particles, and let us have its average value. In agreement with the literature we came to the conclusion that the overwhelming majority of the sputtered particles originates from the surface close some atomic layers [26, 32, 33, 34, 35]. (Nevertheless, the cascade mixing disturbs the material at a depth of about 10 nm [5]). Let us now figure that on the surface there is a sputtering effect different from the one in the bulk material in steady state condition. This sputtering does not happen in stoichiometric ratios, which causes a surplus in one kind of atoms. With the assumptions that the profile of this surplus in the target is linear and the bulk sputtering is according to the steady state condition we suppose that in the middle of the surface close layer, where the disturbation is the strongest (in the third atomic plane below the surface for example) the value of the surplus concentration is equal to the mean value determined above. A linear function recounted to the target concentration therefore shows that the sample is in steady state, but there is preferential sputtering, which means that there is an enriched component on the surface. These linear functions are denoted with the dotted lines in Figs 4, 5 and 6. The thin horizontal lines show the concentration before sputtering.

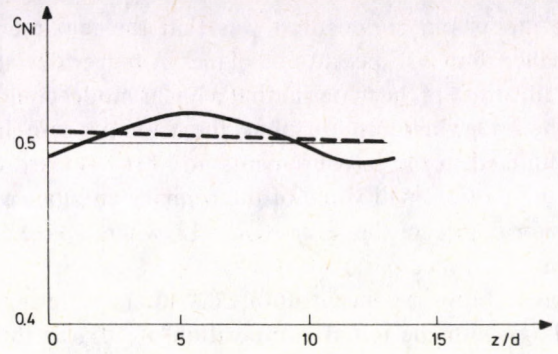

Fig. 4. The Ni concentration after sputtering by 1 keV Ar^+ ions in a Ni—Au target. The initial composition is denoted by the horizontal line. The dotted line shows the linear function according to the conceptual model of surface enrichment

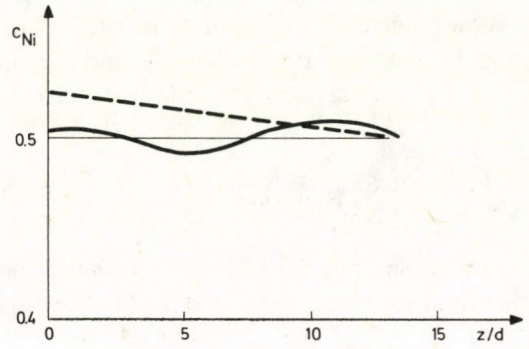

Fig. 5. The Ni concentration after sputtering by 1 keV Ar^+ ions in a Ni—Pd target. The initial composition is denoted by the horizontal line. The dotted line shows the linear function according to the conceptual model of surface enrichment

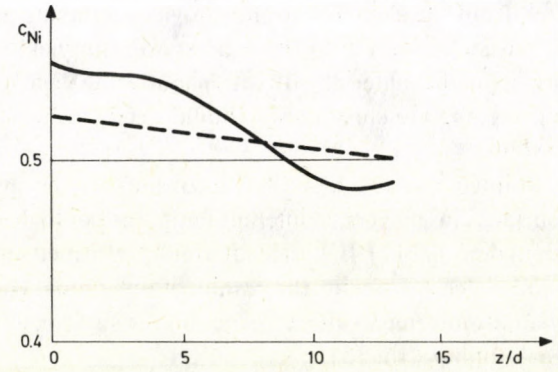

Fig. 6. The Ni concentration after sputtering by 1 keV Ar^+ ions in a Ni—Cu target. The initial composition is denoted by the horizontal line. The dotted line shows the linear function according to the conceptual model of surface enrichment

In the above model our supposition was that the maximum change of the concentration is smaller than 20% per atomic planes. A bigger deviation would mean such a drastical modification of the material that a linear model could not include it in the calculation. The other assumption that the cascades are independent and nonoverlapping is fulfilled in the measurements, too [16]. This is due to the small primary doses. Owing to the small value of the primary energy we may neglect the examination of greater depths of the target ($z/d > 12$, where z is the depth measured from the surface, d is the lattice parameter).

Figures 4, 5 and 6 show the concentration of Ni after sputtering in Ni—Au, Ni—Pd and Ni—Cu alloys with the initial composition of 50% as the function of the normalized depth.

According to the Figures, there is a small Ni enrichment on the surface in the case of the Ni—Au target and no enrichment is found at Ni—Pd within the 10% standard deviation of the computation. There seems to be a significant enrichment of Ni at Ni—Cu. As the experiments show in the third and second case there is a certain amount of Ni enrichment [3, 16] a more significant one for Ni—Cu and a small one for Ni—Pd (2 keV Ar^+). We have no measured data about the surface composition change in Ni—Au systems.

Conclusions

The RETTUPS simulation model developed by the authors can produce valuable and comparable results which in an experimental sense agree well with the sputtering yields of pure targets of the literature (Ar^+). With the parameter values fitted to pure targets we could reach qualitatively good results in the investigation of binary alloys.

It can be seen that the sputtering features of the pure materials survive in alloy sputtering. This fact must be partly due to the assumption that the binding energies are invariantly transferred from the elements to the alloy components. According to our calculations and the measured data [35] the total sputtering yield increases linearly with the concentration from the material with lower sputtering yield to the other with a higher one. For deeper-going conclusions we should need further knowledge of the atomic processes in solids.

Sigmund has pointed out the fact that according to the measurements the composition of the surface close layers is different in the case of high and in the case of low primary ion current density [17]. In his calculations performed on a small intensity primary beam the tendencies agree with the results of our model computations. The component with higher atomic mass value enriches on the surface, if the other features of the components are similar [16, 36].

References

1. H. H. Andersen and H. L. Bay, in Sputtering by Particle Bombardment I, Ed. R. Behrisch, Springer Verlag, Heidelberg, 1981.
2. G. K. Wehner, in Methods of Surface Analysis. Ed. A. W. Czanderna, Elsevier, Amsterdam, 1975.
3. K. Goto, T. Koshikawa, K. Ishikawa and R. Shimizu, Proc. 7th Int. Vac. Congr. and 3rd Int. Conf. Solid Surf. Vienna, 1977.
4. N. J. Chou and M. W. Shafer, Surf. Sci., **92,** 601, 1980.
5. W. O. Hofer and U. Littmark, Phys. Lett., **71A,** 456, 1979.
6. H. H. Andersen, Appl. Phys., **18,** 131, 1979.
7. A. Gras-Marti and P. Sigmund, Proc. Symp. Sputtering., Eds P. Varga, G. Betz and F. P. Viebock. Vienna, 1980.
8. K. Watanabe, M. Hashiba and T. Yamashina, Surf. Sci., **61.,** 483, 1976.
9. H. W. Etzkorn, U. Littmark and J. Kirschner, Proc. Symp. Sputtering, Eds P. Varga, G. Betz and F. P. Viebock. Vienna, 1980.
10. J. Kirschner and H. W. Etzkorn, Appl. Surf. Sci., **3,** 251, 1979.
11. H. W. Etzkorn and J. Kirschner, Nuc. Instr. Meth., **168,** 395, 1980.
12. S. Hofmann, Proc. 7th Int. Vac. Congr. and 3rd Int. Conf. Solid Surf. Vienna, 1977.
13. R. Shimizu and N. Saeki, Surf. Sci., **62,** 751, 1977.
14. H. Shimizu, M. Ono and K. Nakayama, Surf. Sci., **36,** 817, 1973.
15. G. Betz, M. Arias and P. Braun, Nuc. Instr. Meth., **170,** 347, 1980.
16. G. Betz, Surf. Sci., **92,** 283, 1980.
17. P. Sigmund, J. Appl. Phys., **50,** 7261, 1979.
18. R. Shimizu, Appl. Phys., **6,** 241, 1975.
19. D. P. Jackson, Can. J. Phys., **53,** 1513, 1975.
20. R. Behrisch, G. Maderlechner, B. M. U. Scherzer and M. T. Robinson, Appl. Phys., **18,** 391, 1979.
21. D. E. Harrison, Jr., N. S. Levy, J. P. Johnson and H. M. Effron, J. Appl. Phys., **39,** 3742, 1968.
22. T. Ishitani, Jap. J. Appl. Phys., **11,** 125, 1972.
23. V. E. Yurasova and V. A. Eltekov, Proc. Symp. Sputtering, Eds P. Varga, G. Betz and F. P. Viebock, Vienna, 1980.
24. N. Bohr, Kgl. Dan. Vid. Selsk. Mat. Fys., **18**/8, 1948.
25. W. S. Snyder and J. Neufeld, Phys. Rev., **103,** 862, 1966.
26. P. Sigmund, Phys. Rev., **184,** 383, 1969.
27. G. Betz, R. Dobrozemsky and F. P. Viehböck, Int. Mass Spectr., **6,** 451, 1971.
28. H. Öschsner, Zeitschr. f. Phys., **261,** 37, 1973.
29. P. S. Ho, J. E. Lewis and W. K. Chu, Surf. Sci., **85,** 19, 1978.
30. G. Betz, J. Marton and P. Braun, Nuc. Instr. Meth., **168,** 541, 1980.
31. F. G. Rüdenauer, Int. J. Mass Spectr., **6,** 309, 1971.
32. H. W. Werner, Vacuum, **22,** 613, 1972.
33. A. Benninghoven, Surf. Sci., **35,** 427, 1973.
34. H. Liebl, J. Vac. Sci. Techn., **12,** 385, 1975.
35. P S. Ho, Surf. Sci., **72,** 253, 1978.
36. P. K. Haff, Appl. Phys. Lett., **31,** 259, 1977.

Acta Physica Hungarica 54 (3—4), pp. 287—295 (1983)

VIBRATION OF A VISCOELASTIC FLUID SPHERE

K. DOBRÓKA

Department of Physics, Technical University for Heavy Industry, 3515 Miskolc, Hungary

(Received 9 September 1982)

The characteristic equation for the vibration of a viscoelastic (Oldroyd or Maxwell) fluid sphere is derived. It is shown that this equation can be written formally in the form obtained by Chandrasekhar for selfgravitating viscous globe. Real solutions corresponding to the first two aperiodic modes and the complex solutions corresponding to damped oscillatory motions of the Oldroyd liquid sphere are also evaluated.

1. Introduction

Previously it was shown by Tang and Wong [1] that the characteristic equation determining the aperiodic and vibrational modes of an incompressible viscous globe under the action of gravitational or electrical forces (with high, low or zero electric conductivity) and surface tension can be reduced to the form given by Chandrasekhar [2]. This characteristic equation is a very general one. It can be applied in a broad range of phenomena such as vibration of stars, liquid drops and of atomic nuclei, too. Our purpose is to show that under more general conditions, when the fluid has viscoelastic nature, the characteristic equation can also be written in the form of Chandrasekhar's equation.

To describe the viscoelastic nature of some polymers and suspensions Oldroyd introduced the constitutive relation [3]

$$\left\{1+\lambda_1\frac{\mathrm{d}}{\mathrm{d}t}\right\}\left\{\sigma_{ik}+p\delta_{ik}\right\}=\left\{1+\lambda_2\frac{\mathrm{d}}{\mathrm{d}t}\right\}2\eta e_{ik}, \tag{1}$$

where σ_{ik} is the stress tensor, p is the scalar pressure, $\frac{\mathrm{d}}{\mathrm{d}t}$ is the mobil operator, e_{ik} is the rate of strain tensor

$$e_{ik}=\frac{1}{2}\left(\frac{\partial v_i}{\partial x_k}+\frac{\partial v_k}{\partial x_i}\right),$$

η is the coefficient of viscosity, λ_1 is the stress relaxation time, λ_2 is the strain retardation time, δ_{ik} is the Kronecker delta, while v_i, x_i are the velocity and position vector, respectively. With the help of (1) the stress relaxation and strain retardation obtained in some fluid mechanical experiments can be interpreted. In the following we shall treat the small amplitude vibration of an incompressible Oldroyd liquid sphere.

2. The characteristic equation

After Chandrasekhar, the boundary of the vibrating mass is assumed to be sharp and given by

$$r'(\vartheta, \varphi, t) = R + \varepsilon(t) Y_{lm}(\vartheta, \varphi), \tag{2}$$

where R is the equilibrium radius, Y_{lm} is the spherical harmonic and

$$\varepsilon(t) = \varepsilon_0 e^{-\sigma t}, \tag{3}$$

where $\varepsilon_0 \ll R$. We can write the linearized equation of motion as

$$\left\{1 + \lambda_1 \frac{\partial}{\partial t}\right\} \left\{\frac{\partial \mathbf{v}}{\partial t} + \operatorname{grad} w\right\} = \left\{1 + \lambda_2 \frac{\partial}{\partial t}\right\} \nu \Delta \mathbf{v},$$

ν being the kinematic viscosity, ρ is the mass density,

$$w = \frac{\delta p}{\rho} + \frac{\rho^*}{\rho} \delta V,$$

δp and δV are the perturbation of the pressure and of the (gravitational or electrostatic) potential caused by the vibration, ρ^* is the corresponding mass or charge density, as the case may be.

Assuming the time dependence of all quantities in the form similar to (3) we get the only space dependent equation

$$-\sigma \mathbf{u} + \nu \frac{1 - \lambda_2 \sigma}{1 - \lambda_1 \sigma} \operatorname{rot} \operatorname{rot} \mathbf{u} = -\operatorname{grad} w, \tag{4}$$

$\mathbf{u}$ being the amplitude of the velocity. As in the papers [1], [2] the quantity w can be written as

$$w = P_0 \frac{r^l}{R^{l-1}} \varepsilon Y_{lm} + \frac{\rho^*}{\rho} f(l) \frac{r^l}{R^{l+2}} \varepsilon Y_{lm} = (l+1) \Pi_0 r^l \varepsilon Y_{lm}, \tag{5}$$

where P_0 and Π_0 are constants and

$$f(l)=\begin{cases} -\dfrac{3}{2l+1}GM & \text{for self-gravitating globe,} \\ \dfrac{3}{2l+1}kQ & \text{for uniform volume charge,} \\ -\dfrac{l+1}{2l+1}kQ & \text{for surface charge with low conductivity,} \\ 0 & \text{for surface charge with high conductivity.} \end{cases}$$

Here G denotes the gravitational constant, M is the mass of the globe, Q is the electric charge and $k=(4\pi\epsilon_0)^{-1}$, ϵ_0 being the vacuum permittivity. (Whether to take the gravitational field into account in the case of viscoelastic liquid drop is of course a purely academic question; this is done only to complete our discussion.)

By means of Eqs (4), (5) it can be seen, that $\mathbf{u}$ is a poloidal vector with the components in spherical coordinates [4]

$$\mathbf{u}=\begin{cases} \dfrac{l(l+1)}{r^2}U(r)Y_{lm}e^{-\sigma t}, \\ \dfrac{1}{r}\dfrac{\mathrm{d}U(r)}{\mathrm{d}r}\dfrac{\partial Y_{lm}}{\partial\vartheta}e^{-\sigma t}, \\ \dfrac{1}{r\sin\vartheta}\dfrac{\mathrm{d}U(r)}{\mathrm{d}r}\dfrac{\partial Y_{lm}}{\partial\varphi}e^{-\sigma t}, \end{cases} \tag{6}$$

where $U(r)$ is the determining scalar function satisfying the equation

$$\frac{\mathrm{d}^2U}{\mathrm{d}r^2}-\frac{l(l+1)}{r^2}U+\frac{1-\lambda_1\sigma}{1-\lambda_2\sigma}\frac{\sigma}{\nu}U=\frac{1-\lambda_1\sigma}{1-\lambda_2\sigma}\frac{\varepsilon_0}{\nu}\Pi_0 r^{l+1}. \tag{7}$$

The general solution of Eq. (7) is

$$U=Ar^{\frac{1}{2}}J_{l+\frac{1}{2}}(qr)-\frac{\varepsilon_0}{\nu}\Pi_0 r^{l+1}, \tag{8}$$

where $J_{l+\frac{1}{2}}(x)$ is the spherical Bessel function of order $l+\dfrac{1}{2}$ and

$$q=\sqrt{\frac{\sigma}{\nu}\frac{1-\lambda_1\sigma}{1-\lambda_2\sigma}}.$$

The constants appearing in (8) can be determined by means of the boundary conditions:

(i) The u_r radial component of velocity must be compatible with the form of the boundary given by Eq. (2)

$$u_r(r=r') = -\sigma\varepsilon_0 Y_{lm} e^{-\sigma t}. \tag{9}$$

(ii) The tangential stresses

$$\sigma_{r\vartheta} = \rho\nu \frac{1-\lambda_2\sigma}{1-\lambda_1\sigma}\left\{\frac{1}{r}\frac{\partial u_r}{\partial\vartheta} - \frac{u_\vartheta}{r} + \frac{\partial u_\vartheta}{\partial r}\right\},$$

$$\sigma_{r\varphi} = \rho\nu \frac{1-\lambda_2\sigma}{1-\lambda_1\sigma}\left\{\frac{1}{r\sin\vartheta}\frac{\partial u_r}{\partial\varphi} - \frac{u_\varphi}{r} + \frac{\partial u_\varphi}{\partial r}\right\}$$

must vanish on the boundary.

(iii) The (r, r) component of the total stress tensor

$$\sigma_{rr} = p_0 + \delta p - 2\rho\nu \frac{1-\lambda_2\sigma}{1-\lambda_1\sigma}\frac{\partial u_r}{\partial r}$$

on the deformed boundary must be equal to the force acting on a unit surface because of the surface tension and the Coulomb repulsion.

Combining Eqs (6) and (8), the boundary conditions (i), (ii) give

$$A = \frac{2(l-1)\varepsilon_0\sigma R^{\frac{3}{2}}}{l\{2xJ_{l+\frac{3}{2}}(x) - x^2 J_{l+\frac{1}{2}}(x)\}}$$

and

$$\Pi_0 = -\frac{\sigma^2}{l(l+1)R^{l-1}}\left\{\frac{2(l-1)}{2xQ_{l+\frac{1}{2}}(x) - x^2} - 1\right\}, \tag{10}$$

where the notations

$$x = \sqrt{\frac{\sigma R^2}{\nu}\frac{1-\lambda_1\sigma}{1-\lambda_2\sigma}}$$

and

$$Q_{l+\frac{1}{2}} = \frac{I_{l+\frac{3}{2}}(x)}{J_{l+\frac{1}{2}}(x)}$$

were used.

By means of the boundary condition (iii) we can find

$$\{\sigma_{l,0}^2 + l(l+1)\Pi_0 R^{l-1}\}\,\varepsilon Y_{lm} - \frac{2l}{R}\nu\frac{1-\lambda_2\sigma}{1-\lambda_1\sigma}\left(\frac{\partial u_r}{\partial r}\right)_{r=R} = 0, \tag{11}$$

where

$$\sigma_{l,0}^2 = l(l-1)(l+2)\frac{T}{\rho R^3} - \frac{l}{R}B(l) + \frac{\rho^* l}{\rho R^3}f(l),$$

T is the surface tension and

$$B(l)=\begin{cases} -\dfrac{GM}{R^2} & \text{for uniform gravitating globe,} \\ \dfrac{3kQ^2}{4\pi\rho R^2} & \text{for uniform volume charge,} \\ \dfrac{l^2-3l-2}{2l+1}\dfrac{kQ^2}{4\pi\rho R^5} & \text{for surface charge with low conductivity,} \\ (l-1)\dfrac{kQ^2}{4\pi\rho R^5} & \text{for surface charge with high conductivity.} \end{cases}$$

Taking into account Eqs. (10), (11) the following equation can be written

$$\frac{\sigma_{l,0}^2}{\sigma^2}=\frac{2(l^2-1)}{x^2-2xQ_{l+\frac{1}{2}}(x)}-1+\frac{2(l-1)l}{x^2}\left\{1-\frac{2(l+1)Q_{l+\frac{1}{2}}(x)}{x-2Q_{l+\frac{1}{2}}(x)}\right\}, \tag{12}$$

which is formally the same as the Chandrasekhar characteristic equation.

In the special case, when $\lambda_2=0$ Eq. (1) gives the constitutive equation of the Maxwell fluid, so Eq. (12) can be considered as the characteristic equation of a vibrating sphere of Maxwell fluid with $x=\sqrt{\frac{\sigma R^2}{\nu}(1-\lambda_1\sigma)}$. If $\lambda_1=0$ and $\lambda_2=0$ Eq. (1) gives the state equation of the Newtonian liquid. In this case the Eq. (12) is completely the same as the Chandrasekhar equation with $x=\sqrt{\frac{\sigma R^2}{\nu}}$.

In the following we exclude in our considerations the gravitational case and give numerical results concerning the viscoelastic drops.

3. Aperiodic motion

The real solutions of Eq. (12) describe aperiodic motions of the fluid sphere. In order to find numerical results, it is suitable to introduce dimensionless quantities: the relaxation "time" $\alpha_1=\lambda_1\sigma_{l,0}$, the retardation "time" $\alpha_2=\lambda_2\sigma_{l,0}$ and the generalized viscosity $\alpha^2=\frac{\sigma_{l,0}R^2}{\nu}$. So we can write

$$x=\alpha\sqrt{\sigma^*\frac{1-\alpha_1\sigma^*}{1-\alpha_2\sigma^*}}$$

with $\sigma^* = \frac{\sigma}{\sigma_{l,0}}$. The special case of $\alpha_1 = \alpha_2$ also gives the results of Chandrasekhar [2] and Tang and Wong [1]. The viscoelastic nature of the fluid is shown by the fact that $\frac{\alpha_1}{\alpha_2} \neq 1$. On the other hand, it was shown by Oldroyd [3], that $\lambda_1 > \lambda_2 \geqq \frac{1}{9}\lambda_1$, so our numerical calculations are carried out in the case, when the non-Newtonian feature of the fluid is most characteristic: $\frac{\alpha_1}{\alpha_2} = 9$ [3].

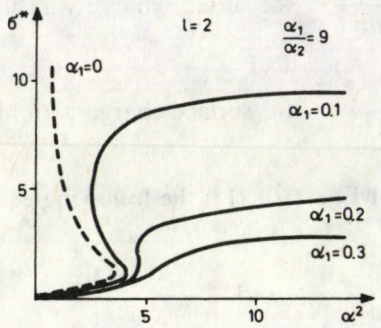

Fig. 1. The real solutions of the characteristic equation for $l=2$ in the interval $0 < \sigma^* < \frac{1}{\alpha_1}$ as a function of α^2 at various values of the parameter α_1 (full curve). The broken curve shows the results of Newtonian case

As is shown by Chandrasekhar, there is an infinite number of intervals of x, where the characteristic equation has real solutions. The first of them for $l=2$ is $0 < x < 2.6656$.

In Oldroyd fluids two regions of real σ^* roots can be separated. In the first one $\sigma^* < \frac{1}{\alpha_1}$ and at small σ^* the solutions concerning the viscoelastic drops are near to those of Newtonian fluid sphere. At the relaxation "times" $\alpha_1 < 0.2104$ the curve $\alpha^2(\sigma^*)$ has a maximum α^2_{max} (Fig. 1). In contradiction with the Newtonian case, this maximum is only a local one, there can also be aperiodic solutions in the range $\alpha^2 > \alpha^2_{max}$. At a value $\alpha_1 = 0.2404$ the curve $\alpha^2(\sigma^*)$ has an inflexion point, where $\alpha^2 = 4.7374$, while at larger values of α_1 the curve is monotonic. The local maxima belonging to various α_1 parameters are in the interval

$$3.6902 < \alpha^2_{max} < 4.7374.$$

In the other range $\sigma^* \geqq \frac{1}{\alpha_2}$, the solutions are plotted in Fig. 2.

For $l=3$ similar results can be found (Fig. 3). The first interval of x in which real solutions exist $0 < x < 4.0019$. The curve $\alpha^2(\sigma^*)$ has a local maximum at the values of the dimensionless relaxation times $\alpha_1 < 0.2229$.

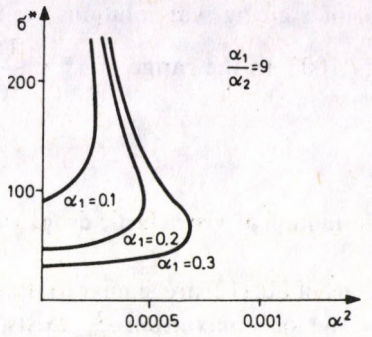

Fig. 2. The real solutions of the characteristic equation for $l=2$ in the range $\sigma^* \geqq \frac{1}{\alpha_2}$ as a function of α^2. They are labelled by the value of α_1

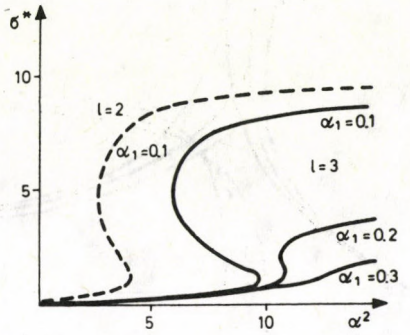

Fig. 3. The real solutions of the characteristic equation for $l=3$ aperiodic modes of decay as a function of α^2, labelled by the value of α_1 (full curve). Broken curve shows the $l=2$ mode with $\alpha_1=0,\ 1$

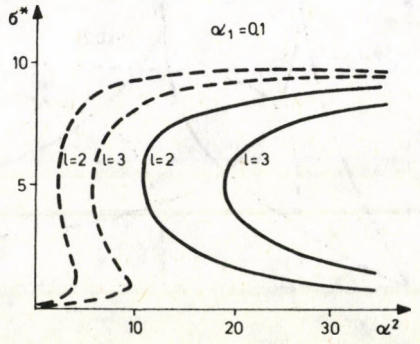

Fig. 4. The first order (broken line) and second order (full line) real solutions of characteristic equation for $l=2$ and $l=3$ with $\alpha_1=0,\ 1$ as a function of α^2

The second interval of x giving real solutions are for $l=2$ $5.3114<x<5.4730$ and for $l=3$ $6.6308<x<7.1003$. In the range of $\sigma^* < \frac{1}{\alpha_1}$ the results for $\alpha_1=0.1$ are plotted in Fig. 4.

4. Periodic motion of viscoelastic drops with damping

The complex solutions of Eq. (12) are similar to those given by Tang and Wong [1] in the sense that when the local maximum α^2_{max} exists, for $\alpha^2>\alpha^2_{max}$ the imaginary part of σ^* rises rapidly from 0 towards 1, and at $\alpha^2=\alpha^2_{max}$ the real part of σ^* coincides with the aperiodic solution. This is shown in Fig. 5 for $l=2$ and in Fig. 6 for $l=3$. As in

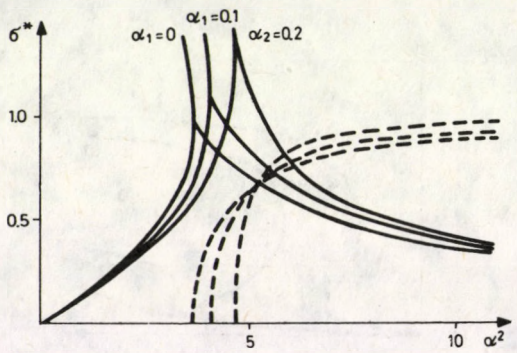

Fig. 5. Complex solutions of the characteristic equation are plotted as a function of α^2 labelled by the parameter α_1. The real part of the σ^* is shown as a full curve, the imaginary part is shown as a broken curve. The order of deformation is $l=2$

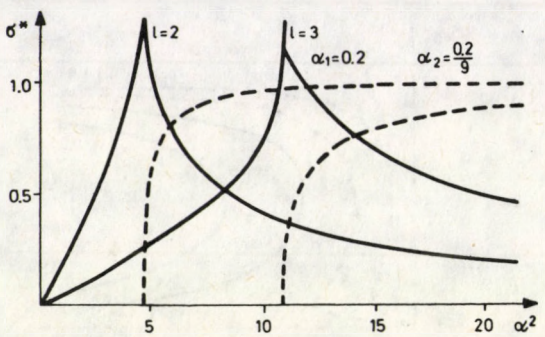

Fig. 6. Complex solutions of the characteristic equation as a function of α^2. The orders of deformation are $l=2$ and $l=3$. The dimensionless relaxation "time" is $\alpha_1=0$, 1

Newtonian liquids there can exist no complex solutions for $\alpha^2 < \alpha_{max}^2$. Because of this fact a critical radius exists, above which periodic motions occur:

$$R_{crit} = \alpha_{max} \sqrt{\frac{\nu}{\sigma_{l,0}}}.$$

In Oldroyd fluids the local maximum α_{max} and also R_{crit} is always greater than that in Newtonian liquids.

5. Conclusions

Applying the constitutive equation of the Oldroyd fluid the Chandrasekhar characteristic equation is derived in a more general form. Our results give both the characteristic equations of vibrating Maxwell and Newton fluid spheres as special cases. Real and complex numerical solutions concerning the Oldroyd fluids are given.

Acknowledgments

The author wishes to thank Professor J. Szabó for helpful discussions and encouragements.

References

1. H. H. K. Tang and C. Y. Wong, J. Phys. A: Math., Nucl. Gen., **7**, 1038, 1974.
2. S. Chandrasekhar, Proc. London Math. Soc., **9**, 141, 1959.
3. J. G. Oldroyd, Proc. Roy. Soc. (London), A **245**, 278, 1958.
4. S. Chandrasekhar, Hydrodynamic and Hydromagnetic Stability. Oxford University Press, 1968, Ch. 10.

Acta Physica Hungarica 54 (3—4), pp. 297—301 (1983)

THE PARTIAL WIDTH OF THE HIGGS BOSON IN $H \to W^+ W^- \gamma$ DECAY

T. TORMA

Astronomical Research Institute, 1121 Budapest, Hungary

(Received 12 October 1982)

The partial width of the process $H \to W^+ W^- \gamma$ is examined in the standard Weinberg–Salam model. The photon spectra are plotted with different $m_H > 2m_W$ values. The decay ratio $R = \Gamma(H \to W^+ W^- \gamma)/\Gamma(H \to W^+ W^-)$ is evaluated and found to be 0(.01). This process may be observed at $m_H \sim 150$ GeV.

The decay modes of the neutral Higgs boson are discussed in the literature [1–4]. The characteristic feature of these processes is that H decays into the heaviest particle kinematically available. This is the result of generating the masses by spontaneously broken Higgs-fermion interaction; so the coupling constant is proportional to the fermion (or W) mass. This makes the decay mode very sensitive to m_H, which is a free parameter of the theory. There are hopes that in photon production processes in the range of small photon energies a propagator can be made small in Feynman graphs, and the decay rates are increased.

In this paper we examine the decay $H \to W^+ W^- \gamma$. The corresponding Feynman graphs are shown in Fig. 1. The interaction is given by the vertices

$$H_I = g \cdot m_W \cdot H(x) \cdot \bar{W}^{\lambda}(x) W_{\lambda}(x)$$

or (1)

$$g m_W \cdot \varepsilon^{\lambda}(W^+_{\text{out}}) \cdot \varepsilon_{\lambda}(W^-_{\text{out}})$$

and

$$-ei\left[(k_3 - k_1)_{\mu_2} g_{\mu_3 \mu_1} + (k_2 - k_3)_{\mu_1} g_{\mu_2 \mu_3} + (k_1 - k_2)_{\mu_3} g_{\mu_1 \mu_2}\right]. \tag{2}$$

The differential decay width is

$$\mathrm{d}\Gamma = \frac{1}{2m_H} \frac{\mathrm{d}^3 p}{2E_p} \frac{\mathrm{d}^3 q}{2E_q} \frac{\mathrm{d}^3 k}{2E_k} \frac{1}{(2\pi)^9} \cdot (2\pi)^4 \delta^4(k + p + q - H) \cdot \sum_{\substack{\text{polar. of} \\ W^+, W^-}} |\mathfrak{M}|^2 , \tag{3}$$

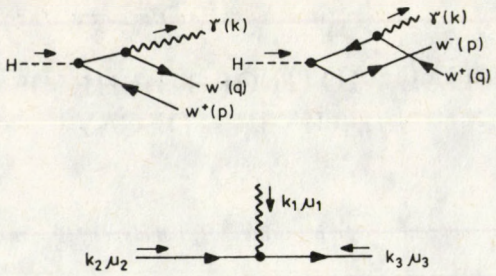

Fig. 1. The γWW vertex and the Feynman graphs for $H \to WW\gamma$

where the S-matrix element has the form

$$\begin{aligned}\mathfrak{M} = &\frac{iegm_W}{(k+q)^2-m_W^2}\cdot\{-2(\bar{\varepsilon}_p\rho_{k+q}\varepsilon_\gamma)(k\varepsilon_q)+\\ &+2(\bar{\varepsilon}_p\rho_{k+q}\varepsilon_q)(\varepsilon_f q)+[\bar{\varepsilon}_p\rho_{k+q}\cdot(k-q)]\cdot(\varepsilon_q\varepsilon_f)\}+\\ &+\frac{iegm_W}{(k+p)^2-m_W^2}\cdot\{\varepsilon_q\rho_{k+p}\cdot(p-k)](\bar{\varepsilon}_p\varepsilon_f)-\\ &-2(\varepsilon_q\rho_{k+p}\bar{\varepsilon}_p)(p\varepsilon_f)+2(\varepsilon_q\rho_{k+p}\varepsilon_f)(k\bar{\varepsilon}_p)\},\end{aligned} \tag{4}$$

where all vector indices are omitted, ε_Q are the polarization vectors for the particle with momentum Q:

$$\rho_Q = \sum_{j=1}^{3}\varepsilon_{jQ}^{\lambda}\varepsilon_{jQ}^{\mu} = -\left(g^{\lambda\mu}-\frac{Q^\lambda Q^\mu}{m_W^2}\right) = (Q^2-m_W^2)D_F(Q) \tag{5}$$

and for the photon

$$\rho_f = \rho_\gamma = k^2\cdot D_F(k).$$

Substituting (4) and (5) into (3) we choose a special coordinate system

$$\begin{aligned}
k^\lambda &= m_W\cdot\frac{y}{\lambda}\left(\quad 1 \quad |0|0| \quad 1 \quad\right) & \lambda &= \frac{m_H}{m_W}\\
H^\lambda &= m_W\cdot\quad\left(\quad \lambda \quad |0|0| \quad 0 \quad\right) & y &= \frac{m_H E_\gamma}{m_W^2}\\
p^\lambda &= m_W\cdot\quad\left(\quad \frac{\lambda}{2}-\frac{x}{\lambda} \quad |0|A| \quad -\frac{\lambda}{2}-x\left(\frac{1}{\lambda}-\frac{\lambda}{y}\right)\quad\right) & \beta &= \Gamma_W/m_W\\
q^\lambda &= m_W\cdot\quad\left(\frac{\lambda}{2}+\frac{x}{\lambda}-\frac{y}{\lambda}|0|-A|-\frac{y}{\lambda}+\frac{\lambda}{2}+x\left(\frac{1}{\lambda}-\frac{\lambda}{y}\right)\right) &&
\end{aligned} \tag{6}$$

$$A^2 = \frac{x}{y}\left(1-\frac{x}{y}\right)(\lambda^2-2y)-1,$$

and integrating over W^+W^- phase space we find

$$\frac{d\Gamma}{dE_\gamma} = \frac{\alpha^2}{8(2\pi)^3 \sin^2 \Theta_W} \cdot \frac{1}{(gm_W)} \cdot \frac{1}{\lambda^2} \cdot \int_{\frac{y}{2}\cdot(1-\sqrt{1-4/(\lambda^2-2y)})}^{\frac{y}{2}\cdot(1+\sqrt{})} dx \cdot \Sigma|\mathfrak{M}|^2 \tag{7}$$

where the physical range for y is

$$0 \leqq y \leqq \frac{\lambda^2}{2} - 2. \tag{8}$$

As a result we have

$$\frac{d\Gamma}{dE_\gamma} = \frac{\alpha^2}{(2\pi)\sin^2 \Theta_W} \cdot \frac{1}{\lambda^2} \cdot \int_{\frac{y}{2}\cdot(1-\sqrt{})}^{\frac{y}{2}\cdot(1+\sqrt{})} dx \cdot$$

$$\cdot \left\{ \frac{F_1(x, y, \lambda)}{x^2+\beta^2} + \frac{F_2(x, y, \lambda)}{[x(y-x)+\beta^2]^2+\beta^2(2x-y)^2} \right\}, \tag{9}$$

where

$$F_1 = 2(x^2-x+y) + A \cdot \left\{ 2 + \left(\frac{\lambda^2}{2} - 1\right)^2 + y - y^2 + (2y-1)\cdot x - x^2 \right\},$$

$$F_2 = 2x^2 - A \cdot \left\{ y + \frac{1}{2}\left(\frac{\lambda^2}{2} - 1\right)y^2 - 1 + \frac{y}{2}\left(\frac{\lambda^2}{2} - 1\right)^2 - \frac{1}{2}\left(\frac{\lambda^2}{2} - 1\right)^2 - \right.$$

$$\left. - \left[y\left(\frac{\lambda^2}{2} - 1\right) + \left(\frac{\lambda^2}{2} - 1\right)^2 + y^2 + 2 \right] \cdot x + 3yx^2 - 2x^3 \right\}. \tag{10}$$

The finiteness of W boson width is taken into account by substituting $m_W \to$ $\to m_W - i\Gamma_W$ in the W denominator.

We have integrated (9) and found an expression we do not display for lack of space. The result is plotted in Fig. 2. To get the width, it was numerically integrated over E_γ. For comparison we computed the total width $\Gamma(H \to W^+W^-)$, and the ratio to $H \to W^+W^-\gamma$ is given on the graphs as

$$R = \Gamma_{H\to W^+W^-\gamma}/\Gamma_{H\to W^+W^-},$$

where

$$\Gamma_{H\to W^+W^-} = \frac{\alpha}{8} m_W \sqrt{\lambda^2-4} \cdot \frac{2 + \left(\frac{\lambda^2}{2} - 1\right)^2}{\lambda^2}.$$

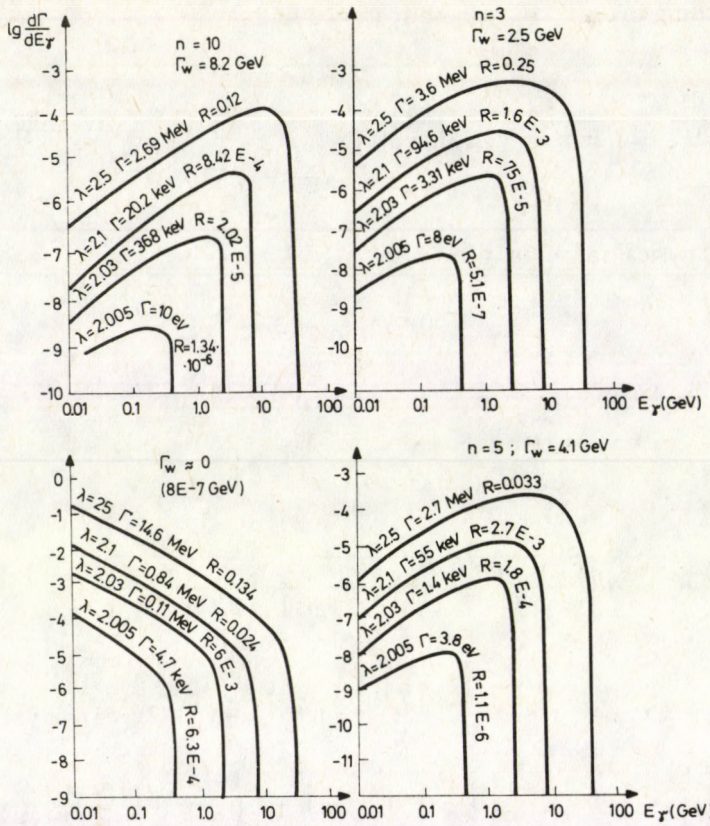

Fig. 2. The $d\Gamma(H\to W^+W^-\gamma)/dE_\gamma$ differential cross section against E_γ. n is the fermion generation number, Γ means $\Gamma(H\to W^+W^-\gamma)$ and $R=\Gamma(H\to W^+W^-\gamma)/\Gamma(H\to W^+W^-)$ and $\lambda=m_H/m_W$

As Fig. 2 shows, the infrared divergencies do not occur because of the finiteness of the W width[(1)].

The best region for detecting $H\to W^+W^-\gamma$ is that of large m_H masses, but it must remain below the next threshold. This is at $m_H=2m_Z$, i.e. $\lambda=\dfrac{2}{\cos^2\Theta_W}=2.6$, where $H\to ZZ$ begins to dominate.

In this region $m_H/m_W=(2.05\ldots 2.5)$ we get an observable value

$$R=(10^{-2}\ldots 10^{-3}).$$

[(1)] In the standard WS model $\Gamma_W=0.882\cdot n$, where n is the fermion generation number, available below the $m_W/2$ limit. The minimum value for n is 3 (see e.g. [4]).

Acknowledgement

I express my gratitude to Prof. G. Pócsik for his constant aid and consultations in preparing this paper.

References

1. G. Pócsik and G. Zsigmond, Phys. Lett., **112B,** 157, 1982.
2. J. Ellis et al., Nucl. Phys., **B106,** 292, 1976.
3. G. Pócsik and T. Torma, Z. Phys., C, **10,** 367, 1981.
4. J. Bernabéu, P. Pascual, Electro-Weak Theory, GIFT, 1981.

Acta Physica Hungarica 54 (3—4), pp. 303—312 (1983)

A SURVEY OF AMORPHOUS Se—Te SEMICONDUCTORS AND THEIR CHARACTERISTIC ASPECTS OF CRYSTALLIZATION

M. F. KOTKATA and M. K. EL-MOUSLY

Physics Department, Faculty of Science, Ain Shams University, Cairo, Egypt

(Received in revised form 30 September 1982)

This paper reviews some work done in our laboratory on the binary amorphous system Se—Te. The compositional dependence of some physical properties such as: density, dc conductivity and thermal conductivity, have been investigated. A number of results are reviewed. The effects of composition, temperature and time of annealing on the dc conductivity are explained in terms of structural changes and crystallization kinetics. The spectrum of the activation energies of crystallization for the amorphous solid and liquid phases is discussed.

1. Introduction

This laboratory has been engaged for some time in studying the transport properties of some different amorphous chalcogenide systems. Although there is still much to be done, it is now possible to discuss a number of common features that appear to be emerging for the system Se—Te. To characterize a material, it is necessary to do a large number of different experiments on the same material.

Series of Se—Te alloys, ranging in chemical composition from pure Se to pure Te, were prepared by melting and quenching the mixture [1]. The vitreous and non-vitreous state was confirmed earlier by DTA measurements [1] and X-ray diffraction [2]. The equilibrium phase diagram of the system Se—Te has been constructed [1]. An eutectic point is observed at the composition of $TeSe_{30}$ at 180 °C during the supercooling process. The diffraction pattern of the vitreous state is characterized by two broad maxima using the wavelength $\lambda = 0.1542$ nm. The phase diagram of the whole system shows the presence of three distinguishable substitutional solid solution phases termed A, A + B, and B phases, where the compositional ranges for these three states were reported [1, 2].

For both the vitreous (glass) and crystallized states, the variation of the density [1], dc conductivity [3, 4], and thermal conductivity [5] with the Te concentration for some Se—Te compositions have been measured. The crystallization kinetics of the vitreous (amorphous solid) materials have been investigated by isothermal [3, 6, 7] and by non-isothermal [8, 9] techniques. Also, the kinetics of liquid-crystal (l—c) phase transformation have been studied for some Se—Te compositions [4].

The aim of the present work is to clarify some of the previous results gained from different physical measurements for various compositions in the system Se—Te together with some aspects of their crystallization. A number of new results for some other compositions $TeSe_x$ are presented. The compositional range of $1000 \geqq x \geqq 2.5$ was covered.

2. Thermal spectrum of electrical conductivity

Figure 1 shows a typical variation of the dc conductivity during a consecutive heating-cooling cycle of the sample $TeSe_{500}$. The characteristic value of E_σ for each of the initial amorphous (line AB), liquid (line FG) and polycrystalline (line IJ) phases are represented in the Figure. The point B (72 °C) represents the beginning of the amorphous—crystal (a—c) transition T_{a-c}, during the heating cycle. The melting point lies between points E and F (210–225 °C).

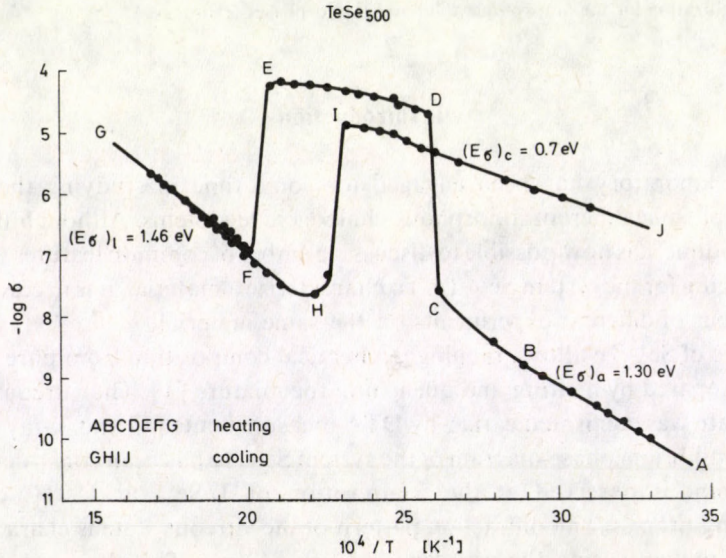

Fig. 1. Thermal spectrum of the electrical conductivity of $TeSe_{500}$

Upon cooling a liquid below its melting point T_m, it either crystallizes or forms a glass. During crystallization the viscosity, energy, volume, internal energy and hence the electrical conductivity change discontinuously, and the transition is first-order. In glass formation, however, these properties change in the vicinity of the glass transition temperature T_g. In Fig. 1, the point H (177 °C) represents the beginning of the l—c transition, T_{l-c}.

Table I

Transition temperatures of Se—Te glasses

Composition	Te [at%]	T_{a-c} [°C]	T_{l-c} [°C]	T_m (DTA) [°C]
Se	0.0	65	157	221
$TeSe_{1000}$	0.099	69	165	
$TeSe_{500}$	0.199	72	177	
$TeSe_{100}$	0.990	72	198	
$TeSe_{80}$	1.235	74	182	
$TeSe_{50}$	1.96	77	132	222
$TeSe_{30}$	3.23	88	163	223
$TeSe_{20}$	4.76	92	170	224
$TeSe_{12.5}$	7.41	92	186	
$TeSe_{10}$	9.09			232
$TeSe_5$	16.67			244,252
$TeSe_{2.5}$	28.57	97	259	273,292
$TeSe_{1.5}$	40.00			308,325
TeSe	50.00			333,354
Te_3Se	75.00			395,423
Te	100.00			454

Table I gives the composition dependence of the transition temperatures T_{a-c} and T_{l-c}. The melting points T_m as determined from DTA measurements are given in Table I. The Table shows that T_{a-c} increases monotonically with increasing tellurium, while T_{l-c} shows a certain minimum at the eutectic composition $TeSe_{30}$. Starting from the composition $TeSe_5$ (16.6 at% Te), the endothermic peak on the thermograms of the DTA splits, which means two melting points, T_{m1} and T_{m2}.

3. Characteristic physical properties

3.1. The glassy and crystalline states

The electrical conductivity $\sigma(T)$ was measured as described previously [8], the thermal conductivity $\chi(T)$ has been measured using a specially developed technique [10] based on the principle of steady-state longitudinal heat flow [11]. The coefficient χ of the samples was determined relative to that of fused quartz.

Figure 2 illustrates the composition dependence of the activation energy of the conduction (E_σ), the conductivity at 20 °C (σ_{20}), the thermal conductivity at 20 °C (χ_{20}), and the density (d) for both the glassy and crystalline states. The values of σ_{20}, χ_{20} and d are higher, while E_σ are smaller in the crystalline state than those of the amorphous state. Thus, the variational trend of the composition dependence of E_σ is opposite to that of σ_{20}. In the glassy state, this may be associated with the conducting regions of the Mott model [12]: with variable range hooping occurs at a different Te-content. A maximum value for E_σ and a minimum for σ_{20} is observed at about 2 at% Te.

In elemental selenium each atom must have two neighbours to satisfy the valence requirements. This is achieved either by the formation of small molecules Se_8 or linear polymeric chains Se_n. These structural groupings do not alter with the isoelectronic additives of Te to Se. However, the addition of Te is associated with the formation of mixed eight-membered rings, i.e., $Se_{8-x}Te_x$. Also, this may be effective in changing the

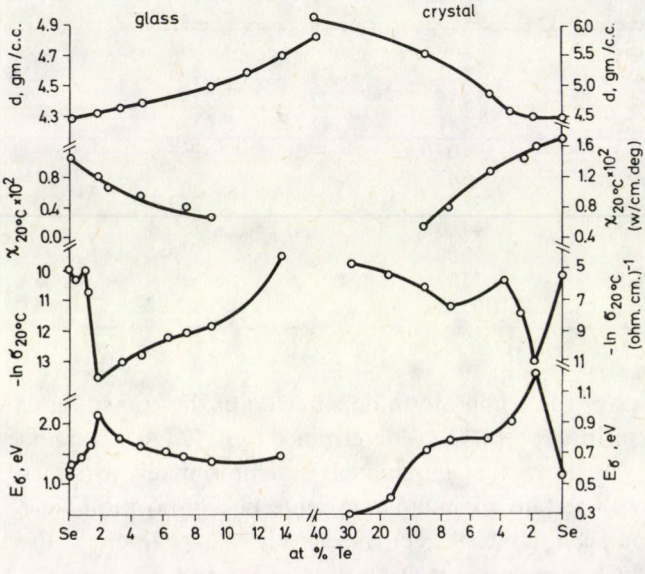

Fig. 2. The composition dependence of E_σ (activation energy of conduction), σ_{20} (electrical conductivity at 20 °C), χ_{20} (thermal conductivity at 20 °C) and d (density) for glasses and crystals Se—Te

length of the selenium chains. This explains the experimental fact according to which the observed variation of E_σ with the tellurium concentration is mainly accompanied by a micro-heterogeneity in the sample structure. The higher value of E_σ at about 2 at% Te indicates a maximum micro-heterogeneity. This means that the formation of monomers (rings) and polymers (chains) with mixed numbers of Te atoms occur with greater probability than a unique number all over the matrix structure.

The monotonic decrease of the measured thermal conductivity χ with Te-content (Fig. 2) is attributed to a decrease in the carrier mean free path. The latter depends on the degree of microheterogeneity, i.e. it is affected by the addition of Te atoms with their greater atomic radius. The computed electronic contribution of the thermal currents (due to both free electrons and electron--hole motion) shows an increase with the Te-content, whereas the main contribution of thermal transport is still due to phonons in the glasses investigated.

3.2. *The liquid state*

Figure 3 shows the composition dependence of E_σ and σ_0 for the liquid alloys Se—Te. The present results for E_σ are compared with those previously published [13–15]. The composition dependence of σ_{20} (the intercept of the lines $\ln \sigma = f(1/T)$ at 20 °C) is also given in Fig. 3. With the increase of the Te-content, the quantities E_σ, σ_0 and σ_{20} vary in a complex manner. This is attributed to the presence of different electron states of the alloys in the different concentration ranges [4].

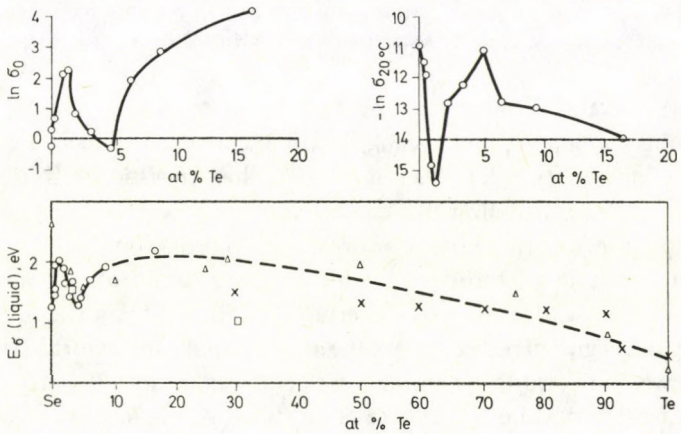

Fig. 3. Composition dependence of E_σ, σ_{20} and σ_0 (temperature-independent pre-exponential factor) for liquid Se—Te
○ our data, △ ref. [13], □ ref. [14], × ref. [15]

The addition of Te dissociates the long Se chains, and this dissociation begins immediately after melting [13]. Apparently, the composition dependence of σ_0 is opposite to that of σ_{20} (Fig. 3). The relative low values of σ_0 for the compositions with a Te-content of about 1.0 and 5.0 at% respectively indicate that the low density of the electron state may be localized in the quasi-gap. The degree of localization is affected by the concentration of Te atoms as well as of their distribution in the liquid phase. The presence of an electron state within the quasi-gap creates another possibility for transferring charge carriers, namely by jumps over the localized states. Assuming an intrinsic conduction in the present liquid alloys, an estimation for the carrier mobility has indicated the presence of thermo-activation for the compositions up to 1.5 at% Te. At higher Te-content, the carrier mobility is temperature-independent. For the latter case, the variation of the conductivity with composition is due to the variation in carrier density rather than mobility.

At very low Te-content, up to about 2 at%, the Te atoms are distributed randomly over the Se chains leading to the increase of both E_σ and σ_0. However, the Te atoms being distributed uniformly over the Se chains facilitate their dissociation, which leads to the observed decrease of E_σ up to 5 at% Te. In the composition range of Te $\simeq$ 5–

15 at%, the molecular size of the liquids Se—Te decreases so markedly that their dissociation energy becomes dependent on the molecular weight and therefore E_σ increases with the Te-content. In other words, the increase of E_σ is due to the decrease in the molecular weight of the chains in this composition range. A further addition of Te, in a concentration > 15 at%, is accompanied by an increase in the predominance of the Te—Te bonds in the molecules. This leads to the apparent gradual decrease in the activation energy of the electrical conductivity with tellurium.

4. Crystallization kinetics

The crystallization kinetics of the Se—Te system was investigated for the amorphous solid and liquid phases using electrical conductivity measurements. Here, the electrical conductivity σ has been used as a characteristic physical quantity to follow the growth of the crystalline phase in the amorphous or in the supercooled liquid phases. The change of σ during both a—c or l—c transformations has been recorded as a function of the time t at different annealing temperatures. At any annealing temperature, σ varies with time t up to a certain limit (point D on the curves of Fig. 4) characterizing the degree of perfectness of the alloy [unpublished work]. The annealing temperatures were selected to be in the range between T_g and T_m.

The measurements of $\sigma = f(t)$ were performed by a stagewise and a continuous technique, respectively. In the former technique, the a—c transformation was carried out step by step by isothermal annealing in an oven preheated at the required temperature. After each step the sample was polished to eliminate the effect of surface crystallization, and the characteristic physical quantity $\sigma(T)$ was measured in the temperature range below T_g, where the crystallization process is practically non-existent. In addition, the continuous technique has been used for the a—c as well as for l—c transformations. In this technique, the conductivity was recorded continuously (1/2 min interval) during an isothermal transformation process:

For a—c investigation, the as-prepared quenched sample was heated at 300 °C for one hour in a pyrex ampoule, sealed under vacuum and provided with two tungsten electrodes, then quenched in ice-water and the function $\sigma(t)$ measured isothermally.

For the l—c experiment, the as-prepared sample was fused at 300 °C for one hour, then quickly transferred to a preheated oven adjusted to the required temperature of annealing.

Figure 4 shows an example for the continuous variation of $\ln \sigma$ with the annealing time during both a—c and l—c transformations carried out at 100 °C for the composition $TeSe_{30}$.

For a—c, the part AB represents a gradual increase of σ as a result of the normal heating of the amorphous solid sample. The transformation a—c passes through two distinguishable time-dependent stages. The first, BC, shows a small increase in the electronic conduction followed by a big increase during the second stage CD.

For l—c, the part AC represents the gradual decrease of σ due to a normal cooling of the liquid sample from 300 °C to 100 °C. The transformation l—c takes place through one smooth stage CD.

At any intermediate point during both transformations a—c and l—c, the measured value of $\sigma(t)$ represents the contribution of two conductivities of two mixed phases: amorphous solid with crystalline (for a—c) or liquid with crystalline (for l—c).

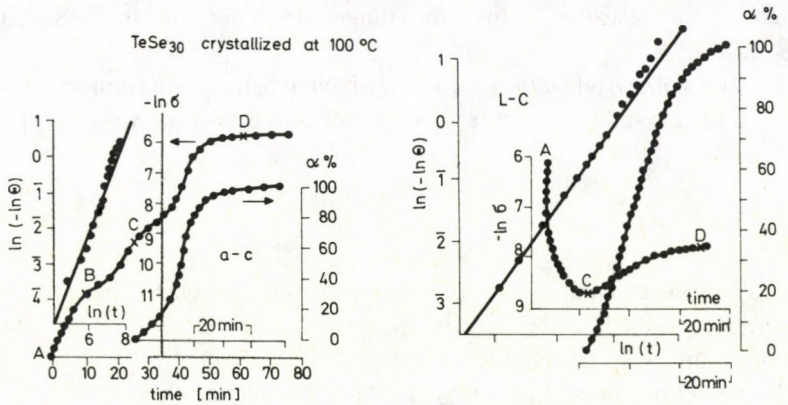

Fig. 4. Crystallization analysis of $TeSe_{30}$ crystallized at 100 °C in the amorphous-crystalline and liquid-crystalline ranges

The fraction transformed at different annealing times $\alpha(t)$ was calculated by using the relative increase in the electronic conduction during the crystallization growth (CD on the curves of Fig. 4). The amount of material left uncrystallized at a time t has been calculated on the basis of the experimental results using the empirical relation previously used for Se and Se—S alloys [16–18],

$$\Theta_t = (\ln \sigma_\alpha - \ln \sigma_t)/(\ln \sigma_\alpha - \ln \sigma_0), \tag{1}$$

where σ_0 and σ_α are the conductivities at the beginning (point C), and end (point D) of the process, respectively, and σ_t is the conductivity at time t between these limits. The untransformed supercooled liquid volume is assumed to be equivalent to the amorphous part. The results of $\alpha = f(t)$ for $TeSe_{30}$ are given in Fig. 4 for both a—c and l—c cases. The obtained curves have a sigmoidal shape indicating an autocatalytic reaction which is often observed in various kinds of solid reactions.

Avrami's equation [19] relating the fraction of the crystalline volume α grown from the amorphous phase to the time of annealing,

$$(1-\alpha) = \Theta = \exp(-Kt^n) \tag{2}$$

has been successfully applied to study the crystallization kinetics of amorphous Se and Se—S alloys [16–18]. The same procedure has been followed here to study quantitatively the crystallization process of amorphous and liquid Se—Te alloys.

The parameter n of the Eq. (2), characterizing the nucleation mechanism and the dimension of crystal growth, has been calculated using the equation:

$$\ln(-\ln \Theta_t) = \ln K + n \ln t. \tag{3}$$

Accordingly, the plot of $\ln(-\ln \Theta_t)$ versus $\ln t$ leads to a straight line of slope n. This has been verified for the investigated compositions during the two transformation processes over the measured temperature ranges, and the results for $TeSe_{30}$ at 100 °C are given in Fig. 4.

The values of crystallization constant, which depends on the temperature and the definition of the crystallization rate K, were calculated for each value of Θ using the equation:

$$K \simeq \ln(\Theta^{-1})/t^n. \tag{4}$$

The last step of the calculation was carried out by a computer to check the reliability and limitation of using $\ln \sigma$ [7] as a sensitive parameter for studying the crystallization kinetics of the investigated samples.

The rate constant K is given by the Arrhenius equation as:

$$K = K_0 \exp(-E/RT), \tag{5}$$

where R is the universal gas constant. For each $TeSe_x$ composition, a plot of $\ln \bar{K}$ (average value over the range of $\Theta \simeq 90\%$–15%) versus $1/T$ could be fitted over a certain temperature range with a straight line whose slope defines the activation energy of the process E. On the other hand, one has to take into account that the constant rate is proportional to $1/\tau$ (the overall time of transformation). Here, also, a plot of $\ln(1/\tau)$ versus $1/T$ could be fitted over a certain temperature range with a straight line whose slope defines E. The activation energy of a particular composition as determined by the two methods; $\ln K$ versus $1/T$ and $\ln(1/\tau)$ versus $1/T$, are in good agreement. Table II gives the calculated values of E with their corresponding temperature ranges for the compositions investigated in both a—c and l—c.

Table II indicates that the crystallization activation energy depends on the concentration of tellurium as well as on the heat treatment of the sample. For the same temperature range, the activation energy of the crystallization of amorphous Se increases gradually with the addition of Te up to the composition of $TeSe_{80}$ (1.235 at% Te). Then, E shows a marked increase at about 2 at% Te followed by a decrease with Te up to about 10 at%, subsequently E increases again with the Te-content. This composition-dependence of E might be attributed to the degree of dispersion and the energy of formation of the chemical bonds in the Se—Te matrix. The highest value of $E = 3.73$ eV at about 2 at% Te corresponds to the maximum micro-heterogeneity in the alloy $TeSe_{50}$ that produces anomalous changes in the various properties.

Table II

Crystallization activation energy of (a) amorphous and (b) supercooled liquid Se—Te alloys

(a)

Composition	E [eV]	Temp. range [°C]
Se	1.3	75–90
	0.83	90–120
	0.23	120–160
$TeSe_{1000}$	1.13	90–120
	0.3	120–160
$TeSe_{500}$	1.35	90–120
	0.3	120–160
$TeSe_{100}$	1.46	90–120
	0.3	120–160
$TeSe_{80}$	2.0	90–120
	0.34	120–160
$TeSe_{50}$	3.73	80–110
$TeSe_{30}$	2.96	80–110
$TeSe_{20}$	2.47	65–90
	2.2	90–110
$TeSe_{12.5}$	2.48	65–90
	1.94	90–110
$TeSe_{10}$	2.39	85–105
$TeSe_{2.5}$	3.54	80–110

(b)

Composition	E [eV]	Temp. range [°C]
Se	1.2	80–110
	0.48	110–160
$TeSe_{50}$	0.76	90–130
$TeSe_{30}$	0.37	90–180
$TeSe_{20}$	0.5	100–150
$TeSe_{15}$	0.6	130–160
$TeSe_{10}$	0.7	100–150

The calculated values of E for the supercooled liquid alloys Se—Te are significantly smaller than those obtained for a—c transformations (Table II). This may be due to the difference of the viscosity of the supercooled liquid and the vitreous states. This decrease should make the diffusion, the self diffusion, and switching of the chemical bonds easier.

References

1. M. F. Kotkata, E. A. Mahmoud and M. K. El-Mously, Acta Phys. Hung., **50,** 61, 1981.
2. M. F. Kotkata, E. A. Mahmoud and M. K. El-Mously, Acta Phys. Hung., **52,** 175, 1982.
3. M. K. El-Mously, M. M. El-Zaidia and S. A. Salam, Egypt. J. Phys., **7,** 1, 1976.
4. M. F. Kotkata, A. A. El-Ela, E. A. Mahmoud and M. K. El-Mously, ICTP Preprints, Trieste-Italy, IC/80/70, 1980, and in Acta Phys. Hung., **52,** 3, 1982.
5. M. El-Zaidia, Ph. D. Thesis, Ain Shams University, Cairo, 1975.
6. M. K. El-Mously and M. M. El-Zaidia, J. Non-Cryst. Solids, **11,** 407, 1973; **27,** 265, 1978.
7. M. F. Kotkata, G. M. Kamal and M. K. El-Mously, Indian J. Technology, **20,** 390, 1982.
8. M. F. Kotkata, E. A. Mahmoud and M. K. El-Mously, Acta Phys. Hung., **47,** 345, 1979.
9. M. F. Kotkata and E. A. Mahmoud, Mat. Science Eng., **54,** 163, 1982.

10. M. F. Kotkata, S. R. Atalla and M. K. El-Mously, Proc. 14th Int. Conf. on Thermal Conductivity, Storrs-U.S.A., 1975, pp. 39–44.
11. A. B. Beck, J. Sci. Instrum., **34,** 186, 1957.
12. N. F. Mott, Electronic Processes in Non-Crystalline Materials. Ed. N. F. Mott and E. A. Davis, Clarendon Press, Oxford, 1971.
13. D. Sh. Abdinov, V. R. Namazov and G. M. Aliev, Neorgan. Mat., **10,** 1960, 1974.
14. F. Mahdjuri, J. Phys. C, **8,** 2248, 1975.
15. J. C. Perron, J. Non-Cryst. Solids, **8,** 272, 1972.
16. M. K. El-Mously, M. F. Kotkata and S. A. Salam, J. Phys. C, **11,** 1077, 1978.
17. M. F. Kotkata, M. K. El-Mously and F. M. Ayad, Acta Phys. Hung., **46,** 19, 1979.
18. M. F. Kotkata, F. M. Ayad and M. K. El-Mously, J. Non-Cryst. Solids, **33,** 13, 1979.
19. M. Avrami, J. Chem. Phys., **8,** 212, 1940.

Acta Physica Hungarica 54 (3—4), pp. 313—331 (1983)

DC CORONA DISCHARGE ON MONOPOLAR BUNDLE WIRES

M. ABDEL-SALAM, M. FARGHALY and S. ABDEL-SATTAR

Electrical Department, Assiut University, Assiut, Egypt

(Received in revised form 19 October 1982)

The solution of monopolar corona equation already reported in literature is extended for bundle conductors using a modified iterative procedure to estimate the corona current contributed by each subconductor of the bundle. The solution is based on underlying assumptions, some of which are waived in the present calculations. The variation of ion mobility with its lifetime as well as the change of the corona onset voltage from point to point on each subconductor are taken into account for the first time. The calculated corona currents from each subconductor are compared with those measured experimentally for a laboratory model.

1. Introduction

HV dc has many advantages over the conventional ac for long transmission [1]. Recent advances in the development of the hv terminal equipment have increased the feasibility of dc transmission. Consequently, various problems associated with it have been studied extensively.

One of these problems is the corona occurring on the transmission lines and the power loss, radio interference, television interference and audible noise associated with it. Theoretical analysis of corona loss on dc transmission lines is very useful for line design.

In this paper, recent approaches [2–4] for calculating corona loss in monopolar configuration are critically reviewed and the underlying assumptions are discussed. Then, an approach is suggested which takes into account for the first time the variation of ion mobility with its lifetime as well as the change of corona onset voltage from point to point on each subconductor of the bundle. This improves the accuracy of theoretical predictions.

2. Monopolar corona equation and the progress in its solution

The main system of equations describing the monopolar corona discharge is:

$$\begin{aligned} \nabla \cdot \bar{E} &= \frac{\rho}{\varepsilon_0}, \\ \nabla \cdot \bar{J} &= 0, \\ \bar{J} &= K\rho\bar{E}, \\ \bar{E} &= -\nabla\varphi. \end{aligned} \tag{1}$$

The first is the Poisson's equation for the electric field; the second is the equation for current continuity; the third is the equation for current density and the fourth equation is the electric field given in terms of the potential [4].

Eq. (1) can be replaced by a single third-order non-linear partial differential equation [4]:

$$(\nabla\varphi\nabla^2\varphi)=0. \tag{2}$$

Eq. (2) is the general form for monopolar corona equation and there is no method known for solving it in the general case without simplifying assumptions.

Deutsch [4] was the first to make an approximate analysis for the line-to-plane geometry. Following Deutsch were Popkov, Tayrlin and Usynin [4] who made a solution more accurate than Deutsch. As reported earlier, [4], the analysis developed by Sarma and Janischewskyj was based on following assumptions:

(i) The electric field at the surface of the hv conductor during corona remains constant at its onset value.

(ii) The mobility of ions is constant independent of their life time.

(iii) Deutsch's assumption as it demonstrates that the space charge affects only the magnitude but not the direction of the electric field.

Although the calculated results agreed reasonably with those measured experimentally for single-conductor lines, the method has never been checked for lines with bundle conductors [5].

Very recently, Sunaga et al [3] reported a new approach for calculating the ionized field of hv dc transmission lines with bundle conductors. They replaced the bundled conductors with an equivalent single conductor having the same electrostatic capacitance. Therefore, the first assumption was replaced with the following two supplementary assumptions:

(ia) The amount of corona current emitted from a bundled conductor is correlated to the conductor surface field by using simplifying relationships having empirical constants.

(ib) The ratio of the corona current density to the applied field for the bundled conductor is not different from the equivalent conductor.

The empirical constants in (ia) are determined [3] from corona current measurements on the available test line. As is well known, the corona current measurements change from place to place and may vary from time to time [6]. This restricts the application of the analysis by Sunaga et al to any general monopolar configuration.

In reality, the field due to space charge at any point in the discharge space can be decomposed into two components; one along the flux line passing it and the other in the normal direction. The first component affects only the magnitude and not the direction of the applied electric field as introduced well in corona loss computation by others [2, 3], while the other component is neglected by them. This latter component has a lateral effect on the applied electric field making them angularly displaced from their trajectories in the absence of space charge as studied previously [4, 7].

3. Underlying assumptions for solving the corona equation

Assumption (i) demonstrates that the electric field at the surface of the hv conductor in corona remains constant at its onset value. When corona occurs on a hv conductor, the electric field at its surface is decreased slightly (5–10%) from the onset by the ion space charge built up around it. The decreased field was measured experimentally [8] and predicted theoretically [9]. Therefore, assumption (i) is not quite justified. In some preliminary calculations, such effect was found to be noticeable only in the region of the onset and becomes negligible at higher voltages. Therefore, all the present calculations take into account that the surface field at each point on the subconductors periphery is constant at its onset value.

On the other hand, when corona occurs on a hv bundle conductor, the onset voltage is no longer assigned a unique value due to a significant change of the applied field from point to point on the subconductor periphery. The corona onset voltage is calculated based on the physical processes involved in corona discharge phenomena [10] (Appendix I). Previous investigators [3, 5] have not taken into account such a change for corona onset voltage around the periphery of subconductors; a phenomenon which has been observed experimentally by Simpson [11].

In the present work, the corona onset voltage is considered to change from point to point over the subconductor surface. This means that the subconductor does not go as whole in corona at one voltage value.

Assumption (ii) demonstrates that the mobility of ions is constant independently of their lifetime. Detailed investigations [12–14] have been made to establish definitely that the mobility of ions is not constant in the corona area. Different empirical relations have been developed [12–14] in literature which correlates the mobility value (k) to the lifetime of ions (t), (Fig. 1).

It is clear that the value of ion mobility obtained by Popkov [12] fits on average the values obtained by Arai and Tsunoda [13] and Vereshchagin and Litvinov [14]

over all the lifetime. Therefore, the values of Popkov for the change of mobility with lifetime have been considered in the present calculations.

Assumption (iii) Deutsch's assumption demonstrates that the space charge affects only the magnitude but not the direction of the electric field. This assumption was aimed at making the calculations possible. It is perfectly valid in symmetrical

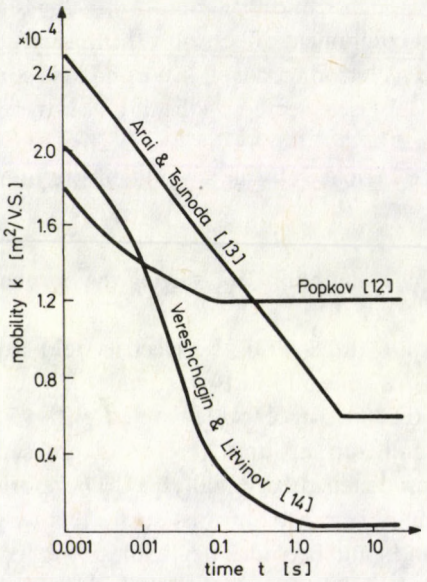

Fig. 1. Variation of ion mobility with its lifetime

configuration (such as the concentric cylindrical geometry). It will be sufficiently close to reality in other configurations where the space charge density in the interelectrode region is not very large [2].

Very recently, Janischewskyj and Gela [15] succeeded to extend the finite elements technique to waive the analysis from this assumption in coaxial cylindrical geometry, for which the field is radial even with the space charge effect.

The object of the present paper is to report an iterative algorithm for calculating corona loss from bundled conductors with Deutsch's assumption being retained in the calculations. The same authors are working now to use the finite elements technique to waive these calculations from this assumption. They hope to make the obtained results public in the very near future.

4. Method of analysis

Defining equations

According to Deutsch's assumption (iii), the space-charge-free field E_1 at any point in the interelectrode region is related to the field in presence of space charge E by:

$$E = \lambda E_1, \tag{3}$$

where λ is a scalar point function of the space coordinates. E and E_1 may be defined in terms of the corresponding space potential φ and φ_1, respectively, in the form

$$\begin{aligned} E &= -\nabla\varphi = -\frac{\mathrm{d}\varphi}{\mathrm{d}s}, \\ E_1 &= -\nabla\varphi_1 = -\frac{\mathrm{d}\varphi_1}{\mathrm{d}s}, \end{aligned} \tag{4}$$

where s is the distance measured along the flux line of the space-charge-free field.

Combining Eqs (3) and (4) and simplifying

$$= \frac{\mathrm{d}\varphi}{\mathrm{d}\varphi_1}. \tag{5}$$

Substituting Eq. (3) into Eq. (1)

$$\nabla \cdot (\lambda E_1) = \frac{\rho}{\varepsilon_0},$$

$$\lambda \nabla \cdot E_1 + E_1 \cdot \nabla\lambda = \frac{\rho}{\varepsilon_0}.$$

But $\nabla \cdot E_1 = 0$ and $E_1 \cdot \nabla\lambda = \dfrac{E_1 \mathrm{d}\lambda}{\mathrm{d}s}$

$$\therefore \frac{\mathrm{d}\lambda}{\mathrm{d}s} = \frac{\rho}{\varepsilon_0 E_1}.$$

Changing the independent variable to φ_1, one can write

$$\frac{\mathrm{d}\lambda}{\mathrm{d}s} = \left(\frac{\mathrm{d}\lambda}{\mathrm{d}\varphi_1}\right) \cdot \left(\frac{\mathrm{d}\varphi_1}{\mathrm{d}s}\right) = -\frac{E_1 \mathrm{d}\lambda}{\mathrm{d}\varphi_1}.$$

Then

$$-\frac{E_1 \mathrm{d}\lambda}{\mathrm{d}\varphi_1} = \frac{\rho}{\varepsilon_0 E_1},$$

$$\frac{\mathrm{d}\lambda}{\mathrm{d}\varphi_1} = -\frac{\rho}{\varepsilon_0 E_1^2}. \tag{6}$$

From Eqs (1) and (3)

$$J = K\rho E_1 \lambda,$$

$$\nabla \cdot J = 0,$$

$$\nabla \cdot (K\rho\lambda E_1) = 0,$$

$$K\rho\lambda \nabla \cdot E_1 + E_1 \cdot \nabla(K\rho\lambda) = 0.$$

Substituting by $\nabla \cdot E_1 = 0$,

$$E_1 \cdot \nabla(K\rho\lambda) = 0,$$

$$E_1 \frac{\mathrm{d}}{\mathrm{d}s}(K\rho\lambda) = 0,$$

$$K\lambda \frac{\mathrm{d}\rho}{\mathrm{d}s} + \rho K \frac{\mathrm{d}\lambda}{\mathrm{d}s} + \frac{\mathrm{d}K}{\mathrm{d}s} = 0$$

or

$$K\lambda E_1 \frac{\mathrm{d}\rho}{\mathrm{d}\varphi_1} + \rho K E_1 \frac{\mathrm{d}\lambda}{\mathrm{d}\varphi_1} + \rho\lambda E_1 \frac{\mathrm{d}K}{\mathrm{d}\varphi_1} = 0.$$

Substituting by Eq. (6),

$$\frac{\mathrm{d}\rho}{\mathrm{d}\varphi_1} = \frac{\rho^2}{\varepsilon_0 \lambda E_1^2} - \frac{\rho}{k} \frac{\mathrm{d}k}{\mathrm{d}\varphi_1}. \tag{7a}$$

Eq. (7a) can be rewritten in the following form by substituting

$$\frac{\mathrm{d}k}{\mathrm{d}\varphi_1} = \frac{\mathrm{d}k}{\mathrm{d}t} \cdot \frac{\mathrm{d}t}{\mathrm{d}s} \cdot \frac{\mathrm{d}s}{\mathrm{d}\varphi_1}.$$

But

$$\frac{\mathrm{d}s}{\mathrm{d}\varphi_1} = -\frac{1}{E_1} \quad \text{and} \quad \frac{\mathrm{d}t}{\mathrm{d}s} = \frac{1^-}{KE} = \frac{1^-}{K\lambda E_1}$$

$$\therefore \frac{\mathrm{d}\rho}{\mathrm{d}\varphi_1} = \frac{\rho^2}{\varepsilon_0 \lambda E_1^2} + \frac{\rho}{\lambda K^2 E_1^2} \frac{\mathrm{d}k}{\mathrm{d}t}, \tag{7b}$$

where $\mathrm{d}t = \mathrm{d}s/v$ is an incremental value of the ion lifetime; $v = K\lambda E_1$ is the ion velocity; $\mathrm{d}s$ is an incremental distance along the flux line. Eqs (5–7) describe the distribution of the electric field and the charge density in the interelectrode spacing providing that the applied electric field is precalculated over all the interelectrode spacing.

The boundary conditions required to solve these equations are given in terms of the voltage applied to the hv bundle conductor and the magnitude of the electric field at its surface. If λ_0 represents the value of the scalar point function (λ) at the subconductor surface, it follows from assumptions (i) and (iii) that $\lambda_e = V_0(\psi)/V$ where $V_0(\psi)$ is the

corona onset at a point described by the angle ψ over the periphery of the subconductor. The details for calculating $V_0(\psi)$ for hypothetic smooth subconductors are given in Appendix I. However for an actual subconductor a reduction surface factor m is assumed for the corona onset voltage. This factor depends on the surface condition of the subconductor and sometimes reaches 0.4 on full-scale transmission lines.

The complete specification of the problem for any particular flux line is, therefore, given in terms of the differential equations (5–7) with the following boundary conditions;

$$\begin{array}{lllll} \text{(i)} & \varphi = V & \text{at} \quad \varphi_1 = V & \left.\right\} & \text{at subconductor} \\ \text{(ii)} & \lambda = \lambda_e = V_0(\psi)/V & \text{at} \quad \varphi_1 = V & \left.\right\} & \text{surface} \\ \text{(iii)} & \varphi = 0 & \text{at} \quad \varphi_1 = 0 & & \text{at ground surface} \end{array} \tag{8}$$

Computational steps of the boundary value problem defined by equations (5–8) at a given value V of the applied voltage

The computational steps are outlined in the flow chart of Fig. 2 and summarized as follows:

1. At a given point P on the subconductor periphery, the electric field E_1 is calculated using the charge simulation technique [16] (Appendix II). The field line emanating from this point is also traced to determine the distribution of the applied electric field along it.

2. The corona onset voltage $V_0(\psi)$ is calculated at the point P (Appendix I). This defines the boundary conditions (i) and (ii) of Eq. (8) at the voltage value V.

3. Assume an arbitrary guessed initial value of space charge density ρ_e at the point P (Appendix III).

4. Integrate the system of equations (5–8) along the already traced field line emanating from the point P, taking into account the variation of ion mobility with its lifetime, (Fig. 1).

5. The resulting value of the potential φ at the end of the field line (i.e. at the ground surface) is compared with the zero value defined by the boundary condition (iii) of Eq. (8).

6a. When the boundary condition (iii) of Eq. (8) is not satisfied in the above step, the assumed initial value of ρ_e is then adjusted and the procedure (steps 3 through 5) is repeated. Appendix III gives how ρ_e can be changed with the aim to maintain the convergence of the solution.

6b. When the boundary condition (iii) is satisfied the charge density ρ and hence the current density J at the point P on the subconductor surface are calculated providing that the electric field at this point is predefined by condition (iii) of Eq. (8).

7. Repeat steps 1 through 6 for all the points on the subconductor surface (n_t). This determines the current density distribution over the subconductor periphery at the voltage value V.

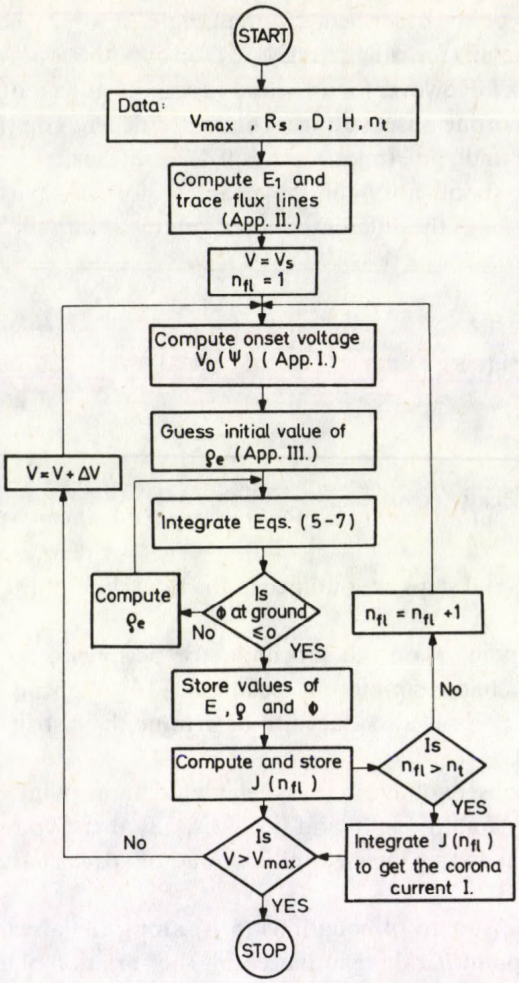

Fig. 2. Flow chart for present method

8. Integrate the resulting current density distribution over the subconductors surface to determine the contributions of each to the total corona current from the bundle.

9. Increment the value of the applied voltage V by an increment ΔV and repeat steps 2 through 8 to determine the subconductor corona current for different voltages up to a maximum voltage V_{max}.

5. Experimental setup

A laboratory model has been strung from smooth wires (0.175 cm in radius and 4.5 m in length) to simulate the subconductors of bundle −4 diamond. The ground plate was simulated by an earthed aluminium plate. The bundle height above the ground was changed by changing the relative position of the aluminium plate with respect to the hv wires. Microammeters were connected at the hv circuit to measure the corona current from each subconductor. This hv circuit was so dimensioned that corona is only generated at the wires under test. To achieve this condition, both ends of each wire were enclosed in metallic spherical caps to avoid corona discharge at these ends. Precautions were also taken for all connections of the measuring circuit to be free from corona.

To measure the lateral distribution of corona current at the ground plate, the earthed aluminium plate has been divided into 30 segments each (5 cm × 4.5 m) spaced 1 mm apart. To each segment, a sensitive microammeter was connected to measure the current received by it. Division of received current by the segment area defines the current density at the segment position.

The available hv source was up to 125 KV, the ripple and harmonic contents of its output were less than 1%. The output voltage was measured accurately using a resistive voltage divider.

6. Results and discussion

a) Corona current from bundle

Figures 3–5 show the calculated and measured values of the total corona current from bundle −4 diamond at different heights above the ground plate. It is satisfying that the present calculations fit reasonably the experimental results. However, the calculated corona current contributed by each subconductor does not fit exactly the corresponding measured value (Figs 6–8).

The authors attributed this discrepancy to the fact that the ions drift along flux lines other than the electrostatic field lines, i.e. Deutsch's assumption is not quite valid for corona generation on laboratory models.

It is quite clear from the experimental results (Fig. 6), that subconductor I which is the nearest one to the ground plate contributes mainly to the total corona current only for small heights above the ground plate. With the increase of the bundle height above the ground plate, side subconductors start to contribute more and the corona current from them exceeds that from subconductor I in contrast to the present calculations.

In reality, the inclusion of the space charge effect in corona loss calculations for complex geometries such as bundled conductors is extremely difficult. Previous

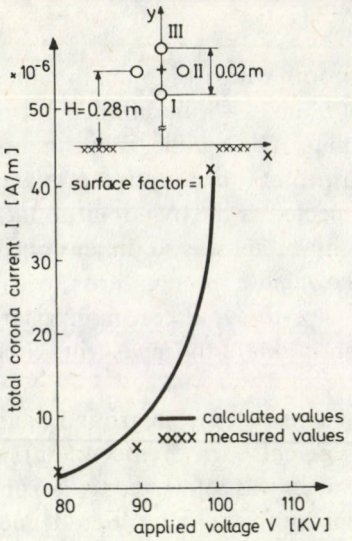

Fig. 3. Calculated and measured total corona *V—I* characteristics for a laboratory model ($H = 0.28$ m)

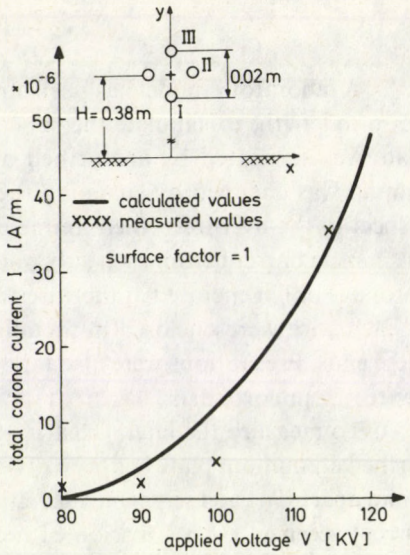

Fig. 4. Calculated and measured total corona *V—I* characteristics for a laboratory model ($H = 0.38$ m)

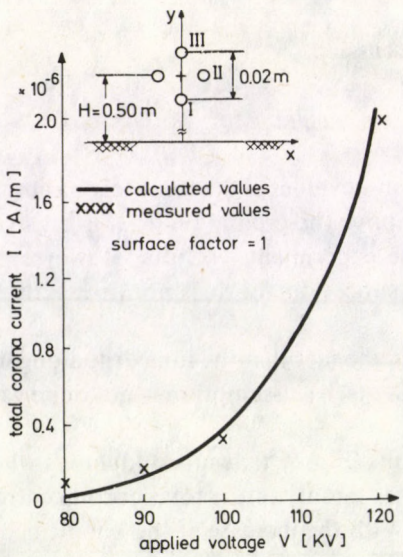

Fig. 5. Calculated and measured total corona *V—I* characteristics for a laboratory model ($H = 0.5$ m)

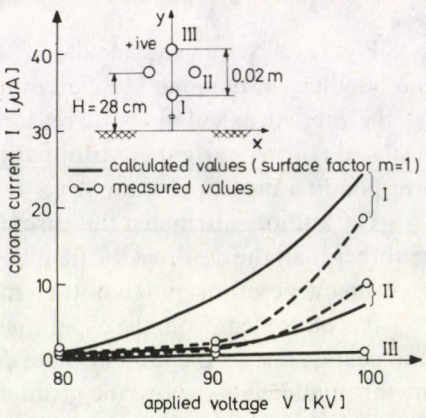

Fig. 6. Calculated and measured corona *V—I* characteristics of each subconductor of the bundle for a laboratory model ($H = 0.28$ m)

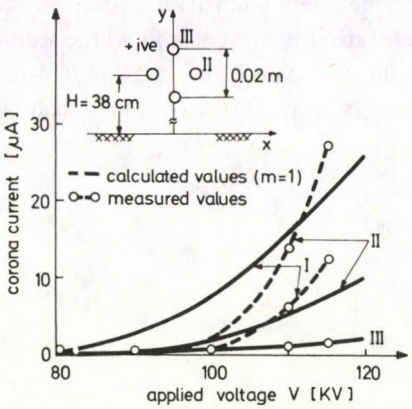

Fig. 7. Calculated and measured corona V—I characteristics of each subconductor of the bundle for a laboratory model ($H = 0.38$ m)

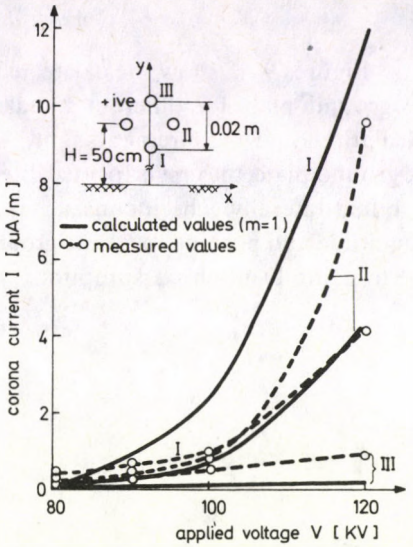

Fig. 8. Calculated and measured corona V—I characteristics of each subconductor of the bundle for a laboratory model ($H = 0.5$ m)

investigations [4, 7] verified that the space charge seems to contract the flux lines of the ionized field with respect to those of the space-charge-free field. For one and the same corona current emitted from the bundle as a whole, the space charge density over the interelectrode spacing increases with decreasing the bundle height above the ground plate. Therefore, the flux lines of the ionized field are expected to be more contracted on decreasing the bundle height above the ground plate. This means that the ions emitted from subconductor I will be convected along flux lines being contracted to be very close to the central axis of the bundle, where the applied field is too high. Subsequently, the corona current contributed by subconductor I is expected to be the high portion of the corona current from the bundle on decreasing its height in agreement with the present calculation (Fig. 6). With the increase of the bundle height above the ground plate, the space charge density and hence its contracting effect for the flux lines starts to be mitigated. Hence, side subconductor II starts to contribute more to the total corona current emitted from subconductor I (Fig. 8). On the contrary, the present calculations showed always that subconductor I contributes the highest portion of the total corona current. This may be attributed to the pertinent inaccuracy on using Deutsch's assumption. Measurements and calculations showed that subconductor III contributes always the smallest portion of the total corona current. This is explained by the fact that the ions emitted from this subconductor are convected along flux lines characterized by length in path and weakness in applied field value.

b) Current density at ground plate

Figures 9–12 show the calculated and measured values of the current density at the ground plate for different bundle heights and different applied voltages. The calculations and measurements show two peaks in the current density distribution over the ground plate, the first is located directly underneath subconductor I and the second is shifted laterally. The inconsistency between the calculated and measured peaks, magnitude and position, over the ground plate may be also ascribed to the inaccuracy due to using Deutsch's assumption.

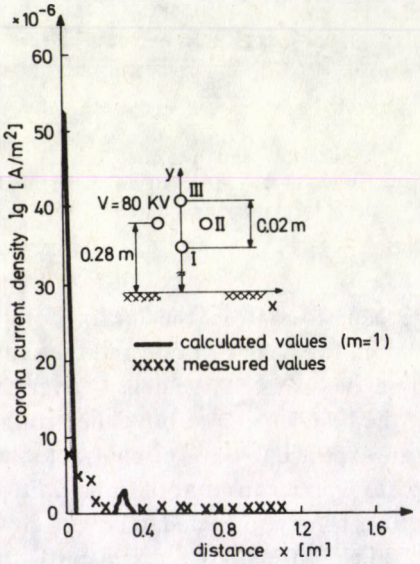

Fig. 9. Calculated and measured current density distributions at the ground plate ($H=0.28$ m and $V=80$ KV)

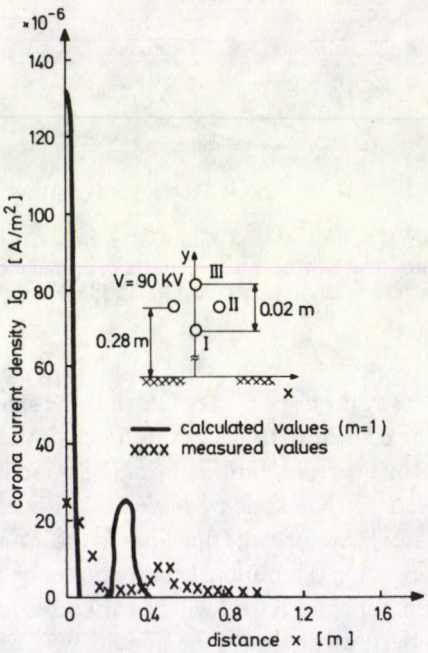

Fig. 10. Calculated and measured current density distributions at the ground plate ($H=0.28$ m and $V=90$ KV)

c) Effect of surface condition

The surface condition of the subconductors decides the corona current contributed from each one and hence affects significantly the total corona current of the bundle. On decreasing the surface factor (m) from 1.0 to 0.9; the total corona current emitted from the bundle increases by about 60%. Hence the current density distribution over the ground plate showed a corresponding increase e.g. 140% at the first peak and 500% at the second peak.

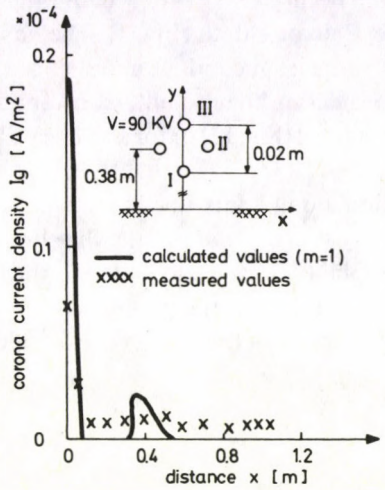

Fig. 11. Calculated and measured current density distributions at the ground plate ($H = 0.38$ m and $V = 90$ KV)

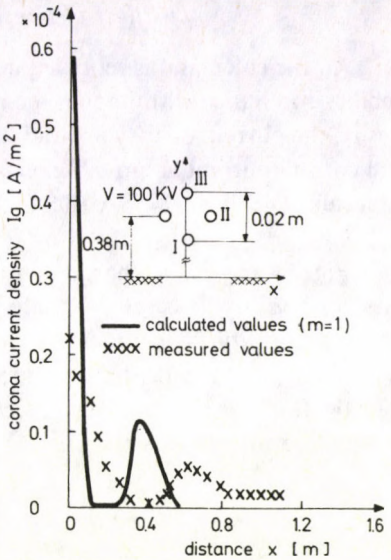

Fig. 12. Calculated and measured current density distributions at the ground plate ($H = 0.38$ m and $V = 100$ KV)

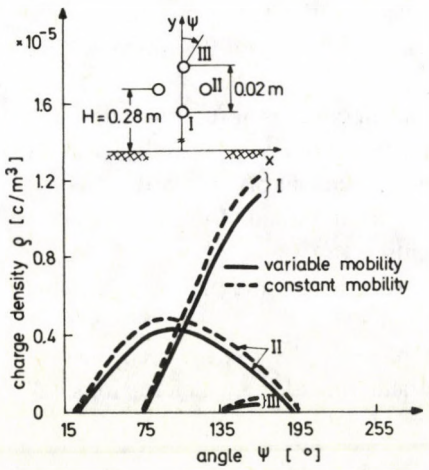

Fig. 13. Corona charge density around the periphery of each subconductor of a laboratory model for constant and variable mobility

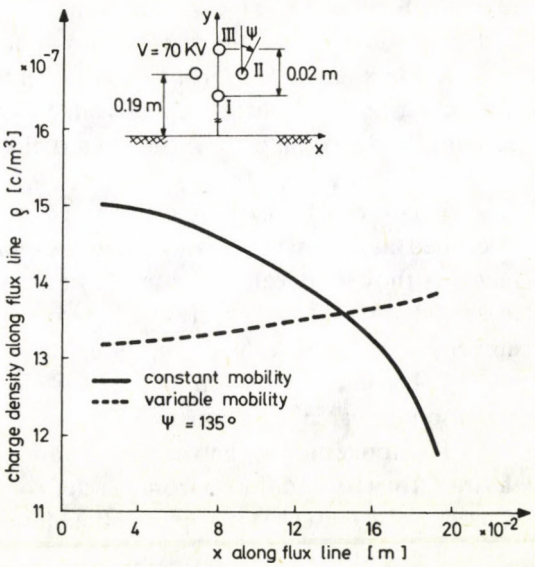

Fig. 14. Corona charge density distribution along a particular flux line

d) Effect of temporal variation of ion mobility

All the calculations reported in the preceding Sections take into account the ion mobility to change with its lifetime according to Popkov's data (Fig. 1). The charge density, the current density around the periphery of each subconductor and hence the total corona current assume higher values on considering the mobility constant at a given value ($=1.5\ m^2/V \cdot S$) either for a laboratory model (Fig. 13) or for a full-scale line [17].

Fig. 14 shows the charge density distribution along a flux line at constant and variable mobility. It is seen that the charge density decreases along the flux line for constant mobility while it increases for variable mobility. This is attributed to the fact that the ion life time for the laboratory model is so short that the mobility decreases along the flux line (Fig. 1). This reflects itself in an increase of the charge density along the flux line to maintain the current continuity (Fig. 14).

7. Conclusions

On the basis of the present analysis, the following conclusions can be drawn concerning monopolar corona on bundle transmission line configurations:

1. The corona onset voltage is calculated for the first time around the periphery of each subconductor of the bundle. It changes from point to point at the subconductor surface in agreement with experimental findings.

2. The monopolar corona equation of the ionized field originating from multi-interacting corona sources is formulated and solved for the first time taking into account the variation of both the ion mobility with its lifetime and the onset voltage around the periphery of subconductors.

3. The corona current contributed by each subconductor of the bundle is calculated and compared with the corresponding measured values on laboratory model. Although the calculated total corona currents fit reasonably the corresponding measured values, the contributed currents from each subconductor showed a discrepancy between calculations and measurements.

4. The lateral distribution of the corona current at the ground plate is calculated and also compared with that measured experimentally.

The above analogy between theory and experiment emphasizes the need to know the trajectory being different from the electrostatic field lines along which the ions will convect; i.e. Deutsch's assumption should be waived.

Appendix I
Criterion of corona onset

The present analysis is restricted to the positive polarity; where the corona onset voltage $V_0(\psi)$ (see Eq. (8)) should be calculated for positive corona.

In the positive corona discharge, one electron is assumed to initiate electron avalanche starting at the ionization zone boundary where the applied field strength is sufficiently high that the ionization coefficient exceeds the coefficient of electron attachment. During the avalanche growth, more electrons and positive ions are produced by ionization collisions. Simultaneously, photons are also produced by exciting atoms and as a result of electron—ion recombinations.

The criterion for corona onset was suggested as follows [10, 18]; the photons reaching the ionization zone boundary are just enough to produce one photo-electron to start a successor avalanche. Having the values of physical parameters involved in the discharge process (namely ionization, attachment and absorption coefficients, etc.), the fulfilment of this criterion depends upon the system geometry, its electric field distribution and the value of the applied voltage. Thus, for a given conductor bundle, its field distribution should be calculated firstly as shown in Appendix II. The corona onset voltage at a given point on the subconductor surface is the voltage which satisfies the above criterion, providing that the avalanche growth takes place along the radial direction passing this point.

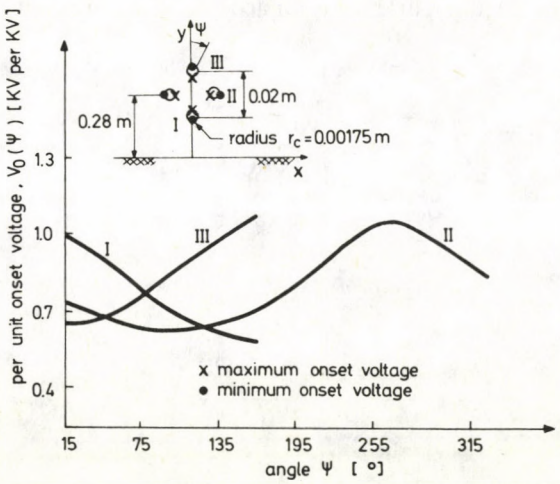

Fig. A-1. Per unit corona onset voltage around the periphery of each subconductor

Figure A-1 shows the calculated corona onset voltage around the periphery of each subconductor of the laboratory model. It is clear that the onset voltage varies from point to point at the subconductor surface and also changes from subconductor

to subconductor. This is attributed to the fact that the applied field changes around the periphery of the subconductor and the point having the highest value of the applied field (Appendix II) goes at first in corona. The onset voltage $V_0(\psi)$ around the periphery of each subconductor can be expressed in the form

$$V_0(\psi) = \frac{V_{0\max} + V_{0\min}}{2} + \frac{V_{0\max} - V_{0\min}}{2} \cos\psi ,$$

where $V_{0\max}$ and $V_{0\min}$ are the maximum and minimum values of the onset voltage where the applied electric field reaches minimum and maximum values, respectively; ψ is the angle measured around the periphery of each subconductor starting from the point having the maximum onset voltage.

The position of the maximum and minimum values of the onset voltage for each subconductor depends on the bundle geometry. Fig. A-1 gives these positions for the diamond geometry.

Appendix II
Calculation of the electrostatic field

The applied (electrostatic) field is calculated using the charge simulation technique [16]. Each subconductor of the bundle-4 is simulated by a number N_q of line charges ($N_q = 4$–6) uniformly distributed around a fictitious cylinder of radius r_f. r_f can take any value between 0.1 r_c and 0.5 r_c for acceptable accuracy of the solution, r_c is the

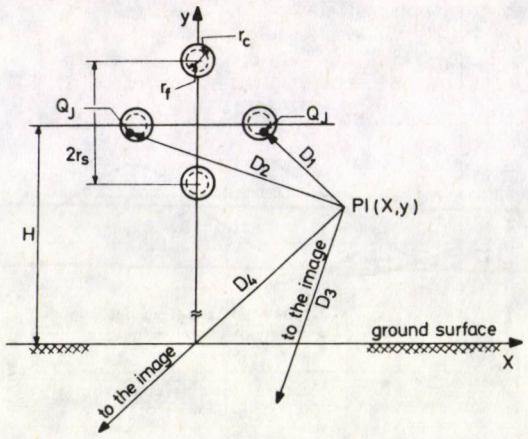

Fig. A-2. Geometry of the charge simulation technique method

subconductor radius. The unknown line charges have magnitudes (Q_j, $J = 1, 2, \ldots 4N_q$) which can be reduced in number to $2N_q$ according to the existing symmetry about the y-axis (Fig. A-2). The images of all these charges with respect to ground are considered.

The potential at any point p_1 in space is the algebraic sum of the potential, at this point produced by each simulating line charge Q_j and its image.

At any point on the subconductor surface, this calculated potential cannot easily equal the applied voltage V. Therefore, the magnitudes for the line charges Q_j are chosen so that the calculated potentials at a large number of point $N_B = 4N_q$ deviate only slightly from the actual potential V. The deviations are minimized by the least square technique [19]. The x- and y-component of the electric field intensity E_1 can be expressed as a function of coordinates of line charges and the point $p_1(x, y)$ at which the field is to be calculated in the form

$$E_x(x, y) = \sum_{J=1}^{4N_q} Q_j \left[-\frac{X_{qj}+x}{D_4} + \frac{X_{qj}-x}{D_3} - \frac{X_{qj}-x}{D_1} + \frac{X_{qj}+x}{D_2} \right],$$

$$E_y(x, y) = \sum_{J=1}^{4N_q} Q_j \left[-\frac{Y_{qj}+y}{D_4} - \frac{Y_{qj}+y}{D_2} - \frac{Y_{qj}-y}{D_3} - \frac{Y_{qj}-y}{D_1} \right],$$

where the distances D_1, D_2, D_3 and D_4 are as shown in Fig. A-2. X_{qj}, Y_{qj} determines coordinates of the Jth line charge.

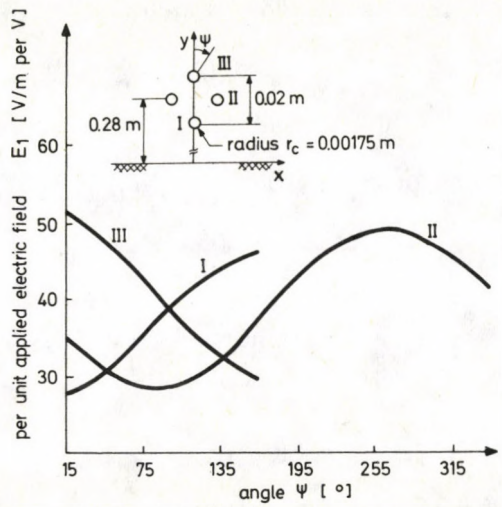

Fig. A-3. Per unit applied electric field around the periphery of each subconductor

Fig. A-3 shows the per-unit applied electric field around the periphery of each subconductor of the bundle under consideration.

The differential equation describing the field line is

$$dy/dx = E_y/E_x .$$

Runge–Kutta and/or corrector-predictor methods [19] were used for solving this differential equation to trace the flux lines emanating from subconductors. The step over the field line was chosen very small close to the subconductors and increased on going far from them.

Appendix III
Guessing of the corona charge density at the subconductor surface

An initial estimate of the charge density at a point defined by the angle ψ on the subconductor surface was considered as a fraction of the mean value of space charge density ρ_m along the field line [2]:

$$\rho_{e_1} = 1.5\,\rho_m,$$

$$\rho_{e_2} = 3.0\,\rho_m,$$

where

$$\rho_m = \varepsilon_0 (V - V_0(\psi)) / \int_0^v \int_{\varphi_1}^v (\mathrm{d}\varphi_1 / E_1^2)\mathrm{d}\varphi_1$$

with $V_0(\psi)$ = onset voltage, V is the applied voltage, E_1 is the electrostatic field. Subsequent values of $\rho_{ei} (i > 2)$ were expressed in the form

$$\rho_{ei} = \rho_{ei-1} + \frac{\delta\varphi_{i-1}(\rho_{ei-1} - \rho_{ei-2})}{\delta\varphi_{i-2} - \delta\varphi_{i-1}},$$

where $\delta\varphi_i$ is the per unit potential error at the ground surface corresponding to iteration i as:

$$\delta\varphi_i = (V - \int_0^v \mathrm{d}\varphi)/V.$$

This approach assures always a convergence to a value of ρ_e where $\delta\varphi_i$ tends to zero.

References

1. Transmission Line Reference Book — HVDC to ±600 KV, EPRI, California, USA.
2. M. P. Sarma and W. Janischewskyj, IEEE Trans., Vol. PAS-**88,** 718, 1969.
3. Y. Sunaga and Y. Sawada, IEEE Trans., Vol. PAS-**99,** 605, 1980.
4. M. Abdel-Salam and M. Khalifa, Acta Phys. Hung., **36,** 201, 1974.
5. M. P. Sarma and W. Janischewskyj, IEEE Trans., Vol. PAS-**89,** 860, 1970.
6. M. Abdel-Salam and S. Abdel-Sattar, Discussion of paper No. 80 SM 712-0, 1980.
7. C. F. Gallo and W. L. Lama, IEEE Trans., Vol. 1GA-7, 420, 1971.
8. R. T. Waters, T. E. Rickard and W. B. Stark, IEEE Conf. publ. 90, 188, 1972.
9. M. Khalifa and M. Abdel-Salam, Proc. IEEE, **120,** 1574, 1973.
10. M. Abdel-Salam and M. Abdellah, Acta Phys. Hung., **40,** 155, 1976.

11. J. H. Simpson, Theoretical and Experimental Studies of Corona Loss from dc Lines. Presented at the Corona Res. Meeting, Montreal, P.Q., Canada, 1966.
12. V. I. Popkov, Elekrichestvo, No. 1, 33, 1949.
13. K. Arai and Y. Tsunoda, paper No. 35.07, Third International Symposium on High Voltage Engineering, Milan, 1979.
14. J. P. Vereshchagin and V. E. Litvinov, Elektrichestvo, No. 3, 30, 1978.
15. W. Janischewskyj and G. Gela, IEEE Trans., Vol. PAS-**98**, 1000, 1979.
16. M. Khalifa et al., IEEE PES paper, No. A75, 563–7, 1975.
17. M. Abdel-Salam, M. Farghaly and S. Abdel-Sattar, Monopolar Corona on Bundle Conductors. Paper submitted at the IEEE PES Winter Meeting, 1982.
18. M. Abdel-Salam et al, IEEE Trans., Vol. PAS-**95**, 1019, 1976.
19. S. D. Conte, Elementary Numerical Analysis, McGraw-Hill Company, New York, 1965.

Acta Physica Hungarica 54 (3—4), pp. 333—335 (1983)

QUARK INTERACTION ENERGIES AND BARYON MAGNETIC MOMENTS

TEJ K. ZADOO and G. Q. SOFI

Department of Physics, S. P. College, Srinagar 190001, India

(Received in revised form 8 November 1982)

It is pointed out that exact values of the magnetic moments of SU(3) baryons can be obtained by assuming the dependence of the magnetic moments on the quark interaction energy.

Introduction

Baryon magnetic moments have attracted great attention during the last few years. Many authors [1–9] employing different techniques have calculated these. The Coleman–Glashow (CG) formulas [10] for the hyperon moments reveal a rather confusing situation; the Σ^+ moment is consistent with the CG formula, the Λ moment which has been measured to good precision deviates significantly from the CG value $\mu_\Lambda = -0.957$. None of the other theoretical approaches used so far have been able to give an overall satisfactory fit.

In this note we present a fit to the magnetic moments of SU(3) baryons in terms of the quark interaction energies.

Magnetic moments of SU(3) baryons

The mass of a baryon which is made up of three quarks q_1, q_1 and q_2 is given by [11]

$$B(q_1, q_1, q_2) = 2m(q_1) + m(q_2) + \frac{3}{4} V(q_1, q_1, 1) +$$

$$+ \frac{1}{2} V(q_1, q_2, 1) + \frac{1}{4} V(q_1, q_1, 0) + \frac{3}{2} V(q_1, q_2, 0) + A, \qquad (1)$$

where $m(q)$ is the mass of the quark q, $V(q_1, q_2, s)$ is the interaction term representing the pairing energy between q_1 and q_2, the third index representing the spin, and A is a constant. In analogy to SU(3) we assume that the magnetic moment of a baryon is

dependent on the charges of the quarks [12] and the interaction energies. In analogy to Eq. (1) we write that the magnetic moment of a baryon B is given by

$$\mu_B = aQ_1 + aQ_2 + aQ_3 + \frac{3}{4}V'(q_1, q_1, 1) + \frac{1}{2}V'(q_1, q_2, 1) +$$

$$+ \frac{3}{2}V'(q_1, q_2, 0) + \frac{1}{4}V'(q_1, q_2, 0), \tag{2}$$

where Q is the charge of the quark 1 and $V'(q_1, q_1, 1)$ means the interaction term, etc.

We assume that in Eq. (2) the interaction energy does not depend on the spin, i.e.

$$V'(q_1, q_1, 1) = V'(q_1, q_1, 0) \quad \text{and} \quad V'(q_1, q_2, 1) = V'(q_1, q_2, 0).$$

Then, the Eq. (2) will be modified to

$$\mu_{(B)} = a(Q_1 + Q_2 + Q_3) + V'(q_1, q_1) + 2V'(q_1, q_2). \tag{3}$$

The magnetic moments of SU(3) baryons will be given by

$$\begin{aligned}
P(uud) &= a + V'(uu) + 2V'(ud) \\
N(udd) &= V'(dd) + 2V'(ud) \\
\Sigma^+(uss) &= a + V'(uu) + 2V'(us) \\
\Sigma^-(dds) &= -a + V'(dd) + 2V'(ds) \\
\Xi^0(uss) &= V'(ss) + 2V'(us) \\
\Xi^-(dss) &= -a + V'(ss) + 2V'(ds) \\
\Lambda(ud_{\text{anti}}, s) &= V'(ud) + V'(ds) + V'(us)
\end{aligned}$$

Fitting the values of a and V as follows

$$a = -0.788$$

$$\begin{aligned}
V(uu) &= 3.738 & V(dd) &= -1.75 & V(ss) &= -0.580 \\
V(ud) &= -0.080 & V(ds) &= -0.224 & V(us) &= -0.310
\end{aligned}$$

The values of the magnetic moments obtained from these values are given in Table I.

Table I

Comparison between the experimental and predicted values of the magnetic moments

Baryon	Predicted value	Experimental value
P	2.79	2.79
N	−1.91	−1.91
Σ^+	2.33	2.33
Σ^-	−1.41	−1.41
Ξ^0	−1.20	−1.20
Ξ^-	−0.240	−1.85 .75
Λ	−0.614	−0.614

Conclusion

From our results one can conclude that the quark—quark interaction, which has been usually neglected, has certain deeper influence on the magnetic moments. The discrepancy between the theory and the experiment may be due to relativistic effects, the effects of the $q\bar{q}$ sea (meson current) which have to be examined thoroughly and due to the fact that the interaction term $V'(q_1, q_2, 1)$ may not be exactly equal to $V'(q_1, q_2, 0)$. These have to be thoroughly examined.

References

1. A. de Rujula, H. Georgi and S. L. Glashow, Phys. Rev., **D12,** 147, 1975.
2. M. Ahmad and Tej K. Zadoo, Il Nuovo Cimento, **36A,** 86, 1976.
3. M. Slaughter and S. Oneda, Phys. Rev., **D14,** 1319, 1976.
4. M. Ahmad and Tej K. Zadoo, Phys. Rev., **D15,** 2483, 1977.
5. A. Bohm, Phys. Rev., **D18,** 2547, 1978.
6. H. J. Lipkin, Phys. Rev. Lett., **41,** 1629, 1978.
7. Y. Tomozawa, Phys. Rev., **D19,** 1626, 1978.
8. H. J. Lipkin, Phys. Lett., **89B,** 358, 1980.
9. G. Brown, M. Rho and V. Vento, Phys. Lett., **97B,** 423, 1980.
10. S. Coleman and S. L. Glashow, Phys. Rev. Lett., **6,** 423, 1961.
11. Tej K. Zadoo and M. Ahmad, Ind. J. Pure and Appl. Phys., **17,** 152, 1979.
12. J. J. Kokkedee, The Quark Model, Benjamin, New York, 1969.

Acta Physica Hungarica 54 (3—4), pp. 337—351 (1983)

NOISE INTERFERENCE WITH ORAL COMMUNICATION

T. TARNÓCZY

Research Laboratories for Natural Sciences of the Hungarian Academy of Sciences
Budapest, Hungary

(Received in revised form 11 November 1982)

Communication by speech is the most direct connection between human beings. Noise disturbs this connection because it masks some components of acoustical features and therefore reduces the information content of speech. Diminishing of intelligibility does not only prevent communication but can bring forth dangerous situations. The paper discusses the mechanism of speech production and the most important peculiarities of speech as information. The chief goal of the treatment is the redundancy of speech which is the most important factor to preserve information in the presence of noise interference. In connection to this the acoustical data of intelligibility measured chiefly by the author, will be given. A new computation method for the determination of intelligibility percentage in the presence of noise interference will be presented.

1. Communication by speech

The English word noise has two meanings. It means statistically fluctuating or simply non-periodical sound whose energy distributions depending on the frequency (so-called Fourier spectrum) consists of continuous, eventually densely located non-harmonic elements or is interspersed with them. According to its other meaning noise is any sound disturbing man in any of his activities. In certain languages there are two separate words for the two meanings.

Sounds with continuous spectrum may, of course, also carry information just as the so-called musical sounds with harmonic components. The former type is characteristic of several consonants, while characteristic examples for the latter are the vowels.

The disturbing noise may be the sound of both physical characters, but disturbance in understanding speech is caused in most cases and to the greatest extent by sounds with continuous spectrum. That is, the two meanings of noise are coinciding at such occasions.

Speech is the most important means of communication for human beings. Its functioning is linked with a bilateral human capability, with the ability of formation and of understanding of speech. Basic conditions of this are the following: intention of communication, the system of signals used according to a common agreement, the perfect condition of organs serving for emission and reception as well as the ability of

understanding. Therefore, the chain of speech communication is a complicated system where brain, nerves, speech organs and hearing all participate (Fig. 1). Feedback serving for the checking of transmission, namely, the fact that the speaker hears also his own voice, is not a basic condition but improves the speed and safety of communication.

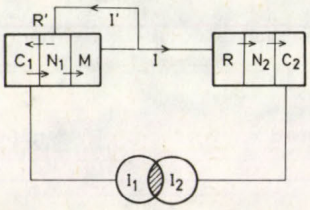

Fig. 1. Diagram of the communication chain; I = information, $C_{1,2}$ = cerebral function, $N_{1,2}$ = nervous connections, M = motoric emission, R = reception, I', R' = feed-back information for the emitter, $I_{1,2}$ = information store of both emitter and receiver

Communication by sounds is known also in the world of animals, but this is different from human speech, because with animals each information is given by a separate signal. Thus, of course, it is inapt for information on thoughts. Human speech is a system of signals built up on 35–40 elements, where meaning relies on various forms of connections between elements. Not only the possibility is given to form a new speech sound compound for any meaning, but also for the construction of a grammatical system in order to develop a literary language semantically perfectly tinged.

Speech is perfectly understandable — under appropriate acoustic circumstances — for healthy people mutually knowing the system of acoustical signals agreed upon (the language). By acoustical circumstances first of all the loudness of speech, the distance between speaker and listener and environmental background noise are meant. "Intelligibility" may decrease depending on them, what is more, it may even be lost. Therefore, the notion of intelligibility has a great importance in the evaluation of speech communication. With noise present both the speaker and the listener are faced with a difficult task: the former is disturbed by noise in thinking and the formation of speech, while the latter in hearing the series of signals and the cerebral evaluation of information content. It is first of all the phenomenon of "masking" that makes communication difficult [1].

Brain-work is, as a matter of fact, the decoding of the acoustical material heard, that will become more and more difficult according to what share and part of information is made unintelligible. Therefore, the harmful effect of speech—noise interference consists not only in the fact that the information is not understood, but also that the establishment of communication requires great efforts both on the side of emission (shouting) and on that of reception (combinative thinking).

That is why Robinson [2] ranks speech interference among primary human effects of noise. Namely, in speech disturbance stress is laid on the cerebral evaluating of

sound material just as in the sensational evolution of loudness and noisiness. However, the similarity is still not full, because in the case of speech interference our brain deals not directly with the determination of some property of noise, but with the decoding of information material distorted indirectly by the masking effect of noise. It is also true that speech interference is not a secondary derivative of such character as impaired hearing, nerval or organic diseases. This chain of thoughts necessitates the insertion of a third kind of noise effect between the two extreme types, the sensational judgement of the quantitative data of noise and the development of harmful effects of noise. To this interstate could be ranked also the sleep-disturbing effect of noise, whose further consequences are tiredness, reduced mental alertness, nervousness, etc. It is characteristic of these categories (speech interference, sleep interference) that they exist only while noise is present. With the elimination of noise also the phenomenon disappears. This is not the case with impaired hearing, nerval taint or organic diseases remaining also in noiseless state. These latter are the real secondary noise effects.

For acoustical communication several examples may be found also in the world of animals. The primary reason for this is the suitability of biological sound for communication purposes. Sound may be easily and rapidly formed, it contains a relatively wide variation of information possibilities and has an adequate distance effect, too. It may be well used also in the presence of natural obstacles (bush, wood, forest). It is also an important characteristic that acoustic signals may be "coded", that is animals belonging to other species do not know what information is contained in the given signal. The sound formed by animals has really all the features to be a carrier of the most important chain of communication.

In the course of investigations it turned out that most animals have a relatively abundant acoustical vocabulary. At least a dozen of animals are known that are able to produce 18–25 various phonetic signals (finch, dolphin, roaring monkey, etc.).

Sound forming is usually of a not too differentiated quality, but it has variable components. Such is first of all the frequency band used. Within one species the band of sound issuing and the sensibility range of the receiver organ are naturally in harmony. But the sound will not necessarily be perceived by the member of another species. It is very interesting that among mammalia examined until now man is perhaps the most sensitive in the range of low frequency sounds, while fully insensitive to very high frequency sounds. The frequency of the highest sound heard by man is 16–18 kHz, while the ears of chimpanzees are sensitive up to 22 kHz, those of dogs up to 38 kHz, of washbears up to 50 kHz, of cats up to 75 kHz, of bats up to 120 kHz. Non-mammals are usually insensitive to high sounds. This is surprising because previously we had thought that crickets, but also birds were sensitive to very high sounds. In reality the upper limit of the hearing of birds is around 8–12 kHz according to experiments [3].

Variation is possible first of all in pitch and time. It seems much less probable that the quality of sound would have an information-carrying role. But for man even this factor results in unlimited combination possibilities, i.e. the multiplication of meaning content.

2. Vibration of vocal cords

The primary source of the formation of speech sounds is the glottis. The originally closed vocal cords are made to vibrate by the flow of air flowing out of lungs. The fundamental tone generated in this way is transformed into speech sounds by various resonator holes, finally the sound will be radiated into the environmental air-space through the oral aperture and/or nostrils (Fig. 2).

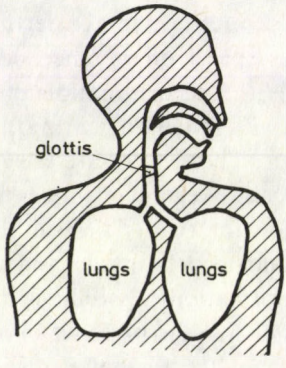

Fig. 2. Schematic view of speech organs

Beneath vocal cords one single large hole — the chest — is to be found. This hole includes the energy source of the sound formation system — the lungs. Since there are several soft and thus largely damping substances in the hole, it is first of all the trachea that has the role of a resonator. Since this resonator has a rather low own resonance, it does not influence the sound quality of speech sounds but may characterize individual timbre. In case of a normal speech sound the pressure of air flowing out of lungs corresponds to that of a water column of about 4 cm. When shouting very loudly and with high pitch it may even reach the pressure of a 20 cm high water column. The energy of the streaming air changes partly into sound energy, but the efficiency of transformation is very low, only some tenths of a thousandth.

Vocal cords block up the way of air as an elastic tightened membrane and form the sound source of speech and singing voice. It is about a pair of folds whose longitudinal tension, setting and gap size may be changed depending on our will. Muscles are partly imbedded into the vocal cords and partly make move the cartilages placed around. Vocal cords adhere to the cartilages and thus the exact setting and control is made by means of these. Cricoid is the basic cartilage of larynx. Above it the thyroid cartilage is located. Vocal cords begin with the inner part of its front wall that may be tightened by the thyroid cartilage. Arytenoid cartilages are placed on the backward side of cricoid. Vocal cords end on them whose approaching or keeping away is regulated by them. The cartilage covering the larynx has a protective role and

has nothing to do with sound formation. In Figs 3a and 3b the cross-section of larynx and the rough layout of vocal cords are presented. The movement of vocal cords may be best explained on the cross-section, but experimentally it may be examined precisely in the two other major directions. Pseudo (or false) vocal cords to be seen in the figure do not participate in sound formation under normal conditions, but in pathological cases and with operative help they may take over — imperfectly — the voice-forming role of vocal cords.

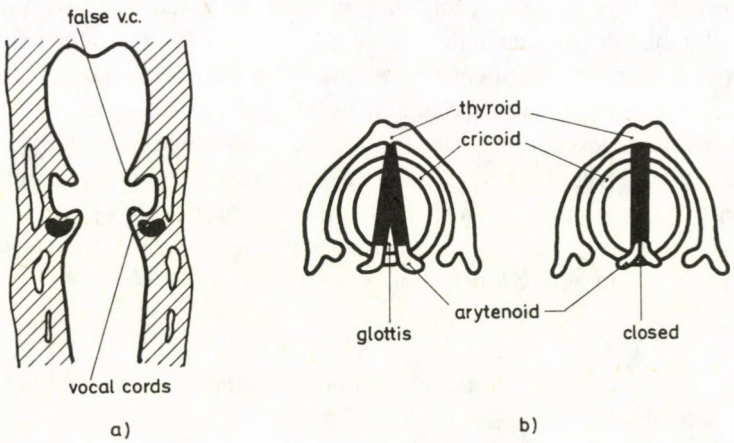

Fig. 3a. Vertical cross section of larynx, b) horizontal sections in the height of glottis with open and closed state

The length of vocal cords is 20–25 mm. Their movement takes place in such a way that the air flow pouring out of lungs knocks against the obstacle raised by closed glottis. If surplus pressure exceeds the compressing strength of vocal cords the flow of air breaks through the closure. In this way the surplus pressure will immediately diminish and resulting from their elasticity vocal cords are closed again. Air flowed out is continuously replaced from lungs, therefore after a certain time it will reach the surplus pressure required for a break-through again, and the movement goes on. Of course, elasticity data of vocal cords and flow data of the air current are in harmony. There is such a relationship between flow velocity in the contraction and pressure that at the narrowest place of larynx (glottis) air pressure will be the smallest. This physical circumstance promotes, what is more, partly governs the closure of vocal cords.

Vocal cords do not form a system opening and closing in plane, but move away and upward, then with an elliptical movement they collide further down and, when closing the edges are pressed together or may even be placed one above the other. Closure does not take place at once along the glottis, either, but the glottis is gradually closed from the front to the back and thus the entire movement has a character of a snake-like movement in space that may be well observed with a stroboscope. After

closing, vocal cords strive for the repetition of the process even by themselves — because of their elasticity —, therefore, they start again towards the opening upwards. The well timed increase of pressure of air coming from lungs assists this movement [4].

Since the basic material of speech sounds comes to being through the movement of vocal cords, also more detailed data of the process should be presented. Such are the form of vibration, the relationship between the duration of opening and closing as well as the harmonic content of the sound thus obtained. The time pattern of the glottis opening is a function of typical triangle form where the opening stage steeply increases. The duration of opening and closing state may be examined either with stroboscopic method or by the form in time of the sound obtained. According to data obtained from oscillograms the opening quotient amounts to 0.2 at the normal pitch of speech sound and may increase quite up to a value of 0.7 with the increase of pitch by two octaves. According to the experiments the absolute value of opening time is constant: 2–2.5 ms [5, 6]. As against this, according to the stroboscopic method the opening quotient hardly depends on the frequency and its value is around 0.7 [7].

It is difficult to make a decision here, because it is very difficult to exactly define what we mean by an acoustically open state.

3. Differentiated phonation

The sound generated by glottis — the voice — is one of the raw materials of speech. Its oscillogram has the form of characteristic saw-tooth just as that of mechanic or electric self-induced vibrations. The harmonics content of the voice decreases by about 12 dB/octave. This raw material is transformed into speech sounds with characteristic timbre by the resonance effect of holes above the glottis.

However, there are also several other methods of forming speech sounds. In the cavities above the glottis closures and narrowings may be established and thus various kinds of noise may be created. Narrow gaps may be formed between lips, lips and teeth, tongue and teeth as well as between tongue and various places of palate. Voiceless fricatives (*f*, *s*, *ʃ*, etc.) are formed in this way. If also voice is made sound the corresponding voiced pairs (*v*, *z*, *ʒ*) will be heard. With the sudden bursting of corresponding closures stops *p*, *t*, *k*, and in a voiced form *b*, *d*, *g* are obtained. The rapid consecutive application of the closure- and gap-forming methods will result in new sounds, they are the so called affricates, e.g. *ts*, *tʃ*. Also the timbre of noise sounds is influenced by holes above the glottis, but the real resonance effect is exercised first of all in the formation of vowels and semi-vowels (*m*, *n*, *l*, *r*, etc.).

Relatively most is known about the physical structure of vowels. Vowel-forming holes transform voiced sounds in their harmonic content as a result of their resonance effect (Fig. 4). Therefore, places of resonance amplification plotted against frequency are called "formants". Helmholtz has created a certain kind of filter theory for the explanation of the generation of vowels. At present this is replaced by a more modern

"tube theory" [8]. According to the drawing in Fig. 2 a tube with varying cross-section is leading from the glottis to the opening of the mouth, its length is about 17 cm. If the vowel-forming tube is considered a system with a quarter of a wavelength, its fundamental tone is around 500 Hz that may, of course, be modified by the formation of the tube (tongue, opening of the mouth). Indeed, the first resonance places (formants) are to be found between 200–1000 Hz. Places of further resonances may be found around 1500 Hz, 2500 Hz, etc. also with very wide modification possibilities (formants 2, 3, etc.).

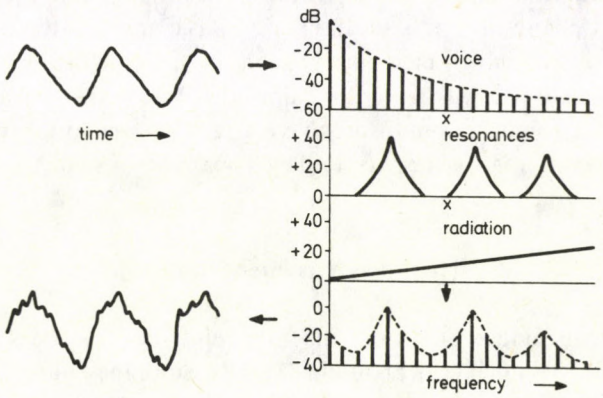

Fig. 4. Evolution of vowel sounds. Upper left: cord tone, right: Fourier-spectrum of cord tone and modifying effects caused by transfer functions, below right: final spectrum, left: final oscillogram

The first two formants show the acoustical character of vowels rather well. The final acoustical form of speech sounds develops but after the radiation through the apertures of resonator cavities. The radiation resistance of oral cavity raises the upper range of spectrum in a first approach by 6 dB/octave. Thus the heard character of upper formants will be stronger.

Therefore, the development of the acoustical character of vowels is a complicated process. In Fig. 4 we tried to outline the individual phases of the process. According to the system theory resonance curves modify the original series of harmonics. The effect of radiation resistance already mentioned is superposed on this that gives the final acoustical form. However, this may only be measured in the axis of the radiation. Laterally the radiation diagram is frequency dependent because of interferences and the shadowing effect of head, respectively. The usual frequency spectrum of speech sounds is distorted laterally or at the back, that makes also intelligibility more difficult.

Much less is known about the physical character of consonants than about that of vowels, but the so-called semi-vowels are formed identically as vowels. In the acoustical quality also elements of noise character may be observed and the formants of surrounding vowels also strongly influence the formation of the character in time. The character of consonant of continuous noise develops in a wide frequency band, but it

may be rather well recognized and identified from analysed patterns. The most complicated mechanical recognizing task is caused by stops. With them attempts are made to achieve some result by the "locus" notion for the time being. Locus is a frequency place to which second — eventually third — formants of surrounding vowels are approaching when changing the form of the vocal tract [9].

With the appropriate formation of cavities a theoretically infinite number of vowel kinds may be created, but within one language usually only 5–15 vowel qualities are really used. Even if not exactly, but about the same consideration holds also for consonants. From the information theoretical viewpoint it is very important that out of the continuously changeable possibilities in very large numbers the language selects a signal store consisting only of a few number of discrete elements. This phenomenon is, of course, connected also with our perception possibilities, but within one language each member of a language community has an "absolute hearing" for distinguishing tone qualities. Most languages build up their vocabulary usually from 35–45 speech sounds.

4. Speech as information

If all speech sounds would have the same relative occurrences, the information content of a phonetic signal were around 5–5.5 bits. Since the velocity of speech can be about 10–12 signals per second, the information capacity of speech is about 50–60 bit/s. The so defined information content of a short sentence reaches 500 bits. If our brain worked like a digital computer, both the sending and the receiving intellect ought to make maximum $2^{500} = 10^{150}$ decisions during this time for coding and decoding the phonetical and linguistical information, respectively. Beside this, the brain can distinguish between real quality informations (i.e. the phonetical contents of the information) and other ones (e.g. individual character, emotion content etc.). All these data indicate how faster (how much more efficiently) the brain performs its evaluating work than computers.

The question will be made even more complicated if we try to determine the information content of speech sounds analyzed from the physical side by artificial recognition. A physical analysis of speech sound will not result in the determination of a single quality, but the analysis is extended to the pitch of sound, duration, intonation and resonance data of 3–4 formant places, etc. The quality of sound should be determined on the basis of these permanently changed 8–10 data.

The solution of the problem has not been possible with our contemporary technical possibilities. However, by means of synthetisation and transformation into acoustical signals of the same information data a well understandable artificial speech may be generated. This fact points to the special activity of brain in decoding speech information. Because of the overlapping of formant places dependent on pronounciation decisions made on the basis of formants are not always unambiguous. It may be added to this that the individual timbre, the connection of the sound in question with

other sounds, and the emotional content of the text give a lot of additional information to the acoustical signal. Physical analysis is not able to distinguish between elements of the recorded information "parcel". It is an elementary observation, for example, that the loudness of speech may alter the formant structures more than it is characteristic for the difference between two vowels. Physical analysis is not able to separate the disturbing "additional information" which sometimes necessarily seems more significant from the "main information" characterizing the real quality, and thus, a simple analysis is not suitable for the mechanical recognition of quality. This parcel character of physical data of speech sounds is one of the important basic principles of research [10].

It results from the foregoing that the brain is likely to take considerably more data into consideration than physically available when making decision concerning quality. Besides, it makes not only short-time analysis within a given sound, but permanently considers also relations with preceding and following sounds, what is more, it even compares the material perceived with its own lingual and intellectual vocabulary and it corrects the eventually wrongly identified signal qualities afterwards. Thus, its work is further enlarged.

As a matter of fact, the interesting technical idea that the automatic recognition and identification of quantized signals may be technically solved, however, with the present technical level this is not possible for continuous ones, was raised even through the failure of the automatic recognition of speech sounds. Namely speech itself is not a succession of information signals, but their total confluence out of which our signal recognition systems are not able to select discrete qualities. First of all two things have to be solved yet: one is the segmentation of individual signals, while the other is their identification with elements of the quantized quality system. However, identification is not fully possible because of the suppressing effect of additional information even if the possibility of correlation analysis is included in the solution.

Therefore, physical data of human communication have developed according to the abilities of man. The speed of formation and of understanding is about the same, and this determines the capacity of elementary information material and the information capacity of speech sound. It is obvious that the most open system types (Morse signals) could not correspond to human needs because of the time-duration of their decoding, while the closest ones (picture-writing) because of their absurd large memory store. Therefore, the number and quality of speech elements had to develop by psycho-physiological reasons.

The carrier of the information material of speech communication is always some series of physical signals. But, this is subject to the interference of environmental physical and biophysical phenomena in the course of their spreading, transformation, perception and even understanding. Only quantitative data of the information material transmitted may be measured, but its contentual value may not. Yet, a relatively small phonetical change may involve considerable contentual deviation. Therefore, the stability of signals is a decisive problem of communication.

The informative effect of signals is not unambiguously influenced by various distortions, for example, the resonances of oral holes are practically distortions in the development of speech sounds, or the dynamical compression of hearing in understanding. All this promotes the adequate development and reception of signals carrying information. As against this, interference with noise always affects in the direction of the reduction of information content.

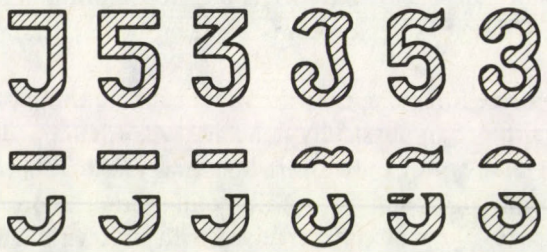

Fig. 5. Example shows the conserving effect of redundancy. The distortion in the second row cannot eliminate the meaning of the redundant form

The signal-noise ratio (difference between signal and noise levels) is one of the most fundamental data of the efficiency of communication. In the understanding of speech sounds the judgement of so-called distinctive features (difference thresholds) has an important part and this judgement is made difficult by the masking effect of noises. It is a general rule of nature that the intelligibility of a series of signals masked by noise may be gained by increasing the redundance of the carrier signals. Redundance may, for example, be increased by the multiplication of distinctive features of the individual elements, the numerical increase of the series of signals or by the repetition of signal processes (phonetical or verbal redundance).

The next redundance possibility is the length of sound signal series designating meanings and grammatical categories. The entire vocabulary of a language could be made up of sound relations of two, three and four elements. All combinations (e.g. four identical consonants one after the other) are, however, usually not made use of by languages in order to ensure intelligibility, i.e. information. Instead, longer words are formed. Longer signal series are less sensitive to noise, because the loss of one or another information element may be easily corrected in the brain. The time for information increases in this way. Shortness increases the amount of information per unit time, but also increases sensitivity to noise. Speech has developed in such a way that these two viewpoints are in balance.

In Fig. 5 the informational effect of two signal series is presented without and with noise interference, respectively. Interference has hardly any harmful effect on the information content of redundant series, while a perfectly informative signal series (containing no insignificant auxiliary signals) will become fully indecipherable [10].

Therefore, with large basic noise redundance should be increased in speech communication. For example, space language vocabularies do not allow the "yes—no" version, but instead the use of "affirmative—negative" is obligatory.

5. Acoustical data of speech and intelligibility

Resulting from the peculiarities of speech sounds acoustical power and spectrum are permanently changing in the course of speech. In order to be able to determine acoustical data for the speech itself certain statistical considerations have to be made. It may be stated concerning a longer speech whether it was too still, of normal intensity or too loud. A similar procedure may be followed also in the course of measurements. The average sound pressure level of normal speech is about 72–76 dB at a distance of 30 cm from the speaker. Measuring data under various circumstances may be found in Table I. The Table contains the average of the Hungarian speech of 18 men, measurements were made by the so-called speech choir method [11, 12].

Table I

Average sound pressure level of man's speech at 30 cm distance from head

Speech	Front	Side	Behind
Murmured	63	–	–
Still	67	62	57
Normal	74	70	64
Loud	81	76	72
Shouted	86	–	–

Beside average levels also the form of the average spectrum of speech has to be known. In Fig. 6 an average spectrum of 8 European languages was indicated for man's voice. Data are plotted in spectrum level (energy level falling to 1 Hz theoretical bandwidth) and with a fluctuation possibility of ± 3 dB are valid for the English, German, Swedish, Russian, Italian, Hungarian [12] as well as Spanish [13] and French [14] languages. In Fig. 6 the zero level is the average (long-time) sound pressure level of speech.

From Fig. 6 speech levels falling to octave bands of 250...4000 Hz medium frequencies may easily be converted. These data are needed if we wish to calculate the intelligibility of speech in advance for noises of various spectral compositions.

Speech sounds are of various intensity and structure, therefore noise does not equally mask them, but the more intensive the noise the more it will mask. According to traditional definition intelligibility is the numerical quotient of the understood elements and all speech elements (sound, syllable, word) communicated. However,

intelligibility percentages determined on the basis of fluent speech are quite different from the values referring to individual syllables or separate (meaningful or meaningless) words [15]. Namely, in the identification of meaningful texts very great deviations may be stated depending on the practice, individual abilities and intelligence as well as on the text. For example, with a 50 per cent syllable intelligibility, speech intelligibility may reach 90 per cent. Therefore, almost exclusively syllable intelligibility is used for investigations.

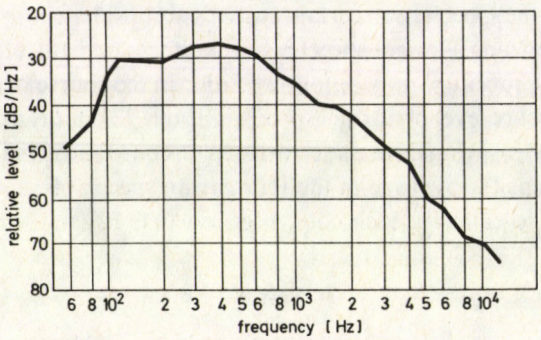

Fig. 6. Average speech spectrum of European languages. All data fall within ±3 dB band of the curve plotted

For direct measuring several procedures are known. Their common feature is that they try to find an answer to the intelligibility of mainly monosyllabic and disyllabic words with identical or similar voice structure as the language investigated. It is not absolutely necessary that the individual words have some meaning. And, if so, then mistakeable words are selected, where, for example, changing one phonem (speech sound occurring in the language in question) causes changes also in the meaning. E.g.: boon-coon-loon-moon-noon-soon.

The intelligibility percentage determined may be used for indicating the suitability for work of the acoustical surrounding. However, because of the clumsiness of subjective measuring also some computation methods have developed in the course of time.

One of them is the estimation method using the total noise level. Following from the data of Table I the masking effect of noise may be somewhat compensated by the increase of sound intensity. An important consideration is the relationship between spectra of speech and of interfering noise. For example, "white noise" (the energy density of spectrum is constant as a function of frequency) masks stops according to Table II. The basic assumption of the data of the Table is that the sound pressure level of speech and noise should be identical, i.e. the signal to noise ratio is 0 dB. In such cases the intelligibility of the individual sounds is called intelligibility stability [16].

Table II

Percentual intelligibility stability of stops for the English and Hungarian languages

Sound	English	Hungarian
p	50.5	46.5
t	76.5	87.5
k	50	78.5
b	75	75
d	73	68
g	59	66.5

Under similar circumstances the intelligibility of vowels may reach even 98 per cent. Therefore the exact knowledge of spectral relations is needed.

Fletcher [15] gave possibilities for other solutions by introducing the term "articulation index". The essence of articulation index lies in that the intelligibility referring to the entire frequency range is made up of partial intelligibilities achieved in the individual frequency bands. On the basis of this the action of speech interference level (SIL), then its modified forms were introduced.

The preferred speech interference level (PSIL) is the simple arithmetical mean value of the noise level to be measured in octave bands with 500, 1000 and 2000 Hz medium frequencies, respectively. As a function of this the admissible distance and sound intensity to be used for intelligibility in speech communication are given. Data are presented in Table III [17].

Table III

Admissible PSIL-values in dB mean values as a function of speech distance and sound intensity

Distance [m]	Normal	Raised voice	Loud	Shouted
0.3	68	74	80	92
0.6	62	68	74	80
0.9	58	64	70	76
1.2	56	62	68	74
1.5	57	60	66	72
1.8	52	58	64	70
3.6	46	52	58	64

The computations presented did not take spectral deviations of speech and interfering noise into consideration. The spectrum of speech may be assumed as given according to Fig. 6. Of course, the spectral forms of speech with intensities deviating from the normal one are also known [12]. The spectrum of the given noise should be compared to them. But this is not enough to forecast intelligibility, since also partial intelligibility percentages falling to the individual octave bands have to be known.

Relevant data are presented in Table IV where partial values falling to the individual octave bands may be found by the author for English [15], Russian [19] and Hungarian [20] languages. The first two result from conversion, while the third one from direct measuring.

Table IV

Partial intelligibility percentages (X) measured in octave bands, without background noise

Centre of band (Hz):	125	250	500	1k	2k	4k	8k
English	3	15	29	28	17	8	–
Russian	1	6	23	32	26	10	2
Hungarian	2	13	18	22	22	20	3
Mean values:	2	11	23	27	22	13	2

It results from Table IV that the octave band with 4000 Hz medium frequency largely contributes to the intelligibility, therefore it cannot be omitted from the computation. The level values of speech and noise components should be determined in five octave bands. Furthermore — according to an idea of D. E. Broadbent [21] — we may agree that if some component of noise level is at least by 30 dB below the speech level, it has no effect to intelligibility, while if it is at least by 20 dB above it, then understanding will be made quite impossible. Transitional cases are handled proportionally. Level data of the individual bands are weighted by partial percentages of intelligibility, then partial results are added. Thus we get an intelligibility index in a given noise:

$$I = \frac{\sum_i (S-N)_i + 20}{50} X_i,$$

where S_i and N_i are the ith octave band levels of speech and of noise, respectively: and X_i is the percentual intelligibility component in the same octave band according to the data of Table IV.

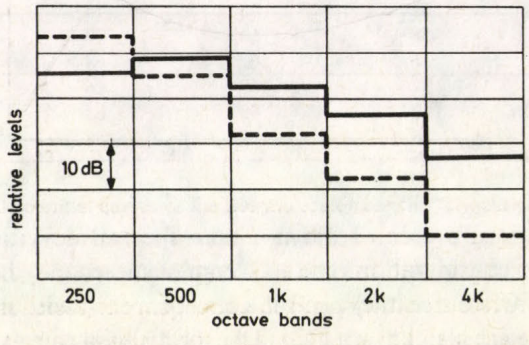

Fig. 7. Diagram for computation of interfering effect of a given noise with speech, i.e. of intelligibility of syllables in a given language. Straight lines: speech spectrum, broken lines: noise spectrum. For details see the text

In Fig. 7 beside octave band data of the average energy spectrum of speech of normal intensity also octave levels of a hypothetical noise source — measured at the ear of the listener — were plotted. If the computation mentioned is made according to the summation of

$$\frac{(S-N)_{250}+20}{50} X_{250} + \frac{(S-N)_{500}+20}{50} X_{500} + \ldots$$

then for these circumstances an intelligibility of 51.4% will be obtained for the English language and that of 54.7% for the Hungarian one. For verification of the computation use data of Table IV and Fig. 7. The achieved values depend, of course, on the speech level and on the noise spectrum in another case.

References

1. E. Zwicker, R. Feldtkeller, Das Ohr als Nachrichtenempfänger. S. Hirzel Vg., Stuttgart, 1967.
2. D. Robinson, Aeronautical Research Control C. P. 1112 London, HMSO, 1970.
3. G. Tembrock, Tierstimmen, A. Ziemsen Vg., Wittenberg, 1959.
4. Jw. van den Berg, J., Speech and Hearing Res., **1,** 227, 1958.
5. M. Joos, Acoustic Phonetics. in: Suppl. to Language. Waverly Press Inc., Baltimore, 1948.
6. T. Tarnóczy, J. Acoust. Soc. Amer., **23,** 42, 1951.
7. R. Timcke, Z. Laryngologie, Stuttgart, **35,** 331, 1956.
8. G. Fant, Theory of Speech Production. Mouton, 'S-Gravenhage, 1960.
9. P. C. Delattre, A. M. Lieberman and F. S. Cooper, J. Acoust. Soc. Amer., **27,** 769, 1955.
10. T. Tarnóczy, Rap. du 5e Congr. Internat. d'Acoust. Liège, 1965, Vol. 2, 371.
11. T. Tarnóczy, Acustica, **23,** 173, 1970.
12. T. Tarnóczy, Acustica, **24,** 57, 1971.
13. V. Bañuls-Terol, Proc. 7th Intern. Congr. on Acoust., Budapest, 1965, Vol. 3, 293.
14. T. Tarnóczy, Acoustique Télécomm. Colloque FASE75, Paris 1975, 123.
15. H. Fletcher, Speech and Hearing in Communication, Van Nostrand, New York, 1953.
16. G. A. Miller and P. E. Nicely, J. Acoust. Soc. Amer., **27,** 338, 1955.
17. L. L. Beranek, Noise Reduction, McGraw-Hill, New York, 1960.
18. J. C. Webster, J. Acoust. Soc. Amer., **37,** 692, 1965.
19. V. K. Jofe and A. A. Janpolsky, Tables and Graphics for Computation in Electroacoustics (in Russian). Moscow–Leningrad, 1954.
20. T. Tarnóczy, Kép és Hangtechnika, **20,** 97, 1974 (in Hungarian).
21. W. Burns, Noise and Man, J. Murray, London, 1973, p. 184.

Acta Physica Hungarica 54 (3—4), pp. 353—359 (1983)

REPARAMETRIZATION OF SUPERGROUP: SUPERSPACE AS A VECTORSPACE

NGUYEN AI VIET

Institute of Physics, Nghia do, Tu liem, Ha noi, VSR

(Received in revised form 18 November 1982)

In this paper we show that, with reparametrization of supergroup, superspace as the homogeneous space of it will be linearized, superfield will be defined uniquely, vector coordinates and spinor coordinates will play the equal rôle... We can list all possible subgroups of supergroup easily in this way of parametrization. The representation of this algebra will be given. The linearization of superspace would lead to new approaches to construct geometrical structures on it. The Abelian translation group would make easier the construction of the harmonic analysis on it. Last of all, the $SU(N)$ internal symmetry of extended superunified theories would be manifest in these models.

1. Introduction

In original works [1, 2], the supertranslation group has been introduced with parametrization by the generators $Q, \bar{Q}, P$ of the pseudo Lie algebra

$$\{Q, \bar{Q}\} = 2\sigma_\mu P^\mu ,$$

$$\{Q, Q\} = \{\bar{Q}, \bar{Q}\} = [P_\mu, Q] = [P_\mu, \bar{Q}] = [P_\mu, P_\nu] = 0 . \tag{1.1}$$

Elements of the supertranslation group can be parametrized as:

$$G(c_\mu, \zeta, \bar{\zeta}) = \exp i(c_\mu P^\mu + \zeta Q + \bar{Q}\bar{\zeta}) . \tag{1.2}$$

The product defined on the group is not linear, not global, even not commutative [3, 4]:

$$\begin{aligned} &G(c_{1\mu}, \zeta_1, \bar{\zeta}_1) \cdot G(c_{2\mu}, \zeta_2, \bar{\zeta}_2) = \\ &= G(c_{1\mu} + c_{2\mu} + i(\zeta_2 \sigma_\mu \zeta_1 - \zeta_1 \sigma_\mu \bar{\zeta}_2), \quad \zeta_1 + \zeta_2, \bar{\zeta}_1 + \bar{\zeta}_2) . \end{aligned} \tag{1.3}$$

Then the superspace and the superfields defined on it can be introduced as:

$$\Phi(x, \vartheta, \bar{\vartheta}) = \exp [i(x_\mu P^\mu + \vartheta Q + \bar{Q}\bar{\vartheta})] \Phi(0, 0) . \tag{1.4}$$

Using the Cambell—Haussdorf identity, by such way of parametrization with $Q, \bar{Q}$ and P^μ we have three different definitions of superfield corresponding to the

following three choices (see [5]):

$$\begin{aligned} &\exp\left[i(x_\mu P^\mu + \vartheta Q + \bar{Q}\bar{\vartheta})\right]\Phi(0,0) \equiv \Phi(x,\vartheta,\bar{\vartheta}), \\ &\exp\left[i(x_\mu P^\mu + \vartheta Q)\right]\cdot\exp\left(i\bar{Q}\bar{\vartheta}\right)\Phi(0,0) \equiv \Phi_1(x,\vartheta,\bar{\vartheta}), \\ &\exp\left[i(x_\mu P^\mu + \bar{Q}\bar{\vartheta})\right]\cdot\exp\left(i\vartheta Q\right)\Phi(0,0) \equiv \Phi_2(x,\vartheta,\bar{\vartheta}). \end{aligned} \tag{1.5}$$

This way of parametrization has some "esthetical" shortcomings:

a) The spinortranslations do not form one-parameter group. This kind of parametrization is not as canonical as the usual techniques treated with Lie groups.

b) The supertranslation group is not commutative. The harmonic analysis and the generalized Fourier transformations have not been discussed yet on the superspace. Because the supertranslation group is not compact, but locally compact only, the commutativity would make this construction easier by the recipe given in [6].

c) Superfields are not determined uniquely.

d) When the geometrical structures on a manifold are constructed, an algebraic structure used to be given on it, so that the manifold will become a vectorspace. Concretely, one always makes an additive group isomorph with the translation group. With the previous parametrization both cannot be realized at the same time, because the supertranslation group is not Abelian. We cannot use the standard techniques to construct a linear geometry on it.

e) Geometrically speaking, up to now the superspace is considered as a fibre bundle [7, 8], not base manifold. The geometry on it is a non-linear one. So vector coordinates and spinor coordinates do not play the same rôle in our formalism.

In this study on the reparametrization of supergroup, we try to overcome all these minor esthetical shortcomings.

2. Reparametrization of supergroup and superspace

In [9] the authors have affirmed that the most general form of the commutator of the Fermi generators of degree 1 is:

$$\{Q^L, \bar{Q}^M\} = c^{LM}\sigma_\mu P^\mu . \tag{2.1}$$

According to them, if $c^{LM} = 0$ then $Q = \bar{Q} = 0$. So in the case of non-vanishing Fermi generators c^{LM} can always be normalized to δ^{LM}. However, it is not true, if we reexamine the analysis in which $\{Q^L, \bar{Q}^M\}$ belongs to the $(1/2, 0)(0, 1/2) = (1/2, 1/2)$ representation of Lorentz group. Because zero belongs to any representation, so in (2. 1) c^{LM} can vanish quite right. For instance, let us take the following non-vanishing Fermi generators:

$$\begin{aligned} Tsp^L &= Q^L + i\bar{\vartheta}^L\sigma_\mu P^\mu , \\ \overline{Tsp}^L &= \bar{Q}^L + i\vartheta^L\sigma_\mu P^\mu , \end{aligned} \tag{2.2}$$

with Q and $\bar{Q}$ given in (1.1). ϑ and $\bar{\vartheta}$ are spinorcoordinate operators of the superspace (1.3). As we know from [3]

$$\{Q, \vartheta\} = \{\bar{Q}, \bar{\vartheta}\} = i\,. \tag{2.3}$$

We have the following minimal extension of Poincaré algebra

$$\begin{aligned} &[P_\mu, Tsp] = [P_\mu, \overline{Tsp}] = \{Tsp, \overline{Tsp}\}\,, \\ &\{Tsp, Tsp\} = \{\overline{Tsp}, \overline{Tsp}\} = 0\,, \\ &[M_{\mu\nu}, Tsp] = 1/2 \cdot \sigma_{\mu\nu}\overline{Tsp}\,, \\ &[M_{\mu\nu}, Tsp] = 1/2 \cdot \tilde{\sigma}_{\mu\nu}\overline{Tsp}\,. \end{aligned} \tag{2.4}$$

We can see that in this case Fermi generators form a Grassman algebra (while the generators given in (1.1) form a Clifford algebra). Supertranslation group will be parametrized as:

$$G(a_\mu, \zeta, \bar{\zeta}) = \exp\left[i(a_\mu P^\mu + \zeta Tsp + \overline{Tsp}\bar{\zeta})\right]. \tag{2.5}$$

The product defined on this group turns to be commutative, linear and global:

$$G(a_{1\mu}, \zeta_1, \bar{\zeta}_1) \cdot G(a_{2\mu}, \zeta_2, \bar{\zeta}_2) = G(a_{1\mu} + a_{2\mu}, \zeta_1 + \zeta_2, \bar{\zeta}_1 + \bar{\zeta}_2)\,. \tag{2.6}$$

Superfield will be determined uniquely if the superspace is parametrized with Tsp, $\overline{Tsp}$ and P^μ:

$$\Phi(x, \vartheta, \bar{\vartheta}) = \exp\left[i(x_\mu P^\mu + \vartheta Tsp + \overline{Tsp}\bar{\vartheta})\right]\Phi(0, 0)\,. \tag{2.7}$$

Let us parametrize the elements of the minimal spinor extension of Poincaré group with generators Tsp, $\overline{Tsp}$, P^μ and $M_{\mu\nu}$ by $\{\Lambda, a_\mu, \zeta\}$. We can get easily the set of all possible subgroups of it, when we fix each parameter:

1. $\{1, 0, 0\} = 1$: it is the trivial group, the unit of the supergroup.
2. $\{\Lambda, 0, 0\} \in \mathfrak{L}$: it is the usual Lorentz group.
3. $\{\Lambda, a_\mu, 0\} \in \mathfrak{P}$: it is the usual Poincaré group.
4. $\{1, a_\mu, \zeta\} \in \mathfrak{S}T$: it is the commutative supertranslation group.
5. $\{1, a_\mu, 0\} \in T$: it is the usual space time translation group.
6. $\{1, 0, \zeta\} \in Tsp$: it is the new spinor translation group.
7. $\{\Lambda, 0, \zeta\} \in \mathfrak{S}\mathfrak{L}$: it is the new super Lorentz group.

It is worth noting that in this way of parametrization we get two new groups Tsp and $\mathfrak{S}\mathfrak{L}$. The consideration of these is an interesting work, and it will be discussed elsewhere.

The superspace now is the set of numbers $(x_\mu, \vartheta, \bar{\vartheta})$ transforming under the action of the element $\{\Lambda, a_\mu, \zeta\}$ of supergroup as follows:

$$\begin{aligned} &x_\mu \to \Lambda_\mu^\nu x_\nu + a_\mu\,, \\ &\vartheta \to A(\Lambda)\vartheta + \zeta\,, \\ &\bar{\vartheta} \to \bar{A}(\Lambda)\bar{\vartheta} + \bar{\zeta}\,. \end{aligned} \tag{2.8}$$

So we come to a natural and general definition of supergroup: *Supergroup is the group of inhomogeneous linear transformations acting on superspace and leaving Minkowski space and spinorspace invariant.*

3. Representation of Tsp algebra

Let us consider the massive case: Take $\vec{P}=0$ and $P_0=m$ $Tsp\cdot\overline{Tsp}$ is Casimir operator then, because it commutes with all other generators. So we have:

i) *Irreducible multiplets with* $\overline{Tsp}\cdot Tsp\,|\varphi\rangle=0$

There are two possibilities:

a) $Tsp\,|m,J,J_3\rangle_0^l=0$: $|m,J,J_3\rangle_0^l$ is the Grassman vacuum with left-handed chirality. This vacuum degenerates with four states forming a complete basis, which spans a 4-dimensional representation space:

$$|m,J,J_3\rangle_0^l;\quad Tsp_\alpha|m,J,J_3\rangle_0^l;\quad Tsp_\alpha Tsp_\beta|m,J,J_3\rangle_0^l. \tag{3.1}$$

b) $Tsp|m,J,J_3\rangle_0^r=0$: $|m,J,J_3\rangle_0^r$ is the Grassman vacuum with right-handed chirality. This vacuum degenerates with four states forming a complete basis, which spans a 4-dimensional representation space:

$$|m,J,J_3\rangle_0^r;\quad \overline{Tsp_\alpha}|m,J,J_3\rangle_0^r;\quad \overline{Tsp_\alpha}\,\overline{Tsp_\beta}|m,J,J_3\rangle_0^r. \tag{3.2}$$

ii) *Irreducible multiplets with* $\overline{Tsp}\cdot Tsp|\varphi\rangle=0$

It occupies 8 states forming a complete basis. It is an octet with neutral chirality:

$$\begin{gathered} Tsp|m,J,J_3\rangle_0^n\neq 0;\quad \overline{Tsp}|m,J,J_3\rangle_0^n\neq 0:\\ |m,J,J_3\rangle_0^n;\quad Tsp_\alpha|m,J,J_3\rangle_0^n;\quad \overline{Tsp_{\dot\alpha}}|m,J,J_3\rangle_0^n;\\ \overline{Tsp_{\dot\alpha}}Tsp_\beta|m,J,J_3\rangle_0^n;\quad \overline{Tsp_{\dot\alpha}}\,\overline{Tsp_{\dot\beta}}|m,J,J_3\rangle_0^n;\\ Tsp_\alpha Tsp_\beta|m,J,J_3\rangle_0^n. \end{gathered} \tag{3.3}$$

In the space of functions on the supergroup, we represent the generators of the minimal spinor extension of Poincaré group as:

$$\begin{aligned} &P_\mu=i\partial_\mu,\\ &M_{\mu\nu}=i(x_\mu\partial_\nu-x_\nu\partial_\mu)+1/2\cdot\left(\sigma_{\mu\nu}\vartheta\frac{\partial}{\partial\vartheta}-\tilde\sigma_{\mu\nu}\vartheta\frac{\partial}{\partial\vartheta}\right),\\ &Tsp_\alpha=i\partial/\partial\vartheta_\alpha;\quad \overline{Tsp_{\dot\alpha}}=i\partial/\partial\bar\vartheta_{\dot\alpha}. \end{aligned} \tag{3.4}$$

Generally speaking, the 16-component superfield is reducible and it can be reduced into the sum of an irreducible quartet with left-handed chirality (independent of $\bar{\vartheta}$), and an irreducible quartet with right-handed chirality and an octet with neutral chirality. At the same time, it is the product of a superfield with right-handed chirality and a superfield with left-handed chirality:

$$\begin{aligned}\Phi(x_\mu, \vartheta, \bar{\vartheta}) &= \Phi^r(x, \vartheta) + \Phi^l(x, \bar{\vartheta}) + \Phi^n(x, \vartheta, \bar{\vartheta}) = \\ &= \Phi'^r(x, \vartheta) \cdot \Phi'^l(x, \bar{\vartheta}) .\end{aligned} \tag{3.5}$$

Let us note that the product of superfields of the same chirality is a superfield of that chirality.

4. Discussion

The construction of Lagrange field theory for *Tsp* algebra is straightforward by the standard method proposed by Salam and Stradee [2]. Here we do not discuss it in detail.

From a geometrical viewpoint, the constructon of geometrical structures on the superspace as a vectorspace is a very interesting work. For this purpose we would define a certain scalar product on superspace as:

$$\langle Z, Z' \rangle = g_{mn} Z^m \cdot Z^n \qquad \text{where} \qquad Z^m = (x_\mu, \vartheta, \bar{\vartheta}) .$$

First we consider the flat superspace, in which g_{mn} is a global supermetric tensor. Only from the scalar nature and from the symmetric property of this product with ϑ and $\bar{\vartheta}$ we come to

$$\langle Z, Z \rangle = f(x_\mu x^\mu, \vartheta, \bar{\vartheta}) = x_\mu x^\mu . \tag{4.1}$$

Proof: From the scalar nature of this product, we must pair ϑ with $\bar{\vartheta}$ in any terms of this product. So:

$$\langle Z, Z \rangle = f(x_\mu x^\mu, \vartheta\bar{\vartheta}) .$$

But because the product is symmetric, if in a certain term of the product there is a $\vartheta\bar{\vartheta} \cdot C(x, \vartheta, \bar{\vartheta})$, there must be $\bar{\vartheta}\vartheta \cdot C(x, \vartheta, \bar{\vartheta})$ terms in the product. However, the two terms destroy each another.

So: *Distance in superspace is the distance is Minkowski space, but the angle in superspace is not that one in Minkowski space.*

So we can see that the spinor coordinates would give contributions to the curvature of manifolds in the superspace. Indeed, if we give a hypersurface by the following equation:

$$\vartheta = \vartheta(x); \quad \bar{\vartheta}(x) = \bar{\vartheta} . \tag{4.2}$$

We can come to a curved Minkowski space as a physical manifold in the superspace with the following metric tensor:

$$
\begin{aligned}
g_{\mu\nu}(x) = g_{\mu\nu} + g_{\mu\alpha} \cdot \partial\vartheta^{\alpha}(x)/\partial x^{\nu} + g_{\mu\dot{\alpha}} \partial\bar{\vartheta}^{\dot{\alpha}}(x)/\partial x^{\nu} + \\
+ g_{\alpha\nu} \partial\vartheta^{\alpha}(x)/\partial x^{\mu} + g_{\dot{\alpha}\nu} \partial\bar{\vartheta}^{\dot{\alpha}}(x)/\partial x^{\mu} + \\
+ g_{\alpha\beta} \partial\vartheta^{\alpha}(x)/\partial x^{\mu} \cdot \partial\vartheta^{\beta}(x)/\partial x^{\nu} + g_{\dot{\alpha}\dot{\beta}} \partial\bar{\vartheta}^{\dot{\alpha}}(x)/\partial x^{\mu} \cdot \partial\bar{\vartheta}^{\dot{\beta}}(x)/\partial x^{\nu} + \\
+ g_{\dot{\beta}\alpha} \partial\bar{\vartheta}^{\dot{\beta}}(x)/\partial x^{\mu} \cdot \partial\vartheta^{\alpha}(x)/\partial x^{\nu} + g_{\alpha\dot{\beta}} \partial\vartheta^{\alpha}(x)/\partial x^{\mu} \cdot \partial\bar{\vartheta}^{\dot{\beta}}(x)/\partial x^{\nu} .
\end{aligned} \tag{4.3}
$$

Specially, if we choose:

$$
g_{mn} = \begin{pmatrix}
1 & 0 & 0 & 0 & 0 & 0 & 0 & 0 \\
0 & 1 & 0 & 0 & 0 & 0 & 0 & 0 \\
0 & 0 & 1 & 0 & 0 & 0 & 0 & 0 \\
0 & 0 & 0 & -1 & 0 & 0 & 0 & 0 \\
0 & 0 & 0 & 0 & 0 & 0 & i & 0 \\
0 & 0 & 0 & 0 & 0 & 0 & 0 & i \\
0 & 0 & 0 & 0 & i & 0 & 0 & 0 \\
0 & 0 & 0 & 0 & 0 & i & 0 & 0
\end{pmatrix} \tag{4.4}
$$

With the assumption that the scalar product is bilinear and symmetric with ϑ and $\bar{\vartheta}$. Then (4. 3) gets the following form:

$$
\begin{aligned}
g_{\mu\nu}(x) = g_{\mu\nu} + i(\partial\vartheta(x)/\partial x^{\mu} \cdot \partial\bar{\vartheta}(x)/\partial x^{\nu} + \\
+ \partial\bar{\vartheta}(x)/\partial x^{\mu} \cdot \partial\vartheta(x)/\partial x^{\nu}) \equiv g_{\mu\nu} + S .
\end{aligned} \tag{4.5}
$$

The S-term will cause the curvature of the space. We stop the discussion with the remark that: *In the superspace we can get all configurations of gravity corresponding to the set of the possible* $\vartheta = \vartheta(x)$; $\bar{\vartheta} = \bar{\vartheta}(x)$ *in it.*

In conclusion, we note that with *Tsp* algebra, the $SU(N)$ internal symmetry will be manifest.

Consider the extended superunified algebra in the general form:

$$
\begin{aligned}
&[P_{\mu}, P_{\nu}] = [P_{\mu}, B_l] = [P_{\mu}, Q^L] = [M_{\mu\nu}, B_l] = 0 , \\
&[M_{\mu\nu}, P_{\rho}] = i(g_{\mu\rho} P_{\nu} - g_{\nu\rho} P_{\mu}) , \\
&[M_{\mu\nu}, Q^L] = 1/2 \cdot \sigma_{\mu\nu} Q^L , \\
&\{Q^L_{\alpha}, Q^M_{\beta}\} = \varepsilon_{\alpha\beta} \Sigma (a_l)^{LM} \cdot B_l , \\
&\{Q^L_{\alpha}, \bar{Q}^M_{\dot{\alpha}}\} = c^{LM} (\sigma_{\mu})_{\alpha\dot{\alpha}} P^{\mu} , \\
&[B_l, B_m] = i \Sigma c^k_{lm} B_k , \\
&[B_l, Q^L] = \Sigma S_l^{LM} \cdot Q^M .
\end{aligned} \tag{4.6}
$$

When $c^{LM}=0$, we get the *Tsp* algebra.

Using Jacobi identity (B_l, Q^L, Q^M) we come to:

$$\Sigma c^{LM} \cdot \bar{s}_l^{MN} + \Sigma s_l^{LM} \cdot c^{MN} = 0 \tag{4.7}$$

or in the matrix form: $c \cdot \bar{s}_l = -\bar{s} \cdot c$.

In usual models, with $c^{LM}=\delta^{LM}$, we have $\bar{s}_l = -s_l$. As we now, s_l matrices are the representations of the internal symmetry group. So the internal symmetry group must be orthogonal. We could get the $SU(N)$ symmetry only after a lengthy manipulation with so called self-duality (see [10]).

In our *Tsp* algebra $c^{LM}=0$, (4.7) satisfies automatically. So we can get a manifest $SU(N)$ superunified theory. This kind of symmetry fits better with reality.

Acknowledgements

Thanks are due to Professor Dao Vong Duc for many helpful discussions. Every technique used in this study has been learned from his lectures on elementary particle physics.

I am also indebted to my master, Professor I. Lovas, who introduced me to elementary particle physics in first steps.

Professor K. Wali (from Syracuse University) gave me encouragement to write this study.

References

1. J. Wess and B. Zumino, Nucl. Phys., **B70,** 39, 1974.
2. A. Salam and J. Stradee, Nucl. Phys., **B76,** 477, 1974.
3. V. A. Aghievetski and L. Mezintchescu, Usp. Fiz. Nauk., **117,** 637, 1975.
4. F. A. Berezin and G. I. Katz, Mat. Sbor. No. 82 (124), 343, 1970.
5. P. Fayet and S. Ferrara, Phys. Report, **32,** 251, 1977.
6. E. Mewitt and K. Rose, Abstract harmonic analysis I, II Springer Verlag, 1963, 1970.
7. P. Nath and R. Arnowitt, Phys. Letters, **56B,** 177, 1975.
8. S. W. McDowell and F. Mansouri, Phys. Rev. Letters, **38,** 139, 1977.
9. R. Maag, J. Lopuszansky and M. Sohnius, Nucl. Phys., **B88,** 257, 1975.
10. E. Crammer, Preprint LPTENS, 80/9 (1980).

Acta Physica Hungarica 54 (3—4), pp. 361—367 (1983)

SHORT COMMUNICATION

COMMENTS ON THE DOPPLER FORMULAS FOR LIGHT DEDUCED BY PODLAHA AND SJÖDIN

J. WILCZYŃSKI

*Wrocław 1, Poland**

(Received 18 January 1983)

1. Introduction

Recently Podlaha and Sjödin [1] have deduced the "relativistic" Doppler formulas for light within the framework of one class of the theories of ether, in which the ratio of transversal to longitudinal contractions is $\psi(w)/\varphi(w) = 1:(1-w^2/c^2)^{1/2} = 1/\beta$ and the frequency changes of (atomic) oscillators are proportional to $\Omega(w) = \beta$; w is the body's speed relative to the ether. They base on the wave theory of light but accept the ether "seulement au sens d'un système de référence préféré".

Podlaha and Sjödin write that "nous nous refusons de réduire la physique en mathématique, mais considérons plutôt tout processus physique comme quelque chose de réel", and that their formula "permet une compréhension meilleure des causes physiques de l'effet que la déduction relativiste habituelle".

The above and other assumptions taken by Podlaha and Sjödin determine unambiguously the definite consequences. Then the velocity of light c is isotropic only in the preferred frame F_P, and in other frames F_M as moving relative to F_P this velocity must be a vectorial sum of c and speed w_M of F_M. To be sure one can do that the velocity of light measured in F_M will be c [2], but the one-way anisotropy will not be liquidated. Further, the relativistic change of the frequency of the oscillators is related exclusively to F_P and is a function of speed w only; they are two absolute magnitudes. The frequency of identical oscillators, as an absolute one, is the greatest and equal to v_0 only when the oscillators are at rest in F_P. The frequency of the same oscillators but at rest in F_M, also as an absolute one, is equal to $v_M = v_0\beta_M$. Thus, each of these frequencies of the same oscillators has the one and only value relative to F_P, F_M, the source's frame F_S, and observer's frame F_B. Nothing but the difference (or relative difference or ratio)

* Mailing address: Skr. p. 2057, Wrocław 1, Poland

depends on the speed of the other frame. For instance, the frequency of oscillators in F_S moving with speed w_S does not depend on the speed w_B of F_B, it does not depend either on the relative speed v between F_S and F_B.

The situation is different in Einstein's special theory of relativity (STR) where the relativistic effect takes place exclusively directly between two inertial reference frames. When one of them is "stationary" ($v=0$), then the other must be "moving" ($v\neq 0$). The relativistic effect arises in the "moving" frame but is observed in the "stationary" frame. This effect is a function of the relative speed v directly and exclusively between the two frames. But each frame can be "stationary" and/or "moving". There exists here a full symmetry between the two frames when, for example, two beams of photons are exchanged between these frames; such a symmetry does not exist in the ether world. The relativistic change of frequency in F_S, when observed or compared in F_B, can be only negative in STR but negative ($w_S > w_B$) as well as positive ($w_S < w_B$) in the ether theory. Thus, it seems rather impossible for the two theories to give the equivalent Doppler formulas, as it follows from formulas (1) and (3) deduced in [1].

It is necessary to remember in short that the *measured* values of both Doppler effects (singly or together) depend on the *methods* of measurement used in the experiments real and . . . imaginary (very often used by authors). In the ether theory with time dilation and length contraction the same photon can have different values, for instance, *when emitted and measured in the same frame* F_M: 1. the simultaneous marking of two neighbouring crests on a measuring rod gives different values in the directions parallel and perpendicular to w_M and it depends on the value of w_M, 2. the measured time of passings two neighbouring crests through the same point always gives frequency ν_0 independently of the value of w_M. In this concrete case, in the ether theory, the quadratic Doppler effect, as one objective and dependent on w_M, must be separated (or calculated) from the result directly received if the used method of measurement warrants its at least theoretical separation (or calculation). Thus both theory and formula of the Doppler effect must show the objective effects independent of the methods of measurement. In practice, unfortunately, the derivation and/or discussion of the Doppler formulas are based on the results (readings) of a selected (sometimes, convenient) method of measurement (e.g., see [3, 4, 5, 2]). We base on the objective effects; the photons, their real energies (represented by frequencies and wavelengths) do not "adopt" to a method of measurement.

2. Contradictions in the statements of [1]

2.1. Podlaha and Sjödin assume that the oscillators moving through the ether really change their frequencies. In consequence, they multiply (revalue) the classical Doppler formula by the factor $\Omega(w_S)/\Omega(w_B)=\beta_S/\beta_B$ in order to obtain the relativistic

Doppler formula valid in the ether theory:

$$\nu = \nu_0 \frac{1 - \dfrac{w_B \cos \beta}{c}}{1 - \dfrac{w_S \cos \alpha}{c}} \frac{\Omega(w_S)}{\Omega(w_B)}, \tag{1}$$

where ν_0 is the proper frequency of the source (oscillator) at rest in F_P, ν is the frequency emitted in F_S and measured by the observer B at rest in F_B, α and β are the angles, measured in F_P, between the speeds w_S and w_B, respectively, and the source-observer direction.

Formula (1) is contradictory to the facts following from the assumptions in [1]. For a simplification of our discussion we exclude the classical expression or take $\cos \alpha = \cos \beta = 0$. Firstly, when $w_S = w_B \neq 0$, $\nu = \nu_0$! for any values of these speeds. This is physically impossible in the ether theory, because then the frequencies both emitted in F_S (as $\nu_S = \nu_0 \beta_S$) and in F_B (as $\nu_B = \nu_0 \beta_B$) are the same and equal to the frequency of the photons emitted in F_S (as ν_S) and observed in F_B (as ν_{SB}). Secondly, when $w_S = 0$, the frequency observed in F_B ought then to be greater than ν_0 (equal to ν_0/β_B)! Thirdly, formula (1) is useless when applied in experiments, because in F_B only two frequencies ν_B and ν_{SB} are attainable.

Podlaha and Sjödin write that formula (1) is similar (semblable) to that derived by Ives (formula (9) in [6]); we say that the two formulas do not differ in the question under discussion. However, Ives treats his formula as a general one in the ether world, but they write that "malheureusement la formule (1) est en général valable seulement dans le système de référence préféré".

2.2. In the ether world with the preferred frame the Doppler formula must be derived in such a manner to be valid in every frame. The frequency of the oscillators at rest in F_S, $\nu_S = \nu_0 \beta_S$, will be obseved (measured) in $F_B \equiv F_P$ (will enter into $F_B \equiv F_P$) as

$$\nu_{SP} = \nu_S / [1 - (w_S \cos \alpha)/c] = \nu_0 \beta_S / [1 - (w_S \cos \alpha)/c] \tag{2}$$

and as

$$\nu_{SB} = \nu_S \frac{1 - (w_B \cos \beta)/c}{1 - (w_S \cos \alpha)/c} = \nu_0 \frac{1 - (w_B \cos \beta)/c}{1 - (w_S \cos \alpha)/c} \beta_S \tag{3}$$

in F_B when $w_B \neq 0$. Frequency ν_0 cannot exist in F_B when $w_B \neq 0$. But ν_0 is represented unambiguously in F_B by the frequency

$$\nu_B = \nu_0 \beta_B \tag{4}$$

of the identical oscillators at rest in F_B. Therefore, formula (3) can be rewritten as

$$\nu_{SB} = \nu_B \frac{1 - (w_B \cos \beta)/c}{1 - (w_S \cos \alpha)/c} \frac{\beta_S}{\beta_B}. \tag{5}$$

Formula (5) is a correct Doppler formula in the ether world and is valid in any (intertial) reference frame of this world. This formula is free from the objections in Section 2.1 referred to (1). Podlaha and Sjödin and Ives overlooked or "lost" the third element, v_B, in the formula of revaluation (see (4)), and this is why one finds v_0 instead of v_B in (1); we find the same mistake in Section V – C [7].

2.3. Let us forget for a "moment" that v_0 is unsuitable in (1). Podlaha and Sjödin use the transformation formulas to transform their formula (1) into the observer's frame, and they get (3) in [1]:

$$v = v_0 \frac{(1 - v^2/c'^2)^{1/2}}{1 - \frac{v}{c'} \cos \Theta_B} \Gamma \tag{6}$$

where v and v_0 keep the same meanings as in (1), $c' = \beta_B c/\psi\Omega$ is the velocity of light in F_B, v is the source's speed relative to F_B, Θ_B is the angle between v and the source-observer direction as measured in F_B, $\Gamma = \beta_B \Omega(w_S)/\beta_S \Omega(w_B)$. Relying on the experimental results or in accepting the Lorentzian world [8], Podlaha and Sjödin put $c' = c$ ($\psi = 1$) and $\Gamma = 1$, and formula (6) becomes also Einstein's formula. Our third objection in Section 2.1 relative to formula (1) is also valid relative to formula (6) as a relativistic formula in the ether theory since frequency v_0 has the same meaning as in (1). Whereas when formula (6) is treated as Einstein's one, frequency v_0 is correct, because the frequency *emitted* in both source's and "stationary" frames is always v_0, which does not take place in the ether world when $w_S \neq 0$ (although the readings can give v_0 when a convenient method of measurement is used).

To compare formulas (1) and (6) we assume that the photons are emitted perpendicularly to w_S and w_B. Then the classical expression in (1) and the expression in the denominator of (6) cancel; the relativistic speed addition gives $v = w_S - w_B$ when both w_S and $w_B \ll c$. Then formulas (1) and (6) can be reduced to, respectively,

$$v = v_0[1 - (w_S^2 - w_B^2)/2c^2] \tag{7}$$

and

$$v = v_0[1 - (w_S - w_B)^2/2c^2]. \tag{8}$$

Thus, firstly, the quadratic effect in (7) can be positive as well as negative, but only negative in (8)! Secondly, it can be though that $w_S < w_B$! Thirdly, the absolute values of the quadratic effects in (7) and (8) differ from one another! This difference is proportional to w_B:

$$\left| \frac{w_S^2 - w_B^2}{2c^2} \right| - \frac{(w_S - w_B)^2}{2c^2} = \frac{2w_B v}{2c^2}, \tag{9}$$

when $w_S \neq 0$ and $w_B \neq 0$. Thus the equivalence between (1) and (6) cannot exist here, too.

2.4. The aberration effect was used in order to derive (Ives, [6]) formula (6) from (1) in the direction of emission perpendicular to w_S or to show the equivalence (Podlaha and Sjödin, [1]) between formulas (6) and (1). The reason for which Ives did so, can be

found in [9, 6]. This problem needs a separate discussion. Note, however, that the quadratic Doppler effect in (6) becomes now a function of two effects: time dilation, and longitudinal Doppler effect due to the aberrational inclination; this is clearly seen in (14) [6]. But then the effect (its value) due to time dilation would have to depend on the direction of emission.

2.5. Podlaha and Sjödin propose a new modification of the rotor experiment to state the value of Γ: emitter-source S and absorber-source A rotate on two different coaxial disks with two independent (linear) speeds, respectively, v_S and v_A. The frequencies of S and A are compared with the frequency of the source comoving with the observer B (with laboratory and axes); formula (6) is used twice. The laboratory speed is w_B relative to F_P. When the directions of all three speeds are parallel and both v_S and $v_A \ll c$, formula (13) in [1] reduces to

$$\Delta\nu = \nu_{SB} - \nu_{AB} = -\nu_0\left(\frac{v_S^2 - v_A^2}{2c^2}\right). \tag{10}$$

Using our formula (5) for the same situation, we have $w_S = w_B \pm v_S$ for S and $w_A = w_B \pm v_A$ for A. The difference between the frequencies ν_{SB} of S and ν_{AB} of A, measured in F_B, is then

$$\Delta\nu = \nu_{SB} - \nu_{AB} = -\nu_B\left(\frac{v_S^2 - v_A^2}{2c^2} \mp \frac{2w_B(v_S - v_A)}{2c^2}\right), \tag{11}$$

when all w_B, v_S and $v_A \ll c$. The difference between (10) and (11) is evident, even if we neglect the difference between ν_0 and ν_B. The two last formulas are identical and correct when $w_B = 0$, that is, when laboratory rests in F_P.

3. Discussion and conclusion

The experiment proposed by Podlaha and Sjödin could test difference (9) and state existing the speed w_B (when $v_A = -v_S$ in formula (11)). But the results of all four Ives—Stilwell experiments [10—13], of all rotor experiments [14—16], and of temperature-dependent experiments [17, 18] compel us to accept that the absolute speed w_B of the laboratory at rest on the Earth's surface is equal to zero! The last two groups of experiments also contradict Einstein's Doppler formula: there is one-way frequency change of the oscillators between F_S and F_A. And in the temperature-dependent experiments there is a *change of the sign* of the effect!; besides, the frequency difference was proportional to $(v_S^2 - v_A^2)$ but not to $(v_S - v_A)^2$.

Somebody can say that in the proposal by Podlaha and Sjödin there exists an analogy to the photons emitted by a star and observed in a free cosmo-space (in the worst case, on the Earth's surface), and, consequently, a difference of pseudo-gravitational potentials can exist in their proposed experiment. But such an objection cannot exist with reference to the second variant of Dos Santos proposal [19] (two rotors with coinciding axes, emission and absorption perpendicular to the angular

rotors' speeds). This variant (with various and different values of v_S and v_A, and with axes parallel and perpendicular to the Earth's absolute speed w_E) enables us to test Einstein's equivalence principle. We expect that the results will confirm expression $(v_S^2 - v_A^2)$, contradict Einstein's equivalence principle, confirm the dependence of the relativistic effect only on the value of speed, and give $w_E = 0$.

The equivalence between (1) and (6) can exist in no way, as Eqs (7), (8), and (9) show; but first of all v_B instead of v_0 must be in (1), as it is in (5). (Note that such two equivalent formulas are written by Buonomano and Moore [20]; they also use the aberration angles in derivation [21].). Our formula (5) is a universal one in the ether world, that is to say it is the one and only one to be used in any (inertial) reference frame.

But formula (5) similarly as formula (6) and formulas derived by others [1, 5, 6, 20, 23], applied to the Ives—Stilwell experiments (then $w_S = w_B \pm v_S$), gives the *positive* quadratic Doppler effect:

$$v_{SB} = v_B(1 \pm v_S/c + v_S^2/2c^2). \tag{12}$$

The positive resultant effect is produced by the classical part which contains term $+v_S^2/c^2$. But formula (12) is contradictory to the results of these experiments (they gave the positive effect but for wavelengths). Besides, we do not find speed w_B in (12). Therefore, the classical Doppler formula needs a separate discussion.

The absence of the dependence on w_B in the results of all three groups of experiments suggests that the ether if any ought to be attached to the Earth's surface. There exists such a possibility if we assume that the ether, a new sort of ether, is a "shadow" of the gravitational fields (with all their properties such as density, density gradient, superimposition, rotary motion). In the terms of our Earth, the Earth's mass can already be large enough for the density of the ether belonging to the Earth on and close to its surface to be predominant against a background of the component density of the ethers belonging to the other celestial bodies, so that the relativistic effects are such as observed. This predominance must diminish with the distance from the Earth's surface (centre), and in such a situation the E-W anisotropy in Hafele and Keating's experiment [22] and its absence in the experiment by Champeney et al [15] ought to be evident.

References

1. M. F. Podlaha and T. Sjödin, Acta Phys. Hung., **48,** 69, 1980.
2. S. J. Prokhovnik, Found. Phys., **10,** 197, 1980.
3. R. A. Waldron, The Wave and Ballastic Theories of Light, Muller, London, 1977, p. 72.
4. H. W. Milnes, Spec. Sci. Techn., **2,** 285, 1979.
5. S. Marinov, Found. Phys., **8,** 637, 1978.
6. H. E. Ives, J. Opt. Soc. Am., **27,** 389, 1937.
7. V. Buonomano, Int. J. Theor. Phys., **13,** 213, 1975.
8. T. Sjödin, Nuovo Cimento, **51B,** 229, 1979.
9. H. E. Ives, J. Opt. Soc. Am., **27,** 177, 1937.

10. H. E. Ives and G. R. Stilwell, J. Opt. Soc. Am., **28,** 215, 1938.
11. G. Otting, Phys. Z., **40,** 681, 1939.
12. H. E. Ives and G. R. Stilwell, J. Opt. Soc. Am., **31,** 369, 1941.
13. H. I. Mandelberg and L. Witten, J. Opt. Soc. Am., **52,** 529, 1962.
14. See Refs in [1].
15. D. C. Champeney, G. R. Isaak and A. M. Khan, Phys. Lett., **7,** 241, 1963.
16. K. C. Turner and H. A. Hill, Phys. Rev. II, **134B,** 252, 1964.
17. R. V. Pound and G. A. Rebka, Phys. Rev. Lett., **4,** 274, 1960.
18. A. J. F. Boyle, D. St. P. Bunbury, C. Edwards and H. E. Hall, Proc. Phys. Soc., **76,** 165, 1960.
19. A. N. Dos Santos, Nuovo Cimento, **32B,** 519, 1976.
20. V. Buonomano and J. E. Moore, Am. J. Phys., **42,** 1021, 1974.
21. V. Buonomano and J. E. Moore, "The Classical and Relativistic Doppler Effects", unpublished.
22. J. C. Hafele and R. E. Keating, Science, **177,** 166 and 168, 1972.
23. B. L. Rawat, Am. J. Phys., **45,** 1211, 1977.

BOOK REVIEWS

Albert Einstein in Berlin, 1913–1933 I–II. Dokumente. Edited by CHRISTA KIRSTEN and HANS-JÜRGEN TREDER, Akademie-Verlag, Berlin, 1979, 286 + 286 pp.

Albert Einstein spent two mature decades in Berlin, in close contact with Planck, Laue and others, enjoying the relaxed atmosphere of the Weimar Republic. Prof. Hans-Jürgen Treder collected all relevant documents of this period (written mainly not by Einstein, but about Einstein) and published them with a detailed analysis of the two Berlin decades. The series of documents starts with the recommendation of Einstein for the Berlin Academy, signed by Planck, Nernst, Rubens, Warburg. One reads the much quoted sentences: "Zusammenfassend kann man sagen, dass es unten den grossen Problemen, an denen die moderne Physik so reich ist, kaum eines gibt, zu dem nicht Einstein in bemerkenswerter Weise Stellung genommen hätte. Dass er in seinen Spekulationen gelegentlich auch einmal über das Ziel hinausgeschossen haben mag, wie z. B. in seiner Hypothese der Lichtquanten, wird man ihm nicht allzuschwer anrechnen dürfen; denn ohne einmal ein Risiko zu wagen, lässt sich auch in der exaktesten Naturwissenschaften keine wirkliche Neuerung einführen."

Not all of the documents are so interesting, most of them are academic red tapes. The police and embassy reports about Einstein's behaviour in Germany and abroad reflect his pacifism and liberalism. The suspicions of the German authorities help us to honour his human greatness.

The careful presentation of even the minor documents may be helpful to the researcher of the history of modern science.

G. Marx

A. BOHR und B. R. MOTTELSON: *Struktur der Atomkerne Bd. I–II.* Akademie-Verlag, Berlin, 1980, 496 + 653 Seiten

Die deutsche Gesamtübersetzung des Werkes "Nuclear Structure I–II" [Benjamin, New York, Amsterdam, 1969, 1975] des Nobelpreisträger Verfasserdoppels erschien erst ein halbes Jahrzehnt nach dem Erscheinen der Originalausgabe. Das grossangelegte, grundlegende Opus unternahm die systematische Darstellung des damaligen Standes unseres Verständnisses der Kernstruktur mittels einer phänomenologischen Analyse der beobachteten Kerneigenschaften. Phänomenologie bedeutet hier: anstatt der vollständigen Reihe von Freiheitsgraden zu arbeiten, schon mit einigen wenigen, aber dem konkreten Problem am besten angepassten Koordinaten herauszukommen. Da das zu erörternde Material ausserordentlich vielfach ist, solch ist auch das Spektrum der angewandten Methoden. Doch gibt es Gesichtspunkte, die sich durch den ganzen Gedankengang ziehen und dessen theoretisch-methodische Einheit gewährleisten. Es soll nur ein allgemeines Prinzip erwähnt werden: Die Auswahl und Entwickelung der diskutierten Modelle erfolgt stets auf Grund der von der elementaren Wechselwirkung erforderten exakten und annähernden Symmetrien.

Band I, "Einteilchenbewegungen", gliedert sich auf drei Kapitel wie folgt: Symmetrien und Erhaltungssätze; Bewegung unabhängiger Teilchen; Einteilchenkonfigurationen. Das eigentliche, kernphysikalische Wesen der Ausführung befindet sich in den oft kurzen Hauptteilen der einzelnen Kapitel. Die als Hintergrund dienenden mathematischen und quantenmechanischen Grundlagen sind in den zahlreichen Anhängen auf hohem Grade ausgearbeitet. Kapitel I setzt zuerst die Raum- und Zeitparität, die isobare Invarianz, die Hyperladungs-

erhaltung und die unitären Symmetrien auseinander. Es kulminiert endlich in der Ableitung der allgemeinsten Form jener Zweikörperkräfte, die die erwähnten Symmetrien befriedigen. Die anschliessenden Anhänge beschäftigen sich mit den Drehungs-, Zeitumkehr- und Permutationssymmetrien. Im Mittelpunkt von Kapitel 2 steht die Einleitung der Begriffe des mittleren Kernpotentials und des optischen Potentials. In den Anhängen werden einige Probleme, wie z. B. die Niveaudichteverteilung, die Stärkefunktioneneigenschaften, mit Hilfe statistischer Methoden gelöst. Kapitel 3 verhandelt die Übergänge zwischen Kernniveaus, hervorgerufen durch elektromagnetische und schwache Wechselwirkungen. Ein Anhang ist der Formulierung der Theorie des β-Zerfalls gewidmet.

Band II, "Kerndeformationen", befasst sich mit der Anregung kollektiver Freiheitsgrade der Nukleonenbewegung. Kapitel 4 stellt die Theorie der Rotationsspektren dar, samt der Kopplung der Rotation zur Einteilchenbewegung und den Eigenschaften der Hochspinniveaus im Yrastgebiet. Kapitel 5 erörtert die Einteilchenbewegung in einem deformierten Potential, im Zusammenhang mit Transferreaktionen. Im Kapitel 6 wird es gezeigt, wie eine Vibration zustandekommt, falls eine primäre Dichteänderung eine solche Änderung der Einteilchenbewegung hervorruft, die ihrerseits eine sekundäre Dichteänderung von derselben Grössenordnung erzeugt. Es werden die Kopplungen Dipol—Quadrupol, Vibration—Rotation und Vibration—Einteilchenbewegung betrachtet. Ein interessantes Problem, die Existenz kollektiver Anregungen, die keine klassische Analogie haben (Rotation im Isospinraum, Vibration durch Ladungsaustausch, Oszillation durch Paarerzeugung) schliesst den Gedankengang.

Trotz dem breiten Kreis des behandelten Materials blieben einige wichtige Probleme in den Hintergrund verbannt. Der Leser sucht umsonst eine Diskussion der leichtesten Kerne. Die Diskussionen des Schalenmodells und der Theorie der Kernmaterie sind je zu einer einzigen Seite zusammengedrängt. Das Fehlen von Themen, wie das zeitabhängige Hartree–Fock Modell, die Generatorkoordinatenmethode oder das Modell der wechselwirkenden Bosonensysteme, ist zur Zeit des Erscheinens der deutschen Ausgabe schon auffallend. Doch ist dieser scheinbare Mangel des Werkes nur der Preis, der für die äusserst sorgfältige, sachmässige, aber zeitraubende Arbeit der Übersetzung zu zahlen ist.

T. Dolinszky

Chronobiologie, Chronomedizin, GDR–USSR Symposium Halle/Saale, July 10–15, 1978. Edited by J. SCHUH, K. HECHT and J. A. ROMANOW, Akademie-Verlag, Berlin, 1981

The book contains the full text of the contributions to the German–Soviet Symposium held in Halle, July 10–15, 1978. The subject of the Symposium was the biological and medical aspect of periodic processes observed in living organisms. In this comparatively new field participants from the GDR and from the USSR presented 52 and 26 papers, respectively. The papers were grouped according to methodical, biological and medical-pharmaceutical aspects.

1. Methodical aspects

In this part of the Symposium 12 German and 2 Soviet papers present the mathematical methods applied in the study of periodic time-processes. The following two papers should be specially noted.

In his paper on "Rhythms in Biology and Medicine" H. Drischel discussed the general characteristics of biological rhythms. The short wavelength tail of the broad spectrum (with periods from milliseconds to several years) is temperature dependent oscillation, while oscillations of longer wavelength are independent of it, but other environmental factors affect them more. The observable macroscopic rhythms may be derived from elementary biochemical and biophysical processes.

R. Sinz dealt with the thermodynamical approach of the problem. In his paper on "Oscillation as a Characteristic of Dissipative Structures and Organic Ordering" he also pointed out the timeliness of this field. The oscillations characterize the so-called dissipative systems on every level of organization and are of fundamental importance in the formation and maintenance of order in biological systems and for the multioscillatory functional order of living organisms.

Regarding the papers in general it can be stated that the biometrical methods of data processing render it possible to separate the stochastic and deterministic components and to analyse the periodic components of the time-series. The separation of these latter was carried out by various orthogonal transformations. Fourier-analysis with trigonometric functions and the use of processes applying Haar und Walsh functions were presented.

W. Meyer and his coworkers analysed the minute-rhythm of the central nervous system and blood pressure in their contribution on "Frequency-

specific method of analysis to determine time-series types." In the processing of time-series they applied smoothing, polynomial regression, cluster analysis, etc.

2. Biological and medical-pharmacological aspects

These papers presented the rhythmicities observed at the different (biochemical, biophysical, genetical, physiological) levels of organization of the living organism.

The contribution of H. J. Müller on "Chronobiological aspects of the seasonal 'niching' of arthropods" is of special interest. The author stressed the importance of the biological rhythm and the regulation and inhibition of development in the synchronization of the autogeneses and the ecological utilization of time niche dimension.*

E. Porzig in his paper on "Chronobiological aspects of livestock production" pointed out that from agricultural aspects the knowledge of the biological rhythm and the adaptation to the existing periodicity may result in a considerable increase of productivity.

According to Yu. A. Romanow in the application of medicaments the knowledge of biological cycles has two significances. On the one hand, the effectiveness of medicaments depends on the time of their administration (i.e. in which phase of the cycle it is administered), on the other, medicaments may affect the cycle itself. ("Chronobiology, chronopharmacology and chronomedicine.")

The paper on "The significance of biorhythms in diagnostics for prognostication of illness" by N. I. Moissejewa and her coworkers may be of interest proposing the use of the biorhythm as a preliminary indicator for the prognosis of an illness. The proposal is based on their results obtained on the heart function and circulation of patients suffering from (cranial and cerebral) nervous trauma and schizophrenia.

The report by I. E. Ganelina and S. K. Tchurina on "Observations on the effect of biorhythm on the onset and development of acute myocardial infarction" summarized the interesting results obtained from the statistical evaluation of the data of a great number of case histories. According to them the existence of a cycle of 42-day duration could be shown. The mortality was highest among persons who had developed the disease in the first and fourth week of the cycle.

The material of the Conference may be of interest not only for the researchers of one particular field. It may serve as a valuable source of information for biologists, physicians, pharmacologists as well as mathematicians, physicists and chemists. It shows a new attitude, taken toward the general assertion of various periodicities on the different levels of biological organization, affecting naturally a wide spectrum of biological sciences. At the same time it points out interesting new possibilities of the application of mathematical and physical methods.

G. Rontó

* In the course of their accommodation living organisms — adjusting themselves to the most different environmental conditions — aim to utilize every part of the territory at their disposal. A similar effect can be found in relation to time period, since in the case of living organisms active and passive phases and favourable and unfavourable periods follow each other, which renders possible the optimal utilization of a given territory for several species.

ERICH LOHRMANN: *Hochenergiephysik*,
B. G. Teubner, Stuttgart, 1981, 248 Seiten

Die zweite, neubearbeitete, erweiterte Auflage dieses ausgezeichneten Büchleins der Teubner Studienbücher-Serie ist ein schönes, nützliches Geschenk von dem Verlag (und von dem Autor) an die Physiker, die sich für die Physik der Elementarteilchen, für die neuen Ergebnisse der Feldtheorie der Teilchen interessieren. Der Fachausdruck "Hochenergiephysik" ist heute ein Synonym für "die Physik der Elementarteilchen": je grösser die verwendete Energie ist, umso tiefer, d. h. in umso kleinerem Zeitraum-Intervall sich die Gesetze der Mikrowelt zu erkennen geben. Seit der ersten Ausgabe des Buches wurde das Lepton-Quark-Modell der Teilchen erwiesen; so ist es selbstverständlich, dass der Verfasser die Behandlung des Themas auf dieses Modell gründet.

Der Inhalt des Buches ist in vier Kapiteln eingeteilt. Das erste Kapitel enthält die Grundlagen des ganzen Themas von der Beschreibung der Beschleunigern über den "Zoo" der Elementarteilchen bis zu den Erhaltungsgesetzen und Symmetrien. Die weiteren Teile des ersten Kapitels dienen der Vertiefung und Erweiterung der erwähnten Themen.

Der Gegenstand des zweiten Kapitels ist die Beschreibung der elektromagnetischen Wechselwirkung, wobei auch die experimentellen Beweise der Quantenelektrodynamik diskutiert werden.

In dem dritten Kapitel wird starke, in dem vierten die schwache Wechselwirkung lehrreich und pädagogisch brilliant behandelt.

Trotz dem kleinen Umfang des Buches werden das farbige Quark-Modell, der Strom-Strom-Typ der schwachen Wechselwirkung, die Cabibbo-

Theorie, die CP-Verletzung, die Hauptprobleme der K^0- und der Neutrinophysik umfangreich und nach dem heutigen Stand der Theorie behandelt.

Das Buch ist übersichtlich und gut verständlich geschrieben. Viele anschauliche Zeichnungen und Tabellen, Literatur- und Sachverzeichnis ermöglichen es dem Leser, sich schnell einen Überblick zu verschaffen. Von der Stoffauswahl her ist das Buch besonders für die Leser von Nutzen, die die Elemente der Atom- und Kernphysik kennen und die sich für die Elementarteilchenphysik interessieren. Für diesen Personenkreis — und für jede Physikbibliothek — ist es wärmstens zu empfehlen!

K. L. Nagy

The Role of Coherent Structures in Modelling Turbulence and Mixing. Proceedings of the International Conference, Madrid, June 25–27 1980. Edited by J. JIMENEZ, Lecture Notes in Physics, Vol. 136, Springer-Verlag, Berlin, Heidelberg, New York, 1981. XIII + 393 pp

This Volume contains 17 contributions presented at the Madrid Conference, organized to help promoting development in the field, where the growing recognition of the existence of large-scale structures in many turbulent flows had already led to a deeper insight into the nature of turbulence, stimulating new ideas for new experiments. On the other hand, in computation and modelling the new ideas have not yet produced the important results expected of them. So the importance of improving the cooperation between experimentalists, engineers and theorists became evident in a field led by experimental researchers.

The papers are grouped essentially in three sections, theory, experiments and applications. The sections are headed by invited review papers, viz. by J. Mathieu's and G. Charney's "Experimental Methods in Turbulent Structure Research", H. E. Fiedler's (and coworkers') "Initiation, Evolution and Global Consequences of Coherent Structures in Turbulent Shear Flows" (experimental section), P. G. Saffman's "Coherent Structures in Turbulent Flow", (theoretical section) and A. Linan's "Lewis Number Effects on the Structure and Extinction of Diffusion Flames Due to Strain" (applications section). The other papers treat closely interrelated subjects in the field of computer analysis, large scale and periodic structures, jet flows, boundary layers, turbulent combustion, etc.

The publication of this Volume will hopefully contribute to a joint development of theoretical and experimental research in the field.

I. Abonyi

N. P. KONOPLEVA and V. N. POPOV: *Gauge Fields*. Harwood Academic Publishers, Chur, 1982

This is a translation from the second Russian edition which appeared in 1980. The subject is timely; gauge fields have become a prominent working tool in quantum field theory and elementary particle physics.

The discussion starts with a crisp review of recent developments in particle theory and gauge fields. Global and local transformations in relativity, spherical solutions of the Yang—Mills equations, gravitation as a gauge field and gauge theories of strong interactions form the menu of the first chapter which has been considerably expanded for the second edition. Chapter II is devoted to the Lagrangian theory of gauge fields, Noether's theorems and to Lie derivatives. This is followed by a more geometrical approach to the subject: essentially, an introduction to fibre bundles. The quantum theory of gauge fields is finally described in detail in Chapter IV. Stress is laid here upon the path integral approach although a section deals also with the canonical quantization of the gravitational field.

I should like to praise the simple and elegant style in which the volume was written for a physicist audience. Much of the flavour of the book is conveyed intact by the excellent translation due to N. M. Queen. References are amply supplied at the end of each chapter.

Very recently, we have seen a series of successes in the treatment of the gauge equations. Among the new techniques applied, the Backlund transformations, complex twistor manifolds or lattice computations deserve mentioning. Unfortunately, this upsurge in the theory occurred after the present book was completed. Considering the past successful efforts of the authors in keeping the volume up-to-date, the reviewer has every reason to expect a third edition, extended also to these tantalizing new ideas.

Z. Perjés

Neutrino Physics and Astrophysics. Proceedings of the Neutrino '80 Conference (Erice, Sicily). Edited by ETTORE FIORINI. Ettore Majorana International Science Series, Volume 12. Plenum Press, New York and London, 1982, 421 pp.

Physicists celebrated the 50th anniversary of the idea of the neutrino at this World Conference in 1980. For fundamental research the discovery of the neutrino indicated the strength of the conservation theorems in the search for understanding Nature.

But in the seventies the neutrino has become an efficient tool for the exploration of the deep structure of matter. With its help one can see the controlled fusion reactor inside the stars. We may hope that the neutrinos may help in catching the view of the first second in the history of the universe. These are the topics and chances to which the International Neutrino Conferences are devoted.

The 1980 Conference was dominated by the semicentenary celebration of the "elusive" neutrino. The Proceedings offers the recollection of R. Peierls about the theoretical search, leading to the concept of neutrino, the description of the early days of experimental neutrino physics by F. Reines, and the flicks of the great moments of the neutrino history by B. Pontecorvo. These pages will become important sources for the experts of the history of science and a good reading for everyone interested in the birth of grand ideas.

1980 was an exciting year anyway. The big machines produced neutrinos in immense quantities for the exploration of the hadron structure and the weak interactions enabling the authors of review talks to draw a conclusion from the high energy physics of the seventies. But at the doorway of the eighties a search started to go beyond the "classic" quark-lepton physics, to look for new peaks beyond the trinity of the strong-electromagnetic-weak interactions.

The first reports about possible neutrino mass, neutrino oscillation, proton decay, grand unification of forces and the related push for new machines and detectors lead the reader into a virgin area. The short reports are omitted from the Volume, a pity for the reporters. But the printed review talks offer a more enjoyable lecture than the conventional conference proceedings.

G. Marx

Nonlinear Phenomena at Phase Transitions and Instabilities. Edited by T. RISTE, NATO Advanced Study Institutes Series, Series B: Physics, Volume 75. Plenum Press, New York and London, 1982, pp. 481

The present NATO Advanced Study Institute held in Geilo, March 29—April 9 1981, was the sixth in a series devoted to the subject of phase transitions and instabilities. The institute provided a useful forum for the review and discussion of nonlinear phenomena associated with instabilities in various systems. The "Nonlinear Phenomena at Phase Transitions and Instabilities", utilizing the experimental and theoretical efforts of the past decade, tries to elucidate the nature of this nonlinearity.

Giving special emphasis to such significant topics as anharmonic properties near structural phase transitions, transports, and fluctuations in linear array of multistable systems, this Volume offers several papers written by the most advanced scientists in their fields. K. A. Müller's lectures give a good review of the experimental evidences and theoretical models for collective anharmonic behaviour near the structural phase transitions in special $SrTiO_3$-type and ferroelectric systems. The new theoretical results of structural phase transitions are clearly presented in A. D. Bruce's lecture in connection with the classical phonon-based theories and renormalisation group methods. An interesting model to study the dynamic correlations in the ordered phase of perovskites is outlined in Meissner, Menyhárd and Szépfalusy's lectures.

The lectures also paid much attention to hydrodynamic instabilities for which the non-linearities and boundary conditions perform the selection and stabilization of certain structures and patterns. A number of Rayleigh—Bénard problems and Lorenz model are described showing that the bifurcation theory is relevant both to the theory of hydrodynamic instabilities and to the transitions between modulated crystal structures. In addition, this Volume gives a detailed picture of nonlinear thermal convection, nonlinear fluctuations, steady states, limit cycles. An intuitive description of fluctuations near the critical points and near the instability points in driven system is studied by V. Degiorgio. One of the most interesting review lectures of the Volume is presented by M. G. Ve Larde in association with the study of some outstanding aspects and features of the time evolution of non-linear systems. This lecture reviews the different pictures of the onset of turbulence, the phase transition picture and the stability of steady states, the dynamical — stability of limit cycles, and finally the present situation and trends of the strange attractor theory.

The last lectures deal with the recent progress in the study of the two-dimensonal melting problem, confirming or denying the existence of the continuous melting process.

The Volume may be interesting for students and gives a thoroughly up-to-date review of this rapidly developing field for the specialists. It is especially valuable to physicists concerned with all types of nonlinear systems.

I. Gyarmati

Manuscript received by Akadémiai Kiadó: 19 November 1982
Manuscript received by the Printers: 3 December 1982
Date of publication: 7 September 1983

PRINTED IN HUNGARY
Akadémiai Nyomda, Budapest

NOTES TO CONTRIBUTORS

I. PAPERS will be considered for publication in Acta Physica Hungarica only if they have not previously been published or submitted for publication elsewhere. They may be written in English, French, German or Russian.

Papers should be submitted to

Prof. I. Kovács, Editor
Department of Atomic Physics, Technical University
1521 Budapest, Budafoki út 8, Hungary

Papers may be either articles with abstracts or short communications. Both should be as concise as possible, articles in general not exceeding 25 typed pages, short communications 8 typed pages.

II. MANUSCRIPTS

1. Papers should be submitted in three copies.
2. The text of papers must be of high stylistic standard, requiring minor corrections only.
3. Manuscripts should be typed in double spacing on good quality paper, with generous margins.
4. The name of the author(s) and of the institutes where the work was carried out should appear on the first page of the manuscript.
5. Particular care should be taken with mathematical expressions. The following should be clearly distinguished, e.g. by underlining in different colours: special founts (italics, script, bold type, Greek, Gothic, etc.); capital and small letters; subscripts and superscripts, e.g. x^2, x_3; small l and 1; zero and capital O; in expressions written by hand: *e* and *l*, *n* and *u*, *v* and v, etc.
6. References should be numbered serially and listed at the end of the paper in the following form: J. Ise and W. D. Fretter, Phys. Rev., **76**, 933, 1949.

For books, please give the initials and family name of the author(s), title, name of publisher, place and year of publication, e.g.: J. C. Slater, Quantum Theory of Atomic Structures, I. McGraw-Hill Book Company, Inc., New York, 1960.

References should be given in the text in the following forms: Heisenberg [5] or [5].

7. Captions to illustrations should be listed on a separate sheet, not inserted in the text.
8. In papers submitted to Acta Physica all measures should be expressed in SI units.

III. ILLUSTRATIONS AND TABLES

1. Each paper should be accompanied by three sets of illustrations, one of which must be ready for the blockmaker. The other sets attached to the copies of the manuscript may be rough drawings in pencil or photocopies.
2. Illustrations must not be inserted in the text.
3. All illustrations should be identified in blue pencil by the author's name, abbreviated title of the paper and figure number.
4. Tables should be typed on separate pages and have captions describing their content. Clear wording of column heads is advisable. Tables should be numbered in Roman numerals (I, II, III, etc.).

IV. RETURN OF MATERIAL

Owing to high postage costs, the Editorial Office cannot undertake to return *all* material not accepted for any reason for publication. Of papers to be revised (for not being in conformity with the above Notes or other reasons) only *one* copy will be returned. Material rejected for lack of space or on account of the Referees' opinion will not be returned to authors outside Europe.

Periodicals of the Hungarian Academy of Sciences are obtainable at the following addresses:

AUSTRALIA
C.B.D. LIBRARY AND SUBSCRIPTION SERVICE
Box 4886, G.P.O., *Sydney N.S.W. 2001*
COSMOS BOOKSHOP, 145 Ackland Street
St. Kilda (Melbourne), Victoria 3182

AUSTRIA
GLOBUS, Höchstädtplatz 3, *1206 Wien XX*

BELGIUM
OFFICE INTERNATIONAL DE LIBRAIRIE
30 Avenue Marnix, *1050 Bruxelles*
LIBRAIRIE DU MONDE ENTIER
162 rue du Midi, *1000 Bruxelles*

BULGARIA
HEMUS, Bulvar Ruszki 6, *Sofia*

CANADA
PANNONIA BOOKS, P.O. Box 1017
Postal Station "**B**", *Toronto, Ontario M5T 2T8*

CHINA
CNPICOR, Periodical Department, P.O. Box 50
Peking

CZECHOSLOVAKIA
MAD'ARSKÁ KULTURA, Národní třida 22
115 66 Praha
PNS DOVOZ TISKU, Vinohradská 46, *Praha 2*
PNS DOVOZ TLAČE, *Bratislava 2*

DENMARK
EJNAR MUNKSGAARD, Norregade 6
1165 Copenhagen K

FEDERAL REPUBLIC OF GERMANY
KUNST UND WISSEN ERICH BIEBER
Postfach 46, *7000 Stuttgart 1*

FINLAND
AKATEEMINEN KIRJAKAUPPA, P.O. Box 128 *SF- 00101 Helsinki 10*

FRANCE
DAWSON-FRANCE S. A., B. P. 40, *91121 Palaiseau*
EUROPÉRIODIQUES S. A., 31 Avenue de Versailles, *78170 La Celle St. Cloud*
OFFICE INTERNATIONAL DE DOCUMENTATION ET LIBRAIRIE, 48 rue Gay-Lussac
75240 Paris Cedex 05

GERMAN DEMOCRATIC REPUBLIC
HAUS DER UNGARISCHEN KULTUR
Karl Liebknecht-Straße 9, *DDR-102 Berlin*
DEUTSCHE POST ZEITUNGSVERTRIEBSAMT Straße der Pariser Kommune 3-4, *DDR-104 Berlin*

GREAT BRITAIN
BLACKWELL'S PERIODICALS DIVISION
Hythe Bridge Street, *Oxford OX1 2ET*
BUMPUS, HALDANE AND MAXWELL LTD.
Cowper Works, *Olney, Bucks MK46 4BN*
COLLET'S HOLDINGS LTD., Denington Estate *Wellingborough, Northants NN8 2QT*
WM. DAWSON AND SONS LTD., Cannon House *Folkstone, Kent CT19 5EE*
H. K. LEWIS AND CO., 136 Gower Street
London WCIE 6BS

GREECE
KOSTARAKIS BROTHERS INTERNATIONAL BOOKSELLERS, 2 Hippokratous Street, *Athens-143*

HOLLAND
MEULENHOFF-BRUNA B. V., Beulingstraat 2, *Amsterdam*
MARTINUS NIJHOFF B.V.
Lange Voorhout 9-11, *Den Haag*
SWETS SUBSCRIPTION SERVICE
347b Heereweg, *Lisse*

INDIA
ALLIED PUBLISHING PRIVATE LTD., 13/14
Asaf Ali Road, *New Delhi 110001*
150 B-6 Mount Road, *Madras 600002*
INTERNATIONAL BOOK HOUSE PVT. LTD.
Madame Cama Road, *Bombay 400039*
THE STATE TRADING CORPORATION OF INDIA LTD., Books Import Division, Chandralok 36 Janpath, *New Delhi 110001*

ITALY
INTERSCIENTIA, Via Mazzé 28, *10149 Torino*
LIBRERIA COMMISSIONARIA SANSONI, Via Lamarmora 45, *50121 Firenze*
SANTO VANASIA, Via M. Macchi 58
20124 Milano
D. E. A., Via Lima 28, *00198 Roma*

JAPAN
KINOKUNIYA BOOK-STORE CO. LTD.
17-7 Shinjuku 3 chome, Shinjuku-ku, *Tokyo 160-91*
MARUZEN COMPANY LTD., Book Department, P.O. Box 5050 Tokyo International, *Tokyo 100-31*
NAUKA LTD. IMPORT DEPARTMENT
2-30-19 Minami Ikebukuro, Toshima-ku, *Tokyo 171*

KOREA
CHULPANMUL, *Phenjan*

NORWAY
TANUM-TIDSKRIFT-SENTRALEN A.S., Karl Johansgatan 41-43, *1000 Oslo*

POLAND
WĘGIERSKI INSTYTUT KULTURY, Marszalkowska 80, *00-517 Warszawa*
CKP-I W, ul. Towarowa 28, *00-958 Warszawa*

ROUMANIA
D. E. P., *Bucuresti*
ILEXIM, Calea Grivitei 64-66, *Bucuresti*

SOVIET UNION
SOJUZPECHAT — IMPORT, *Moscow*
and the post offices in each town
MEZHDUNARODNAYA KNIGA, *Moscow G-200*

SPAIN
DIAZ DE SANTOS, Lagasca 95, *Madrid 6*

SWEDEN
GUMPERTS UNIVERSITETSBOKHANDEL AB
Box 346, *401 25 Göteborg 1*

SWITZERLAND
KARGER LIBRI AG, Petersgraben 31, *4011 Basel*

USA
EBSCO SUBSCRIPTION SERVICES
P.O. Box 1943, *Birmingham, Alabama 35201*
F. W. FAXON COMPANY, INC.
15 Southwest Park, *Westwood Mass. 02090*
READ-MORE PUBLICATIONS, INC.
140 Cedar Street, *New York, N.Y. 10006*

YUGOSLAVIA
JUGOSLOVENSKA KNJIGA, Terazije 27, *Beograd*
FORUM, Vojvode Mišića 1, *21000 Novi Sad*

Index: 26.022